24th International Workshop
on ECR Ion Sources

ECRIS2020

ECRIS'20

CONFERENCE PROCEEDINGS

FRIB **Facility for Rare Isotope Beams**
East Lansing, MI, USA
28-30 September 2020

FOREWORD

The 24th International Workshop on Electron Cyclotron Resonance Ion Sources (ECRIS2020), was held from September 28th–September 30th, 2020 and followed by the North-American Charge Breeding (NACB) workshop October 1st and 2nad. Both events were hosted online by the Facility for Rare Isotope Beams (FRIB) at Michigan State University.

The scientific program was similar to previous editions of the workshop and included progress reports and new development of ECR ion sources. Other topics included plasma modeling, charge breeding, plasma physics and techniques and experimental investigations of ECR plasmas.

Despite the challenges posed by the COVID-19 pandemic that prevented the community to meet in person, many people contributed and attended the workshop online across many different time zones. The program included 24 talks and 27 posters. Unlike previous years posters consisted of a shorter presentation of 8 minutes with 2 minute for questions. Overall approximately 20 students contributed to the workshop.

Highlight of the workshop included recent progress on 4th generation ECRIS working at 45 GHz at IMP and LBNL, the progress of the 3rd generation sources at FRIB and KBSI and the report of several new ion sources at INFN, IMP, IAP, HIMAC, LPSC and JYFL including for this latter a new concept of CUBE-ECRIS. Plasma investigations were presented from INFN using X-ray imaging, by MSU on experimental studies on plasma instabilities and Osaka University on microwave launching. Many contributions of metallic beam production were presented including GANIL, IMP and JINR which remain a very important topic for the community. A very interesting study of plasma chamber cooling was presented by IMP for sustainable high power operation of 28 GHz ion source using microchannels. Finally more theoretical work and modelisation were presented including a model of B-min instabilities by LBNL, a detailed modeling of electron trajectories by LPSC and simulation of electromagnetic waves in ECR cavity by INFN.

The proceedings, which include copies of presentations, are available on the JACoW website.

Finally, after the workshop it was determined that the next workshop will be held at the Institute for Plasma Research in Ghandinagar, India in 2022

Guillaume Machicoane
ECRIS20 Conference Chair

International Advisory Committee (IAC)

Guillaume Machicoane	**Chair**	FRIB-MSU	USA
Sandor Biri		ATOMKI	Hungary
Luigi Celona		INFN-LNS	Italy
Atsushi Kitagawa		NIRS	Japan
Hannu Koivisto		JYFL	Finland
Laurent Maunoury		GANIL	France
Takahide Nakagawa		RIKEN	Japan
Vadim Skalyga		IAP-RAS	Russia
Liangting Sun		IMP	China
Thomas Thuiller		LPSC	France
Klaus Tinschert		GSI	Germany
Richard C. Vondrasek		ANL	USA
Mi-Sook Won		KBSI	South Korea
Daniel Xie		LBNL	USA

Local Organizing Committee (LOC)

Guillaume Machicoane	**Chair**	FRIB-MSU	USA
Alain Lapierre		FRIB	USA
Alexa Allen	**Workshop Admin**	FRIB	USA
Haito Ren		FRIB	USA
Antonio Villari		FRIB	USA

JACoW Editorial Team (JET)

Alexa Allen		FRIB	USA
Bethany Hannon		FRIB	USA
Ana Lesage	**Editor-in-Chief**	FRIB	USA
Maggi Montes-Loera		SLAC	USA
Volker RW Schaa	**Technical Editor**	GSI	Germany
Tasha Summers		MSU	USA

Contents

ISBN: 978-3-95450-226-4 ISSN: 2222-5692 doi:10.18429/JACoW-ECRIS2020-MOWZO01

FECR ION SOURCE DEVELOPMENT AND CHALLENGES*

L. Sun[1,2 †], H. W. Zhao[1,2], W. Wu[1,2], B. M. Wu[1], J. W. Guo[1], X. Z. Zhang[1], Y. Q. Chen[1], E. M. Mei[1], S. J. Zheng[1], L. Zhu[1], X. D. Wang[1], X. J. Ou[1], C. J. Xin[1], M. Z. Guan[1], W. Lu[1], L. B. Li[1], L. X. Li[1,2], J. B. Li[1], Z. Shen[1,2]
[1]Institute of Modern Physics, Chinese Academy of Sciences, Lanzhou, China
[2]School of Nuclear Science and Technology, University of Chinese Academy of Sciences, Beijing, China

Abstract

FECR or the First 4th generation ECR (Electron Cyclotron Resonance) ion source is under development at Institute of Modern Physics (IMP) since 2015. This ion source is aiming to extract intense highly charged heavy ion beams in the order of 1 emA from the dense plasma heated with 45 GHz microwave power. To provide effective magnetic confinement to the 45 GHz ECR plasma, a state of the art Nb_3Sn magnet with min-B configuration is a straightforward technical path. As there are no much precedent references, it has to be designed, prototyped at IMP through in-house development. Meanwhile, other physics and technical challenges to a 4th generation ECR ion source are also tackled at IMP to find feasible solutions. This paper will give a brief review of the critical issues in the development of FECR ion source. A detailed report on the status of FECR prototype magnet development will be presented.

INTRODUCTION

Heavy ion accelerators are the most powerful tools in modern nuclear physics research. Driven by the needs of large scale heavy ion accelerators, such as FRIB at MSU, RIBF in RIKEN, HIRFL at IMP and so on, ECR ion sources have been continuously supported and improved. The recently started national basic science research project called HIAF or High Intensity heavy ion Accelerator Facility in Huizhou [1], which is composed by high performance superconducting ECR ion sources, SRF (Superconducting Radio Frequency) linac, BRing (Booster synchrotron Ring), HFRS (High energy FRagment Separator) and SRing (Spectrometer synchrotron Ring), will accelerate and accumulate 1×10^{11} ppp U^{35+} of 800 MeV/u in BRing (Fig. 1). For this goal, the injector linac iLinac needs to deliver U^{35+} beam with a beam intensity of ~1 emA at the energy of 17 MeV/u. Consequently, the room temperature front end part will be able to produce and deliver high intensity U^{35+} beams. A 70% efficiency is estimated to transport the intense U^{35+} with high quality to iLinac, and as a result ~40 pμA U^{35+} is literally needed for routine operation if the peak performance of HIAF is desired. Given some margin, the ion source should be able to produce 50 pμA U^{35+} when fully optimized to guarantee the routine operation performance.

* Work supported by NSFC with contract No. 11427904 and Chinese Academy of Sciences with contract No. QYZDB-SSW-JSC025.
† sunlt@impcas.ac.cn

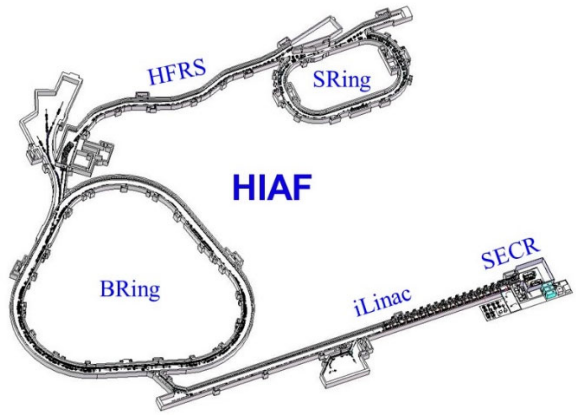

Figure 1: Schematic layout of HIAF.

Modern ECR ion sources with the 3rd generation sources as the iconic machines have been built since 20 years ago. Heated by the microwave of 24~28 GHz and 10 kW maximum power, these sources such as VENUS in LBNL, SCECRIS in RIKEN, SuSI at MSU, SECRAL at IMP and so on, can produce (or potentially) U^{3x+} ion beams of the intensity 10~15 pμA which is more than 10 times the recodes set 20 years ago. But to meet the needs of HIAF, the performance still needs to be boosted by a factor of 3~4. As ECR ion source development is mainly governed by the scaling of $I_q \propto \omega_{ecr}^2$, the straightforward technical path is to develop a 4th generation machine. FECR ion source, which is one of the key components of the LEAF (Low Energy heavy ion Accelerator Facility) project [2], will prototype the first 4th generation ECR ion source in the world.

FECR

The 4th generation ECR ion source concept was proposed more than 10 years [3] when several 3rd generation ECR ion sources had been constructed but seemed to be saturated in performance, which was still not up to the requirements of next generation heavy ion accelerators. FECR ion source is one of the next generation ECR ion sources following the 4th generation concept, which is aiming to be operated the microwave frequency of 45 GHz that can fundamentally increase the ECR plasma density by a factor of 2~3. Table 1 gives the typical design features of FECR. As is mentioned in the table, with the increase of the microwave frequency, the key parameters of the ion source in comparison with a 3rd generation ECR have been obviously changed, which will give the challenges and difficulties in ion source development.

ISBN: 978-3-95450-226-4 ISSN: 2222-5692 doi:10.18429/JACoW-ECRIS2020-MOWZO01

Table 1: Typical Design Features of FECR

Spec.	Unit	FECR	3rd G ECR
ω_{rf}	GHz	45	24/28
RF power	kW	⩾20	~10
Chamber ID	mm	≥Ø140	Ø100~150
Mirror Fields	T	6.4/3.5	~4/2.8
B_{rad}	T	3.2	1.8~2.2
L_{mirror}	mm	500	420~500
B_{max} in conductor	T	~11.8	~7
Conductor	/	Nb_3Sn	NbTi
T_s	keV	80~100	50~60
$(Ne)_{crit}$	cm^{-3}	$\sim 2.6\times10^{13}$	$\sim 1\times10^{13}$
Max. drain	mA	~50	~20

CHALLENGES

To make an operational 45 GHz ECR ion source, FECR has many challenges. As given in Table 1, the key parameters of the ion source will have obvious changes, which might give fundamental impact to the ion source structure or operation conditions. The main expected challenges are given in the following discussions.

Nb_3Sn Magnet

Sextupole Coil Production. A wind and react approach is used in the fabrication of the FECR coils. There are many successful examples of high field solenoids with Nb_3Sn wire, but in terms of sextupole, no much successful information could be the references. The main challenges lie in the precise winding of more than 800 turns single strand in a saddle-like configuration. To have high standard electrical insulation (3~5 kV) of the coil, no damage in the S-glass braided material is allowed during the winding. After successful winding, winded coil will be sent to a programmable oven for heat treatment where the wire will turn into Nb_3Sn conductor. To achieve high quality of electrical insulation and also high RRR value of the superconductor, decarbonization process is mandatory. Finally, the coil will be put in a tooling for Vacuum Pressure Impregnation (VPI) to form the final configuration and more importantly to strengthen the coil and improve the electrical insulation property. To meet the needs of precise installation with bladder and key technology, the 860 mm length sextupole coils should be eventually prepared within a tolerance of ±100 μm.

Cold Mass Structure. There will be complicated forces between the coils. For a 3rd generation ECR ion source, it has already been a big challenge. For FECR, this interaction forces will be more than doubled. Efficient pretension and clamping of all the coils will be the highest priority in the structure design. FECR cold mass design also adopted the state-of-the-art bladder and key technique. The explosive view of FECR cold mass is given in Fig. 2.

Quench Protection. FECR will have totally ~1.6 MJ stored energy at 100% energized currents. Fast and safe extraction of the stored energy when the magnet quenches is crucial. However, compared to NbTi, Nb_3Sn has much slower quench propagation speed that makes fast quench detection and energy extraction more stringent. Passive quench protection widely used on 3rd generation devices is not suitable to FECR. Figure 3 gives the hot-spot temperature for one of the FECR coils. Active quench protection system adaptable to FECR should be developed.

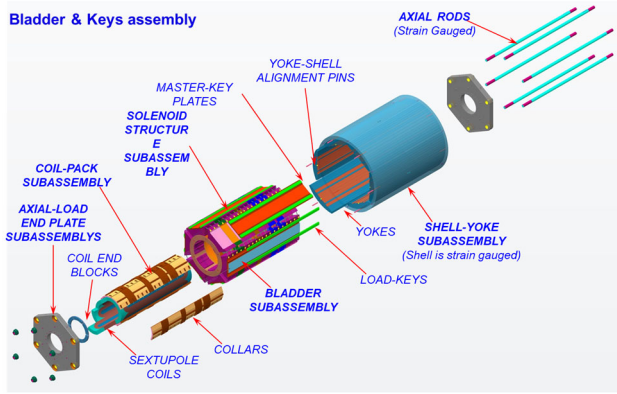

Figure 2: FECR cold mass structure.

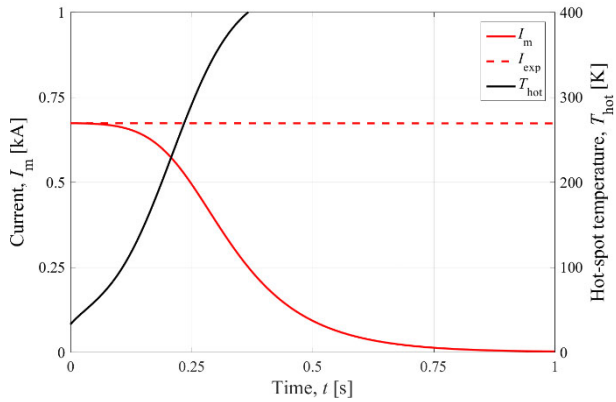

Figure 3: Hot-spot temperature estimation with passive quench protection scheme for one injection solenoid.

Cryogenic System. FECR has a 3.5 tons cold mass. To accommodate it and make it work safely at 4.3 K (liquid helium temperature), many issues should be handled. Radial field homogeneity is very essential for a high performance ECR ion source. Misalignment of the cold mass will possibly cause thermal shortage inside the cryostat, and more importantly, the inhomogeneous radial field on the plasma chamber wall will result in much weaker total magnetic field and consequently much heavier localized heating by plasma flux leakage. Additionally, for efficient energy extraction, active quench protection will use 0.5~2.0 Ω dump resistor which will excite high voltages in the coil circuits. For FECR, a highest voltage of ~1 kV will be seen during the quench energy extraction at 100% design currents [4], which needs a very robust solution to the electrical insulation in the cryostat design and fabrication. Last but not least, much more dynamic heat load is expected to be dumped to the cold mass, and high dynamic cooling capacity is needed at 4.2 K to avoid the loss of boiling-off liquid helium.

ISBN: 978-3-95450-226-4 ISSN: 2222-5692 doi:10.18429/JACoW-ECRIS2020-MOWZO01

Conventional ECR Parts

20 kW/45 GHz Microwave Coupling. As 45 GHz microwave has a wave length of ~6.7 mm, transmission and coupling of high power microwave to ECR plasma may have the potential risk of arcing inside the circular waveguide. Quasi-optical transmission in air from the generator to the microwave window, and then converted to oversized waveguide after the microwave window is proposed and successfully tested at IMP on the SECRAL-II test bench (Fig. 4). This has basically solved the problem of high power transmission and coupling to ECR ion source. However, the efficient coupling to an ECR plasma in terms of highly charged ion production remains unclear, which needs the real test with FECR. Additionally, in recently years several laboratories have demonstrated that multi-frequency heating is essential to stabilize the plasma when the ion source is fed with high power microwave for highly charged ion beam production. For FECR, it is still hard to make a choice in the auxiliary plasma heating frequency. As a baseline, 45 GHz/20 kW + 28 GHz/10 kW will be applied.

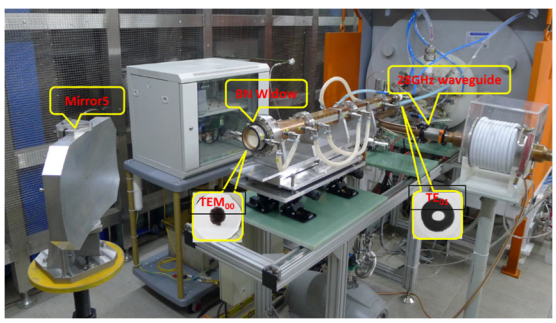

Figure 4: SECRAL-II test bench with 45 GHz microwave coupling system.

Reliability and Stability at 20 kW/45 GHz. Once high power density plasma is built, there will be many challenges. The critical one is the efficient plasma chamber cooling. Many laboratories had the experience of damaged plasma chambers by localized overheating of escaped plasma flux. According to the estimation by T. Thuillier in his paper [5], the peak power sink on the inner wall of plasma chamber can reach to 1.25 MW/cm^2 for 1 kW 28 GHz microwave heating that will cause instant boiling of the cooling water at the weak |B| area on the plasma chamber at high power level. Created bubbles will prevent further cooling with flowing water and plasma chamber damage will happen when chamber material starts to degrade at high temperature. Normally, this damage is an instant process once the heated microwave power reaches the critical value of the chamber (magnetic field configuration, plasma stability also have influences). At 45 GHz, we might face much higher plasma flux density for every kW microwave power launched. Most of the existing plasma chamber can barely take long-time operation at the power level of 10 kW. It is a big challenge for FECR to work at 20 kW/45 GHz.

Strong Bremsstrahlung Radiation. Strong bremsstrahlung radiation is an iconic characteristic of highly charged ECR ion source, which is an evidence of the existence of energetic electrons inside the plasma. For superconducting ECR ion source, this radiation will give additional heat sink to the cryogenic system as mentioned in the former section. This radiation will also cause the degradation of electrical insulators. High voltage (HV) main insulators have been damaged with many 2nd or 3rd generation ion sources. More energetic and dense electrons will be created inside FECR plasma, and the damage to the main insulator column will be devastating. Another possible risk is the radiation to the Nb_3Sn coils. As Nb_3Sn coils have strict requirement on electrical insulation property. Any degradation in the epoxy insulation will affect the performance and even the normal operation of the coils.

Intense Beam Extraction. 3rd generation ECR sources have produced highly charged beams with a total current of 15~20 emA that is 2~3 times the total current from a high performance 2nd generation ECR ion source. FECR is expected to be able to extract 30~50 emA total beam that will raise the challenges in beam extraction, transport and quality control.

Intense Refractory Ion Beam Production. Intense uranium beam is highly desired in most of the heavy ion accelerator laboratories. High temperature oven remains the baseline solution to highly charged intense uranium beam production, despite the sputtering method has also been regarded as an efficient technology in the production of 100 eμA U^{3x+}. As metal uranium is chemically reactive to most crucible materials, UO_2 is favoured for oven application, which needs ~2000°C for intense beam production. At such a high temperature, Lorentz forces, material degradation (or chemical reaction), and thermal stress constitute the challenges in high temperature oven technique. Other than uranium beams, intense beam production of Th, W, Mo, Ca, and so on is also of high challenge with regards to production efficiency and high charge state.

STATUS REPORT

Many research activities oriented to the afore mentioned challenges have been made. In this paper, several typical processes are presented.

FECR Prototype Cold Mass

To validate the cold mass design of FECR, a 1/2 length prototype has been proposed and developed [5]. This prototype is mainly composed by 6 sextupole coils and 2 axial solenoids, which can demonstrate the Nb_3Sn coil fabrication technique, cold mass structure, quench protection and cold mass integration technologies. By the end of August 2020, the prototype cold mass has been developed and recently tested for the 1st round. The prepared prototype cold mass is shown in Fig. 5. In the cold test, we energized the solenoid and sextupole individually. The solenoid was energized to 100 % design current of 600 A without a quench, and the sextupole was energized to 90% design current of 671 A without a quench. But during the training study, we found flux jump signal interference and the power supply stability are problems for stable operation and fast, accurate quench detection.

ISBN: 978-3-95450-226-4 ISSN: 2222-5692 doi:10.18429/JACoW-ECRIS2020-MOWZO01

Figure 5: Picture of completed FECR 1/2 size prototype cold mass ready for test.

Cryogenic System

An engineering design of the FECR cryogenic system has been made recently based on the final structure design of the cold mass. This cryogenic system will provide the LHe operation condition for the 3.5 tons cold mass. Cold alignment with the assistance of on-line field mapping is enabled in the cryostat design. The typical features of FECR cryogenic system is given in Table 2. The choice of the cryocoolers is specified. As given in Table 3, a combination of 1 CH-110 and 3 RDE-418D4 coolers from Sumitomo Inc., and 3 KDE422 coolers from CSIC Pride (Nanjing) Cryogenic Technology Co., Ltd. has been adopted.

Table 2: Cryogenic System Parameters of FECR

Parameters	Value
Operation Temp. (K)	4.3
Magnet Cooling	LHe bathing
Stored Energy (MJ)	~1.6
Required dynamic cooling capacity (W)	≥12
Warm bore ID (mm)	Ø162
LHe volume (liter)	~330
Dimension (mm)	L1456×Ø1200×H2690
Total weight (ton)	~6.1

Table 3: Cryocoolers for FECR

Model	1st Stage	2nd Stage
CH-110	~130 W@50 K	N/A
KDE-422	~20 W@50 K	≥2.2 W@4.2 K
RDE-418D4	~42 W@50 K	≥1.8 W@4.2 K
Total	~316 W@50 K	≥12 W@4.2 K

High Power Operation

Traditional double-wall water cooling aluminium plasma chamber can only safely work at the ECRH microwave power level of 7~8 kW of 24~28 GHz. A recent breakthrough in plasma chamber design by utilizing a microchannel technology can fundamentally improve the cooling capacity of the plasma chamber. In the recent online test, a total power of 11 kW has been fed into the newly developed plasma chamber installed on SECRAL-II. After 48 hours continuous 11 kW operation, the plasma chamber survived and stable highly charged ion beams are also produced, such as >100 eμA Xe^{34+}. This can't guarantee the safe operation at 20 kW/45 GHz, but is a good baseline for the FECR ion source plasma chamber design.

High Temperature Oven

Enlighted by the successful inductive heating oven (IHO) developed at MSU for the reliable operation under 1800°C, a refined IHO has been recently developed at IMP. With several modifications in the oven structure and material design, this oven can work stably up to 2000°C. Recently, this oven has been used to produce intense uranium beams. At 6 kW/24 GHz, 450 eμA U^{33+} was produced and more importantly the oven survived the one-week high temperature operation [6], which gave us confidence in developing reliable high temperature oven for FECR.

Dynamic Heat Load

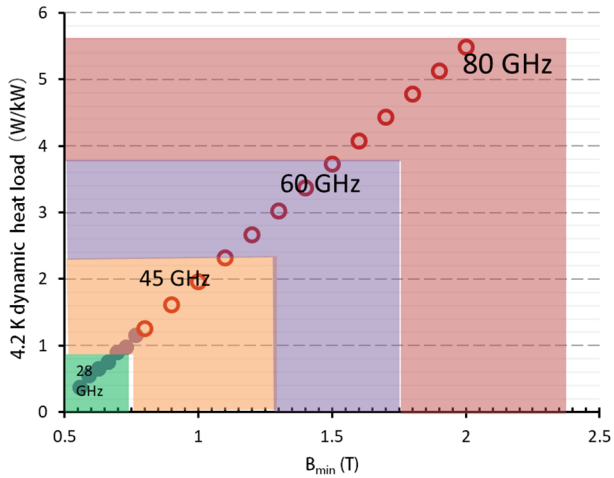

Figure 6: Estimated dynamic heat load to the 4.3 K cryogenic system at different operation B_{min}.

Dynamic heat load to the 4.2 K cryogenic system is mainly caused by the high energy electron bremsstrahlung radiation as most of the existing 3rd generation ECR ion sources have used 1~2 mm Ta shielding that could easily prevent the X-ray of <200 keV from penetration to the cryogenic system. The experimental results from SECRAL-II indicate the dynamic heat load could reach 0.6~1.0 W/kW at 24~28 GHz when B_{min} was set in the range of 0.6~0.7 T, ~0.7 of B_{ecr}. It has been accepted by the community that high temperature electron spectra temperature T_s increases linearly with B_{min} before the cyclotron instability is triggered at B_{min}/B_{ecr}~0.8. For FECR, it will be operated at the B_{min} of 0.9~1.1 T. As illustrated in Fig. 6, 1~2 W/kW dynamic heat load is predicted for FECR which means the cryogenic system will have a total dynamic heat load of 20~40 W during CW operation, which is much beyond the ~12 W design value. Before we can find better solutions, one compromised plan is to lower the operation duty factor by pulsing the microwave power when > 10 kW operation is desired.

ISBN: 978-3-95450-226-4 ISSN: 2222-5692 doi:10.18429/JACoW-ECRIS2020-MOWZO01

SUMMARY

FECR project was officially started in 2015. After 5 years continuous development, we have tackled most of the envisioned challenges. Most of them have got fundamental progresses recently, but there are still many open questions. To develop an operational FECR ion source, there are still many challenges ahead. According to the updated project plan, FECR assembly is about to be ready in 2021. That will be time to check the feasibility and reliability of our designs towards a high performance 45 GHz ECR ion source.

ACKNOWLEDMENT

We acknowledge the fruitful collaboration work on FECR cold mass design between ATAP/LBNL and IMP. The collaboration with RIKEN ion source group on high temperature oven development is appreciated. We are also graceful that so many people from our community and outside of our community have given us suggestive advice. We thank all the commercial vendors who have been supporting us in this challenging research.

REFERENCES

[1] J. C. Yang *et al.*, "High Intensity heavy ion Accelerator Facility (HIAF) in China" *Nucl. Instrum. Meth. B,* vol. 317, pp. 263-265, 2013.
doi.org/10.1016/j.nimb.2013.08.046

[2] L. Sun, H. W. Zhao, W. Lu, J. W. Guo, Y. Yang, H. Jia, L. Lu, W. Wu, "Review of highly charged ion production with ECR ion source and the future opportunities for HCI physics" *X-Ray Spectrometry*, vol. 49, pp. 47-53, 2020.
doi.org/10.1002/xrs.3049

[3] Claude M. Lyneis, D. Leitner, D. S. Todd, G. Sabbi, S. Prestemon, S. Caspi, and P. Ferracin, "Fourth generation electron cyclotron resonance ion sources (invited)", *Rev. Sci. Instrum.*, vol. 79, p. 02A321, 2008.
doi.org/10.1063/1.2816793

[4] E. Ravaioli *et al.*, "Quench Protection of a Nb$_3$Sn Superconducting Magnet System for a 45-GHz ECR Ion Source", *IEEE Trans. Appl. Supercond.,* vol. 28, no. 3, pp. 1-6, Art no. 4700906, 2018.
doi.org/10.1109/TASC.2018.2793891

[5] H. W. Zhao *et al.*, "Superconducting ECR ion source: From 24-28 GHz SECRAL to 45 GHz fourth generation ECR", *Rev. Sci. Instrum.*, vol. 89, p. 052301, 2018.
doi.org/10.1063/1.5017479

[6] W. Lu, L. T. Sun, C. Qian, L. B. Li, J. W. Guo, W. Huang, X. Z. Zhang, and H. W. Zhao, "Production of intense uranium beams with inductive heating oven at Institute of Modern Physics", *Rev. Sci. Instrum.,* vol. 90, p. 113318, 2019.
doi.org/10.1063/1.5128419

ISBN: 978-3-95450-226-4 ISSN: 2222-5692 doi:10.18429/JACoW-ECRIS2020-MOWZO02

LECR5 DEVELOPMENT AND STATUS REPORT

C. Qian,[1,2] L. T. Sun, [1,2] Z. H. Jia,[1,3] W. Lu,[1] L. B. Li,[1] X. Fang,[1] J. W. Guo,[1] J.J. Chang,[1] J.R. An,[1] J.D. Ma,[1] H. Wang, [1] Y. M. Ma, [1] Y.C. Feng[1], X. Z. Zhang, [1] and H. W. Zhao,[1,2]

[1]Institute of Modern Physics, Chinese Academy of Sciences, Lanzhou, China

[2]School of Nuclear Science and Technology, University of Chinese Academy of Sciences, Beijing, China

[3]School of Nuclear Science and Technology, Lanzhou University, Lanzhou, China

Abstract

LECR5 (Lanzhou Electron Cyclotron Resonance ion source No. 5) is an 18 GHz room temperature ECR ion source featuring Ø80 mm ID (Internal Diameter) plasma chamber and high magnetic fields. It has been successfully constructed at IMP recently and has been fully commissioned to meet the requirements of SESRI (Space Environment Simulation and Research Infrastructure) project. According to the test results, LECR5 can meet the requirements of SESRI with sufficient beam intensities within the required the transverse emittances. As LECR5 is designed to be optimal for the operation at 18 GHz, we have explored the source performance at 18 GHz with a maximum microwave power around 2 kW. Recent source test indicates, LECR5 can produce not only high intensity ion beams such as 2.12 emA O^{6+}, 121 eμA of Ar^{14+}, 73 eμA of Kr^{23+}, 145 eμA of Xe^{27+}, but also very high charge state ion beams such as 22 eμA of Bi^{41+}. This paper will present the recent progress with LECR5, especially the intense ion beam production and the beam quality investigation.

INTRODUCION

Space Environment Simulation and Research Infrastructure (SESRI), which is one of the large-scale science projects proposed in the National Twelfth Five-Year Plan of China, will be constructed in Harbin Institution of Technology. It has kinds of accelerators designed and constructed by the Institute of Modern Physics (IMP), the Chinese Academy of Sciences (CAS). The 300 MeV proton and heavy ion accelerator is a significant radiation source, which will supply 100 - 300 MeV protons and 7 - 85 MeV/u heavy ions for studying the interaction of high energy space particle radiation with the material, device, module, and biological entity. Electron Cyclotron Resonance (ECR) ion sources are widely used to produce a multi-charged ion beam for heavy ion accelerators. The SESRI project dedicated to space radiation consists of a high performance ECR ion source, a high intensity ion linac, a synchrotron, and three research terminals to meet the above requirements. As shown in Fig. 1. Table 1 shows the required beam current and quality of the ion source. Some all permanent magnet ECR ion sources (LAPECR1, LAPECR2) and some room temperature ECR ion sources (LECR1, LECR2, and LECR3) have also been successively built at IMP [1].

† qianc@impcas.ac.cn

All permanent Magnet ECR ion source and 14.5 GHz room temperature ECR ion source cannot meet the bismuth ion beam requirement. Referring to the ECR ion source development at IMP [2], 18 GHz ECR ion source can meet this project's needs. As the critical part of the complex, a high performance room temperature ECR ion source (named LECR5) was proposed for various ion beams injection. Ac-cording to the scaling laws of an ECR ion source [3, 4]. Its design is based on LECR4 [5] parameters and optimized for the magnetic field of the SECRAL operating at 18 GHz [6]. Compared with a superconducting ECR ion source, a room temperature 18 GHz ECR ion source has the advantages of more accessible construction, lower cost, and more convenient maintenance.

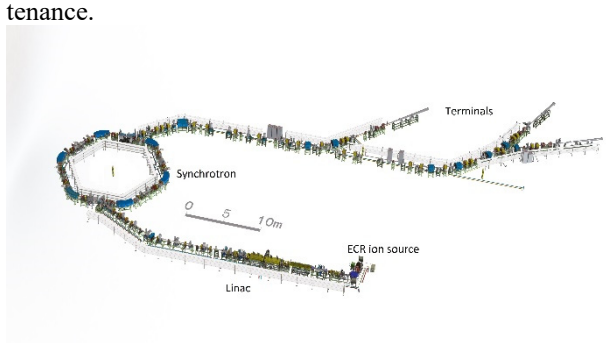

Figure 1: The layout of accelerator of SESRI.

Table 1: The Requirements of the Ion Source (*updated)

Ions	Current (eμA)	4RMS (π.mm.mrad)
H_2^+	≥250	≤0.8
$^4He^{2+}$	≥200*	
$^{84}Kr^{18+}$	≥84	≤0.6
$^{209}Bi^{32+}$	≥50	

DESIGN OF LECR5 AND FEATURES

As shown in Fig. 2. For most room temperature ECR ion source, the axial magnetic field to achieve a mirror field uses two coils that injection and extraction coils. LECR5 designed a third set of coils placed in the middle of the mirror field to control Bmin. It is advantages to tuning on the electron temperature through the magnetic gradient at resonance. Besides, the magnetic field at the injection side is reinforced by a thick iron plug that obtains a high-B mode magnetic profile. The axial field of 2.5 T at the injection is

ISBN: 978-3-95450-226-4 ISSN: 2222-5692 doi:10.18429/JACoW-ECRIS2020-MOWZO02

achievable. A hexapolar system gives the radial magnetic field. The optimum configuration for such a system is given by the so-called Halbach array composed of 36 block permanent magnets (88 mm inner diameter, 188 mm outer diameter, and 320 mm long). Using the higher remanence material N50M NdFeB (Br=1.407 T, Hc=-1043 kA/m) improves the radial magnetic field strength, and uses higher polarization coercivity material N48SH NdFeB (Br=1.386 T, Hc=-1011 kA/m) solves the self-demagnetization problem in the six critical magnetic segments. The radial magnetic field at a chamber wall of 1.2 T is achievable, and the large and long plasma chamber (80 mm in diameter and 340 mm long) allows a long lifetime for the ions to produce high charge states. Table 2 presents the design parameters of the LECR5 ion source. After the assembly, the magnet parameters are up to and better than the design value [7].

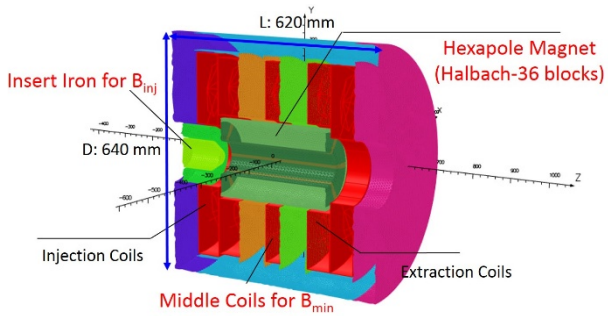

Figure 2: Layout structure of the LECR5 ion source.

Table 2: The Design Parameter of the LECR5 Ion Source

Parameters	value
Microwave frequency (GHz)	14.5 - 18
Maximum power (kW)	2.5
B_{inj} (T)	2.5
B_{ext} (T)	1.4
B_{min} (T)	0.33~0.53
B_{rad} (T)	1.2
Mirror Length (mm)	340
Plasma Chamber D (mm)	80
Maximum HV (kV)	30

COMMISSIONING ION BEAMS

Gaseous Ion Beams Production

The testing of LECR5 was started in August 2019 by producing high charge state ion beams from oxygen and argon plasmas [7]. The first extraction's beam intensity adopted dual-frequency (14.5 + 18 GHz) heating has produced 450 eμA O7+ and 260 eμA Ar12+, which verified the performance of LECR5. At the beginning of 2020. The commissioning of LECR5 for stable beam production was started from oxygen. 2.12 emA O6+ has been obtained after optimization. Depending on 14.5+18 GHz microwave power and comparing with other ECR ion sources given in Fig. 3. It was commissioned with a single frequency of 18 GHz, maximum power was 2 kW, and stainless steel plasma chamber for the SESRI project requirements. Optimization of typical charge states of gaseous ion beams was commissioned to explore the performance of LECR5 ion source. The record intensities for argon, krypton, and xenon are presented in Table 3. The beam results of LECR4 in Table 3 were commissioned with dual-frequency (18 +18 GHz), and microwave power was less than 2.2 kW [8]. Those of SECRAL in Table 3 were commissioned at 18 GHz [9]. It produces a higher charge state ion beam that is better than LECR4 and close to SECRAL operated at 18 GHz. The higher radial magnetic field (>1.2 T) can produce higher charged ion beams at the same conditions. It can meet the demand of ion beam current at less than 1 kW microwave power and supply stable ion beams. For the light ion beam, the magnetic field and microwave power can be reduced to meet its needs.

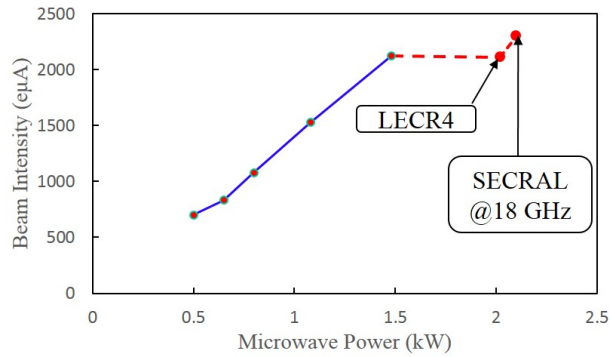

Figure 3: Depending on 14.5+18 GHz microwave power and comparing with other ECR ion sources.

Table 3: Comparison of the Gaseous Ion Beam Results of LECR5 with other ECR Ion Sources

	Q	**LECR5** (eμA)	**LECR4** (eμA)	**SECRAL** (eμA)
^{40}Ar	11+	521	620	
	12+	385	430	510
	14+	121	185	270
	16+	21	21	73
^{84}Kr	18+	220		
	20+	120		
	23+	73		
	26+	32		
^{129}Xe	20+	338	430	505
	23+	263	275	
	26+	200	205	410
	27+	145	135	306
	28+	104	92	

Metal Ion Beams Production

High intensity high charge state metal ion beam is essential for performance presentation of ECR ion source. The

ISBN: 978-3-95450-226-4 ISSN: 2222-5692 doi:10.18429/JACoW-ECRIS2020-MOWZO02

bismuth ion beam has been produced with LECR5 operated at dual-frequency (14.5 +18 GHz) and aluminum plasma chamber. By optimizing of LECR5 conditions, stable high charged bismuth ion beams had been obtained with an oven method at 25 kV extraction voltage. An internal oven was developed at IMP for metallic ion beam production. The central part of the oven (Fig. 4) consists of an alumina ceramic wound with a 0.5 mm diameter tantalum wire, and its working temperature is from 200 ℃ to 1300 ℃ [10]. A 15 A/20 V electrical power supply is used to heat the tantalum wire. Table 4 presents the commissioning beam results compared with LECR4 and SECRAL. Figure 5 shows the typical spectrum when Bi41+ is optimized. The results of higher charged bismuth ion beams are close to and better than those of SECRAL operated at 18 GHz.

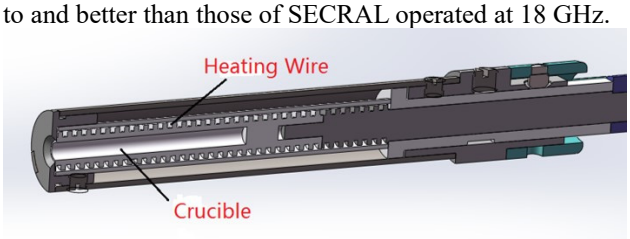

Figure 4: The layout structure of the oven used on the LECR5.

Table 4: Comparison of the Metal Ion Beam Results of LECR5 with Other ECR Ion Sources

	Q	LECR5 (eμA)	LECR4 (eμA)	SECRAL (eμA)
^{209}Bi	30+	119		191
	31+	101	92	150
	32+	81	63	
	41+	22		22
	45+	12.5		15
	50+	3.8		1.5

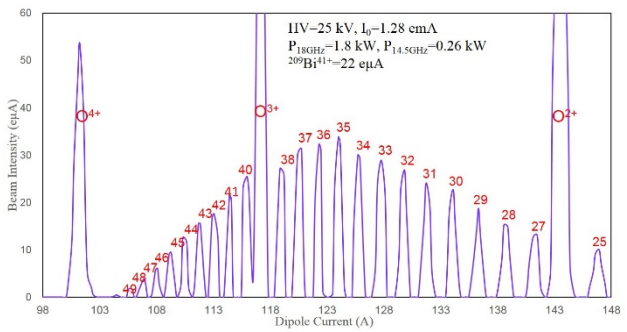

Figure 5: The spectrum of LECR5 optimized for Bi41+ at dual-frequency (14.5 +18 GHz) heating.

ION BEAMS EMITTANCE

LECR5 ion source can improve the efficiency of linac by providing high quality ion beam. It is difficult to control the beam quality of ECR ion source for light ion, but it can be optimized for heavy ion beam. The light ion beam emittance could be controlled by slits in two directions and optimization of low energy beam transmission. During the LECR5 beam commissioning heavy ion beam, 121 eμA Ar^{14+}, 145 eμA Xe^{27+}, 81 eμA Bi^{32+} and 22 eμA Bi^{41+} at 25 kV extraction voltage ion beam emittances were measured by an Allison-type emittance scanner. The results are shown in Fig. 6. It can be seen that normalized emittance of high intensity high charged ion beam is around 0.1 π.mm.mrad and could satisfy the requirement of SESRI.

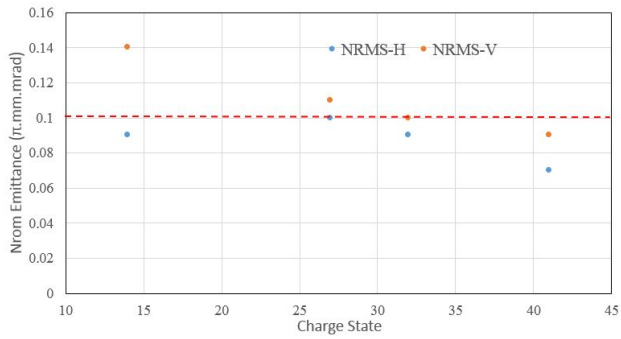

Figure 6: Ion beam Emittance for argon, xenon, and bismuth, H means horizontal, V means vertical.

CONCLUSION AND PERSPECTIVES

A high performance 18 GHz room temperature ECR ion source was successfully constructed. Some outstanding results of medium-high-charge ion beams have been produced. It can produce a higher charged heavy ion beam close to SECRAL operated at 18 GHz. The emittance of the ion beam is reasonable and better than the requirements of the SESRI project. The 18 GHz room temperature ECR ion source's performance can be further improved by increasing the radial magnetic field and effective confinement magnetic field. Better beam results will be obtained by multi-frequency heating and microwave power up to 3 kW in the future.

ACKNOWLEDGMENTS

This project is supported by National Nature Science Foundation of China (Grant No. 11875300) and National Twelfth Five-Year Plan of China. The authors also gratefully acknowledge the helpful advice from every colleague from Ion Source Group of IMP CAS.

REFERENCES

[1] L. T. Sun *et al.*, "Brief review of multiple charge state ECR ion sources in Lanzhou", *Nucl. Instrum. Methods. Phys. Res.*, vol. 235, p. 524529, July 2005. doi:10.1016/j.nimb.2005.03.237

[2] L. Sun *et al.*, "Overview of high intensity ion source development in the past 20 years at IMP", *Rev. Sci. Instrum.*, vol. 91, p. 023310, 2020, doi:10.1063/1.5129399

[3] R. Geller, *Electron Cyclotron Resonance Ion Sources and ECR Plasma*, Philadelphia, PA, USA: Institute of Physics Publishing, 1996, pp. 394-398.

ISBN: 978-3-95450-226-4 ISSN: 2222-5692 doi:10.18429/JACoW-ECRIS2020-MOWZO02

[4] D. Hitz, "Recent Progress in High Frequency Electron Cyclotron Resonance Ion Sources", *Advances In Imaging And Electron Physics,* vol. 144, p. 047075, 2006. doi:10.1016/S1076-5670(06)44001-5

[5] W. Lu *et al.*, "The development of a room temperature electron cyclotron resonance ion source (Lanzhou electron cyclotron resonance ion source No. 4) with evaporative cool-ing technology at Institute of Modern Physics", *Rev. Sci. Instrum.*, vol. 86, p. 043301, 2015. doi:10.1063/1.4916658

[6] H. W. Zhao *et al.*, "Advanced superconducting electron cyclotron resonance ion source SECRAL: Design, construction, and the first test result", *Rev. Sci. Instrum.,* vol. 77, p. 03A333, Mar. 2006, doi:10.1063/1.2149307

[7] C. Qian *et al.*, "A new room temperature LECR5 ion source for the SESRI project", *Rev. Sci. Instrum*., vol. 9i, p. 023313, Feb. 2020, doi:10.1063/1.5128514

[8] W. Lu, et al., "High intensity high charge state ion beam production with an evaporative cooling magnet ECRIS", vol. 87, p. 02A738, Feb. 2016. doi:10.1063/1.4936183

[9] H. W. Zhao *et al.,* "Intense highly charged ion beam production and operation with a superconducting electron cyclotron resonance ion source", *Phys. Rev. Accel. Beams*, vol. 20, p. 094801, Sep. 2017. doi: 10.1103/PhysRevAccelBeams.20.094801

[10] Z. M. Zhang *et al.*, Production of Metallic Ions Beam in ECR Ion Source", *Chinese Physics C*, vol. 14, p. 974978, Oct. 2000.

ISBN: 978-3-95450-226-4 ISSN: 2222-5692 doi:10.18429/JACoW-ECRIS2020-MOWZO03

STATUS OF THE AISHa ION SOURCE AT INFN-LNS*

L. Celona†, G. Calabrese, G. Castro, F. Chines, O. Leonardi, G. Manno, D. Mascali, A. Massara, S. Passerello, D. Siliato, G. Torrisi and S. Gammino
INFN – Laboratori Nazionali del Sud, Catania, Italy
G. Costanzo, C. Maugeri, F. Russo, CNAO, Pavia, Italy

Abstract

The AISHa ion source is an Electron Cyclotron Resonance Ion Source designed to generate high brightness multiply charged ion beams with high reliability, easy operations and maintenance for hadrontherapy applications. The R&D performed by the INFN-LNS team during the 2019/2020 has allowed the improvement of the AISHa performances up to 20% for some of the extracted beams: both injection and extraction flanges has been improved and a movable electrode has been installed. The low energy beam transport has been equipped of an Emittance Measurement Unit (EMU), working through the beam wire scanners principle, for the measurement of the vertical and horizontal emittance of the beams of interest for hadrontherapy applications. Beam emittance has been characterized as a function of q/m and of the beam intensity to highlight space charge effects. If necessary, the beam wire scanners can be used for the characterization of the beam shape. The perspectives for further developments and plasma diagnostics will be also highlighted.

INTRODUCTION

The Advanced Ion Source for Hadrontherapy (AISHa) is an Electron Cyclotron Resonance Ion Source (ECRIS) representing an intermediate step between a 2nd generation ECRIS, unable to provide the requested current and/or brightness, and the 3rd generation ECRIS, too complex and expensive [1].

It has been intended as a multipurpose device and was designed with the typical requirements of hospital facilities in mind, where the minimization of the mean time between failures and the fast maintenance operations are key issues together with the low ripple, high stability, and high reproducibility of the ion beams produced.

For these peculiarities and for the ability to produce highly charged ion beams, it is also a suitable solution to feed accelerators as cyclotrons.

Figure 1 shows a view of the ion source in the experimental area, while the main design features are listed in Table I. The features included in the design exploit all the knowledge acquired from INFN-LNS in the last decades in the ion source design and realization [2].

The AISHa hybrid magnetic system consists of a 36 segment permanent Halbach-type hexapole magnet and a set of 4 independently energized superconducting coils. The coils are enclosed in a compact cryostat equipped with two double-stage cryocoolers that allow us to reach the operating conditions in around 40 h in LHe free operation [3].

The microwave injection system has been designed for maximizing the beam quality through a high-power klystron amplifier operating in the 17.3–18.4 GHz band that allows us to fine tune the frequency by a Digital Fast Tuner System (DFTS). It is scheduled to upgrade the microwave injection system to a higher frequency in order to operate in both single and double frequency modes to exploit at the same time, the Frequency Tuning Effect (FTE) and the Two Frequency Heating (TFH) [4].

A 21 GHz-1.5 kW klystron power amplifier is expected to be delivered by the end of the year and it will be coupled with low losses to the source through the use of an “ad hoc” electromagnetic bandgap device acting as a DC-break.

The plasma chamber, designed to operate around 18 GHz and to hold a maximum power rate of 2 kW is placed at a high voltage (up to 40 kV) and insulated to the ground by a waveguide DC break [5], designed to permit reliable operation up to 50 kV.

The beamline consists of a focusing solenoid placed downstream of the source, a 90° bending dipole for ion selection, and two diagnostic boxes. Each diagnostic box consists of a Faraday Cup (FC), two beam wire scanners, and four slits.

The system of wire scanners and slits has been designed and assembled to allow to beam emittance measurement. The commissioning of the customized Emittance Measurement Unit has started during the late spring with the characterization of the emittance of Argon, Oxygen Carbon, Helium and Proton beams.

Figure 1: Side view of the Advanced Ion Source for Hadrontherapy at INFN-LNS in Catania.

* Work supported by INFN Fifth National Commission
† Celona@lns.infn.it

ISBN: 978-3-95450-226-4 ISSN: 2222-5692 doi:10.18429/JACoW-ECRIS2020-MOWZO03

Table 1: The Main Design Features of the Source AISHa

Parameter	Value
Radial field on plasma chamber wall	1.3 T
Axial field	2.6/0.4/1.7 T
Frequency	17.3/18.4 GHz
Power	1.5 kW
Cryostat length	620 mm
Diameter	650
Extraction voltage	Up to 40 kV
Plasma chamber	92 mm
Extraction aperture	7.2 mm
Resonance zone length	<10 cm

The body source has been totally redesigned paying more attention to the water cooling circuit enabling reliable long time operations. Improvement of the stability of the gas fluxes through the use of mass flow controllers able to provide stable fluxes as low as 0.011 sccm played a key role in the optimization of the source tuning that is in turn beneficial for the emittance minimization.

EXPERIMENTAL RESULTS

The performances of the AISHa ion source has been characterized by the simultaneous measurements of the Charge State Distribution (CSD), of the beam emittance ε and beam brilliance B^q.

The beam emittance has been performed by slicing the beam along the x/y direction and measuring the current for different position of a beam wire scanner, moving parallel to the horizontal/vertical slit. The experimental data have been analysed by means of a home-made code that evaluates the root mean square (rms) normalized emittance.

Normalized emittance is a relativistic invariant, which is expected to be independent of the extraction voltage. Hereinafter we will refer to the rms normalized emittance as the emittance.

The beam brilliance is a measured of the beam current per unit of phase space. Beam brilliance enables us to compare beams characterized by different intensity and emittance. Beam brilliance has been evaluated as the ratio between the ion beam current and the emittance squared:

$$B^q = \frac{I^q}{\varepsilon_x \varepsilon_y}$$

In case of symmetric emittance, $\varepsilon_x \sim \varepsilon_y$, the brilliance can be simply evaluated as:

$$B^q = \frac{I^q}{{\varepsilon_{x,y}}^2}$$

Figures 2, 3 and 4 shows the CSD of the AISHa ion source when producing Argon, Oxygen and Helium respectively. During the test AISHa was able to produce up to 1.3 mA of O^{6+}, 0.35 mA of O^{7+} and more than 5 mA of He^{2+}.

However, it is noteworthy that, for any of the ion beam investigated, maximum brilliance has been always achieved in the highest current conditions.

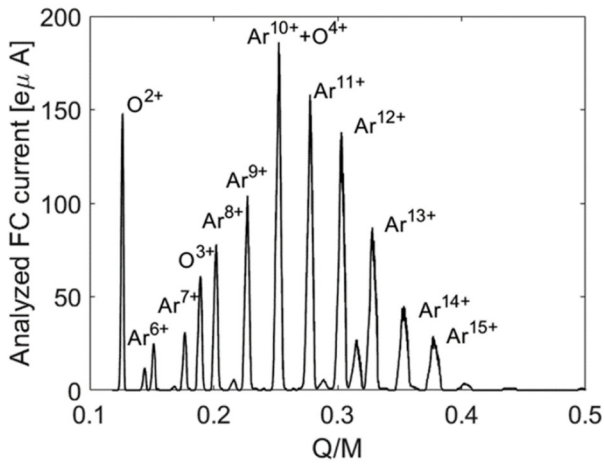

Figure 2: Argon charge state distribution for the ion source tune optimized for the Ar^{11+} charge state.

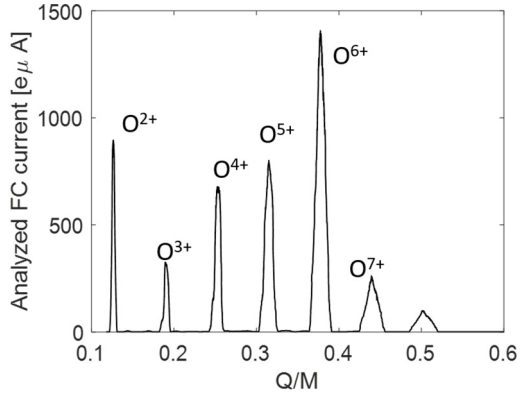

Figure 3: Argon charge state distribution for the ion source tune optimized for the O^{6+} charge state.

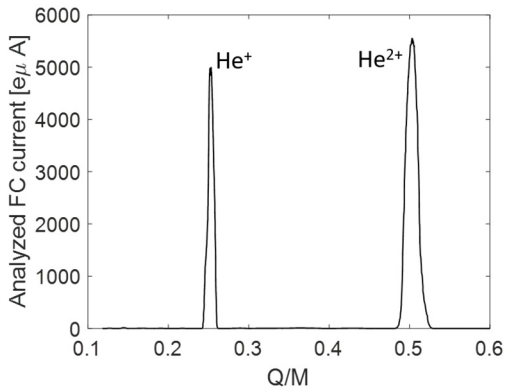

Figure 4: Argon charge state distribution for the ion source tune optimized for the He^{2+} charge state.

Figures 5 and 6 show respectively an example of vertical and horizontal beam emittance acquired by wire scanner system developed at INFN-LNS. The vertical emittance has a spatial dimension larger than the horizontal emittance due to the symmetry breaking introduced by the analysing magnet along the beam transport line. On the other hand, the dimension in the dx/dz dimension is larger in horizontal emittance.

ISBN: 978-3-95450-226-4 ISSN: 2222-5692 doi:10.18429/JACoW-ECRIS2020-MOWZO03

Several studies has been performed with the aim of decreasing the beam emittance for a given ion beam. In particular beam emittance has been characterized versus charge state current I^q. Best value of emittance has been generally obtained for lower values of extracted current. For example, in the case of O^{6+}, the best value has been achieved when producing 0.230 mA (peak value 1.4 mA). In the case of He^{2+}, when producing 0.7 mA (peak value 5.4 mA).

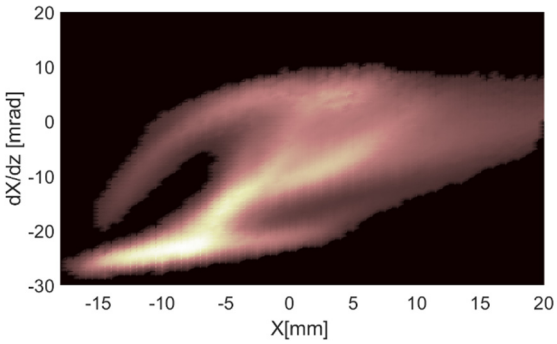

Figure 5: Measure of the vertical emittance of a O^{6+} beam.

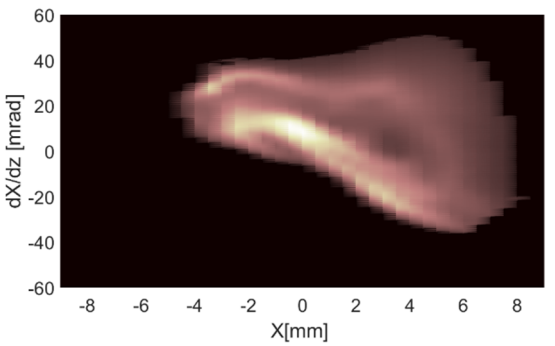

Figure 6: Measure of the horizontal emittance of a O^{6+} beam.

Table 2 summarizes those results in terms of beam current (mA), beam emittance (π·mm·mrad) and beam brilliance (mA/π·mm·mrad²).

Further improvement in terms of peak current and brilliance are awaited as soon as the AISHa shall be upgraded to 21 GHz. Installation of the novel 21 GHz-1.5 kW klystron power amplifier is expected within the end of this year.

CONCLUSION AND PERSPECTIVES

The AISHa ion source is LHe hybrid ECRIS designed in order to work in hospital environment, but is also capable to produce intense highly charged ion beams and for this reason it may be also used in nuclear physics laboratories as a multipurpose source.

The source is going to be moved in a new dedicated laboratory where it is planned to be used for the R&D activities of the LNS ion source group.

A series of experiment and developments have been funded in the next three within the experiment IONS.

Table 2: Best results achieved by the AISHa Ion Source in terms of extracted current (mA), beam emittance (π·mm·mrad) and beam brilliance (mA/π·mm·mrad²)

Charge State	I^q	$\varepsilon_{rms.norm}$	Brilliance
$^{16}O^{6+}$	1.4	0.2198	28.9
$^{16}O^{6+}$	0.23	0.115	17
$^{16}O^{7+}$	0.35	0.247	5.7
$^{12}C^{4+}$	0.65	0.272	8.8
$^{12}C^{4+}$	0.15	0.222	3
$^{12}C^{5+}$	0.17	---	---
$^{40}Ar^{11+}$	0.16	0.201	3.8
$^{40}Ar^{12+}$	0.14	0.201	3.4
$^{4}He^{2+}$	5.4	0.418	30.9
$^{4}He^{2+}$	0.7	0.245	11.6

A second source is under realization for the CNAO hadrontherapy center located in Pavia. Magnetic system have been already realized, the procurement phase is under way and the first assemblies are expected for March-April 2021 at INFN-Pavia. The pre-assembled source is expected to be deployed at CNAO synchrotron room within the fall of the next year.

ACKNOWLEDGEMENTS

The authors would like to acknowledge the support of the INFN technical staff and of the mechanical workshop for the valuable work done in the design and manufacture of several items of the AISHa facility.

REFERENCES

[1] R. Geller, *Electron Cyclotron Resonance Ion Source and ECR Plasmas*, Institute of Physics, Philadelphia, 1996.

[2] S. Gammino *et al.*, "Perspectives of electron cyclotron resonance ion sources beyond the scaling laws," *IEEE Trans. Nucl. Sci.*, vol. 63, pp. 1051-1059, 2016. doi:10.1109/TNS.2016.2514981

[3] L. Celona *et al.*, "Experimental characterization of the AISHa ion source", *Rev. Sci. Instrum.,* vol. 90, p. 113316, 2019. doi:10.1063/1.5128631

[4] F. Maimone *et al.*, "Influence of frequency tuning and double-frequency heating on ions extracted from an electron cyclotron resonance ion source," *Rev. Sci. Instrum.*, vol. 82, p. 123301, 2011. doi:10.1063/1.3665673

[5] O. Leonardi, G. Torrisi, G. Sorbello, L. Celona, and S. Gammino, "A compact dc-break for ECR ion source @ 18 GHz," *Microwave. Opt. Technol. Lett.,* vol.60, p. 3026, 2018. doi:10.1002/mop.31421

ISBN: 978-3-95450-226-4 ISSN: 2222-5692 doi:10.18429/JACoW-ECRIS2020-MOWZO04

GISMO GASDYNAMIC ECR ION SOURCE STATUS: TOWARDS HIGH-INTENSITY ION BEAMS OF SUPERIOR QUALITY*

I. V. Izotov†, A. F. Bokhanov, E. M. Kiseleva, R. L. Lapin, V. A. Skalyga, S. S. Vybin
Institute of Applied Physics of Russian Academy of Sciences, Nizhny Novgorod, Russia

Abstract

GISMO, a CW high-current quasi-gasdynamic ECR ion source, is under development at the IAP RAS. The quasi-gasdynamic confinement regime, featuring high plasma density (up to 10^{14} cm^{-3}) and moderate electron temperature (~100 eV), allowed to extract pulsed beams of H^+ and D^+ ions with current of 450 mA and RMS emittance <0.07 π·mm·mrad [1]. It has been already demonstrated that major benefits of quasi-gasdynamic confinement, previously tested in pulsed mode at SMIS37 facility [1], are scalable to the CW operational mode. In first experiments at GISMO facility, the ion beams were extracted in pulsed mode from the CW plasma of ECR discharge due to technical limitations of cooling circuits. Proton beams with current up to 65 mA were achieved at extraction voltage of 40 kV. A new unique extraction system especially effective for the formation of high current density ion beams was developed.

INTRODUCTION

A distinctive feature of gasdynamic ECR ion sources being under development at IAP RAS is a confinement regime of a high density plasma. It was demonstrated [1–3] that the use of high-frequency gyrotrons is very beneficial for a dense plasma production and high-current ion beams formation. Previously, ion beams of both light (hydrogen) and heavy (nitrogen, argon) elements were extracted from the plasma of ECR discharge sustained by 37.5 [1] and 75 GHz [3] radiation, demonstrating ion beam currents on the level of 100–500 mA with normalized RMS emittance below 0.2 π·mm·mrad in a pulsed operation mode. This success stimulated the construction of the facility named GISMO (Gasdynamic Ion Source for Multipurpose Operation) [4] at IAP RAS, which main application is a powerful neutron generator [5]. The scheme of the facility is shown in Fig. 1. A 28 GHz/10 kW CW gyrotron is used for the plasma heating, manufactured by Gycom. The microwave generator is equipped with power supplies suitable for CW or pulsed operation. The plasma trap has an all-permanent magnet design. To ensure sufficient plasma confinement, the magnetic field configuration is designed to be similar to a simple mirror trap close to the system axis, and the magnetic field strength is 1.5 T at plugs and 0.25 T at the trap center, yielding the mirror ratio of 6. The distance between magnetic mirrors is 12 cm. The magnet bore is 50 mm, thus allowing the use of a water-cooled plasma chamber with a vacuum bore of 32 mm. An ion beam extraction system has been designed to use the acceleration voltage of up to 100 kV. A high source potential requires a development of an appropriate high-voltage insulation of the plasma chamber from unbiased components of the facility. A quasi-optical system, shown in Fig. 1, is implemented instead of a convenient waveguide DC-break. The electro-magnetic radiation of the gyrotron (TE02 mode of a circular waveguide) is converted to the Gaussian beam, which then propagates in open air through the gap of 15 cm, acting as a DC-break. The radiation is received by the horn antenna, converted into a TE11 mode of a circular waveguide, and then focused to the plasma with a microwave-to-plasma coupling system embedded into the vacuum chamber.

GISMO plasma chamber is schematically shown in Fig. 2 together with the simulated temperature on the surface of the chamber touching the magnets (temperature simulations were conducted taking into the account plasma flow and power distributions) and the electromagnetic field distribution inside the chamber (calculated in vacuum, i.e. in absence of the plasma). Simulations show that the unique design of the plasma chamber allows us to safely inject the nominal power of 10 kW with the microwave transmission efficiency close to 95%, (estimated when no reflection from the plasma is present) and without having any cooling issues. Having the plasma volume of 40 cm^3, injected power density reaches 250 W/c^3, whereas conventional ECRISes usually operate at ~1–10 W/cm^3 power density. Such level of deposited power allows to run the ion source in quasi-gasdynamic mode (which is naturally featured with very high energy losses due to low plasma lifetime) while keeping the electrons hot enough to maintain 100% ionization degree.

The main motivation of studies at GISMO facility is the development of a powerful D-D neutron generator [5] capable of producing the neutron flux sufficient for boron neutron capture therapy (BNCT). The D-D neutron generator scheme based on a high-current gasdynamic ECR source should provide the necessary neutron flux once the ion beam current reaches ~1 A at 100 keV energy.

Besides BNCT, neutronography is the application which demands high density neutron fluxes. The use of a high-current ECR ion source with quasi-gasdynamic plasma confinement and heating with gyrotron microwave radiation allows us to produce light ion beams with uniquely low emittance (for a given current level) [6]. Such a low emittance enables the focusing of the ion beam into the spot of several tens of micrometers in diameter. The suggested approach may be exploited for the development of the point-like neutron source with the size of emitting area comparable to

* supported by RFBR, grant #20-32-70002, and within the state assignment of the Ministry of Science and Higher Education of the Russian Federation No. 0035-2019-0002.
† vizot@ipfran.ru

ISBN: 978-3-95450-226-4 ISSN: 2222-5692 doi:10.18429/JACoW-ECRIS2020-MOWZO04

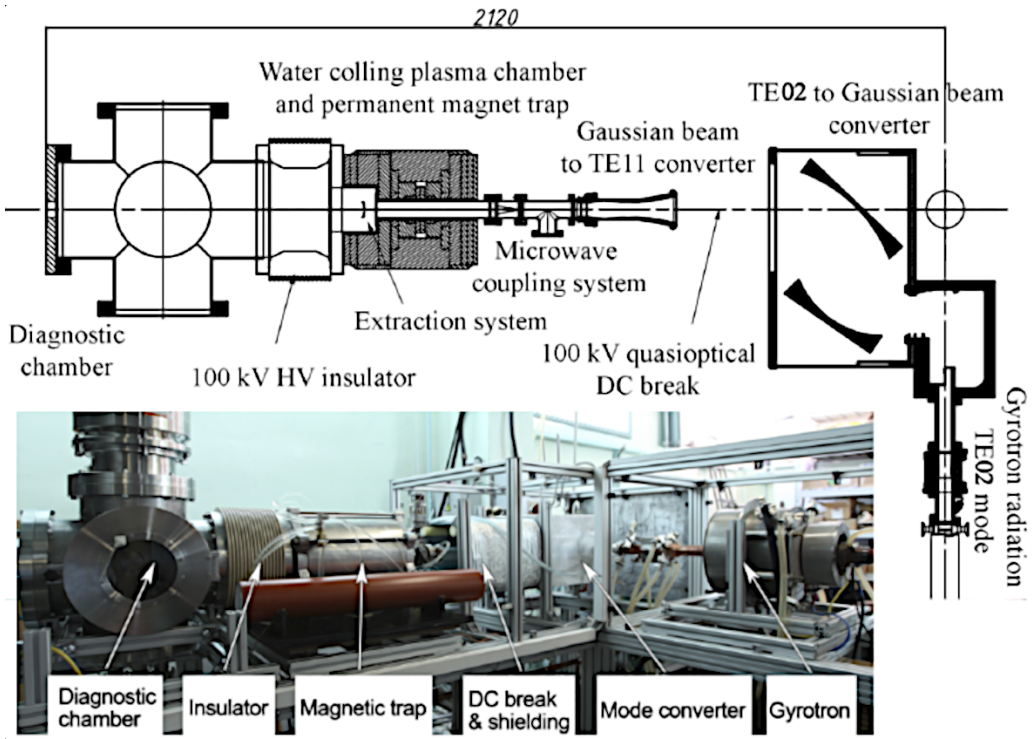

Figure 1: GISMO experimental facility layout.

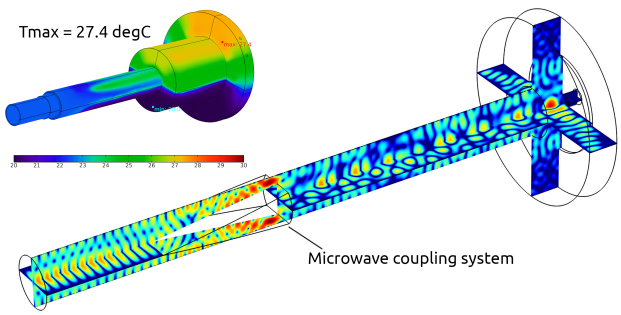

Figure 2: Simulated plasma chamber temperature and RMS electric field distributions at 10 kW of injected power.

femtosecond laser systems, but with significantly higher neutron yield.

FIRST EXPERIMENTS

It has been shown earlier that the plasma density can reach a level of 10^{13} cm^{-3} [7]. As a first step, we have used a simple 2-electrode extraction system for a beam formation. This system is obviously non-optimal for plasma parameters achieved at GISMO, as it has a very long (250 mm) and narrow (30 mm) puller tube, which leads to a more than 90% of beam losses, as was confirmed with IBSimu code [8].

Thus, instead of the extracted ion beam current measured with the conventional Faraday cup, the power supply drain current has been used for a beam current evaluation in the first experiments. The dependence of the drain current on the hydrogen pressure in the plasma chamber is shown in Fig. 3, right axis shows the corresponding current density, assuming 3 mm extraction aperture, the microwave power was equal to 2 kW.

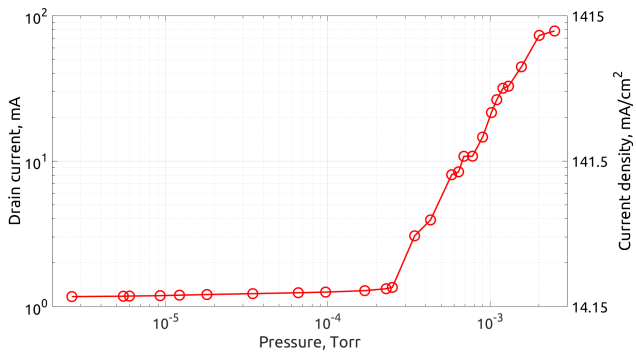

Figure 3: Drain current and corresponding current density as a function of hydrogen pressure in the plasma chamber.

Despite the fact we are not able to extract the whole beam with such extraction system, we estimated the emittance of the beam with pepper-pot method. The beammask was located at the exit of the puller tube (i.e. 260 mm from the plasma electrode), CsI scintillator was placed 50 mm downstream from the mask and its luminescence was captured with synchronized CCD camera. The example of emittance diagram obtained at 1 mTorr pressure and 2 kW of microwave power and 30 kV of extraction voltage is shown in Fig. 4.

RMS normalized emittance calculated from the data in Fig. 5 is equal to 0.019 π·mm·mrad, which seems to be as low as the method precision for the used geometry. We

ISBN: 978-3-95450-226-4 ISSN: 2222-5692 doi:10.18429/JACoW-ECRIS2020-MOWZO04

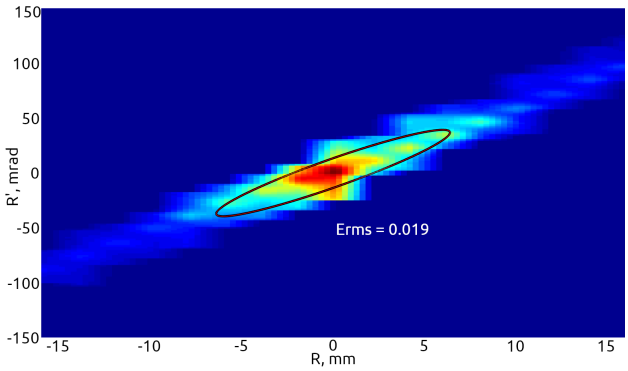

Figure 4: Emittance diagram example, obtained at a hydrogen pressure of 1 mTorr, 2 kW of microwave power and 30 kV of extraction voltage.

would like to underline that once the whole beam would be extracted, the emittance will be likely greater, though these preliminary experiments and IBSimu simulations together indicate that it is reasonable to expect the emittance on the level of 0.1–0.2 π·mm·mrad.

SPHERICAL EXTRACTOR

In order to address the problem of high current density beam formation, the new type of extraction geometry is proposed [9]. The main idea is to change the shape of the electrodes, which exploits an inhomogeneous distribution of the electric field in the accelerating gap of the ion beam formation system. This method may be especially effective in systems with a high current density, mitigating the negative effect of the space charge of the beam on its quality. It allows for significant enhancement of the current and/or reducing the emittance at a certain accelerating voltage and characteristic size of the system, especially when the extraction system operates in the space charge limited regime, which is the case for GISMO facility. The problem of the dense ion beam formation is due to the harmful influence of the self space charge, which distorts the shape of the meniscus, making it convex. Accordingly, the accelerating field near the meniscus forms a diverging beam, which cannot be transported efficiently. The increase in the electric field near the meniscus provides higher beam acceleration gradient and reduces the region with high space charge level. It is proposed to consider the combination of electrodes shown in Fig. 1. Hereinafter we denote such a system as a "spherical" because the puller and the tip of the plasma electrode form plates of a hollow hemispherical capacitor (this region is highlighted with a rectangle in Fig. 5a), whereas the conventional flat structure shown in Fig. 5b forms plates of a flat capacitor.

The use of inhomogeneous accelerating field allows an increase of the electric field magnitude near the plasma meniscus without raising the extraction voltage or reduction of interelectrode distance (see Fig. 5). In this work we consider a new electrode geometry which produces an inhomogeneous electric field providing higher gradients of ion beam

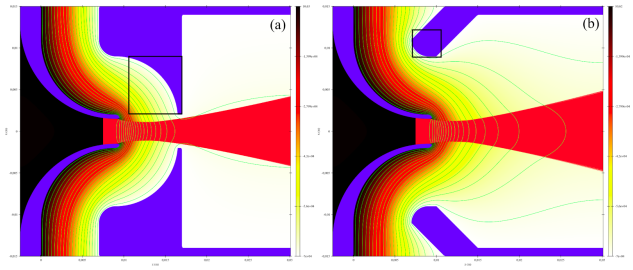

Figure 5: Distribution of the electric field modulus in the interelectrode space (a - spherical, b - flat). Distribution of the electric field along the axis of symmetry (c). The voltage between electrodes is the same and equal to 70 kV.

acceleration and reducing the space charge influence on its quality.

It is of note that the new geometry can be used for a wide range of the ion beam sources and its applications. This approach in extraction system design allows for increase of the current of the beam at proton injectors [10, 11] and multi-charged ion sources for accelerators [12]. The current density can exceed the level of 1 A/cm^2. Such high current densities are available at ion sources for focused ion beams (FIBs) [13] but the total current is lower by several orders of magnitude. On the other hand, the use of a new geometry allows for significant decrease of the extraction voltage and hence it is useful for low energy ion beam production. Such beams are required for ion implantation [14]. The decrease of the optimal extraction voltage can also significantly reduce the co-extracted electron flow in negative ion sources [15]. In many nuclear physics facilities injecting heavy ion beams into cyclotron accelerators the experimental program often requires high currents of medium charge state ions. The currents of such beams often cannot be maximized because the injection energy (source potential), defined by the design of the central region of the cyclotron, is too low to reach the plasma density-limited operation mode of the ion source. The novel approach for the beam extraction system could overcome such limitations and is therefore of interest for various accelerator facilities. In particular, this is relevant for the 3rd and 4th generation ECR ion sources where the plasma density is as high as 10^{12}–10^{13} cm^{-3}, and very high extraction voltages are required to reach the plasma density-limited operation. In this case the new extraction system allows exploiting the full capacity of the ion source in a wider range of extraction voltages. Another technical advantage of the proposed system is the possibility to use puller with much greater aperture than in conventional extraction systems, as the puller aperture barely affects the the shape of the meniscus and the mode of extraction of the beam. The example is shown in Fig. 6, where two significantly different puller apertures are simulated. The reason for that being the puller part highlighted in the Fig. 6a has a weak effect on the electric field distribution, while the highlighted part in the Fig. 6b makes the main contribution.

ISBN: 978-3-95450-226-4 ISSN: 2222-5692 doi:10.18429/JACoW-ECRIS2020-MOWZO04

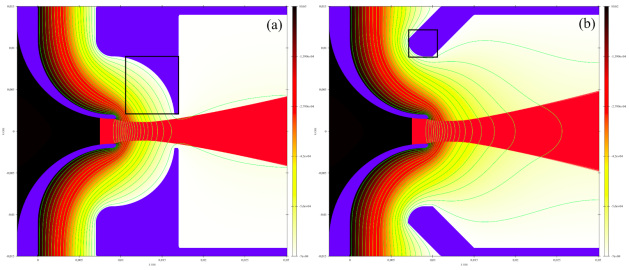

Figure 6: Formation of an ion beam with various puller designs. A significant increase in the aperture of the puller slightly affects the beam.

A set of tungsten electrodes of a new type was designed and fabricated at IAP RAS for initial test on GISMO facility. A photograph of electrodes is shown in Fig. 7. The first experiments with new electrodes are in progress at the moment and will be published soon.

CONCLUSION

New gasdynamic CW ECRIS named GISMO is now operational at IAP RAS. Hydrogen plasma emissivity of >1 A/cm^2 has been demonstrated. A new type of extraction system geometry able to handle beam current densities of >1 A/cm^2 is developed and manufactured. Proton beams with current of 65 mA were successfully obtained at extraction voltage of 40 kV. Judging from conducted experiments and IBSimu numerical investigations, the extraction system consisting of 4 electrodes and new spherical geometry would be able to extract the beam current on the level of 250 mA, Preliminary estimations of normalised RMS emittance suggested that the emittance of such a beam should be lower than 0.2 π·mm·mrad. Thus, GISMO facility may be able to fulfill the requirements of future proton accelerator projects, such as ISIS upgrade (ISIS-II) and DARIA [11].

Figure 7: A photograph of spherical plasma electrode and a set of puller electrodes.

REFERENCES

[1] S. Golubev *et al.*, "High current ECR source of multicharged ion beams", *Nucl. Instrum. Methods Phys. Res., Sect. B*, vol. 256, pp. 537-542, March 2007, doi:10.1016/j.nimb.2006.12.053

[2] V. Skalyga *et al.*, "New progress of high current gasdynamic ion source (invited)", *Rev. Sci. Instrum.*, vol. 87, p. 02A716, 2016, doi:10.1063/1.4934213

[3] V. A. Skalyga *et al.*, "Study of hydrogen ECR plasma in a simple mirror magnetic trap heated by 75 GHz pulsed gyrotron radiation", *Rev. Sci. Instrum.*, vol. 88, p. 033503, 2017, doi:10.1063/1.4978278

[4] V. A. Skalyga *et al.*, "Status of a new 28 GHz continuous wave gasdynamic electron cyclotron resonance ion source development at IAP RAS", *AIP Conf. Proc.*, vol. 2011, p. 030013, 2018, doi:10.1063/1.5053274

[5] V. Skalyga *et al.*, "High yield neutron generator based on a high-current gasdynamic electron cyclotron resonance ion source", *J. Appl. Phys.*, vol. 118, p. 093301, 2015, doi:10.1063/1.4929955

[6] V. Skalyga *et al.*, "High current proton beams production at Simple Mirror Ion Source 37", *Rev. Sci. Instrum.*, vol. 85, p. 02A702, 2014, doi:10.1063/1.4825074

[7] V. Skalyga *et al.*, "First experiments with gasdynamic ion source in CW mode", *Rev. Sci. Instrum.*, vol. 87, p. 02A715, 2016, doi:10.1063/1.4934208

[8] T. Kalvas *et al.*, "IBSIMU: A three-dimensional simulation software for charged particle optics", *Rev. Sci. Instrum.*, vol. 81, p. 02B703, 2010, doi:10.1063/1.3258608

[9] S. S. Vybin *et al.*, "High current ion beam formation with strongly inhomogeneous electrostatic field", arXiv:2009.02757

[10] J. Knaster *et al.*, "Overview of the IFMIF/EVEDA project", *Nucl. Fusion*, vol. 57, no. 5, 2017, doi:110.1088/1741-4326/aa6a6a

[11] S. Grigoriev *et al.*, "Spin-echo Small Angle Neutron Scattering for a Compact Neutron Source Daria", *J. Surf. Invest.*, vol. 13, pp. 1132–1134, 2019, doi:10.1134/S1027451019060314

[12] J. C. Yang *et al.*, "High Intensity heavy ion Accelerator Facility (HIAF) in China", *Nucl. Instrum. Methods Phys. Res., Sect. B*, vol. 317, pp.263-265, 2013, doi:10.1016/j.nimb.2013.08.046

[13] N. S. Smith *et al.*, "High brightness inductively coupled plasma source for high current focused ion beam applications", *J. Vac. Sci. Technol., B*, vol. 24, p.2902, 2006, doi:10.1116/1.2366617

[14] Michiro Sugitani, "Ion implantation technology and ion sources", *Rev. Sci. Instrum.*, vol. 85, p. 02C315, 2014, doi:10.1063/1.4854155

[15] D. Faircloth *et al.*, "ISIS Penning source extraction studies reveal the 3-dimensional Child–Langmuir effect", *Rev. Sci. Instrum.*, vol. 91, p. 043307, 2020, doi:10.1063/1.5129675

ISBN: 978-3-95450-226-4 ISSN: 2222-5692 doi:10.18429/JACoW-ECRIS2020-MOXZO01

STATUS OF THE 45 GHz MARS-D ECRIS*

D. Z. Xie†, J. Y. Benitez, M. Kireeff Covo, A. Hodgkinson, M. Juchno, L. Phair, D. Todd, L. Wang
Lawrence Berkeley National Laboratory, Berkeley, CA, USA

Abstract

Development of MARS-D, a 45 GHz next-generation Electron Cyclotron Resonance ion source (ECRIS) using a NbTi MARS-magnet, continues to move forward at LBNL. All of the key components of MARS-D have been nearly finalized, with recent completion of the magnet stress analyses. This article presents and discusses the status of this new 45 GHz ECRIS, such as the latest design features and the component fabrication plans likely taking place in the near future.

INTRODUCTION

The next generation of ECRIS will operate at substantially higher magnetic fields and microwave frequencies, therefore source development will require addressing a number of challenges. The most critical challenge is constructing a superconducting magnet system capable of producing the needed high-magnetic fields. Compared to the two existing superconducting ECRIS magnet geometries: Sext-In-Sol and Sol-In-Sext, the Mixed Axial and Radial field System (MARS) presents many advantages [1]. The key advantage is the efficiency with which MARS can generate minimum-B fields capable of extending the NbTi conductor to the next generation of ECRIS operating at 45 GHz, whereas using one of the two existing geometries will require higher-current superconductors, such as Nb_3Sn or HTS. To validate and demonstrate the MARS magnet geometry as the superior ECRIS magnet scheme, MARS-D, a demonstrative ECRIS operating at 45 GHz, was proposed and conceptual design of the source system was initiated in 2015 [2]. A NbTi MARS-magnet will be used to produce a minimum-B configuration of field maxima of 5.6 T axially and 3.2 T radially needed for the 45 GHz MARS-D. Over the subsequent years, efforts to further optimize the design of MARS-D have been continuing. In the following sections, the optimized mechanical layout and main features of MARS-D will be presented and briefly discussed, such as the updated magnet dimensions, the coil stress analyses, multiple-frequency plasma heating, preliminary design of the plasma chamber, and plans for the conventional ion source components.

MAGNET OPTIMIZATIONS

The initial magnet design of MARS-D reported in 2015 [2] incorporated a set of hexagonal solenoids to increase the axial mirror fields of the closed-loop-coil to achieve the required minimum-B field for ECRIS operations. Since that time a few changes have been made to optimize the magnet design. First, the closed-loop-coil has been slightly modified for better form aspect ratio and electrically divided into inner and outer subsections with different currents, as shown in Fig. 1a, to keep this coil operating further away from the NbTi critical current. To mitigate the hoop-stress and reduce magnet coil quenching, the hexagonal solenoids have been replaced with a set of round solenoids where some of them are either electrically divided or mechanically divided, as shown in Fig. 1b. Table 1 lists the updated inner and outer diameters, axial widths and locations, and the designed engineering current densities for all coil subsections for 45 GHz operation.

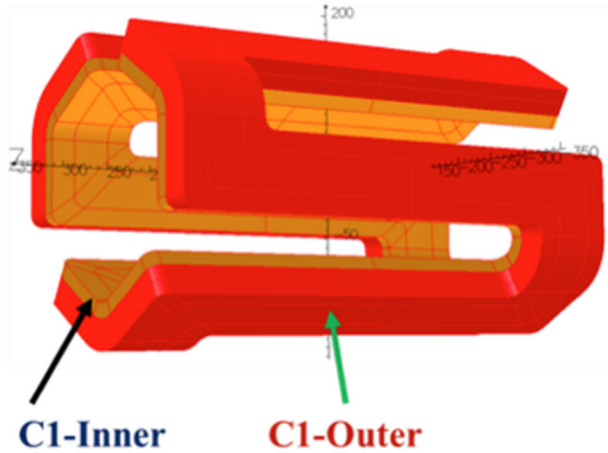

a

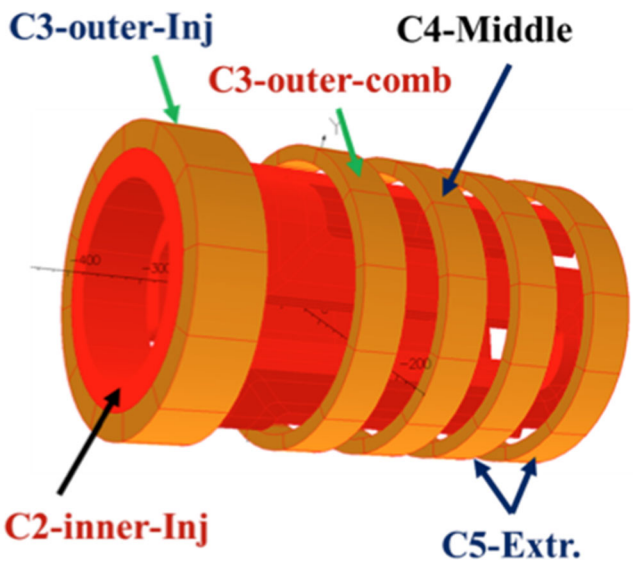

b

Figure 1: **a** and **b** show the optimized layout of the NbTi MARS-based-magnet with electrical subdivisions for a 45 GHz next generation ECRIS: MARS-D.

* Work was supported in part by the U.S. DOE, Office of Science, Office of Nuclear Physics under contract number DE-AC02-05CH11231.

† zqxie@lbl.gov

ISBN: 978-3-95450-226-4 ISSN: 2222-5692 doi:10.18429/JACoW-ECRIS2020-MOXZO01

Table 1: Coil Mechanical Dimensions and Designed Current Densities of the Optimized MARS-D Magnet for Operations at 45 GHz

Coil Subsection	ID/OD/W (mm)*	Axial Z_1: Z_2 (mm)**	Des. J_{eng} (A/mm^2)
C1-Inner	220*/252/78	-270 : 270	140
C1-Outer	252*/316/78	-270 : 270	210
C2-in-Inj	250/320.5/90	-370 : -280	140
C3-out-Inj	320.5/391/90	-370 : -280	180
C3-out-comb	351/391/60	-150 : -90	180
C4-Middle	351/391/60	-30 : 30	-200
C5-Extr. (1 & 2)	351/391/60	80 : 140 200 : 260	180

* Minimum ID and OD of the hexagonal shape of the closed-loop-coil, W is the coil axial length.

** Axial coil location Zs are referenced in the center of the closed-loop-coil.

COIL SUPPORT AND STRESSES

Figure 2 shows a sectional view of the updated MARS-D magnet cold mass comprised of the NbTi coils and the support structure. After exploring the possible schemes for coil clamping, a shell-based technique of Bladder and Key [3], schematically illustrated in Fig. 3, developed by the BCMT (Berkeley Center for Magnet Technology) at LBNL has been chosen to radially clamp the MARS-D magnet coils. 2-D and 3-D stress analyses of the MARS-D magnet system have shown that the MARS-D magnet comes with substantially lower stress compared to either a NbTi or a Nb_3Sn magnet using the existing "Sext-In-Sol" magnet geometry for 28 and 45 GHz operations. Comparisons of the maximum coil stresses for the three high-field ECRIS magnets at designed excitations are tabulated in Table 2. The lower stresses on the NbTi coils of the MARS-D magnet will benefit the operation reliability. Row 4 of Table 2 shows that MARS-D at 45 GHz operation has the lowest stored energy of the three at 560 kJ. The substantially lower stored energy in MARS-D magnet system is a result of its smaller magnet volume since the system stored energy is linearly proportional to both the conductor wire length and wire current squared. A five-cooler wet-closed cryostat with a hexagonally shaped warm bore matching the MARS's closed-loop-coil shape has been planned and will be fabricated by a commercial company.

QUAD-FREQUENCY HEATING

As shown in Fig. 4, a minimum-B field configuration has many closed, nested ECR Heating (ECRH) surfaces, which can be used to energize plasma electrons by injecting appropriate microwave frequencies simultaneously. Double-frequency plasma heating was successfully demonstrated enhancing the ECRIS performance in the 1990's [4] and is commonly employed in high charge state ECRISs. Further benefits were demonstrated with the first use of triple-frequency heating in SECRAL-II [5]. One of the merits of multi-frequency plasma heating in ECRISs is that it can efficiently combine more wave power, from a number of low-power wave sources, through the nested ECRH surfaces into the plasma.

As a 45 GHz 20 kW microwave source is not yet available in the North America, we plan to commission MARS-D using a combination of four-frequencies, 22, 28, 35 and 45 GHz, with a total power of ≃ 4 kW as listed in Table 3, to establish a baseline performance before an eventual power upgrade to ~ 20 kW. Quad-frequency plasma heating should provide an opportunity to further study the effects of multi-frequency plasma heating in high charge state ECRISs, especially for the production of low-intensity ultra-high-charge-state ion beams.

The use of four-frequency heating will also allow investigations into the effects of power density in ECRISs and serve as a test of one of Geller's scaling laws stating that the microwave power P_μ dependence on the angular frequency ω, the optimum charge state q_{opt} and the ECRH volume V (volume enclosed by the ECRH surface), is summarized as [6]:

$$P_\mu/V \sim \omega^{1/2} q_{opt}^3 \quad (1)$$

The third generation sources have seen approximately a doubling of frequency from second generation (2nd: 14-18 GHz, 3rd: 24-28 GHz), while the heating volumes and injected microwave powers have increased a factor of 3-5. For example, P_μ and V in AECR-U (14 GHz) are 2.1 kW and ~ 300 cm^3, while in VENUS (28 GHz) are 10 kW and ~ 1300 cm^3. These parameters result in a P_μ/V ratio of ~ 7.0 W/cm^3 in AECR-U and about ~ 7.5 W/cm^3 in VENUS, i.e., about the same for the two generations of ECRIS. So far it is not clear what and how important a role the ECRH volume plays in the greatly enhanced VENUS performance over AECR-U which seems to contradict Geller's scaling mentioned above [6]. Thus an investigation into the effects of ECRH volume could yield a better understanding of the ECR plasma.

The ECRH volume for each planned frequency in MARS-D is computed and listed in column 4 of Table 3. For instance, the 45 GHz ECRH volume in MARS-D is about 2.3 – 2.5 liters, about a factor of 2-3 of the 28 GHz volume in MARS-D or VENUS. In the future, one could analyze the performance of the four ECRIS generations to explore the advantages and differences for a better understanding and revisit the wave power scaling in question if needed. The quad-frequency heating capability in MARS-D will also make it possible to study the effects of each of the four ECRH volumes in a more systematic and detailed manner.

ISBN: 978-3-95450-226-4 ISSN: 2222-5692 doi:10.18429/JACoW-ECRIS2020-MOXZO01

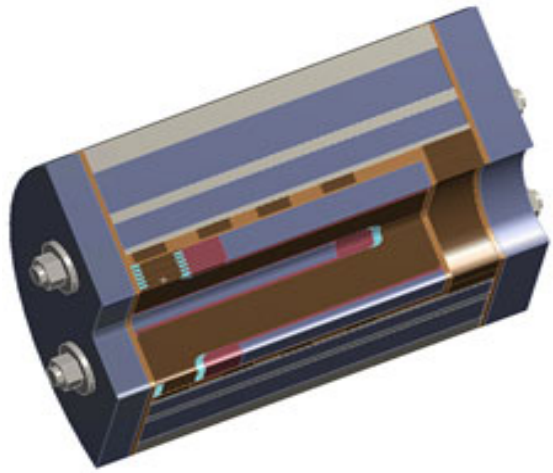

Figure 2: A sectional view of the optimized MARS-D NbTi magnet cold mass.

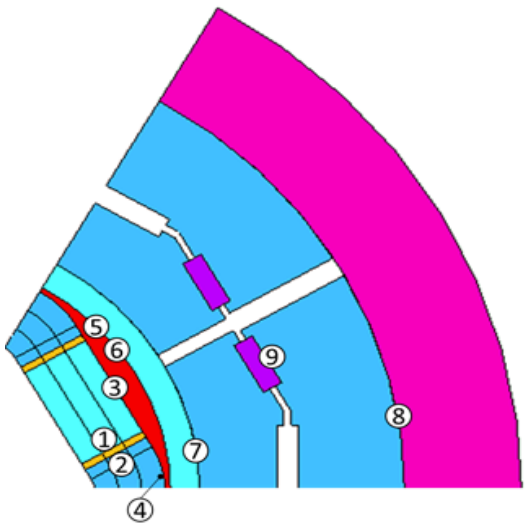

1. Coil to MoCu pole; **2.** MoCu to Iron pole; **3.** Coil/MoCu pole to Mandrel; **4.** Iron pole to Mandrel; **5.** Mandrel to Solenoid; **6.** Mandrel to Mandrel rib; **7.** Mandrel rib/Solenoid to Pad; **8.** Shell to Yoke; **9.** Yoke/pad to Key.

Figure 3: Interfaces between different cold mass materials are indicated. A Bladder and Key system will be used to radially pre-stress the coils of the MARS-D NbTi magnet.

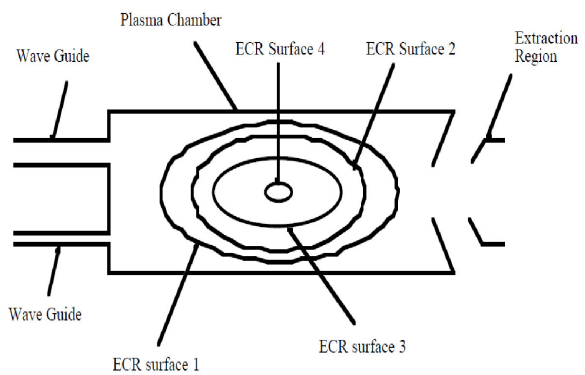

Figure 4. A schematic view of four nested ECR surfaces in a minimum-B field inside a plasma chamber of a high charge state ECRIS [4].

Table 2: Maximum Magnet Coil Stress of Three Magnet Systems for MARS-D, FRIB VENUS and IMP FECR

	FRIB VENUS[1]	IMP FECR[2]	MARS-D[3]
Frequency	28 GHz	45 GHz	**45 GHz**
Sextupole	140 MPa	144 MPa	**80 MPa**
Solenoids	90 MPa	100 MPa	**55 MPa**
Sys. stored Energy	720 kJ	1600 kJ	**560 kJ**
Geometry	Sext-In-Sol	Sext-In-Sol	**MARS**
Conductor	**NbTi**	**Nb_3Sn**	**NbTi**

[1] H. Felice, Report and Review on the FRIB VENUS magnet (Oct 2013) and (Sept 2014, unpublished).
[2] M. Juchno, Report on the IMP 45 GHz ECRIS magnet preliminary design review (Dec 2016, unpublished).
[3] M. Juchno, MARS-D NbTi Magnet Stress Analysis (June 2020, unpublished).

Table 3: Quad-frequency Heating Planned for Energizing the MARS-D Plasma

f (GHz)	Max. Power (kW)	B_{ecr} (T)	ECRH V (Liter)
22	1.5	0.79	0 – 0.4
28	1.0	1.00	0.5 – 0.9
35	1.0	1.25	1.1 – 1.5
45	0.5	1.61	2.3 – 2.5

Total power of 4 microwave sources ≃ 4.0 kW.

CONVENTIONAL SOURCE COMPONENTS AND BEAM OPTICS

A full superconducting ECRIS consists of three component categories: 1. The superconducting magnet; 2. The microwave sources; and 3. The conventional source components. Category 3 is the remainder as it is not addressed in the above Sections. To save engineering efforts and costs, most of the MARS-D conventional source components will be duplicated from the VENUS source system (e.g., beam optics, beam transport line, and ion beam analysis). Some of these duplications will involve minor revisions or simplifications, such as eliminating remote adjustment of the gap between the puller electrode and the extraction aperture, as VENUS is largely insensitive to the gap distance. The injection assembly will undergo somewhat larger changes, shortening it as much as possible to ease routine operations. The plasma chamber for MARS-D should meet a few requirements. First, it should be fabricated with a hexagonal shape matching the warm bore of the cryostat to maximize the utilization of the generated sextupole fields. Second, it should employ high x-ray attenuation in the

ISBN: 978-3-95450-226-4 ISSN: 2222-5692 doi:10.18429/JACoW-ECRIS2020-MOXZO01

plasma chamber to reduce the x-rays getting into the cryostat. Third, it should be able to sustain an anticipated 20 kW of wave power needed for intense ion beam production. A scheme, shown in Fig. 5, is being explored as a good candidate for the desired plasma chamber. A single rectangular water channel of ~ 21 mm^2 cross section is roughly equivalent to a single tube of 5-mm-diameter, and two of these channels near each plasma flute should be able to handle the anticipated maximum power deposition in the walls for ~ 20 kW operation.

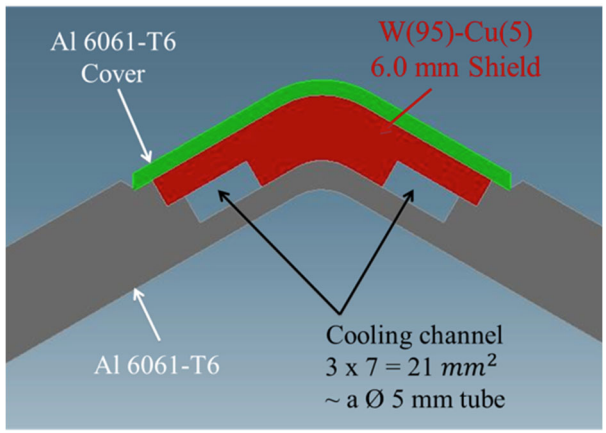

Figure 5. A cross-sectional view of a plasma flute in a hexagonal-shape plasma chamber with a W(95)/Cu(5) x-ray attenuator embedded inside the cooling channel.

For x-ray attenuation, tungsten will be used in place of tantalum as they have approximately the same atomic number, but tungsten is approximately 20% more dense and will attenuate more x-rays for the same thickness. Numerical computations indicate that a 6-mm-thick W(95)/Cu(5), planned for embedding in the MARS-D plasma flutes, will attenuate x-rays of energy ≤ 1 MeV by more than a factor of 2 compared to the 2 mm Ta shielding used in VENUS. This increased x-ray attenuation will help reduce the dynamic thermal load in the cryostat to keep the magnet functional at high frequency and power operation. The goal for the new W/Cu attenuator is to cope with at least the 4 kW power operation and a central field B_{min} of about 0.8 - 1.0 T during the commissioning which is substantially higher than in VENUS and could lead to very high yield of energetic x-rays [7]. The source commission with 4 kW should set up a baseline for future operations with higher power. Future solution is planned for the worst scenario by sacrificing more radial space to increase x-ray attenuation with thicker W/Cu slab and operating the source with as low B_{min} as possible to handle the operations with microwave power up to 20 kW.

DISCUSSION

The above presentation and discussion have shown that the MARS-D ECRIS is converging and nearly finalized on all the technical aspects. The optimized MARS magnet design and its lower coil stress are advantageous and should improve the operational reliability of the NbTi magnet for MARS-D. Once the NbTi MARS-magnet is constructed and tested, we will have passed the most difficult step, leaving only the fabrication of conventional source components and procurement of microwave sources. The utilization of quad-frequency plasma heating, even with limited power up to only 4 kW, will be a first for ECRISs. It could possibly lead to further enhancements of ECRIS performance, especially on the production of ultra-high charge state ion beams. In addition it will provide a new opportunity to study the merits of multiple-frequency plasma heating which will benefit the future ECRISs.

In summary the design of the 45 GHz MARS-D ECRIS has been optimized and source fabrication will begin once funding is available.

ACKNOWLEDGMENT

This work was supported in part by the U.S. Department of Energy, Office of Science, Office of Nuclear Physics under contract number DE-AC02-05CH11231.

REFERENCES

[1] D. Z. Xie, “A new structure of superconducting magnetic system for 50 GHz operations”, *Rev. Sci. Instrum.*, vol. 83, p. 02A302, 2012. doi.org/10.1063/1.3655530

[2] D. Z. Xie, J. Y. Benitez, A. Hodgkinson, T. Loew, C. M. Lyneis, L. Phair, P. Pipersky, B. Reynolds, and D. S. Todd, “Development status of a next generation ECRIS: MARS-D at LBNL,” *Rev. Sci. Instrum.*, vol. 87, p. 02A702, 2016. doi.org/10.1063/1.4931713

[3] S. Caspi *et al.*, "The use of pressurized bladders for stress control of Superconducting Magnets," *IEEE Trans. Appl. Supercond.*, vol. 11, no. 1, pp. 2272–2275, 2001.

[4] Z. Q. Xie, “Production of highly charged ion beams from electron cyclotron resonance ion sources,” *Rev. Sci. Instrum.*, vol. 69, p. 625, 1998. doi.org/10.1063/1.1148462

[5] L. T. Sun *et al.*, “High Power Operation with SECRAL-II Ion Source”, in *Proc. 23th International Workshop on ECR Ion Sources (ECRIS'18)*, Catania, Italy, Sep. 2018, pp. 58-62. doi:10.18429/JACoW-ECRIS2018-TUA5

[6] R. Geller *et al.*, “The Grenoble ECRIS Status 1987 and Proposals for ECRIS Scalings,” in *Proc. of the 8th ECR Workshop*, NSCL Report: MSUCP-47 (unpublished), E. Lansing, MI, USA, 1987, p1.

[7] D. Leitner, C. M. Lyneis, H. Koivisto, T. Ropponen, J. Ropponen, D. S. Todd, J. Y. Benitez, S. Gammino, “Measurement of the high energy component of the x-ray spectra in the VENUS electron cyclotron resonance ion source”, *Rev. Sci. Instrum.*, vol. 79, p. 033302, 2008. doi.org/10.1063/1.2821137

ISBN: 978-3-95450-226-4 ISSN: 2222-5692 doi:10.18429/JACoW-ECRIS2020-MOXZO02

CONCEPTUAL DESIGN OF HEAVY ION ToF-ERDA FACILITY BASED ON PERMANENT MAGNET ECRIS AND VARIABLE FREQUENCY RFQ ACCELERATOR

O. Tarvainen*, A. Letchford, D. Faircloth
STFC Rutherford Appleton Laboratory, ISIS, Harwell, OX11 0QX, United Kingdom
T. Kalvas, J. Julin
University of Jyväskylä, Department of Physics (JYFL), 40500 Jyväskylä, Finland

Abstract

We present a conceptual design of a heavy ion time-of-flight elastic recoil detection analysis (ToF-ERDA) facility based on a permanent magnet (PM) ECRIS and variable frequency RFQ designed to accelerate 1–10 pnA of $^{40}Ar^{8+}$, $^{84}Kr^{17+}$ and $^{129}Xe^{24+}$ ions to 4–7, 10–15 and 13–20 MeV. It is argued that the required beam currents can be achieved using the minimum-B quadrupole CUBE-ECRIS, which is currently being developed at JYFL. Beam dynamics studies demonstrate approximately 95% transmission of the heavy ion beams through the low energy beam transport (LEBT) and 70–80% efficiency through the RFQ. The predicted LEBT and RFQ transmissions of the CUBE-ECRIS with a rectangular extraction slit are almost similar to those of a conventional ECRIS with a circular extraction aperture. It is shown that approximately 10–20% of the ions can be accelerated to the desired energy with an energy spread $\Delta E/E$ below the required limit set by the ToF-ERDA resolution.

INTRODUCTION

Typical ToF-ERDA facilities are based on the concept shown in Fig. 1(a). The heavy ion beams (X^-) are produced with a caesium sputter ion source (see e.g. Ref. [1]). These ions are injected into a tandem-type accelerator where they are first accelerated by the terminal voltage, stripped at the terminal to produce positive ions with a charge state distribution (X^+ ... X^{n+}) and finally accelerated by the terminal voltage into the sample chamber at laboratory ground through an m/q-separation magnet selecting the ion energy.

The concept has benefits and drawbacks. The advantages are: the required beam currents of 1–10 pnA (i.e. particle nanoamperes at the target) can be produced from a wide range of elements; the ion beam energy can be varied over a range of several MeV through the adjustment of the accelerator terminal voltage and selection of the final charge state; the same accelerator can be used for Rutherford Backscattering Spectrometry if equipped with a negative helium (He^-) ion source. By contrast: the stability of the ion source and the lifetime of its cathode can prolong the measurement time and cause downtime of the facility; tandem-based IBA facilities tend to be large in size as the accelerator terminal voltage is on the order of several MV and often needs SF_6-insulation to work, which requires special management (SF_6 is a potent green house gas with an estimated 23,900 times "global warming potential" of CO_2 [2]).

The majority of ToF-ERDA investigations can be carried out with the ion beams (elements) listed in Table 1. All listed beams are halogens, which are easy to produce with the negative sputter ion source from caesium salt targets.

Table 1: Typical Ions (Elements) and Beam Energies Used in ToF-ERDA

Ion	Energy [MeV]
$^{35/37}Cl$	4–10
$^{79/81}Br$	10–15
^{127}I	13–20

PROPOSED ToF-ERDA FACILITY

We introduce an alternative ToF-ERDA concept, shown schematically in Fig. 1(b). The benefits are: increased reliability of the ion source, reduced operational effort and maintenance, lack of SF_6 electrical insulation and smaller

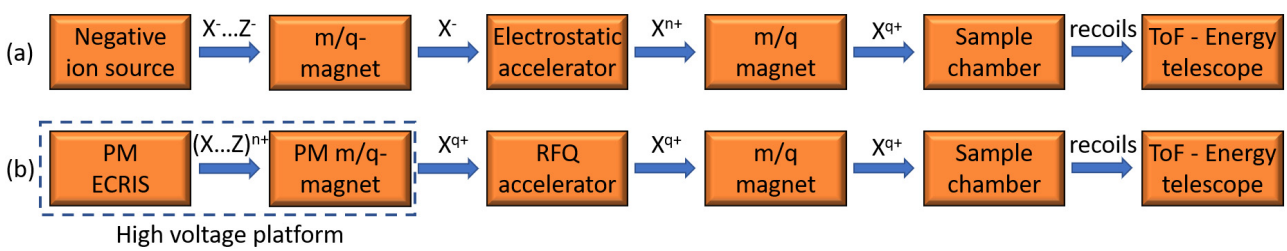

Figure 1: (a) The concept of a typical ToF-ERDA facility based on negative ion source and an electrostatic accelerator. (b) An alternative concept based on permanent magnet ECRIS and variable frequency RFQ accelerator.

* olli.tarvainen@stfc.ac.uk

ISBN: 978-3-95450-226-4 ISSN: 2222-5692 doi:10.18429/JACoW-ECRIS2020-MOXZO02

laboratory footprint in comparison to most tandem-type accelerators. This conceptual study has been carried out to support the planning of the UK National Thin Film Deposition and Characterisation Centre (led by Daresbury Laboratory). The proposed concept is intended to complement the arsenal of quantitative characterisation methods available for users by allowing the measurement of elemental depth profiles of thin films containing both heavy and light elements in nanometer-scale.

The main components of the proposed TOF-ERDA equipment are

- High charge state permanent magnet electron cyclotron resonance ion source (PM-ECRIS).
- Low energy beam transport (LEBT) with electrostatic focusing and permanent magnet m/q-separator.
- Two-stage low energy acceleration platform.
- Variable frequency RadioFrequency Quadrupole (RFQ) accelerator.
- High energy beam transport (HEBT) with energy dispersive separator, i.e. bending magnet.
- Sample chamber with an option of an auxiliary Rutherford Backscattering Spectrometry (RBS) system.
- Time of Flight – Energy telescope for the detection of recoils.

The design is based on a variable frequency RFQ accelerator, approximately 1.9 m long and with a frequency range of 79–107 MHz. Such accelerator would be an SF_6-free solution producing beams listed in Table 2, i.e. with noble gas ions replacing the halogens. The beam currents listed in Table 2 are the m/q-analyzed electric currents (eμA) through the LEBT required to achieve 1–10 pnA at the target with the desired energy spread ($\Delta E/E$ <0.2%).

Permanent Magnet ECRIS

The ion beams in Table 2 can be produced with modern PM-ECRISs with an order of magnitude margin in beam intensities (see the literature survey in Ref. [3]). A conventional minimum-B ECRIS with solenoid and sextupole field components can be considered an overkill for the task. Therefore, the primary candidate for the ion source is the 10 GHz CUBE-ECRIS under construction at JYFL accelerator laboratory. The CUBE-ECRIS is a PM version of the ARC-ECRIS, i.e. it has a minimum-B quadrupole magnetic field topology. The magnet structure is very simple in comparison to conventional PM ECRISs and the resulting field fulfills the semiempirical scaling laws [4] as shown in Fig. 2. The physics design of the CUBE-ECRIS is presented in Ref. [3]. First results from the prototype are expected in 2021.

Table 2: Ions, Beam Energies and Required m/q-analysed LEBT Beam Currents for RFQ-based ToF-ERDA

Ion	Energy [MeV]	Current [eμA]
$^{40}Ar^{8+}$	4–7	0.1–1.0
$^{84}Kr^{17+}$	10–15	0.2–2.2
$^{129}Xe^{24+}$	13–20	0.3–3.0

Low Energy Beam Transport

The expected shape of the beam spot extracted from the CUBE-ECRIS differs from the beam spot of a conventional PM ECRIS. That is because the plasma flux distribution from a quadrupole magnetic field topology favors a rectangular slit instead or a round aperture to extract the beam [3]. Thus, two versions of the low energy beam transport have been simulated comparing the expected LEBT transmissions of the CUBE-ECRIS and conventional ECRIS. The CUBE-ECRIS LEBT is based on a two-stage acceleration with the ion source at approximately +10 kV potential with respect to the LEBT platform, electrostatic quadrupole doublet (EQ1–EQ2), 90° m/q-analysis magnet (DIP) and electrostatic quadrupole triplet (EQ3–EQ5) all on the high voltage platform. Meanwhile, the LEBT design for the conventional ECRIS is based on a 90° m/q-analysis magnet on the platform and a solenoid magnet (SOL) at laboratory ground focusing the beam into the RFQ. The LEBT simulations were

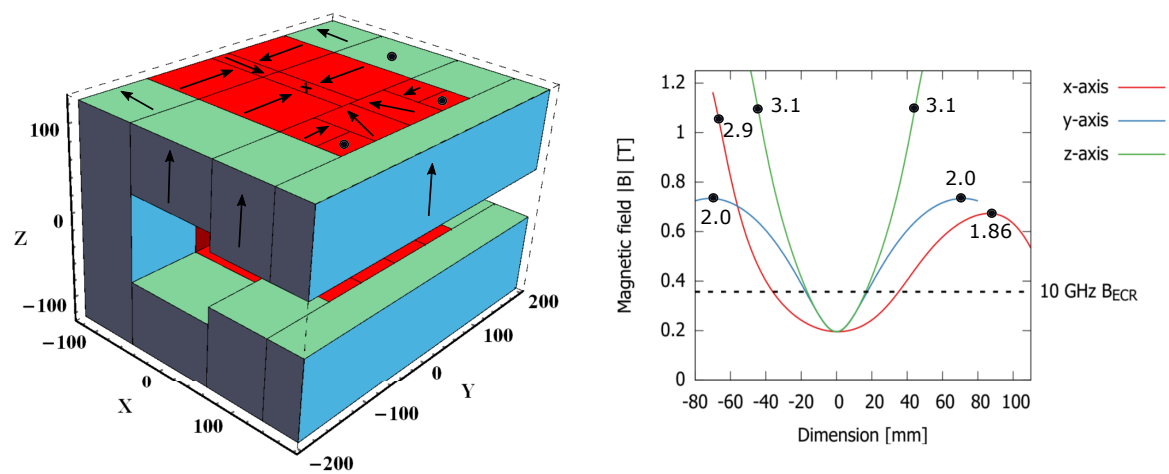

Figure 2: The permanent magnet array and magnetic field of the prototype 10 GHz CUBE-ECRIS. The magnetization vectors are mirrored about the $z = 0$ plane. The mirror ratios (B_{max}/B_{ECR}) on each axis are marked with the black dots.

ISBN: 978-3-95450-226-4 ISSN: 2222-5692 doi:10.18429/JACoW-ECRIS2020-MOXZO02

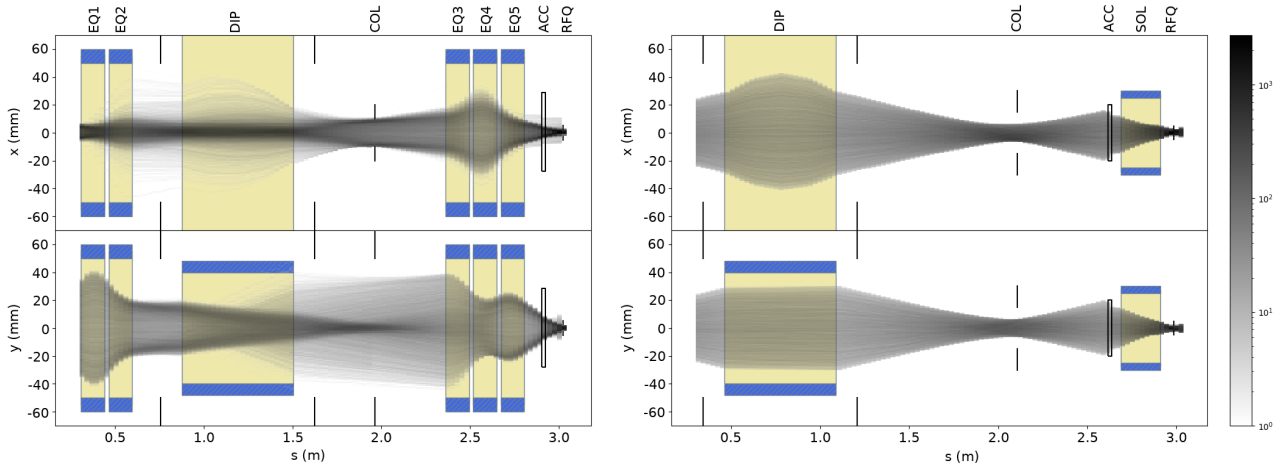

Figure 3: The optimized LEBT solutions for the CUBE-ECRIS (left) and a conventional PM-ECRIS (right).

made with Python-driven Ion Optics Library, PIOL (under development at JYFL), using third order matrices. Figure 3 shows an example of the simulations for Ar^{8+}. The simulation of the conventional ECRIS LEBT assumes similar beam properties to the JYFL 14 GHz ECRIS, i.e. diverging beam with 0.1 mm·mrad normalized rms emittance in both transverse planes. For both LEBT options and beams shown in Table 2 the calculated LEBT transmission is 93–97%. The given number is the total transmission through the LEBT, not the fraction of the beam in the RFQ acceptance, which is discussed later. The expected ~95% transmission is similar to the CUBE-ECRIS prototype beamline with an electrostatic quadrupole doublet and a 135° dipole magnet (loaned from GANIL), under commissioning at JYFL. Thus, the first experimental m/q-analysed beam currents should match those in Table 2 to demonstrate the feasibility of the CUBE-ECRIS concept for the IBA-application.

The two-stage acceleration allows extracting all three noble gas ion species with 10–11 kV ion source potential and using a permanent magnet dipole for the m/q-separation before accelerating the ions into the RFQ. The combined platform + ion source voltage ranges from 18.75 kV to 31.25 kV corresponding to 4 MeV argon and 20 MeV xenon out of the RFQ, respectively. The use of the PM dipole minimizes the power consumption of the LEBT platform. Figure 4 shows a preliminary simulation of a 90° PM bending magnet with 35° entrance and exit angles (used in the LEBT simulation). The magnetic field can be adjusted in the range of 68–91 mT by moving the "magnet cartridge" radially with respect to the apex of the reference beam trajectory. However, for the IBA-application it is more convenient to adjust the ion source potential to select the beam. In Fig. 4 the dipole field is 83 mT, achieved when the cartridge is moved 25 mm outwards from the position corresponding to the maximum field i.e. when the cartridge is perfectly aligned with the gap in the return yoke. The radial uniformity of the field ($\Delta B/B$) is better than 10^{-3} in the volume occupied by the beam (i.e. $-40\,\text{mm} < r < 40\,\text{mm}$). The uniformity of the field is affected by the volume of the PM material in the thin layers between the magnet pole pieces and the return yoke.

Variable Frequency RFQ

The Radio Frequency Quadrupole (RFQ) is an RF accelerator particularly well suited to the acceleration of low velocity ions due to its use of transverse electric rather than magnetic fields for focussing the beam. The RFQ has four symmetrically placed electrodes inside a resonant cavity which concentrate the TE21 quadrupole mode into a small beam channel. By carefully shaping or modulating the beam facing surfaces of the electrodes a component of the transverse field is directed into the longitudinal direction to provide acceleration.

Because it is an RF accelerator a strict requirement for the RFQ is synchronism between the particles and the RF field.

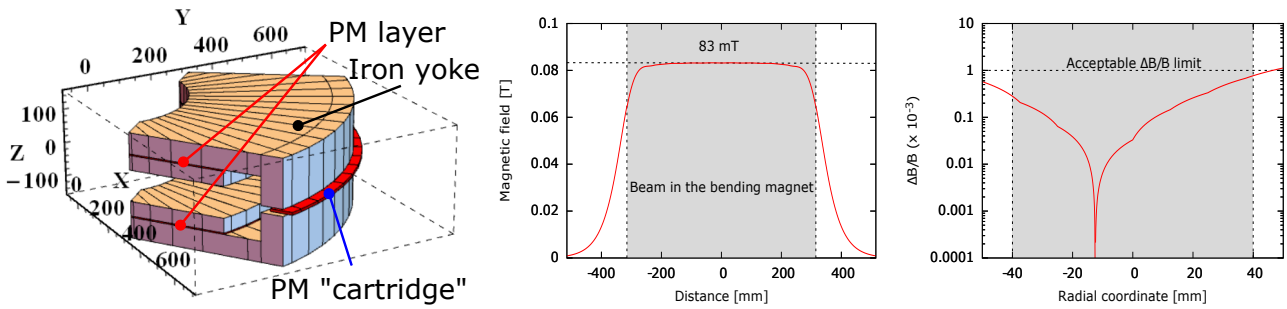

Figure 4: The permanent magnet dipole (left), its magnetic field along the reference particle trajectory (center) and the radial uniformity of the field, $\Delta B/B$ (right).

ISBN: 978-3-95450-226-4 ISSN: 2222-5692 doi:10.18429/JACoW-ECRIS2020-MOXZO02

For a fixed frequency RFQ this translates into a fixed velocity profile. Any ions with the same charge to mass ratio can be accelerated with the final energy being proportional to the mass. Ions with different charge to mass ratios can also be accommodated by varying the strength of the electric field (or RF power level) within the constraint that the maximum surface electric field is not exceeded. In order to achieve variable energy in a single structure it is necessary to adjust the operating frequency. Designing a frequency adjustable, high Q resonant cavity is certainly the biggest challenge in realising a variable energy RFQ however several such devices have been built previously [5–8]. At this stage of the study only the beam dynamics of the RFQ have been considered.

A particular feature of the RFQ is its ability to take a continuous beam from an ion source and bunch it for stable RF acceleration with very high capture efficiency even for high current beams with large space charge forces. This is achieved by a slow, quasi-adiabatic bunching process for which there are well developed design procedures. In the context of low current, high charge state heavy ion beams for IBA this type of design has several disadvantages: (i) Adiabatic bunching can result in a rather long structure. (ii) The slow increase in the electrode modulation can lead to features that are at or beyond the limit of ordinary machining processes. (iii) Constraints on the adiabatic bunching can mean that the longitudinal emittance is not a free parameter resulting in large energy spread.

In order to overcome these disadvantages a different approach has been taken for the IBA RFQ. The long adiabatic bunching section has been replaced by a discrete buncher and drift followed by a capture section. This results in a somewhat shorter RFQ with larger modulation at the beginning and greater control over the energy spread at the cost of reduced total capture efficiency. Figure 5 shows the RFQ parameters. The graphed energy is for the case of $^{129}Xe^{24+}$ accelerated to 20 MeV where the total energy spread is ~0.5%. The total beam transmission η and fraction of beam below 0.2% and 0.5% energy spread are shown in Table 3. These values were calculated by tracking the particle distributions at the end of the LEBT through the RFQ. The total transmission through the RFQ is somewhat better for the conventional ECRIS and its LEBT but the difference to CUBE-ECRIS is very small when the energy spread is restricted (by slits in the high energy beamline).

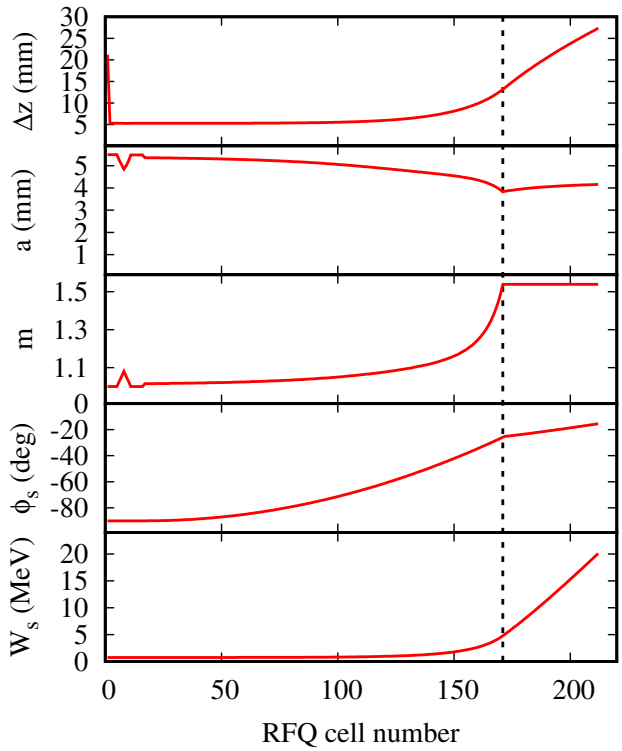

Figure 5: The RFQ parameters along the 1.92 m length of the structure (cell number): Δz is the length of each cell, a the minimum distance of the vane tip from the axis, m the vane modulation, ϕ_s the synchronous phase and W_s the energy of the synchronous $^{129}Xe^{24+}$ ion. The vertical dashed line marks the transition into the accelerating section.

High Energy Beam Transport and Time of Flight – Energy Telescope

The use of the variable frequency RFQ accelerator means that the beam is pulsed at the RFQ frequency with the beam pulses occupying approximately 20% of the time domain, which translates to 2 ns pulses at 10 ns interval for 100 MHz RFQ frequency. The beam can be considered to be semi-continuous if there is sufficient temporal overlap of recoils hitting the first timing detector produced by successive beam

Table 3: The calculated ion beam final energy E, RFQ frequency f and vane voltage V_{vane}, ion source potential V_{source}, total beam transmission η and fraction of beam for which certain $\Delta E/E$. The transmission values are for the CUBE-ECRIS and its LEBT with the corresponding values for the conventional ECRIS and its LEBT in parentheses.

Ion	E [MeV]	f [MHz]	V_{vane} [kV]	V_{source} [kV]	η [%]	$\Delta E/E$ <0.5%	$\Delta E/E$ < 0.2%
$^{40}Ar^{8+}$	4	79.687	56.7	18.75	69 (84)	23 (29)	9 (11)
$^{40}Ar^{8+}$	7	105.416	63.0	32.81	76 (93)	25 (29)	9 (9)
$^{84}Kr^{17+}$	10	86.946	42.4	22.06	70 (87)	20 (27)	8 (13)
$^{84}Kr^{17+}$	15	106.486	63.5	33.09	76 (93)	21 (28)	9 (13)
$^{129}Xe^{24+}$	13	79.995	39.0	20.31	70 (81)	22 (29)	8 (13)
$^{129}Xe^{24+}$	20	99.222	60.0	31.25	70 (87)	25 (29)	8 (10)

ISBN: 978-3-95450-226-4 ISSN: 2222-5692 doi:10.18429/JACoW-ECRIS2020-MOXZO02

pulses. For example, the 100 MHz repetition rate is sufficiently high, depending on spectrometer design, if the recoil times-of-flight span more than 50 ns. Typically, the times-of-flight are in the range of some 100 ns, which implies that for this application the RFQ beam can be considered continuous.

The energy spread of the beam incident on the target can be limited by a high-resolution dipole magnet coupled with a pair of slit plates. The maximum allowed energy spread can be estimated by assuming that the intrinsic ToF spectrometer energy resolution must be greater by some factor than the broadening in recoil spectra caused by incident beam energy variation.

For the proposed beams the energy resolution of the spectrometer for surface recoils can be calculated. One of the figures-of-merit of interest for a ToF-ERDA system is the achievable depth resolution, which is affected not only by instrumentation but fundamental ion-matter interactions like energy-loss straggling and multiple scattering.

Table 4: Relative energy resolution (%) of the proposed time-of-flight spectrometer for various surface recoils, and scattered incident beam ion from ^{197}Au, taking into account timing resolution, kinematic broadening due to finite detector solid angle, and energy loss straggling in the first timing foil.

Ion	E MeV	^{1}H %	^{16}O %	^{28}Si %	^{197}Au (sc.) %
$^{40}Ar^{8+}$	4	0.56	0.41	0.39	0.31
$^{40}Ar^{8+}$	7	0.53	0.42	0.39	0.33
$^{84}Kr^{17+}$	10	0.54	0.42	0.39	0.29
$^{84}Kr^{17+}$	15	0.54	0.46	0.42	0.31
$^{129}Xe^{24+}$	13	0.56	0.41	0.39	0.27
$^{129}Xe^{24+}$	20	0.53	0.45	0.42	0.28

In Table 4 we have considered effects related to ERD kinematics and intrinsic timing resolution (150 ps), kinematic broadening due to finite detector size or position sensitivity (1 mrad), as well as energy loss straggling in the first carbon foil (thickness 2 μg cm^{-2}) for surface recoils in a ToF spectrometer with a flight path length of 600 mm installed to an angle of 40° relative to the beam. The depth resolution degrades rapidly deeper in the sample especially for heavier recoils, so these values of 0.2–0.6% should be considered optimistic estimates of real world performance. It is concluded that an incident energy spread of 0.2% would be sufficiently small to account for the difference between the optimistic estimate and actual performance of the spectrometer. The assumptions made are based on realistically achievable ToF-ERDA spectrometer design [9, 10].

DISCUSSION AND OUTLOOK

The main advantage of the proposed RFQ based IBA-system over the state-of-the-art negative ion based facilities is the use of (high charge state) noble gas ions, which allows the production of these beams with the PM-ECRIS to be automated into a turn-key system with minimal user involvement. The same applies to the tuning of the RFQ once the correct combination of injection energy, RF frequency and electrode voltage (RF power) for each final ion energy has been determined.

In addition to the RFQ, we have considered the possibility of using a high charge state PM ECRIS on a high voltage platform to produce the desired beams. The benefit of the platform option would be the addition of He^{2+} beam into the arsenal, and hence enabling the use of RBS with the same accelerator. However, the platform voltage would need to be 750–800 kV to achieve the same range of final ion energies as with the RFQ. Such platform would be prohibitively large –its reliable operation would require a laboratory space up to 10 squash courts (in volume) – and the RBS energies of 1.6 MeV as a maximum would be only borderline acceptable for the proposed STFC facility.

The proposed ToF-ERDA concept has been submitted to STFCs internal evaluation as a part of the National Thin Film Deposition and Characterisation Centre with the possible funding decision of a technical design study expected in 2020–2021. Meanwhile the development of the CUBE-ECRIS is ongoing at the JYFL accelerator laboratory. The success of the CUBE-ECRIS prototype will define the choice of the ion source for the project.

REFERENCES

[1] R. Middleton, "A versatile high intensity negative ion source", *Nucl. Instrum. Methods Phys. Res.*, vol. 214, no. 2–3, pp. 139-150, 1983. doi:10.1016/0167-5087(83)90580-X

[2] P. Forster *et al.*, "Global Warming Potentials …", in *IPCC Second Assessment Report*, chap. 2.10. https://www.ipcc.ch/site/assets/uploads/2018/02/ar4-wg1-chapter2-1.pdf

[3] T. Kalvas, O. Tarvainen, V. Toivanen, and H. Koivisto, "Design of a 10 GHz minimum-B quadrupole permanent magnet electron cyclotron resonance ion source", *J. Instrum.*, vol. 15, p. P06016, 2020. doi:10.1088/1748-0221/15/06/P06016

[4] D. Hitz, A. Girard, G. Melin, S. Gammino, G. Ciavola, and L. Celona, "Results and interpretation of high frequency experiments at 28 GHz in ECR ion sources, future prospects", *Rev. Sci. Instrum.*, vol. 73, p. 509-512. doi:10.1063/1.1429313

[5] A. Schempp *et al.*, "Development of a Variable Energy RFQ for Cluster Acceleration", *Conference Record of the 1991 IEEE Particle Accelerator Conference*, San Francisco, CA, USA, 1991, pp. 3053-3055 vol. 5. http://jacow.org/p91/PDF/PAC1991_3053.PDF

[6] K. Stiebing *et al.*, "The Frankfurt ECRIS-RFQ facility for materials research with highly charged ions", *Nucl. Instrum. Methods Phys. Res., Sect. B*, vol. 113, no. 1–4, pp. 34-37, Jun. 1996. doi:10.1016/0168-583X(95)01413-6

[7] K. Amemiya *et al.*, "Aluminum Ion Implantation using a Variable Energy RFQ Implanter", in *Proc. EPAC'98*, Stockholm, Sweden, 1998, pp. 2419-2421. http://jacow.org/e98/PAPERS/WEP31C.PDF

ISBN: 978-3-95450-226-4 ISSN: 2222-5692 doi:10.18429/JACoW-ECRIS2020-MOXZO02

[8] K. Amemiya *et al.*, "Development of a continuously variable energy radio frequency quadrupole accelerator for SiC power semiconductor device fabrication", *Nucl. Instrum. Methods Phys. Res., Sect. B*, vol. 188, no. 1–4, pp. 247-250, Apr. 2002. doi:10.1016/S0168-583X(01)01107-7

[9] M. Laitinen, M. Rossi, J. Julin, and T. Sajavaara, "Time-of-flight – Energy spectrometer for elemental depth profiling – Jyväskylä design", *Nucl. Instrum. Methods Phys. Res., Sect. B*, vol. 337, pp. 55-61, 2014. doi:10.1016/j.nimb.2014.07.001

[10] S. Eschbaumer, A. Bergmaier, and G. Dollinger, "A position sensitive time of flight detector for heavy ion ERD", *Nucl. Instrum. Methods Phys. Res., Sect. B*, vol. 371, pp. 125-131, 2016. doi:10.1016/j.nimb.2015.09.036

ISBN: 978-3-95450-226-4 ISSN: 2222-5692 doi:10.18429/JACoW-ECRIS2020-MOYZO01

IMAGING IN X-RAY RANGES TO LOCALLY INVESTIGATE THE EFFECT OF THE TWO-CLOSE-FREQUENCY HEATING IN ECRIS PLASMAS*

R. Rácz†, S. Biri, Z. Perduk, J. Pálinkás, Institute for Nuclear Research (Atomki), Debrecen, Hungary
E. Naselli[1], M. Mazzaglia, G. Castro, L. Celona, S. Gammino, D. Mascali, G. Torrisi, INFN-Laboratori Nazionali del Sud, Catania, Italy
A. Galatá, INFN-Laboratori Nazionali di Legnaro, Legnaro, Italy
[1]also at Name of Universita degli Studi di Catania, Catania, Italy

Abstract

Plasma instabilities limit the ECR Ion Sources performances in terms of flux of the extracted highly charged ions by causing beam ripple and unstable operation conditions. In a 14 GHz ECRIS (Atomki, Debrecen), the effect on the plasma instabilities in an Argon plasma at Two Close Frequencies heating scheme (the frequency gap is smaller than 1 GHz) has been explored. A special multi-diagnostic setup has been designed and implemented consisting of detectors for the simultaneous collection of plasma radio-self-emission and of high spatial resolution X-ray images in the 500 eV - 20 keV energy domain (using an X-ray pinhole camera setup). We present the comparison of plasma structural changes as observed from X-ray images in single and double-frequency operations. The latter has been particularly correlated to the confinement and velocity anisotropy, also by considering results coming from numerical simulations.

INTRODUCTION

Electron Cyclotron Resonance (ECR) Ion Sources (ECRIS) are used to produce highly charged plasmas and ion beams [1]. The ion beams are usually injected into to a high energy accelerator to provide high energy ions mainly for nuclear and particle physics experiments. Demand from the users were strongly motivating the improvement and development of ion source performances since the appearance of the pioneer ECRISs.

To produce highly charged ions hot plasma should be generated. Due to the magnetic confinement of the charged particles the velocity distribution of the energetic electrons is strongly anisotropic in the plasma. This anisotropy can cause plasma kinetic instability [2] limiting the energy content of the plasma and therefore the number of the extracted highly charged ions.

Appearance threshold of the kinetic instability was investigated intensively. Strong correlation between the magnetic field configuration of the source and the onset of the instability was found [3]. The instability always raises when the B_{min}/B_{ECR} exceeds a value around 0.8 (where B_{min} and B_{ECR} are the minimum magnetic field and the resonant magnetic field, respectively). This value slightly varies with the other operation conditions of the ion source (gas pressure, microwave power). Recent study [4] shown that the spectral temperature of the plasma is increasing monotonically toward the threshold value and then saturates. Energy content of the plasma cannot be increased anymore, the electrons losses caused by the unstable condition dominates the plasma processes.

Several experiments demonstrated that the plasma stability and therefore the ion beam stability can be improved by applying two frequency heating of the plasma. Both two far (resulting in two well separated ECR heating zones) and two close (frequency gap is comparable with the scale-length of the resonance) frequency heating were investigated [5, 6].

While the beneficial effect of the multiple frequency heating is proved [7] the mechanism and the dynamics of the processes caused by the second frequency are still not fully known. Therefore, we have investigated the effect on the plasma instabilities in an Argon plasma at Two Close Frequencies Heating (TCFH) scheme using two diagnostic tools; a two-pins RF probe connected to a spectrum analyzer (SA) and an X-ray pinhole camera.

Parameters of the radiofrequency spectra (obtained by the RF probe) can be used as an indication of stable and unstable plasma conditions and a quantitative estimation of the strength of the instability can be done [6].

The high spatial resolution X-ray images (taken by the pinhole camera) are used to monitor the structural changes of the plasma when the second frequency is injected.

Furthermore, numerical simulation to investigate the velocity distribution of the plasma electrons were done to interpret the complex information obtained by the help of the two diagnostic tools.

EXPERIMENTAL SETUP

Argon plasma were generated by the 14 GHz, room temperature Atomki ECRIS [8]. The B-minimum trap consists of two room temperature coils and of a NdFeB permanent magnet hexapole. The radial magnetic field measured at the plasma chamber wall is about 1.1 Tesla while the axial magnetic peak fields along the axes of the plasma chamber are 1.26 T at the injection side and 0.95 T at the extraction side. The minimum value (B_{min}) is 0.39 T.

* Work supported by the 3th Nat. Comm. of INFN, under the Grant PANDORA_Gr3, for the financial support and has received funding from the European Union's Horizon 2020 research and innovation program under grant agreement No 654002 (ENSAR2-MIDAS).
† rracz@atomki.hu

ISBN: 978-3-95450-226-4 ISSN: 2222-5692 doi:10.18429/JACoW-ECRIS2020-MOYZO01

The plasmas were heated by single and double frequency mode. The first 14.25 GHz signal was amplified by a klystron while the second tuneable one was provided by a TWT Amplifier operating in 13.6 GHz - 14.6 GHz frequency range. Microwaves were launched through only one waveguide by mixing the two RF signals before the plasma chamber by a power combiner. Both the forwarded and the reflected powers were measured at the closest possible point to the plasma chamber.

Schematic drawing of the experimental setup can be seen in Fig. 1.

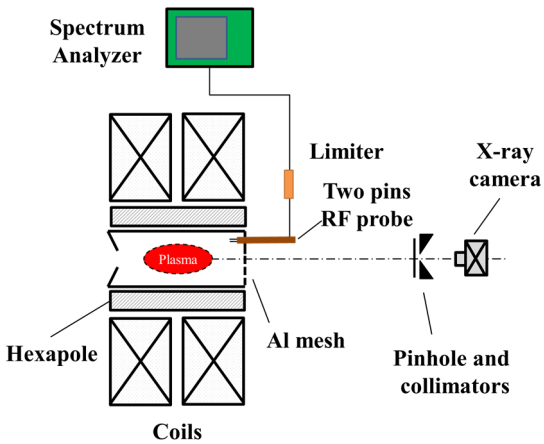

Figure 1. Drawing of the experimental setup with the two diagnostics tools.

The injection plate of the plasma chamber was adapted to the X-ray imaging: the area of the Al made circle shape injection plate was divided into two regions in the ratio 2:1. The smaller area was used for microwave and gas injection, furthermore to insert the RF-probe directly inside the plasma chamber. The larger part was closed by an Al mesh to form closed resonant cavity and to provide transparency for X-ray imaging at same time.

The X-ray pin-hole camera for 2D space resolved spectroscopy [9], consisting in a CCD camera and a lead pinhole. The CCD camera is made of 1024 x 1024 pixels and sensitive the range 500 eV - 20 keV. It was coupled to a Pb pin-hole (thickness 2 mm, diameter Φ = 400 μm) and placed along the axis, facing the chamber from the injection flange. A Titanium window with 9.5 μm thickness was used to screen the CCD from the visible and UV light coming out from the plasma. A multi-disks (disks with the same thickness and different hole diameter) lead collimator [10] was used as extra shielding, developed to acquire X-ray picture at up to 200 W of total incident power with appropriate signal over noise ratios. The magnification of the imaging system was 0.244.

A two-pins RF probe was connected to a Spectrum Analyser (SA) in order to detect the plasma emitted EM waves in GHz ranges characteristics of the kinetics instabilities. The flexible two-pins RF probe has an outer diameter of 4mm and a pin length of 3.5 mm. The pin distance is 2 mm. The Spectrum Analyser is operated in the range 13-15 GHz. The resolution bandwidth was 3 MHz with a sweeping time of 400 ms.

ANIZOTROPY VS. B_{MIN}/B_{ECR}

We have performed simulation of plasma electrons in the magnetic trap of the Atomki ECRIS under ECR conditions in single frequency heating (SFH) mode to investigate the effect of the B_{min}/B_{ECR} to the anisotropy of the plasma electrons by changing the resonant frequency (consequently the resonant field). The simulation was done by TrapCAD [11, 12], which is a numerical code using a single electron approach neglecting the particle-particle interactions. The electron heating using the electron–cyclotron-resonance process is calculated by assuming a simple RF field but using realistic magnetic field configuration. A circularly polarized plane wave is assumed propagating along the z-axis. The electric vector of this type of wave is rotating in the x-y plane of the chamber. A 4th-order Runge-Kutta method is applied for the integration of the magnetic field line equation. The Lorentz force integration is processed by a time-centered leapfrog scheme explicitly solving the motion equations. The time-step of the code was set to be 3ps.

SFH mode was modelled by running the code for 15 configurations. The RF frequency was scanned from 11 GHz to 18 GHz with 500 MHz steps. The corresponding ratio B_{min}/B_{ECR} is increasing from 0.6 to 0.99 by changing the frequency from 18 GHz to 11 GHz. 100,000 electrons were started from the resonant zone with 5.5 eV initial average kinetic energy both for parallel and perpendicular velocity components. Simulation is ended after 200 ns (i.e. after many RF cycles and thus giving the opportunity to the whole simulated electron bunch to interact with the wave), while the RF power was set to 200W which corresponds to 134 V/cm electrical field in the given cylindrical ECRIS plasma chamber.

Figure 2 shows the average kinetic energy of the electrons related to the parallel and the perpendicular components. The “anisotropy parameter” has been then calculated as the ratio of the average kinetic energy corresponding to the parallel and perpendicular velocity component of the electron: An = <E_l>/<Ell>. Dependence of “An” as function of the $Bmin/B_{ECR}$ is plotted in Fig. 3.

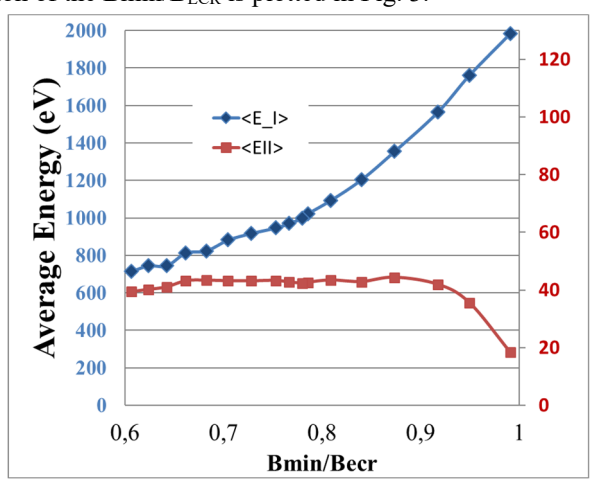

Figure 2. Average Energy of the parallel (EII) and the perpendicular (E_I) velocity components of the non lost electrons.

ISBN: 978-3-95450-226-4 ISSN: 2222-5692 doi:10.18429/JACoW-ECRIS2020-MOYZO01

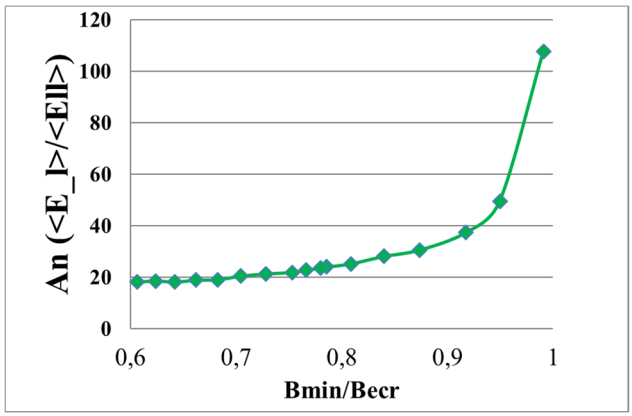

Figure 3. Dependence of the anisotropy parameter.

This plot underlines the escalation of the anisotropy toward higher B_{min}/B_{ECR} ratios. The escalation starts close to the experimentally observed 0.8 threshold value and rapidly rises above 0.95. In the next section we will compare the anisotropy changes effected by the second frequency with the experimental results obtained by the X-ray camera and RF diagnostic system.

RESULTS AND DISCUSSION

We were taking series of X-ray images and RF spectra in single and in two frequency operation mode. In single frequency operation mode the frequency was swept from 13.6 GHz to 14.6 GHz with 50 MHz frequency steps at fixed incident microwave power (200 W). At two close frequency operation the microwave power provided by the TWT was fixed at 120 W (also in this case the frequency was swept from 13.6 GHz to 14.6 GHz with 50 MHz frequency steps) while the power launched by the fixed frequency klystron was always 80 W.

Plasma-self Emitted RF Spectra

In stable plasma conditions cases the observed frequency spectra typically show the pumping RF peak(s) only. However, in unstable plasma cases the spectra characterized by high number of plasma self-emitted sub-harmonics. By considering the number and the intensity of the sub-harmonic peaks a quantitative parameter estimating the instability strength (Is) can be calculated [6]. In the paper [6] we demonstrated that the TCFH regime is able to dump the instabilities: it was possible to observe that the instability strength drops dramatically by adding the second pumping wave, see Fig. 4.

We have also shown that the spectral structure of the self-emitted radiation (subharmonics are detected along with the main frequencies) in TCFH mode always follows an empirical law; every time, the emission has been observed to occur at frequencies lower than the lowest of the two pumping frequencies. As an example, we present two SA spectra recorded at single frequency (13.9 GHz and 14.25 GHz) and one spectra recorded at 14.25 GHz + 13.9 GHz in double frequency heating mode (in all three cases the total net power was 200 W): they are shown, respectively, in the sequence of plots of Fig. 5. This tendency indicates that the plasma density distribution is rearranged at TCFH mode, becoming denser in the central region of the plasma chamber (where the B-field is lower).

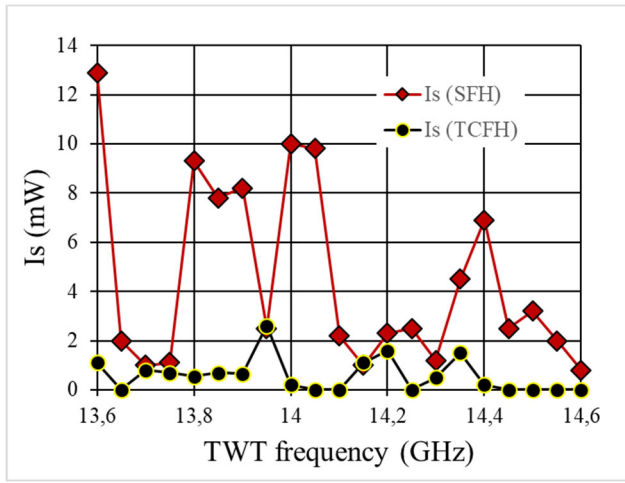

Figure 4. Instability strength as function of the applied frequency in single and in two frequency operation mode.

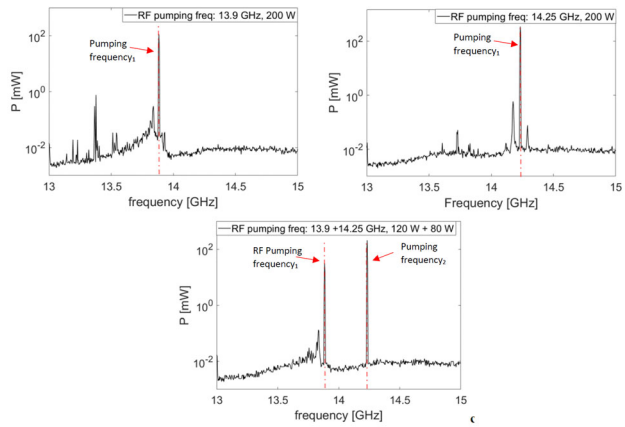

Figure 5. RF spectra measured by the spectrum analyser corresponding to single (13.9 and 14.25 GHz, at 200W) and to double frequency heating (13.9 GHz +14.25 GHz, 120 W + 80 W) operation mode.

Plasma Images

X-ray images of the plasma were taken with long (50 seconds) exposure time, while the read-out rate was 1 MHz. The Analogue Digital Unit (ADU) corresponding to every pixels and finally read by the CCD is proportional to the product of the number of incident photons and their energies. The images are able to reveal the energy content of the plasma. Figure 6. shows a typical plasma images. We can identify several distinctive areas in the image containing information about the Argon plasma, the losses of the electrons on the plasma electrode and on the cylindrical plasma chamber wall. In order to directly observe the structural changes of the plasma we have selected several ROIs (Regions of Interest) corresponding to different radial positions of the plasma. ROI-Hole gives information about the energy content of the plasma centre, while the ROI-Side characterizes the side areas of the plasmoid.

ISBN: 978-3-95450-226-4 ISSN: 2222-5692 doi:10.18429/JACoW-ECRIS2020-MOYZO01

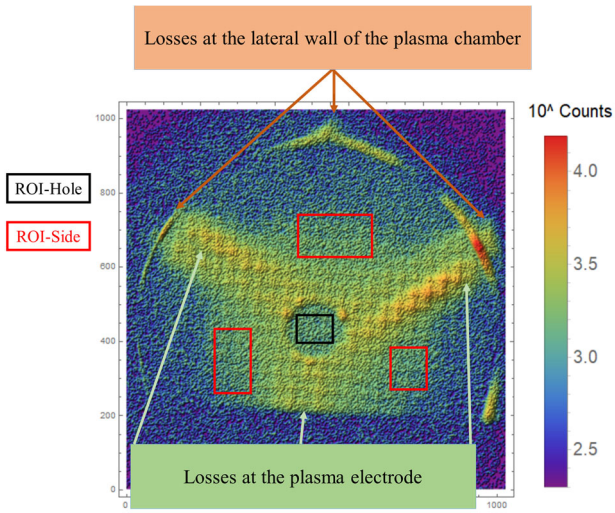

Figure 6. Typical plasma image (in logarithm scale) taken of Argon plasma generated at 13.9 GHz (single frequency mode), 200W. The exposure time was 50s.

We defined a parameter corresponding to every individual image to describe the degree of the concentration of the plasma in the central region of the chamber. This parameter is calculated as the ratio of the (area normalized) ROI-Hole (black rectangle in Fig. 6) counts of the central region and ROI-Side (red rectangle in Fig. 6) counts as the side regions of the plasma.

The higher this ratio, the plasma is more centralized. We have calculated this parameter both for single and double frequency scans and we have compared them at those frequencies where the instability was pronounced (i.e. Is parameter is higher than 7 mW) at single frequency operation mode. These frequencies are 13.6 GHz, 13.8 GHz, 13.85 GHz, 13.9 GHz, 14 GHz, 14.05 GHz. The corresponding centralization parameters are plotted in Fig. 7. This figure together with Fig. 4 clearly demonstrate that at two close frequency heating mode the instability is effectively damped by the second frequency, meanwhile the plasma is rearranged to be denser in a central region of the plasma. This observation is in good agreement with the tendency obtained from the RF spectra, presented in Fig. 5.

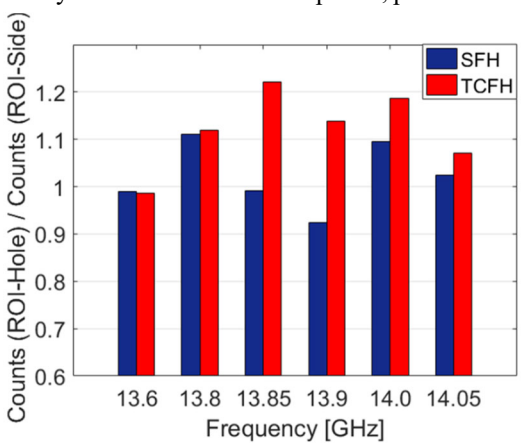

Figure 7. Centralization parameters at single and two frequency operation mode.

Comparison with Simulation Results

The effect of the second frequency to the anisotropy was investigated by the simulation code and compared with the experimentally obtained Is parameters and the centralization parameters. Figure 8 shows these parameters in single and in double frequency operation modes (combination of 13.9 and 14.25 GHz). Each blue bar of the histogram represents the normalized anisotropy. The red curve is the experimentally measured Is parameter, the grey bars indicate the centralization parameter, while the green rectangles report the average energy of the electrons in each simulated configuration. It can be seen that, in addition to the three experimentally investigated working point, we simulated also other two conditions in which the RF power of the two waves used for TCFH has been increased with respect to the experimental case. This plot shows that: at the same net power cases the anisotropy and the average energy decrease when we apply two close frequencies (in the simulation) and the plasma becomes more centralized meanwhile the instability is damped effectively. The additional simulated points when the TrapCAD runs in TCFH at higher total net powers, by increasing the power for both frequencies in parallel, showing that it is in principle possible to increase the average energy of the electrons (even above the energy corresponding to 13.9 GHz) and maintain anyway the anisotropy at low level.

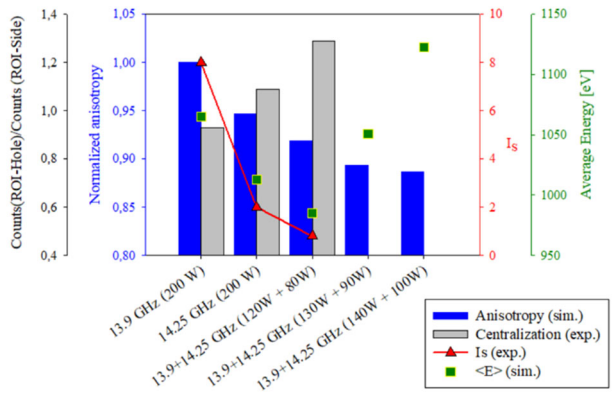

Figure 8. Comparison of simulation (sim.) and the experimental (exp.) results.

SUMMARY

We have presented experimental and simulation results corresponding to stable and unstable plasmas heated in single and two close frequency heating schemes. Non-linear increase of the anisotropy of the simulated electrons in the velocity phase space was observed around the well-known threshold value (B_{min}/B_{ECR} ~0.8) at single frequency. Instability strength and the anisotropy is moderated by applying two close frequency heating. It was also shown that when the instability is effectively damped by the second frequency the structure of the plasma is changes remarkably, the plasma becomes more centralized. One can conclude that the TCFH is making the parameter space broader and improving the plasma confinement allowing to extend the

ISBN: 978-3-95450-226-4 ISSN: 2222-5692 doi:10.18429/JACoW-ECRIS2020-MOYZO01

operation conditions (using a higher amount of RF power) at B_{min}/B_{ECR} values that are impeded by the onset of strong plasma instabilities at single frequency heating.

REFERENCES

[1] R. Geller, *"*Electron Cyclotron Resonance Ion Sources and ECR Plasmas,*" Institute of Physics Publishing*, Bristol, 1996.

[2] S. V. Golubev and A. G. Shalashov, "Cyclotron-Resonance Maser Driven by Magnetic Compression of Rarefied Plasma," *Phys. Rev. Lett.*, vol. 99, p. 205002, 2007.

[3] O. Tarvainen, J. Laulainen, J. Komppula, R. Kronholm, T. Kalvas, H. Koivisto, I. Izotov, D. Mansfeld, and V. Skalyga, "Limitations of electron cyclotron resonance ion source performances set by kinetic plasma instabilities", Review of Scientific Instruments, vol. 86, p. 023301, 2015.

[4] J. B. Li, L. X. Li, B. S. Bhaskar, V. Toivanen, O. Tarvainen, D. Hitz, L. B. Li, W. Lu, H. Koivisto, T. Thuillier, J. W. Guo, X. Z. Zhang, H. Y. Zhao, L. T. Sun and H W Zhao, "Effects of magnetic configuration on hot electrons in a minimum-B ECR plasma", *Plasma Phys. Controlled Fusion,* vol. 62, p. 095015, 2020.

[5] V. Skalyga1,2, I. Izotov1, T. Kalvas3, H. Koivisto3, J. Komppula, R. Kronholm, J. Laulainen, D. Mansfeld and O. Tarvainen, "Suppression of cyclotron instability in Electron Cyclotron Resonance ion sources by two-frequency heating," *Physics of Plasmas*, vol. 22, p. 083509, 2015.

[6] E Naselli, D Mascali, M Mazzaglia, S Biri, R Rácz, J Pálinkás, Z Perduk, A Galatá, G Castro , L Celona, S Gammino and G Torrisi, "Impact of two-close-frequency heating on ECR ion source plasma radio emission and stability," *Plasma Sources Sci. Technol.,* vol. 28, p. 085021, 2019.

[7] A. Kitagawa *et al.*, "Two-frequency Heating Technique for Stable ECR Plasma", in *Proc. 20th Int. Workshop on ECR Ion Sources (ECRIS'12)*, Sydney, Australia, Sep. 2012, paper TUXO03, pp. 10-12.

[8] S. Biri, R. Rácz and J. Pálinkás, "Status and special features of the Atomki ECR ion source," *Rev. Sci. Instrum*., vol. 83, p. 02A341, 2012.

[9] R. Rácz, D. Mascali, S. Biri, C. Caliri, G. Castro, A. Galatà, S. Gammino, L. Neri, J. Pálinkás, F. P. Romano and G. Torrisi, "Electron cyclotron resonance ion source plasma characterization by energy dispersive x-ray imaging," *Plasma Sources Sci. Technol*., vol. 26, p. 075011, 2017.

[10] S. Biri, R. Racz, Z. Perduk, J. Pálinkás, E. Naselli, M. Mazzaglia, G. Torrisi, G. Castro, L. Celona, S. Gammino, A. Galatá, F.P. Romano, C. Caliri and D. Mascali, "Innovative experimental setup for X-ray imaging to study energetic magnetized plasmas," submitted to Journal of Instrumentation.

[11] J. Vamosi and S. Biri, "TrapCAD - program to model magnetic traps of charged particles," Computer Physics Communications, vol. 98, pp. 215-223, 1996.

[12] S. Biri, A. Derzsi, É. Fekete, I. Iván, "The upgraded TrapCAD code," *High Energy Physics and Nuclear Physics - Chinese Edition Supplement,* vol. 31, p. 165, 2007.

ISBN: 978-3-95450-226-4 ISSN: 2222-5692 doi:10.18429/JACoW-ECRIS2020-MOYZO02

HIGH RESOLUTION X-RAY IMAGING AS A POWERFUL DIAGNOSTICS TOOL TO INVESTIGATE ECRIS PLASMA STRUCTURE AND CONFINEMENT DYNAMICS

E. Naselli† [1], D. Mascali, M. Mazzaglia, G. Castro, L. Celona, S. Gammino, G. Torrisi,
INFN-Laboratori Nazionali del Sud, Catania, Italy
R. Rácz, S. Biri, Z. Perduk, J. Pálinkás,
Institute for Nuclear Research (Atomki), Debrecen, Hungary
A. Galatá, INFN-Laboratori Nazionali di Legnaro, Legnaro, Italy
[1]also at Name of Università degli Studi di Catania, Catania, Italy

Abstract

High resolution spatially-resolved X-ray spectroscopy, by means of a X-ray pin-hole camera setup operating in the 0.5-20 keV energy domain, is a very powerful method for ECRIS plasma structure evaluation. We present the setup installed at a 14 GHz ECRIS (ATOMKI, Debrecen), including a multi-layered collimator enabling measurements up to several hundreds of watts of RF pumping power and the achieved spatial and energy resolution (0.5 mm and 300 eV). Results coming by a new algorithm for analyzing Integrated (multi-events detection) and Photon-Counted images (single-event detection) to perform energy-resolved investigation will be described. The analysis permits to investigate High-Dynamic-Range (HDR) and spectrally resolved images, to study the effect of the axial and radial confinement (even separately), the plasma radius, the fluxes of deconfined electrons distinguishing fluorescence lines of the materials of the plasma chamber (Ti, Ta) from plasma (Ar) fluorescence lines. This method allows a detailed characterization of warm electrons, important for ionization, and to quantitatively estimate local plasma density and spectral temperature pixel-by-pixel.

INTRODUCTION

Electron cyclotron resonance ion sources (ECRIS) are able to produce beams of highly charged ions with high intensity and stability, which are necessary for accelerators in applied and nuclear physics research. In order to produce these beams, continuous improvement in the performance of ECR ion sources is required and, since the characteristics of the extracted beam (in terms of current intensity and production of high charge states) are directly connected to plasma parameters and structure. Deeper knowledge of plasma properties becomes thus fundamental. Therefore, at INFN-LNS (Istituto Nazionale di Fisica Nucleare – Laboratori Nazionali del Sud) in collaboration with the Atomki laboratories (Debrecen, Hungary), several non invasive diagnostic tools have been developed, with advanced analytical methods. Among the others, an innovative diagnostic tool consisting of a lead pin-hole, a CCD camera and a multi-disks lead collimator is able to perform high spatial and energy resolution imaging and spectroscopy in the soft X-ray domain.

† eugenia.naselli@lns.infn.it

It represents a very powerful tool to investigate spectrally resolved images, to study the effect of the axial confinement, the plasma radius evaluation and the fluxes of deconfined electrons, also distinguishing fluorescence lines of each material of the plasma chamber (Titanium, Tantalum) from fluorescence lines of plasma (Argon).

Several experiments have demonstrated that the plasma turbulent regimes cause ECRIS performances deterioration in the extracted ion beam, in terms of beam ripple and a decreasing of the high charge state production [1-3]; even if other works have demonstrated that the plasma stability and the ion beam stability can be improved by applying two frequency heating of the plasma [4-6], further studies are necessary in order to investigate in details this phenomena. Moreover, other works [7] predict that turbulent regimes of plasma can generate *precipitations* of the energetic electrons in the loss cones (producing the X-ray burst emission when they impact in the plasma chamber walls) thus increasing the losses compared to the plasma emission.

In 2014 X-ray space resolved-spectroscopy was already performed, but only in low power regimes up to 30 W of RF pumping power [8, 9]. In order to investigate the turbulent regimes, increasing the pumping RF power at least at about 100 W becomes necessary [10]. On this purpose, the whole diagnostic tool for X-ray imaging has been recently improved. The system was re-designed; a new multi-disks lead collimator able to reduce the noise caused by scattering (that becomes very high in high power domain), an innovative plasma chamber design and analytical methods to post-process the acquired images were introduced. Now 200 W operations are possible (one order of magnitude higher than the previous ones) and the diagnostic system can represent an interesting and powerful method to investigate how the turbulences affects the plasma confinement and losses dynamics.

EXPERIMENTAL SETUP

The measurement was carried out in the 2th generation ECRIS installed in the ECR Laboratory of ATOMKI, in Debrecen (Hungary) [11]. The basic operation frequency is 14.25 GHz provided by a klystron amplifier, but it is also possible heating the plasma with a second (tuneable) frequency provided by a travelling wave tube (TWT) amplifier. The axial magnetic field is 1.26 T (injection),

ISBN: 978-3-95450-226-4 ISSN: 2222-5692 doi:10.18429/JACoW-ECRIS2020-MOYZO02

0.39 T (B_{min}) and 0.92 T (extraction), whilst the radial magnetic field produced by a permanent magnet hexapole and measured at the plasma chamber wall (R=29 mm) is 1.1 T. The length of the plasma chamber is 210 mm and the diameter 58 mm.

The non-invasive diagnostic tool consists of:

- a CCD camera, with a sensitive range 2 keV – 20 keV, made of 1024x1024 pixels and having a sensor size 13.3 x 13.3 mm;
- a lead pin-hole of 2 mm of thickness and 400 µm of hole diameter, which is able to reproduce the plasma image in the CCD position-sensitive detector. The magnification *M* of the pin-hole system (developed by the position of the pin-hole with respect to the plasma and to the CCD chip) was optimized: M=0.24;
- two Titanium windows with a total thickness of 9.5 µm in order to reduce UV and visible light;
- a multi-disks collimator consisting of two lead disks of 1 mm of thickness was installed at 40 mm from the pin-hole on the CCD side and 6 mm on the plasma side. The hole diameters are1 mm and 2 mm, respectively.

A sketch of the whole system is shown in the Fig 1.

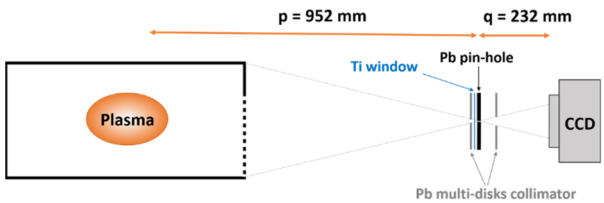

Figure 1. Sketch of the X-ray pin-hole camera setup.

Moreover, a special design of the plasma chamber walls covered by a liner of Tantalum (for the lateral walls) and Titanium and Aluminum (for the extraction and injection endplate, respectively) has been implemented in order to distinguish between fluxes of X-rays coming from walls' bremsstrahlung and fluorescence (produced by the electrons escaping the magnetic trap and impinging on the metals surfaces), from the ones coming from the Argon plasma (due mainly to the fluorescence of the confined ions).

Multi-collimator to Investigate High Power Regimes

By developing the multi-disks lead collimator as extra shielding it has been possible to acquire X-ray picture in relatively high RF-power operation mode, up to 200 W total incident power. This datum still represents the highest operative RF power for which X-ray imaging has been never performed in the field of ECR Ion Sources and ECR compact traps.

Figure 2 shows the two images acquired in the same operative configuration (pumping RF power of 200 W and RF frequency of 13.9 GHz) with an exposure time of 50 seconds have been reported: the image 2.a) has been acquired without the usage of the collimator, the 2.b) with it. It has been demonstrated that using the collimator the noise decrease of 405% outside the plasma chamber (considering the total counts in the region of interest (ROI) squared in green, in the images) and of 152% inside the plasma chamber (considering the total counts in the ROI squared in cyan, in the images). Whilst the signal/noise ratio increase of 70% and 39% outside and inside the plasma chamber, respectively. The signal has been estimated considering the total counts in the ROI white squared.

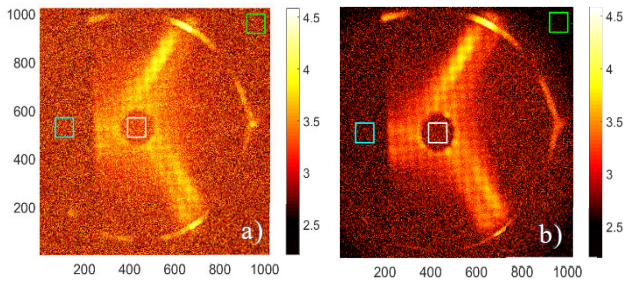

Figure 2. Pseudo-color elaboration of X-ray flux (in logarithmic scale), putting in evidence the ROI where the radiation coming from Ar plasma only (squared in white), and the ROIs where radiation is due to scattering effects (squared in cyan and in green). a) - without the multi-disks collimator. b) - in the pin-hole setup the multi-disks collimator has been used.

Moreover, a very high spatial resolution (500 µm [12]) can be obtained by using the collimator; in the Fig. 2.b) it is in fact possible well distinguish the mesh structure of the Aluminum endplate, manufactured in order to shield microwave but guarantee above 60% of X-ray transmission. The wire diameter is only 400 µm.

THE X-RAY IMAGE OPERATIVE MODES

The photon impinging in the camera generates charge that is proportional to the deposed energy. The Analogue Digital Unit (ADU), corresponding to every pixels and finally read by the CCD, is proportional with the product of the incident photons and their energies. Typically, there are two main operative modes to acquire the images: the *Spectrally Integrated (SpI)* mode and the *Single Photon Counting (SPhC)* mode.

During a long exposure time - for example images collected with several tens of seconds - multi events are registered by the CCD camera, and the spectral information of the incoming X-rays is lost. Therefore, images obtained with long exposure times are called *Spectrally Integrated images*. In this case energy separation of the events is not possible, however, ADUs are revealing the energy content of the plasma and plasma chamber complex. The advantage, in this case, is that these acquisitions are typically fast (tens of seconds) and it is so possible to master, likely "*on line*", the changes of plasma structure and morphology.

The more powerful investigations, able to perform local energy determination, is provided by *Single Photon Counting* mode. Decoupling of photon number versus energy is possible. The technique allows to perform space-resolved spectroscopy (thus evidencing the local displacement of electrons at different energies, as well as of plasma ions highlighted by fluorescence lines emission) versus the

ISBN: 978-3-95450-226-4 ISSN: 2222-5692 doi:10.18429/JACoW-ECRIS2020-MOYZO02

main tuning parameters such as the pumping wave frequency and the strength of the confining magnetic field. It is very useful in order to study how the operative parameters (RF pumping frequency and power, magnetic field and also phenomena such as plasma turbulence) affect the plasma confinement, stability and turbulence onset and to investigate dynamics of plasma versus plasma losses.

The SPhC mode is obtained by fixing a short exposure-time for each of the acquired image-frame (typically in the range of several tens of milliseconds). Multi-images are recorded in SPhC (of the order of thousands image-frames). The SPhC mode allows minimizing the probability that two (or more) photons hit the same pixel during the exposure of a single image-frame with a consequent loss of information about their energies. Only a few number of pixels is illuminated on the full CCD matrix and they can be associated with single photon events and, consequently, they carry the information (in terms of charge) on the energies of the incident photons.

Development of a proper acquisition and processing procedure of the experimental data were required and advanced analytical methods were needed and have been developed on purpose.

THE ANALYTICAL METHOD

Analytical algorithm has been developed to elaborate the raw data acquired using the X-ray pin-hole camera tool, in particular to analyze the Single Photon-Counting images, to perform energy-resolved investigation pixel-by-pixel and deep investigations about confinement dynamics. The analytical method has been developed using the MatLab programming platform.

The developed analytical method for SPhC imaging and spectroscopy consists of six different steps. In this section we describe only the main step, the so called *Grouping process (Gr-p)*, that allows performing the space-resolved spectrum.

Even working in SPhC mode, multipixel events are always present in each of the image-frames acquired during the measurement: they could be associated with *a single photon* that interacts with more than one pixel, or *two (or more) photons* that hit neighboring pixels. The algorithm has been elaborated for recognizing and correcting the group-events.

To ensure the incoming photon energy proportional to the sum of ADU of the loaded pixels, it is necessary that in each acquired image-frame one photon only releases its energy in a given group of pixels. Whilst, if photons are fall to two pixels close to each other, the pixels loaded by the two photons are overlapped or become neighbours forming large clusters and the energy of the photons are summed in this big cluster. Since the isolation of the effect of the two or more photons contributions are impossible, these spurious events have to be filter out by the analytical algorithm. On this purpose, we introduced an input parameter in the algorithm, called *S parameter*, that represents the maximum cluster *size* (*size* is defined as the number of neighbours pixels compounding a cluster) that can be considered due to the impact of only one photon. Consequently, all the clusters of pixels having size larger than *S* have been filtered out by the algorithm. Moreover, also the offset noise contribution has been removed setting a threshold called *L value*.

In a nutshell, the two main input parameters used to characterize the script-run are:

- *L* = count Limit, the threshold to consider a pixel as cluster component, this limit set a noise level;
- *S* = cluster Size, the maximum number of connected pixels to consider them as not overlapping counts.

In more detail, the algorithm works in the following mode: considering a given image-frame, the first phase consists in "*turning off*" all pixels having ADU lower than L, putting to zero all their values; later the procedure scans pixel by pixel each of the image and when an illuminated pixel of coordinates (X, Y) is identified, its neighbouring pixels are checked. If no charge is present into the surrounding pixels, the event is considered to be generated by a single photon and it is associated with a 3-coordinates point (X, Y, E). The coordinate E is the energy associated with the photon. When a group of neighboring pixels is identified during the scan of an image-frame, the algorithm processes this multipixel event to reconstruct its nature (i.e., single or multiple-hit):

- in the group associated with a single photon-event (typically characterized by the presence of a pixel with a maximum intensity, in terms of charge) the code perform the integration of the total charge giving the energy of the photon; the hitting coordinate (X, Y) is fixed to the pixel containing the maximum contribution;
- in case of the groups associated with multiple-hit events (typically characterized by the presence of different relative maxima in a large size of the group of pixels) the processing algorithm filter out them.

When the pixel in the position (X,Y) has been elaborated, the algorithm start to process the subsequent pixel in the position (X+1,Y). The above procedure is repeated pixel by pixel in all the frames.

Considering, for example, a ROI (Region of Interest) of the pixelated matrix (1024x1024 pixels) correspondent to an image-frame, it is possible to observe how the different steps of the Gr-p elaborates the images: we can consider a setting *S=5* and *L=10* as input parameters in the algorithm.

A ROI of 20X30 pixels, by way of example, has been considered in the Fig. 3. The image shown in Fig. 3 a) is corresponding to the first phase, where all pixels having charge lower than *L* (putted to zero). Moreover, in this step, the algorithm finds and checks the clusters size (in red squared the clusters having size larger than *S*, in green squared the other ones). As it is possible to observe, the first ones typically present two or more local maximum, highlighting the contribution does not due by one only single photon. On this purpose, the second step filters out them (the image with the ADU values is shown in Fig. 3. b).

Finally, the third step integrates the charge of all pixels composing a given cluster shown in Fig. 3. c).

ISBN: 978-3-95450-226-4 ISSN: 2222-5692 doi:10.18429/JACoW-ECRIS2020-MOYZO02

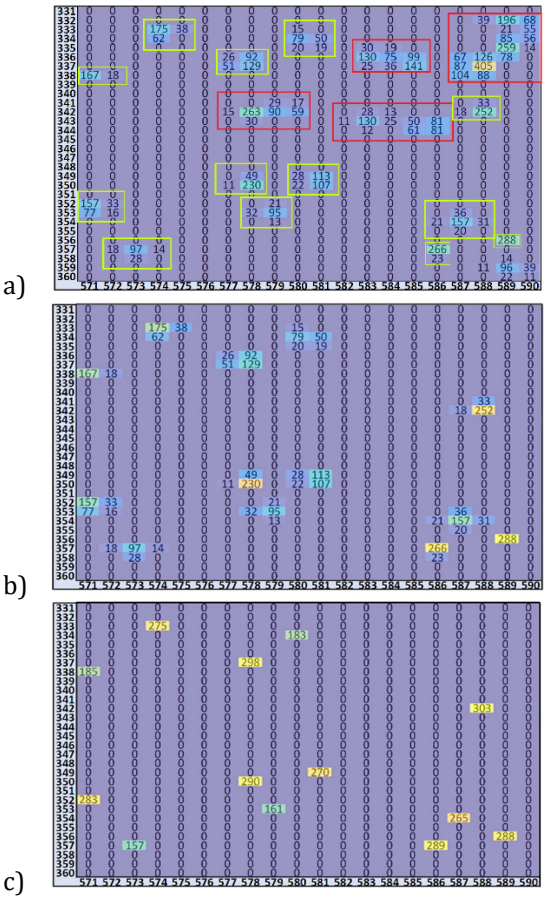

Figure 3: ROI of 20X30 pixels elaborated implementing the three different steps of the grouping procedure: a) after the first step; b) after the second step; c) after the third step.

After that the Gr-p has been performed for all the image-frames composing a measurement, it is assigned a variable N to each coordinate (X,Y) of the CCD matrix; N is the number of photons with energy E in the position (X, Y). N is incremented by a unit during the scansion of all the frames when a photon of energy E is detected in the same position (X, Y) in another frame K.

At the end of the scansion of all the image-frames a set of points with coordinates (X, Y, E, N_{tot}) is obtained. The plot of the total counts N_{tot} versus the energy E is the full X-ray spectrum of the sample under investigation.

THE EXPERIMENTAL RESULTS

In this section an overview of the experimental results concerning both the integrated imaging and the space-resolved spectroscopy in SPhC will be presented.

The Integrated X-ray Imaging

The *Integrated X-ray Imaging* consists in acquiring only one image with a long exposure time of the order of tens of seconds. In this case the total measurement time results to be very fast and the elaboration of the image needs an easy analysis.

An example of a power scaling of the integrated images is shown in Fig. 4 (RF frequency = 13.8 GHz) varying the pumping RF power from 20 W to 200 W at step of 20 W.

From a visual inspection it is possible to highlight how the energy content changes vs. the pumping power.

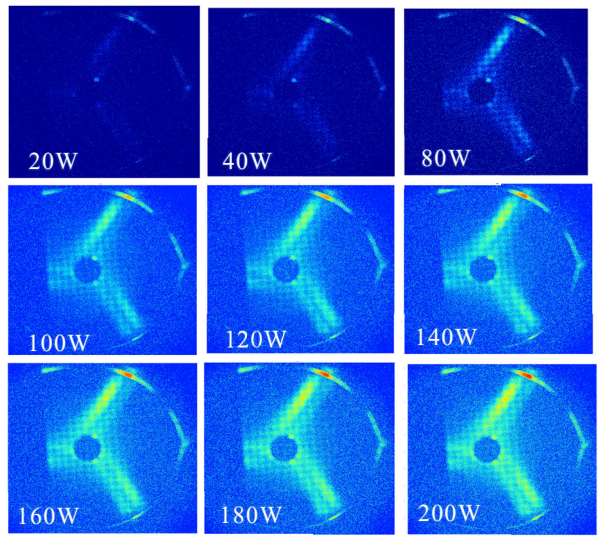

Figure 4: Pseudo-color elaboration of X-ray images (in the same logarithmic scale): power scaling, from 20 W up to 200 W.

Selecting specific ROIs in the images it is also possible to quantitative investigate about the energy content of the emission, comparing the plasma emission vs. the losses emission. It has demonstrated that in the stable regimes the losses decrease [5] and the plasma is rearranged to be denser in a central region of the plasma [13].

Moreover, with integrated imaging it is also possible to *on-line* measure the plasma radius: i.e., at 13.9 GHz of pumping frequency, the experimental radius results 16.04 ± 1.44 mm, which is in very good agreement with the radius of the ECR-ellipsoid (15.50 mm) estimated using the realistic magnetic field of the Atomki-ECRIS.

PhC Imaging and Space-Resolved Spectroscopy

Figure 5 shows the reports of the full field X-ray spectrum of an acquired configuration, with a total net RF pumping power of 200 Watt and a FR frequency of 13.9 GHz amplified by the TWT.

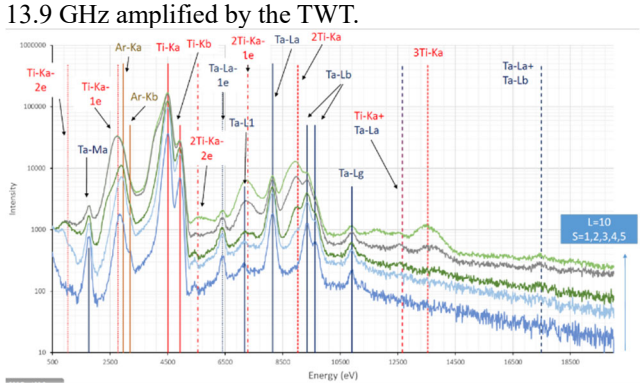

Figure 5: Full field X-ray spectrum of experimental configuration acquired with a total net RF pumping power of 200 Watt and a FR frequency of 13.9 GHz amplified by the TWT.

ISBN: 978-3-95450-226-4 ISSN: 2222-5692 doi:10.18429/JACoW-ECRIS2020-MOYZO02

The thousands of image-frames are gaining the statistics necessary for elaborating high quality X-ray fluorescence spectra and images.

It is possible to distinguish fluorescence lines of each material of the plasma chamber (Ti, Ta) and the fluorescence lines of plasma (Ar). There are also dimer peaks and escape peaks for each fluorescence line. The energy resolution is 0.326 keV at 8.1 keV [12], corresponding to the Ta-Lα line. Separated characteristic peaks in the X-ray spectra, coming from each material, allow to study the confinement dynamics (plasma vs losses X-ray emission) discriminating the radial losses from the axial losses also: X-rays coming from magnetic branches (where electrons are axially deconfined) consist of mostly fluorescence from Ti, X-rays coming from plasma are mostly due to ionized Kα Argon lines and X-rays coming from poles (where electrons are radially deconfined) are mostly due to radial losses impinging on the Ta liner.

Moreover, since the data on the spectrum contains the spatial information on the emitting positions, the definition of a ROI on the fluorescence peaks in the spectrum allows the imaging of the elemental distribution, and it is possible to distinguish the emission (and the correspondent image) coming from each material. As it is possible to highlight in Fig. 6, it is possible to distinguish the emission coming from Ar plasma only (selecting the fluorescence from Ar only), compared to the radial losses (Ta) or the axial losses (Ti), selecting the fluorescence from Titanium and Tantalum, respectively.

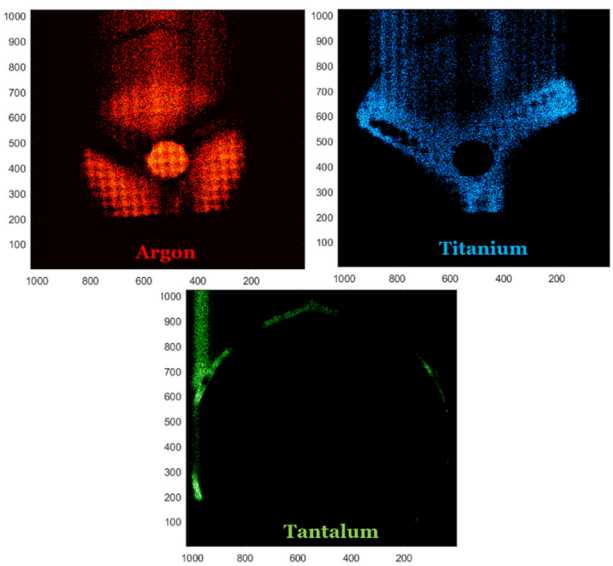

Figure 6: 2D energy filtered images showing fluorescence photons coming from the argon plasma and signals coming from the metallic layers covering plasma chamber walls.

Finally, it is possible also perform a complementary analysis: selecting in the whole image only a "*collection*" of pixels of a ROI, it is possible to investigate about the elemental composition in the given ROI only by means of the correspondent spectrum and, consequently, to perform the plasma parameters (electron density and temperature) estimation.

CONCLUSION AND PERSPECTIVES

The paper reports the tool, the analytical method and the preliminary results of a powerful system for making plasma physics investigation by means of spectrally-resolved imaging and space-resolved spectroscopy. *Live* plasma structure and emission investigations can be performed, using Integrated imaging, and correlating the results vs. ECRIS operative parameters.

The more powerful analysis consists in the Spatial-Resolved Spectroscopy for quantitative estimation of deconfined fluxes in stable vs. unstable regimes, quantitative elemental composition determination pixel-by-pixel and locally plasma parameters (electron density, temperature) measurements.

In perspectives, space-resolved soft X-ray analysis will investigate how plasma turbulence and plasma heating method (i.e. the Two-Close-Frequency Heating) affect plasma confinement and loss dynamics.

ACKNOWLEDGMENTS

The authors gratefully acknowledge the support of INFN by the Grants PANDORA (5th Nat. Comm.) and PANDORA_GR3 (3rd Nat. Comm.).

REFERENCES

[1] S. Gammino, D. Mascali, L. Celona, F. Maimone and G. Ciavola, "Consideration on the role of the magnetic field gradient in ECR ion sources and build-up of hot electron component", *Plasma Sources Science and Technology,* vol. 18, issue no. 4, p. 045016, 2009. doi.org/10.1088/0963-0252/18/4/045016

[2] O. Tarvainen, J. Laulainen, J. Komppula, R. Kronholm, T. Kalvas, H. Koivisto and V. Skalyga, "Limitations of electron cyclotron resonance ion source performances set by kinetic plasma instabilities", *Rev. of Sci. Instrum.*, vol. 86, p. 023301, 2015. doi.org/10.1063/1.4906804

[3] A. Kitagawa *et al.*, "Two-frequency Heating Technique for Stable ECR Plasma", in *Proc. 20th Int. Workshop on ECR Ion Sources (ECRIS'12)*, Sydney, Australia, Sep. 2012, paper TUXO03, pp. 10-12.

[4] V. Skalyga, I. Izotov, T. Kalvas, H. Koivisto, J. Komppula, R. Kronholm, J. Laulainen, D. Mansfeld and O. Tarvainen, "Suppression of cyclotron instability in Electron Cyclotron Resonance ion sources by two-frequency heating", *Physics of Plasmas,* vol. 22, p. 083509, 2015. doi.org/10.1063/1.4928428

[5] E Naselli, D Mascali, M Mazzaglia, S Biri, R Rácz, J Pálinkás, Z Perduk, A Galatá, G Castro , L Celona, S Gammino and G Torrisi, "Impact of two-close-frequency heating on ECR ion source plasma radio emission and stability", *Plasma Sources Sci. Technol.*, vol. 28, p. 085021, 2019. doi.org/10.1088/1361-6595/ab32f9

[6] R. Racz *et al.*, "Effect of the Two-Close-Frequency Heating to the extracted ion beam and to the X-ray flux emitted by the ECR plasma", *JINST,* vol. 13, p. C12012, 2018. doi.org/10.1088/1748-0221/13/12/C12012

ISBN: 978-3-95450-226-4 ISSN: 2222-5692 doi:10.18429/JACoW-ECRIS2020-MOYZO02

[7] A. G. Shalashov *et al.*, "Kinetic instabilities in a mirror-confined plasma sustained by high-power microwave radiation" Phys. Plasmas, vol. 24, p. 032111, 2017. doi.org/10.1063/1.4978565

[8] R. Rácz, D. Mascali, S. Biri, C. Caliri, G. Castro, A. Galatà, S. Gammino, L. Neri, J. Pálinkás, F. P. Romano and G. Torrisi, "Electron cyclotron resonance ion source plasma characterization by energy dispersive x-ray imaging", *Plasma Sources Sci. Technol.*, vol. 26, p. 075011, 2017. doi.org/10.1088%2F1361-6595%2Faa758f

[9] D. Mascali *et al.*, "Electron cyclotron resonance ion source plasma characterization by X-ray spectroscopy and X-ray imaging", *Rev. Sci. Instrum.*, vol. 87, p. 02A510, 2016. doi.org/10.1063/1.4939201

[10] A. G. Shalashov *et al.*, "Kinetic instabilities in a mirror-confined plasma sustained by high-power microwave radiation", *Physics of Plasmas*, vol. 24, p. 032111, 2017. doi.org/10.1063/1.4978565

[11] S. Biri, R. Rácz and J. Pálinkás, "Status and special features of the Atomki ECR ion source", *Rev. Sci. Instrum.*, vol. 83 p. 02A341, 2012. doi.org/10.1063/1.3673006

[12] E. Naselli *et al.*, "Multidiagnostics setups for magnetoplasmas devoted to astrophysics and nuclear astrophysics research in compact traps", *JINST*, vol. 14, issue no 10, 2019. doi.org/10.1088/1748-0221/14/10/C10008

[13] R. Racz *et al.*, "Imaging in X-ray ranges to locally investigate the effect of the Two-Close-Frequency Heating in ECRIS plasmas", presented at the 24th International Workshop on ECR Ion Sources (ECRIS'20), paper MOYZO01, this conference.

ISBN: 978-3-95450-226-4 ISSN: 2222-5692 doi:10.18429/JACoW-ECRIS2020-MOYZO03

THE RELATIONSHIP BETWEEN THE DIFFUSION OF HOT ELECTRONS, PLASMA STABILITY, AND ECR ION SOURCE PERFORMANCE

Bryan Isherwood* and Guillaume Machicoane
National Superconduction Cyclotron Laboratory, East Lansing, MI, USA
Facility for Rare Isotope Beams, East Lansing, MI, USA

Abstract

The diffusion of electrons from ECRIS plasmas results in the emission of a continuous energy distribution of photons from the plasma chamber. Measurements ECRIS bremsstrahlung that are both time and energy resolved of the are often difficult to perform due to the 10's – 100's ms timescale that the plasma evolves over. However, the advancement of low-cost micro-controllers over the last decade makes timing and gating photon spectrometers easier. We present a proof of principle measurement which uses an Arduino micro-controller as a gate-and-delay generator for time resolved ECRIS bremsstrahlung measurements. An example plot of the time resolved spectrum, triggered by beam current variation induced by kinetic instabilities is shown.

INTRODUCTION

Accelerator facilities like the National Superconducting Cyclotron Laboratory (NSCL) and the Facility for Rare Isotope Beams (FRIB) require high intensity, high charge state ion beams for facility operations. These facilities rely on electron cyclotron resonance (ECR) ion sources (ECRISs) to produce stable ion beams for their operations. To that end, researchers have determined different ways to optimize the performance of the ion source [1–3]. In particular, the semi-empirical magnetic field scaling laws have proven to be reliable and important guides to optimizing the performance of ECR ion sources [4].

However, the ECR ion source plasma is prone to microinstabilities that cause quasi-periodic losses of high energy electrons and limit the ion source's performance on the high field and power range of the operating parameter space [5]. These instabilities result from the combination of loss-cone confinement and resonant heating mechanisms that create the ECR plasma. These combined mechanisms create steady-state electron populations that are anisotropic, with large transverse energies, $T_\perp >> T_\parallel$ [6]. These electrons can excite and amplify electromagnetic plasma modes within the plasma chamber and, in doing so, drive themselves into the loss cone [7, 8]. This instability is known as a kinetic cyclotron maser instability and is a type of inverse Landau damping [9, 10].

Electrons driven into the loss cone rapidly escape the plasma chamber, disrupt the plasma quasi-neutrality condition, and alter the confinement characteristics of ions within the system. These imbalances result in the quasi-periodic beam current variations that are characteristic of the instabilities in ECR ion sources [5]. Consequently, the average extracted current of highly charged ions decreases, limiting the ion source's performance, particularly on the high field side of the ion source's operating parameter space. It is difficult to suppress the instabilities as they are a natural consequence of the loss-cone and microwave heating mechanics [11]. Understanding when and how a plasma changes from stable to unstable is essential for optimizing ECRIS performance.

Measurements on AECR at the University of Jyväskylä (JYFL) show that large losses (50 – 90%) of highly charged beam currents occur when operating the ion source with large injected microwave powers and magnetic field strengths, in particular when $B_{min} > 0.7 - 0.8\ B_{RF}$ [5], where $B_{RF} = \omega_{RF}/(28\ \text{GHz})$ (more commonly known as B_{ECR}), and ω_{RF} is the propogation frequency of microwave injected into the plasma chamber. Followup measurements on SuSI at the NSCL demonstrated that the instabilities could occur over a larger subset of the magnetic field parameter space, $B_{min} < 0.55\ B_{RF}$ [12]. The instabilities at lower field values tended to repeat more frequently and perturb the plasma less. However, those measurements focused on the stability characteristics of the magnetic field parameter space as a whole and revealed few details into the effect of the varying field strength on the beam current's transient characteristics.

We report the results of an investigation into the extracted beam current, from an unstable plasma while changing the ion source magnetic field when operating the ion source with magnetic fields lower than those prescribed by the semi-empirical scaling laws. In particular, we focus on the effect of changing magnetic field topologies (extraction side field maximum and global minimum) upon the transience state of extracted Ar^{8+} currents. These results demonstrate a connection between the amplitude and repetition frequency of the plasma instabilities and the longitudinal magnetic field's topology.

APPARATUS AND PROCEDURES

All measurements were taken using the Superconducting Source for Ions (SuSI) at the NSCL[13] (Fig. 1). The ion source's confining magnetic field is created with four superconducting solenoids and a superconducting hexapole coil. The four axial solenoid coils provide longitudinal confinement while allowing for control over the injection and extraction maxima and the field minimum. The system's

* isherwo3@gmail.com

ISBN: 978-3-95450-226-4 ISSN: 2222-5692 doi:10.18429/JACoW-ECRIS2020-MOYZO03

design allows for each of the longitudinal field extrema to vary independently of one another.

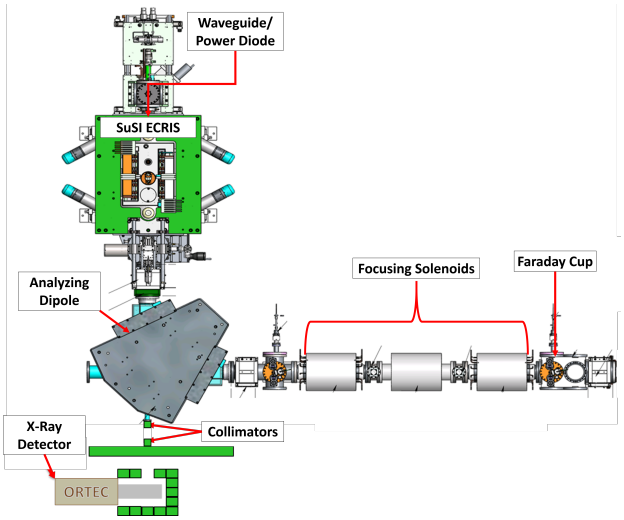

Figure 1: A schematic of the source-beamline configuration used for this measurement.

This measurement acted as a supplemental measurement to Isherwood et al. [14], except in this case, we measured extraction ion currents rather than the diffusing electrons. The dynamics of the diffusion electrons are complicated, however, and a direct 1-to-1 comparison would between these two measurements would be difficult at present. However, these same field parameters allow us to observe the effect of plasma instabilities at less than what is prescribed by the scaling laws. Those fields were based around a "control" magnetic field profile, which all other measurements could be compared against. For our purposes at the moment, the importance of the field profile is that it sets the global minimum and extraction side maximum lower than what is prescribed by the scaling laws (see Table 1).

Table 1: A comparison between the magnetic field topologies of the "standard" field configuration for facility operations and the "control" field configuration used in this study and Ref. [14].

	Standard	Control
B_{min}/B_{RF}	0.71	0.62
$B_{Inj,max}/B_{RF}$	3.96	3.68
$B_{Ext,max}/B_{RF}$	1.94	1.71

The extraction and einzel lens voltages were fixed at 20 kV for the duration of the measurement, with the puller electrode fixed at 0 V. Argon ions were extracted from the plasma chamber with a fixed neutral gas pressure of 213 nTorr, as measured by an ion gauge on the injection side of the plasma chamber. A 90° dipole was used for charge selection and guided the ions into a solenoid focusing lattice to guide the selected charge state current into a Faraday cup. Reflected/emitted microwaves from the plasma chamber were measured with an HP 8473C Low Barrier Schottky Diode connected to a bi-directional waveguide coupler connected to the microwave waveguide. The diode cannot measure the propogation frequency of the emitted microwaves, but does measure the instability repetition rate. The beam current and microwave power signals were measured simultaneously using a Tektronix MDO3054 oscilloscope. Bremsstrahlung measurements were taken on axis using a High Purity Germanium Detector (HPGe), placed in line with the longitudinal axis of the ion source's plasma chamber. Two lead bricks and a cylindrical piece of tungsten collimated the flux of bremsstrahlung radiation emitted from the ion source.

RESULTS

Varying the Extraction Side Field Maximum

We will start by looking at the effect of varying the extraction side field maximum on the extracted Ar^{8+} current. The extraction side field maximum appears to control several characteristics of the unstable plasma, such as the repetition rate and amplitude of individual instability events. Figures 2, 3, and 4 demonstrate these trends through measurements of extracted Ar^{8+} currents and emitted microwave power signals, in time and frequency domains. The increasing field strength correlates with an increasing instability repetition rate and decreasing current variation and microwave emission amplitudes. Furthermore, the higher frequency events tended to occur more randomly, with a larger spread over the frequency domain. Eventually, the microwave power signal beings to resemble electronic noise, albeit large amplitude noise. At this point, the extracted current reaches its minimum over the domain. Figure 5 quantifies these trends by looking at the averaged Ar^{8+} current extracted from the plasma chamber.

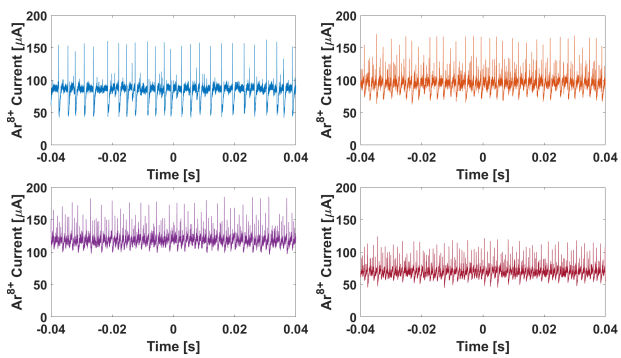

Figure 2: Ar^{8+} beam current for a varying extraction field maxima: (Top Left) $B_{Ext,max}$ = 0.99 T, (Top Right) $B_{Ext,max}$ = 1.07 T, (Bottom Left) $B_{Ext,max}$ = 1.15 T, (Bottom Right) $B_{Inj,max}$ = 1.23 T. B_{min} = 0.4 T, P_{μ} = 350 W, p_{Ar} = 213 nTorr.

Lastly, we find another noteworthy trend in Figs. 2 and 6. As we would expect, the average current increases to a maximum at $B_{Ext,max}$ = 1.15 T ≈ 1.79 B_{RF}, and then decreases as the field continues to increase. However, at this same point, the total number of high energy photons (E_{γ} > 80 keV) begins to decrease. We might expect the total photon intensity

ISBN: 978-3-95450-226-4 ISSN: 2222-5692 doi:10.18429/JACoW-ECRIS2020-MOYZO03

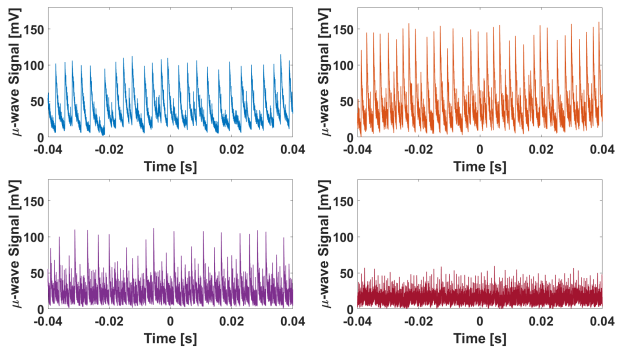

Figure 3: Microwave power signals for a varying extraction field maxima: (Top Left) $B_{Ext,max}$ = 0.99 T, (Top Right) $B_{Ext,max}$ = 1.07 T, (Bottom Left) $B_{Ext,max}$ = 1.15 T, (Bottom Right) $B_{Inj,max}$ = 1.23 T. B_{min} = 0.4 T, P_{μ} = 350 W, p_{Ar} = 213 nTorr. Microwave power has been offset by it's minimum value, over the entire 100 ms measurement period, to account for the AC coupling of the oscilloscope. Signals have been treated with a digital low pass filter using the Matlab signal processing toolkit, with a cutoff frequency of 333 kHz.

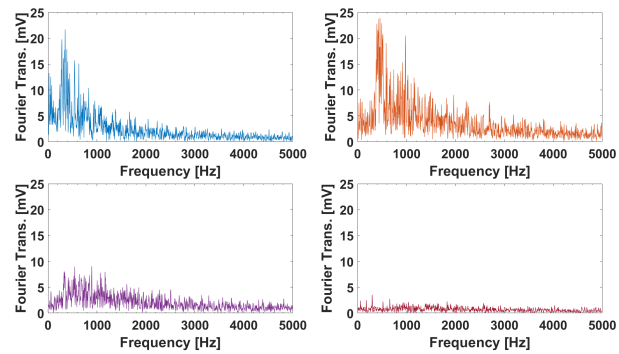

Figure 4: Fourier transform of the microwave power signals emitted from the ion source for a varying extraction field maxima: (Top Left) $B_{Ext,max}$ = 0.99 T, (Top Right) $B_{Ext,max}$ = 1.07 T, (Bottom Left) $B_{Ext,max}$ = 1.15 T, (Bottom Right) $B_{Ext,max}$ = 1.23 T. B_{min} = 0.4 T, P_{μ} = 350 W, p_{Ar} = 213 nTorr.

to decrease with the increasing field (decreasing loss cone pitch angle), but we also see that the photon intensity is relatively insensitive to the field strength for the lower field strengths. In particular, the monotonic decrease appears to begin around a field strength of $B_{Ext,max}$ = 1.1 T, but accelerates beyond $B_{Ext,max}$ = 1.15 T. This trend is *not* reflected in the emitted microwave power, which peaked at $B_{Ext,max}$ = 1.07 T and showed no qualitative change around $B_{Ext,max} \approx 1.8\, B_{RF}$.

Varying the Magnetic Minimum

Varying the magnetic minimum caused a more abrupt change to the beam current's transient characteristics. Figure 7 shows four examples of the changing extracted beam current as the magnetic minimum is varied, as seen by an oscilloscope. For comparison, Figures 8 and 9 show how the

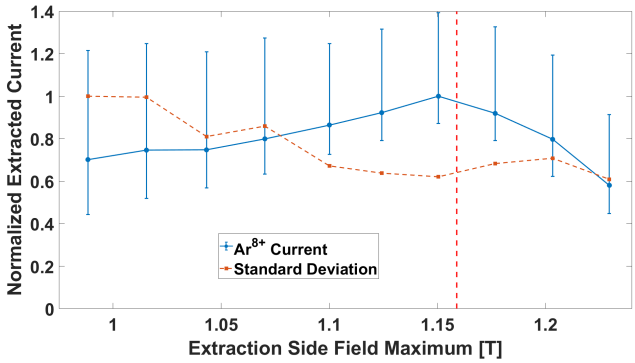

Figure 5: Trends in the average extracted Ar^{8+} beam currents, measured over a 200 ms period, and its standard deviation as the extraction side field maxima is varied. Both data sets are normalized by the largest values in their respective sets. Error bars represent the average positive and negative amplitudes away from the average measured current. B_{min} = 0.4 T, P_{μ} = 350 W, p_{Ar} = 213 nTorr. The vertical dashed lines show where $B_{Ext,max}/B_{RF}$ = 1.8

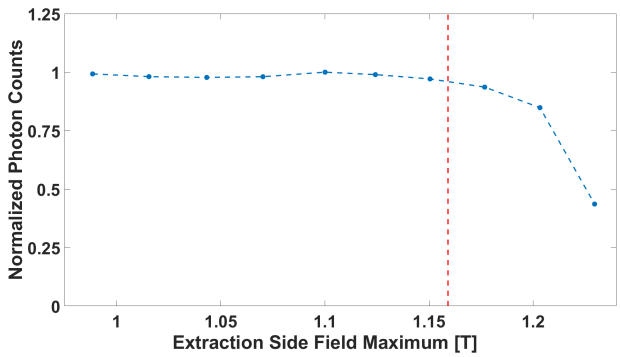

Figure 6: Total number of xray photons, with energies greater than 80 keV, measured while varying the extraction side maximum. B_{min} = 0.4 T, P_{μ} = 350 W, p_{Ar} = 213 nTorr. The dashed vertical line shows where $B_{Ext,max}/B_{RF}$ = 1.8. The data set is normalized by its largest value.

amplitude and frequency microwave signal change throughout this part of the measurement, in both time and frequency domains. At low fields, the amplitude and repetition frequency between subsequent instability events are similar. As the field increases, the amplitude between subsequent instability events becomes more random. The emission of microwave radiation begins spreading over the frequency domain. Eventually, we begin to see larger single instability events that occur less frequently. These events overshadow a set of smaller, but more frequent, instabilities events that do little to perturb the extracted current. At the end of our field domain, B_{min} = 0.47 T, the plasma appears to stabilize. The variations in the extracted current and emitted microwave power become indistinguishable from electronic noise. This does not mean that the plasma is stable, as it may exist in the so-called "CW" mode; however, without more sophisticated diagnostics, this operating point is almost indistinguishable from one that is stable [15].

ISBN: 978-3-95450-226-4 ISSN: 2222-5692 doi:10.18429/JACoW-ECRIS2020-MOYZO03

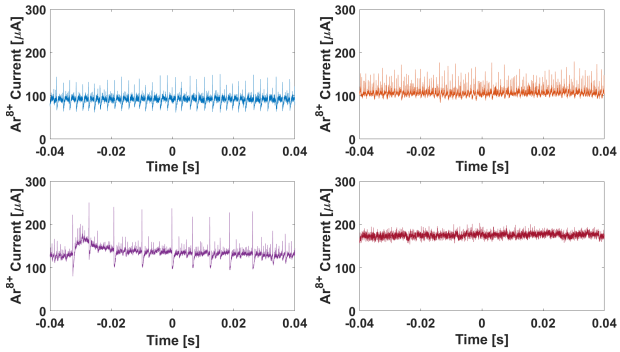

Figure 7: Fourier transform of the microwave power signals emitted from the ion source for a varying magnetic minimum: (Top Left) B_{min} = 0.34 T, (Top Right) B_{min} = 0.40 T, (Bottom Left) B_{min} = 0.44 T, (Bottom Right) B_{min} = 0.47 T. $B_{Ext,max}$ = 1.1 T, P_{μ} = 350 W, p_{Ar} = 213 nTorr.

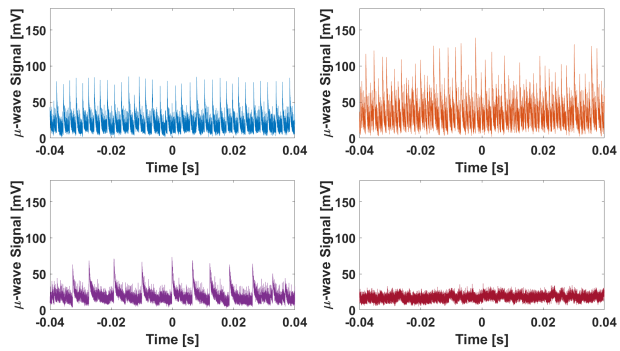

Figure 8: Fourier transform of the microwave power signals emitted from the ion source for a varying magnetic minimum: (Top Left) B_{min} = 0.34 T, (Top Right) B_{min} = 0.40 T, (Bottom Left) B_{min} = 0.44 T, (Bottom Right) B_{min} = 0.47 T. $B_{Ext,max}$ = 1.1 T, P_{μ} = 350 W, p_{Ar} = 213 nTorr.

The average extracted beam current increases over the measured domain (see Fig. 10). At B_{min} = 0.47 T ≈ 0.73 B_{RF}, the beam current reaches its maximum while also minimizing its upward and downward deviations. The field domain was not large enough to determine if the current would continue to increase or begin to decrease beyond 0.47 T, although previous measurements suggest an eventual decrease [5]. In this case, the maximum current correlates with a minimum in the emitted microwave power. Lastly, we can see that intensity of photons emitted from the plasma chamber increased monotonically with the increasing magnetic field strength. In this case, we do not see any qualitative change in the diffusion rate of electrons out of the system.

DISCUSSION

The results of these measurements demonstrated how the ECRIS magnetic field topology affects the stability of its plasma. Figures 2 and 7 show that more frequent instability events tend to correlate with larger amplitude beam current variations, in particular, larger losses. A longer time between instability events may indicate that a larger population of

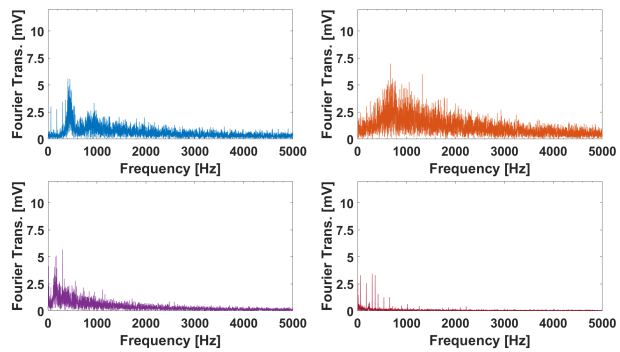

Figure 9: Fourier transform of the microwave power signals emitted from the ion source for a varying magnetic minimum: (Top Left) B_{min} = 0.34 T, (Top Right) B_{min} = 0.40 T, (Bottom Left) B_{min} = 0.44 T, (Bottom Right) B_{min} = 0.47 T. $B_{Ext,max}$ = 1.1 T, P_{μ} = 350 W, p_{Ar} = 213 nTorr. The peaks in the lower right plot are the result of electronic noise that is persistent throughout the facility.

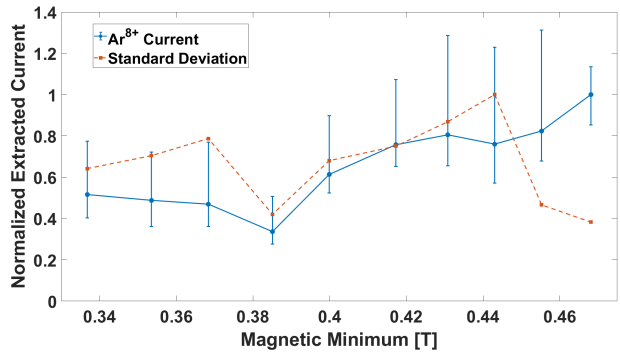

Figure 10: Average, maximum, and minimum Ar^{8+} beam currents, measured over a 100 ms period, for a varying magnetic minimum.

electrons builds up before the instability event. This buildup would result in a larger loss of electrons from confinement per event and perturb the plasma to a greater degree. On the other hand, this hypothesis would also imply a larger release of microwave energy from the plasma per event. However, confirming this hypothesis is difficult, as we cannot measure the propagation frequencies of the emitted microwaves. Without this information, we cannot correct Figs. 3 and 8 for waveguide losses.

Figures 6 seem to suggest that the decreasing extracted ion current above $B_{Ext,max}$ = 1.8 B_{RF} is correlated with a decreasing electron diffusion rate. The more frequent instability events may suppress the accumulation of electrons within the system, effectively suppression the production of highly charged ions. However, the increasing instability rate does not appear to affect the diffusion rate of electrons while the magnetic minimum is increased (Fig. 11). Alternatively, the changing electron diffusion rate may result from the varying pitch angle of the magnetic field's loss cone. However, if that were the case, we would expect to see a change in

ISBN: 978-3-95450-226-4 ISSN: 2222-5692 doi:10.18429/JACoW-ECRIS2020-MOYZO03

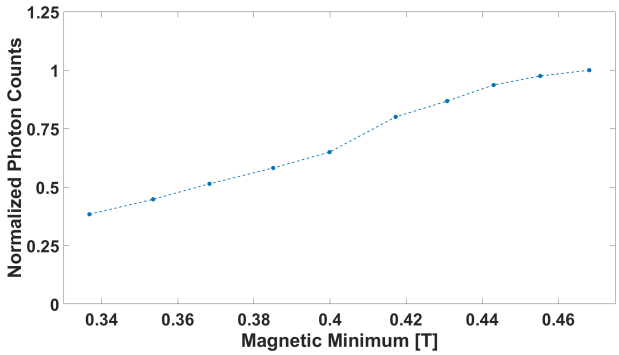

Figure 11: Total number of xray photons, with energies greater than 80 keV, measured while varying the magnetic minimum. $B_{Ext,max}$ = 1.1 T, P_{μ} = 350 W, p_{Ar} = 213 nTorr. The data set is normalized by its largest value.

the electron diffusion rate for lower extraction field maxima, which is not the case.

More work is necessary in order to understand the relationship between ECR ion source performance and the kinetic instabilities within the ion source plasma. The results shown here indicate that the ECRIS performance is not necessarily correlated with the presence of kinetic instabilities. Rather, a more complicated interaction between the magnetic field topology and the electron population appears to limit the extracted ion current. However, these results are limited to the low power regime, and may not represent performance at higher powers. Further studies of the electron diffusion rate, particularly beyond the B_{min}/B_{RF} = 0.8 performance limit, may provide greater insight into the scaling laws.

ACKNOWLEDGMENTS

This research was made possible by the National Science Foundation under NSF Grant 1632761 and U.S. Department of Energy Award Number DE-SC0018362. Thanks are given to the NSCL/FRIB Ion Source group staff Jeff Stetson, Jesse Fogleman, and Larry Tobos. We also thank the NSCL/FRIB facilities and operational managers including Andreas Stolz, Yoshishige Yamazaki, Thomas Russo, Kent Holland, and Steven Lidia.

REFERENCES

[1] R. Geller, "ECR source scaling concepts," in *Proceedings of the 1989 IEEE Particle Accelerator Conference*, Chicago, IL, USA, 1989, pp. 1088–1092. doi:10.1109/pac.1989.73363.

[2] S. Gammino and G. Ciavola, "ECR Ion Sources and Scaling Laws," *Proceedings of the 14th International Conference on Cyclotrons and their Applications, Cape Town, South Africa*, pp. 377–380, 1996.

[3] D. Hitz, A. Girard, G. Melin, S. Gammino, G. Ciavola, and L. Celona, "Results and interpretation of high frequency experiments at 28 GHz in ECR ion sources, future prospects," *Review of Scientific Instruments*, vol. 73, no. 2, p. 509, Feb. 2002. doi:10.1063/1.1429313.

[4] C.M.Lyneis, "Scaling Laws in Electron Cyclotron Resonance Ion Sources," in *Proc. ECRIS'16*, Busan, Korea, Oct. 2016, pp. 1–4. doi:10.18429/JACoW-ECRIS2016-MOAO01.

[5] O. Tarvainen *et al.*, "Limitation of the ECRIS performance by kinetic plasma instabilities (invited)," *Review of Scientific Instruments*, vol. 87, no. 2, 2016. doi:10.1063/1.4931716.

[6] D. Mansfeld *et al.*, "Dynamic regimes of cyclotron instability in the afterglow mode of minimum-B electron cyclotron resonance ion source plasma," *Plasma Physics and Controlled Fusion*, vol. 58, no. 4, p. 045 019, Apr. 2016. doi:10.1088/0741-3335/58/4/045019.

[7] I. Izotov *et al.*, "Microwave emission related to cyclotron instabilities in a minimum-B electron cyclotron resonance ion source plasma," *Plasma Sources Science and Technology*, vol. 24, no. 4, p. 045 017, Jul. 2015. doi:10.1088/0963-0252/24/4/045017.

[8] A. G. Shalashov, E. D. Gospodchikov, and I. Izotov, "Electron-cyclotron heating and kinetic instabilities of a mirror-confined plasma: the quasilinear theory revised," *Plasma Physics and Controlled Fusion*, 2020. doi:10.1088/1361-6587/ab7f98.

[9] D. B. Melrose, "Coherent emission mechanisms in astrophysical plasmas," *Reviews of Modern Plasma Physics*, vol. 1, no. 1, pp. 1–81, 2017. doi:10.1007/s41614-017-0007-0.

[10] C. S. Wu, "Kinetic cyclotron and synchrotron maser instabilities: Radio emission processes by direct amplification of radiation," *Space Science Reviews*, vol. 41, no. 3-4, pp. 215–298, Aug. 1985. doi:10.1007/BF00190653.

[11] V. Skalyga *et al.*, "Suppression of cyclotron instability in Electron Cyclotron Resonance ion sources by two-frequency heating," *Physics of Plasmas*, vol. 22, no. 8, 2015. doi:10.1063/1.4928428.

[12] B. Isherwood, G. Machicoane, D. Neben, G. Pozdeyev, and J. Stetson, "Plasma Instability Studies of the SuSI 18 GHz Source," in *Proc. ECRIS'18*, (Catania, Italy, Aug. 2016), Feb. 2019, pp. 157–161. doi:10.18429/JACoW-ECRIS2018-WEA3.

[13] P. A. Zavodszky *et al.*, "Design of SuSI - Superconducting source for ions at NSCL/MSU - I. The magnet system," *AIP Conference Proceedings*, vol. 749, pp. 131–134, 2005. doi:10.1063/1.1893382.

[14] B. Isherwood and G. Machicoane, "Measurement of the energy distribution of electrons escaping confinement from an electron cyclotron resonance ion source," *Review of Scientific Instruments*, vol. 91, no. 2, p. 025 104, Feb. 2020. doi:10.1063/1.5129656.

[15] A. G. Shalashov, E. D. Gospodchikov, I. V. Izotov, D. A. Mansfeld, V. A. Skalyga, and O. Tarvainen, "Control of electron-cyclotron instability driven by strong ECRH in open magnetic trap," *EPL (Europhysics Letters)*, vol. 124, no. 3, p. 35 001, Dec. 2018. doi:10.1209/0295-5075/124/35001.

ISBN: 978-3-95450-226-4 ISSN: 2222-5692 doi:10.18429/JACoW-ECRIS2020-MOZZO01

PRODUCTION OF ^{48}Ca AND ^{48}Ti ION BEAMS AT THE DC-280 CYCLOTRON

S. L. Bogomolov, D. K. Pugachev†, V. E. Mironov, A. A. Efremov,
V. N. Loginov, A. N. Lebedev, A. E. Bondarchenko, K. I. Kuzmenkov,
Flerov Laboratory of Nuclear Reactions, Joint Institute for Nuclear Research, Dubna, Russia

Abstract

The heaviest known elements (up to ^{118}Og) were synthesized at the U-400 cyclotron (FLNR JINR, Dubna) by using a beam of ^{48}Ca ions.

During the tests of the DC-280 cyclotron an intense beams of ^{48}Ca ions were produced.

For synthesis of the elements 119 and heavier, intense and stable beams of medium-mass elements are required, such as ^{50}Ti and ^{54}Cr. Before starting the main experiments, we test the production of ^{48}Ti ion beam, which is less expensive than ^{50}Ti.

The article describes the method, technique, and experimental results on the production of ^{48}Ca and ^{48}Ti ion beam at the DC-280 cyclotron from the DECRIS-PM ion source.

INTRODUCTION

In last 20 years, at FLNR JINR the super-heavy elements up to 118 have been synthesized using the ^{48}Ca at the U-400 cyclotron.

For further progress in the synthesis of SHE the first in the world Factory of superheavy elements (SHE Factory) was created at the FLNR JINR in 2019 [1]. The main goals of the SHE Factory are experiments at the extremely low cross sections, such as synthesis of new SHE, new isotopes of SHE and study of decay properties of SHE. In addition, experiments requiring high statistics will be conducted, such as nuclear spectroscopy and the study of the chemical properties of SHE.

The factory includes the high-current DC-280 cyclotron and gas-filled separator DGFRS-2. The main parameters of the cyclotron are shown in the Table 1.

Table 1: The Main Parameters of DC-280

Ion sources	DECRIS-PM - 14 GHz
Injection energy	Up to 80 keV/Z
A/Z range	4÷7.5
Energy	4÷8 MeV/n
Magnetic field level	0.6÷1.3 T
K factor	280
Magnet weight	1000 t
Magnet power	300 kW
Dee voltage	2x130 kV
RF power consumption	2x30 kW
Flat-top dee voltage	2x14 kV
Deflector voltage	Up to 90 kV

The cyclotron is equipped with the all-permanent magnet ion source DECRIS-PM [2] (Fig. 1).

† pugachev@jinr.ru

To obtain the requested injection energy, the source is placed at a high-voltage platform. The requests for the ion source are the production of ions with low and medium masses (from He to Kr) such as ^{48}Ca and ^{50}Ti.

The first experiments at the SHE factory will be performed using ^{48}Ca+^{242,244}Pu and the ^{48}Ca+^{243}Am reactions. After completion of these experiments, it is planned to start the synthesis of new superheavy elements in reactions of ^{50}Ti and ^{54}Cr ions with ^{248}Cm, ^{249}Bk and $^{249\text{-}251}$Cf isotopes.

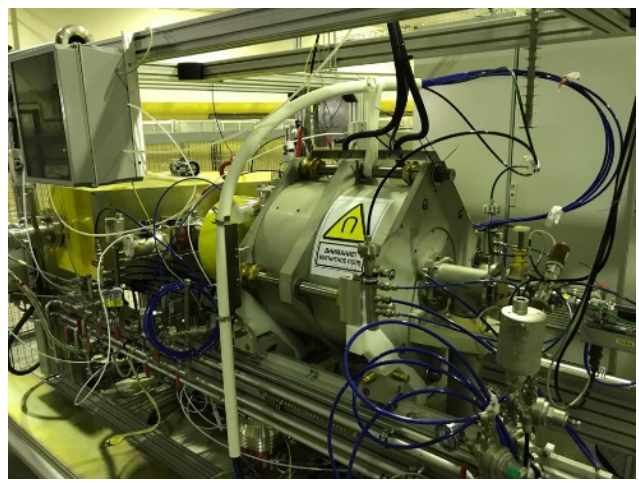

Figure 1: The DECRIS-PM on the high-voltage platform of the DC-280 cyclotron.

THE SOURCE DESIGN

Several different ion sources with permanent magnets are in operation, such as LAPECR2 [3], NANOGAN [4], BIE [5], and others. The sources of this type have the following advantages:

- Low power consumption.
- Low pressure in the water-cooling system.
- Easy tuning.

Disadvantages of these sources are the fixed and relatively small magnetic fields. Despite these disadvantages, the systems typically have a long service life-time.

The magnetic structure of DECRIS-PM consists of hexapole with 24-segments and five 36-segmented axial magnetic rings. The magnetic structure and axial magnetic field are shown in Fig. 2. In the middle part of the source the additional coil is installed for correction of B_{min} value in the range of ±0.075 T, with the maximum current in the coil of 300 A.

The source was tested on a test-bench before installing to the DC-280. The results for metal ions are shown in Table 2 [6].

ISBN: 978-3-95450-226-4 ISSN: 2222-5692 doi:10.18429/JACoW-ECRIS2020-MOZZO01

Table 2: Results of the DECRIS-PM Tests

Q	5^+	7^+	8^+	9^+	10^+	11^+	12^+
^{24}Mg	450	140	40	15			
^{40}Ca				220		158	58
^{50}Ti				90	72	60	23
^{56}Fe				85	80	55	

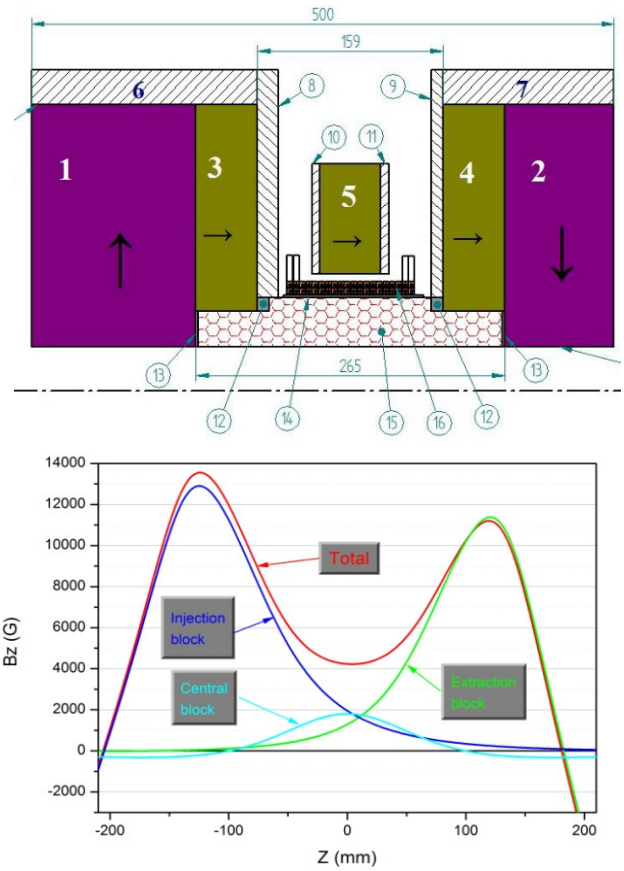

Figure 2: (Top) Magnetic structure of DECRIS-PM: 1÷5 – PM rings; 6, 7 – soft iron rings; 8÷11 – soft iron plates, 12÷14 – auxiliary elements, 15 – hexapole, 16 – coil. (Bottom) Axial magnetic field.

PRODUCTION OF ^{48}Ca BEAM

Production of Ca ions is performed by injecting the calcium vapors into the source chamber from the electrically heated micro-oven installed at the injection side of the source and shifted from the center to the radius of 23-mm.

The oven has a length of 50 mm and the outer diameter of 6 mm. The body of the oven is made of stainless steel; the crucible is made of tantalum. Working diagram for the oven is shown in the Fig.3. The red quadrangle shows the temperature range for the required vapor pressure; the average vapor pressure for calcium in this area is 2.3×10^{-3} Torr.

The crucible is filled with Ca at the stand-alone installation by using the calcium oxide reduction with aluminum in vacuum:

$$3CaO+2Al \rightarrow 3^{48}Ca+Al_2O_3 \quad (1)$$

The required temperature for the reaction is around 1300 °C. In the process of reduction, pure calcium is condensed inside the crucible. The evaporation system is shown in Fig. 4.

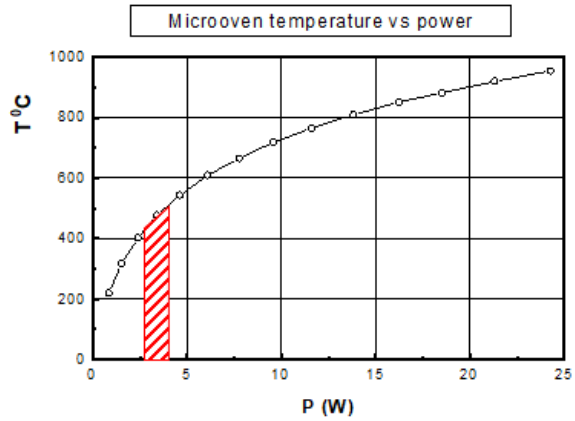

Figure 3: Working diagram of the oven.

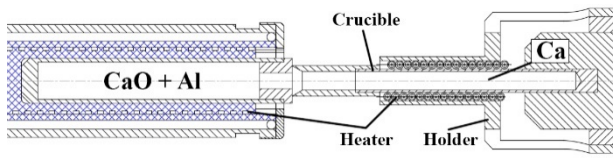

Figure 4: Calcium evaporation system.

The inner volume of the crucible (Fig. 5) is 88 mm^3 that corresponds to 130 mg of calcium. However, the irregular deposition during reduction from the initial volume into the crucible gives a smaller volume of the substance. The crucible is stored in a vacuum container to avoid re-oxidation.

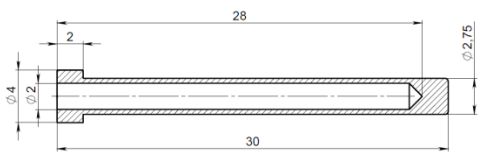

Figure 5: Crucible.

A significant part of the metal vapors evaporated from the oven condenses on the walls of the source chamber and only a small part leaves the source as an ion beam [6]. To prevent deposition of atoms on the water-cooled walls of the chamber, we use a hot tantalum screen. It is placed inside the source with a minimum contact with the surface of the chamber, which reduces heat transfer in the system. During the source operation, the screen is heated by the plasma electrons and microwaves, which contributes to the additional evaporation of the atoms from the surface. As the result, the higher is the injected microwave power, the higher is the temperature of the screen. The injected microwave power of 500 W provides the screen temperature of 550 °C, which is quite enough for the evaporation of calcium from the screen surface [7].

As a support gas, light gases such oxygen and helium are used. The best result for required charge state (Ca^{10+}) is achieved with helium (Fig. 6).

ISBN: 978-3-95450-226-4 ISSN: 2222-5692 doi:10.18429/JACoW-ECRIS2020-MOZZO01

The total operational time with injection of the calcium beam is currently ~1600 hours; the average consumption for the entire working time is 0.7 mg/h at the average intensity of 8 pμA for Ca^{10+}. The average efficiency of the total Ca ion extraction is 16%, for the Ca^{10+}, this value is 5%, excluding regeneration. The dependence of consumption on the ion beam current of Ca^{10+} is almost linear.

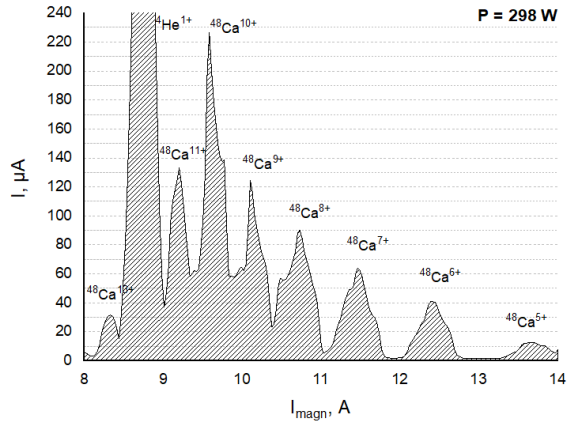

Figure 6: The ^{48}Ca ion spectrum, optimized for Ca^{10+}.

PRODUCTION OF ^{48}Ti BEAM

Operational temperatures of our micro-oven do not allow to use the evaporation technique to produce ^{48}Ti ion beams. Thus, to obtain a stable and high-intensity titanium beam we use the MIVOC method. This method is based on use of organometallic compounds that have a relatively high vapor pressure (10^{-3} Torr) at the room temperature.[8] The vapor pressure is sufficient to operate the source providing the high conductivity of the vapor supply channels. We tried to work with different systems of the gas feeding. The best results were achieved with the gas-regulating valve EVR 116 [9]; it has a smooth adjustment of the gas supply and sufficient gas conductivity, which eliminates clogging of the valve openings by the deposited compound.

The working substance is placed in a glass container (Fig. 7) and after pre-pumping, the glass flask breaks inside the metal casing, which prevents air from entering. The vapor pressure of the substance at the room temperature is sufficient to produce an ion beam without a support gas.

Figure 7: Container with $(CH_3)_5C_5Ti(CH_3)_3$.

The source is equipped with a half-millimeter thick stainless-steel liner to facilitate cleaning of the chamber from carbon contamination. It is a necessary because the change of operating modes should be done in a short period of time. The recently measured charge state distribution of the extracted ion currents for titanium ions is shown in Fig.8. The working time with the titanium beam currently corresponds to ~240 hours on a DC-280 cyclotron. The average efficiency of ion source for ^{48}Ti is 20 %, for the Ti^{7+} this value is 5%.

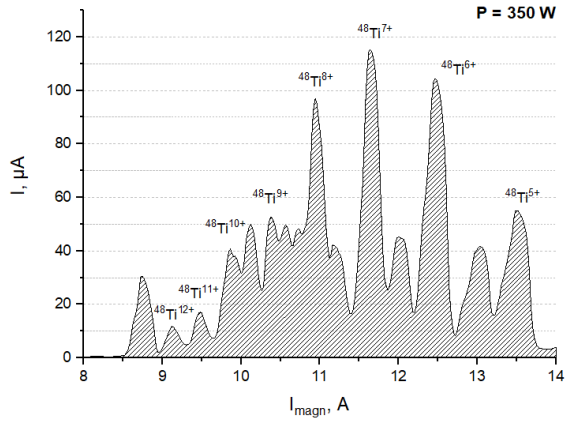

Figure 8: The ^{48}Ti ion spectrum, optimized for Ti^{7+}.

CONCLUSION

During the work was obtained ^{48}Ca and ^{48}Ti. Calcium beam was accelerated, the average efficiency from the ion source to output from the cyclotron is 50%. The average consumption for the Calcium-48 is 0.7 mg/h, for Titanium-48 is 0.55-0.65 mg/h.

ACKNOWLEDGMENT

This work was supported by the Russian Foundation for Basic Research under grant № 20-52-53026/20.

REFERENCES

[1] S. N. Dmitriev *et al.,* "SHE Factory: Cyclotron Facility for Super Heavy Elements Research", in *22nd Int. Conf. on Cyclotrons and their Applications, Cyclotrons'19*, Cape Town, South Africa, JACoW Publishing, pp. 305-310. doi:10.18429/JACoW-Cyclotrons2019-THC01

[2] A. Efremov *et al.*, AIP Conf. Proc. 2011, 040016 (2018). doi:10.1063/1.5053290

[3] L.T. Sun *et al.*, "A high charge state all-permanent magnet ECR ion source for the IMP 320 kV HV platform", *Nucl. Instrum. Methods Phys. Res., Sect. B*, vol. 263, pp. 503–512, 2007. doi:10.1016/j.nimb.2007.07.012

[4] C. Bieth, J. L. Bouly, J. C. Curdy, S. Kantas, P. S. Sole, and J. L. Vieux-Rochaz, "Electron cyclotron resonance ion source for high currents of mono- and multicharged ion and general purpose unlimited lifetime application on implantation devices", *Rev. Sci. Instrum.*, vol. 71, pp. 899–901, 2000. doi:10.1063/1.1150326

[5] Dan. Z. Xie, "The BIE100 ECR ion source", *Rev. Sci. Instrum.*, vol. 73, pp. 531–533, 2002. doi:10.1063/1.1429320

ISBN: 978-3-95450-226-4 ISSN: 2222-5692 doi:10.18429/JACoW-ECRIS2020-MOZZO01

[6] A.A. Efremov *et al.*, "All-permanent Magnet ECR Ion Source DECRIS-PM", in *Proc. HIAT'18*, Lanzhou, China, Oct. 2018, pp. 89-91. doi:10.18429/JACoW-HIAT2018-TUOXA01

[7] V. B. Kutner *et al.*, "Production of intense ^{48}Ca ion beam at the U-400 cyclotron", *Rev. Sci. Instrum.*, vol. 71(2), p. 860, 2000. doi:10.1063/1.1150313

[8] H. Koivisto, J. Arje, and M. Nurmia, "Metal ion beams from an ECR ion source using volatile compounds", *Nucl. Instrum. Methods Phys. Res., Sect. B*, vol. 94, pp. 291–296, 1994. doi:10.1016/0168-583X(94)95368-6

[9] Pfeiffer Vacuum https://www.pfeiffer-vacuum.com

ISBN: 978-3-95450-226-4 ISSN: 2222-5692 doi:10.18429/JACoW-ECRIS2020-MOZZO02

ECR DISCHARGE IN A SINGLE SOLENOID MAGNETIC FIELD AS A SOURCE OF THE WIDE-APERTURE DENSE PLASMA FLUXES*

I. V. Izotov†, A. F. Bokhanov, S. V. Golubev, M. Yu. Kazakov, S. V. Razin,
R. A. Shaposhnikov, S. P. Shlepnev, V. A. Skalyga
Institute of Applied Physics of Russian Academy of Sciences, Nizhny Novgorod, Russia

Abstract

Sources of dense plasma fluxes with wide aperture are extensively used in applied science, i.e. surface treatment, and as a part of neutral beam injectors [1]. Electron cyclotron resonance (ECR) discharge in a solenoidal magnetic field (i.e. with no magnetic mirrors for plasma confinement), sustained by a powerful radiation of modern gyrotrons is under consideration at IAP RAS as a possible alternative to widely used vacuum arc, RF and helicon discharges. The use of a high frequency radiation (37.5 GHz) allows us to obtain a discharge at lower pressure, sustain almost fully ionized plasma with density more than 10^{13} cm^{-3}, whereas the power on the level of several hundreds of kW enables the creation of such a plasma in considerably large volume. In the present work fluxes of hydrogen plasma with the equivalent current density of 750 mA/cm^2 and the total current of 5 A were obtained. A multi-aperture extraction system design capable of forming the non-divergent ion beam was developed with the use of IBSimu code.

INTRODUCTION

The use of the powerful millimetre wavelength range gyrotron radiation for the plasma heating allowed us to create a concept of an unique gasdynamic ion sources at IAP RAS. In such sources the plasma density confined in the simple mirror trap reaches the level of 10^{13}-10^{14} cm^{-3} with the electron temperature on the order of 100 eV [2–5]. The presented research was conducted to investigate the possibility of creation of the plasma with comparable to the gasdynamic ECR ion source (ECRIS) parameters using the sole solenoid field for radial plasma confinement, leaving longitudinal confinement to a self-consistent ambipolar potential, which accelerates ions and slows down electrons. The system based on the single solenoid is very convenient for scaling, much more compact, is free of plasma bremsstrahlung due to the absence of hot electrons, and greatly reduces material costs when compared to the conventional ECRIS traps and with the simple mirror trap.

EXPERIMENTAL FACILITY

The test bench was constructed on the base of SMIS37 facility [3]. The scheme of the experiment is shown in the Figure 1. The microwave radiation with the frequency 37.5 GHz and the power up to 100 kW is launched into the plasma chamber of 68 mm inner diameter through the microwave coupling system. The wedge-like coupling system was located inside the discharge chamber in order to prevent the plasma flux reaching the quartz vacuum window. The microwave launching part has an inner diameter of 38 mm, whereas the plasma chamber has an inner diameter of 68 mm. An influence of that fact on the obtained result is discussed in the conclusion section of the present paper. A stainless steel grid with a transparency of 70% was installed at the farther end of the discharge chamber, opposite to the injection side, in order to create a microwave cavity to improve the efficiency of plasma heating. In the presented research, the metal grid was a part of the discharge chamber and, accordingly, they were under the same potential, namely, they were grounded. The magnetic field in the centre of the coil was varied from 1 to 3 T, while the resonance field value for the radiation frequency of 37.5 GHz is 1.34 T. The plasma chamber is placed inside the pulsed solenoid, which provides the maximum field in its centre of up to 3 T.

The neutral gas is injected into the discharge chamber through the gas feed line embedded into the microwave cou-

* supported by RFBR, project #19-32-90079, and by Presidential Grants Foundation (Grant #MD-2745.2019.2)
† †vizot@ipfran.ru

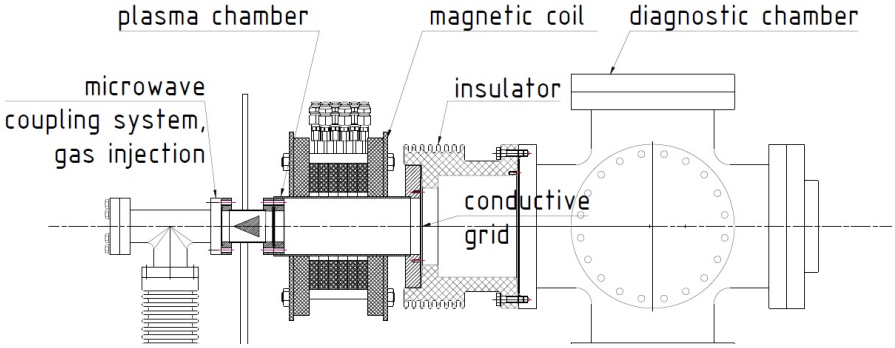

Figure 1: The principal scheme of the constructed experimental bench.

ISBN: 978-3-95450-226-4 ISSN: 2222-5692 doi:10.18429/JACoW-ECRIS2020-MOZZO02

pling system by means of a fast solenoid valve, much alike to SMIS37 facility. The working pressure range was $2{\cdot}10^{-4}$ – $8{\cdot}10^{-4}$ Torr. The residual gas pressure was on the level of 10^{-7} Torr.

EXPERIMENTAL RESULTS

The plasma flux was studied with a single flat Langmuir probe with 1 mm2 square, placed on a 3D movable rod mounted on the back flange of the diagnostic chamber providing measurement both in longitudinal and transverse directions with respect to the magnetic field. The probe was biased negatively, thus measuring the ion saturation current.

The dependence of the plasma flux density on the magnetic field in the solenoid as a function of the injected microwave power is shown in Figure 2.

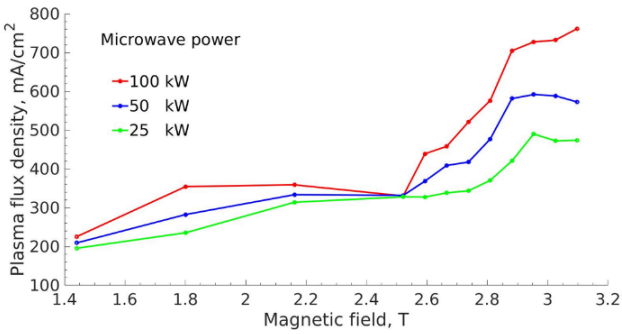

Figure 2: Plasma flux density dependence on the magnetic field value as a function of the injected microwave power.

In this measurement the probe was placed on the system axis as close to the metal grid as possible, resulting in the distance of 74 mm between the probe and the solenoid centre. It is clearly seen from Figure 2 that the plasma flux density increases with the magnetic field magnitude and reaches 750 mA/cm^2 at 3.1 T and the microwave power of 100 kW. A clear change of dependencies behaviour is observed above 2.5 T, which is presumably explained by the fact that at this field strength the farthest from the microwave launching system ECR zone touches the grid. The effect of ECR surface position would be studied in further experiments.

We have also confirmed that the dependence of the plasma flux density on the coordinate along the system axis follows the magnetic field strength, thus the plasma flux is magnetized within the whole volume of the discharge chamber, which may be beneficial for the extractor design providing a flexible tool to control the flux density by moving the extraction system along the system axis.

To study the homogeneity of the plasma flux, we measured the radial profile at the same distance of 74 mm from the solenoid centre, i.e. as close to the grid as possible. The measurement was done with the optimal parameters, being 3.1 T and 100 kW of microwave power and its result is presented in Figure 3. While the maximum density was 750 mA/cm^2, the corresponding total ion current reached 5 A, evaluated straightforward as an integral of the profile over transverse coordinate, assuming the axial symmetry of the flux.

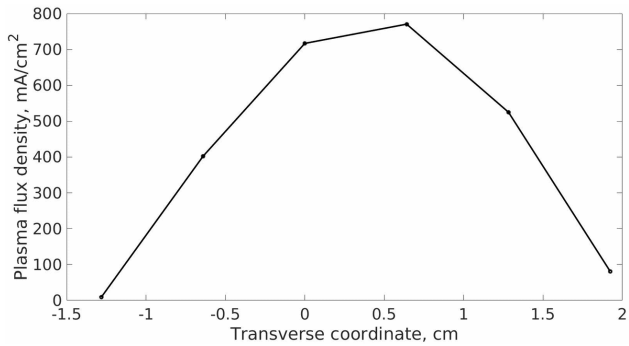

Figure 3: Plasma flux transverse profile at 74 mm from the solenoid centre. Microwave power is 100 kW, gas pressure is $8 \cdot 10^{-4}$ Torr, magnetic field in the coil centre is 3.1 T.

Also, it could be seen that plasma flux FWHM is on the order of 25 mm, while the plasma chamber is 68 mm in diameter. This may be explained by the structure of magnetic field lines together with the plasma chamber geometry. The plasma flux in the system is likely constrained by the diameter of the microwave coupling. This fact additionally underlines the importance of the microwave injection scheme for the discharge parameter optimization. More studies on the microwave coupling scheme are needed even in such a simple configuration.

EXTRACTION SYSTEM DESIGN

n order to form non-divergent beam with current density on the level of 750 mA/cm^2 and total current of several A it is necessary to use a custom multi-aperture or gridded extraction system, as the current density-induced space charge of the beam is considerably high. Simulations of the system capable of dealing with such a beam were performed with IBSimu code [6]. Numerical studies have shown that the least divergent beam may be obtained with the use of 3 multi-aperture electrodes: plasma electrode, middle electrode and puller electrode, separated by 4 and 5 mm respectively. The assembly is intended to be installed at the same position as the grid was installed to in presented experiments, i.e. 74 mm from the solenoid centre, thus the plasma electrode would be acting as a microwave cavity plug. The optimal potentials were numerically found to be +80 kV at the plasma electrode and the plasma chamber, +70 kV at the middle electrode, whereas the puller electrode is conventionally grounded. All of the electrodes have the same shaped holes of 1 mm in diameter and total transparency of 70%. The result if simulation is presented in Figure 4.

According to simulations, it is possible to form a slightly divergent beam with the current density of 750 mA/cm^2 in the accelerating gap and on the level of 500 mA/cm^2 further downstream the beamline.

ISBN: 978-3-95450-226-4 ISSN: 2222-5692 doi:10.18429/JACoW-ECRIS2020-MOZZO02

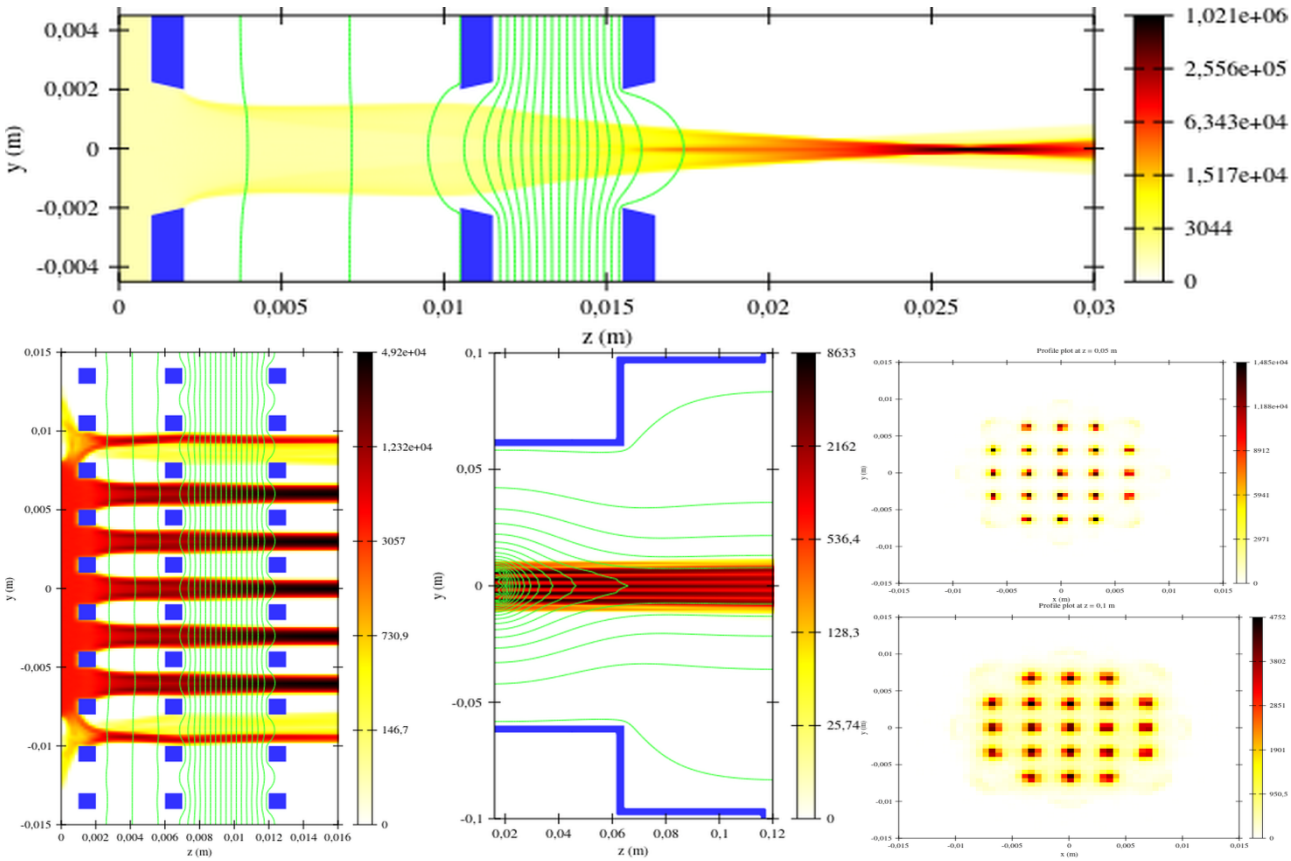

Figure 4: IBSimu simulation of a multi-aperture extraction system. Electric potential (green lines) and current density (false colour) are shown for the single beamlet (top), all beamlets in the extraction region (bottom left), extender region (bottom middle). Cross-sections of the beam current density close to the extraction system (middle right) and 200 mm downstream the beamline (bottom right) are shown in false colour.

CONCLUSION

Wide-aperture plasma fluxes from the ECR discharge in the magnetic field of a single solenoid were obtained. It was found that the flux density increases with the microwave power and magnetic field. The maximum value of the flux density was 750 mA/cm^2, and corresponding total ion current was equal to 5 A. It was also found that the plasma follows magnetic field lines while expanding into the diagnostic chamber.

The obtained results may be supposedly improved with the increase in the frequency and the power of heating microwaves. An increase in the flux aperture could be provided by the use of discharge chambers of larger diameters simultaneously with a specific design of the microwave injection, optimized for more uniform electromagnetic field distribution in the volume.

The obtained results demonstrate perspectives of the proposed system based on a single coil for wide-aperture plasma flux formation, including its probable application for neutral injector development.

Further investigations will be dedicated to the obtaining of plasma fluxes with apertures of 100 cm^2 and a flux density of 1 A/cm^2. The numerically tested extraction system will be tested experimentally.

REFERENCES

[1] L. R. Grisham *et al.*, "Recent improvements to the ITER neutral beam system design", *Fusion Eng. Des.*, vol. 87, p. 1805–1815, 2012, doi:10.1016/j.fusengdes.2012.08.001

[2] V. Zorin, S. Golubev, S. Razin, A. Sidorov, V. Skalyga, and A. Vodopyanov, "High current density ion beam formation from plasma of electron cyclotron resonance discharge", *Rev. Sci. Instrum.*, vol. 75, p. 1675, 2004, doi:10.1063/1.1702086

[3] V. Skalyga *et al.*, "High current proton beams production at Simple Mirror Ion Source 37", *Rev. Sci. Instrum.*, vol. 85, p. 02A702, 2014, doi:10.1063/1.4825074

[4] V. Skalyga *et al.*, "New progress of high current gasdynamic ion source", *Rev. Sci. Instrum.*, vol. 87, p. 02A716, 2016, doi:10.1063/1.4934213

[5] V. A. Skalyga *et al.*, "Study of hydrogen ECR plasma in a simple mirror magnetic trap heated by 75 GHz pulsed gyrotron radiation", *Rev. Sci. Instrum.*, vol. 88, p. 033503, 2017, doi:10.1063/1.4978278

[6] T. Kalvas *et al.*, "IBSIMU: A three-dimensional simulation software for charged particle optics", *Rev. Sci. Instrum.*, vol. 81, p. 02B703, 2010, doi:10.1063/1.3258608

ISBN: 978-3-95450-226-4 ISSN: 2222-5692 doi:10.18429/JACoW-ECRIS2020-MOZZO03

STABLE AND INTENSE ^{48}Ca ION BEAM PRODUCTION WITH A MICROWAVE SHIELDED OVEN AND AN OPTICAL SPECTROMETER AS DIAGNOSTIC TOOL

F. Maimone†, A. Andreev, R. Hollinger, R. Lang, J. Mäder, P. T. Patchakui, and K.Tinschert
GSI-Helmholtzzentrum für Schwerionenforschung, Darmstadt, Germany

Abstract

The CAPRICE ECRIS installed at the High Charge Injector (HLI) of GSI produces highly charged ion beams from gaseous and metallic elements. A high demand of metal ions comes from the nuclear physics, material research, and Super Heavy Element group (SHE), and the most requested element, besides ^{50}Ti, is ^{48}Ca. When this chemical reactive material is deposited inside the plasma chamber at internal components the stability can be compromised. Furthermore, it is difficult to find a working point to guarantee a long-term stability as the oven response time and the reaction of the ECRIS are relatively slow. The monitoring by using an Optical Emission Spectrometer (OES) facilitates immediate reactions whenever plasma instabilities occur. For this reason, a real-time diagnostic system based on an OES has been installed at the ECRIS at HLI for routine operation during the beam-time 2020. The measured spectra revealed a parasitic oven heating by coupled microwaves often compromising the ion source performance. Therefore, a tungsten grid has been installed to shield the oven orifice from the coupled microwaves. The results in terms of ^{48}Ca beam intensity and stability are reported here.

INTRODUCTION

At the high charge state injector (HLI) of GSI highly charged ions are produced by a CAPRICE-type ECRIS. Up to 260 days of beam time per year were served from the ECRIS injector in the last decade. Figure 1 shows the total days of beam-times starting from 2008. In 2013 and 2017 the accelerator was on shut-down mode for maintenance or upgrade.

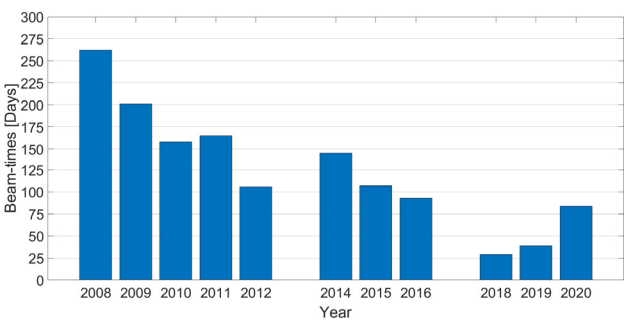

Figure 1: Total days of beam times in the last 12 years by the GSI ECRIS at HLI

† f.maimone@gsi.de

A high demand of metal ions comes from the nuclear physics, material research, and Super Heavy Element (SHE) groups, and the most requested element is ^{48}Ca as shown Fig. 2. Up to 85 days per year of ^{48}Ca were requested in the last years. In order to produce the metallic ion beams with high efficiency and low material consumption, the evaporation technique is used at GSI by means of a resistively heated oven, the STO (Standard Temperature Oven). [1] The ion source performance in producing metallic ion beams has been optimized through the past decades to satisfy the demand of intensity and stability. However, when chemical reactive materials are deposited inside the plasma chamber and at internal components, the stability is compromised. Furthermore, it is difficult to find a working point for a long-term stability because the response time of the oven and the reaction of the ECRIS are relatively slow.

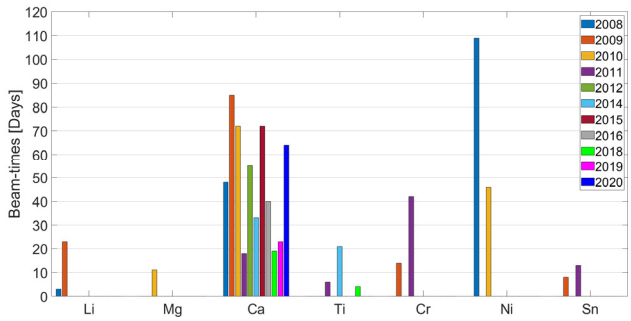

Figure 2: Total days of metallic ion beams produced in the last 12 years by the GSI ECRIS at HLI.

The Optical Emission Spectroscopy has been used to analyse the plasma parameters [2-3] and the continuous monitoring by using an Optical Emission Spectrometer (OES) may facilitate immediate reactions whenever plasma instabilities occur. For this reason, a real-time diagnostic system based on an OES has been installed at the ECRIS at HLI for routine operation and monitoring during the beam time. By means of the OES a parasitic oven heating by coupled microwaves was measured and in case of low melting elements of high vapour pressure like Ca it may compromise the ion source performance [4]. For this reason, the effect of the oven shielding was studied with the OES and a tungsten grid has been installed to shield the oven orifice at HLI during the Ca beam-times of 2020.

EXPERIMENTAL SET-UP

The description of the ion source and of the beamline are reported in [5] and references therein and the details of the

ISBN: 978-3-95450-226-4 ISSN: 2222-5692 doi:10.18429/JACoW-ECRIS2020-MOZZO03

STO are reported in [1]. The sample material has been filled into the STOs and then a tungsten grid has been installed to shield the oven head as show in Fig. 3. A tungsten mesh type 100 holes/inch and 0.0254mm wire with an open area of 81% was used. The geometry of the grid has been selected after several tests with different spacings carried out in December 2019 at the EIS (ECR Injection Set-up) testbench of GSI with ^{40}Ca. No material deposition or condensation was observed after the testing campaign. The microwave power coupled to the ECRIS during the Ca beamtimes was around 650 W at 14.5 GHz.

In order to early detect and prevent instabilities, a diagnostic tool, based on an OES, has been arranged. The set-up is described in [4]. To measure the visible light spectrum, the Ocean Optics QE Pro spectrometer is used [6]. The main specifications include a 25 µm slit, a grating with 600 lines/mm calibrated at 500 nm and a 449-833 wavelength bandwidth determining a 0.95 nm optical resolution. During the beam-runs the optical spectra have been measured together with the plasma images recorded with a CCD camera.

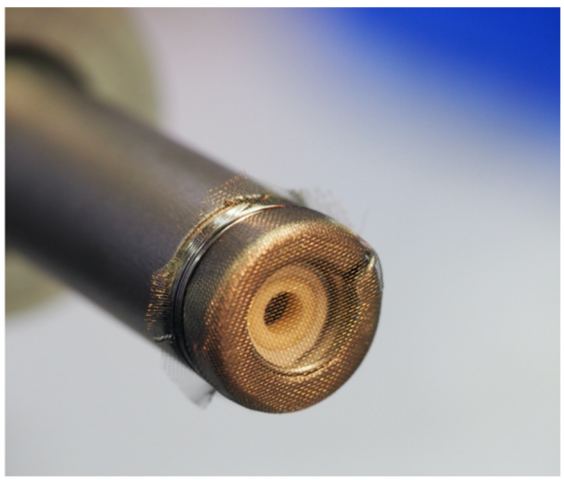

Figure 3: Microwave shielding grid at the oven orifice.

RESULTS AND DISCUSSION

At GSI, ^{48}Ca beams were requested to be delivered from the ECRIS at HLI from February to May 2020 for 64 days of total beamtime in four separate blocks. The ion source parameters were tuned to optimize the production of $^{48}Ca^{10+}$. In table 1 the achieved beam parameters are reported. The maximum intensity achieved in 2020 has been 120 µA and a typical charge state distribution is shown in Fig. 4. With respect to the ^{48}Ca runs of the previous years a much more stable ion source behaviour has been observed implying a huge reduction of tuning intervention for optimization. The use of the tungsten grid improved the long-term beam stability. This result is shown in Fig. 5 where the $^{48}Ca^{10+}$ current measurement at the beam current transformer for almost 10 days, in April 2020, is reported.

Table 1: Ca Beam Runs in 2020: Main Achievements

Date	$^{48}Ca^{10+}$ intensity	Note
19/02-04/03	90-120 µA	No on–call or intervention necessary
17/03-31/03	70-90 µA	Two on–call interventions
02/04-15/04	90-100 µA	Two on–call interventions
19/04-15/05	100-110 µA	No on–call or intervention necessary

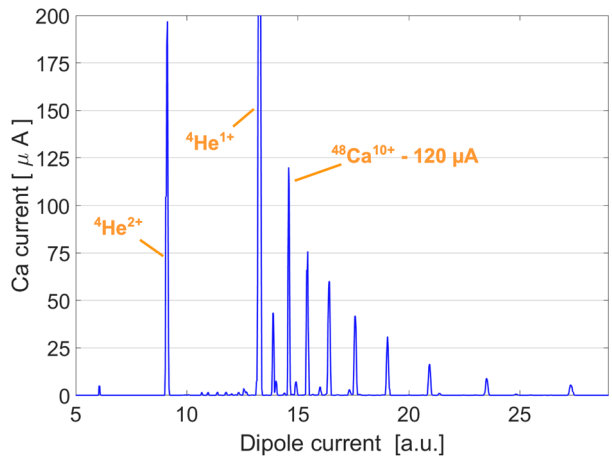

Figure 4: Ca charge states distribution optimized for Ca^{10+}.

The maximum intensity has been achieved at the very begining of ^{48}Ca production as observed for each beam run even in the past years. The intensity drop about 10-15% afterwards can be related to the contamination of the internal components due to the condensed material. A shift hof the intensity towards lower charge states has been observed as well. No ion source parameter has been tuned after the initial optimization and the oven setting has been slightly tuned on 7th and on 10th of April. The two events are underlined in Fig. 5. The first optimization required an increase of oven power in order to compensate the consumed material while the second one required a full ECRIS tuning since an increase of the oven temperature was detected.

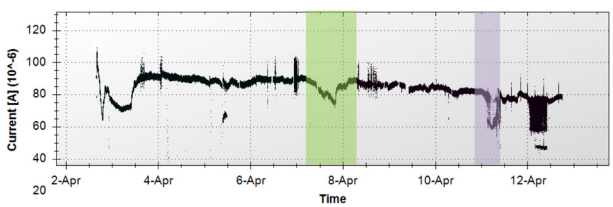

Figure 5: $^{48}Ca^{10+}$ intensity measured at the current transformer for 10 days.

ISBN: 978-3-95450-226-4 ISSN: 2222-5692 doi:10.18429/JACoW-ECRIS2020-MOZZO03

In Fig. 6 the plasma images recorded during these two events are presented. The OES measurements were carried out at the same time frame when the plasma images have been recorded. The optical emission spectra of the plasma images corresponding to the three frames in the upper row of Fig. 6 are shown in Fig. 7. The optical spectra of the last two plasma images, corresponding to the second optimization event of the ECRIS are illustrated in Fig. 8.

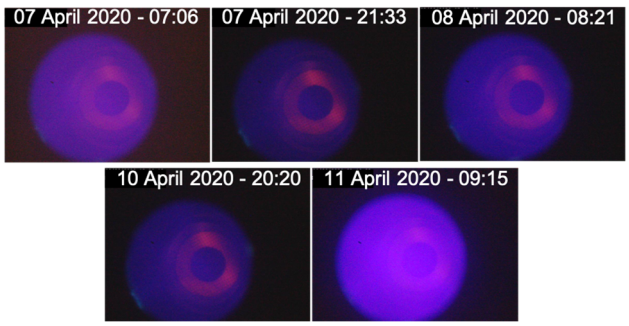

Figure 6: Plasma images recorded at the CCD camera when the optimizations of the ECRIS were requested.

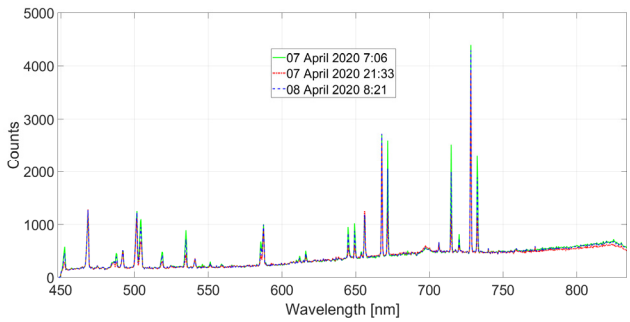

Figure 7: OES measurement at the upper time-frames of Fig. 6 during the first ECRIS optimization (07-08 April).

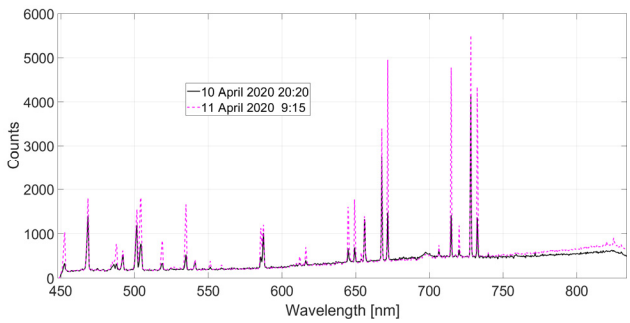

Figure 8: OES measurement at the lower time-frames of Fig. 6 during the second optimization (10-11 April).

With respect to the first optimization, at the second event occurred on the 11th of April an heating of the oven resulted in an increase of counts at higher wavelenghts.

This result ist more clear by analysing figure 9, showing the normalised intensity of the peak at 732 nm and at 827 nm and the integrated counts over the full spectrometer bandwidth. The dashed vertical lines identify the time frames when the plasma images and the optical spectra have been measured and reported. A rise of oven temperture occurred several times during the Ca beam-times of previous years, but with the shielding grid this parasitic heating event was observed only once on 11th of April. Furthermore, the use of the shielding provided an improvement of the material consumption since the reduction of the parasitic heating events avoided the additional and unuseful material evaporation.

Nevertheless, finer meshes or thicker wires will be tested in order to improve the oven shielding to avoid any over heating. It is worth to report that no material condensation has been observed at the oven heads used for all the beamtimes confirming that the shielding can be routinely used even for longer beam time periods.

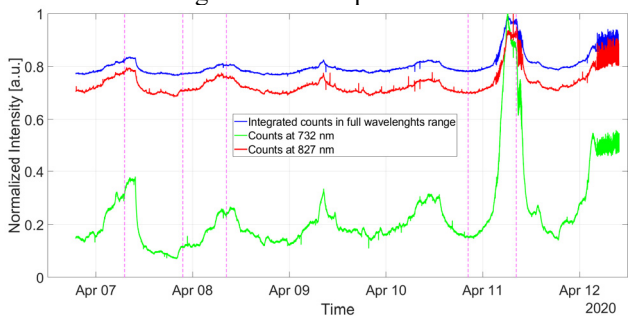

Figure 9: Normalised light intensity at different wavelengths recorded for 5 days (07-08 April)

CONCLUSION

The use of an OES as a diagnostic tool for routine operation of the CAPRICE ECRIS helps to recover the source performances much faster during the metallic ion beam production whenever optimizations are required or instabilities occur. This result has been confirmed during the last ^{48}Ca runs. The monitoring of the spectral components at certain visible wavelengths may help to prevent excessive optimization time.

The grid shielding of the oven head has improved the Ca ion beam production by an ECRIS in terms of stability, intensity and material consumption since the parasitic heating of the ceramic insulating material inside the oven head is strongly reduced.

In future it is anticipated to improve the light transmission between plasma and OES. A spectrometer with a wider range towards the infrared light spectrum would give the opportunity to measure the oven temperature in situ. This would lead to even better control of the evaporation rate.

ISBN: 978-3-95450-226-4 ISSN: 2222-5692 doi:10.18429/JACoW-ECRIS2020-MOZZO03

REFERENCES

[1] K. Tinschert *et al.*, "Metal Ion Beam Production with Improved Evaporation Ovens", in *Proc. 20th Int. Workshop on ECR Ion Sources (ECRIS'12)*, Sydney, Australia, Sep. 2012, paper WEPP15, pp. 140-142.

[2] R. Kronholm *et al*, "ECRIS plasma spectroscopy with a high resolution spectrometer", *Rev. Sci. Instrum*. vol. 91, pg. 013318, 2020. doi:10.1063/1.5128854

[3] O. Tuske *et al*, "Visible light spectrometry measurements for studying an ECRIS plasma and especially applied to the MONO1001 ion source", *Rev. Sci. Instrum*. vol. 75, pg. 1529, 2004. doi:10.1063/1.1691528

[4] F. Maimone *et al*, "Optical spectroscopy as a diagnostic tool for metal ion beam production with an ECRIS", *Rev. Sci. Instrum*. vol. 90, pg. 123108, 2019. doi:10.1063/1.5127571

[5] K. Tinschert *et al*, "Status report on ECR ion source operation at the GSI accelerator facilities", *Rev. Sci. Instrum*. vol. 69, pg. 709, 1998. doi:10.1063/1.1148558

[6] Ocean Insight, https://oceanoptics.com/wp-content/uploads/OEM-Data-Sheet-QEPRO.pdf

ISBN: 978-3-95450-226-4 ISSN: 2222-5692 doi:10.18429/JACoW-ECRIS2020-MOZZO04

NEW METALLIC STABLE ION BEAMS FOR GANIL

F.Lemagnen†, C. Barue, M.Dubois, R.Frigot, N.Lechartier, V.Metayer,
B.Osmond. GANIL, CEA/CNRS, Bd Henri Becquerel, Caen Cedex 5, France

Abstract

GANIL has been producing many stable beams for nearly 40 years. Constant progress has been made in terms of intensity, stability and reliability. The intensity for some stable metallic beams now exceeds or approaches the pμA level at an energy up to 95 MeV/u: 1.14 pμA for ^{36}S (65% enriched) at 77 MeV/u, 0.35 pμA for ^{58}Ni (63%) at 74 MeV/u.

Constant developments are being made to broaden the range of available beams for physics [1]. The presentation highlights recent results obtained for ^{28}Si, ^{184}W and ^{130}Te using the GANIL 's LCO (Large Capacity Oven) [2] on the ECR4 ion source. To produce the tungsten beam, two injection methods were compared. For the first one, we evaporated some tungsten trioxide (WO_3) with GANIL 's LCO. For the second one, the injection in the plasma chamber was made by using MIVOC (Metallic Ions from Volatile Compounds) [3, 4, 5] with a tungsten hexacarbonyl ($W(CO)_6$) compound. It was the first time that we used metal carbonyl compounds and the result is promising. All the tests have been qualified to obtain the level of intensity and beam stability. Theses good results led us to propose them for Physics experiments.

EQUIPMENT CONFIGURATION

The "Oven configuration" of the ECR4 Ion Source

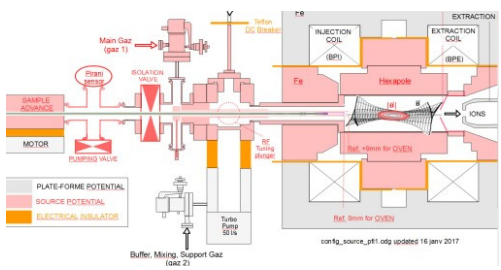

Figure 1: Oven in the ECR4.

The MIVOC Configuration of the ECR4 Ion Source

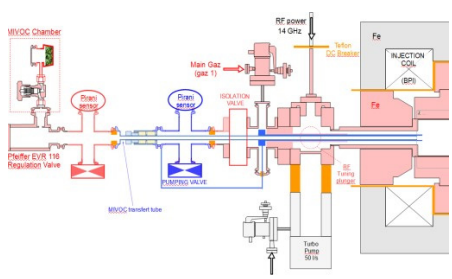

Figure 2: MIVOC chamber with transfer tube connected to the ECR4.

SILICON BEAM WITH ECR4 ION SOURCE

Introduction

The silicon beam was produced using the natural silicon monoxide (SiO) compound which was evaporated with the large capacity oven (LCO). The ^{28}Si beam can also be produced with SiH_4 gas but it's highly flammable and for the safety reason, we don't use this compound.

The Sample Preparation

The compound is a sticky brown powder. This form of compound can be found for several isotopes of silicon (^{30}Si, ^{29}Si). We use an alumina crucible with a useful capacity volume of 140 mm^3. The powder is lightly pressed in the crucible. After filling, we have 130 mg of the SiO in the crucible. To evaporate the compound, we use the high temperature version of the LCO. Before the introduction of the sample in the ion source, we heat the sample up to 500°C for outgazing in the vacuum chamber.

To obtain a vapor pressure of 10^{-2} mbar the temperature of compound should be of 1080°C (1705°C for the melting point).

Production of ^{28}Si with ECR4 Ion Source

Test has been first performed with the natural silicon monoxide. Due to the high temperature required for evaporation we decided to fix, in the first time, the oven position at +9 mm, see on Fig. 1. For the first test, we measured a high consumption (2.45 mg/h of ^{28}Si) with the spectrum op- timized on $^{28}Si^{5+}$. For the second test, we changed the oven position at 0 mm (Fig. 2). The intensity of $^{28}Si^{5+}$ has been delivered by changing various source parameters: RF power, gaz, oven power, we used, like buffer gas, O_2 and we easy obtained the beam stability during 48 hours. The main parameter, which is optimized was the electrical power oven to keep the level of the beam intensity.

The charge state distribution has been optimized on $^{28}Si^{7+}$ with 20μA.e, see on Fig. 3. The consumption was 0.56 mg/h of ^{28}Si with the total ionization efficiency of 6%.

†lemagnen@ganil.fr

ISBN: 978-3-95450-226-4 ISSN: 2222-5692 doi:10.18429/JACoW-ECRIS2020-MOZZO04

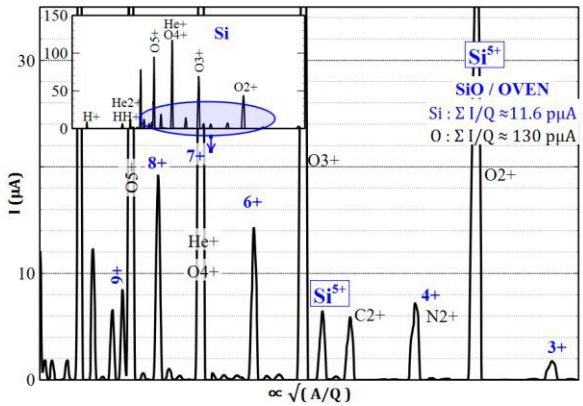

Figure 3: Spectrum optimized on $^{28}Si^{7+}$ (20 μA). RF power: 350 W, buffer gas O_2: 7.4×10^{-6} mbar at injection, 2.3×10^{-7} mbar at extraction, 24.6 kV/1.65 mA, platform 60.5Kv, axial magnetic coils: 1070A/1050A, oven power 23.3 W (~800°C off-line), oven position: +0 mm inside the plasma chamber, no bias. Transport efficiency up to the faraday cup: ~35%.

Conclusion

An intensity of 6μA.e $^{28}Si^{5+}$has been produced for 48 hours. The charge state distribution was better for the second test with 20μA $^{28}Si^{7+}$ due to the change of oven position and more gaz buffer (O_2). With these results, we will be able to increase the list of available beams at GANIL.

TUNGSTEN BEAM WITH ECR4 ION SOURCE

Introduction

Two tests have been scheduled to produce tungsten beam. We choose two different molecules to inject in the ion source. For the first test, we produced the tungsten with the injection of the tungsten hexacarbonyl and for the second we injected the tungsten trioxide. The goal of this experiment is to compare the performance of the beam production with the two injection methods.

Production of ^{184}W with Tungsten Hexacarbonyl Compound

It was the first time that we produced some ions with a neutral carbonyl molecule. To inject the tungsten hexacarbonyl in the plasma chamber, we used the MIVOC method. The scheme of injection is on Fig. 2 and the installation is shown in Fig. 4.

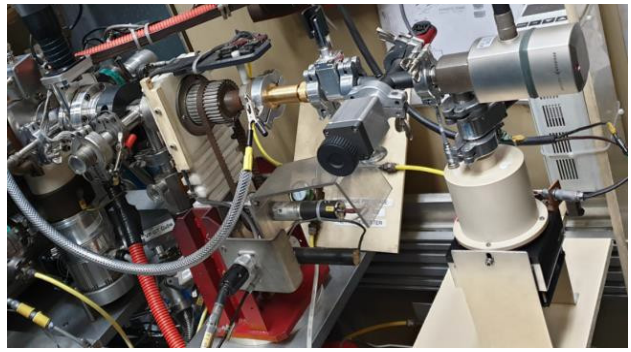

Figure 4: MIVOC process is connected at ECR4 ion source.

Before the production of the beam, we analyzed the compound with the analyser mass spectrometer to see the different atomic masses of molecules and the pollution. The presence of water was important but it was decrease thanks to pumping in MIVOC chamber and the time.

The production test lasted several days, starting the source in the morning and switching it off in the evening, for a cumulative runtime of 33h. A mean intensity of 1.2 μA for $^{184}W^{18+}$ has been maintained.

It corresponds to a total particles current of 0.55 pμA see on Fig. 5. The measured beam transport efficiency of 47% - assumed to be the same for all charge states and spe- cies - leads to an ion flow extracted from the source of about 1.2 pμA. The consumption of ^{184}W was 0.2mg/h and an ionisation efficiency around 5%.

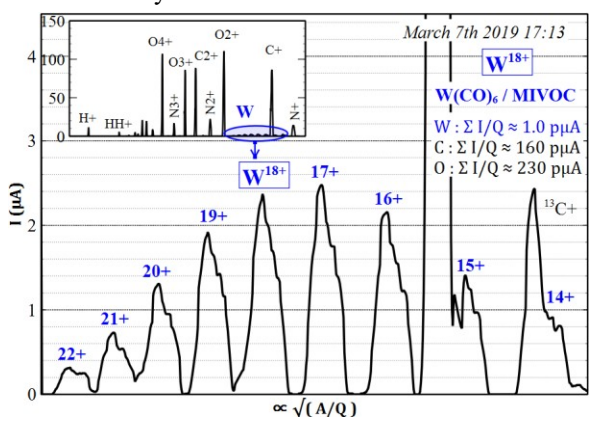

Figure 5: Spectrum obtained with ECR4 ion source and optimized on 184W18+ (2.3 μA). RF power: 170 W, biased tube : -100V/0.0mA, no buffer gas, MIVOC flow 500 mbar.L/s, 4.0×10-7 mbar at injection, 2.0×10-7 mbar at extraction, source 25 kV/1.7 mA, platform 50 kV, injec- tion coil 1060 A, extraction coil 1050 A. Total transport to Faraday cup 47%.

Production of ^{184}W with Tungsten Trioxide

For this test we chose the natural compound of tungsten trioxide (30.6% of 184W). The sample was a very fine green powder which was difficult to stock in the oven's crucible. We obtained a stable beam during 24 hours with 2.8μA of 184W20+ see on Fig. 6. The consumption of 184W was 1mg/h with the total ionization efficiency around 1.4%.

ISBN: 978-3-95450-226-4 ISSN: 2222-5692 doi:10.18429/JACoW-ECRIS2020-MOZZO04

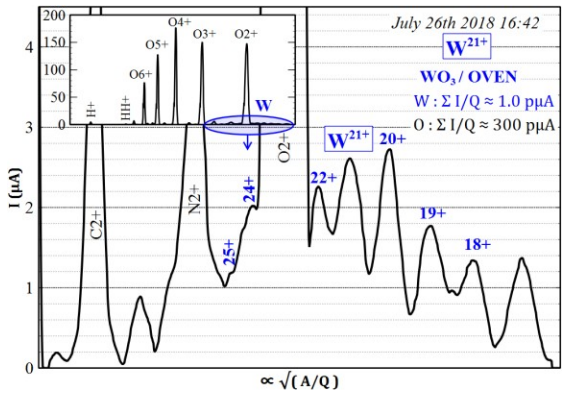

Figure 6: Spectrum obtained with ECR4M and optimized on $^{184}W^{21+}$ (2.5 μA). RF power: 278 W (reflected 110 W), 18 kV/2.0 mA, buffer gas O_2, oven power 33.1 W (~1100°C off line), oven position: +4 mm inside the plasma chamber, no biased tube, coils: 960A/730A. Transport efficiency up to the faraday cup: ~47%.

Conclusion

If we compare the two methods of production, we can see that we have the same level of intensity with a better charge state distribution for the oven methods. We could try to do another test with the oven to reduce the consumption. For the two compounds, if we find the isotopically enriched sample, we will be able to multiply by three the intensity and thus have 7.5μA of $^{184}W^{21+}$.

TELLURIUM BEAM PRODUCTION WITH ECR4 ION SOURCE

Introduction

This beam was developed to answer of the new project of experiment for Agata detector. To produce this test, we took a metallic isotopically enriched sample of 130Te (99.8%).

The Sample Preparation

We use an alumina crucible with a useful capacity volume of 140mm^3. The sample was a metallic form and we put 100mg of the ^{130}Te in the crucible.

To obtain a vapour pressure of 10^{-2}mbar the temperature of compound should be of 360°C (452°C for the melting point). To minimise the influence of plasma heating, a plug with an aperture of 1mm-diameter has been put at the extremity of crucible.

Production of ^{130}Te with ECR4 Ion Source

Due to chemical reaction between oxygen and heated tellurium, we decided to inject nitrogen as a buffer gas

This test has been performed continuously during one week. The charge state distribution has been optimized on $^{130}Te^{18+}$ with 8μA like the spectrum in Figure 7.

The consumption was 0.2 mg/h of 130Te with the total ionization efficiency of 8%.

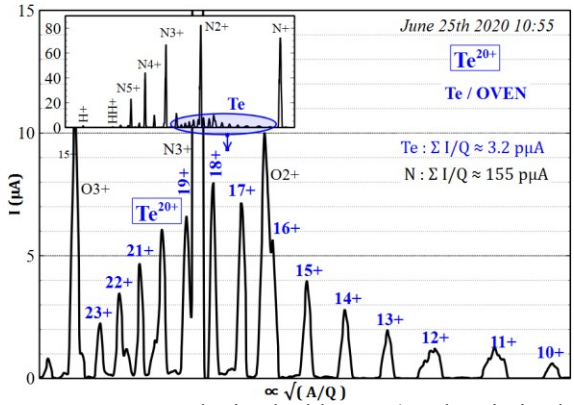

Figure 7: Spectrum obtained with ECR4 and optimized on 130Te18+ (8 μA). RF power: 220 W, buffer gas N2, oven power 2 W (~200°C off line), oven position: +0 mm inside the plasma chamber, no biased tube, coils: 1065A/1065A. Transport efficiency up to the faraday cup: ~35%.

Conclusion

An intensity of 8μA 130Te18+has been produced for 50 hours. The use of Nitrogen gas buffer is good solution to optimise the charge states distribution and to obtain a good stability of the beam. With these results, the AGATA experiment can be programmed for the year.

REFERENCES

[1] C. Barue *et al.*, "Status Report on Metallic Beam Production at GANIL/SPIRAL 2", in *Proc. 22nd Int. Workshop on ECR Ion Sources (ECRIS'16)*, Busan, Korea, Aug.-Sep. 2016, pp. 92-97. doi:10.18429/JACoW-ECRIS2016-WEPP05

[2] P.Lehérissier *et al.,* "Status report on ECR ion source operation at GANIL", *Rev. Sci. Instrum.*, vol. 75, pg. 1488, 2003. doi:10.1063/1.1690447

[3] J. Ärje, H. Koivisto and M. Nurmia., "Operation of the JYFL-ECR Ion Source" in *Proc. 11th Int. Workshop on ECR Ion Sources (ECRIS'93)*, KVI-Groningen, 1993.

[4] H. Koivisto, J. Ärje and M. Nurmia, "Metal ion beams from an ECR ion source using volatile compounds", *Nucl. Instrum Methods Phys. Res., Sect. B.,* vol. 94, pg. 291-296, 1994.

[5] H. Koivisto, J. Ärje and M. Nurmia, "Metal ions from the volatile compounds-method for the production of metal ions beams", *Rev. Sci. Instrum.,* vol. 69, pg. 785-787, 1998.

ISBN: 978-3-95450-226-4 ISSN: 2222-5692 doi:10.18429/JACoW-ECRIS2020-MOZZO06

MICROCONTROLLERS AS GATE AND DELAY GENERATORS FOR TIME RESOLVED MEASUREMENTS

Bryan Isherwood* and Guillaume Machicoane
National Superconduction Cyclotron Laboratory, East Lansing, MI, USA
Facility for Rare Isotope Beams, East Lansing, MI, USA

Abstract

The diffusion of electrons from ECRIS plasmas results in the emission of a continuous energy distribution of photons from the plasma chamber. Measurements ECRIS bremsstrahlung that are both time and energy resolved of the are often difficult to perform due to the 10's – 100's ms timescale that the plasma evolves over. However, the advancement of low-cost microcontrollers over the last decade makes timing and gating photon spectrometers easier. We present a proof of principle measurement which uses an Arduino microcontroller as a gate-and-delay generator for time resolved ECRIS bremsstrahlung measurements. An example plot of the time resolved spectrum, triggered by beam current variation induced by kinetic instabilities is shown.

INTRODUCTION

Accelerator facilities like the National Superconducting Cyclotron Laboratory (NSCL) and the Facility for Rare Isotope Beams (FRIB) require high intensity, high charge state ion beams for facility operations. These facilities rely on electron cyclotron resonance (ECR) ion sources (ECRISs) to produce stable ion beams for their operations. The microwave heated plasmas within these devices can produce beams of highly charged ions. Those ions must undergo multiple ionizing collisions before escaping from the plasma chamber, making the ion confinement time and the electron-ion collision frequency two of the most important characteristic time scales within ECR ion source plasmas [1].

However, the ECR ion source plasma is also prone to microinstabilities that decrease the confinement time of ions. The combined microwave heating and loss-cone confinement creates populations of hot electrons ($E_{kin} > 10$ keV) with large temperature anisotropies, $T_\perp >> T_\parallel$. The anisotropic electrons can excite and amplify electromagnetic plasma modes within the plasma chamber and, in doing so, drive themselves into the loss cone [2, 3]. By driving the hot electrons into the loss-cone, the instabilities limit the confinement time of highly charged ions and cause quasi-periodic losses of extracted beam current [4, 5].

Performing time-resolved measurements can provide insight into the dynamics of the electron and ion populations during unstable operation. To that end, we require non-invasive diagnostic whose acquisition systems can be triggered by the instabilities, rather than an external trigger [6–8]. Doing these kinds of measurements can be difficult, particularly if the measurement must take place over milliseconds. However, we can use Ardunio micro-controllers (AMC) as programmable gate and delay generators to take time-resolved measurements of the ion source bremsstrahlung during unstable operating.

This paper presents a proof-of-principle measurement of this technique using the facilities at the NSCL and seeks to demonstrate its feasibility as a low-cost method of performing time-resolved measurements. In particular, we will show the results of a test measurement where an AMC is used as a gate and delay generator of Bremsstarhlung measurements of the ECRIS plasma chamber, during unstable operation.

APPARATUS

This measurement was performed with the Superconducting Source for Ions (SuSI) at the NSCL[9] (Fig. 1). The ion source's confining magnetic field is created with four superconducting solenoids and a superconducting hexapole coil. The four axial solenoid coils provide longitudinal confinement while allowing for control over the injection and extraction maxima and the field minimum. The system's design allows each of the longitudinal field extrema to be varied independently. The extraction, einzel lens, and puller voltages were fixed at 20 kV, −18 kV, and −0.3 kV, respectively. Oxygen ions were extracted from the plasma chamber with a fixed neutral gas pressure of 131 nTorr, as measured by an ion gauge on the injection side of the plasma chamber. A 90° dipole was used for charge selection and guided the ions into a solenoid focusing lattice to guide the selected

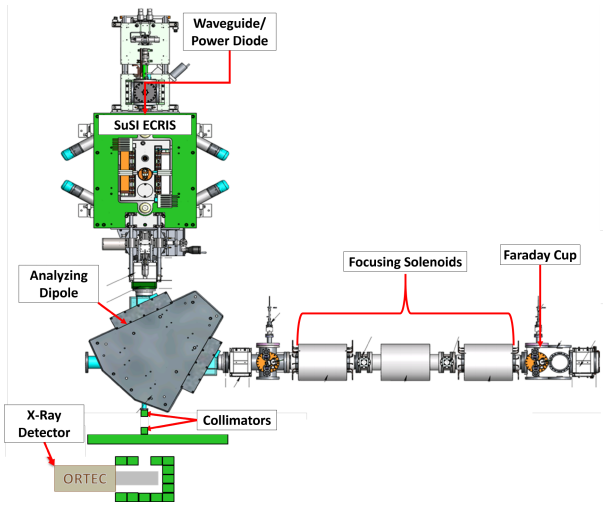

Figure 1: A schematic of the source-beamline configuration used for this test.

* isherwo3@gmail.com

ISBN: 978-3-95450-226-4 ISSN: 2222-5692 doi:10.18429/JACoW-ECRIS2020-MOZZO06

charge state current into a Faraday cup. An Ortec High Purity Germanium (HPGe) detector was placed in line with the longitudinal axis of the ion source's plasma chamber. Two lead bricks and a cylindrical piece of tungsten collimated the flux of bremsstrahlung radiation emitted from the source.

For this test measurement, we used an Arduino UNO microcontroller as our gate and delay generator for the multi-channel analyzer connected to our HPGe. For this test, the AMC (Fig. 2) measured the voltage drop created by the varying current across a variable resistor using the digital input port. Using the ion current as the trigger signal delayed the measurement by the ion the transit time, $\Delta T = 2.7\,\mu s$ for O^{6+} ions. The AMC measured the resulting voltage using the digital input port, which minimized the computational time necessary to trigger the TTL by bypassing the system's internal analog-to-digital converter (ADC), cutting the input-to-output time down to ~0.667 µs. For the duration of the measurement, we stored the AMC in an aluminum mesh cage to prevent sparking, with a BNC bulkhead connecting the AMC to the Faraday cup.

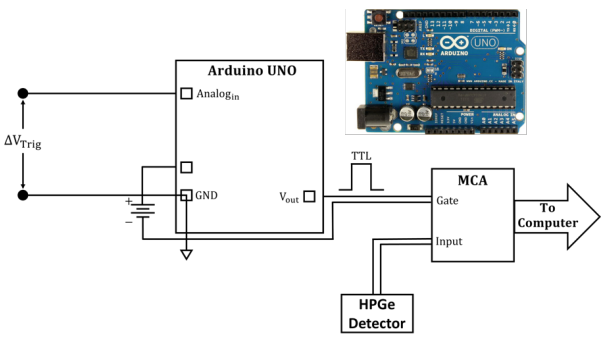

Figure 2: When the AMC measured a decrease in the measured current (voltage drop across a resistor, $V_{sig} < 500$ mV for a digital signal input), it would output a TTL signal to gate the MCA used to collect data from the HPGe detector. The MCA then sent the gated data to a computer running the ORTEC MAESTRO spectrometer program.

We performed two measurements as part of this test, with the goal of observing how the bremsstrahlung distribution would change over the duration of the instability. In the first measurement, the TTL was output immediately following the measured beam current variation, $\delta t = 0.667\,\mu s$. In the second measurement, we manually programmed an 8 ms delay into the micro-controller. The output TTL width was fixed at w = 100 µs and the instability repetition period was approximately 50 ms, for an average duty cycle of 0.2%. Figure 3 shows an example cartoon of the gate timing for both measurements and an example picture of the measured current and gate signals, as seen during the measurement.

RESULTS

Figure 4 shows the results of this test. As we might expect, the total count rate is higher immediately after the instability event (no delay), indicating an increased electron diffusion rate. However, the count rate is at least an order

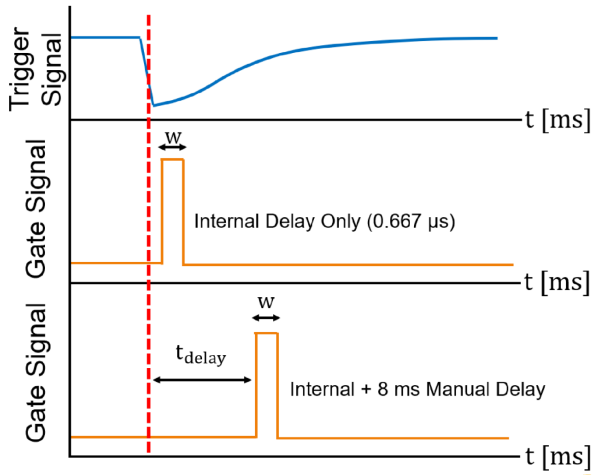

Figure 3: (Top) Two test measurements were performed: one where a TTL was output immediately after the isntability event, within 0.667 µs, and one where the TTL was delayed by 8 ms. (Bottom) Example picture of showing the TTL output along side the measured O^{6+} beam current, on an oscilloscope.

of magnitude lower than what we would expect during time-averaged measurements (see [10, 11]). The low count rates introduce a large uncertainty in the energy-resolved portion of this measurement and make it difficult to observe any

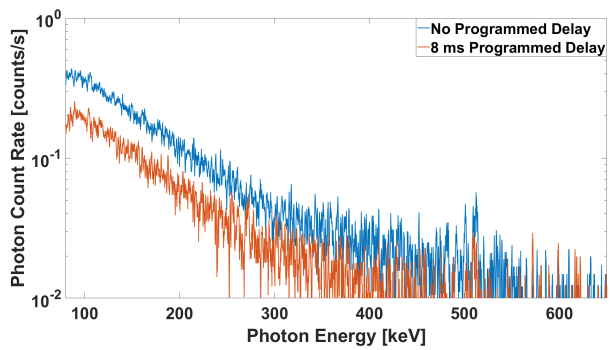

Figure 4: Comparison between the measured bremsstrahlung distributions when the gating TTL is output immediately after (blue) and 8 ms after (orange) the emission triggering of the AMC. The total measurement period for each distribution was 2000 s.

ISBN: 978-3-95450-226-4 ISSN: 2222-5692 doi:10.18429/JACoW-ECRIS2020-MOZZO06

major differences between the two distributions. For example, the spectral temperature, T_s ($\ln I_\gamma = -\hbar\omega/T_s$), between the two distributions are consistent with $T_{s,0ms} = 93\,keV \pm 27\,keV$ and $T_{s,8ms} = 94\,keV \pm 11\,keV$. Time-averaged measurements with the same 'live-time' typically have an order of magnitude lower uncertainty in their spectral temperatures ($\delta T_s \sim 1$–$2\,keV$). Furthermore, Fig. 5 shows that there is little difference between the normalized distributions of each measurement. A higher count rate may demonstrate a larger difference between the two distributions. However, this result may indicate that the instability affects electrons across a broad energy domain, an observation made in some time-resolved measurements of electrons escaping from confinement from an ECR ion source during unstable operation [6].

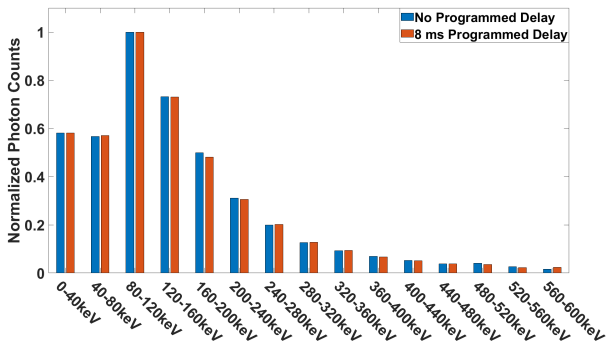

Figure 5: The re-binned and normalized (by largest value) bremsstrahlung distributions show that there is very little difference between the shapes of the two distributions, suggesting that the instability forces electrons of a broad range of energies into the loss cone during, or immediately after, the instability.

ACKNOWLEDGMENTS

This research was made possible by the National Science Foundation under NSF Grant 1632761 and U.S. Department of Energy Award Number DE-SC0018362. Thanks are given to the NSCL/FRIB Ion Source group staff Jeff Stetson, Jesse Fogleman, and Larry Tobos. We also thank the NSCL/FRIB facilities and operational managers including Andreas Stolz, Yoshishige Yamazaki, Thomas Russo, Kent Holland, and Steven Lidia.

REFERENCES

[1] R. Geller, "Electron cyclotron resonance sources: Historical review and future prospects (invited)," *Review of Scientific Instruments*, vol. 69, no. 3, pp. 1302–1310, 1998. doi:10.1063/1.1148797.

[2] I. Izotov *et al.*, "Microwave emission related to cyclotron instabilities in a minimum-B electron cyclotron resonance ion source plasma," *Plasma Sources Science and Technology*, vol. 24, no. 4, p. 045 017, Jul. 2015. doi:10.1088/0963-0252/24/4/045017.

[3] A. G. Shalashov, E. D. Gospodchikov, and I. Izotov, "Electron-cyclotron heating and kinetic instabilities of a mirror-confined plasma: the quasilinear theory revised," *Plasma Physics and Controlled Fusion*, 2020. doi:10.1088/1361-6587/ab7f98.

[4] R. Geller, *Electron Cyclotron Resonance Ion Sources and ECR Plasmas*. Routledge, Dec. 2018. doi:10.1201/9780203758663.

[5] O. Tarvainen *et al.*, "Limitation of the ECRIS performance by kinetic plasma instabilities (invited)," *Review of Scientific Instruments*, vol. 87, no. 2, 2016. doi:10.1063/1.4931716.

[6] I. Izotov *et al.*, "Measurements of the energy distribution of electrons lost from the minimum B-field—The effect of instabilities and two-frequency heating," *Review of Scientific Instruments*, vol. 91, no. 1, p. 013 502, Jan. 2020. doi:10.1063/1.5128322.

[7] O. Tarvainen *et al.*, "The biased disc of an electron cyclotron resonance ion source as a probe of instability-induced electron and ion losses," *Review of Scientific Instruments*, vol. 90, no. 12, Dec. 2019. doi:10.1063/1.5126935.

[8] R. Kronholm *et al.*, "Spectroscopic study of ion temperature in minimum-B ECRIS plasma," *Plasma Sources Science and Technology*, vol. 28, no. 7, Jul. 2019. doi:10.1088/1361-6595/ab27a1.

[9] P. A. Zavodszky *et al.*, "Design of SuSI - Superconducting source for ions at NSCL/MSU - I. The magnet system," *AIP Conference Proceedings*, vol. 749, pp. 131–134, 2005. doi:10.1063/1.1893382.

[10] B. Isherwood, E. Pozdeyev, G. Machicoane, J. Stetson, and D. Neben, "Plasma Instability Studies of the SUSI 18 GHz Source," in *Proc. 23th International Workshop on ECR Ion Sources (ECRIS'18)*, Catania, Italy, 2018, pp. 157–161. doi:10.18429/JACoW-ECRIS2018-WEA3.

[11] B. Isherwood and G. Machicoane, "Measurement of the energy distribution of electrons escaping confinement from an electron cyclotron resonance ion source," *Review of Scientific Instruments*, vol. 91, no. 2, p. 025 104, Feb. 2020. doi:10.1063/1.5129656.

ISBN: 978-3-95450-226-4 ISSN: 2222-5692 doi:10.18429/JACoW-ECRIS2020-TUWZO01

MEASUREMENTS OF PLASMA PARAMETERS NEAR RESONANCE ZONES AND PERIPHERAL REGIONS IN ECRIS

W. Kubo†, S. Harisaki, I. Owada, K. Sato, K. Tsuda, and Y. Kato,
Division of Electrical, Electronic and Infocommunications Engineering, Graduate School of Engineering, Osaka University, 2-1 Yamada-oka, Suita-shi, Osaka 565-0871, Japan

Abstract

Electron cyclotron resonance ion source (ECRIS) has a wide range of application, *e.g.*, cancer treatment and material synthesis. We have constructed the ECRIS which can provide various ion species and investigated how to produce multicharged ions efficiently in Osaka University. In recent years, we have focused on waves propagations in plasma and conducted the upper-hybrid resonance (UHR) experiments. The second microwaves whose frequencies are much higher than fundamental ECR's one are superimposed to the ECR plasma. We have also conducted experiments heating by the coaxial semi-dipole antenna with the aim of enhancing the right-hand polarization (RHP) wave, which contributes to ECR.

We measure simultaneously plasma parameters in those regions by two Langmuir probe inserted into each location under the same operation condition. These probes are set at the upperstream and the downstream of the ECR zone. We measure the electron energy distribution function (EEDF) and the ion saturation current I_{is} in the two regions. We presume RHP waves propagation near the ECR zone by comparing measurements results and the accessibility of the RHP wave in the ECRIS. The accessibility is estimated from the $\boldsymbol{B}$ profiles by the calculation and the n_e profiles obtained by the fitting with the past measurements. In near future, we optimize the coaxial semi-dipole antenna in order to optimize the ECR efficiency by the 2.45 GHz microwave.

INTRODUCTION

Ion sources based on electron cyclotron resonance (ECRIS) have a wide range of applications, *e.g.*, cancer treatment and material synthesis [1, 2]. We have constructed the ECRIS, which can provide various ion species efficiently for those various applications. We have investigated how to produce multicharged ions efficiently in Osaka University [3-6]. We have focused on waves propagations in ECR plasma and conducted the upper-hybrid resonance (UHR) experiments. The second microwave (4-6 GHz) whose frequencies are much higher than fundamental ECR's one (2.45 GHz) are superimposed to ECR plasma as extraordinary (X) mode and got evidences for occurrence of UHR in the experiments [3-5]. We installed coaxial semi-dipole antenna, which is the new type antenna on the mirror end along the geometrical axis of the vacuum chamber. We compared ion beams extracted from the ECRIS with the new antenna and that with conventional one which is the rod antenna installed on the side wall of the vacuum chamber. We obtain the experimental results that the coaxial semi-dipole antenna contributes to stable increase of the multicharged ion beams at high power [7].

Multicharged ion beams have been improved using various methods, *e.g.,* increasing of the magnetic field strength and the microwave frequency, using the DC biased plate-tuner, mixing low z gases, and heating by multiple frequencies. However the position of microwave launching has been empirically determined on conventional ECRIS. There is still room for improvement with the respect to more efficient excitation of the RHP wave propagation. The objective of this research is the estimation of the propagation of the RHP wave near the ECR zone, and in the opposite peripheral region beyond it. We measure simultaneously plasma parameters in those regions by two Langmuir probe inserted into each location under the same operation condition. We can measure plasma parameters, *i.e.,* the electron density n_e, the electron temperature T_e, the I_{is}, and the EEDF. We measure EEDF's and I_{is}'s in the upperstream and downstream regions near the ECR zone. We observe that I_{is}'s and tails of EEDF's measured on the side closer to the microwave launching are higher than those on the other side. These results are consistent with the propagation theory of the RHP wave in the ECR plasma. We compare extracted ion beams by launching microwaves from the coaxial semi-dipole antenna and the rod antenna.

BRIEF THEORICAL BACKGROUND AND EXPERIMENTAL APPARATUS

The RHP waves which give rise to ECR are transverse electric (TE) mode and propagate in the direction parallel to magnetic fields. On the basis of the RHP wave dispersion relationship for the case of no collisions and infinite mass ions, the RHP wave refraction index N_r can be written using the electron plasma frequency f_{pe} and the electron cyclotron frequency f_{ce} as following:

$$N_r^2 = \left(v_\varphi^2 / c^2\right)^{-1} = 1 - \frac{f_{pe}^2}{f(f - f_{ce})} \quad (1)$$

where f is the frequency of incident microwave (RHP wave), v_φ is the phase velocity of the RHP wave, and c is the velocity of light.

Figure 1 shows the typical dispersion relationship of the RHP wave. The vertical and horizontal axes show v_φ^2/c^2 and f respectively. There is three regions A ($f < f_{ce}$), B ($f_{ce} < f < f_R$), and C ($f_R < f$) where f_R is the R-cutoff frequency which is the cutoff of the RHP wave ($N_r \to 0$). A and C regions are propagation regions of the RHP wave ($v_\varphi^2 > 0$) and B region is the non-propagation region ($v_\varphi^2 < 0$). The f_{ce} depends on the magnetic field

† w.kubo@nf.eie.eng.osaka-u.ac.jp

ISBN: 978-3-95450-226-4 ISSN: 2222-5692 doi:10.18429/JACoW-ECRIS2020-TUWZO01

strength B and the f_R depends on B and the n_e. The microwave frequency launched to the vacuum chamber (2.45 GHz) relatively move between the three regions (A, B and C) in the dispersion relationship with the change of the f_{ce} and the f_R.

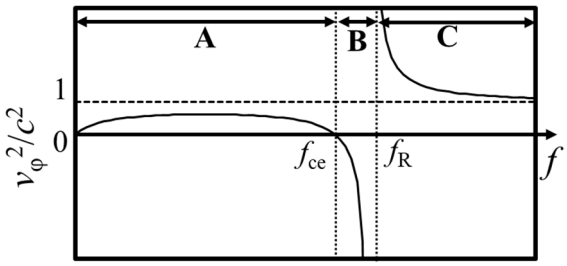

Figure 1: The typical dispersion relationship of RHP waves.

Figure 2(a) and 3(a) shows a schematic drawing of the ECRIS in Osaka Univ. It consists of a cylindrical vacuum chamber (160 mm in inner diameter and 1074 mm in Fig. 2(a)/1054 mm in Fig. 3(b) in length) with several ports at the top and the side wall. We use the cartesian coordinate system (x, y, z) with the origin located at the center of the chamber. The magnetic configuration of the ECRIS is formed by mirror coils (Coil A and B), an additional coil (Coil C), and permanent octupole magnets. Currents of three coils are defined as I_A, I_B, and I_C, respectively. Normally, the I_A and the I_B are 150 A, occasionally 170 A, and the I_C is optimized within ±20 A. The ECR zone is formed in the center of the chamber and is controllable by adjusting the I_C. 2.45 GHz microwaves are generated by the magnetron (incident microwave power 1.3 kW at the maximum) and are introduced into the vacuum chamber of the ECRIS thorough the coaxial window. We launch them from coaxial semi-dipole antenna z=-448 mm, in Fig. 2(b) or the rod antenna z=-175 mm, in Fig. 2(c) installed on the side wall of the vacuum chamber. The coaxial semi-dipole antenna is installed along the geometrical axis of the vacuum chamber in consideration of RHP wave propagation which is parallel to the ***B*** field [7-9]. The shape of the coaxial semi-dipole antenna is L-shape at the tip because we aim to exciting RHP waves by enhancing TE mode [7-9] in Fig. 2(b). The aluminum plate tuner (120 mm in diameter and 2 mm in thickness) is inserted behind the semi-dipole antenna. It is movable horizontally from z=-498 mm to z=-468 mm.

The operating gas is Ar and operating pressures are 10^{-4}~10^{-3}Pa. Langmuir probes LP1 (z=-175 mm) and LP2 (z=175 mm) and L-shape probe (z=364 mm) are inserted from the side port of the vacuum chamber and the plasma electrode in the case I in Fig. 2(a) and II in Fig. 3(a) respectively. LP1, 2 and L-shape probe consist of cylindrical Mo wires of 0.5 mm in diameter and 10 mm for LP1 and LP2 and 15 mm for L-shape probe in length in Fig. 2(d) and in Fig. 3(b). They are movable within x=0-50 mm for LP1 and LP2, and movable in the direction of the rotation for L-shape probe. We can estimate the plasma parameters, *e.g.*, the EEDF, the I_{is} (measured by applying -45V to probes), the n_e, and the T_e. Ion beam extraction electrodes

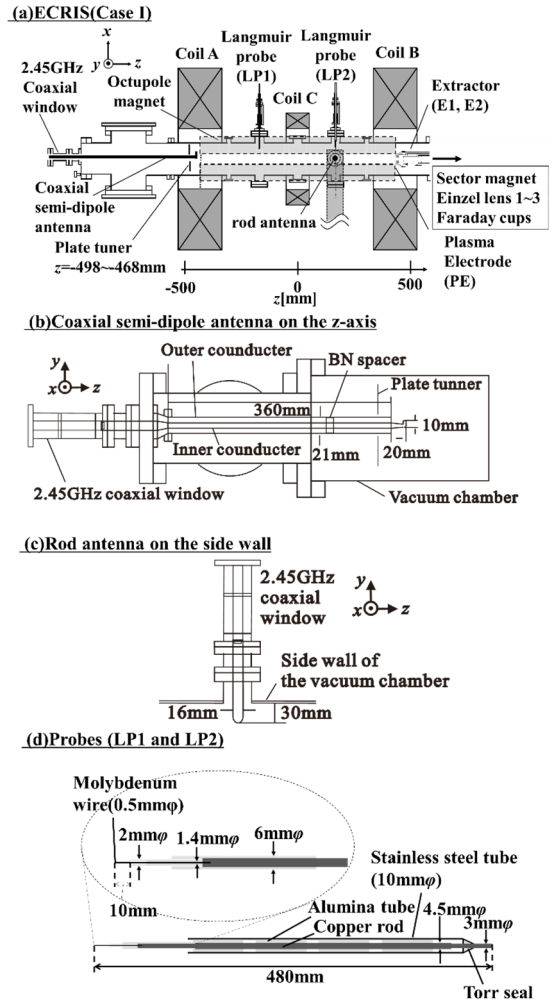

Figure 2: Schematic drawing of ECRIS (Case I) (a). Coaxial semi-dipole antenna installed on the z-axis (b). Rod antenna installed on the side wall of the vacuum chamber (c). Probes inserted from the side port (LP1 and LP2) (d).

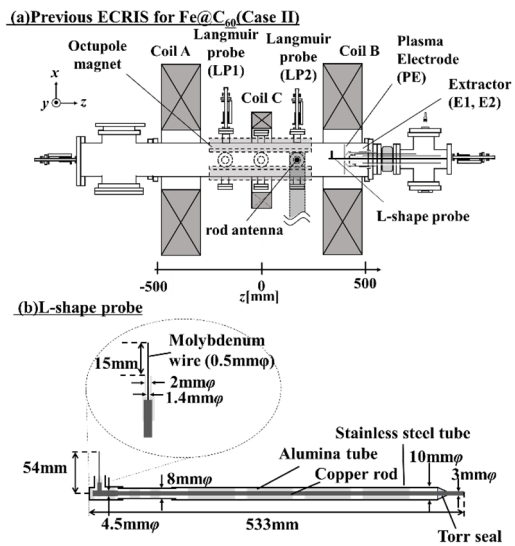

Figure 3: Schematic drawing of previous ECRIS for Fe@C_{60} (Case II) (a). L-shape probe inserted from the extractor (b).

ISBN: 978-3-95450-226-4 ISSN: 2222-5692 doi:10.18429/JACoW-ECRIS2020-TUWZO01

consist of the plasma electrode (PE), the mid-electrode (E1), and the extractor electrode (E2) in Fig. 1(a). Extracted ion beams are focused by the einzel lens and analyzed by a sector magnet. Ion beam currents are measured by several Faraday cups. We can obtain the charge state distribution (CSD) of the extracted ion beam.

Figure 4 shows the typical accessibility condition in the *x*-*z* plane of the vacuum chamber estimated from the past measurements of n_e profiles and calculated *B*. Black and red lines represent the ECR and the R-cutoff regions respectively. It represents the location of the coaxial semi-dipole antenna, the rod antenna, and measurement regions of the LP1 and LP2. There is the B region, which is non-propagation region between the coaxial semi-dipole antenna and the rod antenna. It is considered that the RHP wave launched from each antenna difficult to reach the opposite region beyond the ECR zone. We consider that RHP waves from each antenna produce ECR more efficiently on the closer side with respect to the antenna than on the other side from the point of the accessibility condition. We measure and compare the plasma parameter I_{is} and EEDF in the two regions.

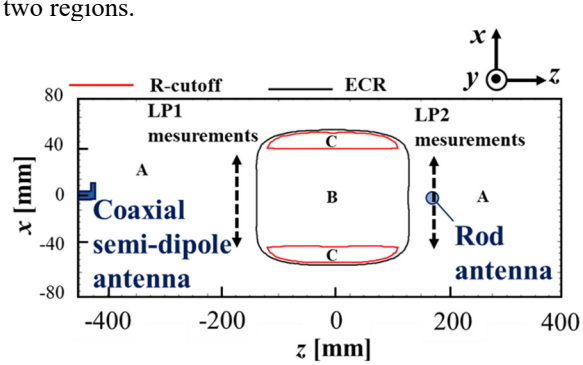

Figure 4: The typical accessibility condition in the *x*-*z* plane.

EXPERIMENTAL RESULTS AND DISCUSSIONS

Comparison of the I_{is}' Measured by LP1 and LP2 in the Case of the Microwave Launching by Each Antenna

Figure 5 shows comparison of the I_{is}'s profiles in the *x* direction measured by LP1 and LP2 in the case of the microwave launching by the coaxial semi-dipole antenna (a) and the rod antenna (b) under conditions which are I_c's are 11 and 15 A respectively. Vertical and horizontal axes are I_{is} and measurement positions *x* respectively. Red and blue plots represent measurement results of LP1 and LP2. In the case of the coaxial semi-dipole antenna, I_{is}'s measured by LP1 are higher than those by LP2. On the other hand, I_{is}'s measured by LP2 are higher than those by LP1 especially in the center of the vacuum chamber in the case of the rod antenna. These results indicate that the ECR on the side closer to the antenna is more efficient than the other side. This is consistent with propagation theory of RHP waves that they cannot pass through the B region above already mentions.

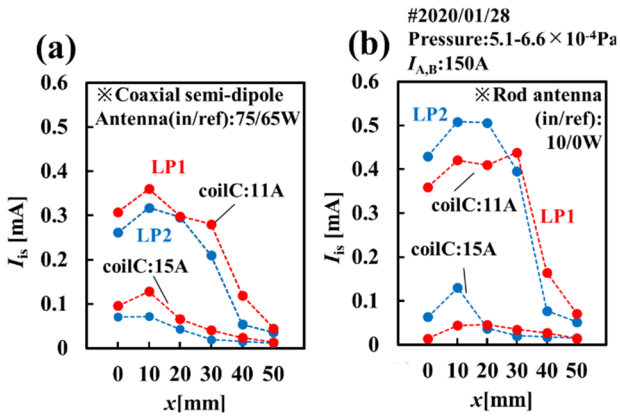

Figure 5: comparison of the I_{is}'s profile in *x* direction measured by LP1 and LP2 in the case of the microwave launching by the coaxial semi-dipole antenna (a) and the rod antenna (b).

Comparison of the EEDF's Measured at z=-175 and 75 mm in ECRIS

Figure 6 shows comparison of the EEDF's measured by LP1 and LP2 at the *x*=0 in the case of the microwave launching by the coaxial semi-dipole antenna (a) and the rod antenna (b). Red and blue plots represent measurement results of LP1 and LP2. In both cases of microwave launching by each antenna, EEDF's measured on the side closer to each antenna have higher tail than the other side. We can calculate the effective electron energy T_{eff} from EEDF's. In the case of the coaxial semi-dipole antenna, T_{eff}'s are 12.9 eV (LP1) and 12.7 eV (LP2). In the case of the rod antenna, T_{eff}'s are 11.0 eV (LP1) and 9.72 eV (LP2). We observe that the EEDF measurement results indicate same tendencies as I_{is}, which are consistent with the propagation theory of RHP waves.

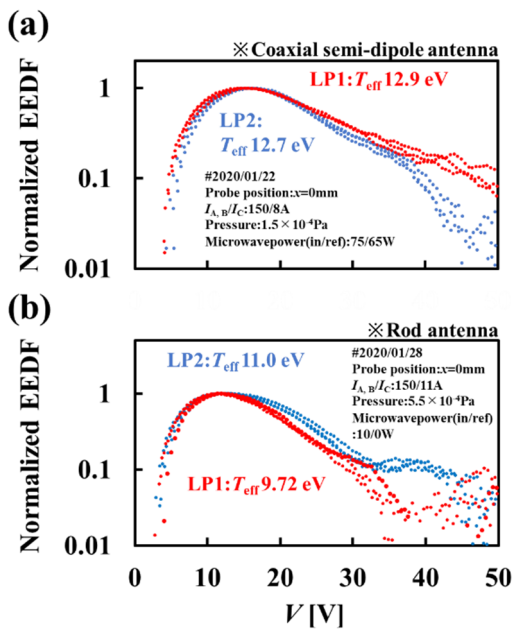

Figure 6: Comparison of the EEDF's measured by LP1 and LP2 at the *x*=0 in the case of the microwave launching by the coaxial semi-dipole antenna (a) and the rod antenna (b).

ISBN: 978-3-95450-226-4 ISSN: 2222-5692 doi:10.18429/JACoW-ECRIS2020-TUWZO01

Typical CSD's of Ion Beams Extracted from Plasmas Produced by Each Antenna at Low and High Power

Figure 7 shows typical CSD of the ion beams extracted from Ar plasmas produced by each antenna at the low power 100W (a) and the high power 280-300W (b). The black and red plots represent the case of the coaxial semi-dipole antenna and the rod antenna respectively. At the low power in Fig. 7(a), the currents of multicharged ions ($Ar^{4\sim7+}$) are higher in the case of the microwave launching by the rod antenna than that by the coaxial semi-dipole antenna. We estimate that this tendency is caused by the location of the rod antenna, which is downstream with the respect to the ECR zone and on the side closer to the extractor. At the high power in Fig. 7(b), multicharged ion currents become unstably and start to decrease in the case of the rod antenna [7]. On the contrary, they continue to increase stably in the case of the coaxial semi-dipole antenna. This is because setting the antenna along the *z*-axis is suitable to the RHP wave propagation [7].

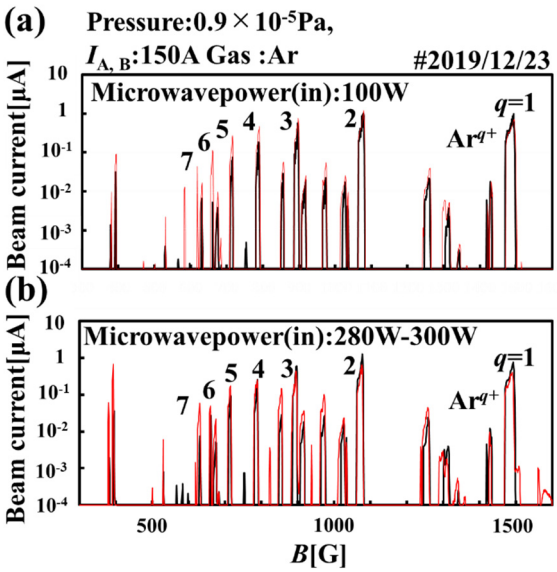

Figure 7: Typical CSD of the ion beams extracted from Ar plasmas produced by two probes at the low power 100W (a) and the high power 280-300W (b).

Plasma Parameters Measured Near the PE-plate by the L-shape Langmuir probe in ECRIS

Figure 8(a) shows PE-plate after experiments of synthesising $Fe@C_{60}$[6] in the previous ECRIS in Fig. 3(a). We can confirm the pattern of the plasma confined by the octupole. We divide it into 8 regions (No. 1~8). We analysis the two regions (No. 5 and 6) by the time of flight mass spectrometry (TOFMS). We observe the spectrum of C_{60}^+ in the No. 5 in Fig. 8(b) and materials which have same *m*/*q* as $Fe@C_{60}$ and $Fe@C_{58}$ in the No. 6 in Fig. 8(c).

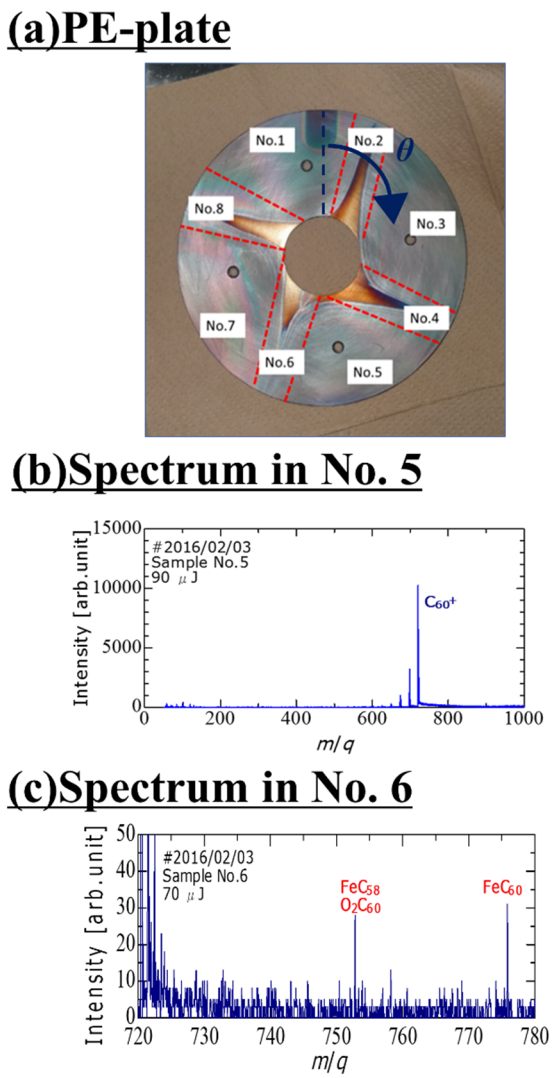

Figure 8: PE-plate after experiments of synthesising $Fe@C_{60}$ (a). Spectrum of the TOFMS analysis in the No. 5 region (b). That in the No. 6 region (c).

Figure 9 shows measurement results by rotating the L-shape probe in Fig. 3(b). We measure the dependence of the I_{is} on the angle θ in Fig. 9(a). The I_{is} peak in the even number regions (No. 2, 4, 6, 8). We measure EEDF's at θ =205° in the No. 6 and those at θ =190° in the boundary region between No. 5 and No. 6 in Fig. 9(b). They are represented by red and black plots respectively. It is observed that the EEDF at θ =205° has higher tail than that at θ =205°. There are higher energy electrons in the No. 6 where productions of $Fe@C_{60}$ and $Fe@C_{58}$ is suggested.

ISBN: 978-3-95450-226-4 ISSN: 2222-5692 doi:10.18429/JACoW-ECRIS2020-TUWZO01

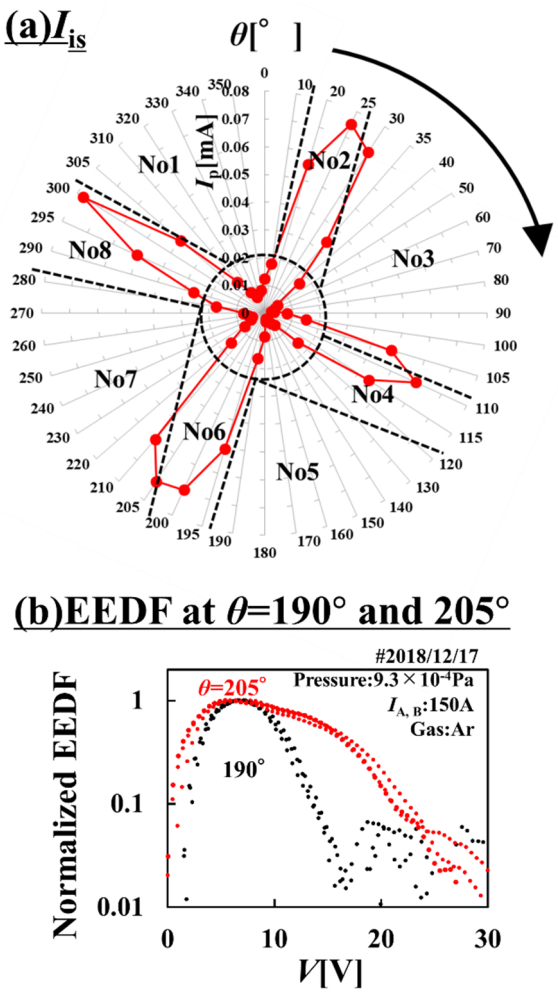

Figure 9: I_{is} measured by L-shape probe (a). EEDF's measured at the θ =205° and 190° (b).

REFERENCES

[1] A. Kitagawa *et al.*, "Status of Ion Sources at HIMAC", in *Proc. 19th Int. Workshop on ECR Ion Sources (ECRIS'10)*, Grenoble, France, Aug. 2010, paper MOCOBK03, pp. 20-22.

[2] T. Uchida, H. Minezaki, K. Tanaka, M. Muramatsu, T. Asaji, Y. Kato, A. Kitagawa, S. Biri, and Y. Yoshida, "Bio-Nano ECRIS: An electron cyclotron resonance ion source for new materials production", *Rev. Sci. Instrum.*, vol. 81, p. 02A306, 2010. doi.org/10.1063/1.3258027

[3] Y. Kato, T. Nishiokada, K. Hamada, K. Onishi, T. Takeda, K. Okumura, T. Omori, W. Kubo, M. Ishihara, and S. Harisaki, "Upper hybrid resonance heating experiments by X-mode microwaves on electron cyclotron resonance ion source', *Rev. Sci. Instrum.*, vol. 91, p. 013315, 2020.

[4] T. Nishiokada, T. Nagaya, S. Hagino, T. Otsuka, M. Masayuki, F. Sato, A. Kitagawa, and Y. Kato, "Experimental results of superimposing 9.9 GHz extraordinary mode microwaves on 2.45 GHz ECRIS plasma", *Rev. Sci. Instrum.*, vol. 87, p. 02A714, 2016. doi.org/10.1063/1.4934212

[5] Y. Kato, T. Nishiokada, T. Nagaya, S. Hagino, T. Otsuka, T. Watanabe, Y. Tsuda, K. Hamada, K. Onishi, T. Takeda and T. Asaji, "Preliminary results of 4.0-6.0 GHz extraordinary mode experiments on 2.45 GHz ECRIS", *AIP Conference Proceedings*, vol. 2011, no. 1, p. 020005, 2018. doi.org/10.1063/1.5053247

[6] Y. Kato, T. Nagaya, T. Nishiokada, S. Hagino, T. Otsuka, T. Watanabe, Y. Tsuda, K. Onishi, K. Hamada, T. Takeda, T. Uchida, M Muramatsu, A. Kitagawa and T. Asaji", Production of nitrogen-fullerene compound ion beams on tandem-type electron cyclotron resonance ion source", *AIP Conference Proceedings*, vol. 2011, p. 090013, 2018. doi.org/10.1063/1.5053394

[7] W. Kubo, K. Hamada, K. Onishi, T. Takeda, K. Okumura, T. Omori, M. Ishihara, S. Harisaki, and Y. Kato, "Coaxial semi-dipole antenna microwave feeding on electron cyclotron resonance multicharged ion source", *Rev. Sci. Instrum.*, vol. 91, p. 023317, 2020. doi.org/10.1063/1.5128576

[8] Francis F. Chen, "*Introduction to Plasma Physics*", New York, Plenum Press, 1974.

[9] Michael A. Lieberman and Allan J. Lichtnberg, in "*Principle of Plasma Discharges and Materials Processing*", New York, NY, USA: Wiley, 1994.

ISBN: 978-3-95450-226-4 ISSN: 2222-5692 doi:10.18429/JACoW-ECRIS2020-TUWZO03

PRODUCTION OF METALLIC ION BEAMS WITH INDUCTIVE HEATING OVEN AT INSTITUTE OF MODERN PHYSICS*

W. Lu†[1], C. Qian[1], L. B. Li, W. H. Zhang, H. Y. Ma, J. D. Ma, Y. C. Feng, L. X. Li[1], J. W. Guo, W. Huang[1], X. Z. Zhang[1], L. T. Sun[1], H. W. Zhao[1]
Institute of Modern Physics, Chinese Academy of Science, Lanzhou, China
[1] also at University of Chinese Academy of Science, Beijing, China

Abstract

A High-Temperature Oven (HTO) with inductive heating technology has been developed successfully in 2019 at Institute of Modern Physics. This oven features durable operation temperature of >2000°C inside the tantalum susceptor. By careful design the oven structure, material compatibility and thermal stress issues at high temperature has been successfully handled, which enables the production of >400 eμA U^{33+} with SECRAL-II. With necessary refinement, this type of oven could also be available with room temperature ECR ion sources, like LECR4 and LECR5. Some improvements in structure have been proposed in this year. The design and testing results will be presented in this contribution.

INTRODUCTION

Most of the advanced heavy ion accelerators need intense metallic ion beams, like MSU-FRIB needs 13 puA of U^{33+} and U^{34+}, RIKEN-RIBF needs 15 puA of U^{35+}, IMP-HIAF needs 20 puA of U^{35+}, and so on. To meet all these requirements, colleagues in the ECR community have developed several methods to produce enough metal vapour in ECR plasma, such as direct plasma heating, MIVOC, Sputtering, Metal oven, Laser ablation, etc. Direct plasma heating method is rarely used in ECR ion source now because the intensity and charge state are very limited and difficult to get very stable plasma. MIVOC is suitable for producing medium charge state ion beams. For sputtering method, it has the advantage of simple structure, and it's also suitable for long-term operation. But the disadvantages are also obvious, like difficult to get very high intensity and charge state. Laser ablation method has been shown to be capable of producing pulsed medium charge state metallic ion beams. But the charge state and reliability still need to be further improved. In general, metal oven method is still the best way to produce intense high-charge-state ion beams. As shown in Fig. 1, it is clear that, for refractory metals, the typical temperature to produce enough metal vapour (0.01–0.1 torr) in an ECR source is 1600–2000°C.

As we know, high performance resistive heating ovens have been developed in the ECR community for more than ten years, and some good results have been produced [1, 2]. But there are also several challenges, like high standard processing technology, strong Lorenz force, and so on. This could be more serious in the next generation ECR ion sources, like FECR and MARS, because the axial magnetic field at the injection side might up to 6 T. compared with a resistive heating oven, the most important feature of an inductive heating oven is that it's Lorenz force free when working in the high magnetic field environment.

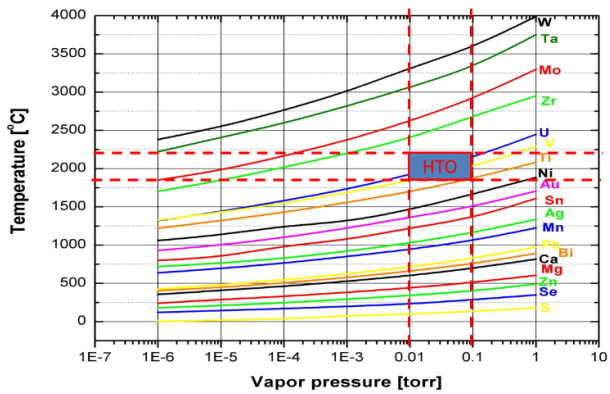

Figure 1: The temperature as a function of metal vapour pressure for refractory metals.

INDUCTIVE HEATING OVEN-2019

The structure of this inductive heating oven is similar to that of MSU [3]. It is composed of a susceptor, zirconia, inductive heating coils, water cooling system, and an AC power supply. The main difference is that a gap has been added between the tantalum crucible and zirconia, as shown in Fig. 2. With this gap, the crucible can only contact the zirconia at the ends, thus effectively avoiding the chemical reaction between each other at the high-temperature region and improving the working temperature and corresponding service life. The newly designed oven also has the following features: 1) end cover structure is designed for easy fixing; 2) Al_2O_3 instead of BN for outer shielding. All of these

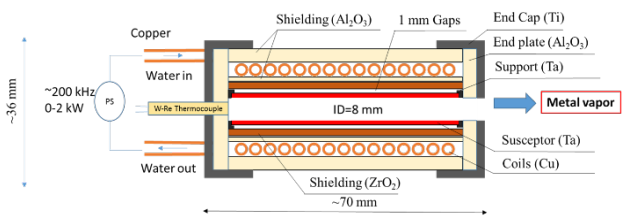

Figure 2: Schematic view of the inductive heating oven-2019.

* Work supported by the West Light Foundation of the Chinese Academy of Sciences & National Nature Science Foundation of China (Grant Nos. 11875300 and 11427904.
† luwang@impcas.ac.cn

ISBN: 978-3-95450-226-4 ISSN: 2222-5692 doi:10.18429/JACoW-ECRIS2020-TUWZO03

make the inductive heating oven-2019 become a reliable, flexible, and low out-gassing high-temperature oven.

Off-line and On-line Test

Figure 3 shows the off-line test platform for the inductive heating oven-2019 at IMP. The test result shows that the temperature of tantalum crucible can reach up to ~2000°C at a maximum AC power of about 1.2 kW. After the off-line test, we installed the oven on the supercon-ducting ECR ion source SECRAL-II, to produce intense high-charge-state uranium ion beams. With 24+ 18 GHz double frequency heating, some preliminary results have been produced with a total microwave power of 6.0 kW in 2019, such as 310 eμA of U^{35+}, 60 eμA of U^{42+}, 9 eμA of U^{50+}, and so on. Detailed information can be found in reference [4].

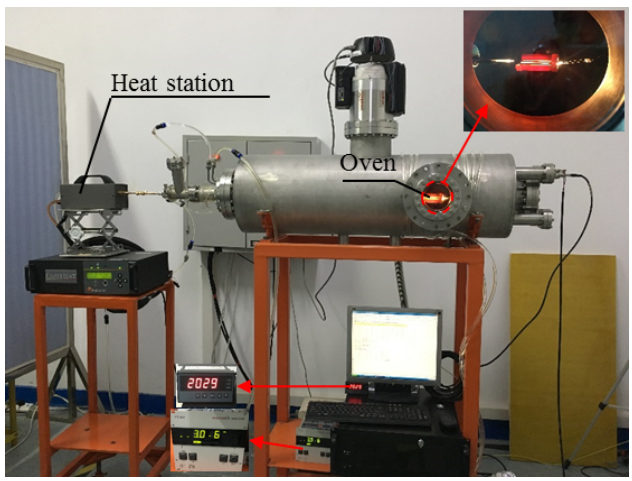

Figure 3: Off-line test platform for the inductive heating oven-2019 at Institute of Modern Physics.

Routine Operation for HIRFL-CSR

HIRFL-CSR has been operating for more than 10 years at IMP since 2007. It needs refractory metallic ion beams for different terminal requirements every year, like $^{27}Al^{8+}$, $^{56}Fe^{17+}$, $^{181}Ta^{35+}$ in 2019. For aluminum and iron, we use the inductive heating oven-2019 instead of the traditional oven. Intensities of 20–30 eμA for $^{27}Al^{8+}$ and 30–40 eμA for $^{56}Fe^{17+}$ have been produced on SECRAL-II ion source with 0.3–0.4 kW of inductive heating power and delivered to HIRFL-CSR for about one week to one month without interrupt, as shown in Table 1. Figure 4 shows long-term stability when delivering $^{56}Fe^{17+}$. For tantalum, we use the sputtering method. 40–60 eμA of $^{181}Ta^{35+}$ has been produced on SECRAL-II ion source with 3.9–4.5 kV negative sputtering voltage and delivered to HIRFL-CSR for more than three weeks without interrupt.

MINI-INDUCTIVE HEATING OVEN-2020

For standard inductive heating oven-2019, the diameter and length is 36 mm and 70 mm, which is suitable for superconducting ECR ion source SECRAL-I and SECRAL-II, but too large for a room temperature ECR ion source,

Table 1: Refactory Metallic Ion Beams Routine Operation for HIRFL-CSR in 2019

Ion	IHO Temp. [°C]	Iq [eμA]	Days
$^{27}Al^{8+}$	1300–1400	20–30	7
$^{56}Fe^{17+}$	1400–1500	30–40	32
$^{181}Ta^{35+}$	Sputtering method	40–60	21

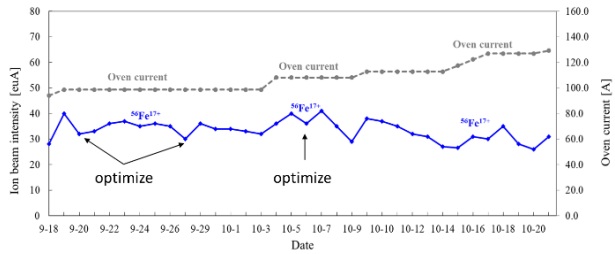

Figure 4: $^{56}Fe^{17+}$ routine operation for HIRFL-CSR with inductive heating oven-2019 in one month.

like LECR4 and LECR5 at IMP. To solve this issue, mini-inductive heating oven-2020 has been proposed this year. As shown in Fig. 5, it is similar to inductive heating oven-2019 in structure, but smaller in diameter and shorter in length. Similar crucible diameter has also been kept to provide enough loading capacity for long-term operation.

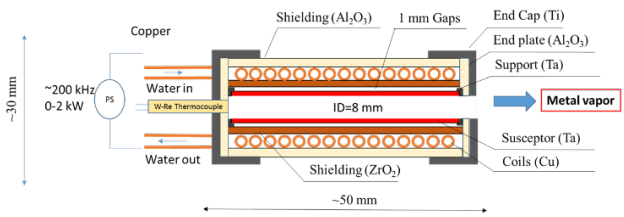

Figure 5: Schematic view of the mini-inductive heating oven-2020.

1st On-line Test

The mini-inductive heating oven-2020 was firstly installed on the room temperature ECR ion source LECR5, to produce intense highly charged calcium ion beams with calcium oxide directly. It is worth to mention that the ion source group at RIKEN has already produced ~50 eμA of $^{40}Ca^{11+}$ with CaO and high-temperature resistive heating oven in 2019 [5].

In the first test, the oven was located close to the plasma in order to utilize the contribution of plasma heating, as shown in Fig. 6. In fact, the plasma contributes too much, which leads to serious outgassing and instability. Only low-charge-state ion beams were produced, like 110 eμA of Ca^{3+}, 60 eμA of Ca^{4+}, and so on, as shown in Fig. 7.

2nd and 3rd On-line Test

To decrease the influence of plasma heating to the oven, we increase the distance between oven and plasma from 40 mm to 60 mm and 100 mm, as shown in Fig. 8. In the second test, plasma heating is still obvious, but much lower.

ISBN: 978-3-95450-226-4 ISSN: 2222-5692 doi:10.18429/JACoW-ECRIS2020-TUWZO03

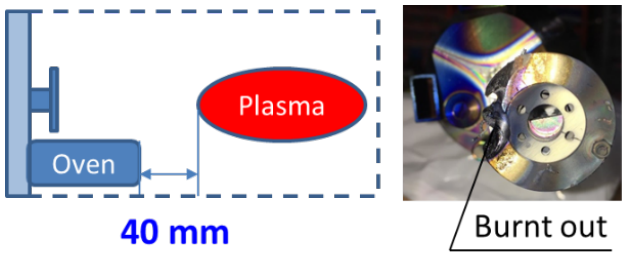

Figure 6: Layout of oven and plasma in the 1st on-line test and photo of oven after tuning.

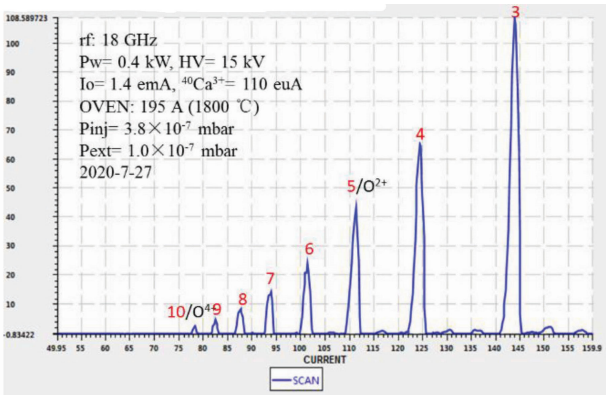

Figure 7: Typical spectrum when oven nearby the plasma in the 1st on-line test.

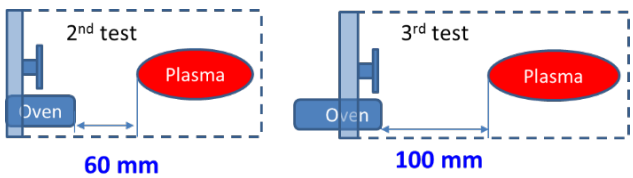

Figure 8: Layout of oven and plasma in the 2nd and 3rd on-line test.

Some medium-charge-state calcium beams have been produced, like 120 eμA of $^{40}Ca^{12+}$, 50 eμA of $^{40}Ca^{14+}$, and so on. In the third test, the oven is located far always from the plasma. Test results demonstrated that the plasma heating influence has been well controlled, and very high charge state calcium beams can be produced, such as 30 eμA of Ca^{16+}, 10 eμA of Ca^{17+}, etc. Figure 9 shows the typical spectrum when Ca^{12+} is optimized.

CONCLUSION

A new type of inductive heating oven with a special gap and fixing structure has been developed at the Institute of Modern Physics. Online test and routine operation have shown that this type of oven can operate at 1600–2000°C for long-term operation without degradation and damage. With necessary refinement, the mini-inductive heating oven-2020 has been fabricated this year and applied to the room temperature ECR ion source LECR5. Some preliminary results have been produced with 0.6–0.8 kW of inductive heating power, like 120 eμA of $^{40}Ca^{12+}$, 50 eμA of $^{40}Ca^{14+}$, 30 eμA of $^{40}Ca^{16+}$, etc.

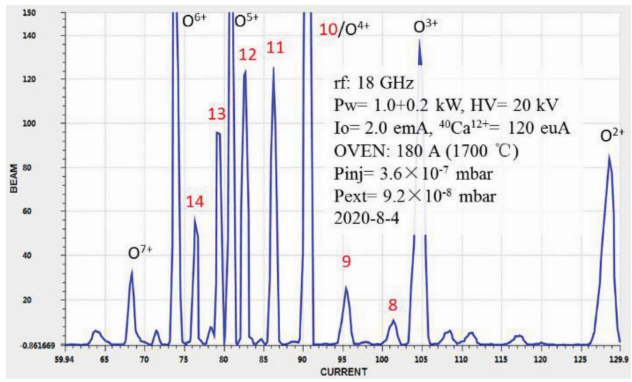

Figure 9: Typical spectrum in the 2nd on-line test.

ACKNOWLEDGMENTS

This project is supported by the West Light Foundation of the Chinese Academy of Sciences and National Nature Science Foundation of China (Grant Nos.11875300 and 11427904).

REFERENCES

[1] J. Y. Benitez *et al.*, "Current Developments of the VENUS Ion Source in Research and Operations", in *Proc. 20th Int. Workshop on ECR Ion Sources (ECRIS'12)*, Sydney, Australia, Sep. 2012, paper THXO02, pp. 153–158.

[2] J. Ohnishi, Y. Higurashi, and T. Nakagawa, "Practical Use of High-Temperature Oven for 28 GHz Superconducting ECR Ion Source at RIKEN", in *Proc. 23th International Workshop on ECR Ion Sources (ECRIS'18)*, Catania, Italy, Sep. 2018, pp. 180–184, doi:10.18429/JACoW-ECRIS2018-WEB4

[3] P. A. Zavodszky *et al.*, "Status report on the design and construction of the Superconducting Source for Ions at the National Superconducting Cyclotron Laboratory/Michigan State University", *Rev. Sci. Instrum.*, vol. 77, p. 03A334, 2006, doi:10.1063/1.2162855

[4] W. Lu *et al.*, "Production of intense uranium beams with inductive heating oven at Institute of Modern Physics", *Rev. Sci. Instrum.*, vol. 90, p. 113318, 2019, doi:10.1063/1.5128419

[5] T. Nagatomo, private communication, 2019.

ISBN: 978-3-95450-226-4 ISSN: 2222-5692 doi:10.18429/JACoW-ECRIS2020-TUXZO01

A PROPOSED EXPLANATION OF HIGH-MINIMUM-B INSTABILITIES

D. S. Todd† and J. Y. Benitez, Lawrence Berkeley National Laboratory, Berkeley, CA, USA

Abstract

It is well-known that electron cyclotron resonance ion sources exhibit instabilities when these sources' minimum magnetic fields are approximately 80% of the resonant field or greater, but the reasons for this instability have yet to be satisfactorily explained. We show that raising the minimum field makes much faster heating modes accessible at lower energies that invite the onset of kinetic instabilities.

KINETIC INSTABILITIES

Electron cyclotron resonance ion sources (ECR ion sources or ECRISs) are an effective means of producing high current, highly-charged ion beams [1,2]. These sources typically rely on a superposition of solenoidal and sextupolar magnetic fields to confine a plasma via magnetic mirroring. Electrons are heated resonantly by injected microwaves near closed surfaces of constant magnetic field that surround the source's minimum magnetic field center. Decades of experience with these sources has shown high-charge-state production is optimized when the axial fields have maxima of approximately twice the resonant field at the beam-extracting end of the source and three-to-four times the resonant field at the opposite end, while maintaining radial fields that are approximately twice the resonant field on the plasma chamber surface. The central field is typically set so that its minimum is in the range of 50-to-80 percent of the resonant field. It has been found for all ECR ion sources that as the minimum field is increased to, and especially beyond, 80 percent of the resonant field the confined plasma becomes increasingly unstable. When this happens, the plasma expels strong bursts of high-energy electrons that have been associated with kinetic instabilities arising when the electron energy distribution increases with energy [3].

Kinetic instabilities can develop in systems where particles gain energy much more quickly than particle-particle interactions can smooth out the energy distribution. ECR ion sources are susceptible to this since scattering cross-sections rapidly decrease with kinetic energy. For advanced sources electron energies can reach the low MeV range, and electrons with energies of 10s of keV or more will spend significant portions of their millisecond-timescale lifetimes without collisions. If an ECR ion source is tuned in a manner that allows for the rapid heating of a significant percentage of electrons to energies where scattering becomes rare, kinetic instabilities become increasingly likely.

SINGLE PASS HEATING

The most effective heating of low-energy electrons takes place where the local magnetic field matches the injected microwave frequency, and as the energy is increased relativistic effects will move the resonance to higher magnetic field surfaces. A rough estimate of the energy gained in crossing the resonance surface can be made as follows. The differential energy gain along path length $d\vec{s}$ is given by $dE = \vec{F} \cdot d\vec{s}$. Maximum electron resonant heating in a magnetic field occurs for a circularly polarized wave of magnitude E in phase with an electron rotating at radius r through an angle $d\theta$: $dE = eErd\theta$. We can use the fact that the transverse and longitudinal (defined to be z-direction) velocities are given by $v_\perp = r\frac{d\theta}{dt}$ and $v_\parallel = \frac{dz}{dt}$, respectively, to rewrite the energy gain as $dE = eE\frac{v_\perp}{v_\parallel}dz$. Reasonable maximum microwave electric fields within the source are likely 10s of kV/m, and for typical high-charge-state producing fields (minimum-field-to-lower-mirror-field ratios of .25 to .4) the velocity ratios are in the range $.5 \lesssim \frac{v_\perp}{v_\parallel} \lesssim .8$. Plugging this all in, it is expected that energy-gain-per-mm of axial travel is in the range of 10s to 100s of eV/mm with higher gains possible as the velocity ratio increases. Single particle simulation agrees with these numbers. For a low-energy electron to reach 10s of keV kinetic energies or greater requires many such crossings, and phase differences will give much lower energy gains on average. However, if regions are accessible where the electron spends a long time in resonance either because of low axial velocity or because it is in a region of near-zero gradient, much larger energy-gains-per-pass are possible.

The minimum magnetic field near the center of the source is a region with zero-gradient, but as mentioned previously it is typically 50-80% of the resonant field. Nearly all ECR ion sources utilize axially-injected microwaves and as electron energies are increased, electron axial velocities can be large enough that the Doppler shift of this incoming wave becomes significant.

In the laboratory frame, microwaves reach a source electron with frequency $f = f_o(1 - \hat{k}_{wave} \cdot \vec{\beta})$, where f_o, $\hat{k}_{wave}$, and $\vec{\beta}$ are the injected wave frequency, its direction, and the electrons velocity divided by the speed of light, respectively. An electron will be in resonance with the shifted wave if the local magnetic field satisfies the cyclotron equation, $\omega = \frac{eB_{res}}{\gamma m}$, which can be solved for the local resonant field:

$$B_{res} = \frac{\omega\gamma m}{e} = \frac{\omega_{rf}(1 - \hat{k}_{wave} \cdot \vec{\beta})\gamma m}{e} = B_{res,\gamma=1} \cdot \gamma(1 - \hat{k}_{wave} \cdot \vec{\beta}) \quad (1)$$

where ω_{rf} is injected microwave's angular frequency and $B_{res,\gamma=1}$ is the magnetic field that a non-relativistic electron would resonate at that frequency.

Increasing the minimum magnetic field decreases the kinetic energy required for a confined (outside loss cone)

† dstodd@lbl.gov

ISBN: 978-3-95450-226-4 ISSN: 2222-5692 doi:10.18429/JACoW-ECRIS2020-TUXZO01

electron to be resonantly heated at the zero-gradient field near the source center. Figure 1 shows the minimum kinetic energy necessary to reach this field ratio for an extraction mirror field (B_{ext}) twice the resonant field. Higher extraction fields move this curve down, but the effect is small over the typical extraction field operating ranges for high charge state production ($1.8 \leq B_{ext}/B_{min} \leq 2.2$).

Access to the zero-gradient part of the axial field curve allows greater kinetic energy changes near this minimum. More importantly, we will see there are other heating modes that become accessible when the electrons have energies that allow them to better utilize fields lower than the injected frequency's natural resonance.

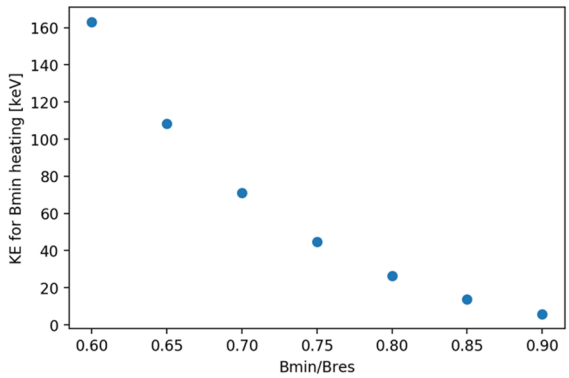

Figure 1: The minimum kinetic energy required for resonant heating at B_{min} as a function of B_{min}/B_{res} is plotted for B_{ext}/B_{res}=2.

ELECTRON RESONANT HEATING

Figure 2 shows a plot of the axial magnetic field in VENUS as a function of axial position along with the fields required for resonant heating by the Doppler-shifted injected waves a simulated, confined electron receives as it moves inside the source. The heating wave is assumed to be two axially-directed, circularly-polarized plane waves with 10 kV/m magnitude traveling in opposite directions, so at any instant the electron is affected by two waves: one Doppler shifted up and one down. Because of these shifted frequencies, the electron resonant fields are also shifted, and this shifted field is also plotted for the electron motion in Fig. 2.

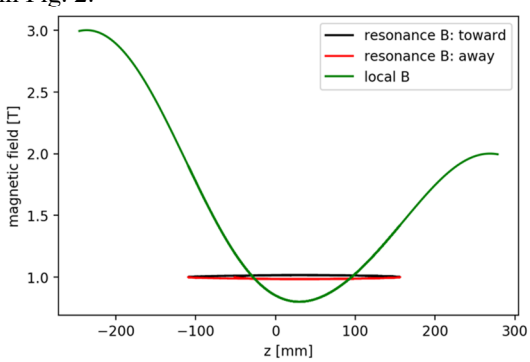

Figure 2: The axial field and Doppler-shifted resonance fields ("away": shifted down, "toward": shifted up) for a confined electron are plotted vs. axial position.

From the plot in Fig. 2, we expect resonant heating to be possible where the resonant field curves overlap with the local magnetic field. The region where these overlaps occur is shown in Fig. 3 with the energy as a function of z plotted below. As can be seen in this figure, the largest energy changes (in the range of 100s of eV, as expected) occur where the local field is close to the Doppler resonant field. For this figure and all following figures of the same format, electron energies and trajectories are selected somewhat randomly as representative of the concept, not the maximum energy gains.

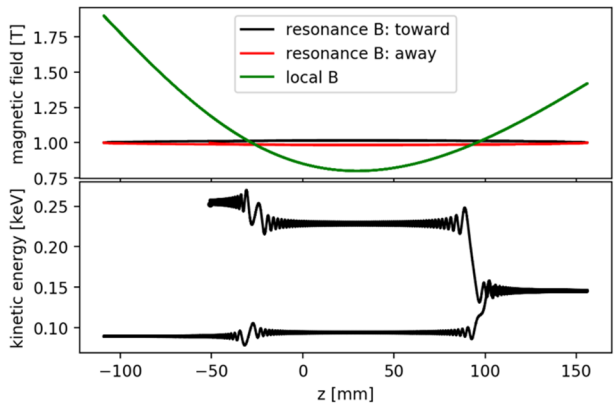

Figure 3: The axial field and Doppler-shifted resonance fields, above, and electron energy, below, are plotted vs. axial position. Energy changes occur when resonant field is near local magnetic field. This and Fig. 4-7 use semi-randomly chosen trajectories that illustrate where energy changes occur, but not the maximum energy change possible, which is phase-dependent.

As mentioned above, it is expected that if the electron spends a long period of time near resonance or interacts with regions of low magnetic field gradient, it will be possible to have especially large energy changes in a single crossing. Figure 4 shows a crossing in the former case where the electron reflection occurs near resonance. Heating in this mode, which can give higher energy changes in a single pass (~keV range) is possible for electrons of all energies in all sources with appropriate ratio of transverse-to-axial velocities, however it is expected that a small percentage of electrons have the proper angle to undergo this heating.

Increasing the minimum magnetic field provides other fast-heating mode as the lowest section of the axial magnetic field becomes accessible. Figure 5 shows what happens when the zero-gradient part of the magnetic field becomes accessible for resonant heating: larger energy gains (again, keV range or higher) become possible in a single pass.

It is not necessary for there to be actual coincident resonance near the minimum field point for there to be large energy gains. Two examples are given in Figs. 6 and 7 where the shape of the lowered resonance curve as a function of z roughly approximates the shape of the local magnetic field along the electron's trajectory. In Fig. 6 there is only one actual resonance match to the local field near each

ISBN: 978-3-95450-226-4 ISSN: 2222-5692 doi:10.18429/JACoW-ECRIS2020-TUXZO01

end of the z axis, but for the remainder of the region between these points it is near-resonance, allowing for large (keV-scale) energy gains in a single source crossing. Fig. 7 has two matches of the resonant and local fields on either side of the minimum field, but even larger gains are made possible by the outer resonances happening near the reflection points.

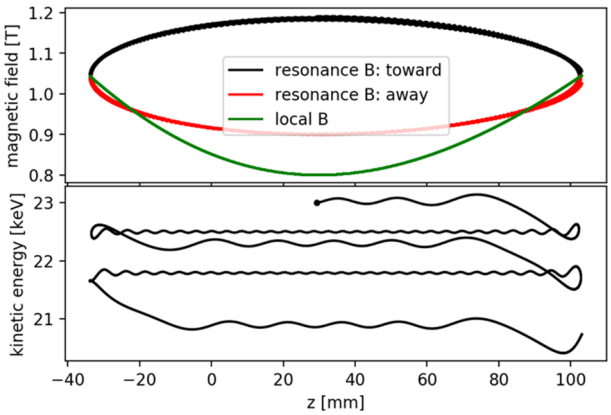

Figure 4: Resonant heating where the reflection point has a resonant magnetic field close to the local electric field. Larger energy gains are possible as the axial velocity is near zero at the ends. (see Fig. 3 for full description)

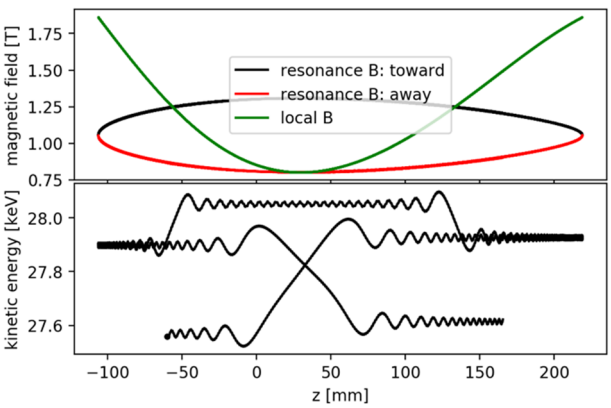

Figure 5: Resonant heating when the axial minimum becomes accessible. (see Fig. 3 for full description)

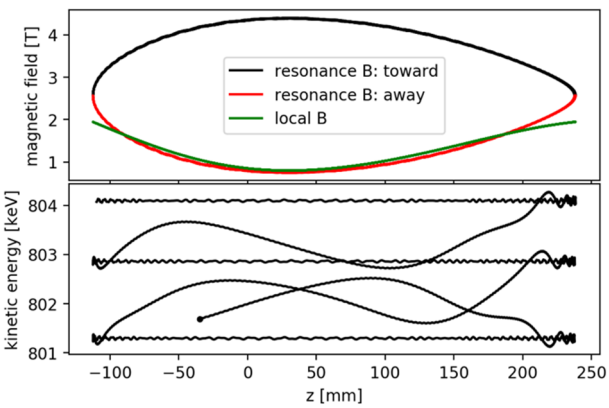

Figure 6: Resonant heating with one resonant match on either side of B_{min} but a near resonance over much of the trajectory. (see Fig. 3 for full description)

The wider availability of heating modes where large electron energy gains can be made with few axial bounces makes kinetic instabilities more probable. Increasing the minimum field makes especially high-energy-gain modes accessible at lower kinetic energy.

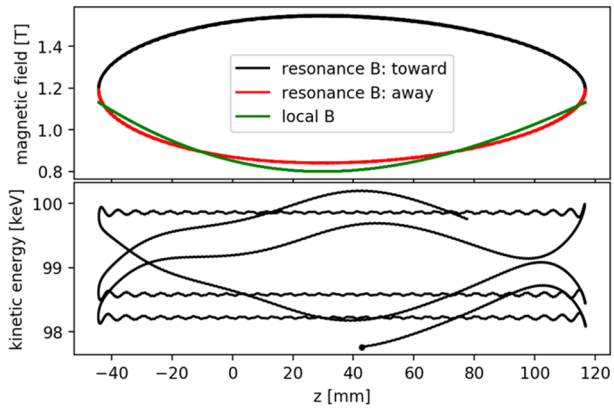

Figure 7: Resonant heating with two resonance matches on either side of the minimum field and a general shape match allowing relatively high energy changes. (see Fig. 3 for full description)

ECR RESONANT HEATING MAP

Utilizing conservation of the first adiabatic invariant ($\mu = \frac{\gamma m v_\perp^2}{B}$), it is possible to determine which near-axial electrons will encounter a resonance point before mirroring based on the kinetic energy and velocity angle away from the source's long axis at the axial location of the minimum field. Figure 8 represents a map of this kinetic energy/velocity angle phase space where resonance heating can occur for any ECR ion source with B_{min}/B_{res}=0.8 and B_{ext}/B_{res}=2.0. In this figure we can see that there is no resonant heating at large angle (electrons don't have sufficient axial velocity to reach resonance) and that the maximum energy electrons that may be resonantly heated are just over 1 MeV. The maximum bremsstrahlung energies measured from advanced ECR ion sources such as VENUS have been in the MeV range [4], and Fig. 8 implies that next-generation sources shouldn't be able to exceed this energy via resonantly heated electrons. Also plotted is the line showing the angle/energy combination allowing resonant heating at the field minimum.

For comparison, Fig. 9 shows a similar phase space plot to Fig. 8 but with a lower minimum field (B_{min}/B_{res}=0.6). It can be seen that there are a number of changes between these two plots. First, the phase space area allowing the resonant heating of confined electrons dramatically decreases when B_{min} is reduced. Second, reducing B_{min} shifts the minimum field resonance line to significantly higher energy for confined particles. Both of these would be expected to result in generally slower electron heating and lower likelihood of kinetic instabilities.

As an aside, it was found experimentally using VENUS that the instability encountered when B_{min}/B_{res}=0.8 and B_{ext}/B_{res}=2.0 went away as the extraction field was reduced to around B_{ext}/B_{res}=1.6 while keeping the minimum field

ISBN: 978-3-95450-226-4 ISSN: 2222-5692 doi:10.18429/JACoW-ECRIS2020-TUXZO01

ratio fixed. Reducing the extraction field moves the loss cone line upwards in Fig. 8, which replicates the trend when the minimum field is reduced: it shifts the kinetic energy required of confined electrons for resonance at minimum field higher and simultaneously reduces the resonant heating phase space for the confined electrons.

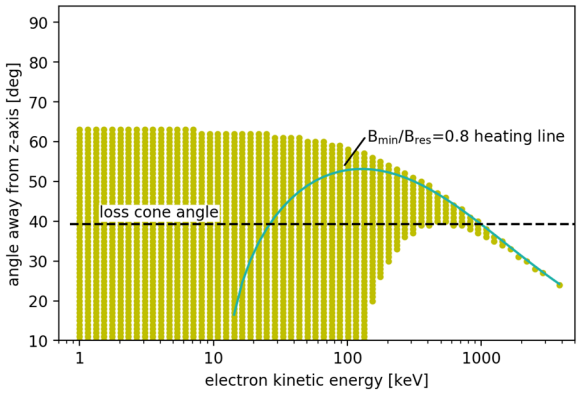

Figure 8: Phase space map indicating kinetic energy/axial angle combinations where resonant heating may occur for B_{min}/B_{res}=0.8.

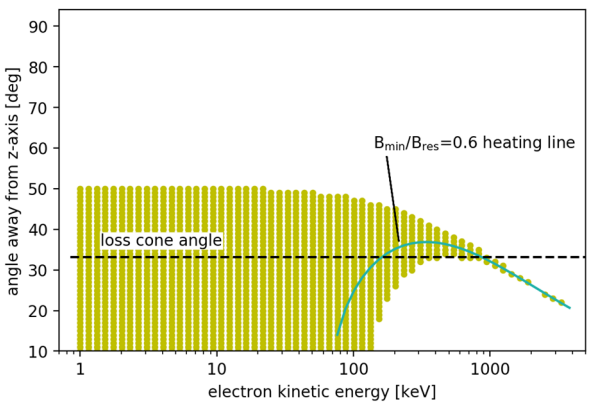

Figure 9: Phase space map indicating kinetic energy/axial angle combinations where resonant heating may occur for B_{min}/B_{res}=0.6.

ADDING SECOND FREQUENCY

The addition of a second heating frequency to an ECR ion source is a well-known means of reducing instabilities. For VENUS, the secondary frequency is 18 GHz, and Fig. 10 repeats the electron simulations above but adds 4 kV/m of the lower frequency. This represents 40% of the 28 GHz field or 16% of the power, and this power ratio is not very different from that used in VENUS.

As can be seen when comparing Fig. 10 to the earlier similar figures, the addition of the second frequency has resulted in a much noisier energy curve. We postulate here that the usefulness of the second frequency comes in its decreasing the possibility of multiple in-phase resonances from occurring as can happen with one frequency. Generally, second frequencies are used at much lower power and we conjecture that the second, lower, frequency may be able to reach to the center of the plasma more effectively than the fundamental frequency, as its resonance zone is smaller (if not non-existent). This will need to be tested experimentally.

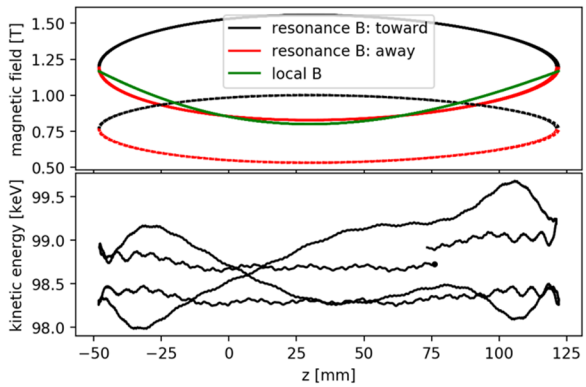

Figure 10: Resonant heating with two frequencies in VENUS (18 and 28 GHz). The resonance curve for the second, lower frequency is the lower oval-like shape in the upper plot. (see Fig. 3 for full description)

FUTURE STEPS

This analysis indicates that raising the minimum magnetic field in an ECRIS could leave the plasma more susceptible to kinetic instabilities as fast-heating modes become more easily accessible at lower energies. More statistics are needed for the simulations and if there are hopes of being accurate in our results we will need to have a better idea of injected microwaves' distribution, both in terms of position and magnitude. As we improve on these fronts, we will use this model to compare with other experimentally seen phenomena such as the seemingly periodic changes in source performance as axial magnetic fields are changed and the resonance zone's length and endpoints change which may indicate more effective heating modes.

REFERENCES

[1] L. Sun *et al.*, "Advancement of highly charged ion beam production by superconducting ECR ion source SECRAL," *Rev. Sci. Instrum.*, vol. 87, p. 02A707, 2016. doi:10.1063/1.4933123

[2] J. Y. Benitez *et al.*, "Recent progress on the superconducting ion source VENUS," *Rev. Sci. Instrum.*, vol. 83, p. 02A311, 2012. doi:10.1063/1.3662119

[3] O. Tarvainen *et al.*, "Limitation of the ECRIS performance by kinetic plasma instabilities," *Rev. Sci. Instrum.*, vol. 87, p. 02A703, 2016. doi:10.1063/1.4931716

[4] D. Leitner *et al.*, "Measurement of the high energy component of the x-ray spectra in the VENUS electron cyclotron resonance ion source," *Rev. Sci. Instrum.*, vol. 79, p. 033302, 2008. doi:10.1063/1.2821137

ISBN: 978-3-95450-226-4 ISSN: 2222-5692 doi:10.18429/JACoW-ECRIS2020-TUXZO03

ANGULAR DISTRIBUTION MEASUREMENT OF ATOMS EVAPORATED FROM A RESISTIVE OVEN APPLIED TO ION BEAM PRODUCTION

A. Leduc[1,2], T. Thuillier[1], L. Maunoury[2], and O. Bajeat[2]
[1]Univ. Grenoble Alpes, CNRS, Grenoble INP*, LPSC-IN2P3, 38000 Grenoble, France
* Institute of Engineering Univ. Grenoble Alpes
[2]GANIL, bd Henri Becquerel, BP 55027,F-14076 Caen, France

Abstract

A low temperature oven has been developed to produce calcium beam with Electron Cyclotron Resonance Ion Source (ECRIS). The atom flux from the oven has been studied experimentally as a function of the temperature and the angle of emission by means of a quartz microbalance. The absolute flux measurement permitted to derive Antoine's coefficient for the calcium sample used : $A = 8.98 \pm 0.07$ and $B = 7787 \pm 110$ in standard unit. The angular FWHM of the atom flux distribution is found to be 53.7 ± 7.3 °at 848K, temperature at which the gas behaviour is non collisional. The atom flux hysteresis observed experimentally in several laboratories is explained as follows: at first calcium heating, the evaporation comes from the sample only resulting in a small evaporation rate. once a full calcium layer has formed on the crucible refractory wall, the calcium evaporation surface includes the crucible's enhancing dramatically the evaporation rate for a given temperature. A Monte-Carlo code, developed to reproduce and investigate the oven behaviour as a function of temperature is presented. A discussion on the gas regime in the oven is proposed as a function of its temperature. A fair agreement between experiment and simulation is found.

INTRODUCTION

This work is dedicated to the study of a low temperature metallic oven dedicated to calcium beam production at the SPIRAL2 facility at GANIL, France [1, 2]. The motivation of the study is to better understand the physics and chemistry of such an oven with the ultimate goal to improve the global conversion efficiency of rare and expensive isotope atom (like ^{48}Ca) to an ion beam in Electron Cyclotron Resonance Ion Source (ECRIS). The long term goal being to build an end-to-end simulation able to optimize and predict the atom to ion conversion yield of oven to produce beams in ECRIS. Here, the differential atom flux from the oven is measured and compared to simulation. Indeed, the angle of atom emission is an important geometrical factor of the whole atom to ion conversion in an ECRIS. In a first part, the calcium oven used is presented in detail. In a second part, the experimental setup used to study the differential atom flux from the oven is described. Next, the Monte Carlo model used to simulate the oven behaviour is presented and the simulation results discussed. In the last section, simulation and experimental results are compared and discussed.

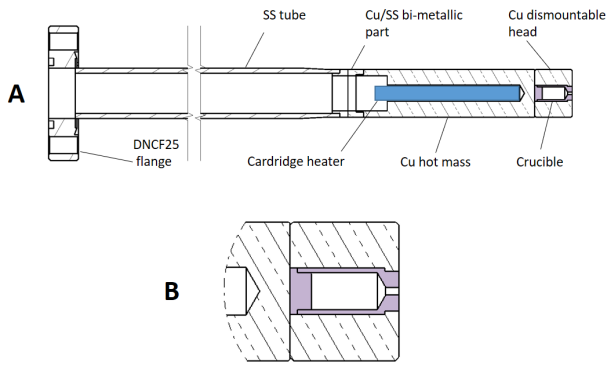

Figure 1: (A) Calcium oven cut away view . (B) Detailed view of the crucible in light purple.

CALCIUM OVEN

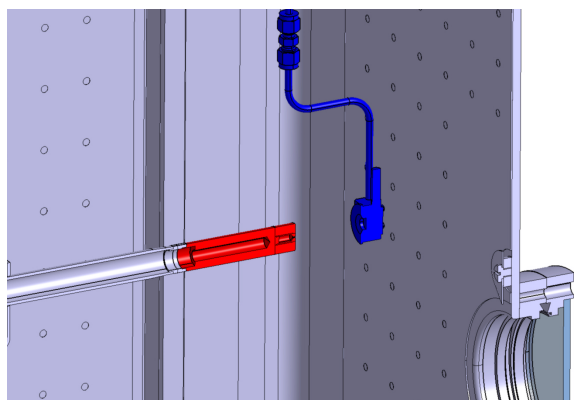

Figure 2: Cutaway view of the vacuum chamber, the rotatable quartz measurement system (blue) and the oven tested (red).

The oven design is derived from an existing technology developed at Lawrence Berkeley National Laboratory [3]. A cutaway view of the oven is presented on Fig.1 with information on its mechanical composition. The oven crucible is made of molybdenum to prevent chemical reaction with the metallic sample. The crucible cavity has a symmetry of revolution and is composed of two parts (see view B of Fig.1): (a) a 5mm diameter and 11 mm long cylindrical container ending on the last millimeter by a 30° cone (shape imposed by the drilling tool geometry), (b) an 1 mm diameter and 2 mm long extraction channel (also referenced later as a nozzle). The oven is heatable up to 875K when a Joule power of 200W is applied. A thermal simulation done with Ansys software has shown that the crucible temperature is

ISBN: 978-3-95450-226-4 ISSN: 2222-5692 doi:10.18429/JACoW-ECRIS2020-TUXZO03

very homogeneous with a maximum temperature gradient of the order of a few degrees Kelvin only. When the electric oven power supply is switched off, the maximum oven temperature at the full microwave power is 500 K, well below the operating range of calcium evaporation in the ECRIS (being 650 to 700 K). Therefore, the design is safe for any experimental operation since, whatever the ion source tuning is, the oven temperature is controlled by adding extra power to the oven cartridge resistor.

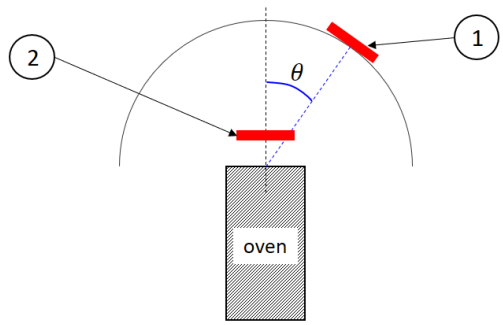

Figure 3: Sketch showing the positions of the quartz balance during the experiments. (1) The quartz describes a circle of radius 60 mm around the oven exit. The quartz and the oven axis form an angle with $-\pi/2 \leq \theta \leq \pi/2$. (2) The quartz is set 10 mm away from of the oven hole.

EXPERIMENTAL MEASUREMENTS

Setup

The oven metallic atom emission has been measured in a dedicated vacuum chamber (see Fig. 2) with a residual pressure $P_0 = 10^{-7}$ mbar. The oven temperature is monitored by the thermocouple included in the oven heater cartridge. The atom flux is measured with a quartz AUDA6 Neyco micro balance. The quartz is inserted into a mechanical support resulting in an active measurement disc diameter of 8.1 mm. The quartz temperature is fixed thanks to a water cooling system. The vertical support is mechanically connected to a rotatable vacuum flange by means of a tube bringing water cooling to the balance. the tube is bent to form two 90° bends so that during a rotation, the quartz describes a circle with a 60 mm radius. The crystal frequency of vibration is 3 MHz when a static electric field is applied. When evaporated metallic atoms are deposited on the quartz surface, its mass increases and thus changes its mechanical resonance frequency. The quartz frequency measurement is done with a dedicated Inficon controller which displays the instantaneous frequency and calculates the mass per cm^2 accumulated during a programmable integration time. During the experiments, the mass flux is calculated after an integration time from 60 to 180 s. In our experimental conditions, The mass limit accuracy of the system has been estimated to be $\approx 0.5 ng/cm^2/s$. The oven axis is horizontal and set perpendicular to the balance axis of rotation. The oven position can be translated along the direction of its axis of revolution. The two experimental configurations reported are displayed on Fig.3. In the configuration (1), the oven exit is placed on the balance axis of rotation. During the quartz rotation, the distance between the oven and the quartz is constant and equals to 60 mm. The angle between the quartz surface and the oven surface is noted θ. In the configuration (2), the quartz is set 10 mm away from the oven exit. The solid angle covered by the quartz is then ≈0.459 sr, with a maximum angle of detection $\theta_1 = 22,0°$.

Table 1: Mass Flow and FWHM Measurements from Protoc ol(2) (see Fig.3)

element	T (K)	$\dot{M}(ng/s)$	FWHM (deg.)
Ca	848	148.9±67	53.7 ±7.3
Ca	873	352.1±67	55.5 ±7.2
Ca	898	649.3±67	62.3 ±4.2

Measurements

The oven run presented used a calcium 40 sample weighting 0.0909 g with a surface $s_{Ca} = 0.8 \pm 0.2\, cm^2$. The overall crucible internal surface is $s_c = 2.8\ cm^2$. The differential metallic mass flow

$$f(\theta) = \frac{1}{r^2}\frac{d\dot{m}}{d\omega} \tag{1}$$

emitted by the oven was measured as a function of θ at T=848, 873 and 898 K (see protocol (1) in Fig.3). Here r is the radial distance between the oven and the balance and $d\omega$ stands for the differential solid angle taken at θ. Results are displayed in fig.4. The errorbar on θ is due to the extended surface of detection ($\sigma_\theta = 0.9°$), the error on angle measurement ($\sigma_\theta \approx 2°$) and the error on alignment ($\sigma_\theta \approx 1.°$), leading to a global error $\sigma_\theta \approx 2.4°$. The mass flux measurement precision is limited by the resolution of the balance for the chosen time of integration of 180 s. The mass flux error is thus estimated to be $\sigma_{\dot{m}} \approx 0.5 ng/cm^2/s$. The full width half maximum (FWHM) of the distributions are reported in Table 5, along with the reconstructed total mass flux $\dot{M}$ integrated over 2π sr (and opportunely averaged on the overabundant range of measurement from $-\pi/2$ to $\pi/2$) :

$$\dot{M} = 2\pi r^2 \left(\frac{1}{2}\int_0^{\pi/2} f(\theta) sin\theta d\theta + \frac{1}{2}\int_0^{-\pi/2} f(\theta) sin\theta d\theta \right) \tag{2}$$

The angular FWHM values are consistent for all data (FWHM 53-63°). Further analysis of the angular mass flow distribution is proposed later in the text helped with a Monte Carlo code. Next, the calcium evaporation rate was measured as a function of the oven temperature in the experimental condition (2) (see Fig.3). The total calcium flux is reconstructed as a function of the temperature using the experimental measurement of $f(\theta)$, by applying the following

ISBN: 978-3-95450-226-4 ISSN: 2222-5692 doi:10.18429/JACoW-ECRIS2020-TUXZO03

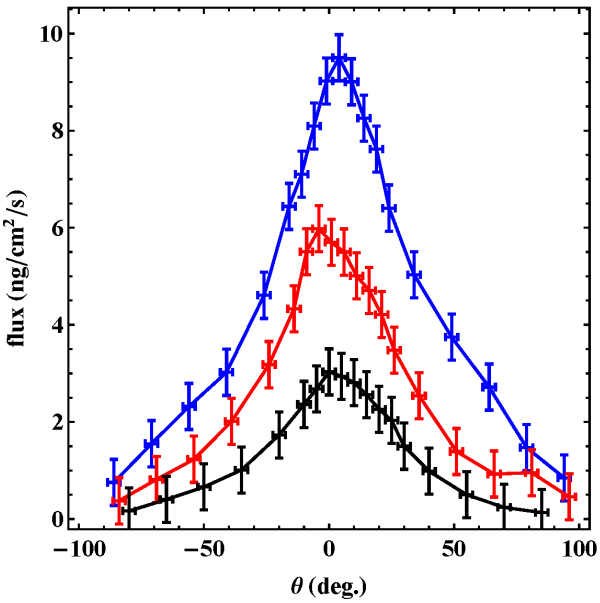

Figure 4: Experimental flux emitted from the oven as a function of the angle θ for calcium. The black, red and blue plots are respectively measured at the temperatures 850, 875, 900°K.

correcting factor:

$$\frac{\int_0^{\theta_1} f(\theta) sin\theta d\theta}{\int_0^{\pi/2} f(\theta) sin\theta d\theta} = 5.565 \tag{3}$$

where f is taken for T=898K, when the precision of experiment (1) is the highest. The experimental data is plotted with blue errorbars on fig. 5. The other solid color plots on fig. 5 are discussed later in the text.

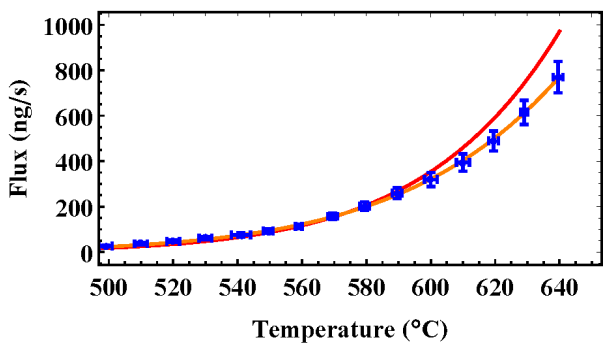

Figure 5: Total calcium flux from the oven as a function of the temperature. Blue symbols: experimental data. Red: theoretical data with $S = s + s_c$ and Ca data from [4]. Orange: least mean square fit of experimental data using $S = s + s_c$ and Antoine's law (see. Eq. 4) coefficients A and B as fit parameters

Table 2: Calcium Antoine's Equation Coefficient Accordi ngto [4] and Calculated in this Study, Expressed in Stan dardunits.

	A	B	C
Ca from [4]	10.34	8.94×10^3	0
Ca this work	8.98 ± 0.07	$7.79 \pm 0.11 \times 10^3$	0

OVEN THERMODYNAMICS AND ANALYSIS

The aperture hole surface of the crucible ($0.78\,mm^2$) is small compared to its internal total surface ($s_c = 2.2cm^2$). See fig.3, view B to visualise the difference. The cavity is thus sufficiently closed to consider it as a Knudsen cell [5, 6]. Consequently, when the metal sample is heated, the local pressure in the crucible raises rapidly to reach the saturating vapor pressure, well above the residual pressure of the vacuum chamber ($P_0 = 10^{-5}$ Pa). The calcium saturation vapor pressures P(Pa) follow the Antoine's law as a function of the temperature :

$$log_{10}P = A - \frac{B}{C+T} \tag{4}$$

where $T(K)$ is the metal temperature and A, B, C are thermodynamics parameters, unique for each chemical element. The evaporated mass rate $\dot{M}$ emitted from the solid metal in the crucible can be expressed using the Hertz-Knudsen equation [7, 8] :

$$\dot{M} = P\sqrt{\frac{m}{2\pi kT}}S \tag{5}$$

where m is the atom mass, P is the metal saturating vapor pressure and S is the surface of evaporation. Another important oven parameter is the sticking time of atoms on the hot crucible surfaces defined by the Frenkel equation [9]:

$$\tau = \tau_0 e^{\frac{H}{kT}} \tag{6}$$

where $\tau_0 \approx 10^{-13}s$ is the atom vibration period on the surface [10], H is the enthalpy of the adsorbed atom, k the Boltzmann constant and T the surface temperature. For the calcium case, two sticking times must be considered. the first is τ_{Ca-Ca}, the sticking time of calcium atom on the metallic Ca surface sample. the other is τ_{Ca-Mo}, the sticking time of Ca on Mo. The adsorbed Ca enthalpy on Ca is well documented : $H_{Ca} = 1.6eV$, giving a sticking time of $1 - 1000ms$ for T $600 - 900K$. On the other hand, the adsorbed Ca on Mo enthalpy value H_{Ca-Mo} was not found in the literature. Nevertheless, H_{Ca-Mo} is expected to be much higher than H_{Ca}. A rough estimate of H_{Ca-Mo} value can be considered from $H_{Sc-Mo} = 5.5eV$ available in [11]. In the present experimental conditions, $\tau_{Ca-Ca} \ll \tau_{Ca-Mo}$ on all the temperature range covered. Hence, when the calcium evaporation starts, a layer of calcium should first be formed

ISBN: 978-3-95450-226-4 ISSN: 2222-5692 doi:10.18429/JACoW-ECRIS2020-TUXZO03

on the Mo crucible wall and stay stuck on Mo. Once the layer is complete, next Ca adsorption on the surface is done on Ca, which strongly reduces the sticking time and transforms the crucible surface to a fresh extra source of calcium. Two experimental confirmations of this phenomenon have been observed: (i) at first start, the calcium flux is very small for a given temperature and, after a sufficiently long time of operation (of the order of an hour), the flux amplifies to reach a much higher stable value. (ii) Immediately after venting the oven used and inspecting its crucible, the presence of a Ca layer is visible on the crucible surface which very rapidly get oxidised to form a white CaO powder. This hypothesis is further investigated helped with the experimental data from experiment (1) (see Fig.3). The theoretical mass flow expected from Eq.4 and Eq.5 using Ca data from [4] is calculated for the temperatures 848, 873 and 898 K, considering the two evaporating surfaces $S = s$ and $S = s_c + s$ and reported in Tab. 3 along with the experimental mass flow from Tab. 1. Clearly, one can see that the sole metal sample evaporating surface (column with $S = s$) is insufficient to reproduce the total mass rate from the oven. But when the crucible surface is added (column with $S = s_c + s$), the matching between theory and experiment becomes very close. The measurement confirms the hypothesis of the transient formation of a Ca layer on the crucible surface which, once completed enhances the evaporation proportionally to the crucible surface.

Table 3: Theoretical Integrated Mass Flow from the Oven in(ng/s) Derived from Eq.4 and 5, Compared with the Experimental Flux for T=848, 873 and 898 K

T (°K)	P (Pa)	$\dot{M}(s)$ ng/s	$\dot{M}(s+s_c)$ ng/s	$\dot{M}$ Exp. ng/s
848	0.627	47.7	179	148.9 ± 67
873	1.26	94.5	354	352.1 ± 67
898	2.42	179	671	649.3 ± 67

Result of experiment in condition (2) (see Fig.3) is next compared with the prediction of eq.5 in the fig.5. The sensitivity to temperature comes here through the pressure and the Antoine's eq.4. The experimental data is the blue errorbar, the mass flow prediction according to the eq.4 using the known tabulated coefficients for calcium, (see Tab.2), is plotted in solid red line. One can see a fairly good fit with experimental data up to 600°C (873K). Above this value, experimental flux is lower than the semi-empirical prediction. Because the total flux has been reconstructed with a sufficiently high precision, alternative Antoine's coefficients are proposed for calcium to fit the data resulting in the orange solid line. The fit value found for the whole temperature range are $A = 8.978 \pm 0.07$, $B = 7787.5 \pm 110$ and $C = 0$ in standard units.

MONTE CARLO SIMULATION

The atom angular distribution from the oven has been investigated by means of a Monte Carlo simulation and compared with the experimental data. The exact 3 dimensions crucible geometry is considered. The oven temperature T is a free parameter and is assumed to be uniform over all the crucible. The metallic sample geometry is not modelled and the initial atom emission position is done randomly along a line following the bottom part of the crucible part (a). The atom emission from the wall follows the Lambert's cosine law:

$$P(\theta) = cos\theta \tag{7}$$

where $P(\theta)$ is the probability of emission at an angle θ with respect to the local normal to the wall. A special care must be taken to inverse this probability distribution function appropriately to use it safely in the Monte-Carlo code [12]. Because the atom emission from the wall is done in a cavity with convex walls, a test is added in the code to check if a fresh reemission occurs toward the cavity and not to the wall. The atom velocity is taken as the mean thermal velocity:

$$v = \sqrt{\frac{3kT}{m}} \tag{8}$$

where m is the considered atom mass. No accomodation from the wall is considered as particles are assumed to be isothermal. Each new adsorption at the wall is counted and re-emission is immediate using the cosine law. The pressure in the part (a) of the crucible is considered constant at the saturating vapor pressure P of eq.4. The pressure in the extraction channel (b) is assumed to decrease linearly from P down to the vacuum chamber pressure $P_0 = 10^{-5}$ Pa. The atom collisions are modelled in the crucible using the atom mean free path λ:

$$\lambda = \frac{kT}{\sqrt{2}\pi l^2 P} \tag{9}$$

where l is the atom diameter ($l \approx 360pm$ for calcium). At each time step, the local pressure is considered and a random number is generated to check whether the atom collides or not. In case of collision, a new atom velocity direction is randomly generated on a uniform sphere. The metallic gas regime in the oven can be assessed with the Knudsen number:

$$K = \frac{\lambda}{d} \tag{10}$$

where d is a characteristic length of the system studied. When $K > 0.5$, the gas is collisionless and atoms exiting the oven are directly those emitted from the walls. An intermediate regime occurs when $0.01 < K < 0.5$ where the volume collisions start to play a role and finally, when $K < 0.01$, the gas becomes fully collisional and the effect from the wall is secondary. In our case, the crucible has 2 characteristic lengths and hence two Knudsen numbers: $K_i = \frac{\lambda}{d_1}$ with d_1=5 mm for the main cylinder and $K_{ii} = \frac{\lambda}{d_2}$ with d_2=1 mm for the crucible exiting channel. In this latter case, we considered the mean pressure in the exit channel $\frac{1}{2}(P + P_0)$

ISBN: 978-3-95450-226-4 ISSN: 2222-5692 doi:10.18429/JACoW-ECRIS2020-TUXZO03

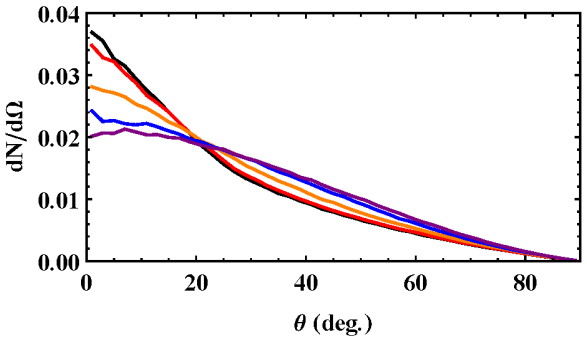

Figure 6: Normalized differential distribution of atoms at the exit of the oven per unit of solid angle as a function of θ for different temperatures: 600K (black), 900K (red), 1000K (orange), 1100K (blue), 1200K (purple).

to calculate λ. The evolutions of λ, K_i and K_{ii} are proposed as a function of T and P in the table 4. For the measurements performed on calcium up to 900K, one can deduce that the calcium gas behaviour is mainly non-collisional. Nevertheless, for T=900K, $K_i = 0.63$ is at the threshold and collision effect, thought not dominant should start to play a role. At 1000K, the calcium gas is collisional in the bulk area (a) while it remains above the transition in the exiting channel. a fully developed collision regime is reached at 1100K with $K_{ii} = 0.12$. The differential angular distribution of exiting atom per unit of solid angle is displayed in Fig.6 as a function of the temperature. The number of particles generated to produce the curves is 1 million. One can clearly see the transition from the non collisional regime at 600K (see black curve) to the intermediate regime at 1000K where the bulk crucible is collisional while the exit channel is not (see orange curve) and finally above 1100K where the whole oven volume is collisional and the extraction emittance is finally defined by the sole exiting channel geometry (see blue and purple curves).

Table 4: Evolution of the Atom Mean Free Path λ and the two Knudsen number K_i K_i fo th Calciu Oven as a Function of the Temperature T and the Saturating Vapor Pressure P

T (K)	P (Pa)	λ (m)	K_i	K_{ii}
600	2.75×10^{-5}	194.4	38895	285348
700	3.70×10^{-3}	1.68	337	3365
800	0.146	0.0488	9.76	97
850	0.66	0.011	2.2846	22.8
900	2.55	0.0031	0.63	6.3
1000	25.19	3.55×10^{-4}	0.071	0.71
1100	163.2	6.01×10^{-5}	0.012	0.12

Figure 7 shows the evolution of the mean numbers of bounce and collision versus the temperature. The temperature at which the volume collision becomes dominant is

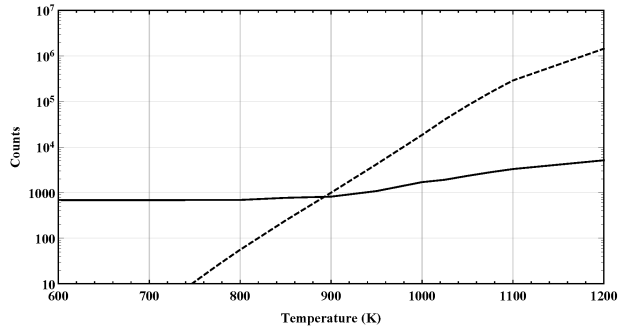

Figure 7: (Black) Mean number of atom adsoption on the crucible wall before atom extraction. (Dashed Black) Number of volume collision in the oven before extraction.

900K. It is worth noting that the mean number of bounce increases much more slowly with temperature than the number of volume collision.

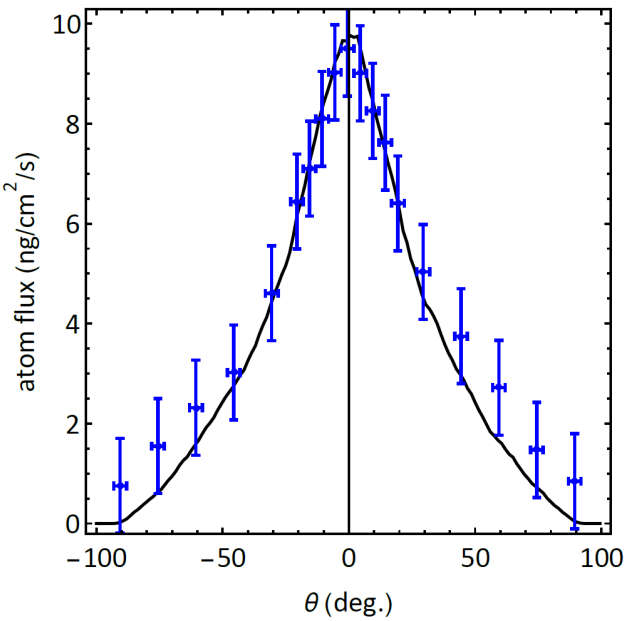

Figure 8: Comparison between the experimental differential mass flux measured in the micro-scale and the Monte-Carlo simulation at T=898K.

Table 5: Comparison between FWHM (in degree) of Angular Differential Mass Flux Measurements and Simulation for Calcium

T (K)	exp. (°)	simulation (°)
848	53.7 ±7	48.6±0.6
873	55.5 ±7	51.4±0.6
898	62.3 ±7	54.45±0.6

ISBN: 978-3-95450-226-4 ISSN: 2222-5692 doi:10.18429/JACoW-ECRIS2020-TUXZO03

COMPARISON OF SIMULATION AND EXPERIMENT

The oven Monte Carlo code is used to simulate the theoretical atom flux expected on the micro scale as a function of the angle θ (see fig.3). An example of the comparison between simulation and measurement is proposed on Fig.8. The simulation reproduces well the general shape of the differential flux as a function of the angle θ. A discrepancy is nevertheless visible for angle larger than 45° where the measurements are higher than the simulation. the difference is nevertheless included in the error bar. The differential flux FWHM is calculated for the simulation and compared with the experimental measurements. The results of the simulation are consistent with the measurements. the experimental FWHM is always higher than the simulation. This systematic difference is likely due to a non simulated physical effect. One could suggest for instance that the actual oven extraction geometry is not exactly as simulated, or that the atom flux continues to collide at the exit of the oven on the first mm. As a conclusion, The Monte Carlo code developed provides satisfactory results compard to experimental measurements and will next be used to study the metallic atom capture in ECR ion source plasma.

REFERENCES

[1] C. Barué, C. Canet, M. Dupuis, J. L. Flambard, R. Frigot, P. Jardin, T. Lamy, F. Lemagnen, L. Maunoury, B. Osmond, C. Peaucelle, P. Sole, and T. Thuillier, "Metallic beam developments for the SPIRAL 2 project", Rev. Scient. Instrum. 85, 02A946 (2014). doi: 10.1063/1.4847236

[2] T. Thuillier, J. Angot, C. Barué, P. Bertrand, J. L. Biarrotte, C. Canet, J.-F. Denis, R. Ferdinand, J.-L.Flambard, J. Jacob, P. Jardin, T. Lamy, F. Lemagnen, L. Maunoury, B. Osmond, C. Peaucelle, A. Roger, P.Sole, R. Touzery, O. Tuske, and D. Uriot, "Status of the SPIRAL2 injector commissioning", Rev. of Scient. Instrum. 87, 02A733 (2016); doi: 10.1063/1.4935227

[3] J. Y. Benitez, K. Y. Franzen, A. Hodgkinson, C. M. Lyneis, M. Strohmeier, T. Thuillier, D. Todd, and D. Xie, "Production of high intensity ^{48}Ca for the 88-Inch Cyclotron and other updates", Rev. Sci. Instrum. 85, 02A961 (2014); https://doi.org/10.1063/1.4854896

[4] S. DUSHMAN and J/M. LAFFERTY – Scientific foundations of vacuum technique. 806 p., 2nd ed. New York, Wiley and Sons (1962).

[5] M. Knudsen, "Die Molekularströmung der Gase durch Offnungen und die Effusion", Ann. Phys. (Leipzig), 29, 179 (1909).

[6] M. Knudsen, Ann. Phys. Leipzig, "Die Gesetze der Molekularströmung und der inneren Reibungsströmung der Gase durch Röhren", 28,75 (1909).

[7] Heinrich Hertz, « Ueber den Druck des gesättigten Quecksilberdämpfes », Annalen der Physik und Chemie, vol. 17, 1882

[8] (de) Martin Knudsen, « Experimentelle Bestimmung des Druckes gesättigter Quecksilberdämpfe bei O° und Höheren Temperaturen », Annalen der Physik, vol. 29, 190.

[9] Frenkel,J., "The Theory of Adsorption and Related Phenomena," Z. Physik 26, 117 (1924).

[10] V. Glebovsky, "Recrystallization in Materials Processing", Intech, ISBN 9789535121961. http://dx.doi.org/10.5772/58713

[11] B. EICHLER and H. ROSSBACH, "Adsorption of Volatile Metals on Metal Surfaces and its Application in Nuclear Chemistry, Calculation of Adsorption Enthalpies for Hypothetical Superheavy Elements with Z around 11", Radiochimica Acta, Vol. 33: Iss. 2-3 (1983). https://doi.org/10.1524/ract.1983.33.23.121

[12] J. Greenwood, "The correct and incorrect generation of a cosine distribution ofscattered particles for Monte-Carlo modelling of vacuumsystems", Vacuum 67 (2002) 217–222. https://doi.org/10.1016/S0042-207X(02)00173-2.

ISBN: 978-3-95450-226-4 ISSN: 2222-5692 doi:10.18429/JACoW-ECRIS2020-TUYZO01

ADVANCEMENTS IN SELF-CONSISTENT MODELING OF TIME- AND SPACE-DEPENDENT PHENOMENA IN ECRIS PLASMA

A. Pidatella*, D. Mascali, B. Mishra, E. Naselli [1], G. Torrisi, INFN-LNS, Catania, Italy
A. Galatà, INFN-LNL, Legnaro, Italy
[1]also at Department of Physics and Astronomy, University of Catania, Italy

Abstract

The resonant interaction of electrons with the microwave radiation in Electron Cyclotron Resonance Ion Sources (ECRIS) plasma leads to a strongly anisotropic electron energy distribution function (EEDF), given as a convolution of two to three electron populations, with the anisotropy that might trigger kinetic instabilities. At the INFN, further efforts have been paid to improve and update the self-consistent 3D numerical codes for plasma electrons kinetics. Progresses have opened several perspectives. It is now possible to derive a space-resolved EEDF, providing local information on the electron properties in the plasma. Also, the code has been updated to provide reaction rates of electromagnetic emissions, including X-ray fluorescence. Estimate of local ion charge state distribution is potentially possible, and first evaluations are ongoing. Dealing with fast-transient mechanisms, such as electromagnetic emission via the electron-cyclotron MASER instability, the code is now updated for locally evaluating EEDF anisotropy. We will present the collected results, which we believe to have a relevant impact both on the ECRIS plasma physics and on the INFN's PANDORA project that plans to use ECR plasmas for fundamental studies in Nuclear and AstroNuclear Physics.

INTRODUCTION AND MOTIVATION

Electron cyclotron resonance ion sources (ECRIS) are able to produce intense and stable beams of highly charged ions, required by accelerators for nuclear and applied physics. Progress and improvements in understanding ECRIS have been made in the past years. However, they mostly consisted in increasing the power of the RF heating-wave, as well as the intensity of magnetic fields, accordingly to the "scaling laws" [1], with constraint represented by present technological limits. In view of this, a deeper knowledge of plasma confinement dynamics and parameters - electron density, temperature, and ion charge state distribution (CSD) - is highly desirable, since the properties of the extracted ion beam (in terms of intensity, average charge state and quality) strictly depend on plasma structure and properties.

ECRIS with a minimum-B magnetic field structure are conventionally employed as source of multicharged ion beams. This magnetic structure consists in a superposition of solenoid and sextupole fields, which topology leads to closed ECR surface, where wave-to-particle resonant coupling and energy transfer take place, and a sufficient plasma confinement for a step-wise ionization to high charge states is realized. However, the resulting electron energy distribution is strongly anisotropic, made at least of two to three main populations: cold (1-100 eV), warm (0.1-10 keV), and hot (10 keV - 1 MeV) electrons. Because of such anisotropic distribution, the system becomes prone to kinetic instabilities, limiting ECRIS performances. These phenomena are mainly driven by warm and hot electrons whose transverse velocity $v_\perp$ (with respect to the magnetic field) dominates over the longitudinal one $v_\parallel$ [2]. These kinetics instabilities can also leave electromagnetic signatures, consisting in powerful bursts of microwave and x-ray radiation, due to a resonant enhancement of plasma waves as an effect of non-linear interactions with hot electrons. This phenomenon is known as electron cyclotron MASER instability [3–5]. Even though many studies have been conducted, the exact mechanism of turbulent regimes of plasmas is still unknown and a deeper investigation is necessary.

The present work shows some preliminary advancements in numerical modeling and studying the aforementioned plasmas, providing space-resolved information both on typical electron energy distribution functions (EEDFs) and on a space-resolved velocity distribution of electron in unstable plasma. These numerical tools will possibly allow exploring space-dependent mechanisms, and to have a better predicting power for both space- and time-dependent phenomena in ECRIS plasma.

3D MODELING OF ECRIS PLASMA

In the case of ECR plasmas, a self-consistent approach is desirable to solve the collisional Vlasov-Boltzmann equations [6]. In this context, the INFN-LNS jointly with the INFN-LNL group, have developed an iterative routine to produce a self-consistent description of ECR *stationary* plasmas. The overall code results from a strict interplay between a kinetic code, or 'particle mover', developed in MATLAB©, and a FEM electromagnetic solver (we used COMSOL - Multiphysics©), for evaluating the electromagnetic (EM) fields once given local charge densities. A self-consistent approach is necessary since the propagating EM field affects electron motion and energy via a resonant interaction. On the other hand, the plasma - being an anisotropic and dispersive medium - presents a 3D dielectric tensor which must be in turn considered in the calculation of the EM field [7]. The 'particle mover' code solves the equations of motion of a given number of particles followed for their entire life (i.e. until they impinge on the chamber walls, meaning they have been de-confined). In this sense, our approach can be

* pidatella@lns.infn.it

ISBN: 978-3-95450-226-4 ISSN: 2222-5692 doi:10.18429/JACoW-ECRIS2020-TUYZO01

defined as a 'stationary' particle-in-cell code, describing the stationary structure of the plasma in the phase space: the local charges densities are evaluated through the 'trick' of density accumulation in a 3D grid. Particles trajectories evolve in parallel (simultaneously) and the local density accumulation is made as single particles move throughout the single cells in the volume contained inside the plasma chamber. During each i-th step of kinetic simulation, the EM field is taken as stationary and coming from the $(i-1)$-th step. The self-consistent loop is run until convergence is achieved between the $(i-1)$-th and i-th step, looking at both 3D density and EM field maps. Further details on the numerical machinery can be found in Ref. [6].

The established numerical code has many times proven its robustness and validity, for instance investigating the so-called frequency tuning effect [8], and reproducing experimental results for light- and heavy-ion dynamics in ECR-based charge breeding devices [9, 10].

SPACE-RESOLVED ELECTRON ANISOTROPY IN THE VELOCITY SPACE

In order to explore the degree of anisotropy of electrons inside a minimum-B trapped ECR-based plasma, we made use of the numerical code described above, to simulate an argon plasma, sustained by microwaves at 12.84 GHz, and 400 W of power. The plasma confinement is supported by a specific magnetostatic minimum-B field profile, having at this frequency a ratio of $B_{min}/B_{ECR} = 0.87$. Only electrons (100 000 particles) have been followed in the numerical simulations, and 3D density and energy density maps were produced. After a simulation time of 250 μs, and one self-consistent simulation loop, the electrons still present in the chamber are around 15 000. Figure 1 shows the distribution

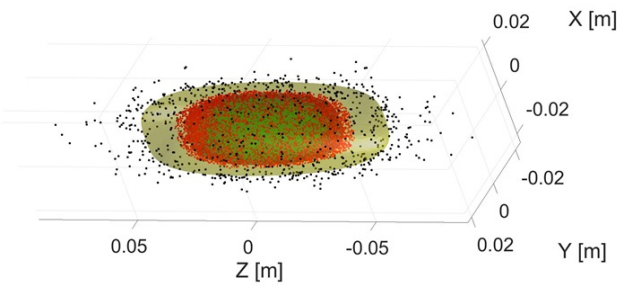

Figure 1: Distribution of electrons in chamber, close to isomagnetic isosurfaces at: $B < 0.96\,B_{ECR}$ (green dots), $B > 1.2\,B_{ECR}$ (black dots - yellow isosurface), and $0.96\,B_{ECR} < B < 1.04\,B_{ECR}$ (red dots - red isosurface).

of bunch of these particles located around three nested and closed isomagnetic surfaces: among the three, the densest one refers to the volume around the isosurface at $B = B_{ECR}$ (red). Here, it is expected the best wave-to-particle coupling and resonant electron's heating. At higher (lower) B-field isosurfaces, particles distribute in the so-called rarefied halo (denser plasmoid) volume. For each spatial region, the transverse $v_\perp$, and longitudinal $v_\parallel$, component of particles' velocity with respect to the magnetic field, has been calculated. Each particle then can be located in the velocity space by a set of coordinates $(v_\parallel, v_\perp)$.

Figure 2 (top-panels) shows a contour plot of the local distribution of particles in the velocity space ($v_\perp$ vs. $v_\parallel$) in the three selected regions. The color refers to the amount of particles with a given $(v_\parallel, v_\perp)$. Figure 2 (bottom-panels) shows the same information, but plotted in terms of $\frac{v_\perp}{|v|}$ and $\frac{v_\parallel}{|v|}$ space, with $|v| = \sqrt{v_\perp^2 + v_\parallel^2}$. The figures provide a set of relevant information: first, there is a different spread of velocity anisotropy in the velocity space which has an evident spatial dependency, and shows a tendency of particles distributing at $v_\perp > v_\parallel$. Second, particles close to the plasmoid show a trend towards a mean isotropic distribution, whereas particles close especially to the ECR surface show a general anisotropic behavior. The halo region has only some particular spot away from the isotropic line. Finally, a *quantitative* idea of the most anisotropic velocity distribution can be appreciated from Figs. 2(d-f), where the ratio $v_\perp/v_\parallel$ in the plasmoid (d) does not go beyond $2 \div 4$. Conversely, the same ratio in the ECR region (f) reaches values even larger than 10. The results promisingly fulfill the experimental/theoretical expectations concerning highly anisotropic electrons, usually located at the ECR surface. On the other side, less anisotropic electrons which are expected lying inside the inner regions of the plasmoid, are evidenced as well by the numerical simulations. Moreover, the simulation parameters (RF Power $P = 400$ W, and $B_{min}/B_{ECR} = 0.87$), characterize a plasma which in the literature is usually referred to as *unstable*, and to be prone to kinetic instabilities [11]. These kind of plasma features are mostly related to strongly anisotropic electrons with a ratio of $v_\perp/v_\parallel \gg 1$ [12], and this aspect has been highlighted by all the spatial regions explored, where generally $v_\perp \geq v_\parallel$.

SPACE-DEPENDENT ELECTRON ENERGY DISTRIBUTION FUNCTION FOR ECR-BASED PLASMA

A study of ECR-based plasma's EEDF has been based on the need to make progress in the space-dependent plasma electron properties characterization, on which several mechanisms and phenomena interesting for ECRIS devices and ECRIS-based technologies depend. It is of fundamental importance to obtain a space-resolved information on the electron energy distribution especially because of the already mentioned ECR plasma features, i.e., high inhomogeneity and strong anisotropy.

Here we present a step-by-step determination of suitable analytic EEDFs that can effectively describe space-dependent properties of minimum-B ECRIS plasma electron populations. The study is based on two main steps. First, we have simulated the same argon ECRIS plasma with same magnetostatic structure, with pumping microwave field frequency at 12.84 GHz, and 30 W of power. The numerical

ISBN: 978-3-95450-226-4 ISSN: 2222-5692 doi:10.18429/JACoW-ECRIS2020-TUYZO01

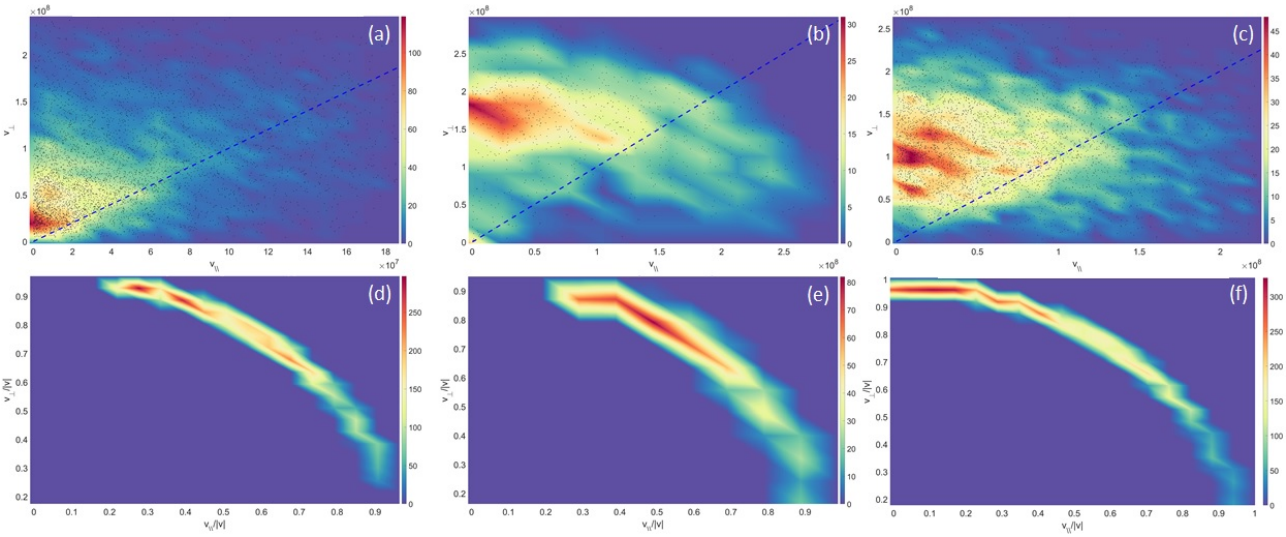

Figure 2: (**Top-panels**) Local distribution of particles in the velocity space ($v_{\parallel}$,$v_{\perp}$) for both particles at the (a) plasmoid, (b) halo, and (c) ECR isomagnetic surfaces. The isotropic line ($v_{\parallel} = v_{\perp}$) is shown (dashed line). (**Bottom-panels**) Same as in the top panels: (d) plasmoid, (e) halo, and (f) ECR region, but in terms of ($\frac{v_{\perp}}{|v|}$, $\frac{v_{\parallel}}{|v|}$).

simulations were settled up to provide 3D density, ρ_i, and energy density, E_i, maps, sliced into seven electron energy intervals, i.e., [0-2] keV, [2-4] keV, ..., [12-∞] keV. Second, based on this first slicing, an average electron energy-based $\langle E\rangle = \sum_{i=1}^{7} \rho_i E_i / \sum_{i=1}^{7} \rho_i$ selection of region of interest (ROI) in the simulation domain has been performed. This consists in grouping cells of the simulation domain whose $\langle E\rangle$ content belongs to the same defined range. Figure 3 shows some isosurfaces of few of these ROIs inside the plasma chamber, where higher $\langle E\rangle$-based ROIs distribute deeper inside the plasmoid region, in a shell-structure shape. Therefore, we have evaluated ROI-averaged electron density

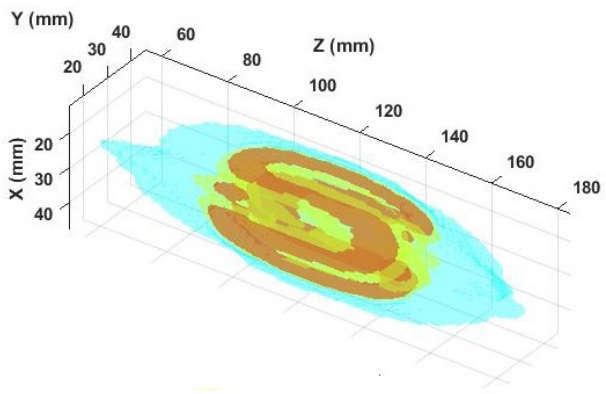

Figure 3: Structure and position in the space of $\langle E\rangle$-based ROIs: $\langle E\rangle \in [0-0.1]$ keV (ROI1, cyan), $\langle E\rangle \in [0.2-0.3]$ keV (ROI3, yellow), $\langle E\rangle \in [0.3-0.4]$ keV (ROI4, red).

and energy density for all the seven energy intervals, with the idea to generate collective data for each ROI, starting from the energy density and density maps produced by the numerical simulation. Next, we have compared the calculated data for each ROI to estimated density and energy density by using 2- and 3-components EEDFs. The nature of plasma properties has suggested a peculiar non-Maxwellian energy distribution, as well as electrons which distribute in two to three populations depending on their energy content. The EEDFs considered in our survey have been constructed as an adequate combination of low- and mid-energy Maxwellian function f_M

$$f_M(E;k_BT_e) = \frac{2}{\sqrt{\pi}} \frac{\sqrt{E}}{(\sqrt{k_BT_e})^3} e^{-\frac{E}{k_BT_e}}, \qquad (1)$$

where T_e is the electron temperature, and k_B is the Boltzmann constant, and functions capturing the high-energy population. The high-energy tails have been described both using Maxwellian or a Druyvesteyn function f_D

$$f_D(E;k_BT_e) = 1.04 \frac{2}{\sqrt{\pi}} \frac{\sqrt{E}}{(\sqrt{k_BT_e})^3} e^{-0.55\frac{E^2}{(k_BT_e)^2}}. \qquad (2)$$

This latter has been considered in the literature as a more accurate function describing high-energy electrons which for some reasons do not thermalize. With this in mind, we have performed this *qualitative* comparison, where estimates of density $(\rho_{ij})_{est}$, and energy density $(E_{ij})_{est}$ are obtained through the several test EEDFs, according to Eqs. (3)

$$(\rho_{ij})_{est} = (\sum_{i=1}^{7} \rho_{ij}) \int_{E_{min}}^{E_{max}} f(E;(k_BT_l)_j;\ldots;(k_BT_h)_j)\mathrm{d}E$$
$$(E_{ij})_{est} = \frac{\int_{E_{min}}^{E_{max}} f(E;(k_BT_l)_j;\ldots;(k_BT_h)_j)E\mathrm{d}E}{\int_{E_{min}}^{E_{max}} f(E;(k_BT_l)_j;\ldots;(k_BT_h)_j)\mathrm{d}E}, \qquad (3)$$

ISBN: 978-3-95450-226-4 ISSN: 2222-5692 doi:10.18429/JACoW-ECRIS2020-TUYZO01

where i and j are the energy intervals and ROI indices, respectively. Also a *quantitative* analysis has been performed cell-by-cell about the goodness of fit parameters, and then of the EEDF, in each of the ROIs, by computing the *mean squared error* (MSE) and the correlation r^2-score coefficient for each EEDF. The function minimizing the MSE value, and maximizing r^2, in all the ROIs has been considered as the most suitable in describing this kind of plasma. Figure 4 shows results for the MSE and r^2 for the EEDFs consid-ered. The best fitting function in all the ROIs is EEDF2, i.e., that one composed by a low-energy Maxwellian and a high-energy Druyvesteyn function. Figure 4 also shows that simulated data are appreciably well approximated by the EEDF2, numerically validating the local information on the electron energy distribution.

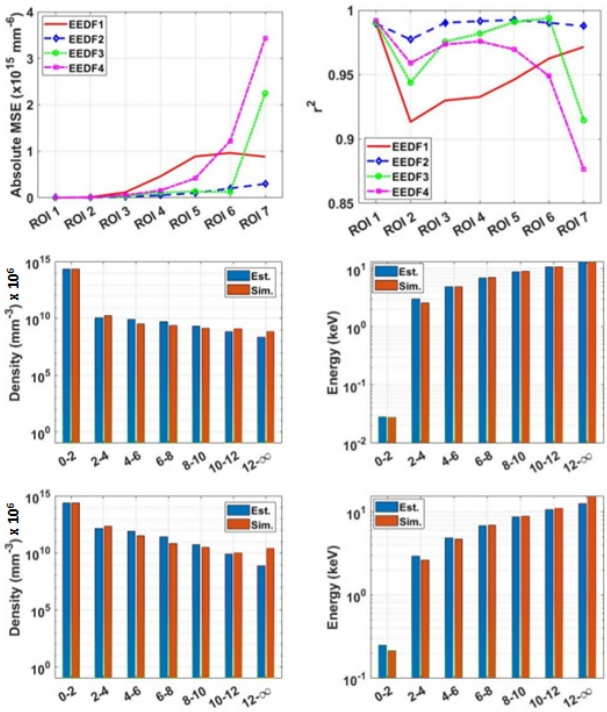

Figure 4: (**Top**). MSE (left) and r^2 (right) score for 4 different EEDFs used to fit data in each of the ROIs. (**Mid**). ROI1 density (left) and energy density (right) simulated data contrasted to the EEDF2 estimated counterparts, according to Eqs. (3). (**Bottom**). ROI3 density (left) and energy density (right) simulated data contrasted to the EEDF2 estimated counterparts.

VALIDATION OF THE CONTINUOUS EEDF

In order to validate the analytic EEDF obtained, we have used it for numerical estimates to be compared with experimental observations and theoretical predictions. One first test bench was provided by the intention to provide a theoretical support to a space-resolved X-ray spectroscopy experiment using quasi-optical methods looking to the fluorescence X-ray emission from K-shells of Ar plasma, conducted jointly by the ATOMKI, Debrecen and the INFN-LNS teams, as a plasma diagnostics tool [13]. The EEDF and simulated density for each individual plasma cell were used to calculate a 3D space-resolved Kα emission rate map. By simulating also the geometrical efficiency of the detector, and other quantities of interest like the quantum efficiency of the CCD camera, as well as the plasma exposure time, the final emission map was obtained. This was compared with the experimental results. Figure 5 shows the results. While the photon counts are not perfectly matching, aspect requiring further analyses, the estimates can be considered close enough in describing the physical experimental imaging. A second test bench for the EEDF validation regarded

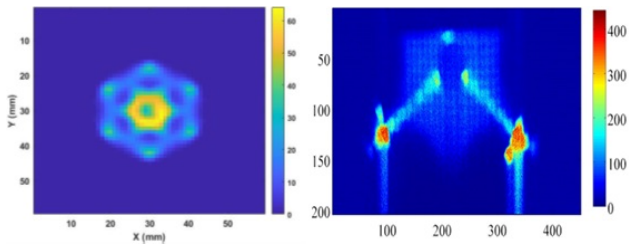

Figure 5: (**Left**) Longitudinally-integrated estimated K-α map at the CCD camera, considering total emission, local geometrical and quantum efficiency. (**Right**) Experimental photon counted images, from Ref. [13].

a first evaluation of the ion CSD for a specific ROI, starting from ROI-averaged plasma density and EEDF inputs. The ion CSD was calculated using the code-suite FLYCHK [14] which required the above mentioned input data as control parameters. Since the code is essentially 0D, each ROI was treated as a single cell, and the collective data generated for the ROI was taken as the spatially-aggregated electron data for that cell. The CSD calculations were performed for Ar ions. Figure 6 displays ROI 1 and 4, together with the extracted collective CSD of Ar ions. It can be seen that the higher the energy of the electrons,the higher the charge states of the ion CSD peak, which is perfectly consistent with expectations.

CONCLUSION

In the present work, we have presented preliminary results obtained from numerical tools developed to explore space-dependent electron properties and structure. Special attention has been devoted to the study of the ECRIS-based plasma electron anisotropy in the velocity space, which is of fundamental relevance in the study of plasma kinetic instabilities, and related transient electromagnetic emissions. A numerical routine has been developed to spatially resolve the electrons velocity distribution, and first promising results have been shown. Experimental evidence of much anisotropic behavior close to the ECR surface, as well as from its inner region, where x-ray burst have been observed [15, 16], have been also captured by the numerical results. Furthermore, a detailed study of a space-resolved EEDF has

ISBN: 978-3-95450-226-4 ISSN: 2222-5692 doi:10.18429/JACoW-ECRIS2020-TUYZO01

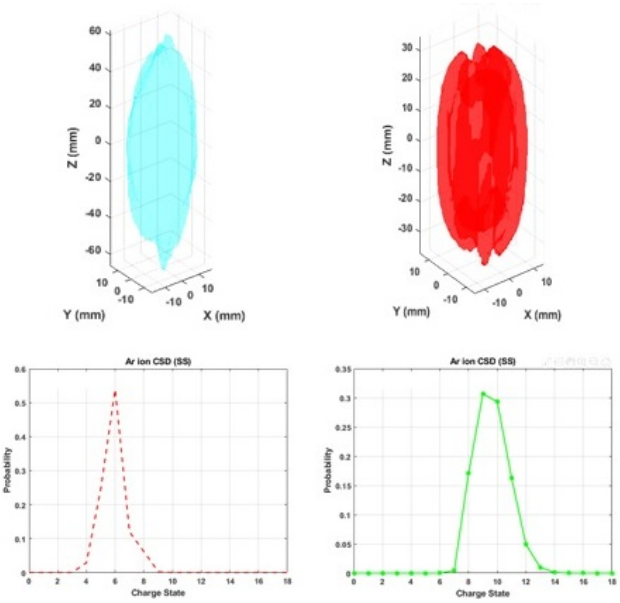

Figure 6: Ion CSD for collective electron data in ROI1 (left) and ROI4 (right) resulting as from FLYCHK code.

been carried out, with preliminary evaluation of analytic EEDF describing the electron properties in a minimum-B ECRIS plasma. The resulting function has been used to contrast experimental results from x-ray spectroscopy and imaging of K-α emission [13], with numerical estimates of the same. The comparison has shown sufficiently good approximation of the experimental results, which require further improvements. The same EEDF has been used for a first evaluation of Ar ion CSD in different regions of interest of the plasma, where the electron density and energy content vary. The resulting CSD shows such spatial dependency, with expected shift of the CSD to higher charge states upon increasing the energy of electrons. This latter result opens to future perspectives, among which, a possible introduction of the space-resolved 0D information on the CSD into the 3D self-consistent machinery, to introduce ion-electron collisional effects with a spatial dependency, and explore this influence on the ECRIS performances. Finally, the same becomes of great relevance - beyond ECRIS purposes - in the Nuclear and AstroNuclear Physics, for studying stellar enhanced nuclear phenomena in plasma, where a certain ion CSD and atomic level population impact on the nuclei's decay mechanisms. The INFN's PANDORA [17] project plans to use these data on ECRIS plasmas for its survey on such phenomena.

ACKNOWLEDGEMENTS

The authors wish to thank the 3rd Nat. Comm. of INFN, under the PANDORA_Gr3 Grant, for the financial support. The authors wish to thank also Dr. Richard Ràcz from ATOMKI - Institute of Nuclear Science (Debrecen, HU) for valuable support in the Kα emission rate evaluation and comparison to experimental results.

REFERENCES

[1] R. Geller, *Electron cyclotron resonance ion sources and ECR plasmas*. Bristol, UK: IOP Publishing, 1996.

[2] I. Izotov *et al.*, "Broadband microwave emission spectrum associated with kinetic instabilities in minimum-B ECR plasmas," *Phys. Plasma*, vol. 24, p. 043515, Apr. 2017. https://doi.org/10.1063/1.4981387

[3] R. A. Treumann, "The electron cyclotron maser for astrophysical application," *Astron. Astrophys. Rev.*, vol. 13, pp. 229-315, Jul. 2006. doi.org/10.1007/s00159-006-0001-y

[4] A. G. Shalashov *et al.*, "Maser based on cyclotron resonance in a decaying plasma," *JETP Lett.*, vol. 84, pp. 314-319, Nov. 2006. doi.org/10.1134/S0021364006180081

[5] O. Tarvainen *et al.*, "Beam current oscillations driven by cyclotron instabilities in a minimum-B electron cyclotron resonance ion source plasma," *Plasma Sources Sci. Technol.*, vol. 23, no. 2, Apr. 2014. doi.org/10.1088/0963-0252/23/2/025020

[6] D. Mascali *et al.*, "3D-full wave and kinetics numerical modelling of electron cyclotron resonance ion sources plasma: steps towards self-consistency," *Eur. Phys. J. D*, vol. 69, p. 27, Jan. 2015. doi.org/10.1140/epjd/e2014-50168-5

[7] G. Torrisi *et al.*, "Full-wave FEM simulations of electromagnetic waves in strongly magnetized non-homogeneous plasma," *Journal of Electromagnetic Waves and Applications*, vol. 28, p. 9, Apr. 2014. doi.org/10.1080/09205071.2014.905245

[8] C. S. Gallo *et al.*, "Self-consistent electromagnetic analysis of the microwave-coupling of an electron cyclotron resonance-based charge breeder," *Rev. Sci. Instrum.*, vol. 91, p. 033501, Feb. 2020. doi.org/10.1063/1.5129622

[9] A. Galatà *et al.*, "A new numerical description of the interaction of an ion beam with a magnetized plasma in an ECR-based charge breeding device," *Plasma Sources Sci. Technol.*, vol. 25, p. 045007, Jun. 2016. doi.org/10.1088/0963-0252/25/4/045007

[10] O. Tarvainen *et al.*, "Diagnostics of a charge breeder electron cyclotron resonance ion source helium plasma with the injection of $^{23}Na^{1+}$ ions," *Phys. Rev. Accel. Beams*, vol. 19, p. 053402, May 2016. doi.org/10.1103/PhysRevAccelBeams.19.053402

[11] V. Skalyga *et al.*, "Kinetic instabilities in a mirror-confined plasma sustained by high-power microwave radiation," *Phys. Plasma*, vol. 22, p. 083509, 2015. doi.org/10.1063/1.4978565

[12] A. G. Shalashov *et al.*, "Kinetic instabilities in a mirror-confined plasma sustained by high-power microwave radiation," *Phys. Plasma*, vol. 24, p. 032111, Mar. 2017. doi.org/10.1063/1.4978565

[13] R. Ràcz *et al.*, "Electron cyclotron resonance ion source plasma characterization by energy dispersive x-ray imaging," *Plasma Sources Sci. Technol.*, vol. 26, p. 075011, Jul. 2017. doi.org/10.1088/1361-6595/aa758f

[14] H.-K. Chung *et al.*, "FLYCHK: Generalized population kinetics and spectral model for rapid spectroscopic analysis for all elements," *High Energy Density Phys.*, vol. 1, no. 1, pp. 3-12, Dec. 2005. doi.org/10.1016/j.hedp.2005.07.001

ISBN: 978-3-95450-226-4 ISSN: 2222-5692 doi:10.18429/JACoW-ECRIS2020-TUYZO01

[15] V. Skalyga *et al.*, "Microwave emission from ECR plasmas under conditions of two-frequency heating induced by kinetic instabilities," *AIP Conference Proceedings (2011)*, p. 020015, Sep. 2018. doi.org/10.1063/1.5053257

[16] E. Naselli *et al.*, "Impact of two-close-frequency heating on ECR ion source plasma radio emission and stability," *Plasma Sources Sci. Technol.*, vol. 28, p. 085021, Aug. 2019. doi.org/10.1088/1361-6595/ab32f9

[17] D. Mascali *et al.*, "PANDORA, a new facility for interdisciplinary in-plasma physics," *Eur. Phys. J. A*, vol. 53, p. 145, Jul. 2017. doi.org/10.1140/epja/i2017-12335-1

ISBN: 978-3-95450-226-4 ISSN: 2222-5692 doi:10.18429/JACoW-ECRIS2020-TUYZO02

A GUIDING CENTRE APPROXIMATION APPROACH FOR SIMULATION ELECTRON TRAJECTORIES IN ECR AND MICROWAVE ION SOURCES*

J. A. Mendez†, T. Thuillier, Université Grenoble-Alpes, CNRS-IN2P3, Grenoble Institute of Engineering (INP), LPSC, Grenoble, France
T. Minea, Université Paris-Saclay, CNRS, LPGP, Orsay, France

Abstract

The present work presents a study on the feasibility of the implementation of the guiding centre (GC) approach in electron cyclotron resonance (ECR) ion sources, with the goal of speeding up the electron's orbit integration in certain regimes. The GC algorithm is compared with the Boris method which is commonly used in plasma simulations. It is shown that the GC approximation reproduces accurately the trajectory drifts and periodic behaviour of electrons in a minimum-B field with magnetic field gradients as high as 40 T/m. A typical confined electron orbit far enough from the source's axis is well reproduced for 1 μs of propagation time, with the GC time-step constrained below 100 ps, providing one order of magnitude gain in computation time with respect to the Boris method. For a confined electron orbit close to the axis a coming out of phase of the electron's trajectory is observed, but the spatial envelope is conserved. A comparative study analyses non-confined electron trajectories in a flatter B-field, that in a microwave discharge ion source, where this method's drawbacks may be avoided given a smaller magnetic field gradient and a shorter electron lifetime in the plasma chamber. In this regime electron trajectories were very well reproduced by the GC approximation. The time-step was constrained below 10 ns, providing up to 30 times faster integration compared to Boris.

INTRODUCTION

The numerical simulation of charged particle trajectories is of interest to model the plasma features of ion sources. The explicit Boris algorithm has become the standard for particle trajectory integration in a magnetic field. The high frequency electron cyclotron motion, in the GHz range, common in ion sources, constrains the time-step below 10 ps, which yields to a longer computation time when such small steps in time are required.

A guiding centre approach neglects the detailed particle's cyclotron motion, describing its trajectory through free motion of the centre of mass along the magnetic field lines and corresponding drifts. This approach is more computationally expensive per step than direct trajectory integration (Boris), a shorter overall computation time may be expected by using a larger time-step (~100 ps).

In this study we investigate the feasibility of using the guiding centre approximation for propagating electrons in ion sources. This was done by developing two otherwise identical algorithms in order to compare the resulting electron mean paths given by the guiding centre approximation and the Boris algorithm.

TRAJECTORY INTEGRATION

Two methods for trajectory integration are investigated, namely the Boris algorithm, as a control, and a guiding centre approximation, whose applicability is the focus of this study.

The Boris Algorithm

The Boris method [1] for particle push is an explicit second order scheme and is the standard used for magnetised plasma simulation. That makes it very stable for long term simulations, property usually associated with symplectic algorithms which is the preservation of the phase space volume. This results on an upper bound to the error in the energy and other dynamic properties of the system. Another reason why the Boris algorithm is so widely used is that it conserves the energy indefinitely in the absence of an electric field or collisions.

The Guiding Centre Approximation

One can divide the motion of the charged particle into the cyclotron motion around the magnetic field lines and the motion of the centre of gyration, the guiding centre (GC). [2] The motion can be described by a guiding centre approximation under the condition that the magnetic field gradient varies in a much larger length-scale compared to the Larmor radius, $\rho \ll B/|\nabla B|$, or written differently:

$$\frac{B}{\rho|\nabla B|} \gg 1 \tag{1}$$

This rends the magnetic moment (μ) an adiabatic invariant. [3] From the covariant equation of motion for the GC, neglecting higher order terms and temporal derivatives, under the assumption that the fields vary slowly with time when compared to the variation due to the particle's movement, one can write the following equations for the GC dynamics: [4]

$$\begin{aligned}\frac{d\mathbf{R}}{dt} = v_{\parallel}\hat{\mathbf{b}} - \frac{\hat{\mathbf{b}}\times\mathbf{E}}{B} + \frac{\hat{\mathbf{b}}}{B\left(1-\frac{E_{\perp}^2}{B^2}\right)} \\ \times\left\{\frac{m\gamma}{q}\left(v_{\parallel}^2(\hat{\mathbf{b}}\cdot\nabla)\hat{\mathbf{b}} + v_{\parallel}(\mathbf{u}\cdot\nabla)\hat{\mathbf{b}}\right.\right. \\ + v_{\parallel}(\hat{\mathbf{b}}\cdot\nabla)\mathbf{u} + (\mathbf{u}\cdot\nabla)\mathbf{u}\big) \\ \left.\left. + \frac{\mu}{\gamma q}\nabla\left[B\left(1-\frac{E_{\perp}^2}{B^2}\right)^{1/2}\right] + \frac{v_{\parallel}E_{\parallel}}{c^2}\mathbf{u}\right\}\end{aligned} \tag{2}$$

* Work supported by the CNRS under the 80|PRIME grant
† mendez@lpsc.in2p3.fr

ISBN: 978-3-95450-226-4 ISSN: 2222-5692 doi:10.18429/JACoW-ECRIS2020-TUYZO02

$$\frac{d(\gamma v_\parallel)}{dt} = \gamma \boldsymbol{u} \cdot \left(v_\parallel (\hat{\boldsymbol{b}} \cdot \nabla)\hat{\boldsymbol{b}} + (\boldsymbol{u} \cdot \nabla)\hat{\boldsymbol{b}}\right) + \frac{q}{m} E_\parallel \quad (3)$$
$$- \frac{\mu}{\gamma m} \hat{b} \cdot \nabla \left[B \left(1 - \frac{E_\perp^2}{B^2} \right)^{1/2} \right]$$

$$\frac{d\left(m\gamma^{*2} v_\perp^{*2}/(2B^*)\right)}{dt} = \frac{d\mu^*}{dt} = 0 \quad (4)$$

$$\boldsymbol{u} = \boldsymbol{E} \times \frac{\hat{\boldsymbol{b}}}{B} \quad (5)$$

An asterisk (*) as upper index in the above equations denotes the quantities in the reference frame moving at the cross fields drift velocity (u), eq. (5).

Equations 2 and 3 were integrated using a fixed time-step (dt) RK4 method. [5] All numerical derivatives were computed at fourth order. The magnetic field gradient was mapped beforehand, in order to avoid having to compute it at each step, thus speeding up the simulation.

ION SOURCES

Two different kinds of ion sources were studied, an ECR ion source, such as PHOENIX V2, and a microwave discharge model, exemplified by the SILHI@GANIL ion source. These ion source designs vary considerably in terms of magnetic field topology and typical electron energy distributions of their corresponding plasmas.

The PHOENIX V2 Ion Source

This compact ECRIS was developed at LPSC and commissioned for the SPIRAL 2 accelerator at GANIL. It operates at 18 GHz microwave frequency and has a cylindrical plasma chamber with a volume of 0.6 L (204 mm long, 63 mm diameter). [6]

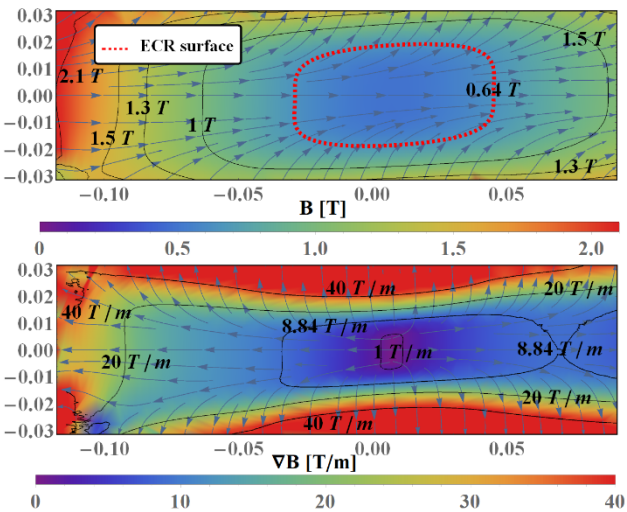

Figure 1: Magnetic field (top) and its gradient (bottom) in a longitudinal cut of PHOENIX V2's plasma chamber. The 18 GHz ECR zone is indicated with a dashed red line.

The magnetic field of PHOENIX V2 (Fig. 1) has 2.1 T at the injection wall, 1.3 T at extraction and a radially confining field strength of 1.35 T. The associated magnetic field gradient is as high as 40 T/m. We also see that for this field geometry the relationship between the field and its gradient is mostly direct, relevant for the validity condition for the GC approximation.

The SILHI@GANIL Ion Source

This Microwave Discharge Ion Source was developed at CEA-Saclay and designed to output a constant high intensity beam of protons or deuteron. As it's typical of this kind of ion sources, it operates with a 2.45 GHz microwave frequency. Its plasma chamber volume is of 0.64 L (100 mm long, 90 mm diameter). [7]

SILHI's magnetic field is produced by three permanent magnet rings located around the plasma chamber (Fig. 2). The maximum field strength is ~0.1 T, which can provide a magnetic mirror for electrons moving towards the extraction wall from the resonance surface. In the absence of other interactions, which are not considered in the present study, electrons undergo at maximum one bounce.

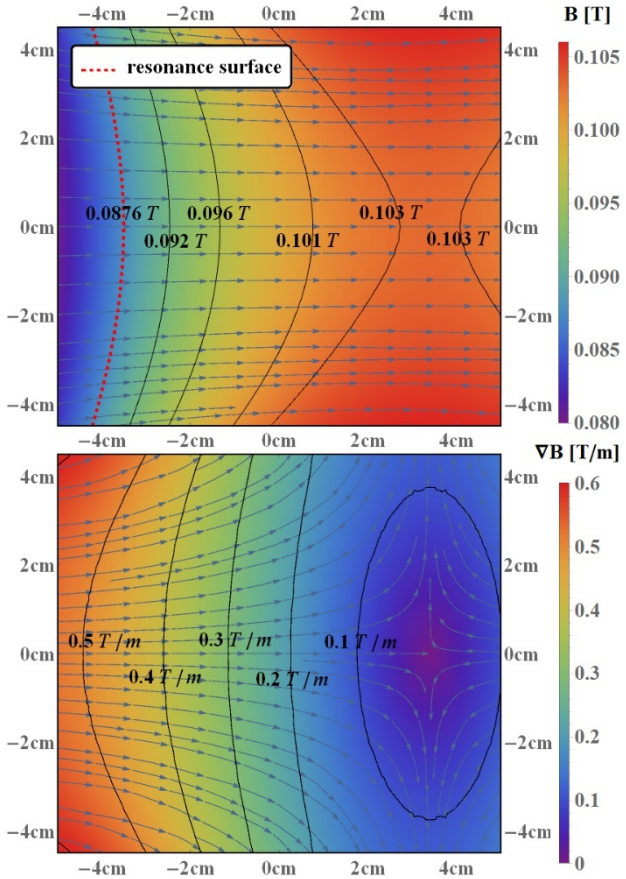

Figure 2: Magnetic field (top) and its gradient (bottom) in a longitudinal cut of SILHI's plasma chamber.

Comparing the magnitude of the field's gradient (Figs. 1 and 2), the one of SILHI is considerably smaller, (0.5 T/m with respect to 40 T/m for PHOENIX V2), pointing to a greater validity of the GC approximation. With this geometry the gradient and field magnitude are inversely related.

Table 1 further suggests that the assumptions made for the GC approximation (see eq. 1) are fulfilled better in the regime given by a microwave resonance ion source, with a typical energy of the order of a few eV and a flatter magnetic field. It also suggests that we would expect the GC

ISBN: 978-3-95450-226-4 ISSN: 2222-5692 doi:10.18429/JACoW-ECRIS2020-TUYZO02

approximation to be useful for electron energies smaller than 10 keV for either source. The Appendix shows the typical evolutions of the validity ratio (eq.1) *vs* time.

Table 1: GC Approximation Validity Ratio, $(B/|\nabla B|)/\rho$, for PHOENIX V2 (near ECR region) and SILHI (near plasma chamber centre) Ion Sources by Electron Kinetic Energy

$E_{kinetic}$	PHOENIX V2	SILHI@GANIL
1 eV	7792	17813
10 eV	2464	5633
100 eV	779	1781
1 keV	246	563
10 keV	78	177
100 keV	24	54
1 MeV	6	13

RESULTS

ECRIS – PHOENIX V2

One kind of typical orbit in an ECRIS is that of confined electrons reasonably Far From the plasma chamber Axis (FFA). This kind of trajectories present bouncing along the longitudinal direction and a precession around the axis.

The electron's energy is physically conserved as no heating is considered in this study. Using a time-step (*dt*) of 1, 10 and 100 ps for the GC algorithm we see that for 1 µs of propagation, this is roughly the case, the overall energy variation is less than 0.1% from the initial value (Fig. 3).

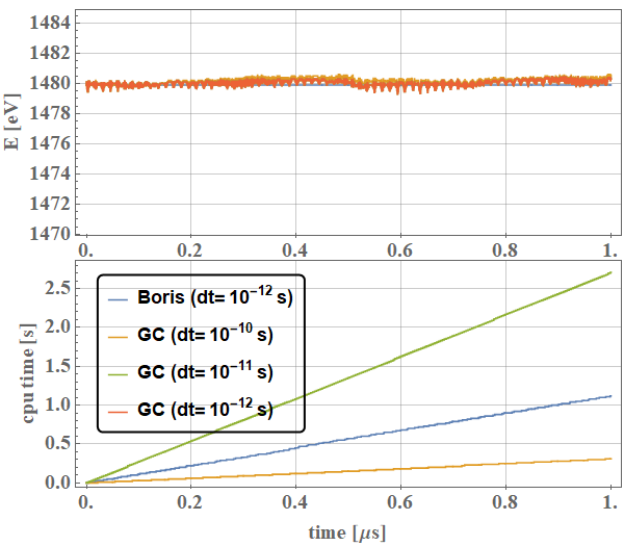

Figure 3: Electron energy (top) and computation time *vs* propagation time for a typical FFA orbit with varied dt.

In terms of computation time, GC was found to be around 20 times more expensive as for Boris' method. A time gain can then be achieved by using a *dt* two orders of magnitude larger (Fig. 3). This gain comes without a noticeable loss of accuracy for this propagation time (Figs. 4 and 5). The simulated GC trajectories agree with Boris' for the valid *dt*. At a *dt* of 1000 ps the GC approximation breaks, shown by diverging residuals (Fig. 5).

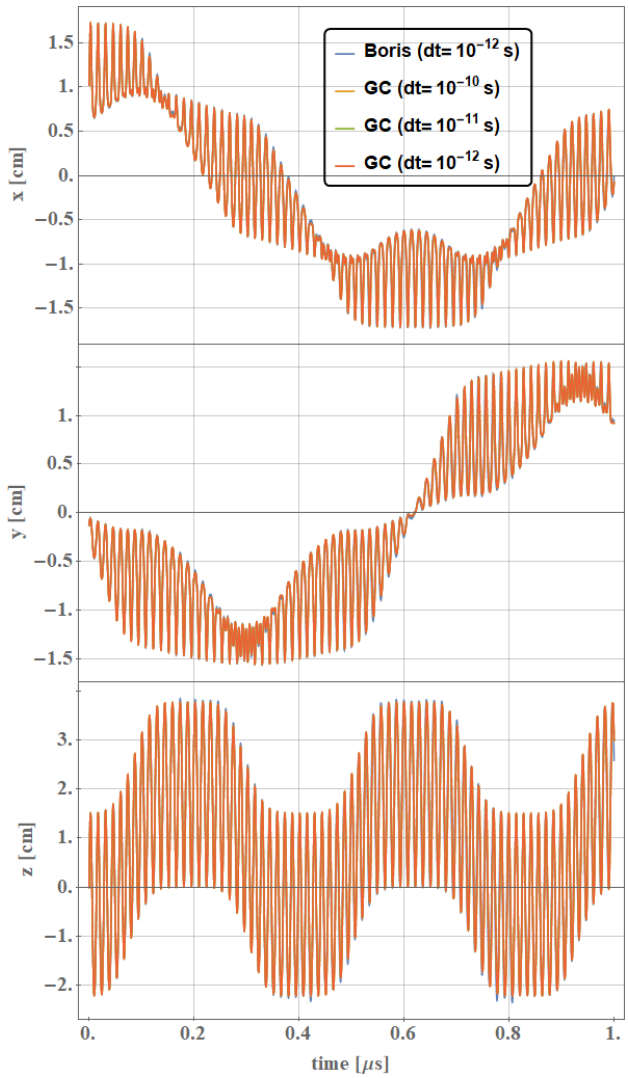

Figure 4: Typical FFA trajectory coordinates. Transversal coordinates x and y and longitudinal coordinate z.

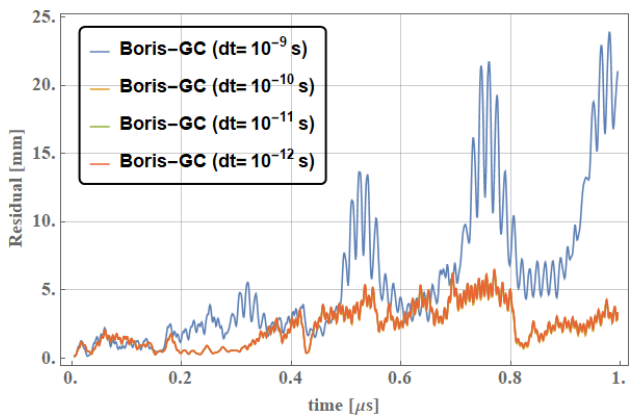

Figure 5: FFA, absolute difference (residual) between simultaneous points during propagation of Boris' and GC.

ISBN: 978-3-95450-226-4 ISSN: 2222-5692 doi:10.18429/JACoW-ECRIS2020-TUYZO02

Another case to consider is that of confined electron Close To the chamber's Axis (CTA). Here we see that the GC and Boris' orbits fall out of phase, but the spatial envelopes remain consistent (Figs. 4 and 6). The residuals (Fig. 7) confirm this observation, but show that the confined trajectories periodically come to agreement, ~1 mm distance. The electron's energy remains practically constant during propagation (Fig. 8). Given that the proposed use case for this algorithm involves a large number of test particles, for very few collisions (very low pressure), this inaccuracy could be averaged out.

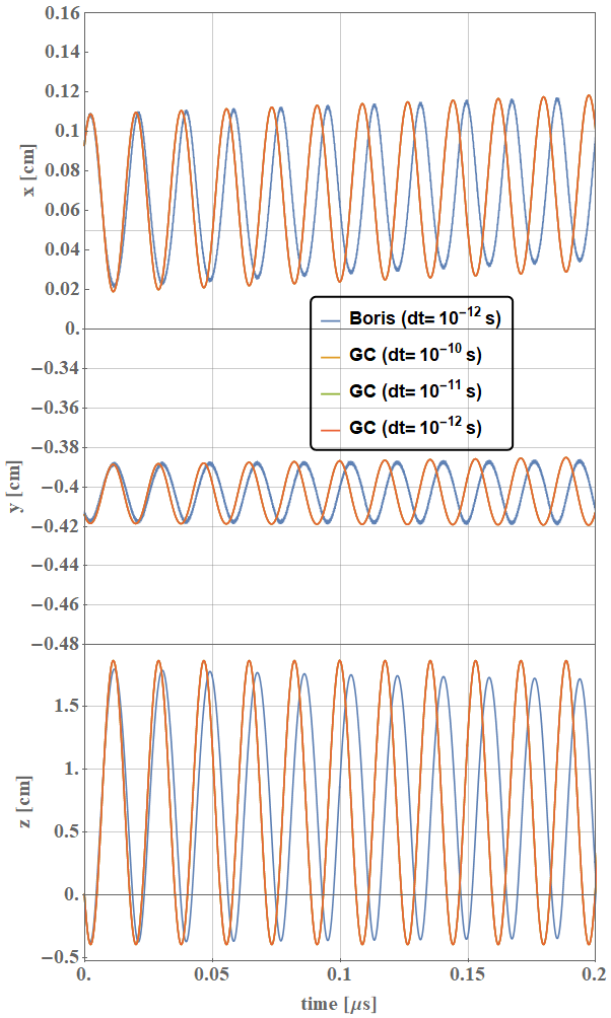

Figure 6: Typical CTA coordinates, for 0.2 µs.

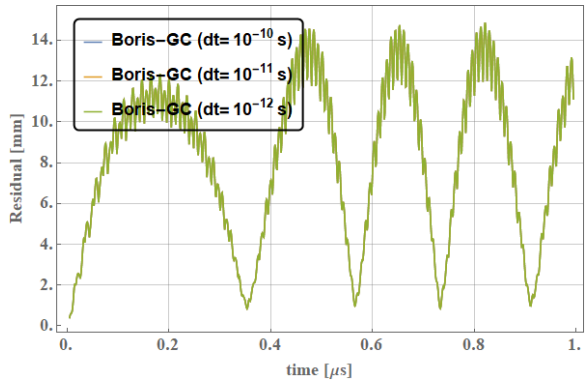

Figure 7: CTA, absolute difference between simultaneous points during propagation of Boris and GC electrons.

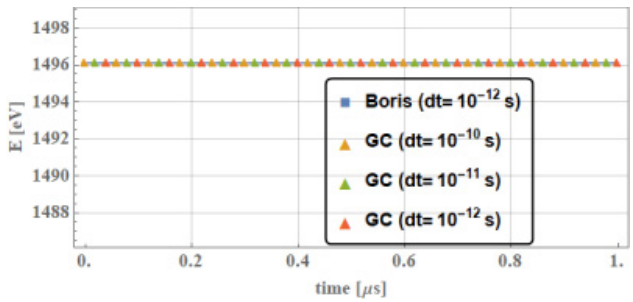

Figure 8: Electron energy *vs* propagation time for a typical CTA orbit with varied *dt*.

Microwave Discharge Ion Source – SILHI

A selected orbit with one bounce in the SILHI ion source shows great coincidence between Boris and GC propagated electrons (Fig. 9). This kind of trajectory was chosen as it represents the most challenging case, excluding higher energy (~100 eV) electrons. A *dt* value of up to 1000 times that of Boris' method still provides good agreement between Boris' and GC orbits.

ISBN: 978-3-95450-226-4 ISSN: 2222-5692 doi:10.18429/JACoW-ECRIS2020-TUYZO02

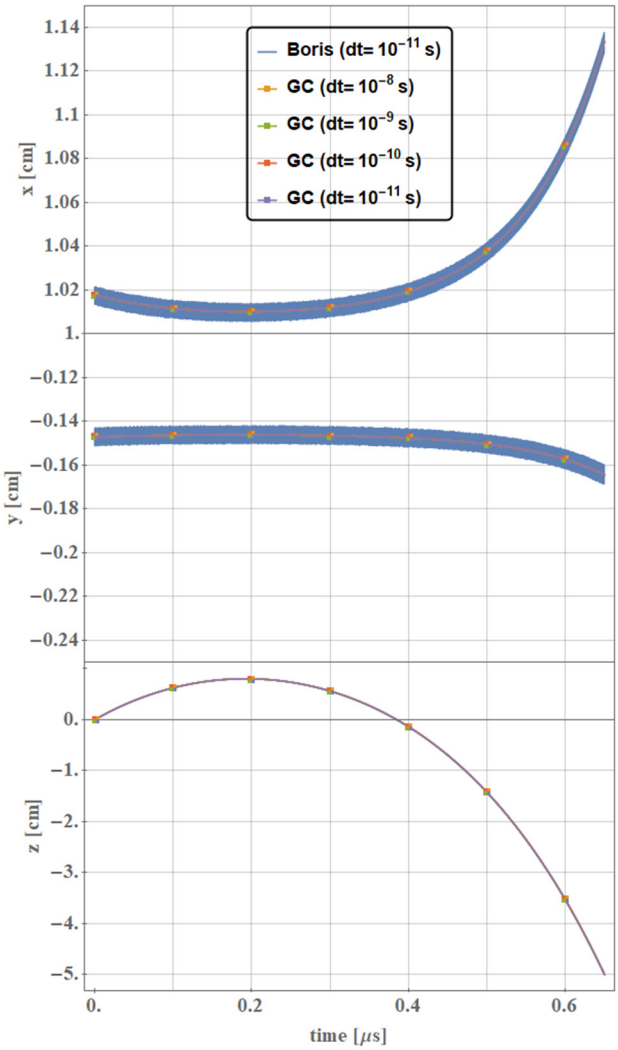

Figure 9: Typical SILHI one bounce electron trajectory coordinates as function of time.

In this case the energy is conserved in the relevant scale for all propagation algorithms, which indicates that the GC approximation's assumption is completely valid in this regime (Fig. 10). With this source's characteristics the GC algorithm was also found to be around 25 times as expensive as Boris, with a time gain obtained from 100 times the *dt* used for Boris: 10 ps (Fig. 11). Using a 10 ns *dt* for the GC provides an almost instantaneous computation, ~30 times faster compared to Boris, and good orbit agreement; however, using such a large *dt* would limit time resolution, therefore its viability depends on the use case.

The residuals show that in this regime (~1eV, SILHI) the GC algorithm breaks at a *dt* = 100 ns, providing an upper usability limit. Good agreement obtained for all smaller *dt* considered (Fig.12).

CONCLUSIONS

The GC algorithm can accurately reproduce electron trajectories in the domain of both studied ion sources and regimes: (i) for the PHOENIX V2 ECRIS being a ~1 T magnetic field and around ~1 keV of electron kinetic energy, and (ii) for the SILHI ion source a lower 0.1 T magnetic field and ~1 eV electron kinetic energy.

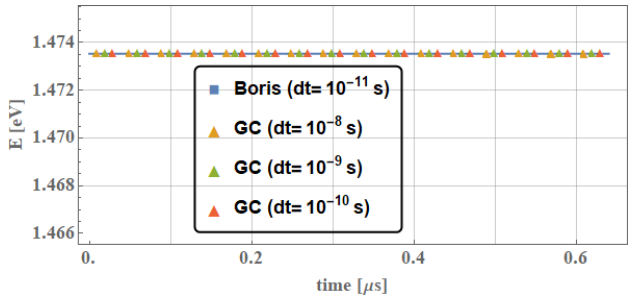

Figure 10: Electron energy *vs* propagation time for a one bounce orbit with varied *dt*.

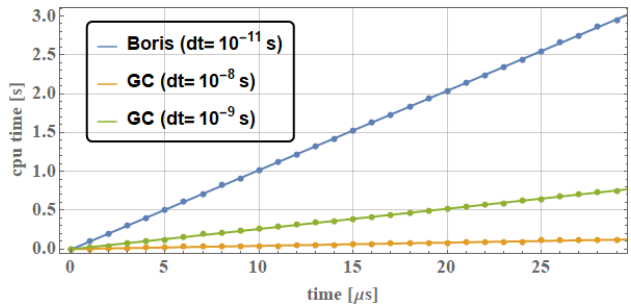

Figure 11: Computation time *vs* propagation time for a 100 sequentially integrated trajectories with varied *dt*.

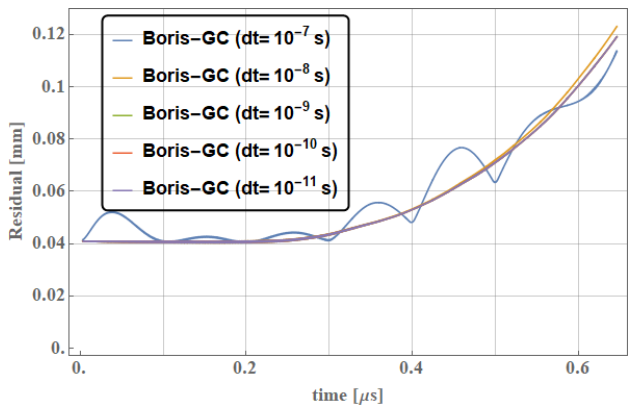

Figure 12: SILHI, absolute difference between simultaneous points during propagation of Boris and GC electrons.

The GC algorithm can provide an advantage in terms of computation time for particle plasma simulations. This advantage is greater for the conditions tested for SILHI, a flatter B-field relative to that of PHOENIX V2. In this regime the time step can be increased by a factor of 10^2 with a computation time ~30 times smaller with respect to Boris' using a 10ps time-step, without considerable loss in accuracy, the time-resolution being the principal limitation.

For the PHOENIX V2 ECRIS the gains are more modest, allowing for a time-step increase of factor of 10^2

ISBN: 978-3-95450-226-4 ISSN: 2222-5692 doi:10.18429/JACoW-ECRIS2020-TUYZO02

providing around one order of magnitude gain in required computation time. In certain cases, a disphasement between Boris' and GC orbits is evident for 1 µs propagation time, however this seems to preserve the spatial orbit envelope. This effect could be neglected in use cases involving many simulated particles and furthermore, the introduction of plasma interactions allows to re-initialize the electron, thus reducing the impact of this effect.

In terms of prospects to follow this study, a smart switcher for orbit integration could be implemented, where the GC approximation is used with a large time-step when valid and a high time resolution isn't required.

APPENDIX

To support the observed greater validity of the GC approximation in SILHI's regime, below its validity ratio is plotted along representative PHOENIX V2 and SILHI trajectories (Fig. 13).

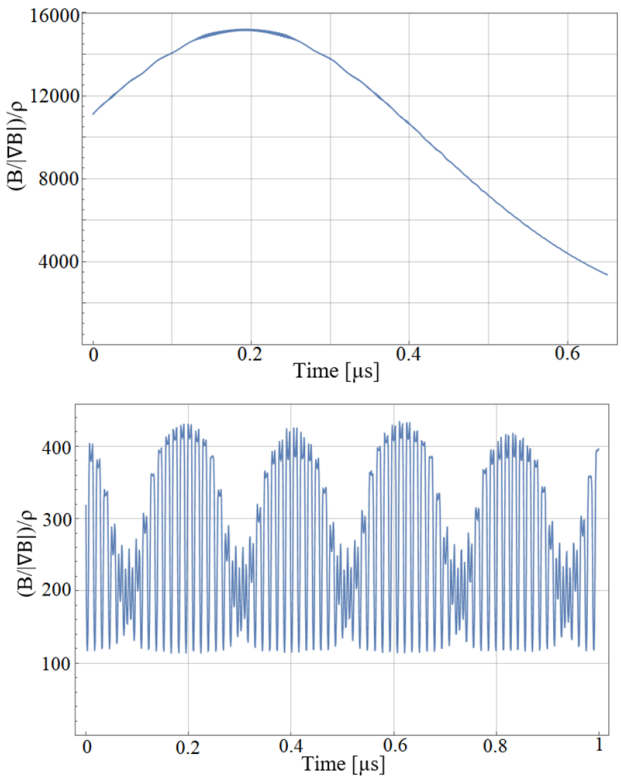

Figure 13: GC approximation validity test ratio along a typical SILHI (top) and PHOENIX V2 (bottom) trajectories.

REFERENCES

[1] H. Qin *et al.*, "Why is Boris algorithm so good?," *Physics of Plasmas*, vol. 20, no. 8, p. 084503, 2013. doi:10.1063/1.4818428

[2] T. G. Northrop, "Adiabatic charged-particle motion," *Reviews of Geophysics*, vol. 1, no. 3, p. 283304, 1963. doi:10.1029/RG001i003p00283

[3] P. O. Vandervoort, "The relativistic motion of a charged particle in an inhomogeneous electromagnetic field," *Annals of* Physics, vol. 10, no. 3, p. 401453, 1960. doi:10.1016/0003-4916(60)90004-X

[4] B. Ripperda *et al.*, "Reconnection and particle acceleration in interacting flux ropes - I. Magnetohydrodynamics and test particles in 2.5D," *MNRAS*, vol. 467, p. 32793298, May 2017. doi:10.1093/mnras/stx379

[5] M. H, I. Saidu, *et al.*, "A simplified derivation and analysis of fourth order Runge Kutta method*," International Journal of Computer Applications*, vol. 9, p. 5155, 2010. doi:10.5120/1402-1891

[6] C. Peaucelle *et al.*, "First A/Q=3 Beams of Phoenix V2 on the Heavy Ions Low Energy Beam Transport Line of SPI-RAL2", in *Proc. 19th Int. Workshop on ECR Ion Sources (ECRIS'10)*, Grenoble, France, Aug. 2010, paper TUCOAK01, pp. 75-77.

[7] R. Gobin *et al.*, "Development of a permanent magnet light ion source at CEA/Saclay", *Review of Scientific Instruments*, vol. 77, no. 3. P. 03B502, 2006. doi:10.1063/1.2164893

ISBN: 978-3-95450-226-4 ISSN: 2222-5692 doi:10.18429/JACoW-ECRIS2020-TUYZO03

ELECTROMAGNETIC SIMULATION OF "PLASMA-SHAPED" PLASMA CHAMBER FOR INNOVATIVE ECRIS

G. S. Mauro*, O. Leonardi, D. Mascali, A. Pidatella, F. Russo, G. Torrisi,
INFN-LNS, Catania, Italy
A. Galatà, C. S. Gallo[1], INFN-LNL, Legnaro, Italy
G. Sorbello[2], Università degli Studi di Catania, Catania, Italy
[1]also with Università degli Studi di Ferrara, Ferrara, Italy
[2]also with INFN-LNS, Catania, Italy

Abstract

The plasma chamber and injection system design play a fundamental role in ECRISs with the aim to obtain an optimized electromagnetic field configuration able to generate and sustain a plasma with a high energy content. In this work we present the numerical study and the design of an unconventionally-shaped cavity resonator that possesses some key advantages with respect to the standard cylindrical cavities, usually adopted in ion sources setups. The cavity geometry has been inspired by the typical star-shaped ECR plasma, determined by the magnetic field structure. The chamber has been designed by using the commercial softwares CST and COMSOL, with the aim to maximize the on-axis electric field. Moreover, a radically innovative microwaves injection system, consisting in side-coupled slotted waveguides, has been implemented, allowing a better power coupling and a more symmetric power distribution inside the cavity with respect to the standard rectangular waveguides. This new "plasma-shaped oriented" design could relevantly improve the performances of the ECRISs while making more compact the overall setup.

INTRODUCTION AND MOTIVATION

Microwave-to-plasma coupling in ECR Ion Sources is based on the matching of the injection waveguide to the plasma-filled cavity. The variation in the performances in terms of extracted current and charge states has been explained by taking into account the different patterns that the electromagnetic field assumes on the resonance surface [1, 2]. In the past years, various approaches to enhance ion source performances through an optimization of the plasma chamber shape [3] or through the use of improved microwave injection systems, have been studied and presented [4–7]. This paper describes the numerical modeling of a novel microwave cavity for plasma confinement whose geometry has been determined by the electron trajectories as they move under the influence of a B-minimum magnetic field. The new cavity shape promotes the excitations of electromagnetic modes that show a field maximum at its center; this could result in an increase of the power absorbed by the plasma and prevent the formation of the typical hollow plasma observed experimentally and demonstrated by numerical simulation [8]. Furthermore, due to the less occupied radial volume, the employment of the presented cavity allows more space for the mid coils and thus a finer tuning of the confining magnetic field could be possible. The second part of the work describes an innovative microwave launching scheme that employs a slotted waveguide placed on the chamber outer wall. This radically new solution greatly improves the number of modes that can be efficiently coupled into the cavity, together with an improved electric field symmetry along the cavity axis. Moreover, the new microwave launch system allows more space on the end flanges of the plasma chamber that can be employed by other ancillary equipment, while offering a distributed and more homogeneous power transfer to the plasma compared to the classical axial injection scheme through rectangular waveguide.

* mauro@lns.infn.it

PLASMA SHAPED CAVITY AND AXIAL MICROWAVE INJECTION

The presented "plasma-shaped" cavity is visible in Fig. 1, along with its dimensions. For the future experimental test on the CAESAR ECRIS setup [9], we set the cavity diameter d and length L equal to 48.5 mm and 150 mm respectively. The cavity geometry has been inspired by the typical star-shaped ECR plasma and is determined by the twisted B-minimum magnetic field structure [10] and also takes into account the electrons trajectories as they move under the influence of the magnetic field.

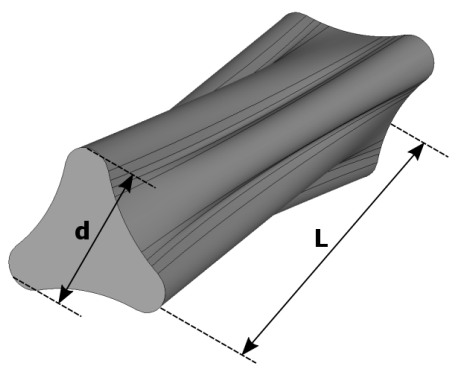

Figure 1: 3D model of the presented "plasma-shaped" cavity with its fundamental dimensions.

In order to study the new cavity driven behaviour, it has been connected to an axial feeding waveguide. Using the

ISBN: 978-3-95450-226-4 ISSN: 2222-5692 doi:10.18429/JACoW-ECRIS2020-TUYZO03

commercial simulator CST Studio Suite, its S-parameters have been calculated and compared to those of a cylindrical cavity with diameter $d = 63.5$ mm and length $L = 150$ mm (CAESAR cavity dimensions), fed by the same feeding configuration. The two geometries are visible in Fig. 2. In particular, both structures: a) consists of a vacuum solid with lossy metal boundary conditions, b) have been fed through a standard WR62 waveguide and c) have been simulated using the same mesh quality (curvature tolerance, number of mesh refinement steps, etc).

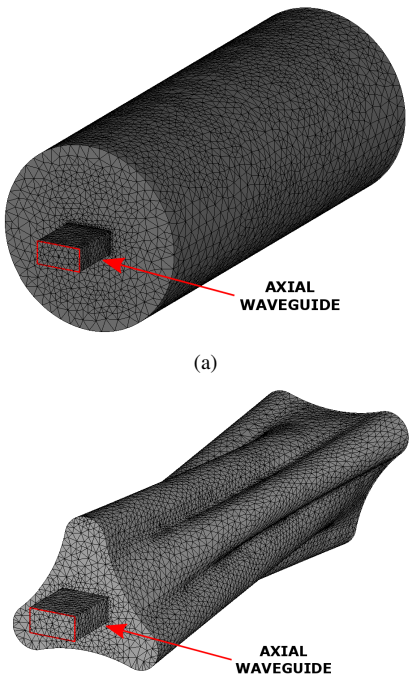

Figure 2: (a) standard cylindrical cavity and (b) "plasma-shaped" cavity models. Applied mesh and axial feeding waveguides are visible.

The performances of both structures have been observed in terms of S-parameters in the frequency range 14-14.5 GHz. Figure 3 shows the $|S_{11}|$ curve for the considered geometries. From the plots it can be seen that in the case of cylindrical cavity the modes inside the considered frequency range are not well adapted (i. e. not optimal power transfer from the feeding waveguide to the cavity). However, in the case of the "plasma-shaped" cavity, more modes are present inside the considered bandwidth and in particular the mode at the frequency of 14.304 GHz has the best coupling ($\simeq -15$ dB). Moreover, the electric field is much more intense than the cylindrical case' one, as can be seen in Fig. 4.

SLOTTED WAVEGUIDE ANTENNA DESIGN

In order to improve the microwave-to-cavity coupling and at the same time have a more uniform and symmetric axial electric field distribution, a slotted waveguide

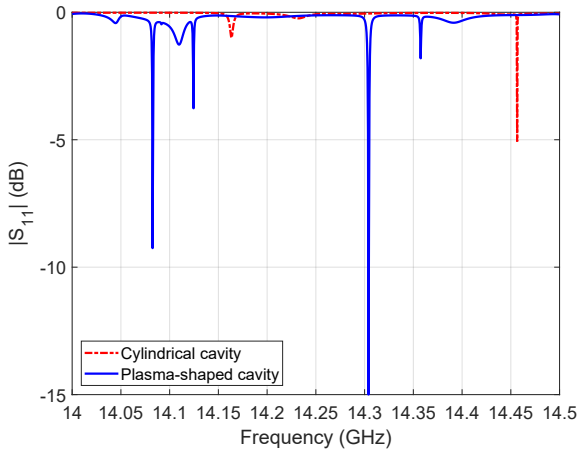

Figure 3: $|S_{11}|$ curve, inside the operational bandwidth of 14-14.5 GHz, for the standard cylindrical cavity and the "plasma-shaped" one.

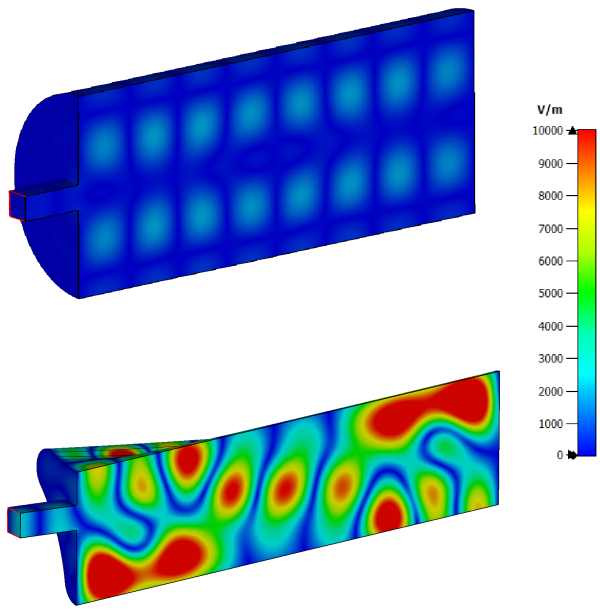

Figure 4: Electric field module plot on cavities slice: cylindrical cavity ($f_0 = 14.457$ GHz) vs. plasma-shaped cavity ($f_0 = 14.304$ GHz). The field has been normalized to the maximum value of 10 kV/m.

has been employed as the microwave injection system and its behaviour has been numerically characterized. Slotted waveguides find many applications in radar and communication systems due to their low-profile design requirements, mechanical robustness, good efficiency, relative ease of realization and wide operational frequency bandwidth [11–13]. The first step has been the design of a slotted waveguide antenna operating in free space. Defining the guided wavelength for the TE_{10} mode of the rectangular waveguide as $\lambda_g = \frac{c}{f}\frac{1}{\sqrt{1-c/(2af)}}$, where f is the operational frequency and a is the waveguide large side, the

ISBN: 978-3-95450-226-4 ISSN: 2222-5692 doi:10.18429/JACoW-ECRIS2020-TUYZO03

guidelines for the design of a slotted waveguide antenna can be found [14, 15]. In the numerical optimization of a slotted waveguide antenna, particular attention must be paid to its critical parameters, and in particular: the distance between the center of the last slot from the closing metallic wall or d_{short}, the width and length of the slots, w_{slot} and l_{slot} respectively. In general, the impedance bandwidth results inversely proportional to the slot number [16]. However, using a low number of slots has a negative impact on the efficiency, so a trade-off for this parameters needs to be chosen depending on the required performances. The antenna shown in Fig. 5 has been optimized through the use of CST. The operational bandwidth is 14.2-15.25 GHz with central frequency 14.7 GHz. We chose to employ eight slots with the scope to maximize the $|S_{11}|$ impedance bandwidth and to obtain an uniform radiation pattern. This value has also been chosen considering the available space along the cavity outer wall, equal to 150 mm. A tuning of the slot width or w_{slot}, a critical parameter that can affect the impedance bandwidth [16], has been performed: the calculated $|S_{11}|$ is shown in Fig. 6 for different slot width values. A good compromise between impedance bandwidth and efficiency has been found when $w_{slot} = 2$ mm.

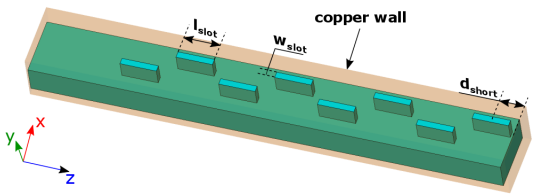

Figure 5: Slotted waveguide antenna model and fundamental parameters: slot length l_{slot}, width w_{slot} and distance from the short circuit d_{short}. The structure consists of an air volume enclosed into a copper block (orange object). The antenna is fed through a waveguide port, not visible in the figure.

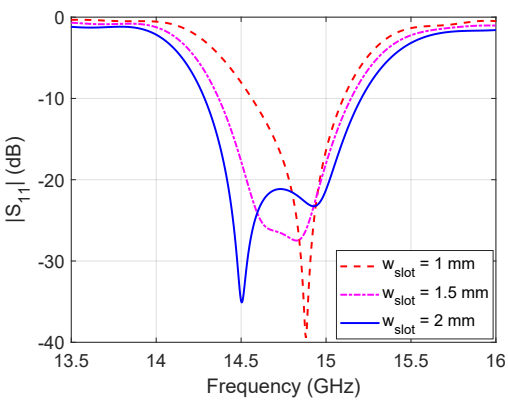

Figure 6: $|S_{11}|$ vs. slot width w_{slot}: it can be seen that this parameter affects the impedance bandwidth.

SLOTTED WAVEGUIDE INJECTION SIMULATIONS

The final step has been the coupling of the slotted waveguide to the cavities, as visible in Fig. 7. In the case of the "plasma-shaped" cavity, the slotted waveguide has also been twisted in order to follow the outer wall shape. Figure 8 shows the $|S_{11}|$ curves for both cavities with the

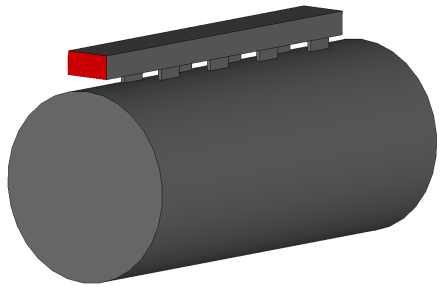

(a)

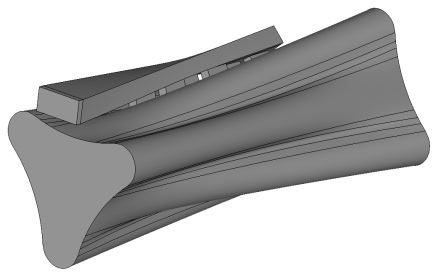

(b)

Figure 7: (a) standard cylindrical and (b) "plasma-shaped" cavities together with the adopted slotted waveguide microwave injection system. In (b) the slotted waveguide has also been twisted in order to follow the cavity profile.

slotted waveguide microwave injection system. From the plot it is immediately evident that the use of the new injection system results in a higher number of modes that are coupled inside the cavities with respect to the standard launch with an axial waveguide; this result could potentially improve ion source performances when applying the frequency tuning technique [17]. Figure 9 shows the electric field plot, at the frequency of 14.466 GHz, for the "plasma-shaped" cavity with the slotted waveguide injection. It can be observed that the field has a maximum at the cavity center and that the field profile has been symmetrized along the cavity axis with respect to the one of Fig. 4, evaluated inside the cavity with the axial waveguide injection. It has to be pointed out that, for the same slotted waveguide injection configuration, the cylindrical cavity presents a predominance of modes with off-axis electric field maximum. The symmetric field leads to a homogeneous power distribution from the multiple radiating waveguide slots to the cavity, with a potential advantage relative to the power absorption from the plasma. Moreover, the use of the slotted waveguide could in principle lead to an increase of the total employable power by creating

ISBN: 978-3-95450-226-4 ISSN: 2222-5692 doi:10.18429/JACoW-ECRIS2020-TUYZO03

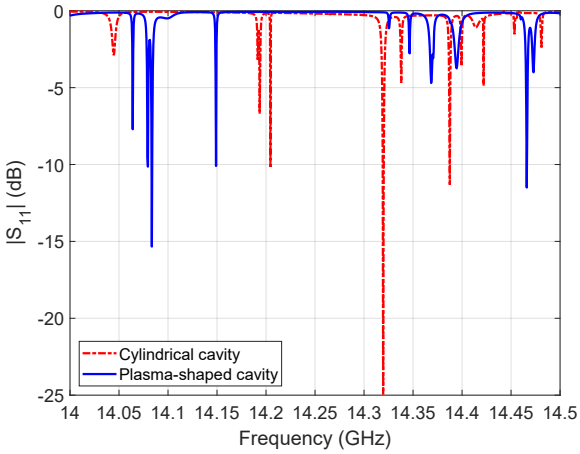

Figure 8: $|S_{11}|$ curve, inside the operational bandwidth of 14-14.5 GHz and with the slotted waveguide microwave injection system, for the standard cylindrical cavity and the "plasma-shaped" one.

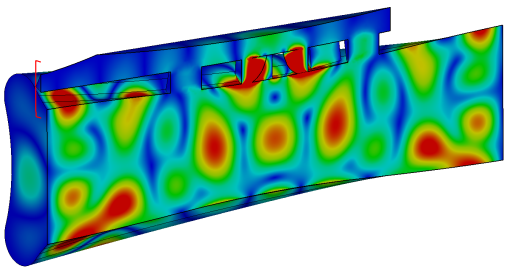

Figure 9: Electric field module plot at the frequency of 14.466 GHz for the "plasma-shaped" cavity with the slotted waveguide injection.

a splitted-injection system composed of multiple slotted waveguides placed radially with respect to the cavity [18].

CONCLUSION AND PERSPECTIVES

In this work, the numerical study of an innovative plasma cavity geometry, inspired by the typical star-shaped ECR plasma, has been presented. The new geometry presents some key advantages with respect to the classical cylindrical cavity; in particular, it is able to excite electromagnetic modes with electric field maximum located near the cavity axis, where the maximum of the resonant absorption takes place. In order to obtain a more symmetric field profile and an homogeneous power transfer to the plasma, a novel microwave injection setup based on a slotted waveguide has been introduced instead of the standard axial waveguide setup. Numerical results show that the new injection system greatly improves the excited modes inside the frequency band of interest, which could be useful in ion source frequency tuning operations. Moreover, the use of the "plasma-shaped" cavity in conjunction with the slotted waveguide results in the symmetrization of the excited modes: this could allow a more uniform power transfer to the plasma when a mode with electric field maximum along the cavity axis is excites, as in the case of the presented geometry. The innovative cavity geometry plus the new microwave injection system solution also releases space from the main injection flange exploitable for other ancillaries.

ACKNOWLEDGMENT

The authors wish to thank the 5th Nat. Comm. of INFN, under the PANDORA Grant, for the financial support. Part of this work has been carried out within the Grant73/IRIS project, also supported by INFN (Italian patent pending n. 102020000001756).

REFERENCES

[1] D. Mascali *et al.*, "Plasma ion dynamics and beam formation in electron cyclotron resonance ion sources," *Rev. Sci. Instrum.*, vol. 81, 2010. DOI: 10.1063/1.3292932.

[2] S. Gammino, G. Ciavola, L. Celona, D. Mascali, and F. Maimone, "Numerical Simulations of the ECR Heating With Waves of Different Frequency in Electron Cyclotron Resonance Ion Sources," *IEEE Trans. Plasma Sci.*, vol. 36, no. 4, 2008. DOI: 10.1109/TPS.2008.927288.

[3] H. Koivisto *et al.*, "A new 18 GHz room temperature electron cyclotron resonance ion source for highly charged ion beams," *Rev. Sci. Instrum.*, vol. 91, no. 2, p. 023 303, 2020. DOI: 10.1063/1.5128860.

[4] D. Hitz, A. Girard, G. Melin, S. Gammino, G. Ciavola, and L. Celona, "Results and interpretation of high frequency experiments at 28 GHz in ECR ion sources, future prospects," *Rev. Sci. Instrum.*, vol. 73, no. 2, pp. 509–512, 2002. DOI: 10.1063/1.1429313.

[5] H. W. Zhao *et al.*, "Intense highly charged ion beam production and operation with a superconducting electron cyclotron resonance ion source," *Phys. Rev. Accel. Beams*, vol. 20, p. 094 801, 9 Sep. 2017. DOI: 10.1103/PhysRevAccelBeams.20.094801.

[6] D. Xie, J. Benitez, W. Lu, C. Lyneis, and D. Todd, "Recent production of intense high charge ion beams with VENUS," in *22nd International Workshop on ECR Ion Sources*, Busan, Korea, 2017, THAO01. DOI: 10.18429/JACoW-ECRIS2016-THAO01.

[7] J. W. Guo *et al.*, "A new microwave coupling scheme for high intensity highly charged ion beam production by high power 24–28 GHz SECRAL ion source," *Rev. Sci. Instrum.*, vol. 91, no. 1, p. 013 322, 2020. DOI: 10.1063/1.5131101.

[8] A. Galatà, D. Mascali, C. S. Gallo, and G. Torrisi, "Self-consistent modeling of beam-plasma interaction in the charge breeding optimization process," *Rev. Sci. Instrum.*, vol. 91, no. 1, p. 013 506, 2020. DOI: 10.1063/1.5130704.

[9] D. Mascali *et al.*, "ECR ion sources developments at INFN-LNS for the production of high brightness highly charged ion beams," in *Proceedings of LINAC2014*, Geneva, Switzerland, 2014, pp. 254–256, ISBN: 978-3-95450-142-7.

[10] G. Torrisi *et al.*, "Non-conventional microwave coupling of RF power in ECRIS plasmas," *AIP Conference Proceedings*, vol. 2011, no. 1, p. 020 014, 2018. DOI: 10.1063/1.5053256.

[11] F. Werner, D. Korzec, and J. Engemann, "Slot antenna 2.45 GHz microwave plasma source," *Plasma Sources Sci. Technol.*, vol. 3, no. 4, pp. 473–481, Nov. 1994. DOI: 10.1088/0963-0252/3/4/004.

ISBN: 978-3-95450-226-4 ISSN: 2222-5692 doi:10.18429/JACoW-ECRIS2020-TUYZO03

[12] A. Woodard, K. Shojaei, C. Berrospe-Rodriguez, G. Nava, and L. Mangolini, "Electron emission from particles strongly affects the electron energy distribution in dusty plasmas," *J. Vac. Sci. Technol., A*, vol. 38, 2020. DOI: 10.1116/1.5134706.

[13] R. V. Gatti and R. Sorrentino, "Slotted waveguide antennas with arbitrary radiation pattern," in *34th European Microwave Conference*, Amsterdam, The Netherlands, 2004, pp. 821–824.

[14] R. S. Elliott and L. A. Kurtz, "The design of small slot arrays," *IEEE Trans. Antennas Propag.*, vol. 26, pp. 214–219, 1978.

[15] R. S. Elliott, "The design of traveling wave fed longitudinal shunt slot arrays," *IEEE Trans. Antennas Propag.*, vol. 27, no. 5, pp. 717–720, 1979.

[16] S. S. Sekretarov and D. M. Vavriv, "A wideband slotted waveguide antenna array for SAR systems," *Progress In Electromagnetics Research M*, vol. 11, pp. 165–176, 2010.

[17] L. Celona, S. Gammino, G. Ciavola, F. Maimone, and D. Mascali, "Microwave to plasma coupling in electron cyclotron resonance and microwave ion sources," *Rev. Sci. Instr.*, vol. 81, no. 2, 02A333, 2010. DOI: 10.1063/1.3265366.

[18] S. Bernal, F. Vega, F. Roman, and A. Valero, "A high-gain, broad-wall slotted waveguide antenna array to be used as part of a narrowband high power microwaves system," in *2015 International Conference on Electromagnetics in Advanced Applications (ICEAA)*, Torino, Italy, 2015, pp. 618–621. DOI: 10.1109/ICEAA.2015.7297190.

ISBN: 978-3-95450-226-4 ISSN: 2222-5692 doi:10.18429/JACoW-ECRIS2020-TUZZO01

CHARACTERIZATION OF 2.45 GHz ECR ION SOURCE BENCH FOR ACCELERATOR-BASED 14-MeV NEUTRON GENERATOR

Sudhirsinh Vala†[1,2], Ratnesh Kumar, Mitul Abhangi[1], Rajesh Kumar[1,2] and Mainak Banyopadhyay[1,2]
[1] Institute for Plasma Research, Bhat, Gandhinagar, 382428, Gujarat, India
[2] Homi Bhabha National Institute (HBNI), Anushaktinagar, Mumbai, 400094, India

Abstract

The 2.45 GHz Electron Cyclotron Resonance Ion Source (ECRIS) has been indigenously developed. This development of ECRIS aims to provide high brightness, stable, and reliable D+ ion beam of 20 mA beam current in a continuous (CW) mode operation for an accelerator-based D-T neutron generator. The ECR ion source setup consists of a microwave system, a magnet system, a double wall water-cooled plasma chamber, a high voltage platform, a three-electrode ion extraction system, and a vacuum system. The ECR ion source test setup is installed, and deuterium plasma is generated. A three-electrode extraction system is designed and fabricated for the ion beam extraction. A ~10 mA deuterium ion beam is extracted from the ECR ion source. The paper covers the detailed experimental setup of ion beam characterization and diagnostics used for measurement of beam profile, beam current, and beam emittance measurements. It also covers the latest results of beam emittance measurements.

INTRODUCTION

The 2.45 GHz ECR ion source is one of the main components of the 14-MeV neutron source. It plays an important role in the operation of the neutron source, particularly in the stability, reliability, and performance of the entire system. Therefore, it gives us the motivation to us for developing the 2.45 GHz ECR ion source for the upcoming neutron source facility at IPR. In the last three decades, many international laboratories had worked on the development of a 2.45 GHz ion source and achieved good performance. The list of some of the high current 2.45 GHz ECRIS is shown in Table 1. The designs of the referred (Table 1) 2.45 GHz ECR ion sources have been studied for the development of 2.45GHz ECRIS for a 14-MeV neutron generator. The 2.45 GHz ECRIS has been designed and developed based on three Coaxial NdFeB permanent magnet Ring type of magnetic system and three-electrode extraction system to produce the 20 mA deuterium ion beam. The results of the deuterium ion beam extraction and emittance measurements were published in this paper.

The 14-MeV neutron generator and deuterium ion irradiation facility is being developed at the Institute for Plasma Research. It will be used for the fusion neutronics activities to support the Indian as well as international fusion program. The neutron is generated by a D-T fusion reaction in which the accelerated deuterium ion beam hits the tritium target and produces the neutrons in order of 10^{12} per second [1].The facility consists of a 2.45 GHz ECR ion source, low energy beam transport system, 300 kV electrostatic acceleration system, medium energy beam transport system, rotating tritium target, vacuum system, and tritium handling & recovery system. The footprint layout of the facility is shown in Fig-1. The entire 14-MeV neutron generator facility will be installed in the 15m x 15m x 9m neutron generator hall, which has 1.8 m thick concrete wall and 0.5 m roof for biological shielding [2]

Table 1: Parameter of the 2.45 GHz ECR Ion Sources

Parameter of 2.45 GHz Source	SILHI (SPIRAL - 2) FRANCE	CEA/Saclay (IFMIF) FRANCE	PKUNIFTY CHINA	LBNL USA
Power	1200	2000 W	800 W	700 W
Magnet System	Three Coaxial NdFeB	Two sole-noid con-figuration	Three Co-axial NdFeB	Two sole-noid con-figuration
Beam Op-tics/ ex-traction system	5 elec-trode 50 kV max,	5 electrode 55 kV max,	3 electrode 50 kV max,	3 electrode 60 kV max,
Extraction aperture	3 mm	9mm	5mm	3mm
Emit-tance(π mm mrad)	< 0.1	0.25	0.2	0.04
Max Beam Current	10 (D)	140(D)	100(D)	44(D)

The deuterium beam is generated by the 2.45 GHz ECR ion source bench. It further transports to the low energy beam transport system, where other ion spices (D2+, D3+) of the deuterium beam will be separated from D+ ion beam by using the dipole magnet and diagnosed through the Beam Diagnostic System (BDS). The only D+ ion beam will transport for further acceleration. The ion beam properties will be measured by an integrated BDS which con-sists of a beam profile monitor, a X-Y slit, and a Faraday cup. To achieve the quality of the deuterium beam for ac-celeration, it will again focus through the quadrupole triplet and further accelerated up to 300 keV through an electro-static accelerator system. The properties of the accelerated deuterium beam are measured for the second time by a sim-ilar integrated BDS and the focused by quadrupole triplet to the switching magnet. Inside the switching magnet, the deuterium beam is splitted into three separate beamlines (-45°, 0°, +45°). The zero-degree beamline will be used for 14MeV neutron production by bombarding the deuterium

† sudhir@ipr.res.in

ISBN: 978-3-95450-226-4 ISSN: 2222-5692 doi:10.18429/JACoW-ECRIS2020-TUZZO01

beam on a rotating water-cooled Tritium target (TiT). The other two numbers of ± 45° beamline used for the deuterium ion beam irradiation experiments. The Tritium Handling and Recovery System (THRS) will be integrated with the exhaust of the beamline system to recover the sputtered tritium from the tritium target during the bom-bardment [3].

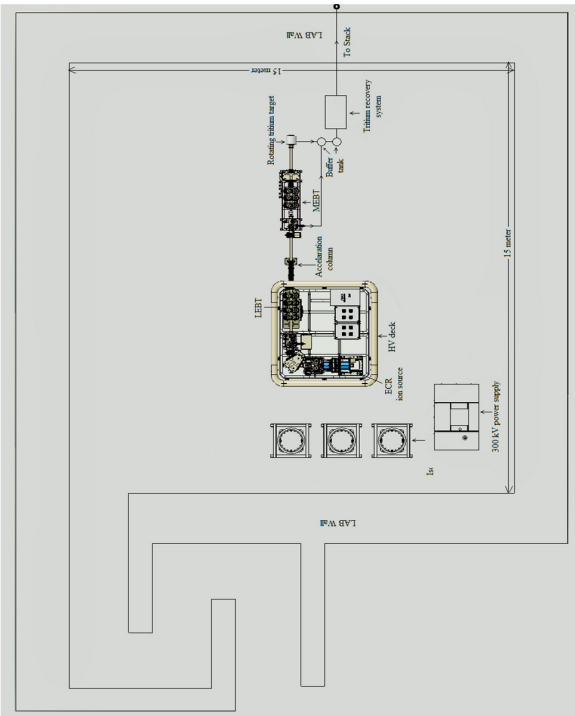

Figure 1. Layout of the 14-MeV neutron generator.

EXPERIMENTAL SETUP

Figure 2 shows the photograph of the experimental setup for the beam characterization experiments. It consists of the 2.45 GHz magnetron based microwave source followed by three stub tuner, 50kV DC high voltage break, 3-step ridge waveguide, plasma chamber with three coaxial NdFeB permanent magnet ring type of magnetic system, three electrodes extraction system, magnetic lens, vacuum chamber, dual Allison emittance scanner, and Faraday cup. A Pfeiffer make (EVR 116) mass-flow controller is used to feed deuterium gas into the plasma chamber to create deuterium plasma.

The three-electrode extraction system consists of a plasma electrode, accel electrode, and decel electrode to extract the deuterium ion beam, which has a 6 mm, 8mm, and 8 mm aperture diameter, respectively. The plasma electrode is kept at positive potential up to 30 kV, accel electrode, and decel electrode at negative potential up to 3 kV and ground potential, respectively. The extracted deuterium ion beam is focused by the magnetic lens, which had a 0.350 T magnetic field with a length of 255mm and 40 mm half aperture. Earlier, we were using an Einzel lens for the focusing of the ion beam, which is now replaced with a magnetic lens for better focusing on the high

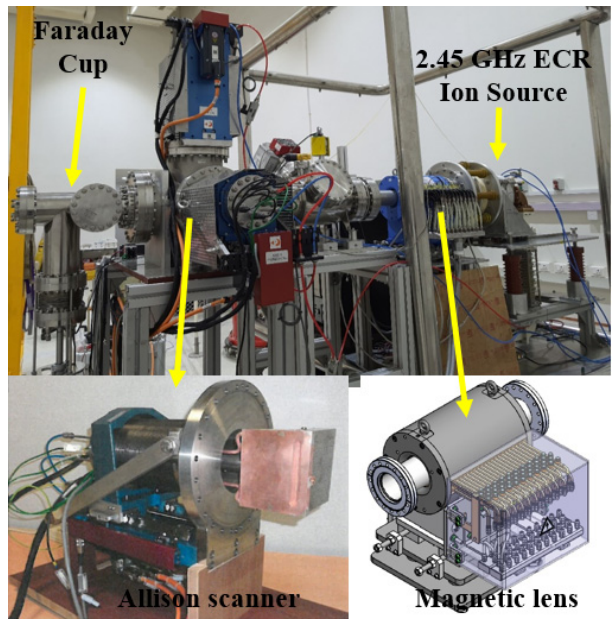

Figure 2: Photo graphic view of experimental setup.

current ion beam [4]. The emittance and current are measured using a dual Allison emittance scanner system and a Faraday cup, respectively.

Before the D ion beam generation, the system was evacuated to a base pressure ~ 10^{-6} mbar. The deuterium plasma was produce using 100 to 400 watt of microwave power with a gas flow rate of 1 to 5 x 10^{-4} mbar l/sec. The ion beam current is measured as a function of the extraction voltage for different MW power. The X-Y emittance is measured at various solenoid current in the magnetic lens system for beam focusing.

RESULTS & DISCUSSIONS

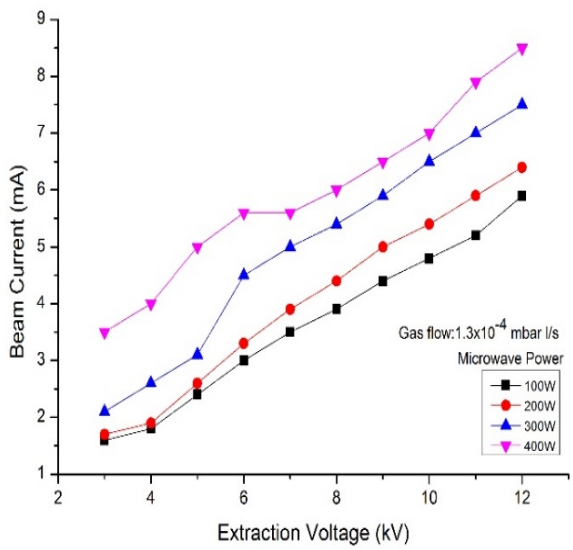

Figure 3 Measurement of deuterium ion beam current as a function of extraction voltage & microwave power.

The ECR ion source has been tuned for the extraction of the deuterium ion beam. The beam current as a function of the extraction voltage for different microwave power is

ISBN: 978-3-95450-226-4 ISSN: 2222-5692 doi:10.18429/JACoW-ECRIS2020-TUZZO01

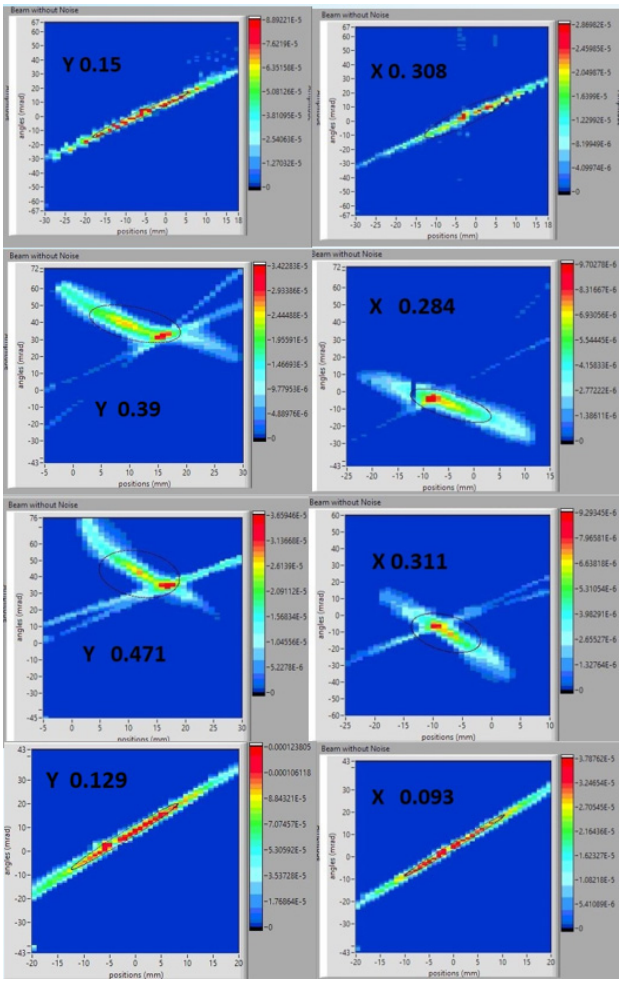

Figure 3. Beam emittance with various solenoid current with fix extraction voltage of 15 kV.

shown in Fig. 3. The preliminary emittance measurement has been done in both X and Y plans. The extraction voltage and acceleration voltage are fixed at 15 kV and -0.8 kV, respectively during the emittance measurement. The results of the emittance measurements are shown in Fig. 4 at various solenoid current. It is observed that there is a variation between the X-plan and Y-plan emittance measurements. The value of normalizing emittance for 90% beam envelop is between 0.093 to 0.308 π.mm.mrad and 0.129 to 0.471π.mm.mrad for X-plan and Y- plan, respectively. The analysis of the results of the emittance measurement is going on.

SUMMARY

For the better focusing of the ion beam into the LEBT, the Einzel lens has been replaced with the magnetic lens (Solenoid).To measure the beam emittance dual Allison emittance scanner has been integrated into the test bench. The beam characterization experiments have been performed. The beam emittance, as well as beam profile, have been measured as a function of solenoid current. The normalized emittance is between 0.093 to 0.308 π.mm.mrad and 0.129 to 0.471π.mm.mrad for X-plan and Y- plan, respectively. The beam diameter is < 20 mm.

REFERENCES

[1] S. Vala, *et al*., "Development and performance of a 14-MeV neutron generator", *Nucl. Instrum. Methods Phys. Res., Sect. A*, Vol. 959, p. 163495, 2020. doi:10.1016/j.nima.2020.163495

[2] H. L. Swami *et al.*, "Occupational radiation exposure control analyses of 14 MeV neutron generator facility: A neutronic assessment for the biological and local shield design", *Nuclear Engineering and Technology*, vol. 52, p. 17841791, Aug. 2020, doi:10.1016/j.net.2020.01.006

[3] S. Vala *et al.,* "Rotating tritium target for intense 14-MeV neutron source", *Fusion Engineering and Design*, vol. 123, p. 7781, June 2017. doi:10.1016/j.fusengdes.2017.05.117

[4] S. J. Vala, M. Abhangi, M. Bandyopadhyay, R. Kumar, and R. K. Kumar, "Development of Test Bench of 2.45 GHz ECR Ion Source for RFQ Accelerator", in *Proc. 23th International Workshop on ECR Ion Sources (ECRIS'18)*, Catania, Italy, Sep. 2018, pp. 198-201. doi:10.18429/JACoW-ECRIS2018-THC2

ISBN: 978-3-95450-226-4 ISSN: 2222-5692 doi:10.18429/JACoW-ECRIS2020-TUZZO02

ELECTRON CYCLOTRON RESONANCE ION SOURCE RELATED RESEARCH AND DEVELOPMENT WORK AT THE DEPARTMENT OF PHYSICS, UNIVERSITY OF JYVÄSKYLÄ (JYFL)*

M.S.P. Marttinen†, B.S. Bhaskar[1], A. Ikonen, T. Kalvas, H. A. Koivisto, S.T. Kosonen, R.J. Kronholm, O.A. Tarvainen[2], O.P.I. Timonen, V. Toivanen
Department of Physics, University of Jyväskylä, 40500 Jyväskylä, Finland
I. Izotov, V. Skalyga
Institute of Applied Physics of Russian Academy of Sciences, 603950 Nizhny Novgorod, Russia
J. Angot, T. Thuillier, Université Grenoble Alpes, 38000 Grenoble, France
L. Maunoury, Grand Accélérateur National d'Ions Lourds, 14076 Caen, France
[1]also at Université Grenoble Alpes, 38000 Grenoble, France
[2]also at STFC ISIS Pulsed Spallation Neutron and Muon Facility, Rutherford Appleton Laboratory, OX11 0QX Harwell, UK

Abstract

Recent research work of the JYFL ion source team covers a wide variety of ion source related projects. The instability measurements have been expanded from the pulse-periodic kinetic instabilities to the cw maser regime, characterized by continuous microwave emissions at high $B_{\mathrm{min}}/B_{\mathrm{ECR}}$ ratio. It has been observed that with appropriate settings, this regime can offer islands of stability with improved performance.

The ion beam transient studies have focused on developing diagnostics methods for studying the confinement times of highly-charged ions in ECR plasmas utilizing the 1+ injection method with a charge breeder and the sputtering method with a conventional ECRIS. These studies imply that long enough confinement times can exist in the plasma offering a potential explanation for the high ion temperatures measured with the high-resolution plasma optical emission spectrometer setup (POSSU), developed at JYFL. POSSU itself is currently being upgraded to enable time-resolved measurements of the emission line profiles.

The commissioning status of the unconventional CUBE-ECRIS with a minimum-B quadrupole magnetic field topology is also presented. The topology, realized with all-permanent magnet structure, is based on the ARC-ECRIS [1] and is optimized for 10 GHz frequency. The status and operational experience with HIISI is reported as well.

PLASMA INVESTIGATIONS

The plasma instability studies with the 14 GHz ECRIS at JYFL have recently concentrated on exploring the plasma maser regime achieved at high $B_{\mathrm{min}}/B_{\mathrm{ECR}}$ ratio. This regime, characterized by continuous microwave emission, and the mechanism of the plasma maser formation in the ECRIS plasma was first discussed by Shalashov et al. [2, 3]. It was recently confirmed that the transition from the pulse-periodic instability regime to the cw maser regime is sometimes (with appropriate tuning and plasma heating frequency) accompanied by increased output of high charge state ions [4] exceeding the beam currents achieved below the instability threshold at $B_{\mathrm{min}}/B_{\mathrm{ECR}}$ of 0.8–0.85. The maser regime corresponds to the "islands of stability" at $B_{\mathrm{min}}/B_{\mathrm{ECR}}$ of 0.9 or higher. It is argued that the maser regime improves the extracted beam currents by enhancing the hot electron losses through the continuous particle-wave interaction, which in turn increases the ion flux by acting on the electrostatic ion confinement. The experiments in the maser regime have been carried out with plasma heating frequencies of 10.8–12.4 GHz because of the excessively high solenoid coil currents required to reach $B_{\mathrm{min}}/B_{\mathrm{ECR}} > 0.9$ with 14 GHz operation.

The JYFL-LPSC collaboration has been developing a code that describes the real 3D magnetic field topology of ECRIS by expanding the on-axis field to $r > 0$ with a 6^{th} order polynomial and superimposing it with an ideal sextupole field [5]. The main objective of the work is to extract all relevant field parameters and compare them to the experimentally found plasma instability threshold. The work aims to define the most influential parameter concerning the onset of plasma instabilities. Figure 1 shows, as an example, the distribution of the magnetic field gradient on the ECR surface of the JYFL 14 GHz ECRIS with nominal coil currents. The code has already been used to correlate the magnetic field properties, especially magnetic gradient distribution, and occurrence of plasma instabilities for SECRAL-II [6] and JYFL 14 GHz ECRIS [7].

The JYFL-GANIL-LPSC collaboration has been developing diagnostic methods for measuring and studying cumulative and population confinement times of ions in the ECRIS plasmas. The temporal evolution of the ion populations is defined by ionization and charge exchange processes, and ion confinement time as per the balance equation [8]. The confinement time must be long enough to allow highly charged ion formation via the stepwise ionization process, but also as short as possible to produce high extraction currents. It is a critical parameter especially in the production

* Work supported by the Academy of Finland (Project funding No. 315855)
† email address: miha.s.p.marttinen@jyu.fi

ISBN: 978-3-95450-226-4 ISSN: 2222-5692 doi:10.18429/JACoW-ECRIS2020-TUZZO02

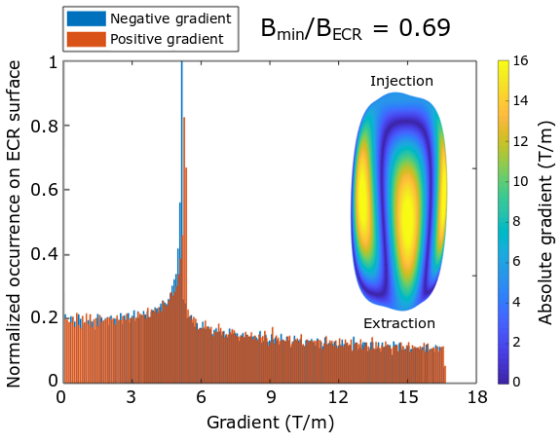

Figure 1: An example of the magnetic field gradient distribution on the (cold electron) ECR surface of JYFL 14 GHz ECRIS with nominal solenoid currents.

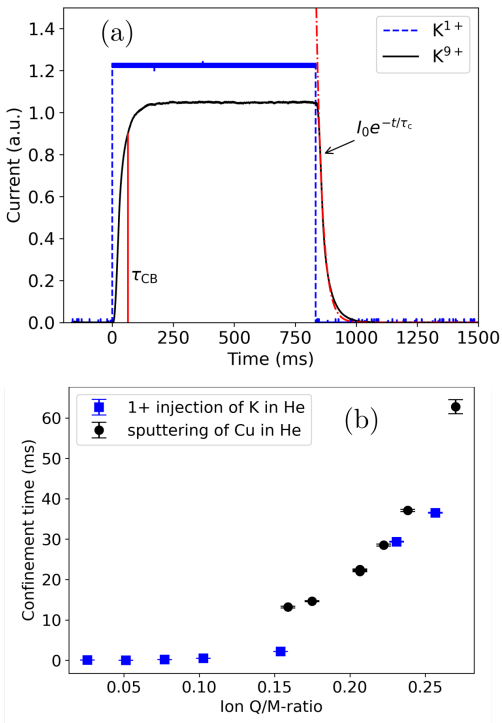

Figure 2: An example of extracted K^{9+} (black line) with pulsed injection of K^+ (dashed line) into a helium buffer (a) and a comparison of obtained τ_c^q using 1+ injection in a CB-ECRIS and sputtering in a conventional ECRIS (b). The exponential fit defining τ_c as well as the conventional charge breeding time τ_{CB} are also plotted.

of Radioactive Ion Beams (RIBs) for nuclear physics studies due to the decay of the injected isotopes.

The confinement time has been studied via transient methods using 1+ injection into a charge breeder and sputtering in a conventional ECRIS. The basic principle of the transient method is to inject material in pulses into a support plasma, and observe the time structure of the extracted ion currents.

Figure 2 (a) shows a current transient resulting from injection of potassium into a Charge Breeder ECRIS (CB-ECRIS). The cumulative confinement time τ_c is determined by means of an exponential fit to the decaying current transient as indicated in Fig. 2 (a). It has been argued to represent the total ion lifetime in plasma, as the decaying current is fed by ionization from lower states and charge exchange from higher states and conversely diminished by ionization to higher and charge exchange to lower states [10]. The conventional measure for the charge breeding time τ_{CB} (the 90 % rise time of the current) is also indicated in the figure. Alternative methods for determining the charge breeding time based on short pulse injection have been presented in Ref. [9].

Mutually corroborative results have been obtained from CB and conventional ECRIS as shown in Fig. 2 (b) [10]. The τ_c values obtained from the measurements have been shown to be long enough to allow ion heating via electron drag to temperatures on the order of 10 eV, offering a potential explanation for the observed ion temperatures ranging from 5 eV to 28 eV [11].

A high-resolution spectrometer POSSU, developed at JYFL, has proven to be a very powerful tool for ECRIS plasma diagnostics. It has been used to probe densities of ions and neutral atoms [12], temperature of the cold electron population [13] and ion temperature [11]. POSSU has a Fastie-Ebert type monochromator with two slits (entrance and exit) and rotating diffraction grating. The scanning time of an emission line profile with this configuration is approximately 10 minutes. The ongoing technical development to improve the spectrometer beyond its present capabilities aims to enable time-resolved measurement of the line profiles of relatively strong emission lines such as 488 nm of Ar^+ and 553 nm of Ar^{9+} with ms-level temporal resolution [14]. The modifications required to achieve this include the minimization of the astigmatism with circular entrance slit, optimization of the throughput of the monochromator and replacing the photomultiplier detection system with a high-sensitivity, high-speed, peltier cooled sCMOS detector. The experiments that become available after the ongoing upgrade include time-resolved measurements of the ion temperatures.

SOURCE DEVELOPMENT

The HIISI ECR ion source [15–17] was designed and constructed during 2015-2017. The testing, which was started in Fall 2017, demonstrated the feasibility of an innovative permanent magnet cooling scheme and a capability of HIISI to produce very high charge states, like Xe^{44+}, required by the user community of the JYFL Accelerator Laboratory. The commissioning experiments were started with 24-segment hexapole ($B_{rad} \approx 1.32$ T). As a result of an unexpected overheating problem the tuning range and operational time of HIISI were strongly limited. The problem was resolved for the stronger 36-segment hexapole structure ($B_{rad} \approx 1.42$ T) construction of which was started in the beginning of 2018. Together with the stronger radial confinement and increased

ISBN: 978-3-95450-226-4 ISSN: 2222-5692 doi:10.18429/JACoW-ECRIS2020-TUZZO02

microwave power (up to 3 kW) available for the plasma heating the intensity of e.g. Ar^{16+} ion beam has increased from 54 µA to 130 µA.

After a short commissioning period, HIISI has been used for the nuclear physics program always when high beam intensity, high charge states or high beam stability is required. Figure 3 shows the injection structure of HIISI: the center of the bias disk is made of magnetic iron (AISI 1006) to maximize the injection magnetic field value (2.8 T). The figure also shows V and Au samples mounted in the plasma flux area on the surface of the non-magnetic part of the bias disk (SAE316). As a result of the arrangement, the ion flux of $1 \cdot 10^5$ particles/s/cm^2 on the experimental target was easily exceeded in the case of $^{51}V^{18+}$ and $^{197}Au^{54+}$ ion beams.

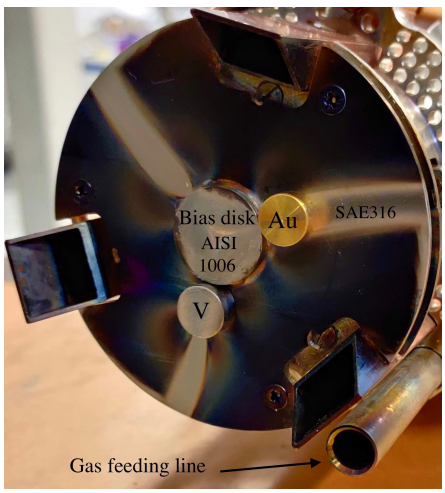

Figure 3: Injection geometry of HIISI including samples for V and Au ion beam production.

Another ion source currently under development at JYFL is the CUBE-ECRIS. It has a minimum-B quadrupole field topology which conforms to the conventional ECRIS scaling laws for 10 GHz microwave operation. A detailed description of the design is presented in Ref. [18]. The magnetic field structure is based on the ARC-ECRIS concept [1], but realized with an all permanent magnet assembly. The aim of the CUBE-ECRIS project is to study the production of highly charged ion beams with a quadrupole field topology and demonstrate beam formation and transport with a slit extraction system, comparing the performance to a conventional ECRIS. Being successful, this alternative topology could have high potential for future ECRIS development, as it has been shown to be scalable to reach appropriate mirror ratios for 100 GHz operation using the existing superconductor technology [19].

The construction of the CUBE-ECRIS was commenced in Spring 2020 and the permanent magnet assembly was completed in September 2020. The assembly is presented in Fig. 4. The resulting magnetic field was verified by measuring the B_y and B_x components of the field along the y direction through the magnetic structure, crossing $B_{\min}$ at $y = 0$. The measured and simulated fields are presented in Fig. 5. The first plasma is expected in the first quarter of 2021.

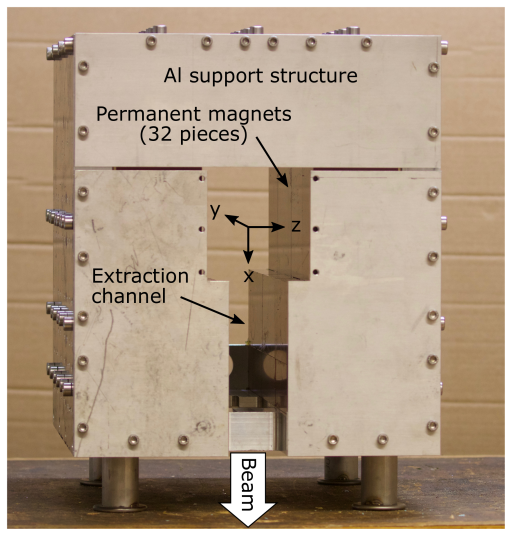

Figure 4: The CUBE-ECRIS permanent magnet assembly inside the Al support structure.

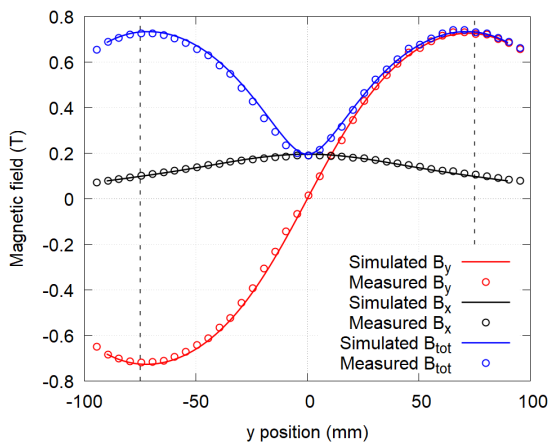

Figure 5: Comparison of simulated and measured magnetic field of the CUBE-ECRIS. Plasma chamber walls are indicated with dashed vertical lines.

REFERENCES

[1] P. Suominen, T. Ropponen, and H. Koivisto, "First results with the yin-yang type electron cyclotron resonance ion source," *Nucl. Instrum. Methods Phys. Res., Sect. A* vol. 578, issue 2, pp. 370–378, Aug. 2007. doi:10.1016/j.nima.2007.05.324

[2] A. G. Shalashov, E. D. Gospodchikov, I. V. Izotov, D. A. Mansfeld, V. A. Skalyga, and O. Tarvainen, "Observation of Poincaré-Andronov-Hopf Bifurcation in Cyclotron Maser Emission from a Magnetic Plasma Trap," *Phys. Rev. Lett.*, vol. 120, issue 15, p. 155001, Apr. 2018. doi:10.1103/PhysRevLett.120.155001

ISBN: 978-3-95450-226-4 ISSN: 2222-5692 doi:10.18429/JACoW-ECRIS2020-TUZZO02

[3] A. G. Shalashov, E. D. Gospodchikov, I. V. Izotov, D. A. Mansfeld, V. A. Skalyga, and O. Tarvainen, "Control of electron-cyclotron instability driven by strong ECRH in open magnetic trap," *Europhys. Lett.*, vol. 124, no. 3, p. 35001, 2018. doi:10.1209/0295-5075/124/35001

[4] V. A. Skalyga *et al.*, "Controlled turbulence regime of electron cyclotron resonance ion source for improved multicharged ion performance," submitted to Phys. Rev. Lett. (2020).

[5] J. R. M. Vaughan, "Representation of axisymmetric magnetic fields in computer programs," *IEEE Trans. Electron Devices*, vol. 19, issue 2, pp. 144–151, Feb. 1972. doi:10.1109/T-ED.1972.17390

[6] J. Li *et al.*, "Effects of magnetic configuration on hot electrons in a minimum-B ECR plasma," *Plasma Phys. Controlled Fusion*, vol. 62, no. 9, p. 095015, 2020. doi:10.1088/1361-6587/ab9d8f

[7] B.S. Bhaskar *et al.*, to be published.

[8] G.D. Shirkov, C. Mühle, G. Musiol, and G. Zschornack, "Ionization and charge dispersion in electron cyclotron resonance ion sources," *Nucl. Instrum. Methods Phys. Res., Sect. A*, vol. 302, no. 1, pp. 1–5, 1991. doi:10.1016/0168-9002(91)90485-9

[9] J. Angot *et al.*, "Charge breeding time investigations of electron cyclotron resonance charge breeders," *Phys. Rev. Accel. Beams*, vol. 21, no. 10, p. 104801, 2018. doi:10.1103/physrevaccelbeams.21.104801

[10] M. Marttinen *et al.*, "Estimating ion confinement times from beam current transients in conventional and charge breeder ECRIS," *Rev. Sci. Instrum.*, vol. 91, no. 1, p. 013304, 2020. doi:10.1063/1.5128546

[11] R. Kronholm *et al.*, "Spectroscopic study of ion temperature in minimum-B ECRIS plasma," *Plasma Sources Sci. Technol.*, vol. 28, no. 7, p. 075006, 2019. doi:10.1088/1361-6595/ab27a1

[12] R. Kronholm *et al.*, "The effect of microwave power on the Ar^{9+} and Ar^{13+} optical emission intensities and ion beam currents in ECRIS," *AIP Conf. Proc.*, vol. 2011, p. 040014, 2018. doi:10.1063/1.5053288

[13] R. Kronholm, T. Kalvas, H. Koivisto, and O. Tarvainen, "Spectroscopic method to study low charge state ion and cold electron population in ECRIS plasma," *Rev. Sci. Instrum.*, vol. 89, no. 4, p. 043506, 2018. doi:10.1063/1.5023434

[14] R. Kronholm *et al.*, "ECRIS plasma spectroscopy with a high resolution spectrometer," *Rev. Sci. Instrum.*, vol. 91, no. 1, p. 013318, 2020. doi:10.1063/1.5128854

[15] H. Koivisto *et al.*, "HIISI, new 18 GHz ECRIS for the JYFL accelerator laboratory," in *Proc. ECRIS'14*, Nizhny Novgorod, Russia, Aug. 2015, p. TUOMMH05, ISBN 978-3-95450-158-8.

[16] T. Kalvas, O. Tarvainen, H. Koivisto, and K. Ranttila, "Thermal design of refrigerated hexapole 18 GHZ ECRIS HIISI," in *Proc. ECRIS'14*, Nizhny Novgorod, Russia, Aug. 2015, p. WEOMMH04, ISBN 978-3-95450-158-8.

[17] H. Koivisto *et al.*, "A new 18 GHz room temperature electron cyclotron resonance ion source for highly charged ion beams," *Rev. Sci. Instrum.*, vol. 91, no. 2, p. 023303, 2020. doi:10.1063/1.5128860

[18] T. Kalvas, O. Tarvainen, V. Toivanen, and H. Koivisto, "Design of a 10 GHz minimum-B quadrupole permanent magnet electron cyclotron resonance ion source," *J. Instrum.*, vol. 15, no. 06, p. P06016, 2020. doi:10.1088/1748-0221/15/06/P06016

[19] P. Suominen and F. Wenander, "Electron cyclotron resonance ion sources with arc-shaped coils," *Rev. Sci. Instrum.*, vol. 79, no. 2, p. 02A305, 2008. doi:10.1063/1.2805209

ISBN: 978-3-95450-226-4 ISSN: 2222-5692 doi:10.18429/JACoW-ECRIS2020-TUZZO04

STATUS OF THE 60 GHZ ECR ION SOURCE RESEARCH

T. André*[1], T. Thuillier[1], P. Sole[1], M. Baylac[1], J. Angot[1], F. Debray[2], I. Izotov[3], and V. Skalyga[3]

[1]Université Grenoble-Alpes, CNRS-IN2P3, LPSC, 38000 Grenoble, France
[2]LNCMI, CNRS-UGA-UPS-INSA, 25, avenue des Martyrs, 38042 Grenoble, France
[3]Institute of Applied Physics, RAS, 46 Ulyanova St., 603950 Nizhny Novgorod, Russian Federation

Abstract

SEISM (**S**ixty gigah**E**rtz **I**on **S**ource using **M**egawatt magnets) is a compact ECR ion source operating at 60 GHz. The prototype uses a magnetic CUSP to confine the plasma. This simple magnetic geometry was chosen to allow the use of polyhelix coils (developed at LNCMI, Grenoble) to generate a strong magnetic confinement featuring a closed ECR surface at 2.14 T. The plasma is sustained by a 300 kW microwave pulse of 1 ms duration and with a 2 Hz repetition rate. Previous experiments at LNCMI have successfully demonstrated the establishment of the nominal magnetic field and the extraction of ion beams with a current density up to ~1 A cm^{-2}. The presence of "afterglow" peaks was also observed, proving the existence of ion confinement in a CUSP ECR ion source. The last run was prematurely stopped due to an incident but the project restarted in 2018 and new experiments are planned in 2021. A new transport beam line has been designed to improve ion beam transport towards the beam detectors. Short and long-term research plans are presented, including numerical simulations of the beam transport line and future upgrades of the ion source with the main goal to transform the high current density measured into a useable high intensity ion beam.

MOTIVATION

In 2014, the experimental 60 GHz ECR ion source, SEISM, produced ion beams with a current density up to $J \approx 1$ A cm^{-2} [1] using a CUSP magnetic configuration [2] with a closed ECR surface. These results were obtained with a 1 mm diameter plasma electrode to manage the beam in a low acceptance beam line. Such a high current density in a CUSP configuration is so far unique in the field of the ECR ion source and it opens new potential applications for next generation particle accelerators. The experiment was incidentally stopped in 2014 by the presence of a stainless steel wire in the water cooling system which created a short cut between two of the four ion source coils and destroy them. At the restart of the project in 2018, an analysis was launched to improve the implantation and the performances of the experiment installed in one of the LNCMI experimental hall.

* thomas.andre@lpsc.in2p3.fr

SHORT TERMS PLANS

Experiment upgrade

First, the two coils that were damaged during the previous experimental campaign have to be reconstructed. Second, the analysis beam line originally solely composed of a bending magnet has beam revised in order to improve the transmission of the beam line. To do so, numerical simulations were performed with the Tracewin code [3], and a new design using existing available equipements was decided. Figure1 shows the new implantation of the experiment. In this configuration, the transport line is composed of a quadrupole triplet with 150 mm gap to ensure focusing of the ion beam and the original dipole with a 60 mm gap was replaced by an existing dipole with a larger gap of 90 mm and a horizontal aperture of 300 mm. Transport simulations indicate that the theoretical transmission could reach 90 % for a 1 mm plasma electrode diameter.

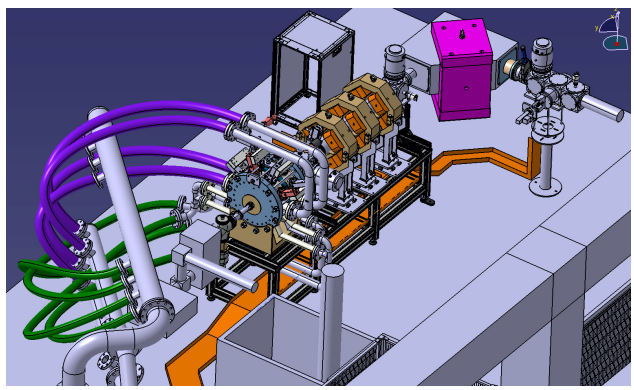

Figure 1: 3D view of the new implantation of the SEISM ion source at LNCMI laboratory.

Another upgrade concerns the range of pressure available in the source. Indeed the existing plasma chamber had a vacuum leak limitating its base pressure to 10^{-5} mbar. A new plasma chamber design was done to solve the issue and reach 10^{-7} mbar. This improvement will also allow to increase the voltage applied on the extraction of the source from 25 up to 40 kV to improve the beam line transport.

Objectives of future experimental sessions

A new experimental campaign is scheduled in 2021 on the SEISM source. Thanks to the upgrade of the beam line, one should be able to reliably reproduce the data obtained in 2014. One experimental goal is to characterize the high

ISBN: 978-3-95450-226-4 ISSN: 2222-5692 doi:10.18429/JACoW-ECRIS2020-TUZZO04

density plasma as a function of the source parameters such as, magnetic field, gas pressure, HF power and the radial biased ring voltage, located between the the two CUSP coils (see Fig. 2).

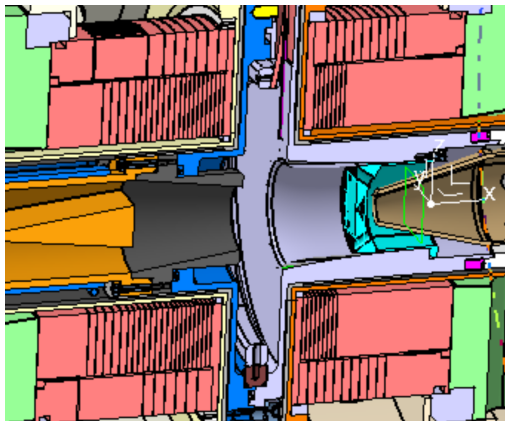

Figure 2: 3D cut view of the SEISM source. Polyhelix (pink), plasma chamber (light grey and blue).

A concomitant monitoring of the plasma stability will be done during the experiments using the technique described in reference [4] . Another point of interest for measurements will be to measure lost electron energy distribution (LEED) which is unknown from a CUSP. Finally, a complete characterisation of the ion beam will be performed. The beam current will be measured in different location, giving information on the transport of very intense beam, and the emittance will be measured by a pepperpot device [5].

LONG TERM PLANS

PACIFICS is a joint project carried by IN2P3 and CEA dedicated to perform high level research and development in the field of particle accelerators. The collaboration answered in 2020 to the EQUIPEX call by the French Agence Nationale de la Recherche. The answer to the call is pending at the time of writting of this document. PACIFICS includes a work package dedicated to the enhancement of high intensity beams for the next generation accelerators. It includes a significant budget for equipements and the priority is first to relocate the SEISM source from LNCMI to LPSC. This action requires to replace the existing resistive coils by a set of superconducting ones [6] . Indeed, experiments at LNCMI are limited to roughly two weeks per year which slows down the research (magnetic field time at LNCMI is shared among several users and must be approved by the European European Magnetic Field Laboratory through calls for experiment). A second priority is to upgrade the 60 GHz gyrotron high voltage power supply from pulsed to 20 kW continuous working (CW) operation. Next, the main goal is to enlarge the plasma electrode extraction hole of SEISM to investigate the production of high intensity beams of medium charge state ions in pulsed and CW operation. It is planned to install an extraction system identical to the SILHI ion source and study the beam emittance and beam neutralisation in a simple LEBT equiped with a diagnostic box and a beam dump. A study was done to investigate the possible geometry of the superconductive coils of the ion source, the goal being to produce a closed 2.14 T ECR surface with two coils arranged in a single cryostat. The parameter varied in the study is the diameter of the plasma chamber taken as 150 mm, 200 mm and 250 mm. The cable used for these simulations has a rectangular section of 1.08×0.68 mm with a Cu:NbTi ratio of 1.35:1 from Oxford Instruments [7]. For each configuration, one considers two coils of rectangular section with opposite current applied to reproduce the CUSP configuration. Dimensions of the coils were adjusted to obtain the closed ECR surface at 2.14 T with an added criteria to have a 10 mm minimum distance between the ECR zone and the plasma chamber wall . Table 1 summarizes the coils main parameters for the 250 mm case.

Table 1: Coils Parameters for a 250 mm Plasma Chamber Diameter

	Solenoid 1	Solenoid 2
Axial position [mm]	-60	+60
Inner Diameter [mm]	165	165
Depth [mm]	40	40
Width [mm]	200	200
Turn/layer	185	185
Number of layer	59	59
Turn /coil	10915	10915
Design current [A]	272	272
Length of cable [km]	9.6	9.6
B_{max} at coil (at design current) [T]	5.9	5.9

Figure 3 shows the fieldmap in the case of the 250 mm diameter for the plasma chamber. In this figure, the white rectangle represents the coils, and the blue line represents the plasma chamber wall. In this example, one can see that a closed surface at 2.14 T, corresponding to the magnetic field needed to achieved resonance at 60 GHz, is present. The closed surface is here located 1.6 cm (see Fig. 5) away from the plasma chamber wall, value well above the minimum target design value of 1 cm.

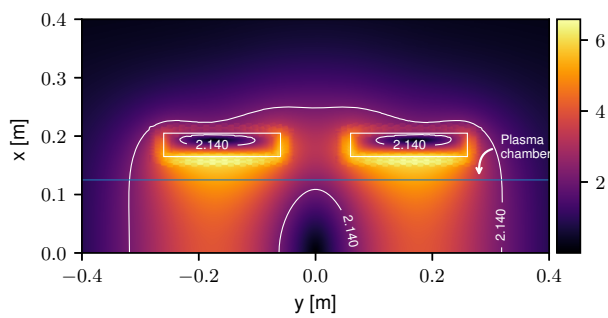

Figure 3: Field map for 250 mm diameter plasma chamber . Plasma chamber (blue). Surface of 2.14 T

To verify the feasibility of the magnetic configuration, one of the important criteria is to verify if the coil loadline

ISBN: 978-3-95450-226-4 ISSN: 2222-5692 doi:10.18429/JACoW-ECRIS2020-TUZZO04

is not too close of the critical curve of the superconducting cable at 4.2 K. Figure 4 shows the loadlines for the three cases studied . For every case, the coil loadline are always under 85 % of the critical current.

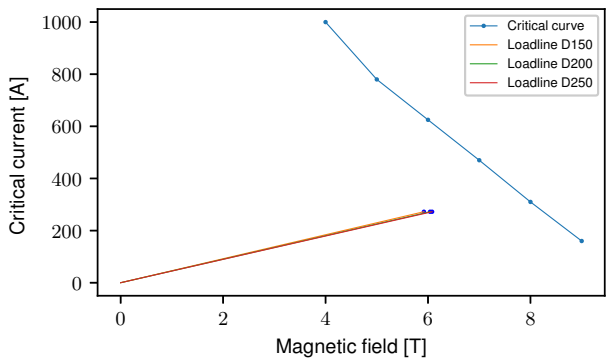

Figure 4: Load lines for the different plasma chamber diameter.

Figure 5 presents the evolution of the distance between the ECR zone and the chamber wall as a function of the diameter of the plasma chamber. One can see that, for all cases, the distance is always above 1 cm, the minimum distance wanted.

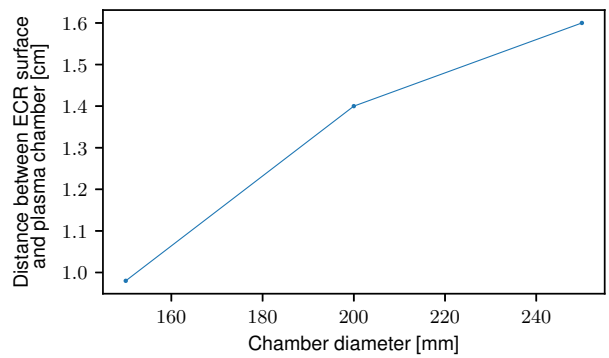

Figure 5: Evolution of the distance between the plasma chamber and the ECR surface for different plasma chamber diameter.

The stored energy in the system is display in Fig. 6 as a function of the chamber diameter.

Figures 7 and 8 respectively present the axial ($r = 0$) and radial ($z = 0$) magnetic field for the three configurations corresponding to the three diameter of the plasma chamber. Table 2 summarizes the magnetic fields properties for each configuration.

Table 2: Magnetic Field Properties

Plasma chamber diameter [mm]	150	200	250
B_{z-max} [T]	4.07	4.08	4.02
B_{r-max}[T]	2.45	2.54	2.47

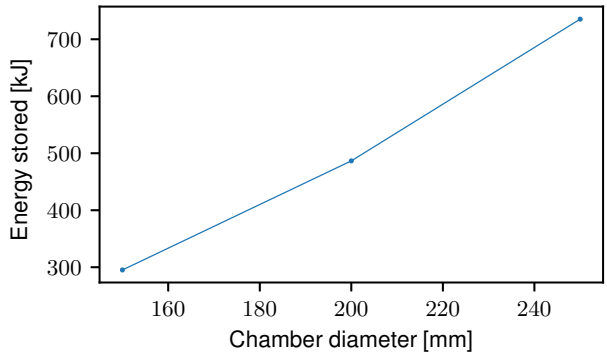

Figure 6: Magnetic energy stored in the system for different plasma chamber diameter .

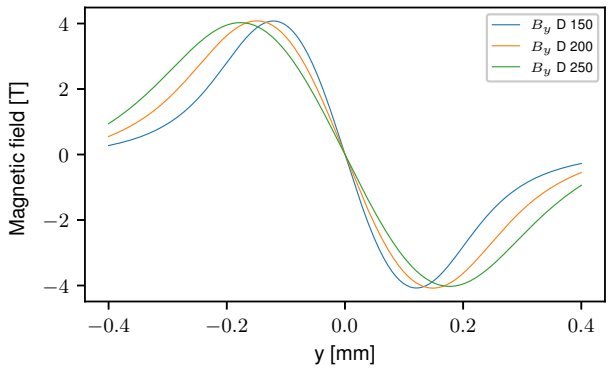

Figure 7: Axial magnetic field on axis (r=0) for the different configuration corresponding to the different plasma chamber diameter.

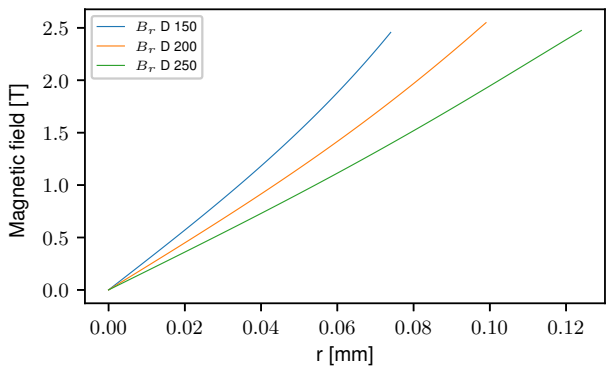

Figure 8: Radial magnetic field at the center of the chamber different configuration corresponding to the different plasma chamber diameter.

CONCLUSION

SEISM ion source R&D will resume in 2021 when a new experimental campaign will happen. Long term plan aims to relocate the ECRIS at LPSC to ease the research and demonstrate the production of very intense CW beam of medium charge state ions.

ISBN: 978-3-95450-226-4 ISSN: 2222-5692 doi:10.18429/JACoW-ECRIS2020-TUZZO04

REFERENCES

[1] T. Lamy, J. Angot, M. Bakulin, F. Debray, J. Dumas, A. Eremeev, C. Grandclement, I. Izotov, J. Jacob, B. Movshevich, et al. 60 ghz ecr ion sources. In *13th Heavy Ion Accelerator Technology Conference (HIAT2015), Yokohama, Japan, 7-11 September 2015*, pages 277–281. JACOW, Geneva, Switzerland, 2016.

[2] L. Latrasse et al.: "A 60 ghz cusp electron cyclotron resonance ion source." Rev. Sci Instrum, vol. 81, p. 02A324, 2010.

[3] Tracewin software, http://irfu.cea.fr/en/Phocea/Page/index.php?id=780

[4] O. Tarvainen et al. "Plasma diagnostic tools for ecr ion sources—what can we learn from these experiments for the next generation sources." Rev. Sci Instrum., vol. 90, p. 113321, 2019.

[5] M. Zhang. Emittance formula for slits and pepper-pot mea-surement. Technical report, Fermi National Accelerator Lab., Batavia, IL (United States), 1996.

[6] T. Thuillier et al. "Prospect for a 60 ghz multicharged ecr ion source." *Rev. Sci. Instrum.* vol. 89, p. 052302, 2018.

[7] Oxford Instruments, https://www.oxinst.com

ISBN: 978-3-95450-226-4 ISSN: 2222-5692 doi:10.18429/JACoW-ECRIS2020-TUZZO05

MULTI-SPECIES CHILD-LANGMUIR LAW WITH APPLICATION TO ECR ION SOURCES * †

Chun Yan Jonathan Wong‡, Oak Ridge National Laboratory, Oak Ridge, USA
Steven Mocko Lund, Facility for Rare Isotope Beams, East Lansing, USA

Abstract

We generalize the classical single-species Child-Langmuir Law to analyze multi-species beams from ECR ion sources. The formulation assumes the relative weight of each species in the extracted beam is known. We apply the results to charge state distribution data from Artemis- and Venus-type sources at the NSCL and LBNL respectively. The total measured beam current is close to the maximum current predicted by the multi-species Child Langmuir law in each case, which indicates that beam extraction occurs close to space-charge-limited flow conditions. Prospects for application of the results and further studies on the topic are outlined.

INTRODUCTION

The classical Child-Langmuir law [1, 2] describes the maximum steady state current that can be transported within a diode given the following assumptions: 1) the diodes are infinite planes with uniform emission which renders the problem one-dimensional; 2) the charged particles are emitted with zero initial velocity (i.e. cold); 3) there is only one species of charged particles; and 4) the particles are non-relativistic. In such a system, space charge forces limit the current that can be transmitted and the maximum current density is given by:

$$J = \frac{4\sqrt{2}}{9}\epsilon_0\sqrt{\frac{q}{m}}\frac{V_0^{3/2}}{d^2} \tag{1}$$

where q and m are the charge and mass of the charged particle, V_0 and d are the potential difference and distance between the cathode and anode, and ϵ_0 is the permittivity of free space. Only ions are considered in this study so we take q to be always positive. If the current density exceeds the limit in Eq. (1), the E-field at the emitting surface would reverse its polarity and "choke" the flow. This space-charge-limited current, also called the Child-Langmuir (CL) current, scales as V_0 to the power 3/2.

* Work supported by the U.S. DOE Office of Science under Cooperative Agreement DE-SC0000661 and the NSF under Grant No. PHY-1565546 while Chun Yan Jonathan Wong was previously at the National Superconducting Cyclotron Laboratory, East Lansing, USA.

‡ wongchu1@msu.edu

In this paper, we discuss how the classical Child-Langmuir law can be generalized to a multi-species case, i.e. when the beam consists of charged particles with multiple distinct charge-to-mass ratios. The generalized solution is applied to Electron Cyclotron Resonance (ECR) ion sources which typically extract ions with many different charge states.

MULTI-SPECIES CHILD-LANGMUIR LAW

To generalize the single-species Child-Langmuir law to multi-species, we first observe that the single-species solution is derived from a set of three equations:

$$\text{Poisson equation:} \quad \frac{d^2}{dz^2}\Phi = \frac{1}{\epsilon_0}\rho \tag{2}$$

$$\text{continuity equation:} \quad J = \rho v = \text{const} \tag{3}$$

$$\text{energy conservation:} \quad \Phi = \frac{1}{2}\frac{m}{q}v^2 \tag{4}$$

where z is the axial coordinate and $\Phi = V_0 - \phi$ with ϕ being the electric potential and V_0 being the potential difference between the two electrodes. Φ so defined gives $\Phi(z = 0) = 0$ at the cathode and $\Phi(z = d) = V_0$ at the anode, which simplify the equations when q is positive. ρ is the charge density, v is the beam velocity and the other quantities have the same definition as in Eq. (1). Note that Φ, ρ and v are all functions of z.

For the same diode system with n distinct species:

$$\text{Poisson equation:} \quad \frac{d^2}{dz^2}\Phi = \frac{1}{\epsilon_0}\sum_{i=1}^{n}\rho_i \tag{5}$$

$$\text{continuity equations:} \quad J_i = \rho_i v_i = \text{const} \tag{6}$$

$$\text{energy conservation:} \quad \Phi = \frac{1}{2}\frac{m_i}{q_i}v_i^2 \tag{7}$$

where all symbols with subscript i denote the respective variables of the i-th species. The Poisson equation couples all species, whereas each species has its own continuity equation and energy conservation equation. Hence the multi-species system is described by a total of $(2n + 1)$ equations.

Inspired by the two-species solution in the problem set of [3], one way to solve for the maximum current density in the multi-species case is to recast the $(2n + 1)$ equations into 3 equations that resemble the form of Eq. (2) - (4) as follows:

$$\text{Poisson equation:} \quad \frac{d^2}{dz^2}\Phi = \frac{1}{\epsilon_0}\rho \tag{8}$$

$$\text{continuity equation:} \quad J = \rho v_{\text{eff}} = \text{const} \tag{9}$$

$$\text{energy conservation:} \quad \Phi = \frac{1}{2}\left[\frac{m}{q}\right]_{\text{eff}} v_{\text{eff}}^2 \tag{10}$$

ISBN: 978-3-95450-226-4 ISSN: 2222-5692 doi:10.18429/JACoW-ECRIS2020-TUZZO05

where v_{eff} is an effective velocity and $[m/q]_{\text{eff}}$ is an effective mass-to-charge ratio. The total charge and current densities ρ and J are given by:

$$\rho = \sum_{i=1}^{n} \rho_i \tag{11}$$

$$J = \sum_{i=1}^{n} J_i \tag{12}$$

If such a transformation exists, the multi-species problem is reduced to single-species and the classical Child-Langmuir solution immediately follows:

$$J = \frac{4\sqrt{2}}{9}\epsilon_0 \sqrt{\left[\frac{q}{m}\right]_{\text{eff}}} \frac{V_0^{3/2}}{d^2} \tag{13}$$

where

$$\left[\frac{q}{m}\right]_{\text{eff}} \equiv \left(\left[\frac{m}{q}\right]_{\text{eff}}\right)^{-1} \tag{14}$$

The effective velocity v_{eff} in Eq. (10) is fixed by Eq. (9) and is just the proportionality constant between J and ρ. Therefore, the key to solving the multi-species Child-Langmuir law is finding the correct effective mass-to-charge ratio $[m/q]_{\text{eff}}$ such that Eq. (10) holds. We prove in the Appendix that the effective mass-to-charge ratio is:

$$\left[\frac{m}{q}\right]_{\text{eff}} = \left(\sum_{i=1}^{n} c_i \sqrt{\frac{m_i}{q_i}}\right)^2 \tag{15}$$

where

$$c_i \equiv J_i / J \tag{16}$$

denotes the current weight of the i-th species which we presume to be specified.

A comparison between the multi-species solution in Eq. (13), and the single-species solution in Eq. (1), of the Child-Langmuir law shows that the only difference lies in the charge-to-mass ratio. This means that all information relevant to the multi-species nature of the problem is encapsulated in the effective charge-to-mass ratio given by Eq. (15), and the dependence of the maximum current density on all other parameters remains identical. This is also precisely the reason it was possible to reduce the multi-species problem to single-species in the first place.

APPLICATION TO ECR ION SOURCES

Beams from ECR ion sources typically contain $\gtrsim$ 10 species whose respective currents are routinely measured to obtain the charge state distribution (CSD). With knowledge of the current weights c_i in Eq. (15) via the CSD, the multi-species Child-Langmuir law is readily applicable to the beam extraction system to determine the maximum transmittable current and to analyze whether the extraction process is consistent with space-charge-limited flow.

In terms of atomic number A and charge state Q, the maximum current density can be expressed as:

$$J = 5.47 \times 10^{-8} \sqrt{\left[\frac{Q}{A}\right]_{\text{eff}}} \frac{V_0^{3/2}}{d^2} \left[\text{A/m}^2\right] \tag{17}$$

where

$$\left[\frac{Q}{A}\right]_{\text{eff}} = \left(\sum_{i=1}^{n} c_i \sqrt{\frac{A_i}{Q_i}}\right)^{-2} \tag{18}$$

For a circular emitting surface with radius R, ignoring 2D effects, the multi-species Child-Langmuir current is:

$$I = \pi R^2 J = 5.43 \left[\frac{Q}{A}\right]_{\text{eff}}^{1/2} \left(\frac{R}{d}\right)^2 (V_0[\text{kV}])^{3/2} \,[\text{mA}] \tag{19}$$

We applied Eq. (19) to CSD measurements of the ECRs ARTEMIS-A [4] from the NSCL and VENUS [5] from LBNL. The CSDs are plotted in Fig. 1 with a summary of the results in Table 1. The total measured current is the sum of the measured currents of all species. Due to beam losses between the source and the Faraday cup, the total measured current should be $\leq$ the drain current supplied to the source. Ideally, the drain current is expected to be a better estimate of the current that is extracted from the ECR. Table 1 also lists extraction system parameters and the associated maximum currents predicted by the single- and multi-species Child-Langmuir law. The target species is used in the single-species case as is conventional.

Table 1: Measurement results, extraction parameters and predictions of single- and multi-species Child-Langmuir (CL) law for the data sets shown in Fig. 1.

Parameter	**ARTEMIS-A**	**VENUS**
Number of species meas.	8	20
Target species	$^{16}O^{4+}$	$^{238}U^{33+}$
Total measured current	0.74 mA	2.97 mA
Drain current	1 to 2 mA	no data
Extraction aperture R	4 mm	4 mm
Extraction gap d	40 mm	40 mm
Extraction voltage V_0	20 kV	30 kV
$[Q/A]_{\text{target-species}}$	0.250	0.139
$[Q/A]_{\text{effective}}$	0.191	0.131
Target species CL current	2.43 mA	3.32 mA
Multi-species CL current	2.12 mA	3.23 mA

In both data sets, the effective charge-to-mass ratio calculated from all measured species is smaller than that of the target species. The difference can be over 20%. The total measured beam current or drain current is close to the multi-species Child-Langmuir current which indicates that the ECR extraction region may be operating at, or close to, space-charge-limited flow.

ISBN: 978-3-95450-226-4 ISSN: 2222-5692 doi:10.18429/JACoW-ECRIS2020-TUZZO05

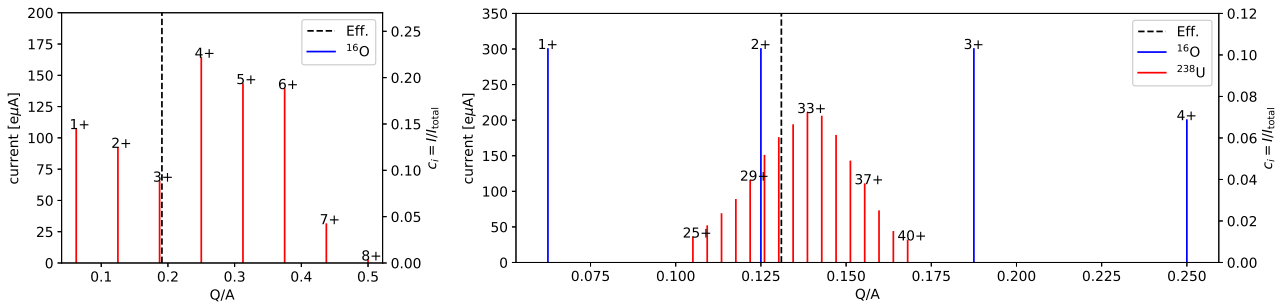

(a) ARTEMIS-A from NSCL

(b) VENUS from LBNL

Figure 1: Measured charge state distribution and the corresponding effective charge-to-mass ratio (dashed line) for: a) ARTEMIS-A producing ^{16}O [6] ;and b) VENUS producing ^{238}U with ^{16}O as the support gas [7]. Each plot shows both the species current (left scale) and its proportion in the total current (right scale).

CONCLUSION

We generalized the classical single-species Child-Langmuir law to study the maximum transportable current in a multi-species system. The solution is found to depend on the charge-to-mass ratio of each component species and its relative weight in the total current. When applied to data sets from ARTEMIS-A and VENUS, the maximum current predicted by the multi-species Child-Langmuir law is close to the total extracted current. These results suggest that the extraction region of ECR ion sources are operating near space-charge-limited flow. This phenomenon may have interesting implications - at fixed extraction parameters, desired increase in the current of high charge state target species must be accompanied by a decrease in currents of other species.

Further studies are required to investigate whether the multi-species Child-Langmuir law can be extended to include the effects of initial ion temperature, electron neutralization and finite emitting region which renders the problem two-dimensional. In particular, escaping electrons not immediately swept back into the plasma chamber may alter the singular charge density at the emission plane associated with CL-type solutions. Progress in extending the model should enhance physical insight on space-charge-limited transport and provide a more accurate limit on the maximum current in an ECR extraction system.

While preliminary comparisons have shown that the multi-species Child-Langmuir current is close to the total extracted current for one extraction configuration, performing experiments to check whether the extracted current varies as $V_0^{3/2}$ will constitute a stronger test on whether ECR beam extraction is space charge limited. During such studies, it will also be interesting to observe whether the effective charge-to-mass ratio changes with extraction voltage, and, if it does, one can explore the implications of individual species not following the $V_0^{3/2}$ scaling. One can also investigate whether ECR scaling relations can be used to constrain the current weights c_i and hence the effective charge-to-mass ratio. This would enable the multi-species Child-Langmuir law to make predictions in the absence of CSD measurement results and enhance its utility in planning and design.

ACKNOWLEDGEMENTS

The authors would like to thank Masanori Ikegami, Guillaume Machicoane, Eduard Pozdeyev, Jeff Stetson and Qiang Zhao from Facility for Rare Isotope Beams and Bryan Isherwood from Michigan State University for fruitful discussions and for their support in obtaining and interpreting ECR measurement results.

APPENDIX: VERIFICATION OF EQ. (15)

To verify that Eq. (15) is the correct effective mass-to-charge ratio that leads to a solution of the multi-species Child-Langmuir law, we have to prove Eq. (10). Referring to the class of energy conservation equations Eq. (7), it suffices to prove that:

$$\frac{1}{2}\left[\frac{m}{q}\right]_{\text{eff}} v_{\text{eff}}^2 = \frac{1}{2}\frac{m_i}{q_i} v_i^2 \tag{20}$$

for any i. Without loss of generality, we show this is true for the last species, i.e. for $i = n$.

The class of energy conservation equations in Eq. (7) imply:

$$\frac{m_i}{q_i} v_i^2 = \frac{m_n}{q_n} v_n^2 \tag{21}$$

for any i. This enables us to derive the following relation

$$\begin{aligned}\sum_{i=1}^{n} c_i \sqrt{\frac{m_i}{q_i}} &= \frac{1}{J}\sum_{i=1}^{n} J_i \sqrt{\frac{m_i}{q_i}} \\ &= \frac{1}{J}\sum_{i=1}^{n} \rho_i v_i \sqrt{\frac{m_i}{q_i}} \\ &= \frac{1}{J}\sum_{i=1}^{n} \rho_i v_n \sqrt{\frac{m_n}{q_n}}\end{aligned} \tag{22}$$

where the last equality sign results from the square root of Eq. (21).

ISBN: 978-3-95450-226-4 ISSN: 2222-5692 doi:10.18429/JACoW-ECRIS2020-TUZZO05

Using Eq. (22) and the definition of ρ and J as the total charge and current density, one obtains

$$\begin{aligned}\left[\frac{m}{q}\right]_{\text{eff}} v_{\text{eff}}^2 &= \left[\left(\sum_{i=1}^{n} c_i \sqrt{\frac{m_i}{q_i}}\right) v_{\text{eff}}\right]^2 \\ &= \left[\left(\sum_{i=1}^{n} c_i \sqrt{\frac{m_i}{q_i}}\right) \frac{1}{\rho}\left(\sum_{j=1}^{n} \rho_j v_j\right)\right]^2 \\ &= \left[\frac{1}{J}\left(\sum_{i=1}^{n} \rho_i v_n \sqrt{\frac{m_n}{q_n}}\right) \frac{1}{\rho}\left(\sum_{j=1}^{n} \rho_j v_j\right)\right]^2 \\ &= \left[\frac{1}{J}\left(\sum_{i=1}^{n} \rho_i\right) \frac{1}{\rho}\left(\sum_{j=1}^{n} \rho_j v_j\right)\right]^2 \frac{m_n}{q_n} v_n^2 \\ &= \frac{m_n}{q_n} v_n^2 \end{aligned} \tag{23}$$

which explicitly proves that Eq. (20) holds for $i = n$.

REFERENCES

[1] C. D. Child, "Discharge from hot CaO," *Phys. Rev. (Series I)*, vol. 32, pp. 492–511, 5 May 1911. doi : 10 . 1103 / PhysRevSeriesI.32.492.

[2] I. Langmuir, "The effect of space charge and residual gases on thermionic currents in high vacuum," *Phys. Rev.*, vol. 2, pp. 450–486, 6 Dec. 1913. doi:10.1103/PhysRev.2.450.

[3] S. Lund, "MSU Physics 905: Fundamentals of accelerator physics," course offered at Michigan State University, 2016.

[4] H. Koivisto *et al.*, "Artemis-the new ecr ion source for the coupled cyclotron facility at nscl/msu," in *Conference Proceedings-Italian Physical Society*, Editrice Compositori; 1999, vol. 72, 2001, pp. 135–140.

[5] D. Leitner *et al.*, "Next generation ECR ion sources: First results of the superconducting 28 GHz ECRIS–VENUS," *Nucl. Instrum. Methods B*, vol. 235, no. 1, pp. 486–493, 2005. doi: 10.1016/j.nimb.2005.03.230.

[6] B. Isherwood, private communication, 2016.

[7] E. Pozdeyev, private communication, 2016.

ISBN: 978-3-95450-226-4 ISSN: 2222-5692 doi:10.18429/JACoW-ECRIS2020-TUZZO06

BEAMS WITH THREE-FOLD ROTATIONAL SYMMETRY: A THEORETICAL STUDY * †

Chun Yan Jonathan Wong‡, Oak Ridge National Laboratory, Oak Ridge, USA
Steven Mocko Lund, Facility for Rare Isotope Beams, East Lansing, USA

Abstract

Beams from ECR ion sources have 3-fold transverse rotational symmetry induced by the ECR sextupole. The symmetry imposes equality constraints among transverse beam moments, which can be derived using a theoretical framework we developed. Since the constraints are solely a consequence of the rotational symmetry of external fields, they hold for a multi-species beam with arbitrary composition and space charge intensity. These constraints provide a new tool to analyze phase space properties of ECR beams and their impact on low-energy transport. We prove that, regardless of their triangulated spatial density profile, beams with 3-fold rotational symmetry have the same RMS emittance and Twiss parameters along any transverse direction. These counter-intuitive results are applied to the FRIB Front End to show how symmetry arguments challenge long-standing assumptions and bring clarity to the beam dynamics.

INTRODUCTION

In theoretical studies, a beam is commonly assumed to have inherited the rotational symmetry of the source or beam line. The symmetry arises from the fact that the system is identical under different rotated transverse coordinate systems, which is true in the idealized case when there is no misalignment and when all elements are perfect.

Two symmetries that often occur are: 1) continuous rotational symmetry in a beam line consisting of solenoids or einzel lens; and 2) 2-fold discrete rotational symmetry in quadrupole transport. In the subsequent discussion, we denote a rotational symmetry by the notation of its respective symmetry group. A beam with n-fold discrete rotational symmetry is said to have C_n symmetry or is called a C_n beam. SO(2) refers to continuous rotational symmetry, which is often called axisymmetry.

Beams extracted from ECR ion sources have C_3 symmetry imposed by the ECR sextupole. As an example, simulation results of an ECR beam at the extraction plane are shown in Fig. 1 where a rotation by $2\pi/3$ would leave the beam distribution unchanged. Concerning the the transverse RMS emittances ε_x and ε_y, three questions can be asked which are central to the quality and transport of such an ECR beam:

- Are ε_x and ε_y different due to the triangulated spatial distribution?
- Do ε_x and ε_y depend on the orientation of the transverse coordinate system (with respect to the sextupole)?
- Do ε_x and ε_y change upon x-y coupling in solenoid transport?

We perform a theoretical analysis on 2nd order moments of C_3 beams to prove that the answers to all three questions are negative. These results are counter-intuitive and contradict conventional assumptions. The significant role they can play in clarifying ECR beam dynamics is demonstrated at the Facility for Rare Isotope Beams (FRIB) Front End.

MOMENT CONSTRAINTS FROM ROTATIONAL SYMMETRY

This section examines the consequences of rotational symmetry as a property of the beam's phase space distribution. We show that rotational symmetry imposes constraints on transverse beam moments and briefly overview a framework for deriving such constraints. A thorough treatment is presented in a manuscript in preparation [1].

Define transverse beam moments

$$\left\langle x^{b_1} x'^{b_2} y^{b_3} y'^{b_4} \right\rangle \equiv \frac{\int_{-\infty}^{\infty}\int_{-\infty}^{\infty}\int_{-\infty}^{\infty}\int_{-\infty}^{\infty} F(x,x',y,y') x^{b_1} x'^{b_2} y^{b_3} y'^{b_4} dx dx' dy dy'}{\int_{-\infty}^{\infty}\int_{-\infty}^{\infty}\int_{-\infty}^{\infty}\int_{-\infty}^{\infty} F(x,x',y,y') dx dx' dy dy'}$$

where $F(x,x',y,y')$ is the distribution function in transverse phase space and b_1, b_2, b_3, b_4 are non-negative integers. F can refer to the phase space distribution of a single species or multiple species. The moment is said to be of k-th order with $k = b_1 + b_2 + b_3 + b_4$. The definition assumes all 1st order moments vanish - it must be true when the beam has non-trivial rotational symmetry (see proof in [1]) which is the subject of this study.

If a beam has rotational symmetry, there are angles θ for which the beam moments are invariant under the phase space transformation:

$$\begin{pmatrix} x \\ x' \\ y \\ y' \end{pmatrix} \mapsto \begin{pmatrix} \widetilde{x} \\ \widetilde{x}' \\ \widetilde{y} \\ \widetilde{y}' \end{pmatrix} = \begin{pmatrix} \cos\theta & 0 & -\sin\theta & 0 \\ 0 & \cos\theta & 0 & -\sin\theta \\ \sin\theta & 0 & \cos\theta & 0 \\ 0 & \sin\theta & 0 & \cos\theta \end{pmatrix} \begin{pmatrix} x \\ x' \\ y \\ y' \end{pmatrix} \quad (1)$$

* Work supported by the U.S. DOE Office of Science under Cooperative Agreement DE-SC0000661 and the NSF under Grant No. PHY-1565546 while Chun Yan Jonathan Wong was previously at the National Superconducting Cyclotron Laboratory, East Lansing, USA.

‡ wongchu1@msu.edu

ISBN: 978-3-95450-226-4 ISSN: 2222-5692 doi:10.18429/JACoW-ECRIS2020-TUZZO06

For C_n symmetry, $\theta = 2k\pi/n$, whereas for an SO(2) beam, θ is arbitrary. For every beam moment, invariance under rotation by θ is equivalent to:

$$\left\langle x^{b_1} x'^{b_2} y^{b_3} y'^{b_4} \right\rangle = \left\langle \widetilde{x}^{b_1} \widetilde{x}'^{b_2} \widetilde{y}^{b_3} \widetilde{y}'^{b_4} \right\rangle \tag{2}$$

which constitutes a constraint equation on beam moments because the right hand side can be expanded using Eq. (1). The class of Eq. (2) contains all information on how rotational symmetry constrains beam moments, but the information does not easily reduce into clean expressions since the expanded equations contain many terms. To simplify the analysis, we developed a method to derive the constraints imposed by rotational symmetry using complex coordinates.

If we define two complex conjugate pairs composed of transverse phase space coordinates:

$$\begin{pmatrix} w \\ \overline{w} \\ w' \\ \overline{w'} \end{pmatrix} \equiv \begin{pmatrix} x + iy \\ x - iy \\ x' + iy' \\ x' - iy' \end{pmatrix} \tag{3}$$

these complex coordinates transform under rotation by θ as follows:

$$\begin{pmatrix} w \\ \overline{w} \\ w' \\ \overline{w'} \end{pmatrix} \mapsto \begin{pmatrix} e^{i\theta} & 0 & 0 & 0 \\ 0 & e^{-i\theta} & 0 & 0 \\ 0 & 0 & e^{i\theta} & 0 \\ 0 & 0 & 0 & e^{-i\theta} \end{pmatrix} \begin{pmatrix} w \\ \overline{w} \\ w' \\ \overline{w'} \end{pmatrix} \tag{4}$$

We can construct a k-th order complex moment $\left\langle w^{a_1} \overline{w}^{a_2} w'^{a_3} \overline{w'}^{a_4} \right\rangle$ where a_1, a_2, a_3, a_4 are non-negative integers and $a_1 + a_2 + a_3 + a_4 = k$. The real and imaginary parts of $\left\langle w^{a_1} \overline{w}^{a_2} w'^{a_3} \overline{w'}^{a_4} \right\rangle$ each comprises sums of physical k-th order beam moments. Upon a rotation by θ, the complex moment undergoes the following transformation in accordance with Eq. (4):

$$\left\langle w^{a_1} \overline{w}^{a_2} w'^{a_3} \overline{w'}^{a_4} \right\rangle \mapsto e^{i(a_1 - a_2 + a_3 - a_4)\theta} \left\langle w^{a_1} \overline{w}^{a_2} w'^{a_3} \overline{w'}^{a_4} \right\rangle$$

If rotation by θ is a symmetry of the beam, $\left\langle w^{a_1} \overline{w}^{a_2} w'^{a_3} \overline{w'}^{a_4} \right\rangle$ remains unchanged upon the transformation which gives:

$$\left\langle w^{a_1} \overline{w}^{a_2} w'^{a_3} \overline{w'}^{a_4} \right\rangle = e^{i(a_1 - a_2 + a_3 - a_4)\theta} \left\langle w^{a_1} \overline{w}^{a_2} w'^{a_3} \overline{w'}^{a_4} \right\rangle \tag{5}$$

Eq. (5) is the key equation that efficiently generates equality constraints among beam moments due to symmetry. For every 4-tuple (a_1, a_2, a_3, a_4) where $e^{i(a_1 - a_2 + a_3 - a_4)\theta} \neq 1$, $\left\langle w^{a_1} \overline{w}^{a_2} w'^{a_3} \overline{w'}^{a_4} \right\rangle = 0$ which give two constraints:

$$\mathrm{Re}\left(\left\langle w^{a_1} \overline{w}^{a_2} w'^{a_3} \overline{w'}^{a_4} \right\rangle \right) = 0 \tag{6}$$

$$\mathrm{Im}\left(\left\langle w^{a_1} \overline{w}^{a_2} w'^{a_3} \overline{w'}^{a_4} \right\rangle \right) = 0 \tag{7}$$

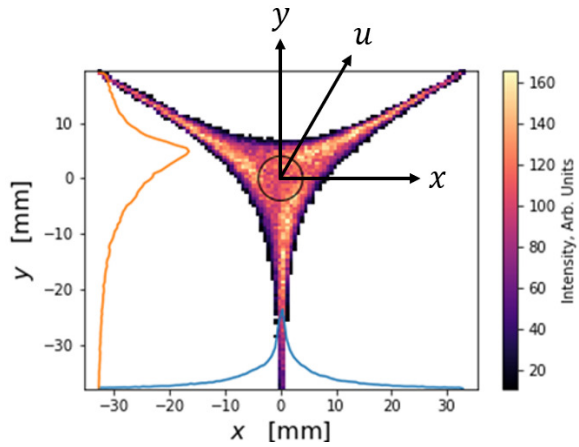

Figure 1: Simulated spatial distribution of Ar^{9+} ions at the extraction plane of the ARTEMIS [2] ECR ion source at FRIB. The inner circle indicates the extraction aperture. Simulation results courtesy of the code developed by Vladirmir Mironov and his colleagues at JINR [3, 4].

.

THREE-FOLD ROTATIONAL SYMMETRY

We employ the theoretical framework developed in the previous section to derive 2nd order moment constraints imposed by C_3 symmetry. For $\theta = 2\pi/3$, one can use Eq. (5) to find three (actually six, but three of them are redundant, see [1]) 2nd order complex moments that must vanish. They generate six unique constraints:

$$\begin{aligned} \mathrm{Re}\left(\langle ww \rangle\right) = 0 \quad &\Rightarrow \quad \langle xx \rangle = \langle yy \rangle \\ \mathrm{Re}\left(\langle ww' \rangle\right) = 0 \quad &\Rightarrow \quad \langle xx' \rangle = \langle yy' \rangle \\ \mathrm{Re}\left(\langle w'w' \rangle\right) = 0 \quad &\Rightarrow \quad \langle x'x' \rangle = \langle y'y' \rangle \\ \mathrm{Im}\left(\langle ww \rangle\right) = 0 \quad &\Rightarrow \quad \langle xy \rangle = 0 \\ \mathrm{Im}\left(\langle ww' \rangle\right) = 0 \quad &\Rightarrow \quad \langle xy' \rangle = -\langle x'y \rangle \\ \mathrm{Im}\left(\langle w'w' \rangle\right) = 0 \quad &\Rightarrow \quad \langle x'y' \rangle = 0 \end{aligned} \tag{8}$$

It is known in literature [5], and we can easily derive using the above framework, that 2nd order moments of an SO(2) beam also obey the set of constraints in Eq. (8). This renders a C_3 beam effectively axisymmetric in the following sense: in terms of 2nd order moments, C_3 and SO(2) beams obey the same constraints and are thus indistinguishable. Only higher order moments can tell them apart.

The indistinguishability entails that 2nd order moments of C_3 and SO(2) beams must have the exact same properties. This argument enables us to prove a counter-intuitive theorem regarding the 2nd order moments of C_3 beams:

Theorem 1. *Take $u(\phi) = x\cos\phi + y\sin\phi$ to be a rotated coordinate. If a beam has C_3 symmetry, the equalities*

$$\begin{aligned} \langle uu \rangle &= \langle xx \rangle \\ \langle uu' \rangle &= \langle xx' \rangle \\ \langle u'u' \rangle &= \langle x'x' \rangle \end{aligned} \tag{9}$$

hold for any ϕ.

ISBN: 978-3-95450-226-4 ISSN: 2222-5692 doi:10.18429/JACoW-ECRIS2020-TUZZO06

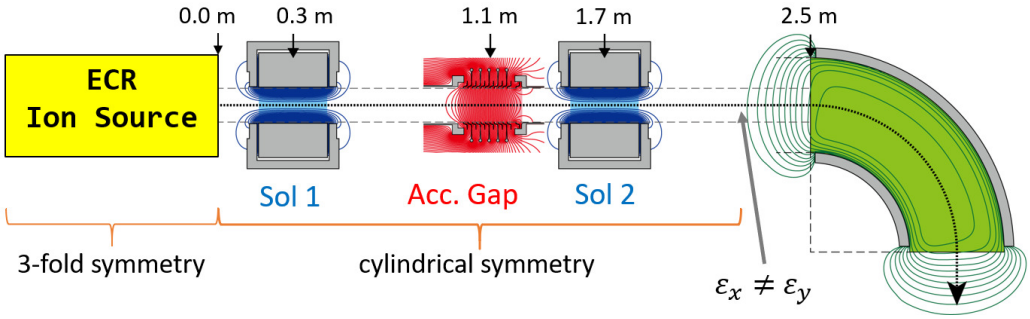

Figure 2: Schematic of the ARTEMIS beam line at the FRIB Front End. Ideally, the ECR ion source has C_3 symmetry while the transport line consisting of two solenoids and an electrostatic acceleration gap is axisymmetric. Image based on original from Ref. [6].

The proof relies on the fact the three equalities in Eq. (9) always hold for an SO(2) beam which looks identical along any direction. Since the theorem only concerns 2nd order moments, and 2nd order moments of SO(2) and C_3 beams have the same properties, the theorem must hold.

Figure 1 shows a beam with C_3 symmetry at an ECR extraction plane and a u-axis that makes angle ϕ with the x-axis. What theorem 1 says is that, although the beam's projected distribution in u-u' phase space varies significantly with ϕ, all 2nd order phase space moments, and hence the RMS phase space ellipse, always remain identical.

An immediate consequence of theorem 1 is:

Corollary 1.1. *A C_3 beam has identical RMS envelope and emittance along any transverse direction*

In particular, the Twiss parameters and emittance in x of a C_3 beam are always equal to their y counterparts.

APPLICATION TO FRIB FRONT END

Corollary 1.1 can help answer long-standing questions about beam emittances in ECR beam extraction and transport. To illustrate the arguments, we describe how theoretical results on C_3 beams were applied to analyze beam dynamics at the FRIB Front End [7]. Figure 2 shows a schematic of the ARTEMIS [2] beam line and depicts the rotational symmetries of the respective segments. In the ideal case, the beam should have C_3 symmetry up to non-zero dipole fields illustrated by the green curves.

Phase space diagnostics are located downstream of the dipole and their measurements on the target species often show $\varepsilon_x \neq \varepsilon_y$. While it is possible for ε_x to increase due to dispersion generated by the dipole, and for ε_y to couple to ε_x via space charge, the sign and magnitude of the difference between ε_x and ε_y were found to depend on the solenoid strengths. Since $\varepsilon_y > \varepsilon_x$ also occurred, dispersion cannot be the sole reason for $\varepsilon_x \neq \varepsilon_y$ downstream of the dipole, and we conclude that $\varepsilon_x \neq \varepsilon_y$ upstream of the dipole as depicted in Fig. 2.

$\varepsilon_x \neq \varepsilon_y$ prior to the dipole in an ECR beam line is often deemed an unsurprising empirical phenomenon caused by the beam's triangulated spatial density profile and x-y solenoid coupling. However, we have proved corollary 1.1 which states that $\varepsilon_x = \varepsilon_y$ if the beam has C_3 symmetry. The statement is a consequence of symmetry alone, so it holds even in the presence of chromatic aberrations, radial field nonlinearities and multi-species space charge with arbitrary intensity and charge state distribution.

Instead, the contrapositive of corollary 1.1 enables us to deduce: there is only one fundamental cause for $\varepsilon_x \neq \varepsilon_y$ in an axisymmetric beam line downstream of an ECR ion source and it is broken symmetry. At FRIB, the argument motivated a search for the source of broken symmetry in the transport line. The first solenoid was found via 3D magnet simulations [8] to have strong multipole fields due to a non-optimal design of the current leads.

CONCLUSION

We proved that 3-fold rotational symmetry guarantees identical RMS emittances and beam envelopes along x and y (and indeed along any transverse direction). These results were derived using a theoretical framework that describes how rotational symmetry imposes constraints on beam moments. The results are counter-intuitive and disprove common assumptions that triangulated distribution or ideal x-y coupling in solenoids would render $\varepsilon_x \neq \varepsilon_y$ in ECR beams. The only fundamental cause of $\varepsilon_x \neq \varepsilon_y$ is broken symmetry, which may arise from misalignments, imperfect elements or neutralization effects from back-flowing electrons. Such arguments are readily applicable to ECR beam lines and successfully clarified beam dynamics at the FRIB Front End.

The theoretical framework we developed also allows us to derive constraints imposed upon 3rd or higher order moments by C_3 symmetry. Their results and implications are discussed in Ref. [1]. In addition to being analytic tools in beam dynamics, symmetry-imposed moment constraints may also serve as a benchmark for ECR simulation models via consistency checks between simulation results and moment constraints. Preliminary work in this regard showed that 2nd order moment constraints are in agreement with the models provided by Vladimir Mironov from JINR that are described in Ref. [3, 4].

ISBN: 978-3-95450-226-4 ISSN: 2222-5692 doi:10.18429/JACoW-ECRIS2020-TUZZO06

ACKNOWLEDGEMENTS

The authors are grateful to our colleagues from NSCL/FRIB: Yue Hao, Peter Ostroumov and Vladimir Zelevinsky for many fruitful discussions on the theory; and Guillaume Machicoane, Felix Marti, Tomofumi Maruta, Alexander Plastun, Eduard Pozdeyev and Jeff Stetson for supporting the analysis on the FRIB Front End. We also thank Vladimir Mironov from the JINR for providing cutting-edge simulation results on ECR ion sources.

REFERENCES

[1] J. C. Wong and S. M. Lund, "Moment constraints in beams with discrete and continuous rotational symmetry," manuscript in preparation.

[2] G. Machicoane, D. Cole, J. Ottarson, J. Stetson, and P. Zavodszky, "ARTEMIS-B: A room-temperature test electron cyclotron resonance ion source for the National Superconducting Cyclotron Laboratory at Michigan State University," *Rev. Sci. Instrum.*, vol. 77, no. 3, 03A322, 2006. DOI: 10.1063/1.2165749.

[3] V. Mironov, S. Bogomolov, A. Bondarchenko, A. Efremov, and V. Loginov, "Numerical model of electron cyclotron resonance ion source," *Phys. Rev. ST Accel. Beams*, vol. 18, p. 123 401, 2015. DOI: 10.1103/PhysRevSTAB.18.123401.

[4] V. Mironov, S. Bogomolov, A. Bondarchenko, A. Efremov, and V. Loginov, "Numerical simulations of gas mixing effect in electron cyclotron resonance ion sources," *Phys. Rev. Accel. Beams*, vol. 20, p. 013 402, 2017. DOI: 10.1103/PhysRevAccelBeams.20.013402.

[5] K.-J. Kim, "Round-to-flat transformation of angular-momentum-dominated beams," *Phys. Rev. ST Accel. Beams*, vol. 6, p. 104 002, 2003. DOI: 10.1103/PhysRevSTAB.6.104002.

[6] K. Fukushima, private communication, 2016.

[7] E. Pozdeyev *et al.*, "FRIB Front End Construction and Commissioning," in *Proc. 9th International Particle Accelerator Conference (IPAC'18), Vancouver, BC, Canada, Apr.-May 2018*, pp. 58–62. DOI: 10.18429/JACoW-IPAC2018-MOZGBF1.

[8] A. Plastun, private communication, 2019.

ISBN: 978-3-95450-226-4 ISSN: 2222-5692 doi:10.18429/JACoW-ECRIS2020-WEWZO02

PRECISE IDENTIFICATION OF EXTRACTED ION BEAM SPECTRUM INITIALLY OBTAINED IN SYNTHESISING IRON-ENDOHEDRAL FULLERENES ON ECRIS

I. Owada†[1], T. Omori[1], W. Kubo[1], S. Harisaki[1], K. Sato[1], K. Tsuda[1],
M. Muramatsu[2], A.Kitagawa[2],Y. Yoshida[3], and Y. Kato[1],
[1]Graduate School of Engineering, Osaka University, Suita, Osaka, Japan
[2]National Institutes of Quantum and Radiological Science and Technology, Chiba, Chiba, Japan
[3]Faculty of Science and Engineering, Toyo University, Kawagoe, Saitama, Japan

Abstract

We have been trying to produce iron endohedral fullerenes in the electron cyclotron resonance ion source (ECRIS). They are expected to be used as quantum computing and contrast agents with high sensibility for MRI. We have conducted initial experiments on producing them only in the second stage of the ECRIS. We have been using iron vapor source by induction heating (IH) from the mirror end along to the geometrical axis, and C60 crucible from the side wall, respectively. We succeeded in realizing ECR plasma that fullerene and iron ions coexist on the single stage ECRIS, even by 1kV extraction voltage. We have performed a detailed identification of the ions of endohedral fullerene by the typical charge state distribution (CSD) using different criteria. By these experimental series, it is suggested that there is possibility of slight formation of iron endohedral fullerenes. We have confirmed the reproducibility of the spectrum of the ions corresponding to Fe@C60+ in several data sets. We will increase the amount of iron vapor and conduct additional experiment.

INTRODUCTION

We have produced the electron cyclotron resonance ion source (ECRIS) plasma to generate a synthetic ion beam in Osaka university [1,2]. The ECRIS has been applied in various fields such as heavy ion cancer therapy and space propulsion [3]. In the field of bionanomaterials, various kinds of atoms have been studied to be encapsulated in fullerenes. Fullerenes have a cage shape, and their scientific and physical properties are dependent on the atoms they contain [4]. Iron endohedral fullerenes are expected to be used as quantum computing or magnetic resonance imaging (MRI) contrast agents. In previous work, various synthesis technologies for producing endohedral fullerene have been developed, e.g. laser-vaporization, arc-discharge, and ion irradiation technique [5-8]. We have been trying to produce endohedral fullerene by collision reaction in the vapor phase in the ECR plasma. We have already succeeded in generating a plasma in which iron and fullerene ions coexist [9]. We have also improved the iron evaporation source for iron ion production. In this study, we have been developing an evaporation source using an induction heating method that allows for non-contact, high-purity material vapor to be extracted. The coexistence of iron and fullerene ions in the ECR plasma was observed in the experimental system. From the analysis of the mass/charge (m/q) value distribution and the result of detailed identification of the ions, the spectrum of the endohedral fullerene ion is confirmed around C_{60}^{+}. We have confirmed the reproducibility of the spectrum in several data sets. We will increase the amount of iron vapor and conduct additional experiment. In this paper, we report the schematic diagram of the constructed system and the results of the detailed identification of charge state distribution (CSD). We also show the results of preliminary experiments conducted without using the iron evaporator is also presented.

EXPERIMENTAL APPARATUS

A. ECR Ion Source

The top view of ECRIS in Osaka Univ. is shown in Fig. 1. The magnetic configuration is formed by the two mirror coils (Coil A, Coil B), additional coil (Coil C), and permanent octupole magnets. The current in coils A, B, and C are I_A, I_B, and I_C, respectively. The I_C is used for controlling the resonance region. We take the center of the vacuum vessel as the origin of the cartesian coordinates system. The IH iron evaporation source is located at z=-280mm and the fullerene crucible is at z=175mm.

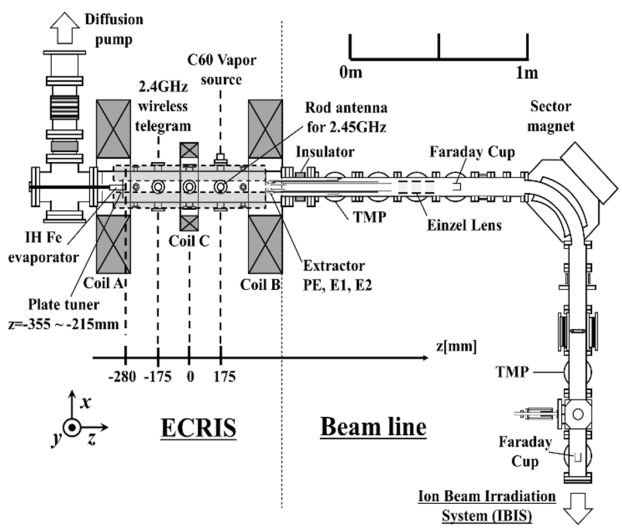

Figure 1: The top view of the ECRIS (Osaka Univ).

† issei0211@me.com

ISBN: 978-3-95450-226-4 ISSN: 2222-5692 doi:10.18429/JACoW-ECRIS2020-WEWZO02

The 2.45 GHz and 2.4 GHz micro wave are usually launched by magnetron (5~100W, z=175mm) and wireless telegram (0.1~0.9W, z=-175mm), respectively. A plate tuner installed on the z-axis. It can be moved at z=-355~-215mm and the introduction of microwaves can be optimized by moving it. It is effective when we manipulate low power micro wave. The extracted ion beam is separated by sector magnet for mass-charge ratio (m/q), detected by a faraday cup, and the CSD of the extracted ion current was obtained.

B. Induction Heating Iron Evaporator and Fullerene Vapor Source

The diagram of inducting heating iron evaporator [10] in Osaka Univ. is shown in Fig. 2. A radio frequency (RF) power supply is used as the power source, and the input power is usually about 600~800W. It is located at z=-280mm.

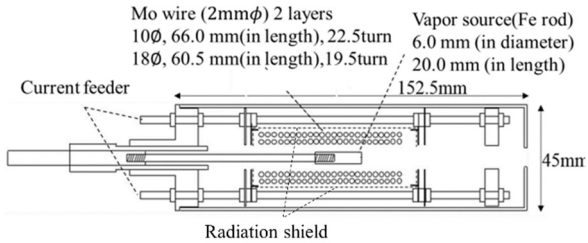

Figure 2: IH Fe evaporator.

The diagram of Fullerene crucible in Osaka University, is shown in Fig. 3. A direct current (DC) power supply is used as the power source, and the input power is usually about 10 W. It is located at z=175mm.

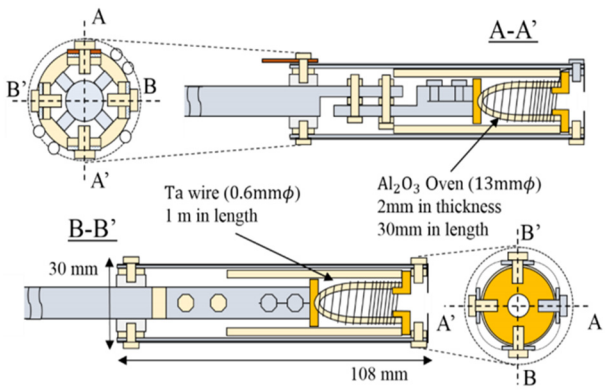

Figure 3: C_{60}^{+} crucible.

C. Experimental Procedure

We mainly use argon or xenon as the support gas. It is suitable for generating iron ions in high power micro wave and high extraction voltage. However, in generating fullerene ions, low power microwave and low extracted voltage is preferred. It is difficult to coexist both iron ion and fullerene ion. At first we preheat Fe evaporator and C_{60} crucible and set the extraction voltage at 10 kV to generate iron ions. The microwave about 10~20 W are launched from the magnetron. After confirming the generation of iron ions on the CSD, we decrease the extraction voltage to 2kV gradually. Likewise, the introduction of microwaves is switched to the wireless telegram and the power is reduced to less than 1W. It is necessary to generate fullerene ions while maintaining the existence of iron ions. Finally, we optimize the magnetic field conditions for production of endohedral fullerenes ions.

EXPERIMENTAL RESULTS AND DISCUSSIONS

A. Typical CSD of Fe^{+}, C_{60}^{q+}, and Their Compound Ions

Figure 4 (a) shows the typical CSD of fullerene ions. The horizontal axis represents the magnetic field and the vertical axis represents the amount of beam current. We can confirm the coexistence of C60+ ~ C603+ ions, Fe ions and residual Xe ions. Fig. 4(b), shows the right-hand side of the spectrum of C60+. From the identification of them, the spectrum to the right-hand side of the spectrum of C60+ are considered as Ar@C60+, Fe@C60+, Xe@C56+ and C70+. We used magnetron microwaves with 10W power, IH iron evaporation source was performed at 700 W input power. The extraction voltage is 2 kV. The support gas is argon with xenon remaining in it.

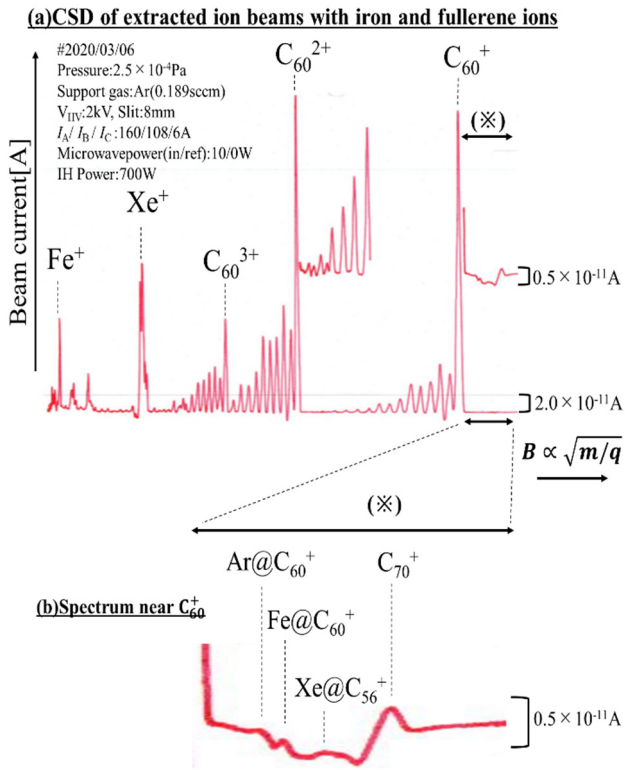

Figure 4 (a): CSD of extracted ion beams with iron and fullerene ions v.s.$\sqrt{m/q}$ (b): Spectrum near C_{60}^{+}.

ISBN: 978-3-95450-226-4 ISSN: 2222-5692 doi:10.18429/JACoW-ECRIS2020-WEWZO02

B. Error Evaluation

We performed relative error evaluation with different combinations of identification criteria. The relative error [%] is defined by the following Eq. (1).

$$\text{relative error}[\%] = \left|\frac{\alpha_1 - \alpha_2}{\alpha_1}\right| \times 100 \qquad (1)$$

α_1 : theoretical mass/charge (m/q) value
α_2 : mass/charge (m/q) value measured by CSD

The results of the evaluation are shown in Table 1. We conduct using a combination of various ions, including fullerene. We were able to identify the spectrum corresponding to the endohedral fullerene with an average relative error of 0.36%~1.35%. The spectrum corresponding to the iron endohedral fullerene were identified with an average relative error of 0.68%.

C. Typical CSD without Iron Ions

The results of the fullerene ion beam generation without the iron ions are shown in Fig. 5.

Table 1: Relative Error Evaluation in Each of the Identification Criteria. [%]

Identification creteria	ArC_{60}^+	FeC_{60}^+	XeC_{56}^+	C_{70}^+
C_{60}^+ & C_{60}^{2+}	0.10	0.50	0.34	0.24
C_{60}^+ & C_{60}^{3+}	0.05	0.44	2.08	0.19
C_{60}^+ & Fe^+	0.60	0.44	1.07	0.47
C_{60}^{2+} & Fe^+	1.47	1.32	1.92	0.52
Ave. error	0.56	0.68	1.35	0.36

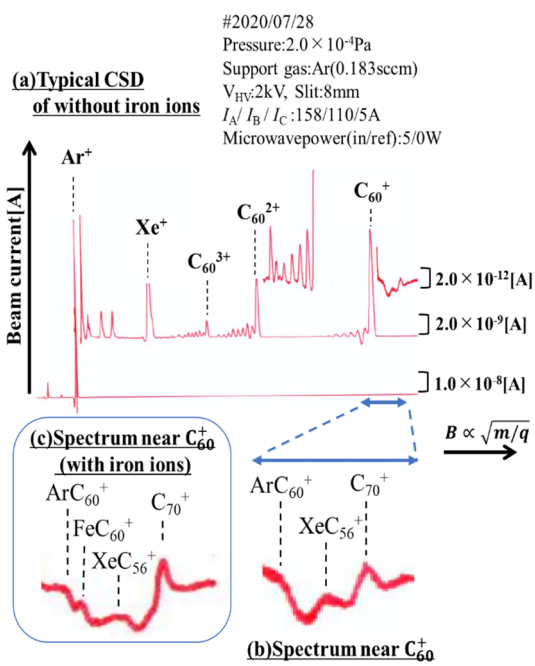

Figure 5: CSD of no iron ion introduction.

It is showed that Fig. 5(a) is the typical CSD of without iron ions and Fig. 5(b) focus on the right side of C60+. Fig. 5(c) is in the case of introducing the iron ions and focusing on the right side of C60+. The results of the similar identification with different criteria, we find the spectrum corresponding to ArC60+, XeC56+, and C70+, but no spectrum corresponding to FeC60+. This shows the reliability of the spectrum corresponding to Fe@C60+ when iron ions are introduced.

D. Conclusions and Future Planning

We have conducted experiments on the formation of iron endohedral fullerene using the inductively heated iron evaporation source. The spectrum corresponding to the iron endohedral fullerene were identified with an average error of 0.68% by using different combinations of the reference ions. We have confirmed the reproducibility of the spectrum of the ions corresponding to Fe@C60+ in several data sets. Additional experiments performed without the introduction of iron ions confirmed that the spectrum corresponding to $Fe@C_{60}^+$ were not seen in the CSD.

We will conduct time-of-flight and chemical analyses of actual products. We are also planning to improve the iron evaporater to produce high-purity iron ions and conduct additional experiment in a situation of increased iron vapor.

REFERENCE

[1] Y. Kato *et al.*, "New tandem type ion source based on electron cyclotron resonance for universal source of synthesized ion beams," *Rev. of Scientific Instrum.* vol. 85, p. 02A950, iss.2, 2014. doi:10.1063/1.4857975

[2] Y. Kato *et al.*, "Production of nitrogen-fullerene compound ion beams on tandem-type electron cyclotron resonance ion source," *Rev. of Scientific Instrum.,* vol. 87, p. 02A711, iss. 2, 2016. doi:10.1063/1.4933122

[3] K. Okumura *et al.*, "Improving transport and optimizing deceleration of ion beams from electron cyclotron resonance multicharged ion sources," *Rev. of Scientific Instrum.* vol. 91, p. 023311, 2020. doi:10.1063/1.5128465

[4] T. Nagaya *et al.*, "Producing multicharged fullerene ion beam extracted from the second stage of tandem-type ECRIS," *Rev. of Scientific Instrum.,* vol. 87, p. 02A723, 2016. doi:10.1063/1.4934644

[5] Y. Chai *et al.*, "Fullerenes with Metals Inside," *Journal of Physical Chemistry*, vol. 95, no. 20, pp. 7564-7568, 1991. doi:10.1021/j100173a002

[6] Y. Lian *et al.*, "High-yield preparation of endohedral metallofullerenes by an improved DC arc-discharge method," *Carbon,* vol. 38, iss. 15, 2117, 2000. doi:10.1016/S0008-6223(00)00070-1

[7] T. Uchida *et al.*, "Status of the Bio-Nano electron cyclotron resonance ion source at Toyo University," R*ev. of Scientific Instrum.*, vol. 85, p. 02C317, 2014. doi:10.1063/1.4862212

[8] S. C. Cho *et al.*, "Nitrogen-atom endohedral fullerene synthesis with high efficiency by controlling plasma-ion irradiation energy and C60 internal energy," *Journal of Applied Physics*, vol. 117, no. 12, p. 123301, 2015. doi:10.1063/1.4916247

ISBN: 978-3-95450-226-4 ISSN: 2222-5692 doi:10.18429/JACoW-ECRIS2020-WEWZO02

[9] Y. Kato *et al.*, "Experimental Condition and Optimization for Coexistence of Fullerene and Iron Ions on ECRIS" *IIT2018, IEEE Conf. Publ*, pp.172-175, 2019.

[10] Y. Kato *et al.*, "Production of electron cyclotron resonance plasma by using multifrequencies microwaves and active beam profile control on a large bore electron cyclotron resonance ion source with permanent magnets," R*ev. of Scientific Instrum.*, vol. 81, p. 02A313, 2010. doi:10.1063/1.3277195

ISBN: 978-3-95450-226-4 ISSN: 2222-5692 doi:10.18429/JACoW-ECRIS2020-WEWZO03

HIGH-INTENSITY VANADIUM-BEAM PRODUCTION TO SEARCH FOR A NEW SUPER-HEAVY ELEMENT WITH $Z = 119$

T. Nagatomo†, Y. Higurashi, J. Ohnishi, H. Nakagawa, O. Kamigaito,
RIKEN Nishina Center, Wako, Japan

Abstract

We have begun synthesizing a new super-heavy element (SHE) with an atomic number, Z, of 119 using a very powerful vanadium-beam (V-beam) to overcome the very small production cross section. We investigated the correlation of the V-beam intensity, the total power of 18- and 28-GHz microwaves, and the consumption rate of metallic V powder that was proportional to the amount of the vapor in the plasma chamber. Consequently, we obtained approximately 600 eμA at a microwave power of 2.9 kW and a consumption rate of 24 mg/h. In addition, we found that the position of the crucible used as an evaporator of the V sample and the strength of the mirror field at the extraction side B_{ext} from 1.34 to 1.51 T did not have a significant effect on the beam intensity.

INTRODUCTION

A new project for the synthesis of new super-heavy elements (n-SHEs) with an atomic number greater than 118 has been conducted at RIKEN heavy-ion linear accelerator RILAC [1] since 2016. As the first step of this project, we attempt to produce an SHE with $Z = 119$, through the nuclear reaction between a vanadium-beam (V-beam) and a curium target. In order to achieve a higher acceleration energy than previously possible, we have installed ten superconducting acceleration cavities that were newly developed to generate a gap voltage of more than 2 MV [2,3] despite the spatial constraints in the existing facility. The cryosorption of the cavity surface, which is cooled by liquid helium, cannot be ignored, because the particulate matter adsorbed on the surface increases the surface resistance, which in turn reduces the acceleration voltage. In order to minimize the generation of the particulate matter due to the ion beam sputtering on the beam duct, we efficiently controlled the transverse emittance of the beam by the "slit triplet" in the LEBT [4]. After the first beam acceleration test this year [5], we successfully accelerated argon- and vanadium-ion (V-ion) beams with a 4 rms emittance of approximately 80 π mm*mrad ($\beta = v/c \sim 0.3\%$). However, the emittance limitation using the slit triplet reduces the beam intensity by approximately 1/3 compared to that of the beam separated by the analyzing the magnet, and it is desirable to obtain the highest intensity beam possible. Furthermore, it is not easy to increase the "brightness" of the beam extracted from the electron cyclotron resonance ion source (ECRIS). In addition, the synthesis of SHE requires a long experimental period that lasts approximately one month without interruption. Therefore, we focused on the effects of V vapor and microwave power on the beam intensity and investigated the optimal parameters that would allow long-term experiments with the highest possible beam intensity.

EXPERIMENTAL

Experiments were performed using the two superconducting ECRISs at RIKEN Nihina center, both of which have essentially the same ion-source structure [6,7]. One superconducting ECRIS is used as the ion source for RILAC, renamed as RIKEN 28-GHz SCECRIS "*KURENAI*" (R28G-K) [4], and the other for the RIKEN Radioactive Isotope Beam Factory (RIBF) [8], renamed as RIKEN 28-GHz SCECRIS "*SUI*" (R28G-S) [6,7]. The main feature of both of the ion sources is their ability to generate the mirror field with "classical" or "flat" B_{min} [9] using six superconducting solenoids and a superconducting hexapole magnet. The 18- and 28-GHz microwaves, which were used for the ECR plasma heating, were generated by a 1.5-kW klystron power amplifier and a 10-kW gyrotron system, respectively. The microwave power was estimated from the temperature rise and flow rate of the cooling water flowing through three channels in the plasma chamber wall.

The V vapor was produced by a high-temperature oven HTO heated by Joule heating using high-power direct currents [10]. The amount of vapor was proportional to the consumption rate of the solid V sample, which was measured as a function of the heating power of the HTO. The HTO crucible can be operated up to ~2,000 K using a high current DC power supply. The crucible had a double structure, namely, a thin tungsten crucible containing a second crucible made of yttrium oxide. The yttrium-oxide crucible contained 2.2 g of granular metallic V sample and suspends the chemical reaction between the sample and the crucible. In the present study, we modified the injection flange in order to use two HTO crucibles (three crucibles at maximum) at the same time, as shown in Fig. 1. Both of the crucibles were placed at positions where the plasma could not reach in order to avoid the additional heat inflow from the plasma. This straightforward modification doubled the amount of the stable V vapor supply. In order to observe the dependence of the beam intensity on the position of the HTO crucible, we compared the optimized $^{51}V^{13+}$-beam intensities obtained using HTO 1 and 2 crucibles individually.

The intensity of the $^{51}V^{13+}$-ion beam was measured by a Faraday cup located near the focal point of the analyzing magnet as a function of the total microwave power and consumption rate. The extraction voltage was also fixed to 12.6 kV, which accelerated the V^{13+} ion to an adequate speed for the following accelerator in RIBF. For each of the experimental conditions, the maximized beam intensity was recorded by adjusting the support gas pressure and the

† nagatomo@riken.jp

ISBN: 978-3-95450-226-4 ISSN: 2222-5692 doi:10.18429/JACoW-ECRIS2020-WEWZO03

position and voltage of the biased disk. In order to avoid the admixture of the $^{16}O^{4+}$-ion beam, which is close to the mass-to-charge ratio of $^{51}V^{13+}$, we chose $^{14}N_2$ gas as a support gas, which stabilized the ECR plasma.

In addition, the mirror field at the beam extraction region B_{ext} was changed from 1.31 to 1.51 T in order to observe the effect on the beam intensity.

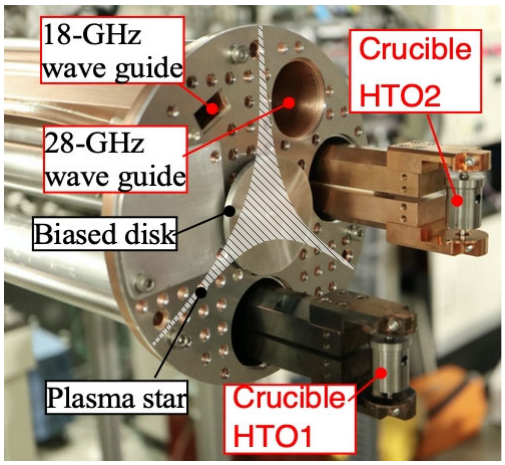

Figure 1: Two HTO crucibles, HTO1 and HTO2, stuck into the plasma chamber. The biased disk was located at the center of the flange and was movable along the axis of the ion source. The rectangular and circular outlets were the ends of the 18- and 28-GHz microwave guides, respectively.

RESULTS AND DISCUSSIONS

Figure 2 shows obtained contour plots of the optimized V^{13+}-beam intensity as a function of the consumption rate and the total microwave power by individually using differently positioned HTO 1 and 2 in Fig. 1 using R28G-K. The mirror fields B_{inj}, B_{min}, B_{ext}, and B_r were fixed as 2.3, 0.48, 1.4, and 1.47 T, respectively. As shown in Fig. 2, the beam intensity increases with increasing consumption rate and microwave power. For example, the beam intensity of 260 eμA was obtained at a consumption rate of 6.6 mg/h and a microwave power of 1.5 kW for HTO 1. For HTO 2, we obtained almost the same beam intensity of 262 eμA under the same conditions. Comparing the contour lines in the panels of Fig. 2, the beam intensity appears to be independent of the oven position.

Using the two crucibles of HTO 1 and 2 simultaneously, we could extend the contour plot to a higher consumption rate region, as shown in Fig. 3 using R28G-S. The mirror fields B_{inj}, B_{min}, B_{ext}, and B_r were 2.3, 0.48, 1.4, and 1.47 T, respectively, and were almost the same as those for the case of Fig. 2. Due to the double ovens, the total amount of the V sample increased to 4.4 g. Thus, for a month of uninterrupted beam supply, the consumption rate should be limited to approximately 6 mg/h. According to Fig. 3, an approximately 400-eμA (30-particle-μA) V^{13+} beam is available for the long-term experiment with microwaves of approximately 2.5 kW.

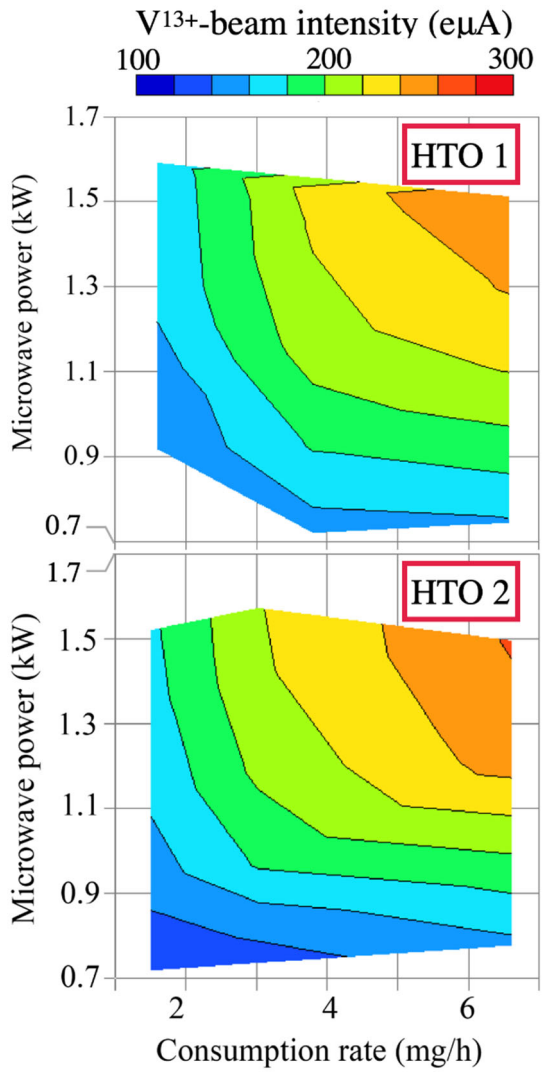

Figure 2: Obtained contour plots of the $^{51}V^{13+}$-beam intensity as a function of the total power of the 18- and 28-GHz microwaves and consumption rate of the V sample using HTO 1(top) and HTO 2 (bottom).

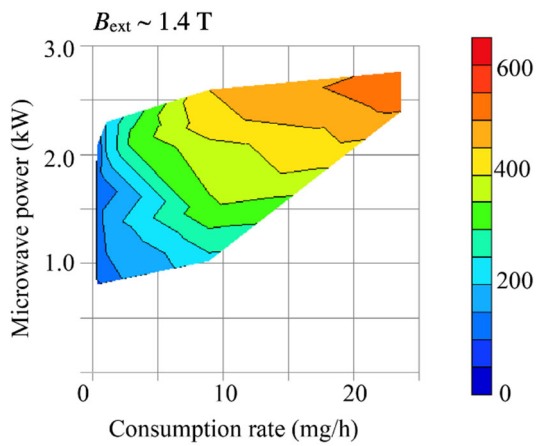

Figure 3: Expanded contour plot of the 51V13+-beam intensity using both HTO 1 and 2 crucibles.

ISBN: 978-3-95450-226-4 ISSN: 2222-5692 doi:10.18429/JACoW-ECRIS2020-WEWZO03

Furthermore, from Fig. 3, the intensity appears not to be saturated yet and increases as the microwave power and the consumption rate increase. By increasing the microwave power and consumption rate to 2.9 kW and 24 mg/h, respectively, we obtained a V^{13+} beam with a very high intensity of 600 eμA, as shown in a mass-to-charge-ratio spectrum in Fig. 4. Such a high-intensity beam, which lasts approximately one week, is also essential for the development of the production targets that require high-intensity exposure.

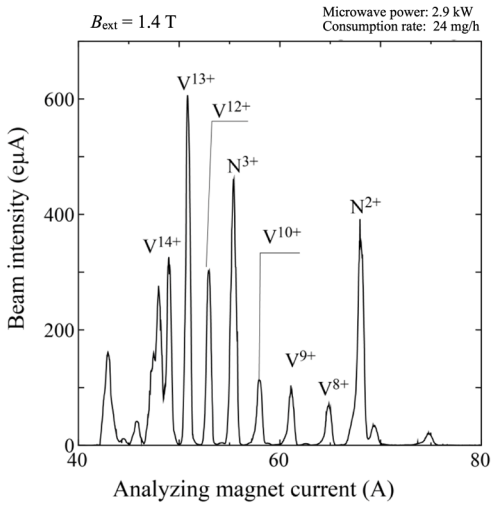

Figure 4: A mass-to-charge-ratio spectrum was obtained with a total microwave power of 2.9 kW and a consumption rate of 24 μg/h

Figure 5 shows the beam intensity of V^{13+} as a function of microwave power for different magnetic field strengths using R28G-K. The consumption rate was fixed to be 6.5 mg/h for all cases. The beam intensity increases linearly with increasing microwave power and is independent of the magnetic field strength for three cases of B_{ext} of 1.34, 1.41, and 1.51 T. Comparing these results, no significant effect of B_{ext} on the V^{13+}-beam intensity was observed in the experimental condition. However, it is possible that some beam quantities, such as the density distribution of the beam in the phase space, which was not observed in this measurement, may have changed by changing the B_{ext} and/or position of the crucible mentioned above. Thus, we plan to measure the ion beam distribution in the transverse phase space $\{x, x', y, y'\}$ using a pepper-pot-type emittance meter while changing B_{ext} and the position of the crucible.

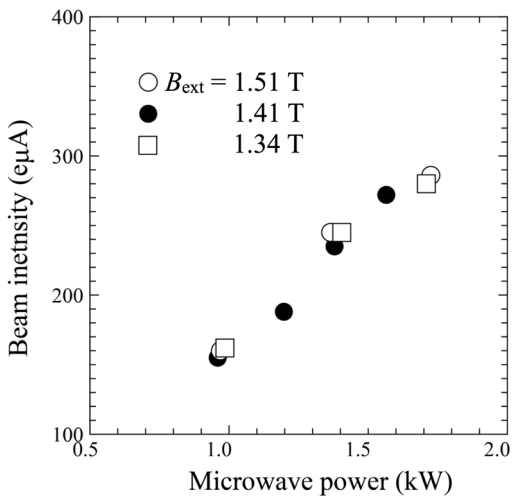

Figure 5: Beam intensity of V^{13+} as a function of microwave power for mirror fields for extraction regions B_{ext} of 1.51 T (open circles), 1.41 T (closed circles), and 1.34 T (open squares).

CONCLUSIONS

We measured the beam intensity of V^{13+} as a function of both the consumption rate of the vanadium sample and the microwave power. The optimized beam intensity was found to clearly depend on these two parameters. In the two-dimensional space of these parameters, the beam intensity is plotted as contour lines. As a consequence of the dependencies, it was found that a V^{13+}-beam with an intensity of 400 eμA can be produced at a consumption rate of approximately 6 mg/h and a microwave power of 2.5 kW. Simultaneously using both HTO crucibles allows us to execute SHE synthesis, which lasts approximately one month without interruption. Furthermore, we also obtained a V^{13+} beam with an intensity of 600 eμA at a consumption rate of 24 mg/h and a microwave power of 2.9 kW. The extra-high-intensity beam lasts for one week, and is suitable for experiments such as the essential development of the production target.

On the other hand, significant effects by changing the oven position and varying B_{ext} between 1.34 and 1.51 T on the beam intensity were not observed within the scope of the simple measurement using only a Faraday cup.

REFERENCES

[1] E. Ikezawa *et al.*, "Heavy-Ion Beam Acceleration at RIKEN for the Super-Heavy Element Search", in *Proc. 13th Int. Conf. on Heavy Ion Accelerator Technology (HIAT'15)*, Yokohama, Japan, Sep. 2015, paper WEPB14, pp. 222-224.

[2] O. Kamigaito *et al.*, "Present Status and Future Plan of RIKEN RI Beam Factory", in *Proc. 7th Int. Particle Accelerator Conf. (IPAC'16)*, Busan, Korea, May 2016, pp. 1281-1283. doi:10.18429/JACoW-IPAC2016-TUPMR022

[3] N. Sakamoto *et al.*, "Development of Superconducting Quarter-Wave Resonator and Cryomodule for Low-Beta Ion Accelerators at RIKEN Radioactive Isotope Beam Factory", in *Proc. 19th Int. Conf. RF Superconductivity (SRF'19)*, Dresden, Germany, Jun.-Jul. 2019, pp. 750-757. doi:10.18429/JACoW-SRF2019-WETEB1

[4] T. Nagatomo *et al.*, "High intensity vanadium beam for synthesis of new superheavy elements with well-controlled emittance by using 'slit triplet'"," *Rev. Sci. Instrum.*, vol. 91, p. 023318, 2020. doi:10.1063/1.5130431

[5] N. Sakamoto *et al.*, Proceedings of the 17th annual meeting of Particle Accelerator Society of Japan, 2020.

[6] T. Nagatomo *et al.*, "First results from the new RIKEN superconducting electron cyclotron resonance ion source (invited)," *Rev. Sci. Instrum.*, vol. 81, p. 02A320, 2010. doi:10.1063/1.3259232

ISBN: 978-3-95450-226-4 ISSN: 2222-5692 doi:10.18429/JACoW-ECRIS2020-WEWZO03

[7] Y. Higurashi *et al.*, "Recent development of RIKEN 28 GHz superconducting electron cyclotron resonance ion source," *Rev. Sci. Instrum.*, vol. 85, 02A953, 2014. doi:10.1063/1.4848976

[8] H. Okuno *et al.*, "Progress of RIBF accelerator" *Prog. Theor. Exp. Phys*, p. 03C002, 2012. doi:10.1093/ptep/pts046

[9] G. D. Alton and D. N. Smithe, *Rev. Sci. Instrum.*, vol. **65**, p. 775, 1994.

[10] J. Ohnishi, Y. Higurashi, and T. Nakagawa, "Practical Use of High-Temperature Oven for 28 GHz Superconducting ECR Ion Source at RIKEN", in *Proc. 23th International Workshop on ECR Ion Sources (ECRIS'18)*, Catania, Italy, Sep. 2018, pp. 180-184. doi:10.18429/JACoW-ECRIS2018-WEB4

ISBN: 978-3-95450-226-4 ISSN: 2222-5692 doi:10.18429/JACoW-ECRIS2020-WEWZO04

PRODUCING MULTICHARGED IONS BY PULSE MODULATED MICROWAVES AT MIXING LOW Z GASES ON ECRIS

S. Harisaki†, W. Kubo, I. Owada, K. Sato, K. Tsuda, and Y. Kato
Division of Electrical, Electronic and Infocommunications Engineering,
Graduate School of Engineering, Osaka Univ., 2-1 Yamada-oka, Suita-shi, Osaka 565-0871, Japan

Abstract

The multicharged ion source on the basis of electron cyclotron resonance (ECR) plasma has been constructed for producing various ion beams in Osaka Univ. We are aiming at producing and extracting multicharged, molecular, and synthesized ion beams ranged over wide mass/charge numbers (m/q) in the single device. Among them, we are now trying to increase the yield of multicharged ion beams. We try to enhance production efficiency of multicharged ions by enhancing loss channel of low Z ions and then cooling them with gas mixing and pulse modulated microwaves. Through these experiments, we explore the feasibility of selectively heating specific ions with pulse modulated microwaves. These experiments are conducted by keeping the total operating pressure constant and changing the mixing ratio of low Z gases. These effects are investigated by measuring charge state distributions (CSD's) of the extracted ion beams. Also, we can measure the plasma parameters using Langmuir probes. In this paper, we mainly describe the results of these active experiments at the ECRIS.

INTRODUCTION

We are aiming at increasing the yield of multicharged ions by advanced wave-heating mechanisms other than fundamental ECR. As a previous study, for example, we obtained the result that the multicharged ion yield of Xenon (Xe) increased in the upper hybrid resonance (UHR) heating experiment using 4-6 GHz X-mode microwaves [1]. Now we are focusing on heating in the frequency band much lower than conventional ECR, and trying to generate another resonance heating, *e.g.* ion cyclotron resonance (ICR), and lower hybrid resonance (LHR). Our ultimate goal is to increase the multicharged ion beam currents by using these resonances to selectively heat low Z ions during gas mixing to enhance loss channels of low Z ions, and then cooling multicharged ions. As a preliminary step, we conducted experiments to generate ECR plasma with pulse modulated microwaves under gas mixing.

Gas mixing is a well-known and effective method for producing multicharged ion beams [2]. In order to increase the yield of multicharged ions of Xe, we perform the gas mixing experiments using Argon (Ar) for low Z gas. These experiments are conducted by keeping the total operating pressure constant and changing the mixing ratio of Xe and Ar. After optimizing the Ar mixing ratio for producing multicharged Xe ions, pulse modulated microwaves are introduced to it. We survey and optimize the pulse frequency for producing multicharged ion beams. The optimum time scale of pulse modulated microwave is several tens of microseconds. We succeeded in further increasing the yield multicharged Xe ion beams by pulsing the microwaves. Also, the pulse frequency at that time is nearly equal to the ion cyclotron frequency of Ar^+. We plan to conduct emittance measurements in near future to further ensure that selective heating of ions is possible. In addition, we also plan to conduct experiments to actively launch RF waves to the ECR plasma under gas mixing.

EXPERIMENTAL APPARATUS

Figure 1 shows the top view of the ECRIS in Osaka Univ. [3]. Vacuum chamber is 160mm in diameter and 1074mm in length. Magnetic field is formed by mirror coils (Coils A and B), a supplemental coil (Coil C), and four permanent magnets (octupole magnets). We use the cartesian coordinates system (x,y,z) with the origin located at the center of the vacuum chamber. Xe and Ar gases are introduced to the vacuum chamber by mass flow controllers, and pressures are monitored directly by Bayard-Alpert (B-A) gauges. 2.45 GHz microwave is generated by a magnetron and launched from a rod antenna which installed on the top of the vacuum chamber (z=175mm). Microwave oscillation can be switched between continuous wave (CW) mode and external input mode, it can be modulated into waveforms according to the external pulses. The operating range of pulse modulation is usually 1-100 kHz in frequency and 20-80% in duty ratio. The incident power of microwaves is defined by P_{in}. Magnetic flux density B is controlled by currents fed to each coil (defined as I_A, I_B, and I_C). In these experiments, I_A=I_B=150A, and P_{in}=100W. Plasma parameters, namely the electron density n_e and the electron temperature T_e are measured by the Langmuir probe 1 (LP1, z=−175mm) and the Langmuir probe 2 (LP2, z=300mm) which have cylindrical Mo electrode (0.25mm in diameter) and can be moved vertically within x=0mm and ±50mm.

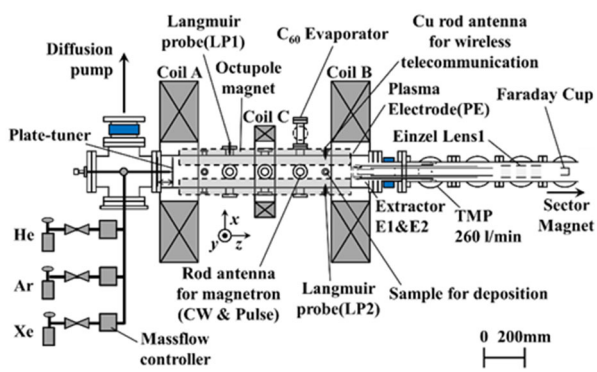

Figure 1: The top view of the ECRIS (Osaka Univ.).

† harisaki@nf.eie.eng.osaka-u.ac.jp

ISBN: 978-3-95450-226-4 ISSN: 2222-5692 doi:10.18429/JACoW-ECRIS2020-WEWZO04

Ion beam is extracted to the beam line, which is composed of extractor and einzel lens 1 (EL1). The extractor assembly is constituted by a plasma electrode PE (15mm in single hole diameter, 10kV applied voltage), mid-electrode E1 (13mm in single hole diameter), and E2 (13mm in single hole diameter, usually grounded voltage). Voltages applied to the PE, the E1, the E2 electrodes, and the EL1 are defined as V_{PE}, V_{E1}, V_{E2}, and V_{el1}, respectively. They are used in optimizing extraction of each ion species. Ion beam is bent by the sector magnet. Ion beam currents are measured by several Faraday cups, and we obtain charge state distributions (CSD's) of them.

In addition, Ion Beam Irradiation System (IBIS) is connected to the rear end of the beam line [4]. The ECRIS and the IBIS are separated by gate valve 1 (GV1), and the IBIS itself is also divided into two parts by gate valve 2 (GV2). We call GV1 to GV2 the measurement part, and GV2 and later the irradiation part. It is described in detail in Ref. [4].

EXPERIMENTAL RESULTS AND DISCUSSION

Typical CSD's with and without Gas Mixing Application

Figure 2 shows typical CSD's of extracted Xe ion beams. Operating pressure is 7.0×10^{-4}Pa. The I_A and the I_B are 150A. P_{in} is 100W. The V_{PE} is 10kV. The I_C, the V_{E1} and the V_{el} are optimized for extracting Xe^{7+} ion beam. The black line is the CSD of Xe ion beams without Ar gas mixing. We can confirm Xe of q=1~7, and the beam current of Xe^{7+} is 1.1×10^{-8}A. Where q is charge state. The blue line is the CSD of Xe ion beams with Ar gas mixing. The current of Xe^{7+} is further increased than that of no gas mixing, and the beam current is 1.8×10^{-8}A.

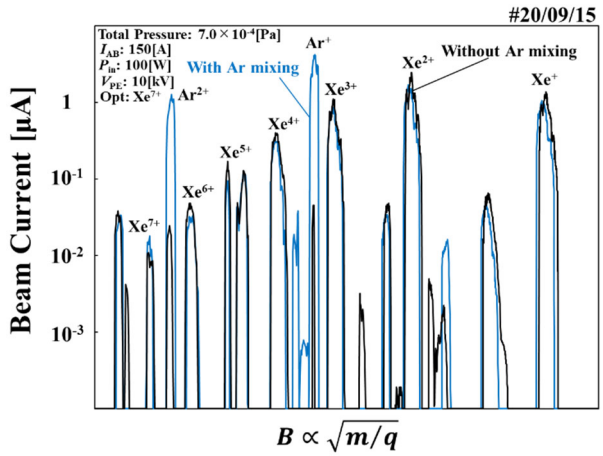

Figure 2: Comparison of typical CSD's of Xe ion beams with and without gas mixing.

The Dependence of Xe Ion Beams on Ar Mixing Ratio

Figure 3 shows the dependence of each Xe ion beam current on Ar mixing ratio. The horizontal axis is the Ar mixing ratio, which is determined by the partial pressures of Xe and Ar under the operation. The experiment is conducted at a constant total operating pressure, which is 7.0×10^{-4}Pa. The V_{PE} is 10kV. The I_C, the V_{E1} and the V_{el1} are optimized for extracting Xe^{7+} ion beam. As the Ar mixing ratio is increased, the extracted Ar^{+} beam current increases, and the Xe^{7+} ion beam reaches the maximum value at Xe:Ar=50:50.

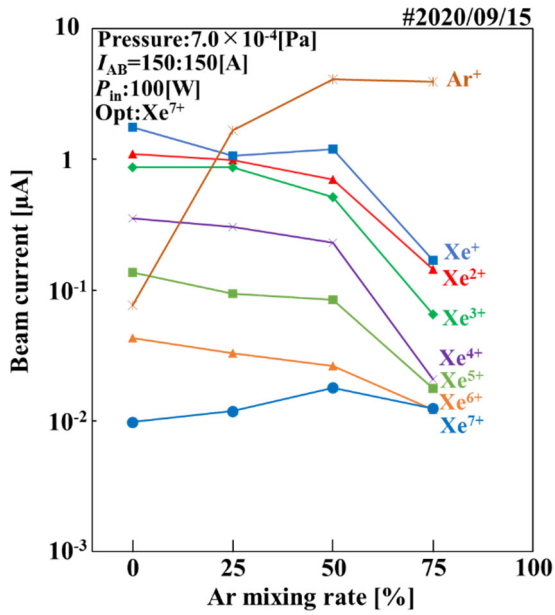

Figure 3: The dependence of each Xe ion beam current on Ar mixing ratio.

Typical CSD's with and without Pulse Modulated Microwaves Application

Figure 4 shows typical CSD's of extracted Xe ion beams. Operating pressure is 7.0×10^{-4}Pa. The I_A and the I_B are 150A. P_{in} is 100W. The V_{PE} is 10kV. The I_C, the V_{E1} and the V_{el} are optimized for extracting Xe^{7+} ion beam. The blue line is the CSD of Xe ion beams under simple gas mixing.

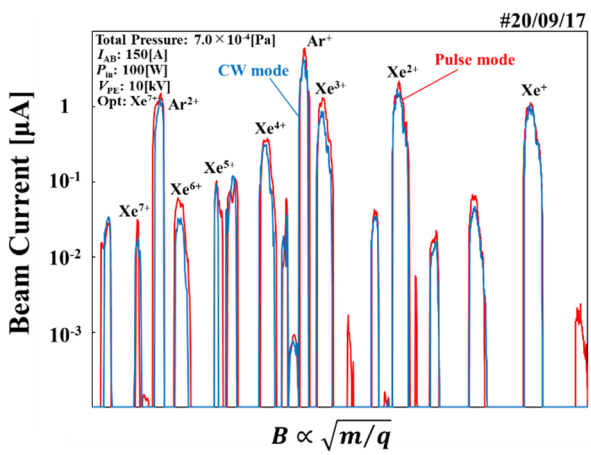

Figure 4: Comparison of typical CSD's of Xe ion beams in CW and Pulse mode.

ISBN: 978-3-95450-226-4 ISSN: 2222-5692 doi:10.18429/JACoW-ECRIS2020-WEWZO04

We can confirm Xe of q=1~7, and the beam current of Xe^{7+} is 1.1×10^{-8}A. The red line is the CSD when pulse wave is applied under gas mixing. The yield of Xe^{7+} is further increased than that of simple gas mixing, and the beam current is 3.5×10^{-8}A.

Microwave Pulse Period Dependence of Multicharged Xe Ion Beam

Figure 5 shows the dependence of Xe^{7+} ion beam current on microwave pulse period. The horizontal axis is the pulse period, and the vertical axis is the beam current of Xe^{7+}. The experimental conditions except for microwaves operation are the same as in Fig. 3. Pulsed microwaves are launched against the mixed gas of Xe:Ar=50:50. When the pulse period is changed in the range of 10-100 microseconds, the yield of Xe^{7+} changed and peaked at a period of 25 microseconds. The time-averaged incident and reflected microwave powers are almost the same in CW and pulse mode. This period corresponds to the ion cyclotron frequency of Ar^{+} in the magnetic field of our ECRIS. The current of Xe^{7+} when microwaves are incident in CW mode is shown by the dotted red line, and the value is 1.8×10^{-8}A. On the other hand, the maximum current of Xe^{7+} in pulse mode is 3.5×10^{-8}A.

Comparison of the Plasma Parameters between CW and Pulse Mode

Figure 6 shows the distribution of the n_e and the T_e in CW mode and pulse mode. The period in pulse mode is 25 microseconds. The measurement is performed three times at each x position by using the LP1, and the figure shows the average value and standard error. When pulse mode is introduced, the n_e is slightly higher than that of CW mode at x=0~40mm. The T_e is lower than that of CW mode at all x positions. Therefore, the increase in multicharged ion beam yield is not considered to be the effect of plasma parameters. We expect that the cause of the increase in the multicharged ion beam yield is the enhancement of the gas mixing effect by pulse waves.

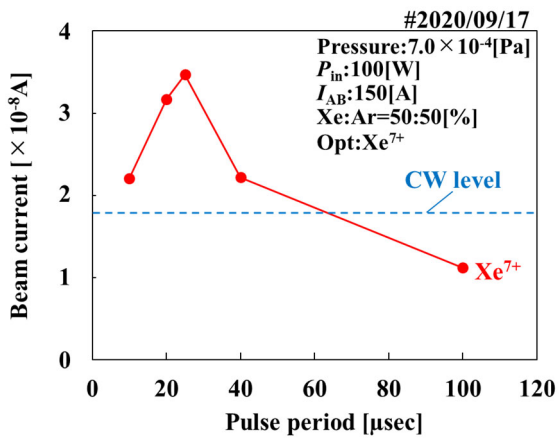

Figure 5: The dependence of Xe^{7+} ion beam current on microwave pulse period.

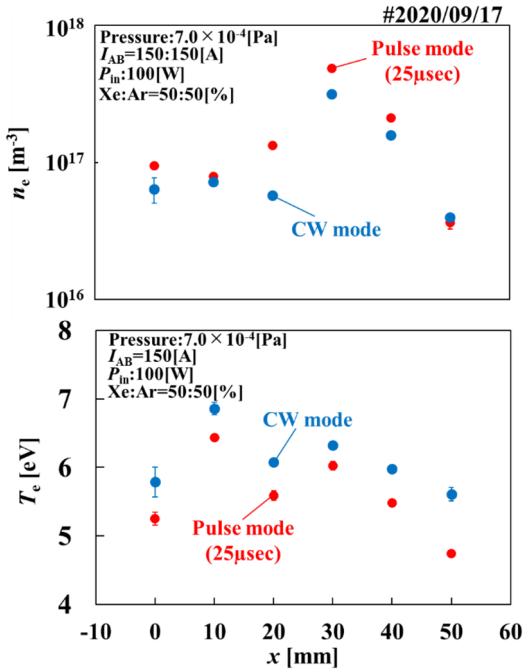

Figure 6: The distribution of the n_e and the T_e in CW mode and pulse mode.

Summary and Future Planning

We launched pulse modulated microwaves under simple gas mixing to increase the yield of multicharged Xe ion beams. The yield of Xe^{7+} was increased by 3.2 times compared with pure Xe ion beams. Furthermore, the probe measurements were conducted to confirm that these results were not due to the effects of the plasma parameters. Except for the enhancement of the gas mixing effect, the afterglow effect may affect the production of multicharged ions.

To obtain more confirmation about selective heating of low Z ions, we plan to perform emittance measurements to estimate the ion temperature T_i before and after the introduction of pulsed microwaves. In addition, we also plan to conduct the experiments that cause ICR and LHR by injecting RF waves into the ECR plasma under gas mixing.

REFERENCES

[1] Y. Kato *et al.*, "Upper hybrid resonance heating experiments by X-mode microwaves on electron cyclotron resonance ion source", *Rev. Sci. Instrum.*, vol. 91, p. 013315, 2020. doi:10.1063/1.5127315

[2] M. Muramatsu *et al.*, "Improvement of microwave injection for heavy-ion production at a compact ECR ion source", *Rev. Sci. Instrum.*, vol. 87, p. 02C110, 2016. doi.org/10.1063/1.5053392

[3] Y. Kato *et al.*, "New tandem type ion source based on electron cyclotron resonance for universal source of synthesized ion beams", *Rev. Sci. Instrum.*, vol. 85, p. 02A950, 2014. doi.org/10.1063/1.4857975

[4] K. Okumura *et al.*, "Improving transport and optimizing deceleration of ion beams from electron cyclotron resonance multicharged ion sources' *Rev. Sci. Instrum.*, vol. 91, p. 023311, 2020. doi.org/10.1063/1.5128465

ISBN: 978-3-95450-226-4 ISSN: 2222-5692 doi:10.18429/JACoW-ECRIS2020-WEWZO05

BEAM PROFILE MEASUREMENTS OF DECELERATED MULTICHARGED Xe IONS FROM ECRIS FOR ESTIMATING LOW ENERGY DAMAGE ON SATELLITES COMPONENTS

K. Sato†, K.Okumura, S. Harisaki, W. Kubo, I. Owada, K. Tsuda, and Y. Kato,
Division of Electrical, Electronic and Inforcommunications Engineering, Graduate School of Engineering, Osaka University, 2-1 Yamada-oka, Suita-shi, Osaka 565-0871, Japan

Abstract

Electron cyclotron resonance ion source (ECRIS) has been constructed for producing synthesized ion beams in Osaka Univ. Xe is used as fuel for ion propulsion engines on artificial satellites. There are problems of accumulated damages at irradiation and sputtering by low energy Xe ion from the engine. It is required to construct experimentally sputtering yield databases of ion beams in the low energy region, since there are not enough data of satellite component materials. Therefore, we are trying to investigate experimentally sputtering yield on materials by irradiating the low energy single species Xe^{q+} ion beams. However, there is a problem that if the low extraction voltage, the amount of beam currents is not enough to obtain ion beam flux for precise evaluation of sputtering yield data. Thus, we conduct to decelerate Xe^{q+} ion beams required low energy region after extracting at high voltage, *e.g.*, 10kV. We measured the decelerated beam profile with x-y direction wire probes. Then we were able to estimate precise dose of ion fluxes. We are going to conduct irradiation experiments to estimate spattering yield damage on various satellite component materials.

INTRODUCTION

An electron cyclotron resonance ion source (ECRIS) are widely applied for plasma processing and ion beam applications [1]. In our ECRIS, we aim at producing and extracting various ion beams in the single device. It plays an important role in medical field of carbon cancer therapy and aerospace engineering field of satellite engine [2, 3]. The satellite engine uses an ion engine, and Xe is widely used as fuel. Recently, life time of satellites is typically required over 10 years. There are problems of accumulation damages at irradiation and sputtering by low energy Xe ion from the engine. It is necessary to predict lifetime of satellite materials for the design of artificial satellites. It is required to construct sputtering yield experimentally since there are not enough data of satellite component materials by ion beams in the low energy region from several hundred eV to 1keV. In recent years, research on the sputtering yield of satellite materials has been conducted. There is a few data the sputtering data of single species Xe^{q+} ion beams. Therefore, we are trying to investigate experimentally sputtering yield on their materials by irradiating the low energy single species Xe^{q+} ion beams. However, there is a problem that if the extraction voltage is 1kV and Xe^{q+} is extracted, the amount of beam currents is not enough for irradiation. Then the ion beams are usually extracted from high voltage about 10 kV and transported. And we decelerate and irradiate ion beams to the materials in the ion beam irradiation system (IBIS) where we have constructed. In low energy irradiation experiments, there is a problem with uniformity of beam profile on the sample about $1cm^2$(10mm×10mm). We first conduct deceleration experiment to measure the current value of the decelerated low-energy ion beam. We confirmed that the enough amount of current in the low energy region (100~200eV). We measure the two-dimensional profiles of the decelerated beam and the beam position. When we determine that the beam position cannot irradiate the center of the target, we correct the beam position by changing the parameters of the laboratory equipment. The full width at half maximum (FWHM) can be measured from the profile. We can calculate the beam area and the current density from FWHM. We estimated irradiation time and the sputtering yield of the material from the current density. We evaluated the dose amount with high accuracy in the low energy region.

EXPERIMENTAL APPARATUS

Figure 1 shows the top view of our ECRIS and the beam line. The magnetic field of the ECRIS consists of octupole magnet and mirror field by two coils (Coil A, B) and additional coil (Coil C). The currents of Coil A and B are usually fixed 150A and that of coil C is adjusted to optimizing the ion beam current. We use the Xe and Ar gas. The Xe and Ar gases are introduced to the vacuum chamber by mass flow controllers. Then the pressures are monitored by a B-A gauge. The typical operation pressure of Xe and Ar gases are from 3×10^{-4}~1×10^{-3}Pa. The z axis shows the distance from center of the ECRIS along to the geometrical axis. 2.45GHz frequency microwaves are launched by the rod antenna through a coaxial window. The microwave powers are usually 10~50W.

The ion beam is extracted with three-electrodes from ECR plasma. The extractor consists of the PE, the E1 and the E2 electrodes. The voltages are V_{PE}, V_{E1} and V_{E2}, respectively. The V_{PE} is usually 10kV and the V_{E2} is grounded. The V_{E1} can change from 0kV to -6kV. We optimize the V_{E1} to extracted multicharged ion beam within wide range of mass/charge numbers and to reduce the loss of the beam current [4]. Einzel lens 1 (EL1) is set between the E2 and sector magnet. The voltage of EL1 is V_{el1}. V_{el1} is used to control transport of the ion beams. Ion beams are transported into the beam line consisting of sector magnet for analysing and acquiring charge state distribution (CSD) of

† itiko1809@gmail.com

ISBN: 978-3-95450-226-4 ISSN: 2222-5692 doi:10.18429/JACoW-ECRIS2020-WEWZO05

the ion beam currents. Beam currents are measured by the faraday cups (FC1, FC).

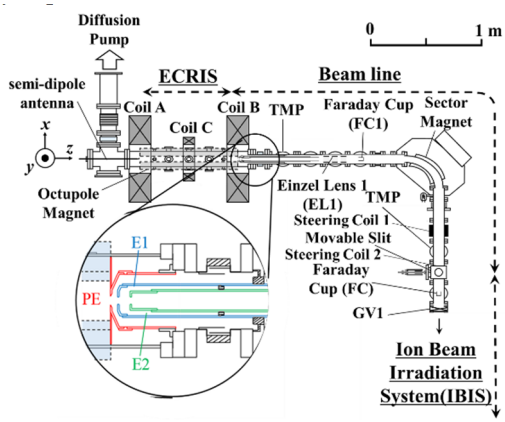

Figure 1: The top view of the ECRIS (Osaka Univ.).

The diameter of the FC is 51mm. The diameter of the FC1 is 50mm. We set the movable slit in front of the FC. It can control absolute value of currents and resolution of the CSD by changing the width with 0~40mm.

Figure 2 shows the side view of the IBIS. The IBIS and the ECRIS are separated by gate valve (GV1). The IBIS is divided by the gate valve (GV2). We call as the beam measurement part from GV1 to GV2, and the beam irradiation part from GV2 or the later. Even during the irradiation experiment, we can exchange irradiation sample easily and quickly by loadlock system of the beam irradiation part. Einzel lens 2 (EL2) is set between the GV1 and GV2. The voltage of the EL2 is V_{el2}. And we use einzel lens 3 (EL3) in the irradiation part. The voltage of the EL3 is V_{el3}.

Figure 3 shows the detail of the beam irradiation part. We measure beam current at FCi in deceleration experiment. The diameter of the FCi is 50mm. X-Y wire probe is used for measuring the two-dimensional profiles of the decelerated beam. Wire probe is made of molybdenum. The diameter of wire probe is 0.5mm. We rotate wire probe when we measure X-direction profile. We move up and down wire probe when we measure Y-direction profile. Casing covers FCi and wire probe. Casing reduces the effects of secondary electrons emitted from FCi and wire probe.

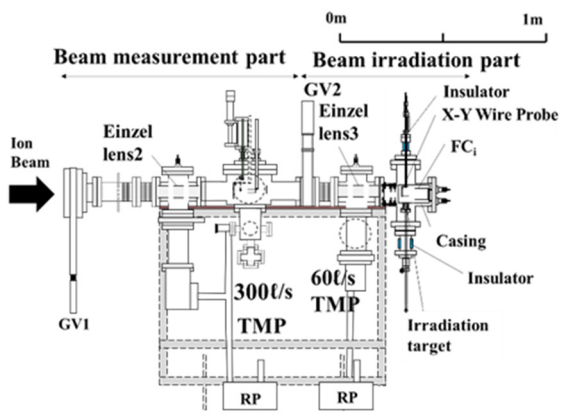

Figure 2: The side view of ion beam irradiation system.

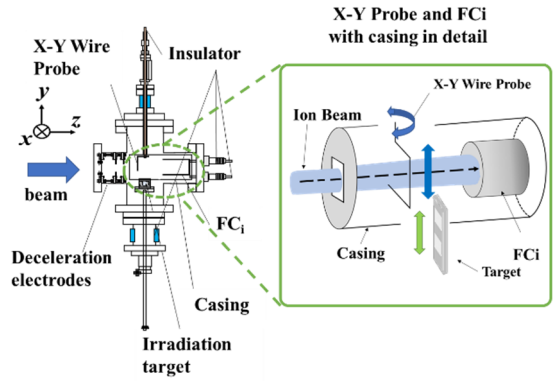

Figure 3: Detail of beam irradiation part.

When we conduct low energy irradiation to the sample, it is necessary to reduce influence of space charge effect of Xe^{q+} ion beams caused by deceleration. Therefore, we construct deceleration electrode (D). We set irradiation target which is rotatable and can apply deceleration voltage. In the irradiation experiment, the target can be irradiated with a decelerated ion beam current by setting the voltage of V_D and the target to the same voltage. We apply voltages V_D to electrodes. In the deceleration experiment and beam profile measurement, the decelerated ion beam current can be applied to each of the V_D voltage and the Faraday cup, Casing and X-Y wire probe at the same voltage.

EXPERIMENTAL RESULTS AND DISCUSSIONS

A. Typical Xe CSD

Figure 4 is typical Xe CSD before deceleration. The *x*-axis represents the magnetic field of the sector magnet, and the *y*-axis represents beam current [μA]. The extraction voltage of ion beam (V_{PE}) is 10kV. Slit width is 40mm. Ion beam is optimized with Xe^+. Operating pressure is 1.3×10^{-4}Pa. Incident microwave power is 30W. Reflected microwave power is 10W. Beam currents of Xe^+ is 66.2μA, Xe^{2+} is 35.6μA, Xe^{3+} is 3.1μA.

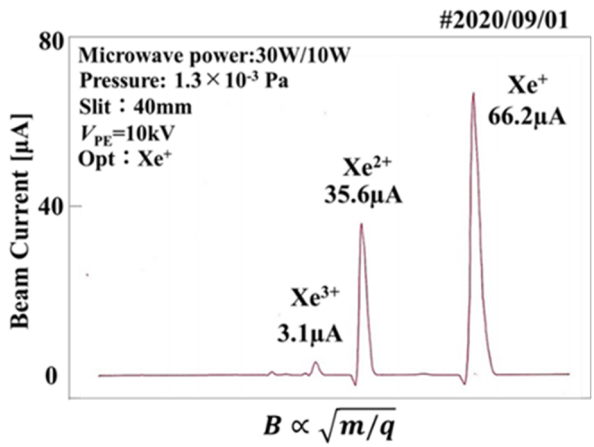

Figure 4: CSD before beam transport.

ISBN: 978-3-95450-226-4 ISSN: 2222-5692 doi:10.18429/JACoW-ECRIS2020-WEWZO05

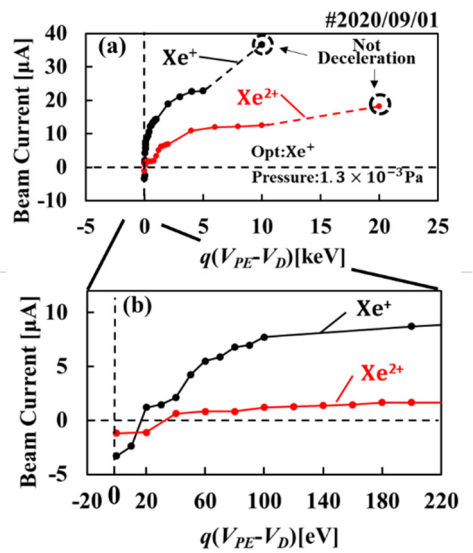

Figure 5: Xe deceleration experiment.

B. Xe Deceleration Experiment

Figure 5(a) and (b) show results of deceleration experiments of $Xe^{+,2+}$. The x-axis represents the energy of the ion beam. V_{PE} is beam extraction voltage and V_D is the beam deceleration voltage. The y-axis is beam current [μA] measured by the FCi. Figure 5(b) shows detail behavior from -20eV to 220eV. The experimental result of Xe^+ is shown in black, and the result of Xe^{2+} is shown in red. We fixed V_{PE} at 10kV and changed V_D from 0kV to 10kV. When we slowed down the beam to reduce the beam energy, the current decreased. We confirmed that beam current is decreased when we decelerated the beam. But we found that there was sufficient current to conduct irradiation experiments in the low energy region.

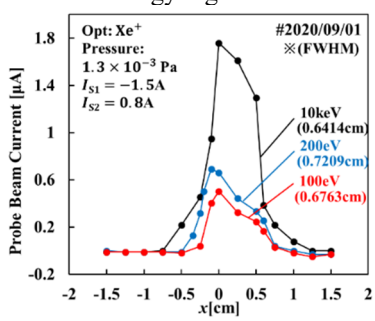

Figure 6: X direction beam profile.

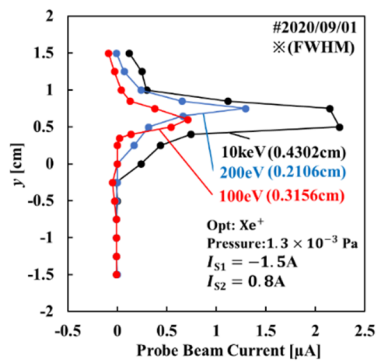

Figure 7: Y direction beam profile.

C. Measurements of Decelerated Xe^+ Ion Beam Profiles

Figure 6 and 7 show profiles of decelerated Xe^+ ion beam. Figure 6 is the x direction profile. Figure 7 is the y direction profile. Black, blue, and red data are 10kV (not deceleration), 200eV (deceleration), 100eV (deceleration). FWHM is descripted under each beam energy. We adjust the beam position by operating currents of steering coil 1 (I_{S1}) and steering Coil 2 (I_{S2}). The current values I_{S1} and I_{S2} are -1.5A and 0.8A. The maximum value of the beam current in the x direction is almost concentrated at x=0. The maximum value of the beam current in the y direction is concentrated at y=0.5~1.0. We need to adjust the beam position so that the maximum value is measured at the center in the future.

SUMMARY AND FUTURE PLAN

We measured the current value of the Xe ion beam in the low energy region by deceleration experiments, and confirmed that sufficient amount of currents for conducting irradiation experiments. We succeeded in acquiring the profile of decelerated Xe^+ ion beam. We evaluate the dose amount with high accuracy from beam profile. In the future, we plan to improve the equipment to obtain a larger dose and conduct irradiation experiments for various materials.

REFERENCE

[1] T. Nagaya, T. Nishiokada, S. Hagino, T. Uchida, M. Muramatsu, T. Otsuka, F. Sato, A. Kitagawa, Y. Kato, and Y. Yoshida, "Producing multicharged fullerene ion beam extracted from the second stage of tandem-type ECRIS" *Rev. Sci. Instrum.,* vol. 87, no. 2, p. 02A723, 2016. doi.org/10.1063/1.4934644

[2] A. Kitagawa, A. G. Drentje, T. Fujita, M. Muramatsu, K. Fukushima, N. Shiraishi, T. Suzuki, K. Takahashi, W. Takasugi, S. Biri, R. Rácz, Y. Kato, T. Uchida, and Y. Yoshida, "Recent developments of ion sources for life-science studies at the Heavy Ion Medical Accelerator in Chiba" *Rev. Sci. Instrum., vol.* 87, p. 02C107, 2016. doi.org/10.1063/1.4934843

[3] T. Takeda, T. Otsuka, S. Hagino, K. Onishi, K. Hamada, T. Omori, K. Okumura, and Y. Kato, "Improving multipole magnets and background vacuum conditions on electron cyclotron resonance ion sources" *Rev. Sci Instrum.,* vol. 91, p. 013308, 2020. doi.org/10.1063/1.5128472

[4] T. Otsuka *et.al.*, 21st Int. Conf. on IIT, IEEE Xplore Digital Library, IEEE Conf.Pub, 7882900, pp.1-4, 2016.

ISBN: 978-3-95450-226-4 ISSN: 2222-5692 doi:10.18429/JACoW-ECRIS2020-WEXZO02

^{39}Ar ENRICHMENT SYSTEM BASED ON A 2.45 GHz ECR ION SOURCE*

Z. H. Jia†, L. T. Sun, Y. G. Liu, J. L. Liu, J. Q. Zhang, Y. Yang,
Q. Hu, Y. H. Guo, Y. J. Li, T. X. Zhan, X. Fang, Q. Wu
Institute of Modern Physics, Chinese Academy of Sciences, Lanzhou, China
Z. H. Jia, School of Nuclear Science and Technology, Lanzhou University, Lanzhou, China
L. T. Sun, Y. G. Liu, Q. Wu, School of Nuclear Science and Technology,
University of Chinese Academy of Sciences, Beijing, China
Z. -T. Lu, W. Jiang, Hefei National Laboratory for Physical Sciences at the Microscale,
CAS Center for Excellence in Quantum Information and Quantum Physics,
University of Science and Technology of China, Hefei, China

Abstract

Aimed at improving the ATTA's (Atom Trap Trace Analysis) dating efficiency with ^{39}Ar radioactive isotope, an isotope enrichment system has been developed at IMP (Institute of Modern Physics) to increase the abundance of ^{39}Ar in the incident sample gas. In this enrichment system, a 2.45 GHz ECR ion source was designed to ionize sample gas and produce isotopes beams with several mA, and the isotopes beam is transported and separated in the separation beam line, which is consisted of two quadrupoles and an analysis magnet. The separated isotopes are collected by a rotated aluminium foil target. According to the recent cross-checked results with ATTA, high enrichment factor of ^{39}Ar isotope has been successfully reached. This paper will give a general introduction to the platform setup. The isotope enrichment efficiency is the critical issue for such a platform and will be specially discussed.

INTRODUCTION

^{39}Ar (half-life is 269 yr) is an ideal isotope for water or ice dating on the time scale of 50 ~ 1,000 years [1]. ^{39}Ar is produced in the atmosphere through cosmic ray induced nuclear reactions and equilibrates at an isotopic abundance of 8×10^{-16}, which makes it extremely challenging for all analytical methods [2]. Up to now, only three effective methods have been successfully applied to environmental sample analysis, i.e. low-level decay counting (LLC) [3], accelerator mass spectrometry (AMS) [4], and the recently developed ^{39}Ar-ATTA [5].

In term of research convenience and feasibility for small samples, ^{39}Ar-ATTA has demonstrated itself the most promising method for ^{39}Ar dating research with significantly higher selectivity [6]. However, typical applications of ATTA such as ocean ventilation would expect Ar sample of only 2 mL STP (standard temperature and pressure) of argon, which can be extracted from 5 L of water [7]. To improve the counting efficiency and counting rate of Ar-ATTA, a variety of improvements such as gas recirculation has been realized. But to improve the counting rate of ^{39}Ar by a factor of 10~100 to lower the analytical uncertainties for practical analyses, ^{39}Ar enrichment might be a more straightforward technical solution.

Noble gas enrichment with an electromagnetic separation system has been previously validated as a successful approach [8]. As ^{39}Ar has a very low abundance in sample Ar gas, to have efficient enrichment within hours, a high intensity beam mass separator system is needed. At IMP, we developed an electromagnetic separation system integrated with a high current 2.45 GHz ECR ion source capable of producing 1~10 mA Ar^+.

SYSTEM DEVELOPMENT

To enrich ^{39}Ar and increase its concentration with high efficiency, crucial factors are intense Ar^+ beam production and effective separation of the Ar isotopes on the target plane. A high-resolution spectrometer system can separate Ar isotopic ion beam well on the target plane. A 2.45 GHz ECR ion source can produce mono-charged ion beams up to 100 mA. Besides, an ECR ion source can realize a very high ionization efficiency of the incident sample gas compared to other types of high current ion sources, which is very advantageous for limited Ar sample gas. Therefore, a 2.45 GHz ECR ion source [9, 10] is utilized as the Ar ion beam production ion source. High beam current can obviously shorten the needed enrichment time, but the beam transport efficiency in the spectrometer system will become lower as a result of beam lose, which is mainly caused by space charge effect of the intense ion beam. Increasing ion beam extraction high voltage can mitigate the influence of space charge effect and therefore improve the transport efficiency. However, higher ion source extraction voltage means higher beam energy and that will imply higher rigidity of the magnetic separator system, and consequently a bulkier system, more power consumption, higher project budget and so on. Additionally, higher beam energy will cause trouble in unwanted beam and en richment target design. The final design of this enrichment system is a compromise of all the afore crucial factors.

The layout and picture of the IMP ^{39}Ar enrichment system is given in Fig. 1. In addition to a 2.45 GHz ECR ion source and a high-resolution spectrometer system consisting of a 95-degree dipole and two quadrupoles, a target chamber and a gas circulating system are also shown in the picture. The total length of the system is about 6 meters. All elements of this system have been meticulously designed to satisfy the projects goals.

* Work supported by National Key Research and Development Project (contract No.2016YFA0302202)
† email address: jiazehua@impcas.ac.cn.

ISBN: 978-3-95450-226-4 ISSN: 2222-5692 doi:10.18429/JACoW-ECRIS2020-WEXZO02

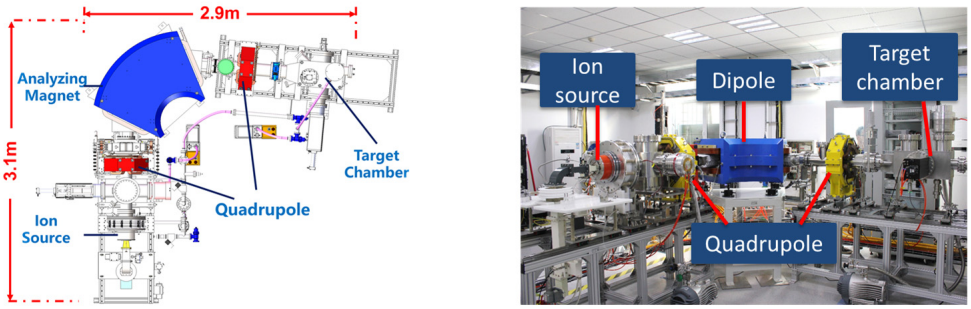

(a) (b)

Figure 1: Layout (a) and picture (b) of ^{39}Ar enrichment platform.

Ion Source

The typical parameters of the ion source are given in Table 1. A 2.45 GHz ECR ions source has been developed for this system. This ion source features a permanent magnet structure and ϕ 200 mm×100 mm dimension for compactness and easy-operation. Although maximum 5 mA Ar^+ is required for the routine operation, more than 10 mA Ar^+ beam extraction has been tested to demonstrate the ion source capacity.

Table 1: Typical Parameters of the Ion Source

Ion Species	Ar^+
Maximum Current	> 10 mA
Operation Model	DC
Ion Energy	40 keV
Beam Stability	≤ 1%

When treating real samples, only limited gas (typically < 5 ml STP) is available, and thus a high ionization efficiency is desired to improve the enrichment efficiency (as only the ionized Ar atoms can reach the target). Figure 2 shows the ionization efficiency and beam current at different gas consumption rates with microwave power of 300 W, which indicates that this ECR ion source could reach an ionization efficiency of >40% with Ar gas.

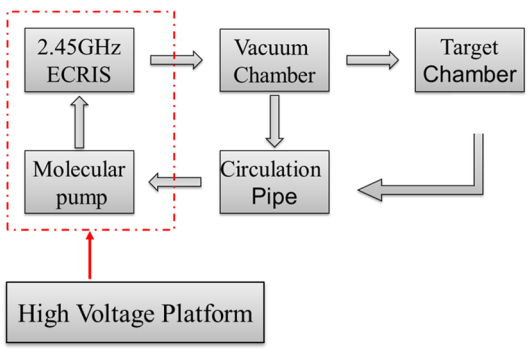

Figure 2: Sketch map of gas circulation.

As presented in Fig. 3, to have a reasonable ionization efficiency, the ion source needs to be operated with an extraction beam current of 1 mA to 3 mA.

Gas Circulation

As the typical Ar ionization efficiency is 50% ~ 60%, to maximize the enrichment efficiency up to 80%, Ar recirculation is necessary. The sketch map of gas circulation is shown in Fig. 3. The working gas that is suctioned from vacuum chamber and target chamber will be injected into ECR ion source to ionize again. In addition, the assistant molecular pump and ECR ion source are set on a high voltage platform.

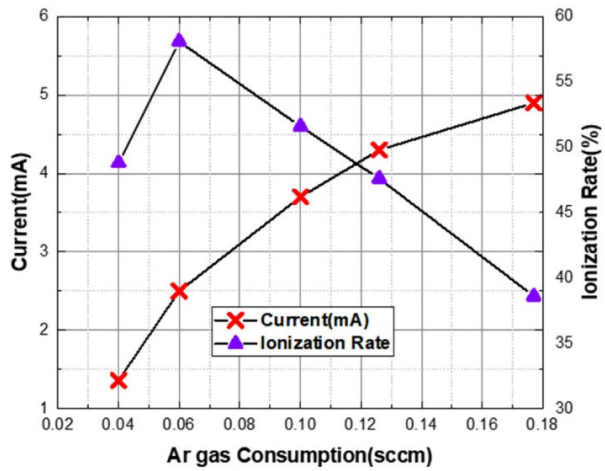

Figure 3: Ionization rate of ion source at different Ar gas consumption and beam current.

Moreover, Non-Evaporable Getter (NEG) pumps have been utilized in the ^{39}Ar enrichment platform vacuum system. Once the enrichment system starts to enrich ^{39}Ar, the vacuum evacuation system will be switch to recirculation operation mode, and the vacuum condition will be maintained via the NEG pumps. More information about this system has been indicated in former report [11].

EXPERIMENTS

According to the project schedule, some experiments have been finished to check this system's properties. Test experiment was finished to check Ar isotopic positions and some enrichment experiments to check project indicators. All these samples were enriched with Al foil, which had been heated in vacuum enrichment to remove gas on the surface of Al foil.

ISBN: 978-3-95450-226-4 ISSN: 2222-5692 doi:10.18429/JACoW-ECRIS2020-WEXZO02

Test Experiment

In order to cross-check the positions of the ^{39}Ar isotopic positions and indicate them directly, a temporary target was made to do this. A piece of heat-sensitive paper fixed on Al foil has been used to detect the Ar isotopic ion beams at the target plane. Ion beams of ^{36}Ar, ^{38}Ar and ^{39}Ar will bombard the heat-sensitive paper, while the high power ^{40}Ar beam will be indicated by the Al foil. As shown in Fig. 4, the resultant burning marks by bombarded ion beams are consistent with simulation results.

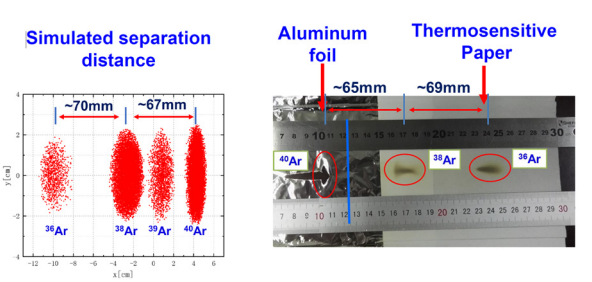

Figure 4: Analysis of the Ar isotopic positions: simulation results (left) and burning marks test (right).

Enrichment Experiments

Based on previous work, serval experiments have been finished to check system enrichment effect. And all enrichment results were validated by ATTA test. The enrichment system was operated for 6-hours and the Al foil containing the enriched samples were sent to USTC for ATTA analysis. Figure 5 shows count rate of natural abundance Ar and after enrichment Ar. Compared with natural Ar's count rate, enrichment samples' have been improved larger than 100 times.

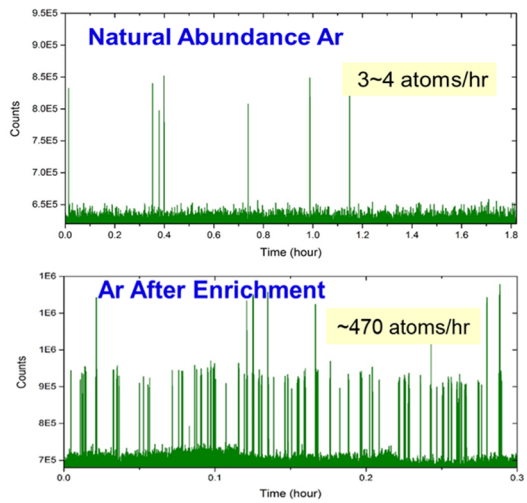

Figure 5: ^{39}Ar detection counts rate of natural abundance Ar gas and enriched samples.

Recently, two experiments with constant sample gas (natural Ar, 5 mL STP) were finished. As shown in Fig. 6, within the error of ATTA, the ^{39}Ar/^{38}Ar ratio of enriched samples are consistent with natural Ar's, which means these enrichment process can preserve sample's dating information completely.

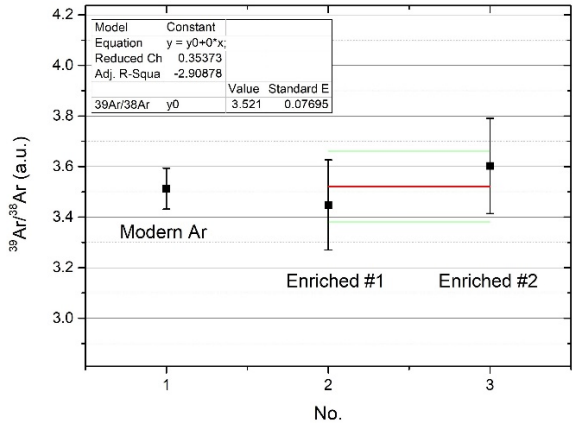

Figure 6: ^{39}Ar/^{38}Ar ratio detection with ATTA of Enriched samples and modern Ar.

CONCLUSION

This ^{39}Ar enrichment has been developed successfully. Moreover, recent experiments show that the ^{39}Ar abundance could be improve more than 100 and this system can preserve dating information well in enrichment process.

REFERENCE

[1] B. Lehmann *et al.*, "Radioisotope dynamics—the origin and fate of nuclides in groundwater", *Applied Geochemistry*, vol. 12, no. 6, p.727738, Nov. 1997. doi:10.1016/S0883-2927(97)00039-5

[2] H. Loosli *et al.*, "A dating method with ^{39}Ar", *Earth and Planetary Science Letters*, vol. 63, no. 1, p. 5162, 1983. doi:10.1016/0012-821X(83)90021-3

[3] P. Schlosser *et al.*, "The distribution of ^{14}C and ^{39}Ar in the Weddell Sea", *Journal of Geophysical Research: Oceans*, vil.99, no. C5, p. 1027510287, May 1994. doi:10.1029/94JC00313

[4] P. Collon *et al.*, "Development of an AMS method to study oceanic circulation characteristics using cosmogenic ^{39}Ar", *Nucl. Instrum. Methods Phys. Res., Sect. B*, vol. 223, p. 428434, Aug. 2004. doi: 10.1016/j.nimb.2004.04.081

[5] W. Jiang *et al.*, "Ar-39 Detection at the 10(-16) Isotopic Abundance Level with Atom Trap Trace Analysis", *Physical Review Letters*, vol. 106, no. 10, p. 103001, Mar. 2011. doi:10.1103/PhysRevLett.106.103001

[6] Z. T. Lu *et al.*, "Tracer applications of noble gas radionuclides in the geosciences", *Earth-Science Reviews*, vol. 138 p. 196214, Nov. 2014. doi: 10.1016/j.earscirev.2013.09.002

[7] Ebser, S *et al.*, "^{39}Ar dating with small samples provides new key constraints on ocean ventilation", *Nature Communications*, vol. 9, p. 17, Nov. 2018. doi:10.1038/s41467-018-07465-7

[8] Lavielle, B *et al.*, "Development toward a double focusing isotopic separator for noble gas isotope enrichment", *Journal of Mass Spectrometry*, vol. 51, no. 10, p. 908913, 2016 doi:10.1002/jms.3800

[9] Wu, Q *et al.*, "A 2.45 GHz intense proton source and low energy beam transport system for China Initiative Accelerator Driven Sub-Critical reactor system", *Review of Scientific Instruments*, vol. 85, no. 2, p. 02A703, Oct. 2013. doi:10.1063/1.4824804

ISBN: 978-3-95450-226-4 ISSN: 2222-5692 doi:10.18429/JACoW-ECRIS2020-WEXZO02

[10] Wu, Q *et al.*, "Development of 2.45 GHz ECR ion sources at IMP", *Journal of Instrumentation*, vol. 14, p. C02009, Feb. 2019. doi:10.1088/1748-0221/14/02/C02009

[11] Jia, Z *et al.*, "An electromagnetic separation system for the enrichment of ^{39}Ar", *Review of Scientific Instruments*, vol. 91, no. 3, p.033309, Feb. 2020. doi: 10.1063/1.5128697

ISBN: 978-3-95450-226-4 ISSN: 2222-5692 doi:10.18429/JACoW-ECRIS2020-WEXZO03

CONCEPTUAL DESIGN OF AN ELECTROSTATIC TRAP FOR HIGH INTENSITY PULSED BEAM*

W. Huang†, L. T. Sun, Y. G. Liu and H. W. Zhao
University of Chinese Academy of Sciences/IMP/CAS, Lanzhou, China
D. Z. Xie, LBNL, USA

Abstract

Highly charged ion sources play an important role in the advancement of heavy-ion accelerators worldwide. Demands of highly-charged heavy ions for new and existing accelerators have driven the performance of ion sources to their limits and beyond. In parallel to developing new technologies to enhance the performance of ECR ion source, this paper presents a conceptual design of an ion trap aiming to convert a CW ion beam into a short beam pulse with high compression ratios. With an electron gun, a solenoid and a set of drift tubes, the injected ions will be trapped radially and axially. By manipulating the potential of the drift tubes, ions can be accumulated with multiple injections and extracted at a fast or a slow manner. This paper presents the simulations and design features of the envisioned ion trap.

INTRODUCTION

The ion kinetic energy produced with accelerators is either proportional to the square of the ion charge state Q (Cyclotrons) or linear to Q (Linac). Therefore, if the beam intensity can meet the requirement, future and existing heavy-ion accelerators can benefit from injecting ion beams of higher charge state Q which could not only achieve the required accelerator performance but also possibly lead to substantial cost savings. After more than 40 years' continued development, the state of the art Electron Cyclotron Resonance Ion Source (ECRIS) has advanced to a 3rd generation with full-superconducting magnets operating at 24 to 28 GHz microwaves, such as VENUS at LBNL, SECRAL & SECRAL 2 at IMP, SC-ECR at RIKEN and SUSI at MSU, etc. [1-5] To advance science research and enhance its capabilities, future and existing heavy-ion accelerators worldwide demand intense highly-charged ion beams. For example, FRIB at MSU needs 13 pμA of CW (continuous wave) $^{238}U^{34+}/U^{33+}$ [6], FAIR at GSI needs 15 emA of pulsed $^{238}U^{28+}$ beam [7], High Intensity heavy ion Accelerator Facility (HIAF) at IMP needs U^{34+} ion beams with an intensity of 1.7 emA in pulsed mode [8], which is far beyond the record what SECRAL 2 can achieve, 390 eμA of U^{34+} [9].

Presently the 4th generation of ECR ion source is under development to meet the heavy ion beam intensity demands with as high charge state as possible. The development of the next generation of ECR ion source requires great efforts/resources and is a time consuming process as it has to overcome many technical challenges, such as how to fabricate the magnet system to mitigate the much higher em interaction forces, more demanding quench protection, sufficient cooling the plasma chamber under high microwave power operation, etc. [10] While benefitting from the 4th generation ECR ion sources, those heavy-ion accelerators requiring intense pulsed ion beams can also benefit from a relatively low-cost device that can convert a CW ion beam of lower intensity but with higher charge state into an intense beam pulse. This is the reason we plan to develop a CW ion beam compressor that could trap and accumulate the highly-charged ions from an ECR ion source to convert those ions into a much higher peak intensity pulsed beam. The simulation details of this conceptual Ion TRap for high Intensity Pulsed beams (ITRIP) are presented and discussed below.

* Work supported by the program of China Scholarships Council (No. 201904910324).
† whuang@impcas.ac.cn

PRINCIPLE OF THE ION TRAP

The structure of the ion trap is very similar to an Electron Beam Ion Source (EBIS), as schematically shown in Fig. 1. Highly charged ions produced with an ECR ion source are injected into the ion trap where the ions get slowed down for accumulation and extraction. A cathode of high emissivity produces an electron beam to provide a negative potential well to radially confine the ions. The axial confinement of the ions is achieved by 1. a high gate potential at the left end (as shown in Fig. 1) to keep the ions from escaping the Trapping Section; 2. a set of drift tubes at the injection side (Bunching Section) to generate a repeating traveling electric potential wave (Vbunch) to accept and move the ions into the Trapping Section and at the same time minimize the ion axial escaping. The Trapping Section accumulates the ions until the ions are extracted out, through manipulating the electric potential at the left hand and other electrodes, to form an intense beam pulse.

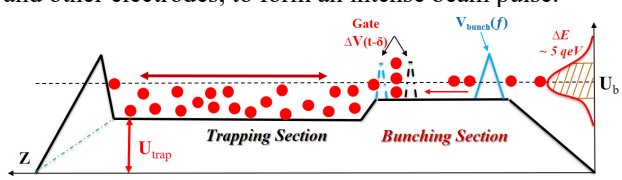

Figure 1. Schematic layout of the ion trap.

The most important key factor of the ion trap is the ion trapping efficiency. Some of the ions will get lost during the accumulation and extraction periods. The ion trap should preserve the ion charge state, in addition to confining the ions. The charge state of ions can be lower due to charge exchange with the background gas, radiative recombination (RR) with the electrons, etc. An ultrahigh vacuum should be provided to reduce the charge exchange. Some of the electrons will also get trapped moving back

ISBN: 978-3-95450-226-4 ISSN: 2222-5692 doi:10.18429/JACoW-ECRIS2020-WEXZO03

and forth which leads to an increased electron density resulting in higher space charge potential for better ion confinement.

The repetition rate requirement for HIAF is 1 Hz with an injection time of about 400 μs and the CW beam intensity of U^{34+} or higher charge state uranium ions is typically 0.2 to 10's pμA produced with SECRAL 2 ion source. So if the ion trap can catch 50% of an injected 1 pμA of U^{34+} ions in the Bunching Section and with a 25% accumulation efficiency in the Trapping Section, the number of U^{34+} ions in the Trapping Section would be ~ 7×10^{11} assuming the capacity of Trapping Section is high enough. If the extraction efficiency of the ion trap can reach 50% which would lead to ~ 3.5×10^{11} ions/pulse.

DESIGN OF THE ELECTRON GUN

A magnetic field is needed for confinement of the electrons. To minimize the simulation time for the conceptual design, the length of the ITRIP is chosen to be ~ 0.5 m. The magnetic field is produced by a solenoid located inside an iron yoke, as shown in Fig. 2 (a). The current density of solenoid is 9 A/mm^2. The inner and outer radius of solenoid are 10 cm and 15 cm, respectively. The length of solenoid is 0.5 m. The thickness of the iron yoke is 2 cm. The computed magnetic field distribution with Vector Field TOSCA [11] is shown in Fig. 2 (b). The maximal magnetic field in the trap is ~ 5570 G which can be produced by room temperature solenoid with water cooling.

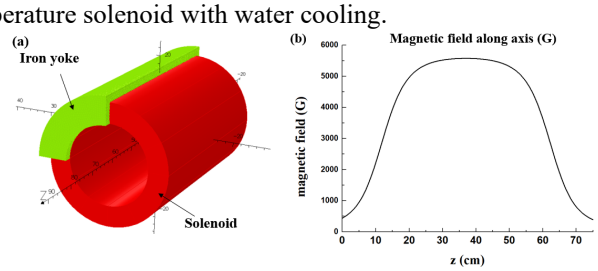

Figure 2. (a) Magnet structure. (b) Magnetic field profile.

Ions are to be injected from one side and extracted from the other side of the ion trap. An electron hollow cathode of a convex surface located at the extraction end is designed with an adequate aperture for ion extraction. A portion of the electron beam, with energy loss due to collision, is trapped between the cathode and reflecting electrode in the confining magnetic field. The corresponding thermionic current density on the cathode is described by Richardson-Dushman as follows [12]:

$$j = A_G T^2 \exp(-\frac{\varphi}{k_B T}) \quad (1)$$

Where A_G is generalized Richardson constant, T is the cathode temperature in K, φ is the work function in eV and k_B is Boltzmann constant.

The radius of drift tube along axis should meet the following equation to maintain a uniform potential distribution in the trap with the same potential on all drift tubes [13]:

$$R_t(z) = R_{t,0} \cdot \sqrt{\frac{B_0}{B(z)}} \quad (2)$$

Where $R_t(z)$ is the inner radius of drift tubes at a location of axial coordinate z and magnetic field $B(z)$ and $R_{t,0}$ is in the point with the maximum value of $B(z)$, notated as B_0.

LaB_6 is widely used in fabricating thermionic electron cathode. Its operating temperature is over 1500 K with generalized Richardson constant of 29 A·cm^{-2}·K^{-2} [14]. The anode consists of two rings to let electron go through between them. The electron gun is simulated with Vector Field SCALA [11]. The hollow electron beam oscillates between the cathode and reflecting electrode, i.e., back and forth through the Trapping Section and the Bunching Section. To get a convergent result, the 9th drift tube and the reflecting electrode after that are omitted in the simulation, as shown in Fig. 3. The temperature of cathode in simulation is 1600 K, the relative potential of all the electrodes including cathode from left to right are 0, 2.5 kV, 4 kV, 1.1 kV, 1.1 kV, 1.1 kV, 1.1 kV, 2.5 kV, 1.1 kV, 1.1 kV. The potential of gate electrode is 2.5 kV when it's closed.

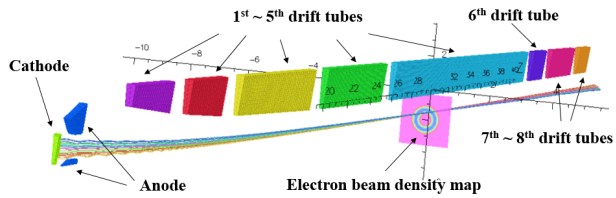

Figure 3. Simulation result of the electron gun.

The electron beam current is ~ 430 mA according to the simulation, with inner r_1 of ~ 0.3 cm and outer radius r_2 of ~ 0.46 cm, as shown in Fig. 4 (a). The trap potential of an electron beam with uniform distribution of radius r_e has the shape [15]

$$V_e(r) = \begin{cases} \dfrac{U_e r^2}{r_e^2} & for \quad r \le r_e \\ U_e(2\ln\dfrac{r}{r_e} + 1) & for \quad r > r_e \end{cases} \quad (3)$$

Where $U_e = I_e/(4\pi\varepsilon_0 v_e)$. The hollow electron beam shown in Fig. 4 (a) can be regarded as a combination of a positive electron beam with radius of r_1 and a negative electron beam with radius of r_2. Assume the relative potential on the drift tube with radius R_t is 0, the space charge potential of the hollow electron beam of 430 mA and 1.1 keV can be calculated with equation (3), as shown in Fig. 4 (b). The depth of the space charge potential of electrons is ~ 0.29 kV. Increase the beam current can increase the potential depth which can lead to better ion confinement.

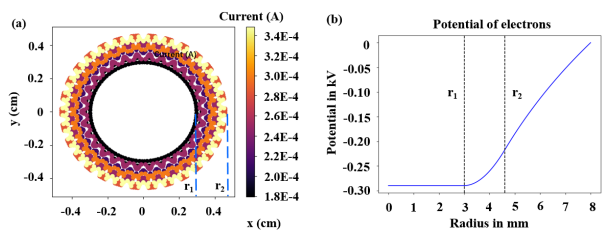

Figure 4. Space charge potential distribution according to the current distribution of electrons. (a) Current distribution. (b) Space charge potential of electron beam.

ISBN: 978-3-95450-226-4 ISSN: 2222-5692 doi:10.18429/JACoW-ECRIS2020-WEXZO03

SIMULATION OF THE ION TRAP

Assume the energy of U^{34+} ions at the exit of an ECRIS are the same which is $21.13 \cdot q$ keV where q is the charge state. The energy of U^{34+} ions will be decreased to $0.03 \cdot q$ keV if the 8th drift tube is on 21.1 kV. Assume a parallel beam of U^{34+} of radius of 5 mm prior to its injection into the ion trap with magnetic field, Fig. 5 shows the simulation of the injected U^{34+} beam profile with code IBSIMU [16]. The electron beam in the trap is omitted to simplify the simulation. The potential of these 4 electrodes from left to right are 17 kV, 20.7 kV, 21.1 kV, 21.1 kV. The potential of the left boundary is 0 V. The left boundary, reflecting electrode and the 9th drift tube can be regarded as an einzel lens that focus ion beam at injection.

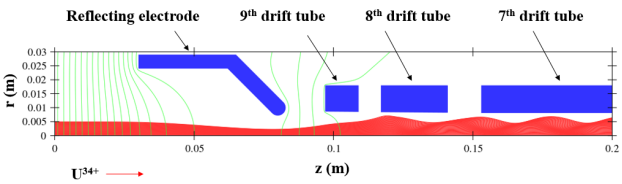

Figure 5. Simulated profile of U^{34+} ions injection.

A PIC simulation software VSim [17] is used to simulate the accumulation of ions in the trap with electrons and the process is extremely time consuming. To get a feel of the trapping, the collisions including charge exchanges and RR (Radiative Recombination) processes among the particles are neglected but take into account the effects of the em field and space charge force on the U^{34+} ions. The electrostatic potential varies depending on the space charge potential of electron beam. The energy of U^{34+} ions can vary from $(10 \sim 100) \cdot q$ eV in the Bunching Section.

Potential on the 9th drift tube will be raised to trap the ions when the Bunching Section is full. Potential on the 8th drift tube will be raised when compressing the ions. Potential on the 6th drift tube will be lower (the gate is open) to dump the U^{34+} ions into the Trapping Section when compression of ions is completed. Potential on the 7th potential will be raised to push the remaining ions into the Trapping Section, and potential on the 6th potential will be raised (the gate is closed) after that. Repeat these processes several times until the Trapping Section is full. The trajectory of one bunch of U^{34+} at 9.6 μs when dumping of ions is completed is shown in Fig. 6 (a). The green points are electrons and the red points are U^{34+} ions in which a good portion of the ions is trapped. The velocity distribution of ions along axis is shown in Fig. 6 (b). Some of the ions with larger energy are reflected by the 1st drift tube while the lower energy ions remain in the Bunching Section.

Due to the time consuming computation and the capability limit of a desktop computer, only 5 bunches of U^{34+} ions are conducted in the simulations. The time for each bunch in injection is ~ 10 μs which consists of ~ 3 μs of injection time, ~ 4 μs of compression time and ~ 3 μs of dumping time. The accumulation results of electrons and U^{34+} ions in the trap are shown in Fig. 7. The accumulation of electrons is essentially saturated after 40 μs with electrons of ~ 5×10^{12} in the trap, which means the theoretical capacity of the trap for U^{34+} is ~ 1.4×10^{11} that should be increased further. The calculated number of trapped U^{34+} ion at 50 μs is ~ 1.8×10^{8} in the simulation. A fitting plot of quadratic function predicts the number of trapped U^{34+} ions to reach 3.4×10^{10} after 1 s, which is only a quarter of the theoretical capacity of the trap. Assume the extraction efficiency is ~ 50%, the intensity of U^{34+} after extraction without considering charge exchange and RR processes will be 1.7×10^{10} ions/pulse.

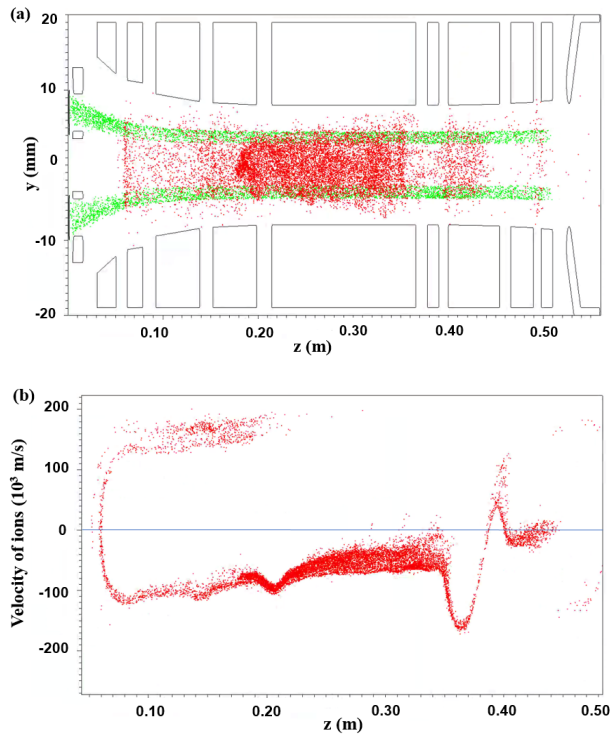

Figure 6. Simulation of one bunch of injection. (a) Particle distributions. (b) Ion velocity distribution.

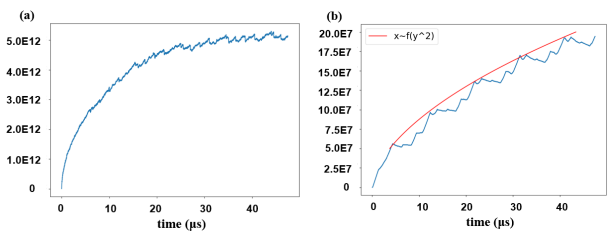

Figure 7. Simulation of the accumulation of electrons (a) and U^{34+} ions (b).

The ions will be extracted from the ion trap at 1 s to accommodate HIAF injection frequency. To simulate the extraction of a high intensity ion beam, assume the extracted instantaneous peak current of U^{34+} is 1 A with $150 \cdot q$ eV, the simulated result is shown in Fig. 8. The outer ring of anode is omitted for simplicity. An einzel lens is used to focus the U^{34+} ions to mitigate the strong space charge force. During the extraction, the voltage of anode decreases to 21.1 kV while the voltage of cathode remains on 20 kV. The voltages of einzel lens from left to right are 19.1 kV, 11.1 kV, 10.1 kV.

ISBN: 978-3-95450-226-4 ISSN: 2222-5692 doi:10.18429/JACoW-ECRIS2020-WEXZO03

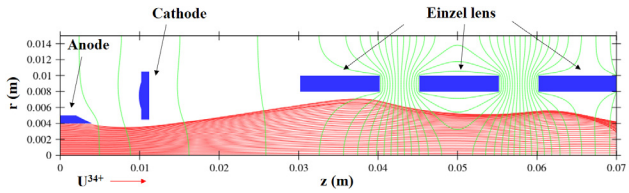

Figure 8. Simulated profile of U^{34+} ions extraction.

DISCUSSION

The capacity of the discussed trap for both electrons and ions is proportional to the trap length to certain extend that means a higher trapping capacity feasible with a longer trap. A larger line density of electrons will lead to a better confinement for ions, which means the current of electron gun can be higher. Increasing the voltage of the anode is a direct way to get a higher current electron beam. However, a too high electron energy can lead to ion ionization resulted in ion loss.

The balance equation of ions considering ionization, RR, charge exchange and the loss of heated ions by Coulomb collisions can be found in reference [18]. Consider the evolution of charge state of uranium ions in 3 cases: (a) 0.15A of electrons with 500 eV in the trap; (b) 0.5 A of electrons with 1100 eV in the trap; (c) 4.7 A of electrons with 5000 eV in the trap. Assume the initial U^{34+} ions in the trap is 3.4×10^{10}, namely ~ 6×10^{8} cm^{-3} in the trap for a confining column of cross section of ~ 1 cm^2. At a background vacuum of 1×10^{-10} Torr, the calculated charge state evolution of uranium ions for the 3 cases mentioned above are shown in Fig. 9. In the 1st case (Fig. 9 (a), (d)), the loss of U^{34+} ions due to charge exchange and RR processes makes up only 3% of the total loss, which means U^{34+} ions are lost mainly due to poor confinement caused by the low current of electrons. In the 3rd case (Fig. 9 (c), (f)), The loss of U^{34+} ions due to charge exchange and RR processes makes up almost the total loss, which means the confinement for ions is good enough. Some U^{34+} ions are ionized, as the ionization potential of U^{34+} is only 1.4 keV, by the high energy of electrons resulted in more loss of U^{34+} in comparison to the 2nd case (Fig. 9 (b), (e)) after 10 ms. The loss of U^{34+} ions due to charge exchange and RR processes makes up 40% of the total loss in case 2 and goes up as increase the current of electron beam. Increasing the energy of electrons to get a higher electron beam current is feasible but the electron energy should depend on the tolerable loss of ions to be trapped.

Assume the U^{34+} ions accumulate as the fitting curve in Fig. 7 (b), the evolution of charge state of ions considering only charge exchange and RR processes is shown in Fig. 10 with an electron beam current of 0.4 A and 1100 eV when the vacuum is 1×10^{-10} Torr. The trapped U ions will be 1.24×10^{10} after 1 s. As a result, the intensity of U^{34+} for ITRIP after extraction will be 6.2×10^{9} ions/pulse with an extraction efficiency of 50% and that means more efforts needed to increase output.

Experimental proof of principle is needed to verify the validity of the design. The structure design of the ITRIP is almost completed, the machining and experiments will be taken place in the near future.

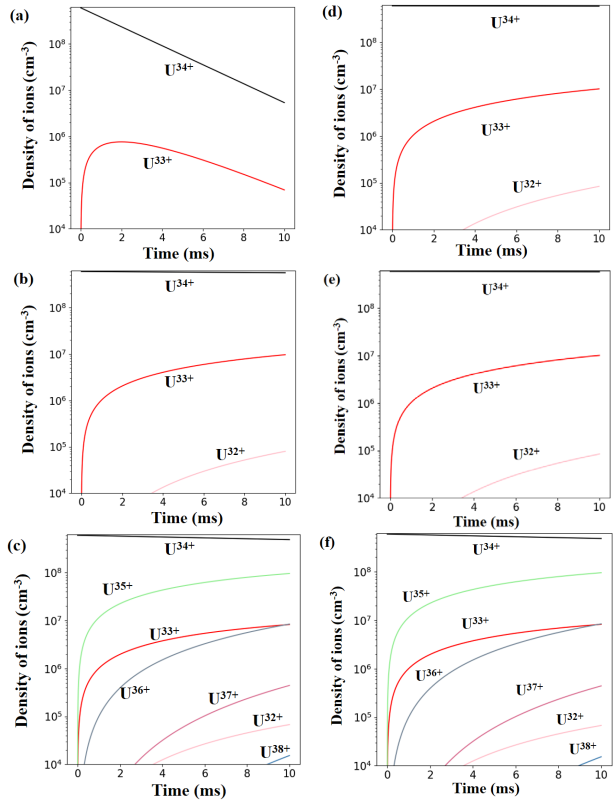

Figure 9. Evolution of charge state of ions for different cases considering all the loss processes (a), (b), (c) and only charge exchange, RR processes (d), (e), (f).

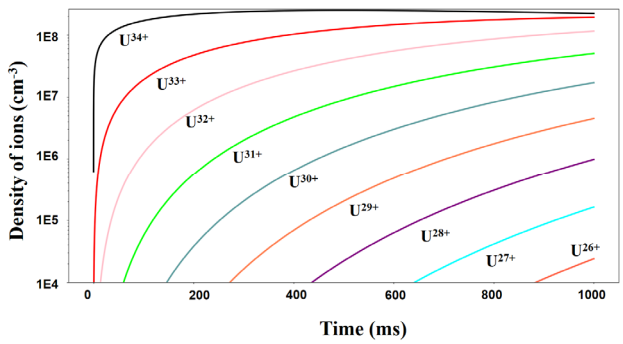

Figure 10. Evolution of charge state of ions in 1 s.

ACKNOWLEDGEMENTS

This work has been supported by the program of China Scholarships Council (No. 201904910324).

REFERENCES

[1] J. Y. Benitez et al., "Current Developments of the VENUS Ion Source in Research and Operations", in Proc. 20th Int. Workshop on ECR Ion Sources (ECRIS'12), Sydney, Australia, Sep. 2012, paper THXO02, pp. 153-158.

[2] H. W. Zhao *et al.*, "New development of advanced superconducting electron cyclotron resonance ion source

ISBN: 978-3-95450-226-4 ISSN: 2222-5692 doi:10.18429/JACoW-ECRIS2020-WEXZO03

SECRAL", *Rev. Sci. Instrum*. Vol. 81, p 02A202, 2010. doi: 10.1063/1.3273058

[3] L. T. Sun et al., "SECRAL II Ion Source Development and the First Commissioning at 28 GHz", in Proc. 22nd Int. Workshop on ECR Ion Sources (ECRIS'16), Busan, Korea, Aug.-Sep. 2016, pp. 43-47. doi:10.18429/JACoW-ECRIS2016-TUAO04

[4] Y. Higurashi *et al*., "Recent development of RIKEN 28 GHz superconducting electron cyclotron resonance ion source", *Rev. Sci. Instrum*. Vol. 85, p 02A953, 2014. doi: 10.1063/1.4848976

[5] G. Machicoane *et al.*, "Performance Investigation of the NSCL 18 GHz Superconducting ECR Ion Source SUSI", in *Proc. 23rd Particle Accelerator Conf. (PAC'09)*, Vancouver, Canada, May 2009, paper MO6RFP035, pp. 432-434.

[6] J. Wei, "The Very High Intensity Future", in *Proc. 5th Int. Particle Accelerator Conf. (IPAC'14)*, Dresden, Germany, Jun. 2014, pp. 17-22. doi:10.18429/JACoW-IPAC2014-MOYBA01

[7] O. K. Kester, "Status of the FAIR Facility", in *Proc. 4th Int. Particle Accelerator Conf. (IPAC'13)*, Shanghai, China, May 2013, paper TUXB101, pp. 1085-1089.

[8] X. Guoqing *et al*., "HIAF and CiADS National Research Facilities:Progress and Prospect", *Nucl. Phys. Rev*.,Vol. 34, p. 275283, 2017. Doi: 10.11804/NuclPhysRev.34.03.275

[9] W. Lu *et al.,* "Production of intense uranium beams with inductive heating oven at Institute of Modern Physics", *Rev. Sci. Instrum*., vol. 90, p. 113318, 2019. doi: 10.1063/1.5128419

[10] H. W. Zhao *et al*., "Superconducting ECR ion source: From 24-28 GHz SECRAL to 45 GHz fourth generation ECR", *Rev. Sci. Instrum*., vol. 89, p. 052301, 2018. doi: 10.1063/1.5017479

[11] OPERA 3d, Vector Fields Ltd., https://www.3ds.com/products-services/simulia/products/opera/.

[12] A. Modinos, *Field, Thermionic and Secondary Electron Emission Spectroscopy*, New York, USA: Springer, 1984.

[13] A. I. Pikin *et al.*, "Tandem EBIS", in *Proc. 12th Int. Conf. on Heavy Ion Accelerator Technology (HIAT'12)*, Chicago, IL, USA, Jun. 2012, paper PO18, pp. 101-104.

[14] K. Torgasin *et al.*, "Thermally assisted photoemission effect on CeB_6 and LaB_6 for application as photocathodes", *Phys. Rev. Accel. Beams*, vol. 20, p. 073401, 2017. doi: 10.1103/PhysRevAccelBeams.20.073401

[15] G. Zschornacka *et al.*, "Electron Beam Ion Sources", *CERN Accelerator School (CAS)*, Senec, Slovakia, May – Jun. 2012. doi: 10.5170/CERN-2013-007.165

[16] T. Kalvas *et al*., "IBSIMU: A three-dimensional simulation software for charged particle optics", *Rev. Sci. Instrum*., vol. 81, p. 02B703, 2010 doi: 10.1063/1.3258608.

[17] VSim, Tech-X, https://www.txcorp.com/vsim/.

[18] R. Becker *et al*., "Simulation of charge breeding for trapped ions ", *J. Phys.: Conf. Ser*., vol. 58, p. 443, 2007. doi: 10.1088/1742-6596/58/1/102

ISBN: 978-3-95450-226-4 ISSN: 2222-5692 doi:10.18429/JACoW-ECRIS2020-WEXZO05

PRODUCTION OF METAL ION BEAMS FROM ECR ION SOURCE

A.E. Bondarchenko†, S. Bogomolov, V. Loginov, A. Lebedev, V. Mironov, D. Pugachev,
Joint Institute for Nuclear Research, FLNR, Dubna, Russia
M. Zdorovets, I. Ivanov , E. Sambayev, M. Koloberdin,A. Kurakhmedov, D. Mustafin,
M. Abdigaliyev, Astana branch of Institute of Nuclear Physics, Nur-Sultan, Kazakhstan

Abstract

The paper describes the production of metal ion beams from ECR ion sources by the MIVOC (Metal Ions from Volatile Compounds) method. The method is based on the use of volatile metal compounds having high vapor pressure at room temperature: for example, $Cr(C_5H_5)_2$, $(CH_3)_5C_5Ti(CH_3)_3$ and several others. Using this method, intense beams of chromium, titanium, iron, and other ions were obtained at the U-400 FLNR JINR and DC-60 cyclotrons (Astana branch of the INP, Alma-Ata, Kazakhstan Republic).

PRODUCTION OF METAL IONS FROM ECR ION SOURCE USING THE MIVOC METHOD

This method is based on the use of organometallic compounds having a relatively high vapor pressure (10^{-3} Torr) at room temperature. Such a vapor pressure is sufficient for the operation of the ECR ion source with corresponding conductivity of the feed line [1].

The necessary preparation of the substance is performed depending on the chemical properties of each compound. For example, titanium and nickel compounds are prepared in an argon box under a red light, both substances are afraid of air, humidity and light. Whereas, the iron compound can be placed into container in air. After preparation all containers with compounds are pumped to the forevacuum, and connected to the ECR ion source through a mechanical or automatic valve for supplying substances [2].

THE CYCLOTRON U-400 OF FLEROV LABORATORY NUCLEAR REACTION (JINR, RUSSIA)

The cyclotron U-400 is designed for production of accelerated ion beams of atomic mass in the range A=4 ÷ 209 and energy 3 ÷ 29 MeV/nuclon. U-400 isochronous cyclotron has been in operation since 1978 [1]. Cyclotron is 4 m in diameter, D=4 m, with K=650 energy factor. Charge exchange technique is used for beam extraction. Axial injection channel with external ion source has been in operation at U-400 since 1996. An ECR ion source ECR-4M is installed at the U-400 cyclotron [3]. Ion source ECR-4M was modernized to improve its performance: higher magnetic field in the injection region; new hexapole; the increase of the discharge chamber from 64 to 74 mm; direct UHF injection.

BEAMS OF METAL IONS FROM ECR-4M ION SOURCE AT THE CYCLOTRON U-400

At the U-400 cyclotron, stable beams of metal ions were produced by the MIVOC method for various research areas:

- ^{52}Cr, ^{56}Fe – study of fusion-fission processes, quasi-fission and multi-nucleon transfer reactions
- ^{54}Cr, ^{50}Ti – alpha, beta and gamma spectroscopy of isotopes of heavy and super heavy elements
- ^{56}Fe – study of reactions with beams of stable and radioactive nuclides leading to the formation of exotic nuclei

Figures 1-4 show the spectra of chromium, titanium and iron ions at the U-400 cyclotron.

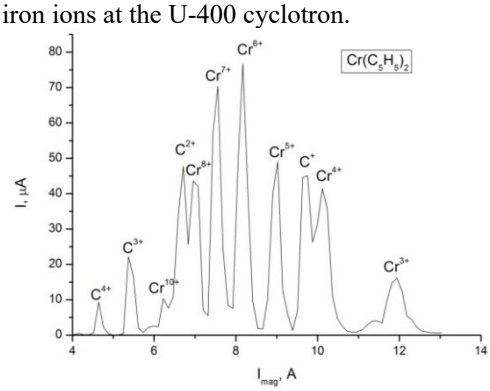

Figure 1: The spectrum of ^{52}Cr ions, the source settings are optimized for $^{52}Cr^{6+}$ – 74 μA. UHF power – 49 W.

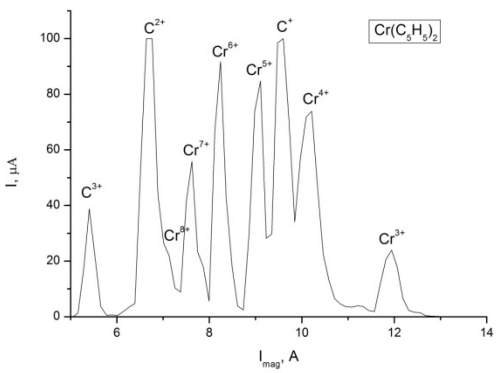

Figure 2: The spectrum of ^{54}Cr ions, the source settings are optimized for $^{54}Cr^{6+}$ – 95 μA. UHF power – 58 W.

† bondarchenko@jinr.ru

ISBN: 978-3-95450-226-4 ISSN: 2222-5692 doi:10.18429/JACoW-ECRIS2020-WEXZO05

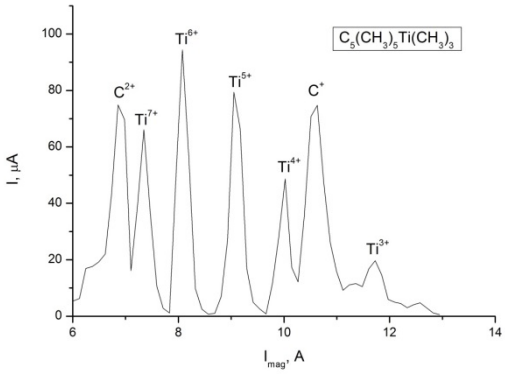

Figure 3: The spectrum of ^{50}Ti ions, the source settings are optimized for $^{50}Ti^{5+}$ – 78 μA. UHF power – 51 W.

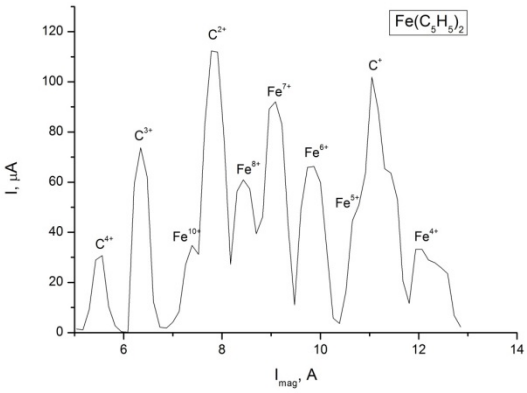

Figure 4: The spectrum of ^{56}Fe ions, the source settings are optimized for $^{56}Fe^{7+}$ – 90 μA. UHF power – 65 W.

THE ACCELERATOR COMPLEX DC-60 OF ASTANA BRANCH OF THE INP (ALMA-ATA, KAZAKHSTAN REPUBLIC)

The cyclotron DC-60 is designed for production of accelerated ion beams of atomic mass in the range A=4 ÷ 132 and energy 0,35 ÷ 1,7 MeV/nuclon [4]. Main objectives: scientific research; education; production of track membranes with special properties; creation of micro and nano structures; surface modification of standard materials, creation of new materials with required properties. The cyclotron is equipped with the ECR ion source DECRIS-3 [5].

Beams of ions of titanium ($(CH_3)_5C_5Ti(CH_3)_3$), chromium ($Cr(C_5H_5)_2$), cobalt ($Co(C_5H_5)_2$), nickel ($Ni(C_5H_5)_2$), iron ($Fe(C_5H_5)_2$), germanium ($Ge(CH_3)_4$) and hafnium ($(C\text{-}_5H_5)_2Hf(CH_3)_2$) after preliminary preparation were produced by the MIVOC method of the DECRIS-3 ion source at the DC-60 cyclotron shown in Figs. 5-11.

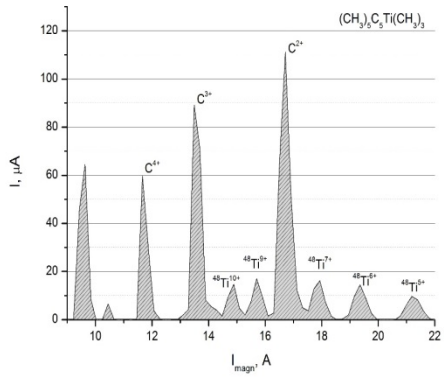

Figure 5: The spectrum of Ti ions, the source settings are optimized for $^{48}Ti^{9+}$ - 18 μA. UHF power – 156 W.

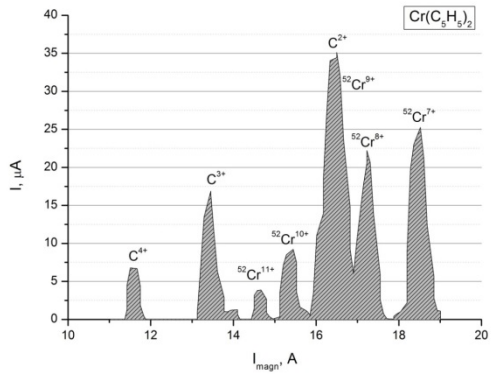

Figure 6: The spectrum of Cr ions, the source settings are optimized for $^{52}Cr^{10+}$ - 9 μA. UHF power – 72 W.

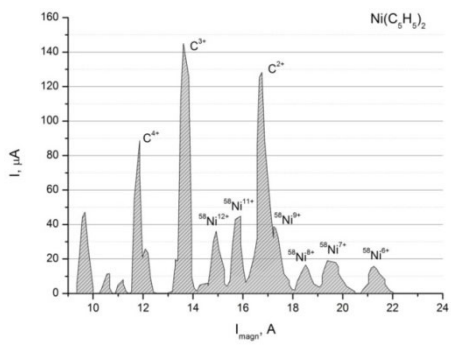

Figure 7: The spectrum of Ni ions, the source settings are optimized for $^{58}Ni^{11+}$ - 43 μA. UHF power – 260 W.

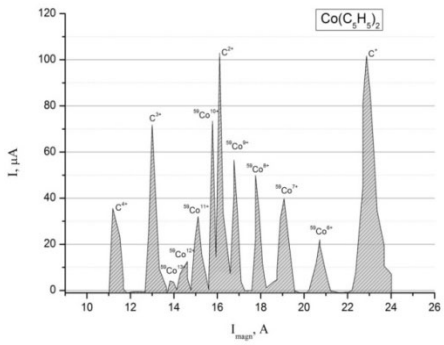

Figure 8: The spectrum of Co ions, the source settings are optimized for $^{59}Co^{12+}$ - 12 μA.

ISBN: 978-3-95450-226-4 ISSN: 2222-5692 doi:10.18429/JACoW-ECRIS2020-WEXZO05

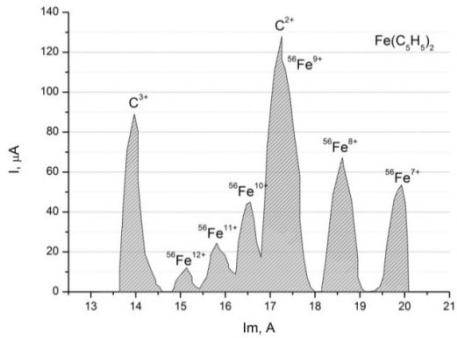

Figure 9: The spectrum of Fe ions, the source settings are optimized for $^{56}Fe^{10+}$ – 44 μA. UHF power – 120 W.

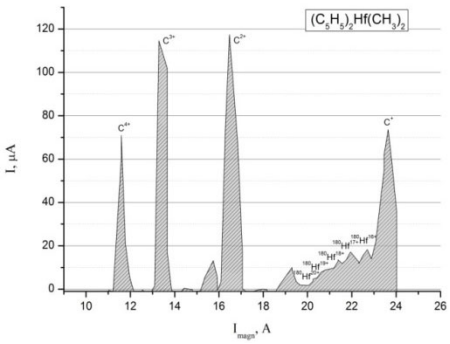

Figure 10: The spectrum of Hf ions, the source settings are optimized for $^{180}Hf^{17+}$ - 19 μA. UHF power – 230 W.

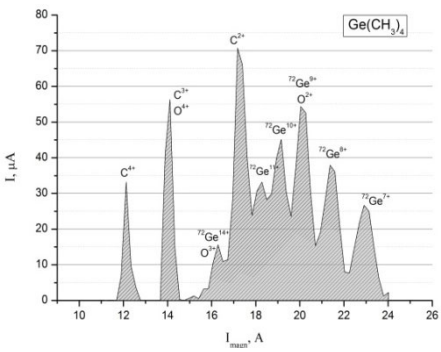

Figure 11: The spectrum of Ge ions, the source settings are optimized for $^{72}Ge^{10+}$ - 46 μA. UHF power – 270 W.

CONCLUSION

The main goal of this work was to employ the MIVOC method for production of ions of solid and extend the spectrum of accelerated ions at the FLNR cyclotrons and at the DC-60 cyclotron. With the expansion of the spectrum of accelerated elements, it becomes possible to set up new experiments in the field of experimental nuclear physics, radiation solid state physics, and various applied problems, which makes the research objective particularly relevant. As a result of the work done, for the first time at the DC-60 cyclotron, the modes of obtaining ion beams $^{48}Ti^{9+}$, $^{58}Ni^{11+}$, $^{59}Co^{12+}$ and $^{52}Cr^{10+}$ were worked out for the first time.

REFERENCE

[1] H.Koivisto *et al*., "Metal ion beams from an ECR ion source using volatile compounds", *Nuclear* Instruments *and Methods in Physics Research B* 94, 1994, pp. 291-296.

[2] S. Bogomolov *et al*., "Production of Intense Metal Ion Beams from ECR Ion Sources Using the MIVOC Method", *Physics of Particles and Nuclei Letters*, 2015, vol. 12, no. 7, pp. 824–830. doi:10.1134/S1547477115070043

[3] B. Gikal *et al.*, "Development of FLNR JINR Heavy Ions Accelerator Complex (DRIBs III)", in *Proc. 21th Int. Conf. on Cyclotrons and their Applications (Cyclotrons'16)*, Zurich, Switzerland, Sep. 2016, pp. 278-280. doi:10.18429/JACoW-Cyclotrons2016-THA03

[4] B. Gikal *et al*., "DC-60 heavy ion cyclotron complex: The first beams and project parameters", *Phys. Part. Nuclei Lett.* 5, pp. 642–644. doi:10.1134/S1547477108070248

[5] V. Loginov *et al*., "Production of intense metal ion beams at the DC-60 cyclotron", *Journal of Instrumentation*, 2019, 14, C02007-C02007. doi:10.1088/1748-0221/14/02/C02007

ISBN: 978-3-95450-226-4 ISSN: 2222-5692 doi:10.18429/JACoW-ECRIS2020-WEYZO01

PRESENT STATUS OF HIMAC ECR ION SOURCES

M. Muramatsu†, A. Kitagawa, QST-NIRS, Chiba, Japan
S. Hashizaki, M. Kawashima, T. Kondo, F. Ouchi, T. Sasano, T. Suzuki, M. Sei, T. Shiraishi, K. Takahashi, AEC, Chiba, Japan
Y. Iwata,NIRS, Chiba-shi, Japan

Abstract

High-energy carbon-ion radiotherapy is being carried out at Heavy Ion Medical Accelerator in Chiba (HIMAC). Over 12000 cancer patients have been treated with carbon beams having energies of between 56-430 MeV/u since 1994. There are two injectors in the HIMAC for medical and experimental use. First injector consists of two ECR ion sources and one PIG ion source, the RFQ linac and the DTL. Usually, this injector suppling the carbon ion for cancer therapy and various ion such as H, He, Fe, Xe are accelerated for biological and physical experiment. The 10 GHz NIRS-ECR ion source produce the carbon ion for cancer therapy. The 18 GHz NIRS-HEC ion source produce He to Xe ions for experimental use. Second injector consists of the compact ECR ion source with all permanent magnet, the RFQ linac and the APF IH-DTL. This injector supplies the carbon ion for experimental use. Additionally, we tried production of the Indium and the Tin ions by using the $In(C_5H_5)$ and the $Sn(i\text{-}C_3H_7)_4$ at the NIRS-HEC. Beam current of the $^{115}In^{20+}$ and $^{120}Sn^{18+}$ were 90 and 15 μA, respectively.

INTRODUCTION

The National Institute of Radiological Sciences (NIRS) was founded by the Japanese Government in 1957 as a core research institute concerning the interactions between radiation and human beings. The National Institutes for Quantum and Radiological Science and Technology (QST) was established in April 2016 to combine NIRS and several institutes that were previously under the Japan Atomic Energy Agency (JAEA). The main aims of QST-NIRS are comprehensive research and development on: (1) the effects of radiation on the human body; (2) protection from radiation, including diagnosis and treatment of radiation injuries; and (3) medical applications of radiation.

Four ion sources produce various ions for medical use, biological and physical experiment in the Heavy Ion Medical Accelerator in Chiba (HIMAC) [1] at the NIRS. The multi-ion irradiation with dose distribution and Liner Energy Transfer (LET) optimization is being studied at NIRS [2, 3]. Helium, carbon, oxygen and neon ions are considered as ion species for multi-ion irradiation. When we use more than one ion sources, it is possible to switch different ion species easily. However, we considered the switching method with only one ion source. Ionization gases were helium, CO_2 and neon to produce He^{2+}, C^{2+}, O^{3+} and Ne^{4+} ions. Present status of ion sources in 2019 and development of gas switching system for multi-ion irradiation and production of Indium and Tin ion production at the 18 GHz NIRS-HEC ion source [4] are described in this paper.

† muramatsu.masayuki@qst.go.jp

OPERATION OF THE HIMAC ION SOURCES IN 2019

The project to develop the world's first medical dedicated heavy-ion synchrotron was started in 1984 as the HIMAC. Since HIMAC was fully developed by NIRS as an accelerator complex. HIMAC has four different types of ion sources, a penning ion source, named NIRS-PIG [5] a 10 GHz electron cyclotron resonance ion source, named NIRS-ECR, an 18 GHz electron cyclotron resonance ion source, named NIRS-HEC, and a 10 GHz permanent magnet electron cyclotron resonance ion source, named Kei2 [6]. The HIMAC ion sources were produced various ion beam for medical and experimental use. Figure 1 shows ratio of operation time and ion species in 2019. Carbon ion is the most utilized the various ion species. The carbon bean from NIRS-ECR was used for medical use. Beam from Kei2 was used for biological experiments. Total number of the patient in 2019 was 876.

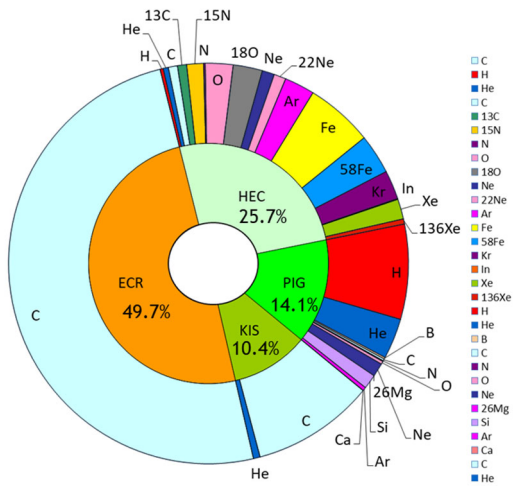

Figure 1: Ratio of operation time and ion species in 2019. ECR: 10 GHz NIRS-ECR, HEC: 18 GHz NIRS-HEC, PIG: NIRS-PIG, KIS: Kei2-source

Figure 2 shows the operation time of various ion species in 2019. Total operation time of ion sources were 9787.16 hours in fiscal year 2019. Operation time of the carbon was higher than other ion species. Operation times of NIRS-ECR and Kei2 sources for carbon ion production were 4865.3 and 969.5 h. Boron and silicon ions were produced by NIRS-PIG with spattering method. We can operate the PIG source during 1 week without maintenance. Iron, krypton and xenon were produce by HEC. Operation

ISBN: 978-3-95450-226-4 ISSN: 2222-5692 doi:10.18429/JACoW-ECRIS2020-WEYZO01

time of Fe, Kr and Xe were 533, 228 and 158 h, respectively. Ions of isotope such as 13C, 15N, 18O and 58Fe were also produced at 18 GHz NIRS-HEC ion source.

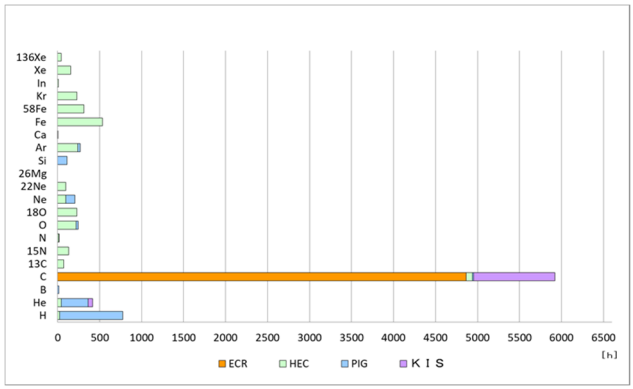

Figure 2: Operation time of various ion species in 2019. ECR: 10 GHz NIRS-ECR, HEC: 18 GHz NIRS-HEC, PIG: NIRS-PIG, KIS: Kei2-source

DEVELOPMENT OF NIRS-HEC

Gas Switching System for Multi-Ion Irradiation

In previous tests, switching time of the ion species using existing gas system could be shortened by using a solenoid valve [7]. Helium, CO_2 and neon gases were used for production of He^{2+}, C^{2+}, O^{3+} and Ne^{4+} ions. A new gas switching system for multi-ion irradiation was manufactured and an ion species switching test was conducted in this time. Figure 3 shows photograph of gas switching system at NIRS-HEC. The high speed solenoid valve (Parker, Series 9) and controller (Parker, Iota One) were used for CO_2, Helium and Neon gases line.

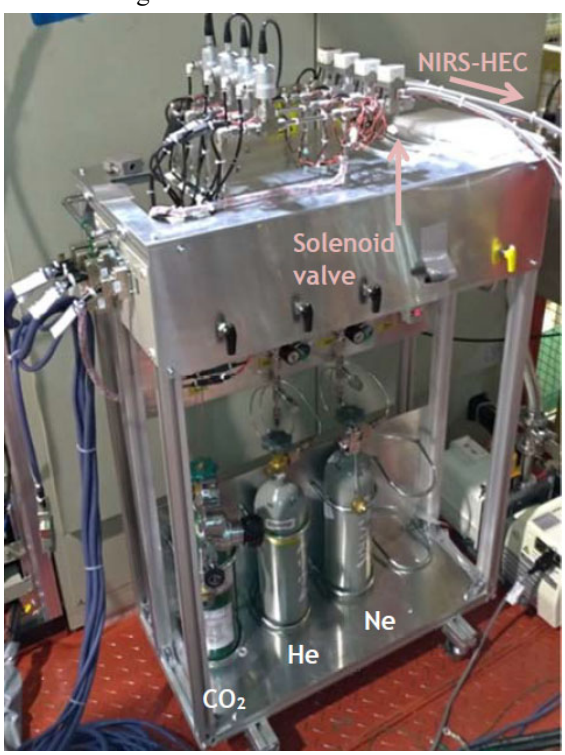

Figure 3: Photograph of gas switching system.

First, the gas was pulsed and the gas exhaust time was measured. Figure 4 shows exhaust time of CO_2. It took 11 seconds for the degree of vacuum in the upstream vacuum box to drop below 1E-5Pa after the gas supply was stopped. In the case of helium and neon, it took 5 and 7 seconds, respectively. Table 1 shows condition of solenoid valve.

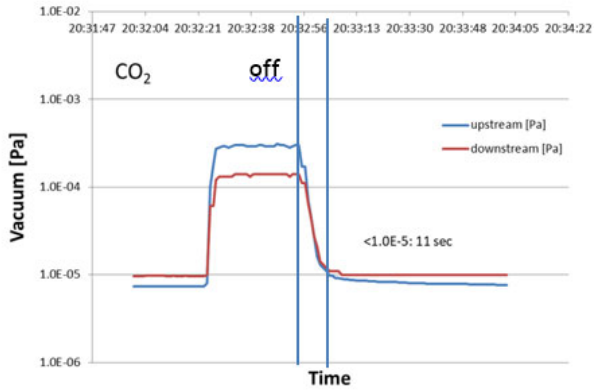

Figure 4: Exhaust time of CO_2. Blue line is vacuum pressure in upstream chamber. Red line is vacuum pressure in downstream chamber.

Table 1: Condition of Solenoid Valve

Gas	Pulse width [msec]	Repetition frequency [Hz]	Pressure [MPa]	Time to 1E-5Pa [sec]
He	0.12	1.2	0.00	5
CO2	0.3	1.2	-0.05	11
Ne	0.25	1.2	0.00	7

Next, an ion beam switching test was performed. As in the previous experiment, we try to produce He^{2+}, C^{2+}, O^{3+} and Ne^{4+} ions by using helium, CO_2 and neon gases with new gas switching system.

Figure 5 shows beam switching time from He^{2+} to Ne^{4+}. In the previous gas system, it took 20 seconds for the beam to stabilize, but in the new system it took 7 seconds. When switching from CO2, where gas exhaust was slow, the beam is stabilized at 35 seconds at the time of switching to Ne^{4+}. (Fig. 6)

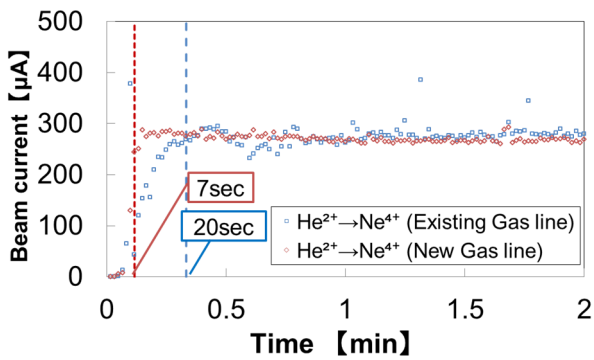

Figure 5: Beam switching time from He^{2+} to Ne^{4+}.

ISBN: 978-3-95450-226-4 ISSN: 2222-5692 doi:10.18429/JACoW-ECRIS2020-WEYZO01

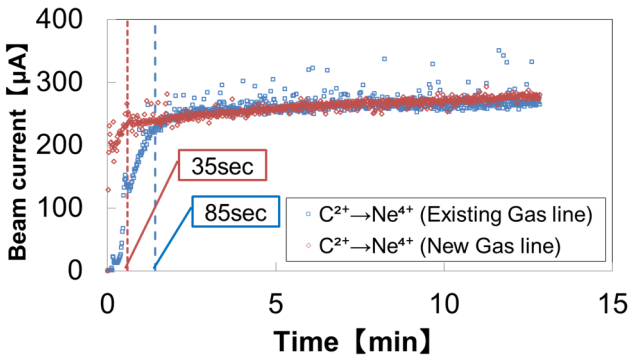

Figure 6: Beam switching time from C^{2+} to Ne^{4+}.

Indium and Tin Ion Production

Production of Indium and Tin ion were tested using $In(C_5H_5)$ and $Sn(i\text{-}C_3H_7)_4$ at NIRS-HEC. A beam test was performed by cooling the container using a Peltier device, because, the vapor pressure at room temperature is high [8]. Figure 7 shows charge state distributions of Indium (a) and Tin (b). The operating parameters of the ion source have been optimized for In^{20+} and Sn^{18+}. The temperatures of the Indium and Tin containers were 6.2 and 9.2 degrees, respectively. The beam currents for In^{20+} and Sn^{18+} were 90 and 15μA, respectively. The extraction voltages at this time were 31 and 32 kV, respectively. In the case of tin, $^{120}Sn^{18+}$ could not be separated due to the presence of isotopes.

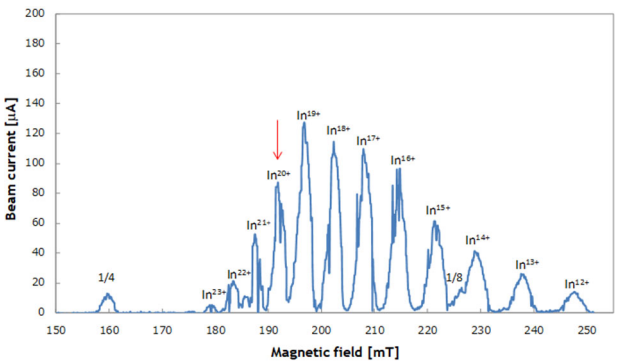

(a)

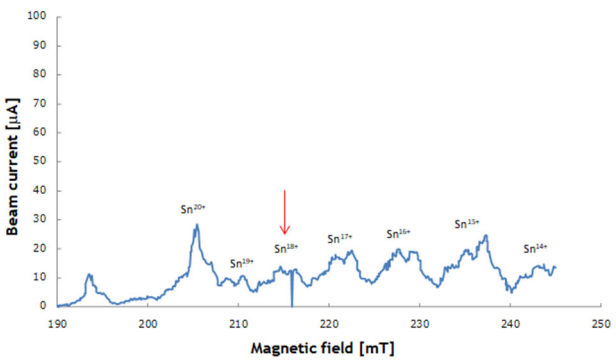

(b)

Figure 7: Charge state distributions of Indium (a) and Tin (b) ions.

CONCLUSION

Total operation time of ion sources were 9787.16 hours without big problem in fiscal year 2019. Operation time of the carbon was higher than other ion species. We made new gas switching system for the multi-ion irradiation at 18 GHz NIRS-HEC. We obtain result of switching time of less than 35 sec using solenoid valve. Indium and Tin ions were produced by using $In(C_5H_5)$ and $Sn(i\text{-}C_3H_7)_4$at NIRS-HEC. The beam currents for In^{20+} and Sn^{18+} were 90 and 15μA, respectively.

REFERENCES

[1] Y. Hirao *et al.*, "*Nucl. Phys*. A 538, 541c, 1992.

[2] T. Inaniwa and N. Kanematsu, "Effective particle energies for stopping power calculations in radiotherapy treatment planning with protons and helium, carbon, and oxygen ions" Phys. Med. Biol. vol. 61, pp. 542–550, Oct. 2016. doi:10.1088/0031-9155/61/20/N542

[3] T. Inaniwa, N. Kanematsu, K. Noda and T. Kamada "Treatment planning of intensity modulated composite particle therapy with dose and linear energy transfer optimization" *Phys. Med. Biol.,* vol. 62, no. 12, pp. 5180–5197, 2017. doi:10.1088/1361-6560/aa68d7

[4] A. Kitagawa et al. "Development of 18 GHz electron cyclotron resonance ion source with high-voltage extraction configuration" Rev. Sci. Instrum. vol. 69, p. 674, 1998. doi:10.1063/1.1148589

[5] Y. Sato *et al.*, "Performance of a low-duty pulsed Penning source for the medical synchrotron facility at NIRS" *Rev. Sci. Instrum.*, vol. 63, p. 2904, 1992. doi:10.1063/1.1142794

[6] M. Muramatsu et al, "Development of a compact electron-cyclotron-resonance ion source for high-energy carbon-ion therapy," Rev. Sci. Instrum., vol. 76, p. 113304, 2005. doi:10.1063/1.2132267

[7] M. Muramatsu et al., "Production of Various Ion Species by Gas Pulsing Technique for Multi Ion Irradiation at NIRS-HEC Ion Source", in *Proc. 23th International Workshop on ECR Ion Sources (ECRIS'18)*, Catania, Italy, Sep. 2018, pp. 79-81. doi:10.18429/JACoW-ECRIS2018-TUP03

[8] W. Takasugi *et al.*, "MIVOC method with temperature control," *Rev. Sci. Instrum.*, vol. 81, 02A329, 2010. doi:10.1063/1.3266143

ISBN: 978-3-95450-226-4 ISSN: 2222-5692 doi:10.18429/JACoW-ECRIS2020-WEYZO02

DESIGN OF A 2.45 GHz SURFACE WAVE PLASMA SOURCE FOR PLASMA FLOOD GUN*

S. X. Peng[1, †], W. B. Wu[1], T. H. Ma[1], A. L. Zhang[2], Y. X. Jiang[1], K. Li[1], B. J. Cui[1], J. F. Zhang[1], T. Zhang[1], J. M. Wen[1], Y. Xu[1], Z. Y. Guo[1], J. E. Chen[1]
[1]State Key Laboratory of Nuclear Physics and Technology & Institute of Heavy Ion Physics, Peking University, Beijing, China
[2]State Key Laboratory of Particle Detection and Electronics, Department of Modern Physics, University of Science and Technology of China, Hefei 230026, China

Abstract

Microwave ion sources have the characteristics of high stability, high plasma density, no metallic contamination, long life, and low gas consumption, which make them excellent candidates for plasma flood gun (PFG) with superior charge neutralization performance for ion implanters. Attempt to develop a large scale PFG based on 2.45 GHz microwave driven sources was launched at Peking University (PKU). A prototype one is a miniaturized 2.45 GHz permanent magnet electron cyclotron resonance (ECR) source to produce point-like electron beam. In previous experiments, more than 8 mA electron beam has been extracted through an Ø6 mm extraction hole at an input microwave power of 22 W with argon gas. Recently, studies are focused on the possibility of producing of ribbon electron beams as PFG with 2.45GHz microwave driven surface wave plasma (SWP) source. A cylindrical chamber surface wave plasma generator with a cylindrical dielectric waveguide and a 70 mm×3 mm extraction slit was designed and fabricated. More details of this PFGs will be discussed in this work.

INTRODUCTION

PFGs are widely used to neutralize wafer charge during the doping process in modern ion implanters. Compared with traditional dc arc discharge with filament and RF discharge, the microwave driven source that has long lifetime and no metallic contamination is regarded as a potential choice of PFG. For an example, Axcelis has developed a microwave electron cyclotron resonance (ECR) PFG for low pressure wafer charge neutralization, a ribbon electron beam with current as high as 20 mA has been obtained with microwave power less than 70 W with xenon gas [1]. Besides, a miniaturized ECR plasma flood gun was developed at PKU, more than 8 mA point-like electron beam has been extracted from this ion source at an input microwave power of 22 W with argon gas [2].

However, there are still some challenges for ECR ion sources to generate large-scale uniform plasmas due to the existence of magnetic field [3], which limit their applications as PFGs in large-area wafers. Fortunately, it has been widely reported that large-area planar surface wave plasmas (SWPs) can be excited with 2.45 GHz microwave energy [4, 5]. In addition, there are some other advantages for the SWP sources compared with the ECR ones. On the one hand, large-area uniform plasmas can be easily obtained by the systematic design of the antenna. On the other hand, there are no external magnetic fields for the SWP sources, which make it simpler and more economic than the ECR sources. Therefore, the 2.45 GHz microwave driven SWP sources are expected to be the potential PFGs for charge neutralization of large-area wafers.

At PKU, a 2.45 GHz ECR ion source was designed for the production of high intensity singly charged ion beams. In this work, this source is updated to a SWP source for the generation of ribbon electron beam. More details of the microwave driven PFG will be discussed in this paper. In addition, some physical analysis including the microwave coupling and thermal analysis will be presented.

MICROWAVE DRIVEN PFG

A schematic diagram of the 2.45 GHz ECR ion source is presented in Fig. 1. It can be briefly divided into microwave matching parts, plasma chamber and permanent magnet rings. A dielectric microwave window is used for microwave coupling and vacuum sealing, which is composed of three pieces of alumina ceramic blocks (Ø32 mm×10 mm) and a piece of thick boron nitride (Ø32 mm×2 mm). The plasma chamber is made of stainless steel (SS) (Ø85 mm × L51 mm). In addition, two NdFeB permanent magnet rings are installed outside of the plasma chamber to provide a resonance magnetic field of 875 Gs. The plasma electrode is made by SS with an Ø6 mm hole.

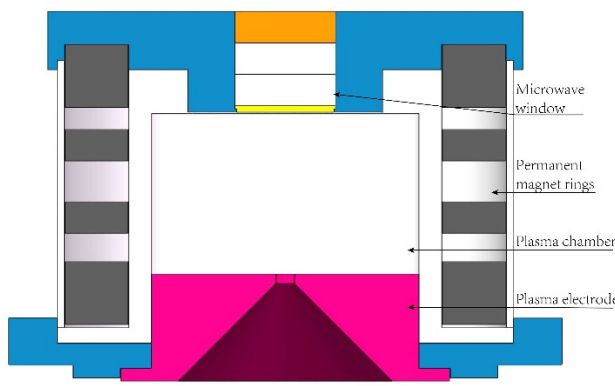

Figure 1. A schematic diagram of the 2.45 GHz ECR ion source at PKU.

* Work supported by the National Natural Science Foundation of China (Grant Nos. 11575013, 11775007 and 11975036).
† sxpeng@pku.edu.cn

ISBN: 978-3-95450-226-4 ISSN: 2222-5692 doi:10.18429/JACoW-ECRIS2020-WEYZO02

In this work, the ECR ion source shown in Fig. 1 is updated to a SWP source for large-area electron beam generation. To realize this function, as presented in Fig. 2, several important improvements are made in this microwave driven PFG.

- The boron nitride is replaced by a ceramic cylinder that stick into the plasma chamber with a length of 40 mm.
- The NdFeB permanent magnet rings are removed.
- A plasma electrode with a 70 mm×3 mm extraction slit is installed.

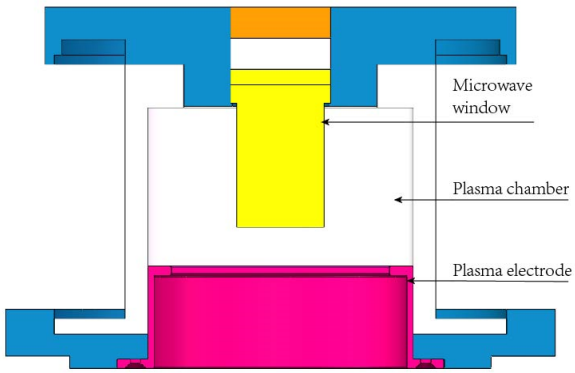

Figure 2. A schematic diagram of the 2.45 GHz the microwave driven PFG.

PHYSICAL ANALYSIS

Although the modification scheme of the microwave driven PFG is proposed, further analysis is necessary for the comprehension of this source. On the one hand, we want to know if the new microwave window is beneficial to the generation of SWP. On the other hand, we should make sure that the water-cooling is enough since the SWP sources usually work under continuous wave (CW) mode with higher microwave power. Therefore, the results of microwave coupling and thermal analysis will be performed in this section.

Microwave Coupling

According to the SWP theory, the surface wave can transmit along the interface between plasma column and dielectric without extra waveguide. The radius of the dielectric cylindrical ceramic rod is assumed as a, and electromagnetic wave propagating along the cylindrical rod can be expressed as [6]

$$R \le a \quad \vec{E}_{z1} = \vec{E}_{m1} J_m(k_d R)\cos m\varphi e^{-ik_z z}, \tag{1}$$

$$\vec{H}_{z1} = \vec{H}_{m1} J_m(k_d R)\sin m\varphi e^{-ik_z z}, \tag{2}$$

$$R > a \quad \vec{E}_{z2} = \vec{E}_{m2} K_m(k_p R)\cos m\varphi e^{-ik_z z}, \tag{3}$$

$$\vec{H}_{z2} = \vec{H}_{m2} K_m(k_p R)\sin m\varphi e^{-ik_z z}. \tag{4}$$

Here m is the number of standing wave of field in the circumferential direction, k_z is the wave number in the axial direction of dielectric rod, k_d and k_p are the wave number along the radial direction in rod and in plasma, respectively. In addition, the dispersion relations of cylindrical surface wave can be written as

$$k_d^2 = \omega^2 \mu_0 \varepsilon_0 \varepsilon_d - k_z^2, \tag{5}$$

$$k_p^2 = k_z^2 - \omega^2 \mu_0 \varepsilon_0 \varepsilon_p, \tag{6}$$

$$\left[\frac{J_m'(k_d a)}{k_d J_m(k_d a)} + \frac{K_m'(k_p a)}{k_p K_m(k_p a)}\right]\left[\frac{\omega^2 \mu_0 \varepsilon_0 \varepsilon_d J_m'(k_d a)}{k_d J_m(k_d a)} + \frac{\omega^2 \mu_0 \varepsilon_0 \varepsilon_p K_m'(k_p a)}{k_p K_m(k_p a)}\right] = \frac{m^2 k_z^2}{a^2}\left(\frac{1}{k_d^2} + \frac{1}{k_p^2}\right). \tag{7}$$

Here ε_d is the relative permittivity of rod, which equals to 9 for the ceramic, and ε_p is the relative permittivity of plasma and can be written as:

$$\varepsilon_p = 1 - \frac{\omega_p^2}{\omega^2}, \tag{8}$$

Where ω is microwave angular frequency and ω_p is plasma angular frequency that is proportional to square root of electron density and can be given by

$$\omega_p = \sqrt{\frac{e^2 n_e}{\varepsilon_0 m_e}}. \tag{9}$$

When the plasma density is low, k_p is an imaginary number which means the electromagnetic wave can propagate in both the axial and the radial directions. The electromagnetic energy can transmit into the plasma chamber and then ignite the plasma. When the plasma density increase to greater than the critical value, k_p becomes a real number. This state is called propagating mode, indicating that the electromagnetic wave will evanesce in the radial direction and propagate only in the axial direction. To verify if the microwave coupling scheme of our PFG is reasonable, the electric field distribution inside the plasma chamber is simulated for the ε_p=1. As presented in Figs. 3 and 4, the electromagnetic wave can transmit along the ceramic and then emitted into the chamber, and the highest electric field norm is about 800V/m.

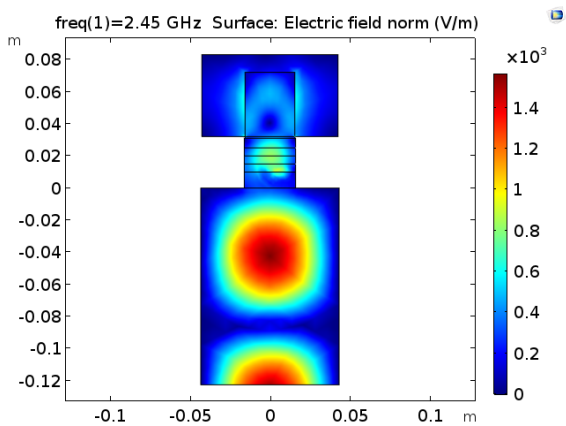

Figure 3. Simulated electric field (V/m) in the plasma chamber (X-Z plane).

ISBN: 978-3-95450-226-4 ISSN: 2222-5692 doi:10.18429/JACoW-ECRIS2020-WEYZO02

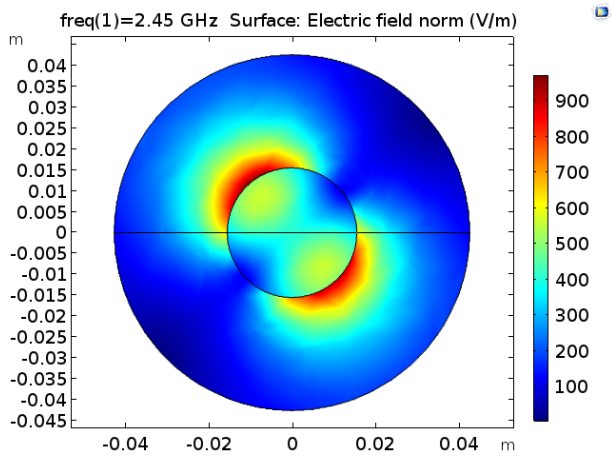

Figure 4. Simulated electric field (V/m) in the plasma chamber (X-Y plane).

Thermal Analysis

Due to the high CW microwave energy deposition during discharge, special design of the water cooling structure of this source is carried out. As presented in Fig. 5, the groove around the microwave window is used for the circulation of cooling water, which has a depth of 4 mm and a width of 5 mm. And a simulation with Ansys Workbench was performed to evaluate the effect of water cooling structure.

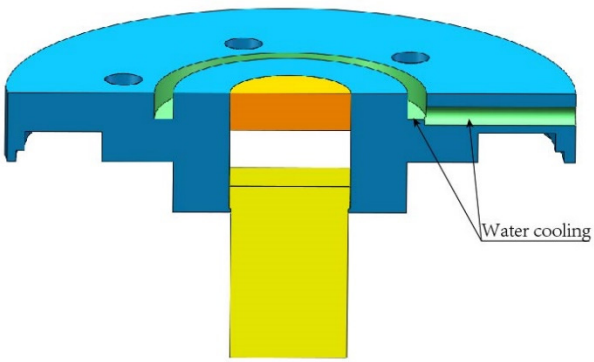

Figure 5. The water cooling structure of the microwave window flange.

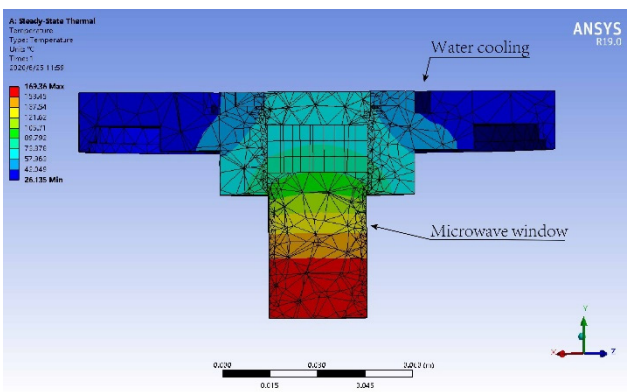

Figure 6. The temperature distribution of the microwave window flange.

The temperature distribution of the microwave window flange is presented in Fig. 6. Since the heat on the ceramic rod is mainly derived from the energy of the input microwave, we assume that the thermal power deposited on the ceramic rod is 100 W and the temperature of the cooling water is set to 22 °C. For the ceramic rod, the highest temperature is 169 °C at the end of the antenna and the lowest temperature is about 50 °C at the starting position of the antenna. The simulated results indicate that the water cooling design of the microwave window is reasonable.

DISCUSSION AND OUTLOOK

In this paper, to generate ribbon electron beams for charge neutralization of large-area wafers, a cylindrical chamber surface wave plasma generator with a cylindrical dielectric waveguide and a 70 mm×3 mm extraction slit was fabricated based on a 2.45 GHz ECR ion source at PKU. The details of this PFG are presented in this paper. In addition, the microwave coupling and thermal analysis are also discussed.

In the future, this microwave driven PFG will be installed and tested. The influence of gas pressure, microwave power, and antenna length on the electron current will be studied systematically. Also, the plasma physics inside this PFG will be followed with interest. All of these work are in process and will be presented later.

ACKNOWLEDGEMENTS

This work is supported by National Natural Science Foundation of China (Grant Nos. 11975036, 11775007 and 11575013). The support from State Key Laboratory of Nuclear Physics and Technology, Peking University is appreciated.

REFERENCES

[1] B. Vanderberg, et al., “Microwave ECR plasma electron flood for low pressure wafer charge neutralization”, AIP Conference Proceedings, vol. 1496, no. 1, p.356, 2012.
doi: 10.1063/1.4766562

[2] Y. X. Jiang, et al., “A miniaturized ECR plasma flood gun for wafer charge neutralization”, Rev. Sci. Instrum. vol. 91, p. 033319, 2020.
doi: 10.1063/1.5128522

[3] R. Geller, “Electron cyclotron resonance sources: Historical review and future prospects”, Rev. Sci. Instrum. vol. 69, p. 1302, 1998.
doi: 10.1063/1.1148797

[4] M. Nagatsu, et al., “Effect of slot antenna structures on production of large-area planar surface wave plasmas excited at 2.45 GHz”, J. Phys. D: Appl. Phys. vol. 33, p. 1143, 2000.
doi: 10.1088/0022-3727/33/10/302

[5] Z. Q. Chen, et al., “A Novel Structure of Slot-Antenna Array for Producing Large-Area Planar Surface-Wave Plasmas”, Plasma Science and Technology, vol. 10, p. 655, 2008.
doi: 10.1088/1009-0630/10/6/01

[6] Z. H. Wu, et al., “Experimental Investigation of Surface Wave Plasma Excited by a Cylindrical Dielectric Rod”, Plasma Science and Technology. vol. 16, p. 118, 2014.
doi:10.1088/1009-0630/16/2/06

ISBN: 978-3-95450-226-4 ISSN: 2222-5692 doi:10.18429/JACoW-ECRIS2020-WEZZO01

ROLE OF THE 1+ BEAM OPTICS UPSTREAM THE SPIRAL1 CHARGE BREEDER

L. Maunoury†, O. Kamalou, S. Damoy, M. Dubois, R. Frigot, S. Hormigos and B. Jacquot,
Grand Accélérateur National d'Ions Lourds, Caen, France

Abstract

The SPIRAL1 charge breeder (SP1CB) is under operation. Radioactive ion beam (RIB) has already been delivered [1] to Physicist for experiments. Charge breeding efficiencies demonstrated high performances for stable ion beams than RIB's. The beam optics, prior to the injection of the 1+ ions into the SP1CB, is of prime importance [2] for obtaining such high efficiencies. Moreover, the intensities of the RIB's are so low, and indeed difficult to tune the SP1CB. A stable beam having a close Brho is required to find out the set of optic parameters preceding the tuning of the RIB. Hence, it has been decided to focus our effort on the control of 1+ beam optics leading to high charge breeding efficiencies whatever the 1+ mass, energy and Target Ion Source System (TISS) used. This contribution will show the strategy undertaken to overcome that problem and the results obtained.

INTRODUCTION

Now, the SPIRAL1 facility has been upgraded and is under operation. Obviously, more time is needed to get a full control over the entire facility as it got more complicated to operate: new Target ion Source System (TISS) [3]; a charge breeder (SP1CB) [4] and reshuffled beam lines. Mainly there are two operational modes for running the facility providing Radioactive Ion Beams (RIB's) to physicist: Shooting Through mode (ST) and 1+/N+ mode [5]. The ST mode carries out the NanoganIII TISS [6] providing RIB's of gas element type transported to the post-accelerator CIME cyclotron [7] through the 6 mm plasma electrode of the SP1CB. The 1+/N+ mode combines the FEBIAD TISS with the SP1CB and has successfully provided a ^{38m}K@9MeV/u beam [8] to physicists in 2019. But challenges ought to be overcome for having a daily routine facility. Indeed, the preparing phase prior to the RIB delivery is too long and a unique set of beam optics parameters must be found for each mode. Concerning the R&D, it is important to understand what are key parameters of the ion beam (Twiss parameters and energy spread) upstream the SP1CB in order to achieve the highest charge breeding efficiency

THE 1+ BEAM LINE

1+ Beam Line Layout

Figure 1 displays the layout of the 1+ beam line. It starts with a combination of two einzel lenses: Einz1 and Einzl2. It is followed by a triplet of magnetic quadrupoles and a magnetic sextupole prior to a magnetic mass analyzing dipole. Next, a triplet of electrostatic quadrupoles is settled just before the 1+ ion injection into the SP1CB. For the diagnostics, there are two beam profilers (upstream PR11 and downstream PR13 the mass analyzing dipole), sets of slits (vertical - horizontal) and one faraday cup CF13 shielded regarding the ion beam extracted backwards from the SP1CB. After the second mass analyzing dipole D3P sorting out the multi-charged ions extracted from the SP1CB, a Faraday cup with a beam profiler is used to check the selected multi charged ion beam intensity and its profile.

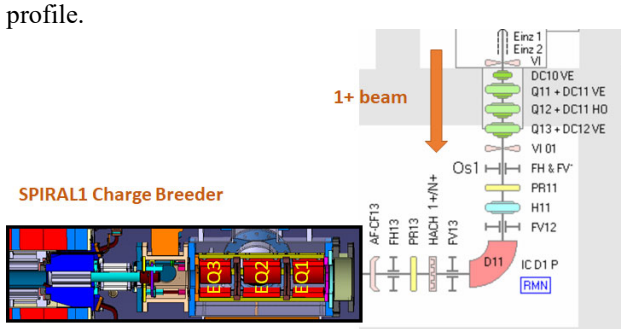

Figure 1: Layout of the 1+ beam line.

Shooting Through Mode (ST)

In this mode, the TISS NanoganIII is operated. The specificity is the large emittance of that Electron Cyclotron Resonance (ECR) ion source type. Moreover, the ion beam must be transported across the SP1CB plasma electrode of 6 mm diameter coercing it to be really focused at that location. The experimental data (beam profilers and efficiency of transport) of a stable ion beam of $^{14}N^{3+}$@19.751kV have been considered. As the twiss parameters for the transverse emittances are not known for the NanoganIII ECR ion source, they were let as free parameters. Using the TraceWin code [9], the ion beam envelopes as well as the initial beam twiss parameters are obtained, see Fig. 2. The ion beam is focused, thanks to the coils of the charge breeder, and transported as much as possible across the SP1CB plasma electrode. The calculated transverse emittances of the initial beam is around 106 π.mm.mrad (4 RMS, X and Y planes) and it is a diverging ion beam. The beam profiler values are also replicated. But, to find those results, the TraceWin code applied a factor of 0.6 on the complete magnetic field intensity of the SP1CB. It implies that the simulation doesn't reproduce quite well the measurements. Moreover, in the N+ line (the beam line transporting the multi-charged ion beam from the SP1CB plasma electrode up to the CIME injection), there is a burst of the ion beam envelope in X plane which cannot be really explained. To find out the issue and fix the problem, a pepper-pot emittance meter (Pantechnik type) will be installed in the N+ beam line to constrain the TraceWin simulation. New data will be recorded and compared to the simulations.

† laurent.maunoury@ganil.fr

ISBN: 978-3-95450-226-4 ISSN: 2222-5692 doi:10.18429/JACoW-ECRIS2020-WEZZO01

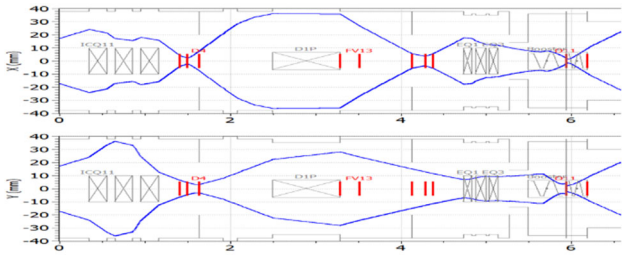

Figure 2: Transverse beam envelopes for the case ST mode and the beam $^{14}N^{3+}$@19.751kV.

Beam Optics for 1+/N+ Mode

For many years, the TISS NanoganIII has been used in combination with a unique set of beam optics suitable for elements up to Brho of 0.136 T.m. Following the upgrade of the SPIRAL1 facility, it is possible nowadays to get RIB's characterized with a $B\rho_{max}$ of 0.22 T.m. The enlargement of Brho involves some restrictions regarding beam optics element in the 1+ beam line. Indeed, the magnetic quadrupoles Q11 Q12 and Q13 cannot be scaled up using the previous beam optics parameters. Henceforth, the idea is to find out a single set of beam optics parameters matching the injection of the SP1CB maintaining as much as possible the SP1CB efficiency over the whole range of Bρ.

Concerning the data, $^{85}Rb^{1+}$ ion has been our probe at different Bρ's defining the 1+ ion beam energy. The two beams were: $^{85}Rb^{1+}$@10kV – Brho = 0.133 T.m (previous beam optics parameters) and $^{85}Rb^{1+}$@27.5kV – Brho = 0.221 T.m. (new beam optics parameters). The $^{85}Rb^{1+}$ ion beam is generated thanks to an ion gun developed at GANIL [2] using a HeatWave pellet [10], up to several hundreds of nA. Fig. 3 shows the SP1CB efficiencies for those two cases.

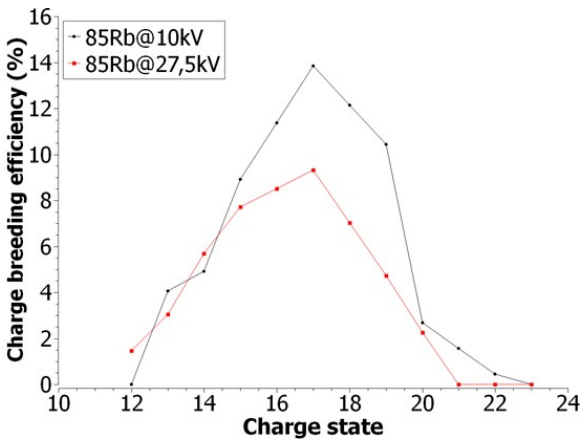

Figure 3: SPIRAL1 charge breeding efficiencies for the mode 1+/N+ and the two cases: $^{85}Rb^{+}$@10kV (black curve) and $^{85}Rb^{+}$@27.5kV (red curve).

Both charge state distributions are close with FWHM (5 - 6 charge states). They are both peaked on the $^{85}Rb^{17+}$ with charge breeding efficiencies of 13.8% (10kV) and 9.3% (27.5kV) associated with global efficiencies of 70.3% (10kV) and 49.8% (27.5kV) respectively. At the same time, beam profiler values have been recorded to coerce the simulations.

Simulations and Ion Beam Injection into the Charge Breeder

Simulations have been undertaken to find out the new beam optics as well as to learn how the 1+ particles are injected into the SP1CB. For that purposes, two software's have been operated: SIMION [11] and TraceWin [9] to do a complete simulation of the total SPIRAL1 beam line. To note here, simulations are achieved with no plasma model implemented in the SP1CB.

SIMION is employed to generate the ion beam from the ion gun up to exit of the second einzel lens Einz2. One example is displayed on Fig. 4. The geometry included in the simulation is as close as possible to the real one and the voltages applied are exactly those used during experiment.

The twiss parameters are deduced and they will become the input for the TraceWin code. Inside TraceWin, there is a tool box with the different types of optic elements. Beam line has been built to reproduce the 1+ and N+ beam line of the SPIRAL1 facility. For the magnetic as well as for the electrostatic quadrupoles, mass analyzing dipole and einzel lenses, in-house boxes are set in the simulation; gradient (T.m) or voltages are applied to the quadrupoles and the ion beam Brho is used to define the ion beam trajectory inside the mass analyzing dipoles. Finally, evolution of the transverse beam envelopes (in both planes X and Y) can be calculated as well as the beam profiler values. On Fig. 5, in italics and blue are the beam profiler values of experiment and in red are the calculated ones. As it can be seen, values are very close except for the PR13 X one. In that case, experimental beam profile was polluted by a huge background.

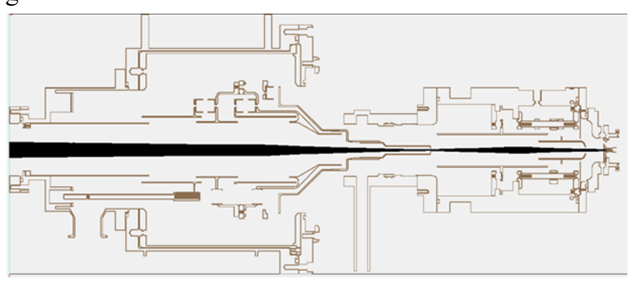

Figure 4: SIMION simulation of 85Rb+@10kV.

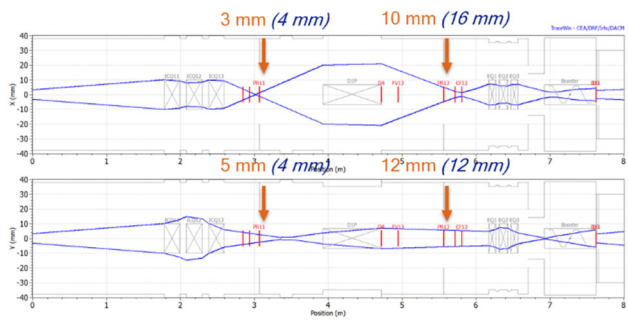

Figure 5: Transverse beam envelopes for the case 1+/N+ mode and the beam $^{85}Rb^{+}$@10kV.

Again, twiss parameters are deduced just at the exit of the EQ3 and inserted as input parameters for the last step of the simulation: evolution of the 1+ beam injected into

ISBN: 978-3-95450-226-4 ISSN: 2222-5692 doi:10.18429/JACoW-ECRIS2020-WEZZO01

the charge breeder and slowed down. The real 3D magnetic field (coils and hexapole), also containing the fringe field, is included into the SIMION simulation.

On Figure 5: the ion beam is firstly divergent and is focused in both transverse planes to the object plane of the mass analyzing dipole (D1P). After the mass analyzing dipole, ion beam is relatively large in vertical plane but again well focused in horizontal plane to get a good resolution. The electrostatic quadrupole focuses in both planes the ion beam to be transported along the deceleration tube of 28 mm of inner diameter. Figure 6 shows the axial magnetic field and the positions where the 2D transverse 1+ beam profile has been calculated. Figure 7 exhibits how the ion beam propagates inside the SP1CB. From the TraceWin calculation, twiss parameters are obtained just after the EQ3. These parameters are the inputs to the next SIMION simulation for SP1CB injection. The ion beam is smoothly convergent to rush through the deceleration tube into the SP1CB. Till the magnetic field is null, ion beam squeezes (X = 170, 300, 358). As soon as the ions feel SP1CB magnetic field, it explodes (X = 410) and therefore it pinches (X = 500, 541) to turn out to be very small. Entering the plasma core zone (X = 675.6, 700), the monocharged particles of the ion beam are magnetically controlled due to their low energy (star shape owing to the combination of magnetic field produced by hexapole and coils). In reality, this is not the truth because, they collide with charge particles (X^{q+}) of the plasma to be slowed down and captured. Figure 8 shows the same evolution depending on the electromagnetic field in use. The "E+B" case is identical to the one of Fig. 7 c). The "E" case corresponds to the exclusion of the magnetic field and the "B" case represents the withdrawal of the deceleration electric field. From the cases "E" and "B", it is demonstrated that only the combination of both electromagnetic fields leads to the formation of a tiny ion beam transporting the 1+ ions at the right energy (few eV) up to the core of the SP1CB plasma to be efficiently captured and charge bred.

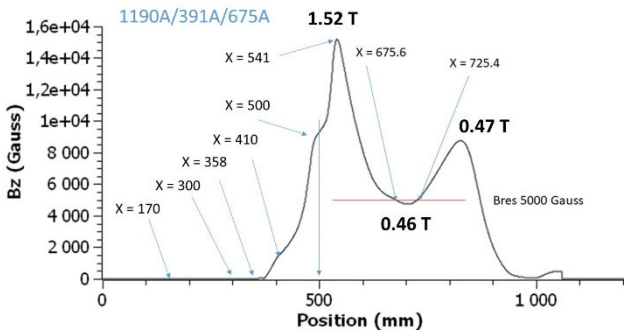

Figure 6: Axial magnetic field profile (Bz in Gauss) with the longitudinal positions corresponding to the Figs. 7, 8 and 10.

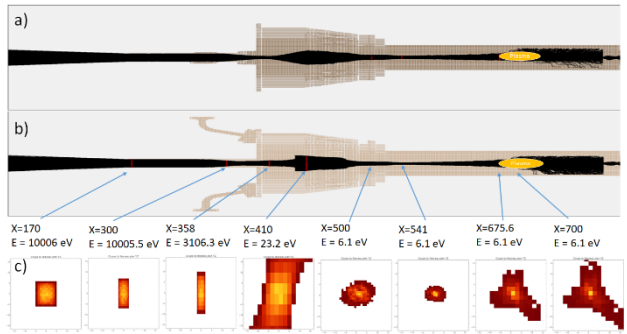

Figure 7: Evolution of the $^{85}Rb^{+}$@10kV injected and slowed down into the SP1CB. a) and b) are the pile-up of 1+ trajectories in both transverse planes. c) images representing the evolution of the 2D transverse 1+ beam profile along the SP1CB.

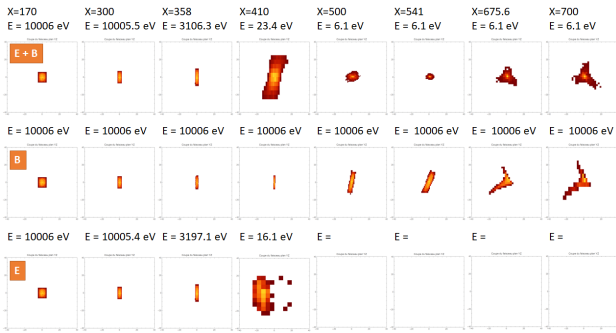

Figure 8: Evolution of the $^{85}Rb^{+}$@10kV injected into the SP1CB for three cases: E+B (both electric field and magnetic field); B (electric field is removed); E (magnetic field is removed).

Same method can be applied to the case of $^{85}Rb^{+}$@27.5kV. But a new beam optics has been found to overcome the magnetic quadrupole (Q11 – Q12 – Q13) restriction. Indeed, to determine the new values of magnetic optic elements, it is scaled regarding Bρ's. As the $^{85}Rb^{+}$@10kV and $^{85}Rb^{+}$@27.5kV are characterized by Brho of 0.133 T.m and 0.221 T.m respectively, the currents applied to the magnetic elements must be multiplied by a factor 1.66 (ratio of square root of the acceleration voltages $\sqrt{\frac{27.5}{10}}$). So a new beam optics has been calculated and tested experimentally. Figure 3 displays the charge state distribution (CSD) of charge bred ions (red curve) at this new energy. Figure 9 is totally similar to Fig. 5. Some discrepancies can be noticed:

- for X beam envelope, global shape is quite comparable except at the end where the beam explodes into the SP1CB
- for Y beam envelope, it blows up after the first magnetic triplet, similarly it is huge passing through the EQ2 before being pinched while entering in the SP1CB

ISBN: 978-3-95450-226-4 ISSN: 2222-5692 doi:10.18429/JACoW-ECRIS2020-WEZZO01

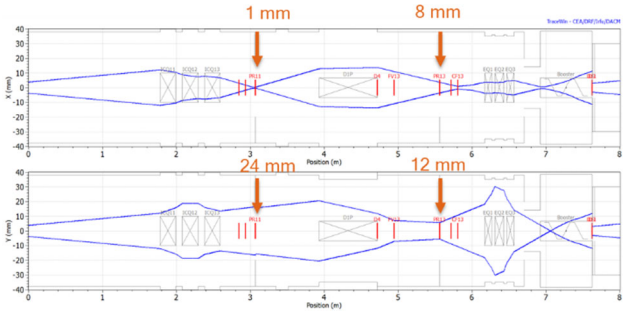

Figure 9: Transverse beam envelopes for the case 1+/N+ mode and the beam $^{85}Rb^{+}$@27.5kV.

But the value of the beam profiler on PR13 are quite similar for both cases prior to the injection inside the SP1CB: X plane 10 mm (10kV) – 8 mm (27.5kV) and Y plane 12 mm (10kV) – 12 mm (27.5kV). Figure 10 displays equivalent behavior regarding Fig. 7. The 2D transverse profiles have comparable shapes at the same locations. But, as it is larger in Y plane (cf. above), it looks likewise in Fig. 9. As the beam in Y plane is a bit larger than the deceleration tube inner diameter, there is some losses which can explain the decrease of the global efficiency in that case (Fig. 3 red curve).

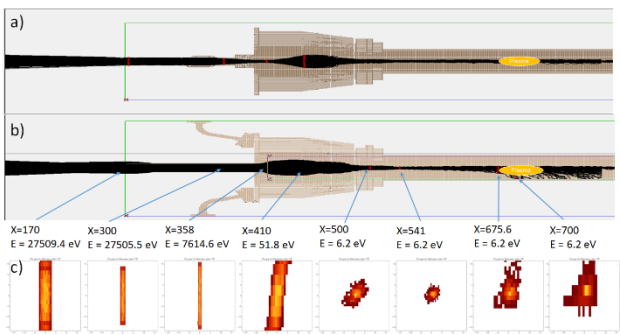

Figure 10: Evolution of the $^{85}Rb^{+}$@27.5kV injected and slowed down into the SP1CB. a) and b) are the pile-up of 1+ trajectories in both transverse planes. c) images representing the evolution of the 2D transverse 1+ beam profile along the SP1CB.

Blind Tuning Test

What is it important to know for this type of facility is the fact that the RIB's are orders of magnitude lower in terms of intensity than stable beams. So, it is not possible to tune the beam optic elements likewise the SP1CB using a classical faraday cup. So the typical method to adjust such a beam, is to use a stable one with an intensity in the range of hundred nA or more. The process is to sweep from the stable ion beam to the RIB by scaling the magnetic optic elements with the Brho and the electrostatic optic elements with the energy corresponding for the 1+ ion beam to the acceleration voltage.

Such test has accomplished successfully using the two isotopes of the rubidium: ^{85}Rb (stable) and ^{87}Rb (stable like because its half-life is $4{,}92\times10^{10}$ years). The abundances of ^{85}Rb and ^{87}Rb are ~72.2% and 27.8% respectively. The ion gun delivered ion beam intensities of ~300 nA of ^{85}Rb and 120 nA of ^{87}Rb well mass resolved. The test has been done at acceleration voltage of 10 kV and using He as buffer gas for the SP1CB. The full SPIRAL1 was tuned for getting a charge bred beam of $^{85}Rb^{19+}$ (Brho = 0.0305 T.m) from $^{85}Rb^{1+}$ (Brho = 0.1332 T.m). At same acceleration voltage, the Bρ's of the $^{87}Rb^{1+}$ and $^{87}Rb^{19+}$ ion beam become 0.1347 T.m and 0.0309 T.m (ratio of square root of the masses $\sqrt{\frac{87}{85}}$) meaning a factor of 1.0117. Figure 11 shows the CSD of charge bred ions. They are both peaked on the $^{85}Rb^{17+, 18+, 19+}$ ions with a maximum charge breeding efficiency of 12.2% ($^{85}Rb^{17+}$) and 10.2% ($^{87}Rb^{18+}$) associated with global efficiency of 70.6% (^{85}Rb) and 53.6% (^{87}Rb) respectively. The SP1CB as well as 1+ and N+ beam lines were tuned exactly in the same manner. Only the magnetic optic elements were scaled regarding the Bρ's ratio above. The ΔV value remained constant to 5.4V (ΔV is the additional voltage applied on the ion gun to get energy enough for the Rb^{1+} beam to be efficiently captured by the SP1CB plasma).

That result goes to prove that bling tuning is possible as long as the relative Brho difference is of the order of few %.

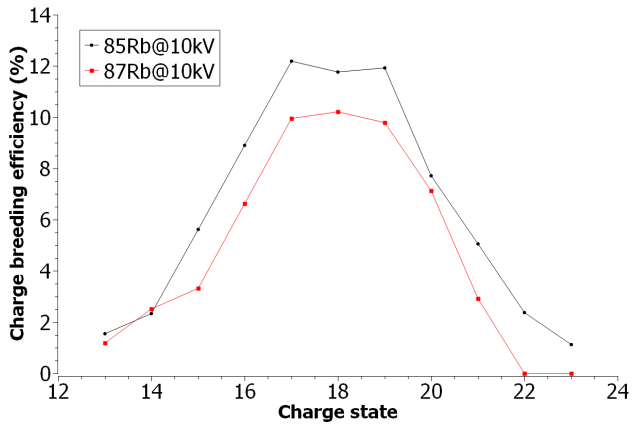

Figure 11: Charge state distribution of ^{85}Rb (black) and ^{87}Rb (red) charge bred ions at 10keV of total energy.

CONCLUSION

That paper focuses on the beam optics. Concerning the ST mode, more work and diagnostic is requested to better understand why TraceWin code must decrease the magnetic field of the SP1CB by a factor 0.6 to reproduce the experimental beam profiler values. A pepper-pot emittance meter type will be mounted in the N+ beam line to constrain the TraceWin simulation. One additional work to be achieved is to seek if there is a possible optimization between the three electrostatic quadrupoles and the magnetic field created by the SP1CB coils such that the transmission across the SP1CB plasma electrode can be increased.

About the 1+/N+ mode, a new beam optics has been found to overcome the limitation of the magnetic quadrupoles (Q11 Q12 Q13) designed previously to go up to Brho of 0.136 T.m instead of the current maximum Brho of 0.22 T.m. That new beam optics leading to close performances of the SP1CB shows a similar propagation of the ion beam inside the SP1CB. It has been established that

ISBN: 978-3-95450-226-4 ISSN: 2222-5692 doi:10.18429/JACoW-ECRIS2020-WEZZO01

both deceleration electric field and magnetic field are requested to transport 1+ incoming ions to the core of the SP1CB plasma. Next work will be the validation of that new beam optics over several ion beams of Na and K at few different energies covering the full range of Bρ's available at the SPIRAL1 facility. Finally, the final validation will be achieved using the TISS FEBIAD in the 1+/N+ mode.

ACKNOWLEDGEMENTS

The authors would like to thanks the fruitful discussions with Dr Olli Tarvainen (STFC Rutherford Appleton Laboratory, ISIS, UK) leading to new insights reported in this paper. Also, the authors want to thank Mr Clément Michel and Mr Alexandre Gognat (GANIL, France) for their computer-assisted design works beneficial to the simulation achievements presented in this paper.

REFERENCES

[1] L. Maunoury *et al.*, "SPIRAL1: A Versatile User Facility", in *Proc. 23th International Workshop on ECR Ion Sources (ECRIS'18)*, Catania, Italy, Sep. 2018, pp. 29-33. doi:10.18429/JACoW-ECRIS2018-MOC4

[2] A. Annaluru, "Beam optics transport and fundamental processes involving a charge breeder in the upgraded SPIRAL1 facility" Ph.D. thesis, GANIL, Université Caen Normandie, France, 2019

[3] P. Chauveau *et al.*, "A new FEBIAD-type ion source for the upgrade of SPIRAL1 at GANIL", *Nucl. Instr. Meth. Phys. Res. B*, vol. 376, pp. 35-38, 2016. doi.org/10.1016/j.nimb.2016.01.039

[4] J. Angot *et al.*, "Recent improvements of the LPSC charge breeder", *AIP Conference Proceedings*, vol. 2011, p. 070005, 2018. doi.org/10.1063/1.5053347

[5] C. Tamburella *et al.*, "Production of multicharged radioactive ion beams: The 1+ to n+ charge state transformation for the Production, Ionisation, Accélération de Faisceaux Exotiques project", *Rev. Sci. Instr.*, vol. 68 iss. 6, pp 2319, 1997. doi.org/10.1063/1.1148142

[6] L. Maunoury, "Production de faisceaux d'ions radioactifs multicharges pour SPIRAL : Etudes et realisation du premier ensemble cible-source", Ph.D. thesis, GANIL, Université Caen Normandie, France, 1998.

[7] L. Boy, "Problèmes posés par l'accélération d'ions radioactifs dans le projet SPIRAL. Réglage et stabilisation de l'accélérateur" Ph.D. thesis, GANIL, Université Caen Normandie, France, 1997.

[8] L. Maunoury *et al.*, "Charge breeding at GANIL: Improvements, results, and comparison with the other facilities", *Rev. Sci. Instr.*, vol. 91, p. 023315, 2020. doi.org/10.1063/1.5128661

[9] http://irfu.cea.fr/dacm/logitiels

[10] https://www.cathode.com

[11] https://simion.com

ISBN: 978-3-95450-226-4 ISSN: 2222-5692 doi:10.18429/JACoW-ECRIS2020-WEZZO02

CONTAMINANTS REDUCTION IN ECR CHARGE BREEDERS BY LNL LPSC GANIL COLLABORATION

J. Angot*, T. Thuillier, M. Baylac, M. Migliore, P. Sole
Univ. Grenoble Alpes, CNRS, Grenoble INP, LPSC-IN2P3, France, Grenoble, France
A. Galatà, INFN-Laboratori Nazionali di Legnaro, Legnaro, Italy
L. Maunoury, Grand Accélérateur National d'Ions Lourds, CEA-DRF/CNRS-IN2P3, Caen, France

Abstract

Contaminants reduction in Electron Cyclotron Resonance Charge Breeders (ECRCB) is a key point for the future experiments foreseen at LNL and GANIL Isotope Separation On Line (ISOL) facilities. According to the mass separator resolution set downstream the ECRCB, the radioactive ion beam study can be challenged in case of low production rate. An ongoing collaboration between LNL, LPSC and GANIL laboratories aims to improve the beam purity, acting on all the pollutant causes. Comparative experiments will be done at LPSC using different techniques, like covering the plasma chamber wall with liners of different materials. Different configurations of the ECRCB will also be tested, with the enhancement of the efficiency and charge breeding time parameters as additional objectives. A presentation of this program is proposed together with the recent upgrade of the LPSC 1+N+ test bench, with the aim to improve the vacuum quality.

INTRODUCTION

The PHOENIX type charge breeder (CB) has been developed at LPSC since 2000 [1]. It is a minimum-B Electron Cyclotron Resonance (ECR) ion source working at 14.5 GHz which is tested on the 1+N+ test bench. Its latest improvements led to progress in terms of efficiency and charge breeding time [2]. Another important parameter to qualify the ECRCB is the contamination yield. In the present European context, with the SPES and SPIRAL1 upgrade projects respectively under construction and already into operation [3, 4], the contaminants reduction is a key point with regard to the foreseen Radioactive Ion Beam (RIB) production yield and resolving power of downstream separators. These facilities are equipped with PHOENIX Charge Breeders in configurations close to the LPSC one. Thus, LNL, LPSC and GANIL decided to collaborate on the contaminants reduction acting on all the polluting sources, on the basis of a previous agreement signed between LNL and LPSC in 2018. A development plan was defined for the LPSC CB to continue improving its performances and to test the solutions retained by the collaboration. The first step, aiming to improve the 1+N+ test bench vacuum and verify the experimental technique to measure the contaminants level was completed in January 2020. The next two steps will consist in modifying the source magnetic structure and the plasma volume.

* julien.angot@lpsc.in2p3.fr

CONTAMINANTS PROBLEM

The ECRCB principle is based on the use of an ECR plasma to multi-ionise an injected 1+ beam. In addition to the injected ion species and the support gas species, contaminants ion beams are extracted from the CB. The origin of these contaminants has already been studied [5–8]. Taking into account the PHOENIX CB configuration and the measurements previously done, the contaminants and their estimated fluxes are indicated below as a function of their origin.

The first cause is the species in the residual vacuum, including the potential leaks with ambient atmosphere, wall outgasing, o-rings permeation and vacuum parts cleaning. Analysing A/q spectrum from the CB running in the 1+N+ configuration, these fluxes are estimated between 10^{12} and 10^{13} pps.

The second one comes from the impurities and unwanted isotopes present in the support gas. 99.999% purity gas are typically used in the CB, and impurities like H_2O, O_2, N_2, CO or hydrocarbons are present with proportions of 20 ppm or less for the gas species usually used (H_2, He, O_2). Taking into account the support gas fluxes deduced from the measured spectrum, the contaminants flux originating from the support gas is estimated at 10^9 pps.

Finally, the plasma confinement being imperfect, the plasma ions intercept the chamber wall. Depending on their charge state and the plasma potential, their energy can reach several hundreds of eV, leading to sputtering of the wall material. Thus, the plasma parameters influence the contamination. It was also demonstrated that an unstable plasma regime could lead to a higher production of contaminants [9]. From this last data, the contaminants fluxes caused by sputtering can be estimated at 10^{12} to 10^{13} pps.

On the other hand, RIB fluxes in the 10^2 to 10^{10} pps range are expected to be injected into the SPES and SPIRAL1 upgrade charge breeders [10]. Taking into account the CB efficiency and the resolving power of the downstream separators, these contaminant yields must be minimised not to compromise physics experiments [8, 11].

SOLUTIONS TO CONTAMINATION PROBLEM

To reduce efficiently the contamination yield, all the sources must be reduced [8].

First, particular attention must be paid to the vacuum chambers and vacuum parts cleaning. Several techniques

ISBN: 978-3-95450-226-4 ISSN: 2222-5692 doi:10.18429/JACoW-ECRIS2020-WEZZO02

have shown their efficiency. The vacuum level must be as low as possible using Ultra High Vacuum (UHV) standards, suppressing o-rings and baking-out sections and parts [12]. The use of the same material is mandatory for the parts surrounding the plasma and for the electrodes. The material has to be as pure as possible, being preferably mono-isotopic. A possible choice could be the deposition of a specific material, the disadvantage being that depending on the thickness and the CB operation conditions, the layer can have a short lifetime. Concerning the support gas, in the case of H_2 or He, one solution proposed by ANL [13], consists in adding a cryogenic system on the gas circuit in order to condensate the contaminants. A baking system could also be added to outgas the circuit before operation.

PRESENT CONFIGURATION OF THE LPSC 1+N+ TEST BENCH AND CHARGE BREEDER

1+N+ Test Bench

The 1+N+ test bench was assembled in 2002 to test the charge breeding method with a PHOENIX type ion source [14]. The "1+" beam line is used to generate the 1+ beam and inject it into the CB. It is composed of the 1+ source, a 90° dipole magnet, two emittance scanners, one Faraday cup (FC) and the injection optics. The analysis of the beams extracted from the CB is done in the "N+" beam line. It consists of the CB extraction and optics, a 120° dipole magnet, two emittance scanners and one FC.

Along the years, the 1+N+ test bench was gradually modified for example to increase the high voltage insulation and adapt new diagnostics. Most of the sealing was done using o-rings. The vacuum system was composed of 16 turbo pumps with pumping speed between 240 and $3601 \cdot s^{-1}$. Oil sealed rotary primary pumps were used in the past and after years of operation, dust accumulated on some surfaces, notably because of pumping oil vapors backstreaming. The vacuum level in the beam line was between 2×10^{-7} mbar and 5×10^{-7} mbar, the typical vacuum level at the CB injection during operation being 7×10^{-7} mbar.

Charge Breeder

Like the other PHOENIX type ion sources, the LPSC charge breeder structure is modular, see Fig. 1. The external part aims to generate the axial magnetic field. It is composed of three pairs of coils (orange) stack assembled with soft iron rings (blue). Inside, the central core is made up of the stainless steel plasma chamber (black) surrounded by the hexapole (green). The plasma chamber has an internal diameter of 72 mm and the hexapole generates a 0.8 T radial magnetic field strength in front of the poles, at the plasma chamber wall surface. The injection plug, extraction plug, surrounding hexapole rings and additional injection plug (blue) set under vacuum into the plasma chamber, parts of the central core, complete the axial magnetic field system.

Two wave guides are machined directly into the additional plug for the microwave coupling; in addition a piece of wave guide made of brass is fixed at the plug extremity. In this configuration, the plasma chamber wall is cylindrical without port. A 40 µm Nickel plating was done on the extraction plug and on the additional injection one to reduce the outgassing under vacuum. A 5 µm Silver plating was added on the additional injection plug to increase the electrical conductivity. A vented plasma electrode with a 8 mm hole, made of 2017A aluminum alloy, closes the plasma chamber at extraction. In this configuration, a great number of material is present in front of the plasma.

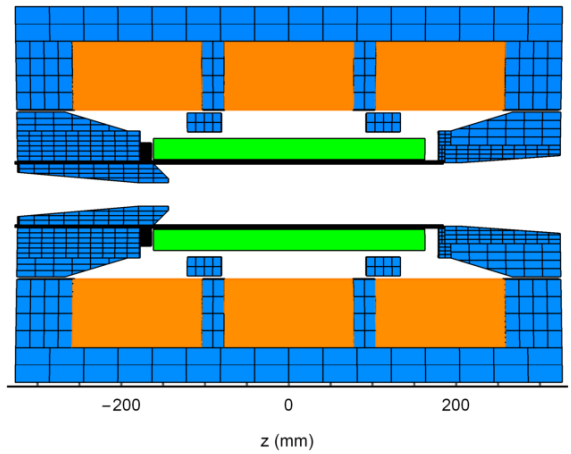

Figure 1: Cut view of the CB configuration.

In order to improve the CB performances, LPSC defined a 3 steps development plan, in collaboration with LNL and GANIL to address contaminants reduction. The first step, completed in January 2020, aimed to improve the vacuum and devices alignment of the 1+N+ beam line. The next step goal will be to modify the axial magnetic system to optimize the field profile while reducing the cross talk between the coils. In this configuration, contaminants reduction experiments will be tested. Comparative measurements will be done to check the efficiency of the different solutions adopted, measuring A/q spectra. A resolving power as high as possible will be necessary to separate the peaks. The measurement method will be verified and the limits evaluated. Finally, the last step will consist in increasing the plasma volume to increase the production of higher charge states [15] and pursuing studies on the contaminants reduction.

CONTAMINANTS MEASUREMENT METHOD

Considering that the contaminant ions originate from the CB plasma, the experiments will be carried out with the CB in "source mode" that is without 1+ beam injection. First, spectra will be acquired with the N+ FC to obtain the absolute value of the more intense species. Then emittance measurements will be done in the horizontal N+ emittance scanner FC. In this case, the 0.2 mm slits will produce a higher resolution, at the expense of cutting a large fraction part of the beam. In order to measure the spectrum, the potential applied to the deviating plate of the emittance scanner

ISBN: 978-3-95450-226-4 ISSN: 2222-5692 doi:10.18429/JACoW-ECRIS2020-WEZZO02

will have first to be optimised on a peak. The comparison of the spectra measured in the FC and in the emittance scanner will allow defining a rough correction factor that will be used to obtain an estimate of the absolute value of the contaminant peaks.

CB DEVELOPMENT PLAN

1+N+ Beam Line Upgrade

The 1+N+ beam line upgrade was realized between September 2018 and January 2020. To minimize the duration of the shutdown, all beam line sections were disassembled at the same time and many modifications were done simultaneously.

Modifications Different solutions were used to upgrade the seven vacuum chambers to UHV standards. The conflat (CF) standard was chosen for all flanges. Three vacuum chambers were replaced by new ones whereas the others were modified. The vacuum valves mounted on the chambers were either cleaned or replaced by new ones.

For alignment, an optical level was set on the beam axis and beam line elements, equipped with removable centered targets, were positioned. This method requires to place targets on the room walls and to have a clear view through the beam line. For this last reason, two view ports were added on the 1+ and N+ dipole magnet chambers and corresponding grooves were machined on their yoke.

All the beam optics elements under vacuum were replaced to be UHV compatible, using alumina as insulating material and 304L stainless steel for metallic parts. The electrical feedthroughs were also replaced, using only brazed alumina sealing. A new 1+ beam electrostatic deviating system was manufactured. To reduce aberrations, the injection double lens assembly was redesigned: the new electrodes have an internal diameter of 80 mm (previously 60 mm).

At extraction, a new assembly composed of the puller and the Einzel lens was designed and manufactured. The new puller has a conical shape to improve the beam extraction and 32 holes were machined to enhance the vacuum pumping. The extraction lens, earlier realized by a simple cylinder set into the extraction chamber [16], was replaced by a three cylindrical electrodes Einzel lens, having a 80 mm inner diameter.

Concerning the diagnostics, the three FC were replaced by new electrostatic ones, based on the same design and with a fully shielded cup. Two new emittance scanners will be adapted and installed on the 1+ section. The N+ emittance scanners were modified to allow pumping, replace the insulation parts by alumina ones and replace the cables under vacuum by UHV models. Their support flange was also upgraded to CF standard.

The vacuum system was completely revised. For the UHV pumping, a new Agilent Twistor 304 FS (2501 $\cdot$ s^{-1} pumping speed) was installed on the 1+ source section. Six Oerlikon turbovac 361 pumps were modified to CF160 flange standard and cleaned by the manufacturer. In this configuration, their pumping speed is 4001 $\cdot$ s^{-1}. One was installed on the 1+ diagnostic section, two on the injection section, two on the extraction section and one on the N+ diagnostics section. All UHV gauges were replaced by Pfeiffer IKR 251 model on CF flanges. The whole vacuum circuit was disassembled and cleaned. A maintenance and a cleaning of the primary dry pump, model Agilent triscroll 300, was also realized.

The largest parts, including the vacuum chambers and most of the flanges, were degreased, etched, rinsed with high pressure water, rinsed with demineralized water and dried. The other parts were degreased, ultrasonic cleaned and dried. All the parts were re-assembled, aligned and set under vacuum. In this configuration, twelve sealings with o-rings remain on the beam line, notably two for the 1+ source, six at the CB injection and three at the CB extraction. In the next CB configuration, the number of o-rings will be reduced, using new alumina CB insulators with brazed metallic flanges. Section by section, a methodical vacuum leak detection was applied to all the welds and connections. In this configuration, without baking the chambers, the pressure in the beam line sections is in the range 3×10^{-8} mbar to 6×10^{-8} mbar, the pressure at the CB injection being 4×10^{-8} mbar. Therefore the residual pressure was reduced by an order of magnitude thanks to the performed modifications while reducing the number of pumps.

Qualification experiments To qualify the test bench, it was decided to compare the charge breeding spectra of K with respect to the one obtained before the upgrade, the tuning being optimised for the K^{10+} charge breeding with He as support gas, see Fig. 2. The new performances being in good agreement with the previous ones, the 1+N+ test bench operation was validated.

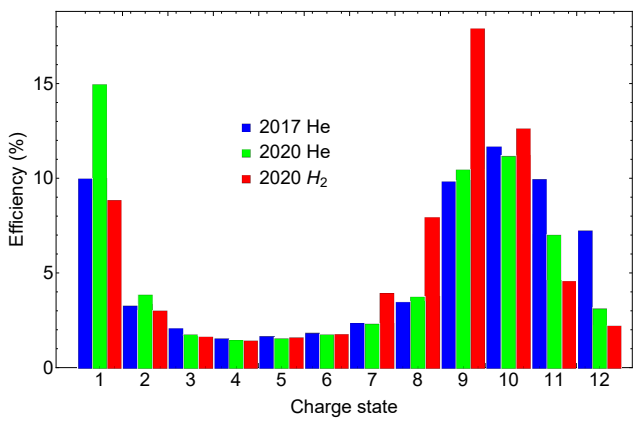

Figure 2: Measured K charge breeding spectra blue) in the previous configuration with He as support gas, green) after the 1+N+ test bench upgrade with He as support gas and red) after the 1+N+ test bench upgrade with H_2 as support gas.

The K^{10+} efficiency is measured at 11.2% and found slightly lower than the previous best measured efficiency at 11.7% [2]. A slight shift toward lower charge states is also noticed together with a lower 1+ beam capture. The

ISBN: 978-3-95450-226-4 ISSN: 2222-5692 doi:10.18429/JACoW-ECRIS2020-WEZZO02

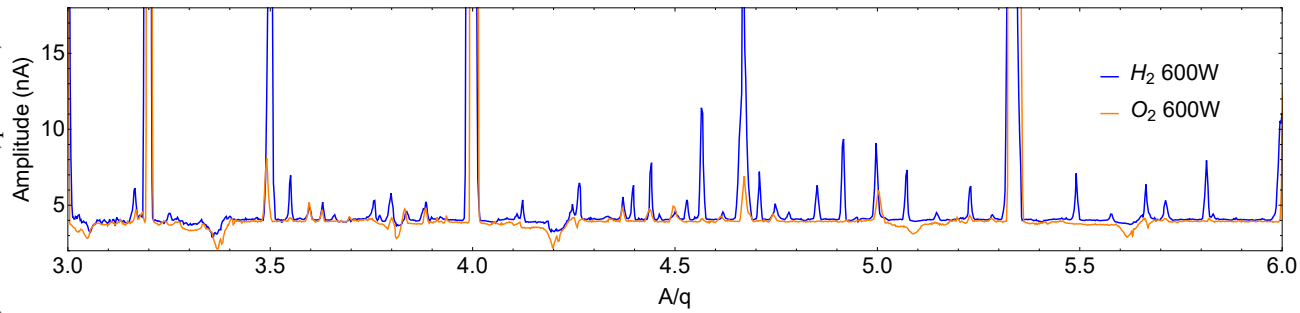

Figure 3: High resolution spectra with H_2 and O_2 as support gas and 600 W of microwave power.

difference is attributed to an incomplete conditioning of the CB before the experiments. Using H_2 as support gas, the best efficiency was found at 17.9% for K^{9+}.

Contaminants Reduction Preliminary Experiments
To estimate the resolving power of the contaminants measurement method, the CB was operated with natural Xenon as support gas and a spectrum was measured with the horizontal emittance scanner. By analysing the separation of the $^{131}Xe^{19+}$ and $^{132}Xe^{19+}$ peaks, which have a A/q ratio near 7 and similar peak amplitudes, the resolving power was estimated at 1:150.

After this experiment, the contaminants measurement method was tested by studying the influence of the support gas species and of the microwave power on the contaminant beams. As a similar operating regime cannot be reached for different support gas, we decided for each support gas species, to tune the CB (support gas dosing, coils...) optimizing the K^{10+} charge breeding efficiency with the same microwave power 600 W. Contaminant spectra were recorded in this configuration, without 1+ beam injection, together with 100, 300 and 450 W microwave power values, as illustrated in Fig. 3.

The measurements analysis shows several limitations. First, the signal over noise ratio is low, the minimum measurable peak amplitude being on the order of 100 epA. This level corresponds roughly to an absolute level of contaminants of 10^{10} pps in the FC. As a comparison, a 10^8 pps flux at the CB entrance would give a 10^7 pps flux in the N+ FC, considering a 10% efficiency. Moreover the minimum step in A/q is too large which leads to imprecise peak value measurement. This limitation comes from the poor resolution of the data acquisition system which generates the analog signal driving the dipole power supply. Finally, dips with negative intensity values are also visible in the spectra, probably due to secondary emission electrons, induced by a neighbour intense beam touching the wall, coupling to the emittance scanner FC through the device pumping holes.

The measurement method will be implemented to solve these problems. The resolution of the data acquisition system will be improved to allow smaller steps in A/q. Instead using the emittance scanner, a slit will be set in the N+ diagnostics section and the measurements will be done in the N+ FC. In this way, at ANL, 1 epA contaminants peaks was measured [8]. Other type of detectors could also be tested with a principle based on the use of a channeltron or a plastic scintillator coupled with a photodiode, the goal being to increase the sensitivity.

For each high resolution spectra, the A/q value of all the peaks was listed. After analysis, the most probable species found for these distributions is in good agreement with the elements cited in the "Charge Breeder" section as possible contaminants with notably Fe, Ni, Mo, Sn, Zn, Cu coming from the wall sputtering and gaseous elements like H, N, O, Xe, Kr or Ar originating from the residual vacuum.

The resolving power is insufficient to separate all the species, most of the peaks being due to the superposition of several possible species. Some peaks are also found to correspond to a single species. For some isotopes, the evolution of the peak amplitude is represented as a function of the microwave power and support gas species, see Fig. 4.

The contaminants production is favoured when using H_2 as support gas, this is also true for most of other peaks, see Fig. 4. $^{96}Mo^{15+}$ and $^{12}C^{5+}$ clearly increase with microwave power whatever the support gas which shows a dependency to the microwave power and so to the plasma density. For $^{40}Ar^{7+}$ the yield is almost constant when increasing the microwave power.

Five Coil CB Configuration

The next step of the development plan consists in optimizing the CB magnetic configuration. The new design was simulated to enhance the magnetic field profile by rearranging the yoke and coils structure and changing the shape of the soft iron plugs (see Fig. 5). One coil of the central pair will be removed and the distance between the coils will be increased to reduce the cross talk. The length of the CB will decrease from 640 mm to 560 mm. The injection and extraction plugs will be shortened, improving the beam injection and extraction. This new configuration is called "Five coil configuration".

The modification of the LPSC CB assembly is planned before the end of 2020, the last parts are being manufactured. Contaminants reduction experiments will be done by introducing liners to cover the plasma chamber wall, the injection plug and the plasma electrode. These measurements will be compared to results previously obtained without liners. Three different liner materials will be tested: Nb, Ta and alu-

ISBN: 978-3-95450-226-4 ISSN: 2222-5692 doi:10.18429/JACoW-ECRIS2020-WEZZO02

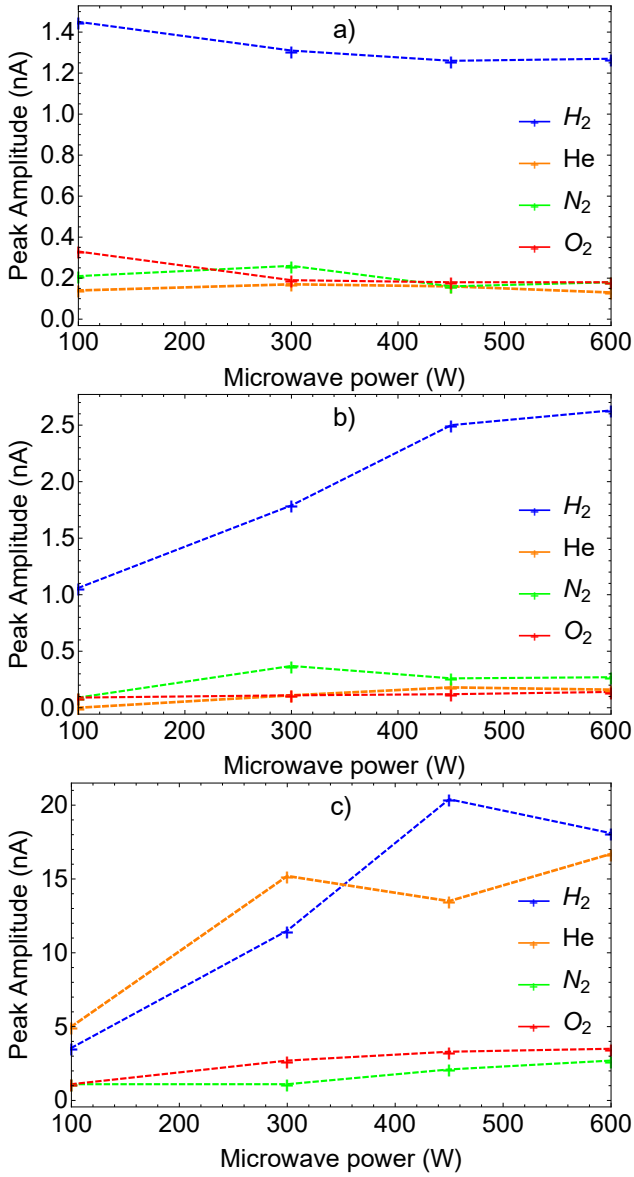

Figure 4: Evolution of a) $^{40}Ar^{7+}$, b) $^{96}Mo^{15+}$ and c) $^{12}C^{5+}$ peak amplitude as a function of microwave power and CB support gas plasma species.

mina. For this last case, the Metal Dielectric liner technique developed at NIPNE [17] is foreseen. A few micron alumina layer is created by special electrochemical deposition on a 99.999% purity aluminum foil. In this five coil configuration, liner parts will be installed through the CB injection port only, without dismounting the extraction. A gas circuit, still to be designed, will also be implemented for the support gas contaminants reduction.

Large Diameter Configuration

The last step of the development plan is called "Large diameter CB configuration". The goal in this case will be to favour the production of highly charged ions by increasing the plasma volume and consequently the ions lifetime within the plasma. This solution, successfully tested on the

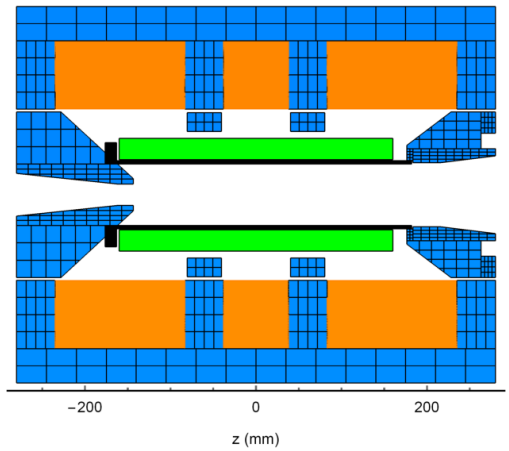

Figure 5: Cut view of the CB five coils configuration.

PHOENIX V3 ion source [15], will be applied to the CB: the plasma chamber diameter will be increased to 100 mm. This configuration should also reduce contamination thanks to a more favorable volume over surface ratio for the plasma cavity [11]. The hexapole was designed to obtain a 1.0 T radial magnetic field at the new plasma chamber wall, in front of the pole. Preliminary magnetic simulations were performed to conceive the axial field system, but the definitive design remains to be done. The material tested for the liners experiments in the five coil CB configuration could be used to manufacture some central core parts of the large diameter CB.

CONCLUSION

A collaboration between LNL, LPSC and GANIL, was inititated on the contaminants reduction and a R&D program was defined and integrated into the LPSC CB development plan. The 1+N+ test bench upgrade reduced the residual pressure throughout the beam line by a decade. Preliminary experiments have shown a high level of contaminants, notably originating from sputtering of the walls surrounding the plasma. The pollutant level was found to be higher with H_2 as support gas and some species tend to increase with the plasma density. Limitations in the detection method were observed and solutions were identified to enhance the sensitivity and precision of the measurements. The LPSC CB will be assembled in the new five coil configuration before the end of 2020 and the solutions defined to reduce the contaminants, like the use of liners, will be tested.

REFERENCES

[1] P. Sortais *et al.*, "Electron cyclotron resonance charge breeder", *Rev. Sci. Instrum.*, vol. 71, p. 617, 2000. doi:10.1063/1.1150331

[2] J.Angot *et al.*, "Recent improvements of the LPSC charge breeder", *AIP Conference Proceedings 2011*, p. 070005, 2018. doi:10.1063/1.5053347

[3] A. Galatà *et al.*, "Towards the First Beams from the ADIGE Injector for the SPES Project", in *Proc. IPAC'19*, Mel-

ISBN: 978-3-95450-226-4 ISSN: 2222-5692 doi:10.18429/JACoW-ECRIS2020-WEZZO02

bourne, Australia, May 2019, pp. 3647–3649. doi:10.18429/JACoW-IPAC2019-THPGW030

[4] L. Maunoury *et al.*, "SPIRAL1: A Versatile User Facility", in *Proc. ECRIS'18*, Catania, Italy, Sep 2018, pp. 29–33. doi:10.18429/JACoW-ECRIS2018-MOC4

[5] N. Imai *et al.*, "KEKCB electron cyclotron resonance charge breeder at TRIAC", *Rev. Sci. Instrum.*, vol. 79, p. 02A906, 2008. doi:10.1063/1.2828070

[6] S. C. Jeong *et al.*, "KEKCB-18 GHz ECR charge breeder at TRIAC", *Nucl. Instrum. Methods Phys. Res., Sect. B*, vol. 266, pp. 4411-4414. doi:10.1016/j.nimb.2008.05.072

[7] R. Vondrasek *et al.*, "Operational experience with the Argonne National Laboratory Californium Rare Ion Breeder Upgrade facility and electron cyclotron resonance charge breeder", *Rev. Sci. Instrum.*, vol. 85, p. 02B903, 2014. doi:10.1063/1.4826329

[8] R. C. Vondrasek, "Addressing Contamination in ECR Charge Breeders", in *Proc. ECRIS'18*, Catania, Italy, Sep 2018, pp. 90–93. doi:10.18429/JACoW-ECRIS2018-TUP07

[9] O. Tarvainen *et al.*, "Plasma instabilities of a charge breeder ECRIS", *Plasma Sources Sci. Technol.*, vol. 26, p. 105002, 2017. doi:10.1088/1361-6595/aa8975

[10] P. Delahaye *et al.*, "New exotic beams from the SPIRAL 1 upgrade", *Nucl. Instrum. Methods Phys. Res., Sect. B*, vol. 463, pp. 339–344, 2020. doi:10.1016/j.nimb.2019.04.063

[11] T. Thuillier *et al.*, "Challenges and Prospects of Electron Cyclotron Resonance Charge Breeding", in *Proc. ECRIS'18*, Catania, Italy, Sep 2018, pp. 14–19. doi:10.18429/JACoW-ECRIS2018-MOC1

[12] A. Galatà *et al.*, "Adige: the radioactive ion beam injector of the SPES project", in *Proc. IPAC2017*, Copenhagen, Denmark, May 2017, pp. 2281–2283. doi:10.18429/JACoW-IPAC2017-TUPVA087

[13] R. Vondrasek, private communication, Jun. 2018.

[14] T. Lamy *et al.*, "ECRIS charge breeding: High resolution spectra and emittance", *Rev. Sci. Instrum.*, vol. 75, p. 1624, 2004. doi:10.1063/1.1691472

[15] T. Thuillier *et al.*, " Effect of the plasma chamber radius on the high charge state production in an ECR ion source",*AIP Conference Proceedings*, vol. 2011, p. 040020, 2018. doi:10.1063/1.5053294

[16] J. Angot, T. Lamy, M. Marie-Jeanne, P. Sortais, and T. Thuillier, "LPSC PHOENIX ECR Charge Breeder Beam Optics and Efficiencies", in *Proc. 20th Int. Workshop on ECR Ion Sources (ECRIS'12)*, Sydney, Australia, Sep. 2012, paper THYO02, pp. 167–171.

[17] L. Schachter *et al.*, "Enhanced highly charged ion production using a metal-dielectric liner in the KVI 14 GHz ECR ion source", *Rev. Sci. Instrum.*, vol 73, p. 570, 2002. doi:10.1063/1.1430274

ISBN: 978-3-95450-226-4 ISSN: 2222-5692 doi:10.18429/JACoW-ECRIS2020-WEZZO03

ECR3 COMMISSIONING AND PLANNING FOR C-14 ION BEAMS AT THE ARGONNE TANDEM LINAC ACCELERATOR SYSTEM*

R.H. Scott†, R.C. Vondrasek,
Argonne National Laboratory, Lemont, IL, USA

Abstract

The Electron Cyclotron Resonance Ion Source ECR3 has recently been commissioned at the Argonne Tandem Linac Accelerator System (ATLAS) at Argonne National Laboratory. While ECR3 can provide many of the stable ATLAS beams, its other intended purpose is the production of C-14 ion beams which were previously produced by a now-retired negative ion source. This paper will discuss the final installation and commissioning of the ion source as well as the preparations for running C-14. A stable C-13 ethylene gas was used as a surrogate to determine the expected level of N-14 contamination when running C-14 since they are inseparable at ATLAS. We were also able to confirm consumption rates and charge state efficiencies under different C-13 running conditions in order to optimize the upcoming C-14 beam production.

INTRODUCTION

The BIE100 [1] Electron Cyclotron Resonance Ion Source (ECRIS), configured with permanent magnets for both axial and radial plasma confinement, was originally conceived by Berkeley Ion Equipment [2]. After use by the Argonne National Laboratory (ANL) Physics Division for off-line research, the ECRIS and a new low energy beam transport (LEBT) section have been incorporated into the Argonne Tandem Linac Accelerator System (ATLAS) [3]. The BIE100, named chronologically as ECR3 within ATLAS, is intended to provide carbon-14 (C-14) ion beams thereby limiting radioactive contamination at ECR2. ECR3 will also lessen the burden of ECR2 which has essentially been the sole provider of stable ion beams at ATLAS since 2015.

INSTALLATION AT ATLAS

The planning, installation and commissioning schedule of ECR3, concurrent with ATLAS operation, was stretched over several years to accommodate personnel and equipment conflicts. In mid-2017 construction began. Electrical service for the area was installed. Relay racks were populated, beamline stands and a high voltage (HV) platform were placed as well (see Fig. 1). Milestones in 2018 included installation of vacuum components, safety systems, air, cooling water and electrical service to the HV platform. Early 2019 was dedicated to installation of the ECRIS onto the HV platform, interlock verifications on the vacuum, high voltage and x-ray protection systems, and the incorporation of all devices into the ATLAS control system.

*This work was supported by the U.S. Department of Energy, Office of Nuclear Physics, under Contract No. DEAC02-06CH11357 and used resources of ANL's ATLAS facility, an Office of Science User Facility.
† rscott@anl.gov

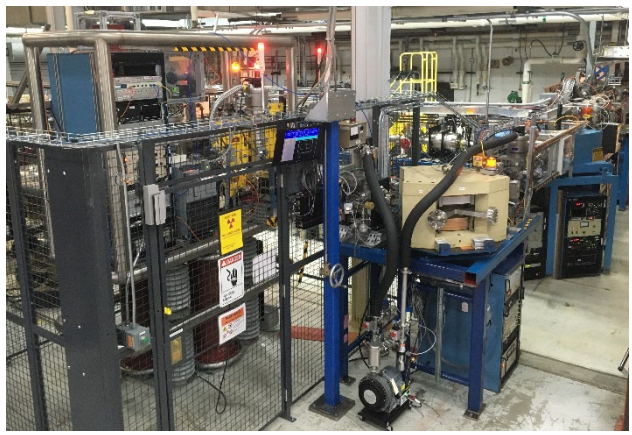

Figure 1: ECR3 ion source on platform inside fenced enclosure (left) and LEBT with m/q selecting dipole (right).

ECR3 Commissioning

Approval for ECR3 operation at ATLAS was obtained in June 2019. At this time RF conditioning was started, and beam identification and transport studies soon followed. Helium, oxygen, neon, argon and krypton production were verified. In October, the first ECR3 beam for the ATLAS experimental program, $^{14}N^{6+}$ using background gas was delivered to target. This was followed by $^{12}C^{4+}$ using methane in December. Ion beam transmission for these experiments ranged from 21% to 38% from the first faraday cup of m/q analysis to the last faraday cup before target, with room for improvement mostly in the ECR3 LEBT. For comparison, transmission from ECR2 is typically near 55% and has been as high as 64% in the last two years.

C-14 PREPARATIONS

C-14 production paused at ATLAS upon retirement of the ATLAS Tandem Van de Graaff in 2013, and the ECR3 ion source was envisioned as the subsequent producer. To eliminate radiocarbon transmission into the facility, the source and beamline pump exhaust is channeled to the CARIBU exhaust stack. Procedures have been written for use of C-14 at ECR3, and a Dual Alpha and Beta Radioactive Assay System has been moved to the adjacent work area to assist radiation protection technicians in field measurements during ion source and beamline entry.

The most stringent requirements of two currently approved ATLAS experiments are an energy of 210 MeV, target intensity of 100 pnA, and ratio of C-14 to N-14 contaminant ≥ 4:1. We have set out to verify that these requirements can be met in a way that minimizes consumption of C-14. It is planned to deliver ethylene gas (C_2H_4) saturated in C-14 supplied by ViTrax, Inc. [4] using a Varian Model 951 variable leak valve. Preliminary tests were performed with ethylene gas enriched with 99% C-13 as a substitute,

ISBN: 978-3-95450-226-4 ISSN: 2222-5692 doi:10.18429/JACoW-ECRIS2020-WEZZO03

C-12 was not used due to large m/q contaminants in $^{12}C^{3+}$ and $^{12}C^{6+}$.

Energy Verification

Achievable energy was predicted using in-house software that takes into account active accelerating components and their maximum energy gain. ATLAS is divided into three accelerating sections with stripping available after the first and second section. It was determined ≥ 210 MeV can be achieved with various accelerator configurations. The first is with ECR3 producing $^{14}C^{6+}$ and accelerating to target. The other option would be to start with charge state (C.S.) 3+ (or 4+) and strip to 6+ using a 50 μg/cm^2 carbon foil after the first accelerating section with a calculated stripping fraction of 40%. Resultant predicted energies are shown in Table 1 for the different configurations available.

Table 1: C-14 Beam Energy Calculations

Source	Stripping			Maximum
	Energy		Fraction	Energy
q	[MeV]	q		[MeV]
3+	25.7	3+	-	122.2
3+	25.7	6+	0.4	210.8
4+	27.9	4+	-	156.3
4+	27.9	6+	0.4	212.3
5+		5+	-	186.4
6+	30.6	6+	-	214.3

Intensity Verification

In Table 2, we determine source intensity requirements for 100 pnA at target assuming a minimum 20% transmission of unstripped beam from source to target and 8% transmission accounting for the additional stripping fraction. Tests were performed with C-13 ethylene gas to determine if a target intensity of 100 pnA is achievable. Maximum stable beam current for $^{13}C^{6+}$ was found to be 13 pnA with 100 W of RF input at 11.49 GHz. $^{13}C^{6+}$ output was limited by a combination of gas and RF input levels causing discharges in a downstream focusing lens. For $^{13}C^{3+}$, stable beam of greater than 7000 pnA was easily produced with 50W RF input power at the same frequency.

Table 2: C-14 Beam Intensity Calculations

Source		Transmission	Target	
q	I [pnA]	[%]	q	I [pnA]
3+	1250	8	6+	100
4+	1250	8	6+	100
6+	500	20	6+	100

From an intensity perspective, the $^{14}C^{3+}$ or $^{14}C^{4+}$stripped to $^{14}C^{6+}$ options are immediately viable. If at all possible, shifting the charge state distribution higher so that $^{14}C^{6+}$ out of the source could be used would make set-up and tuning of the accelerator simpler.

Nitrogen Contamination Levels

Given the concentration of nitrogen in air, it is not surprising an ECRIS produces some level of N-14 ion beams. These beams are inseparable from C-14 of the same charge state at ATLAS. For the upcoming ATLAS experiment a ratio of C-14:N-14 ≥ 4:1 is requested. We were able to look at C-13 and background N-14 beam intensities to determine what the expected ratio might be during a C-14 run under various conditions. The C:N ratio measured for $^{13}C^{6+}$ at 13pnA was 1:1. The ratio improved at lower RF input, with a cost to beam current. Increased RF power resulted in unstable beam dropouts, however overall 6+ output increased, while C:N ratio worsened. Helium gas mixing also improved $^{13}C^{6+}$ current, but did not favor carbon over nitrogen.

Figure 2 shows the relationship of C:N ratio to beam intensity. C:N ratios ≥4:1 were seen at beam intensities >1000 pnA for $^{13}C^{3+}$ and 500 pnA for $^{13}C^{4+}$ at the ion source. Measurements were taken for best intensity with RF input ranging from 13 to 50 W. This information confirms the argument for stripping downstream of ECR3.

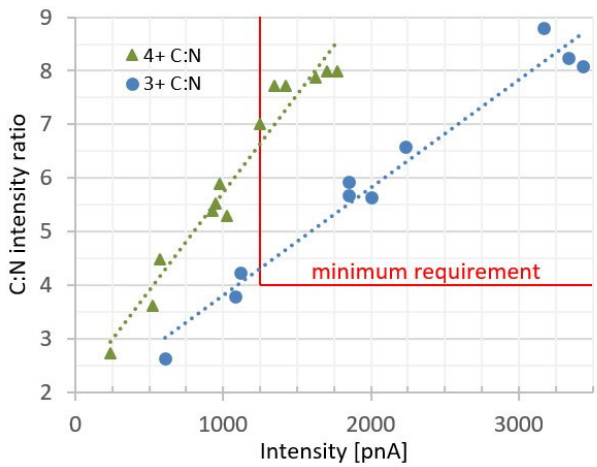

Figure 2: Ratio of C:N intensities vs. ^{13}C intensity at two different charge states (3+,4+).

One further consideration for C:N ratio is that less favorable stripping for carbon occurs than for nitrogen into the 6+ charge state. We calculate the fraction for carbon at 42.6% and nitrogen at 52.9%. This reduces C:N measured at the source by ~20% after stripping. Ratio data shown in Fig. 2 is corrected for this reduction

Ethylene gas pressure upstream of the leak valve had an effect on the C:N ratio as well. This should be noted as we intend to use a small amount of gas (25 ml at STP) that will slowly drop in pressure throughout an experiment. Figure 3 shows the beam current relationship to C:N ratio (corrected for C and N stripping efficiency differences) of $^{13}C^{4+}$ for line pressures of 0.3 atm and 2.2 atm as an example. Since the ECR charge distribution favors 3+ in the range of tested operation, we infer source intensity and C:N are also maintained for $^{13}C^{3+}$ even at low backing pressure.

ISBN: 978-3-95450-226-4 ISSN: 2222-5692 doi:10.18429/JACoW-ECRIS2020-WEZZO03

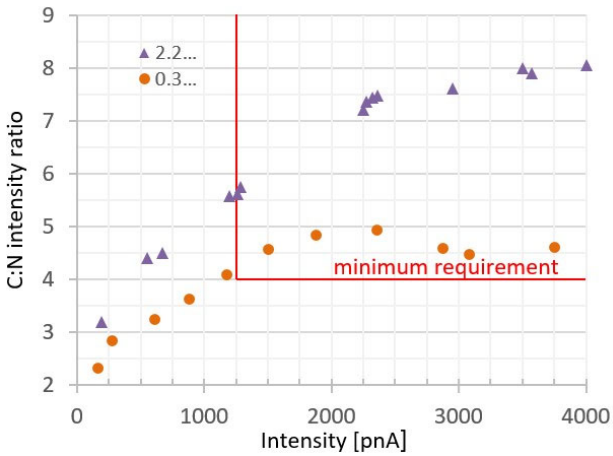

Figure 3: C:N ratio vs. $^{13}C^{4+}$ intensity with ethylene gas feed line before leak valve at 2.2 atm and 0.3 atm.

Carbon Consumption Rates

It is important to consider the consumption of C-14 on two bases. First is to limit the amount of radioactive contamination in the source, downstream beamline and exhaust. We also prefer to conserve the material as a cost savings to facility operation. A measured volume of 8.25 ml was filled with C-13 ethylene during the intensity and contamination tests. Pressure of the volume was measured before and after a test run using an Omega model DPG2001B digital pressure gauge. Ideal gas law was used to calculate number of moles at the start and end of a test run, which was then converted to mg of C-13. From there a consumption rate in mg/hour was derived.

Beam current improvements were obtained by adding ethylene gas, thereby increasing consumption rate and the C:N ratio making the three parameters interrelated. The minimum carbon consumption rate in which required $^{13}C^{3+}$ intensity and C:N ratio (corrected for stripping differences) are met is ~.04 mg/hr (see Fig. 4). This rate would yield ~30 days of continued experiment time for 25 ml of C-14 ethylene gas at STP.

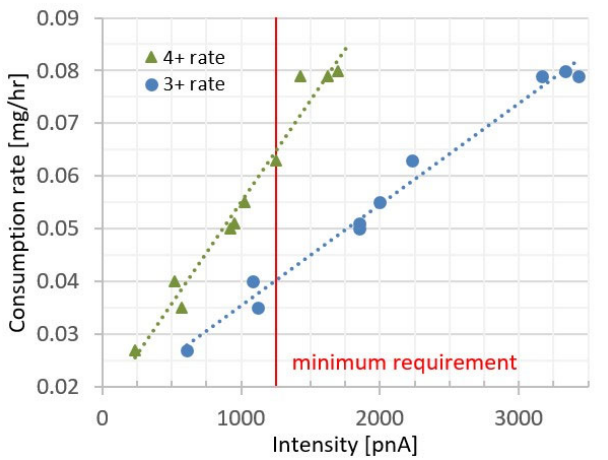

Figure 4: Consumption rate vs. intensity for C-13 3+ and 4+ with ethylene gas feed.

Ion Source Efficiency

Efficiency into a single charge state at the ion source was also examined during these test runs by dividing number of ions intercepting the m/q analysis faraday cup by the number of atoms introduced to the ECRIS over the same time period. For simplicity Table 3 shows the range of efficiencies seen over a variety of gas feed, RF power and frequency conditions used. Under any single condition, 3+ efficiency exceeded that of 4+.

Table 3: C-13 Charge State Efficiencies

q	Source Efficiency
3+	1.0% - 2.1%
4+	0.5% - 1.5%
5+	0.05% - 0.17%

CONCLUSION

An ECR ion source has been installed at the ANL ATLAS facility and will fulfill two needs: the returned production of C-14 after seven year hiatus, and added flexibility as a second ion source for the delivery of stable beams for the experimental program. The source has completed its commissioning phase and is in use at ATLAS. We plan to address the limitations involving the discharging lens with further investigation into root cause and by increasing the gap between electrode and ground. If the discharges are resolved, we can further examine production of $^{13}C^{6+}$ at the source. We are also looking at beam optics in the LEBT to see if transmission can be improved. Even with limitations to overall performance noted above, ECR3 has demonstrated the ability to produce stable C-14 ion beams at the energy, intensity and ratio of carbon to nitrogen required for approved experiments at ATLAS with 3+ out of the source stripped to 6+ downstream.

REFERENCES

[1] D. Z. Xie, "The BIE100 ECR ion source", *Rev. Sci. Inst.*, vol. 73, no. 2, pp. 531-533, Feb. 2002.

[2] D. Z. Xie, "A high efficiency electron cyclotron resonance ion source system for the production of radioactive ion beams," Rep. DOE00 SBIR Phase II Project (Grant No: DE-FG-99ER82750) Nov. 2002

[3] R. H. Scott, C. Dickerson, R. C. Pardo, and R. C. Vondrasek, "A New ECRIS Installation at the Argonne Tandem Linac Accelerator System", in *Proc. 22nd Int. Workshop on ECR Ion Sources (ECRIS'16)*, Busan, Korea, Aug.-Sep. 2016, pp. 105-107. doi:10.18429/JACoW-ECRIS2016-WEPP14

[4] https://www.vitrax.com

ISBN: 978-3-95450-226-4 ISSN: 2222-5692 doi:10.18429/JACoW-ECRIS2020-WEZZO04

IMPROVEMENT OF THE EFFICIENCY OF THE TRIUMF CHARGE STATE BOOSTER (CSB)

Joseph Adegun[1,2†], Friedhelm Ames[1], Oliver Kester[1,2]
[1]TRIUMF, Vancouver BC, Canada, [2]University of Victoria, Victoria, BC, Canada

Abstract

The Electron Cyclotron Resonance Ion Source (ECRIS) is a versatile and reliable ion source to charge-breed rare isotopes at the TRIUMF's Isotopes Separation and Acceleration (ISAC) facility. Significant research work has been done by different groups worldwide to improve the efficiency and performance of the ECRIS. The most recent result of these activities is the implementation of the two-frequency plasma heating. At the ISAC facility of TRIUMF, a 14.5 GHz PHOENIX booster which has been in operation since 2010 was recently upgraded to accommodate the two-frequency heating system using a single waveguide to improve its charge breeding efficiency. Besides, a program has been launched to improve and optimize the extraction of charge bred isotopes in terms of beam emittance. A detailed investigation of the effect of the two-frequency heating technique on the intensity, emittance, and the efficiency of the extracted beam is presently being conducted and the status will be presented.

INTRODUCTION

Different techniques and methods have been explored and employed to improve the performance and efficiency of the Electron Cyclotron Resonance Ion Source (ECRIS) since it was first developed. Examples are plasma-wall coating, biased disks, the increase of the magnetic field strength which allows increasing the RF-frequency, and operation of the ECRIS in two frequencies mode. The operation of the ECRIS with these techniques listed above has demonstrated increased performance of the ECRIS in view of the application as a charge state booster [1-4]. Investigations of the 1+ to n+ conversion processes in the community demonstrated that the efficiency of the process and quality of the highly charged ion beam produced by a Charge State Booster (CSB) can be significantly enhanced by optimizing the plasma conditions and the beam formation in the extraction region [5]. However, the 1+ to n+ conversion rate depends on the flexibility of the injection optics, the plasma conditions, and the beam formation upon ion extraction. TRIUMF embarks on further investigations of ECRIS performance as an ECRIS is used at TRIUMF to boost the charge state of rare isotopes before injection into the linear accelerator (LINAC) of ISAC for post-acceleration.

THE TRIUMF ECRIS CSB

The 14.5 GHz PHOENIX booster of TRIUMF from PANTECHNIK was originally designed as a conventional single-frequency-plasma-heating source. The booster is equipped with a three-electrode extraction system with an aperture radius of 3 mm and an extraction gap of 25 mm. This source has been installed and commissioned in 2010 [6]. The typical operating parameter of the source is listed in Table 1. To optimize the charge breeding results, the plasma chamber wall, the injection, and the extraction electrodes were coated/replaced in 2012 with aluminum/aluminum electrodes to reduce the intensity of the background ions that are introduced into the bulk plasma through plasma-wall interaction. As reported in [7], the intensity of some of the background ions was reduced by about 2 orders of magnitude with aluminum wall coating.

Table 1: Typical Operating Parameters of the TRIUMF CSB

Parameters	Values
Beam energy	11.27*Q keV
Binj	1.15 T
Bmin	0.35 T
Bext	0.87 T
Becr	0.52 T
Br	1.2 T
ECR frequency	14.5 GHz

The preliminary result obtained after the implementation of a two-frequency RF-system is a topic that will be addressed in this paper. A program to improve the beam quality of the CSB has been started. It comprises simulations of the injection and the extraction systems using the code IGUN©. Besides, the result of the magnetic field distribution of the booster that was modelled and simulated in OPERA in preparation for the extraction system simulation in IGUN© will be presented as well.

TWO FREQUENCY OPERATION

The TRIUMF charge state booster (CSB) was recently upgraded to implement the two-frequency heating technique using a single waveguide because the booster was not originally designed to accommodate the conventional two-waveguide approach. The layout of the new rf system upgrade is shown in Fig. 1. The output signals of the two rf signal generators (from BNC with model numbers 845 and 845-20) both with a frequency range of 9 kHz – 20 GHz and output power between -30 – 20 dBm are combined using a high-frequency microwave power combiner (from Mini-circuits with model number ZX10-2-183-S+) with a frequency range of 1.5 – 18 GHz. The combined microwave is fed to a newly installed travelling wave tube amplifier (TWTA) (from CPI with model number VZM6993J4) with a maximum output power of 400 W and a frequency range of 8 – 18 GHz. The amplified microwave

† jadegun@triumf.ca

ISBN: 978-3-95450-226-4 ISSN: 2222-5692 doi:10.18429/JACoW-ECRIS2020-WEZZO04

is fed into the booster through WR-65 waveguide with a frequency range of 12 – 18 GHz.

Before the two-frequency heating technique was implemented on the CSB, a bench test was conducted to ensure the two frequencies launched from the signal generators are fed into the plasma of the ECRIS. The frequencies of 13.65 GHz and 14.5 GHz were set on the signal generators, the launched microwaves were added using the power combiner, the output of the combiner was fed into the TWTA, and an attenuated sample from the TWTA was recorded on a low-power-high-frequency spectrum analyzer.

Figure 2 shows a picture of the spectrum analyzer screen showing the two distinct frequencies launched from the signal generators.

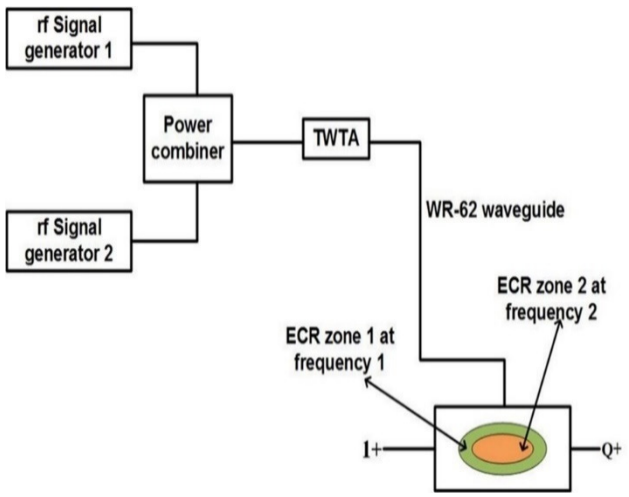

Figure 1: Layout of the TRIUMF two-frequency heating technique.

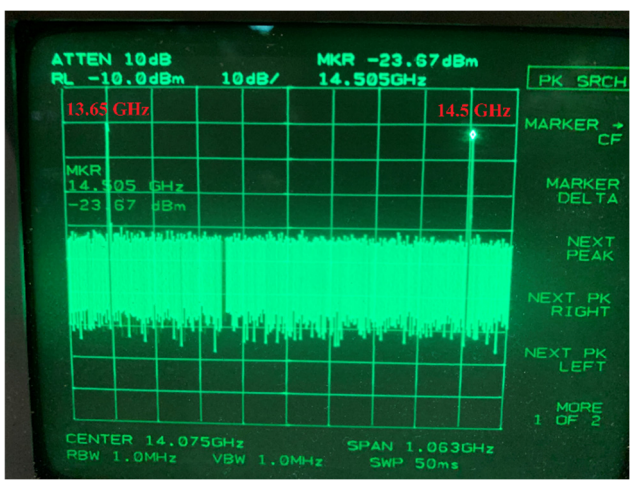

Figure 2: An image of a spectrum analyzer showing the combined microwaves of two frequencies 13.65 GHz and 14.5 GHz launched from the signal generators.

The effect of feeding microwaves with two frequencies into the plasma chamber was investigated by the influence on the extracted charge bred ion current.

INITIAL CHARGE BREEDING RESULT

A Cesium (Cs) test ion source (CTIS), located upstream of the booster for injection and extraction optics tuning, was used to inject a 1+ beam of Cs of about 11 nA into the booster. The booster and the extraction system were optimized for the extraction of Cs^{29+}. One of the rf signal generator's frequency was set to 13.65 GHz while the other signal generator was set to a frequency of 14.5 GHz. The TWTA output power was set to 150 W, the operating parameters listed in Table 1 were used and the Cs charge state distribution (CSD) was measured. The measured charge state distribution was compared with the charge state distribution recorded for the single frequency heating of the replaced rf system.

The replaced rf system comprises a signal generator and a CPI travelling wave tube amplifier (TWTA). The TWTA has a narrow frequency bandwidth between 13.75 – 14.5 GHz. However, because of the upper band of the TWTA's frequency coincides with the designed frequency of the booster, the TWTA was routinely operated at an rf frequency of 14.46 GHz to preserve the life of the TWTA. With the replaced rf system, a 1+ beam of Cs of about 9 nA was injected into the booster, the rf frequency was set to 14.46 GHz and rf power was set to 200 W, while the beam optics and the booster were tuned for the extraction of Cs^{27+}. The two distinct measurements were compared solely to test the newly installed two-frequency heating system as the booster was not well optimized for the operation of the two-frequency heating. The optimization of the booster for two-frequency heating is ongoing. Meanwhile, the Cs charge states could be detected up to 29+ with the two-frequency heating compared to the single frequency heating with Cs charge state up to 27+. More systematic measurements will follow soon.

MAGNETIC FIELD SIMULATIONS

The extraction system of the TRIUMF CSB is currently being investigated by the simulation to further improve the performance of the booster. The correct magnetic field at the extraction region of the booster is an integral part of the extraction system simulation of the ECRIS. It has been reported in [8] that the decreasing axial magnetic field at the extraction region is the dominant cause of an increased emittance of the extracted beam from the ECRIS.

The magnetic field of the TRIUMF CSB has been modelled and simulated in OPERA and benchmarked against the measured field of the GANIL SPIRAL1 booster [9] that is similar to TRIUMF ECRIS CSB. The magnetic field configuration of the booster is composed of three solenoid coils (injection, middle and extraction coils) and a hexapole permanent magnet. The booster is typically operated with the solenoid coil current of 1050 A, 250 A, and 750 A defined on the injection, middle, and extraction coils, respectively. The solenoid coils and the hexapole permanent magnet are encapsulated in an ARMCO soft iron case. There are also ARMCO soft iron plugs at the injection and the extraction regions of the booster to shield stray fields. Besides, two ARMCO soft iron rings are installed around

ISBN: 978-3-95450-226-4 ISSN: 2222-5692 doi:10.18429/JACoW-ECRIS2020-WEZZO04

the hexapole magnet at the center of the booster to properly define the ECR zone in the plasma chamber.

Figure 3 shows the OPERA 3D model of the CSB and Fig. 4 shows the axial magnetic field distributions for different relative permeability values. Figure 5 shows the axial magnetic field distribution of TRIUMF CSB compared with the GANIL SPIRAL1 CSB measured field. The simulated field matched the measured field. The simulated magnetic field of the TRIUMF CSB will be benchmarked against Hall probe measurement in the future.

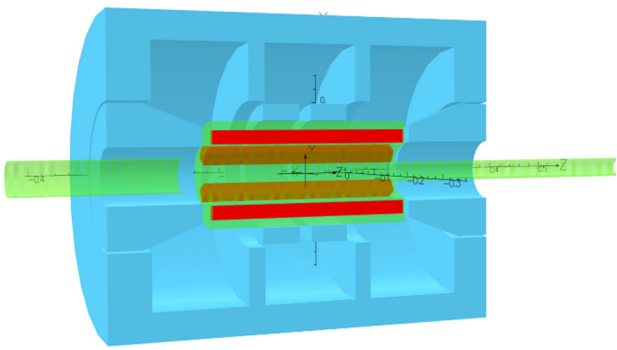

Figure 3: OPERA 3D model of the TRIUMF CSB.

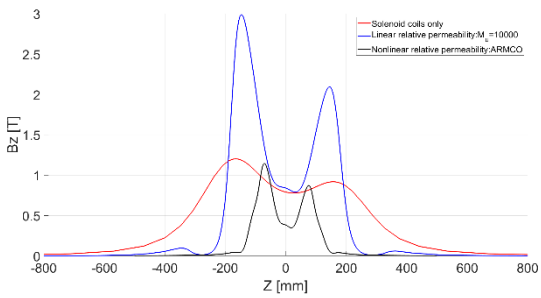

Figure 4: Axial magnetic field distribution of the TRIUMF CSB for different relative permeability values (the blue plot is the magnetic field with linear relative permeability, the black plot is the magnetic field with nonlinear relative permeability, and the red plot is the solenoid coils field only). Coil current (1050/250/750 A).

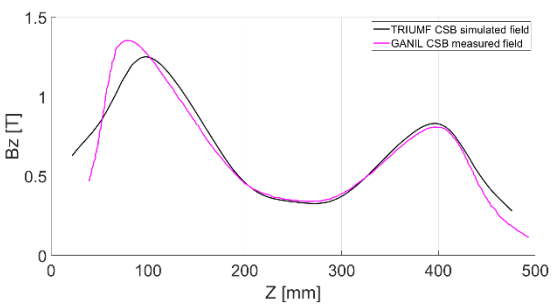

Figure 5: Axial magnetic field distribution of the TRIUMF CSB simulated in OPERA compared with the measured field of GANIL SPIRAL1 CSB. Coil current (1200/250/700 A).

EXTRACTION SYSTEM SIMULATIONS

The extraction system of the TRIUMF ECRIS CSB is being simulated with the code IGUN© to systematically investigate the effect of extraction parameters such as magnetic field, extraction voltage, extraction aperture, and extraction gap on the emittance of the extracted ions to further improve the performance of the booster.

The first simulations used the intrinsic routine of IGUN© to calculate solenoid fields, meanwhile, the calculation does not include the iron yoke or the permanent magnets. Besides, a magnetic field distribution on-axis can be calculated by a different code like OPERA and then import in to the IGUN© code for extraction system simulation. To compare the effect of the magnetic field in the extraction region of the CSB, simulations have been performed with the IGUN-calculated magnetic field and the OPERA-calculated magnetic field. The field distribution for both cases is shown in Fig. 6. It can be seen that with the OPERA-calculated field, the peak of the magnetic field at the injection, middle and extraction is narrow and well-defined while magnetic field distribution calculated with IGUN is broad. This is because the magnetic materials around the solenoid coils are defined and included in the OPERA simulation but not in the IGUN simulation.

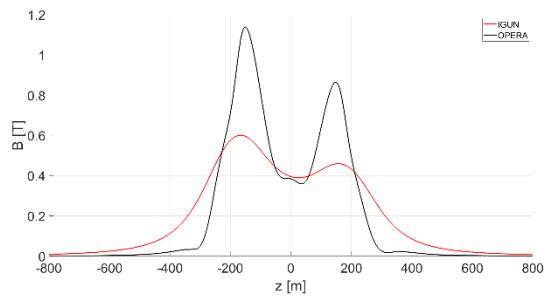

Figure 6: The IGUN-calculated field compared with the OPERA-simulated field. Coil current (1050/250/750 A).

The parameters of the simulated beam in IGUN© code are $^{16}O^{5+}$ with a beam energy of 11.27*Q keV, electron plasma temperature, Te=5 eV, and ion temperature, Ti=0.2 eV. The currents of the solenoid coils are as defined above. The results of the simulation show that the trajectories of the ions simulated with the only solenoid field calculated by the IGUN have less divergent angle compared with the trajectories of the ions simulated with the OPERA-calculated field as shown in Fig. 7. The ions simulated with the OPERA-calculated field have high divergence because of the reduced magnetic field at the end of the extraction system compared with the case of the IGUN-calculated field. The reduced field strength imposes a weaker focusing on the extracted beam resulting in larger beam size. This reduced field strength is caused by the ARMCO soft iron case around the solenoid coils that shield the stray fields.

As the effect of the magnetic field on the beam quality is understood and we have a realistic magnetic field distribution available from OPERA, a systematic parameter scan of voltages using IGUN© can be performed.

ISBN: 978-3-95450-226-4 ISSN: 2222-5692 doi:10.18429/JACoW-ECRIS2020-WEZZO04

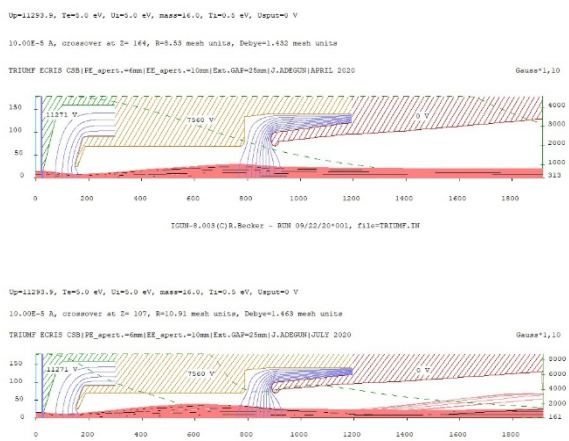

Figure 7: The extraction system of the TRIUMF CSB. The green dash line is the magnetic field. (Top picture is the extraction system simulation with IGUN-calculated field while the bottom picture is the extraction system simulation with OPERA-calculated field).

CONCLUSION AND OUTLOOK

The two-frequency heating system has been implemented at the TRIUMF CSB and the first beam test with two-frequency heating could be performed. The initial result obtained from the source with this operation suggests that the two-frequency heating has a significant effect on the plasma heating and therewith on the charge breeding performance of the booster. Also, a systematic investigation of extraction property using simulations has been started. Therefore, the magnetic field distribution of the CSB has been modelled and simulated in OPERA in preparation for the systematic parameter scans with the extraction system simulation to further improve the beam emittance of the TRIUMF CSB. The magnetic field distribution simulated has been benchmarked against the measured field of the GANIL SPIRAL1 charge state booster, and the simulated field matched the measured field very well.

ACKNOWLEDGEMENT

The project is funded by the Natural Sciences and Engineering Research Council of Canada (NSERC), TRIUMF, and the University of Victoria, BC.

REFERENCES

[1] R. Vondrasek *et al.*, "ECRIS operation with multiple frequencies," in *AIP Conference Proceedings*, 2005, vol. 749, pp. 31–34.

[2] S. C. Jeong et al., "KEKCB-18 GHz ECR charge breeder at TRIAC," *Nucl. Instrum. Methods Phys. Res. Sect. B Beam Interact. with Mater. Atoms*, vol. 266, no. 19–20, pp. 4411–4414, 2008.

[3] Z. Q. Xie, "State of the art of ECR ion sources," *Proc. IEEE Part. Accel. Conf.*, vol. 3, 1998.

[4] A. G. Drentje, A. Kitagawa, T. Uchida, R. Rácz, and S. Biri, "Experiments with biased side electrodes in electron cyclotron resonance ion sources," *Rev. Sci. Instrum.,* 2014, vol. 85, no. 2.

[5] R. Vondrasek, A. Levand, R. Pardo, G. Savard, and R. Scott, "Charge breeding results and future prospects with electron cyclotron resonance ion source and electron beam ion source (invited)," *Rev. Sci. Instrum*., vol. 83, no. 2, 2012.

[6] F. Ames, R. A. Baartman, P. G. Bricault, K. Jayamanna, and T. Lamy, "Commissioning of the ECRIS Charge State Breeder at TRIUMF", in *Proc. 19th Int. Workshop on ECR Ion Sources (ECRIS'10)*, Grenoble, France, Aug. 2010, paper WECOBK01, pp. 178-180.

[7] F. Ames, R. A. Baartman, P. G. Bricault, K. Jayamanna, and A. Mjøs, "Operation of an ECRIS Charge State Breeder at TRIUMF", in *Proc. 20th Int. Workshop on ECR Ion Sources (ECRIS'12)*, Sydney, Australia, Sep. 2012, paper THYO01, pp. 163-166.

[8] M. A. Leitner, D. C. Wutte, and C. M. Lyneis, "Design of the extraction system of the superconducting ECR ion source VENUS," in *Proceedings of the IEEE Particle Accelerator Conference,* 2001, vol. 1, pp. 67–69.

[9] A. Annaluru, "Beam optics transport and fundamental processes involving a charge breeder in the upgraded SPIRAL 1 facility," University of Caen Normandy, 2019.

ISBN: 978-3-95450-226-4 ISSN: 2222-5692 doi:10.18429/JACoW-ECRIS2020-WEZZO10

ELECTRON CYCLOTRON EMISSION IMAGING OF ELECTRON CYCLOTRON RESONANCE ION SOURCE PLASMAS*

L.E. Henderson†, H.L. Clark, C.A. Gagliardi, D.P. May
Texas A&M University, Cyclotron Institute, College Station, TX, USA

Abstract

A new imaging system for electron cyclotron resonance ion sources (ECRIS) has been designed and is being built. This K- and Ka-band camera will extract localized measurements of absolute energy and relative number density for ECRIS plasma electrons by imaging their electron cyclotron emission (ECE) spectra, as the frequency, shape, and strength of the ECE harmonics correlate directly with the local magnetic field, electron energy, and plasma density. The design of the overall quasi-optical system will be presented, including novel ceramic optics for the radial viewports of the Cyclotron Institute's ECRIS and metamaterial mirrors with electronically controllable reflectivity. Spatial resolution sufficient to distinguish important plasma regions and temporal resolution sufficient to study dynamic plasma processes is expected.

INTRODUCTION AND MOTIVATION

A non-disruptive, high spatial resolution, general-purpose diagnostic tool that can measure the energy distribution of the magnetically confined plasma electrons in electron cyclotron resonance ion sources (ECRIS) would be highly useful for investigating and monitoring ECR plasmas. Many plasma diagnostics exist, but extracting electron population parameters from current diagnostics generally relies upon making assumptions about certain correlations between different plasma regions or certain interactions in the electron and ion populations. Direct diagnostics such as Langmuir probes are also not necessarily practical for use in an ECRIS while generating beams for particle accelerators. It would greatly assist routine particle accelerator operations and ECRIS modeling efforts if the ECRIS electron energy distribution was known during routine use, especially given that the myriad of parameters contributing to practical ECRIS plasmas are generally not known to sufficient accuracy a priori.

As some ECRIS plasma electrons are known to be both in cyclotron motion and mildly relativistic, we can expect those plasma electrons to exhibit electron cyclotron emission (ECE). Furthermore, if we assume the electrons in a particular region of the plasma interact sufficiently to produce local Maxwellian populations, the shape of the ECE spectrum from that region will correlate directly and distinctly to an electron temperature in that region [1]. Measuring such a spectra in an ECRIS is complicated, however, by the wide spread of cyclotron frequencies in the min-B magnetic field configuration. ECE spectra observed from ECRIS by simple line-of-sight measurements overlap into a nearly continuous spectrum [2].

The split hexapole design of the conventional 6.4 GHz ECRIS at the Cyclotron Institute allows for radial access ports, which in turn have enabled a novel solution to the problem of studying the ECE of ECRIS plasmas. This paper will discuss an imaging system design capable of simultaneously capturing the ECE spectra from various regions of the plasma.

CAMERA DESIGN

The ECE harmonics expected for the 6.4 GHz ECRIS primarily fall into the K/Ka-band. In order to spatially resolve the origin of ECE signals in the plasma, a novel K/Ka-band microwave imaging system has been designed that consists of ceramic optics, metamaterial quasi-optical elements, and superheterodyne receiver electronics.

The primary optics will be placed under vacuum inside an access pipe for the radial plasma chamber port. These optics will transport the ECE signal from the plasma chamber to an exit vacuum window, where the signal can be routed by secondary optics through air to the data capture tower located beyond the ECRIS x-ray shielding and safety fence (Fig. 1).

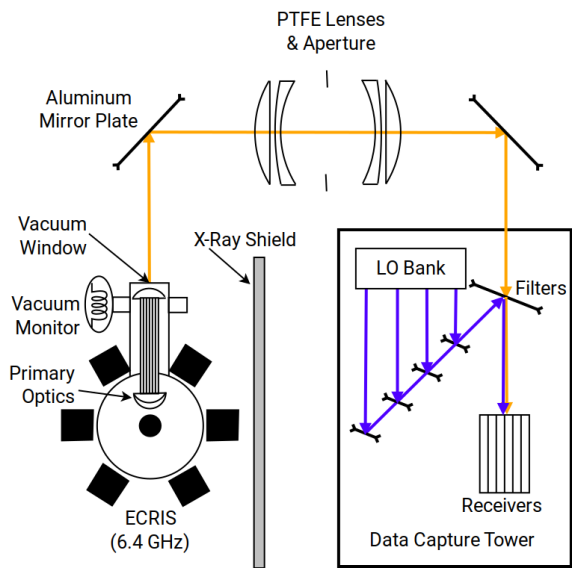

Figure 1: Camera layout (not to scale).

* Work supported in part by the Cyclotron Institute and by the U.S. Department of Energy, Office of Nuclear Science, under Grant No. DE-FG02-93ER40773.
† ethan.henderson@tamu.edu

ISBN: 978-3-95450-226-4 ISSN: 2222-5692 doi:10.18429/JACoW-ECRIS2020-WEZZO10

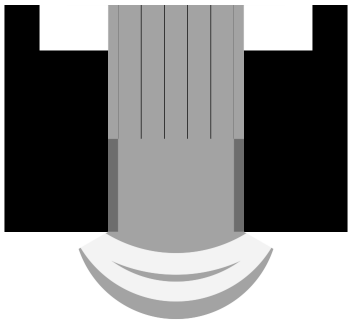

Figure 2: Dielectric structure of the primary optic inside the radial port.

Primary Optics

The main optic (Fig. 2) is a cemented stack of alumina and PTFE lenses that protrudes from the radial plasma chamber port approximately 1/2". The space occupied by this cemented lens is well removed from the plasma flutes and the ECR heating shell, and care has been taken to minimize RF heating. The cemented lens focuses ECE from the central plane of the plasma into the entrance of a 5x5 array of alumina-filled, 0.125" square waveguides. The exit face of the waveguide array will be bonded to an exit lens sitting below the vacuum window which allows for the ECE image to be transmitted into air outside the ECRIS.

Alumina and PTFE were chosen as optical materials due to their flat dispersion curves and low loss tangents across the K/Ka-bands. Alumina's high index of refraction (n = 3.1) also allows for a particularly important trick: diffraction in the 3/4" radial ports would normally destroy any usable image at our frequencies of interest, but once the port is filled with alumina diffraction can be made negligible. PTFE increases the performance of the primary optic by suppressing total internal reflections (increasing the numerical aperture) and diminishing Fresnel reflection. A microwave-absorbing lining is also employed to reduce unwanted stray reflections and cavity modes inside the radial port.

The initial design of the primary optical stack was improved iteratively through ray-tracing with the BEAM4 open-source software package [3] and finite-difference-time-domain (FDTD) simulations of Maxwell's equations with the MEEP open-source software package [4]. The finalized design simulations show good separation of ECE signals from different plasma regions into corresponding waveguides (Fig. 3). The resolution of the optics is Rayleigh-limited at the low end of their operating frequency range (approx. 17 GHz).

Signal Preparation

The ECE signal beam will be passed through a quasi-optical beamsplitter arrangement (Fig. 4) of electronically variable reflective surfaces (EVRS), which are metamaterial mirrors designed for this project and formed by an array of resonators interconnected with resistive silver ink traces and PIN diodes (Fig. 5). The purpose of the PIN diodes is to provide a resonance-clamping AC impedance to the EVRS cell when the array is biased by the proper DC current. Simulations of EVRS supercells in MEEP have shown this clamping behavior for electromagnetic waves at oblique incidences (Fig. 6) and have also shown the EVRS are largely transparent across all other frequencies in the K/Ka-band. A set of EVRS with different resonant frequencies can therefore be stacked to create a broadband mirror with electronically selectable frequency transmission notches.

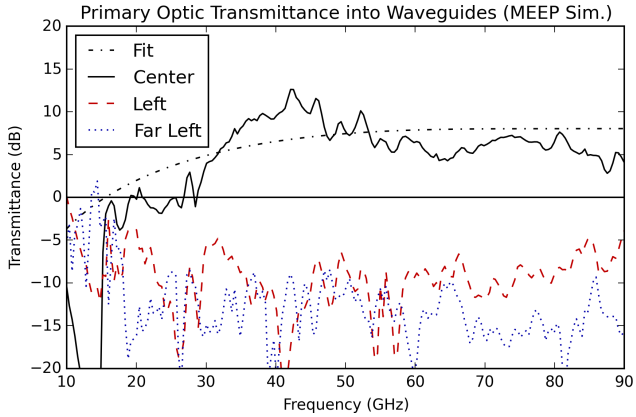

Figure 3: Simulated transmittance of an electromagnetic point source at the center of the plasma chamber into the waveguide array.

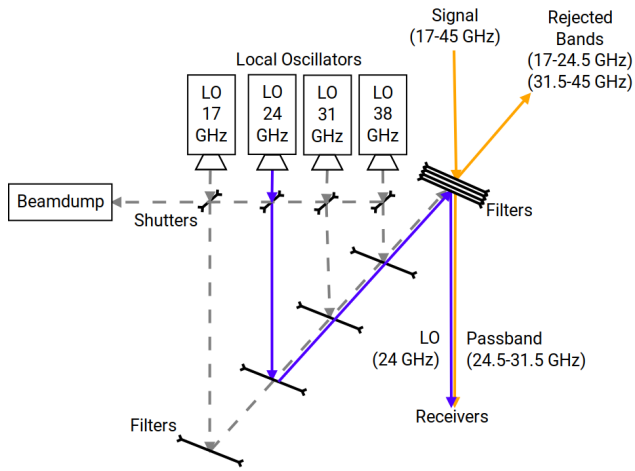

Figure 4: Quasi-optical signal bandpassing scheme.

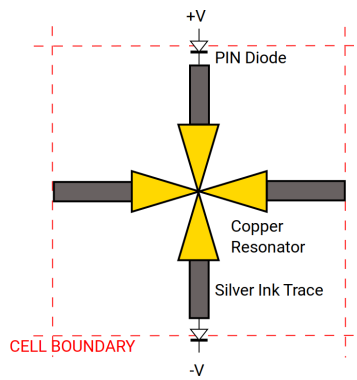

Figure 5: EVRS cell conceptual diagram.

ISBN: 978-3-95450-226-4 ISSN: 2222-5692 doi:10.18429/JACoW-ECRIS2020-WEZZO10

The EVRS beamsplitter stack greatly simplifies bandpassing the signal, and back-illumination of the beamsplitter stack (Fig. 4) also allows for a known local oscillator (LO) frequency to be overlaid onto the passband signal beam. As soon as the combined beam of passband signal and LO is received by a broadband antenna, it can be immediately passed into a mixer diode for frequency down-conversion.

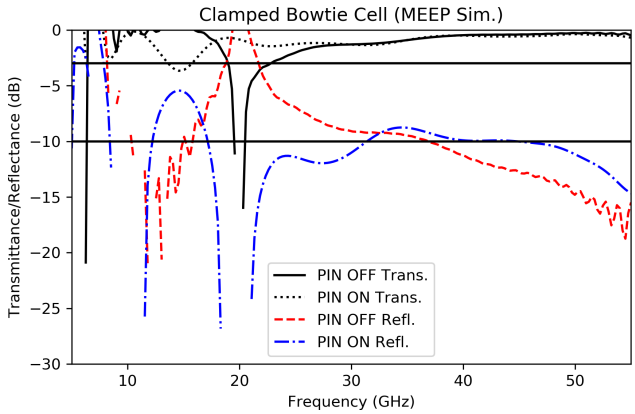

Figure 6: Simulated response to oblique electromagnetic waves by EVRS with lattice parameter a=5.5 mm.

Receiver Electronics

A 5x5 array of broadband antennas will immediately shunt the optically-processed signal into mixer diodes. This will convert the K/Ka-band 17-45 GHz signal into a 0-8 GHz signal that can be easily handled by conventional microstrip electronics. In order to eliminate the rolling shutter effect, the mixers will feed into 25 independent superheterodyne receiver circuits that step down the signal frequency further until it can be digitized by integrated 12-bit, 250 MS/s analog-to-digital (ADC) converters. Finally, in order to maximize the frame rate, the ADC samples will be transmitted to the data capture computers (DAQ) by 25 independent USB 3.1 connections. The maximum data rate for the imaging system is expected to be 100 Gbit/s.

The imaging system will have several operating modes for arbitrary frame rates and partial spectral coverages. The EVRS power supply switching, voltage monitors, and superheterodyne receiver controls will all be tied to a handful of microcontrollers so that the operation of the entire system can be monitored and reconfigured by the DAQ over USB.

COMPONENT DEVELOPMENT

An anechoic chamber with turntables is being assembled for testing the frequency response of each optical component at various angles of incidence. The device-under-test (DUT) and receiver microwave horn will have independent angular positioning, and a 12.4 GHz network analyzer equipped with step-up and step-down mixers will sweep through the entire design band of 17-45 GHz to log the S_{21} scattering parameter for the DUT. This will generate a frequency response curve for every optical component and implicitly create a calibration curve for the final system assembly.

3D-printed PLA optical mounting hardware was developed while access to the lab was limited during the Spring of 2020. The use of entirely plastic frames for mounting most optical elements will greatly reduce paraxial reflections that can otherwise cause significant self-interference in the microwave signal.

INITIAL PLANNED MEASUREMENTS

Once the full imaging system has been assembled, the first measurement that will be attempted is a comparison of the relative electron temperature in the ECR plasma core and in the ECR heating shell during steady-state ECRIS operation. If that proves successful, high frame rate observations of the ignition and afterglow processes will be made.

REFERENCES

[1] G. Bekefi, *Radiation Processes in Plasmas*. New York, NY: John Wiley and Sons, Inc., 1966.

[2] R. Geller, *Electron Cyclotron Resonance Ion Sources and ECR Plasmas*, Bristol, UK: CRC Press, 1996.

[3] Stellar Software, *Beam Four*. Berkeley, CA: Stellar Software, 2015. https://www.stellarsoftware.com/

[4] A. Oskooi, D. Roundy, M. Ibanescu, P. Bermel, J.D. Joannopoulos, and S.G. Johnson, "MEEP: A flexible free-software package for electromagnetic simulations by the FDTD method," *Comput. Phys. Commun.*, vol. 181, pp. 687-702, 2010. doi:10.1016/j.cpc.2009.11.008

ISBN: 978-3-95450-226-4 ISSN: 2222-5692 doi:10.18429/JACoW-ECRIS2020-NACB01

DEVELOPMENT OF A COMPACT LINEAR ZAO NEG PUMPING SYSTEM*

S. Kondrashev†, E. Beebe, B. Coe, J. Ritter, T. Rodowicz, R. Schoepfer, S. Trabocchi,
Brookhaven National Laboratory, Upton, USA

Abstract

An upgrade of RHIC EBIS, the extended EBIS, is presently under development at Brookhaven National Laboratory to increase the intensity of the Au^{32+} ion beams by 40%–50% to $2.1 \cdot 10^9$ Au^{32+} ions/pulse at the booster ring entrance. Generation of intense beams of polarized $^3He^{2+}$ ions with up to $\sim 5 \cdot 10^{11}$ ions/pulse for the RHIC and the future electron–ion collider is a goal of the EBIS upgrade project as well. Ultra-high vacuum is extremely important for stable and reliable operation of EBIS/T devices. We have developed a linear pumping module based on the ZAO NEG unit commercially available from SAES Getters. This pumping system will be used for the Extended EBIS Upgrade which is presently under development at BNL. The new ZAO NEG material has a higher pumping speed and, more importantly, significantly higher sorption capacity for all active gasses compared to previously available types of getters. A ZAO NEG module has been modified to be heated up to 600 °C by passing up to 120 A of DC current through a stainless-steel cage for required NEG activation and reactivation temperature cycles. A method of pumping speed measurements using pulsed gas injection into the vacuum chamber has been developed and used for characterization of the ZAO NEG-based linear pumping system. The results of tests and design of the new ZAO NEG-based linear pumping system are presented and discussed.

DEVELOMENT OF A COMPACT LINEAR ZAO NEG MODULE

New so-called ZAO (Zr-V-Ti-Al) NEG material became commercially available from SAES Getters several years ago. According to SAES Getters, ZAO NEG has multiple advantages compared to previously used getters:

- Larger sorption capacity for all active gases
- Higher pumping speed for all active gases
- Ability to withstand more reactivation cycles
- More robust and has higher embrittlement limit
- Generates fewer micro particles.

The larger sorption capacity of the ZAO NEG is the most important advantage for EBIS applications. ZAO NEG can pump all active gases (especially hydrogen, which is the dominant species in ultra-high vacuum systems) for a year or longer even at a vacuum level of about 10^{-8} Torr without a significant decrease in pumping speed. Commercially available from SAES Getters, a linear ZAO NEG pumping unit with 470x28x8 mm^3 dimensions is shown in Fig. 1.

Figure 1: Photo of linear ZAO NEG pumping unit.

Fifty-four ZAO NEG discs are contained inside 316L stainless steel cage providing 500 l/s pumping speed for hydrogen. The pumping module can be activated by raising the temperature either to 500 ºC for 1 hour or to 450 ºC for more than 24 hours. In the latter case it can be done during high temperature bake-out of the vacuum chamber containing the ZAO NEG pumping module. From operational point of view and previous negative experience with high temperature bake-out (gate valves damage etc.) we strongly prefer ZAO NEG activation at 500 ºC temperature for 1 hour using heating of just pumping module and not the whole vacuum chamber for long period of time.

Activation of Linear ZAO NEG Pumping Unit by DC Current

To keep the ZAO NEG pump as compact as possible we decided to activate pumping module by passing DC current through the stainless-steel cage. The first heating test was done using the cage without ZAO NEG discs inside to prove that cage can transmit the current required to reach 500 ºC over the entire cage length without any damage. The cage has been mounted on high current vacuum feedthroughs with four thermocouples attached along the entire cage length in Fig. 2 (a). Dependence of electric power on transmitted current and dependences of temperatures along the cage on electric power are presented in Figs. 2 (b, c).

One can see that 550 W (85 A/6.5 V) electric power is required to reach temperatures in the range of 500 - 600 ºC along the cage. There was no damage to the cage under these conditions.

The second heating test was done using a pumping module containing ZAO NEG discs. A photo of the pumping module heated to 600 ºC in the middle of the cage inside of the vacuum chamber is presented in Fig. 3.

Pumping Speed Measurements

Schematic of experimental setup for pumping speed measurements is shown in Fig. 4.

A pulsed gas injection system has been assembled to allow injection of a small amount of gas of interest into the main vacuum chamber. It consists of a small buffer chamber with a volume of about 0.5 l, a needle valve, an electromagnetic pulse valve, and a turbomolecular pump (TMP)-based pumping station.

* Work supported by the US Department of Energy under contract number DE-SC0012704 and by the National Aeronautics and Space Administration.
† skondrashev@bnl.gov

ISBN: 978-3-95450-226-4 ISSN: 2222-5692 doi:10.18429/JACoW-ECRIS2020-NACB01

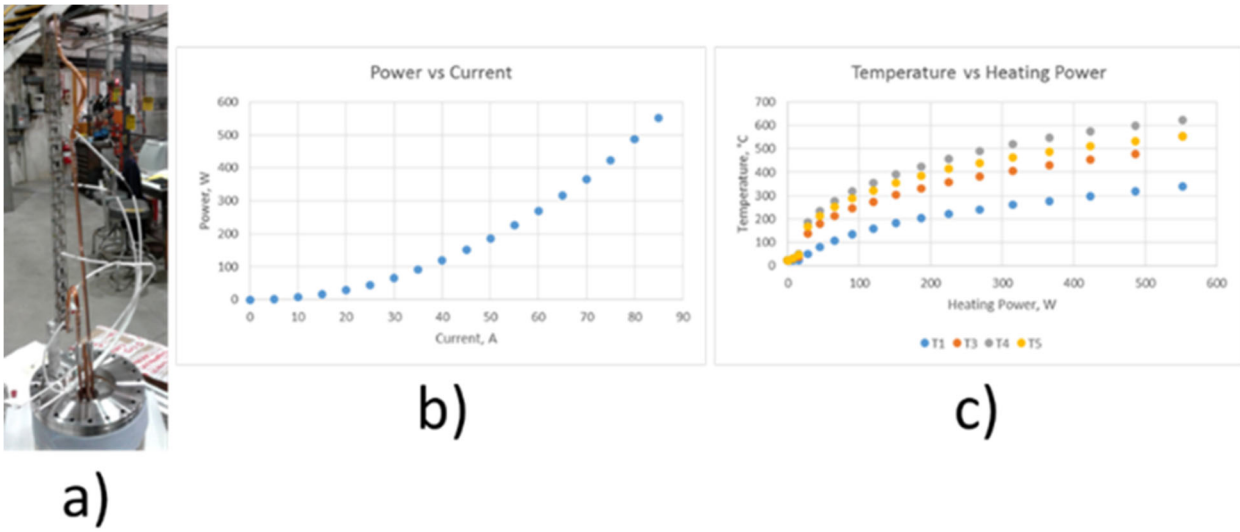

Figure 2 (a, b, c): Cage heating without NEG discs inside: a – cage mounted at high current vacuum feedthroughs with four thermocouples attached, b – dependence of electric power on transmitted current, c – dependences of temperatures along cage on electric power (blue dots – cage end, red dots – ¼ cage length, grey dots – ½ cage length, yellow dots – ¾ cage length).

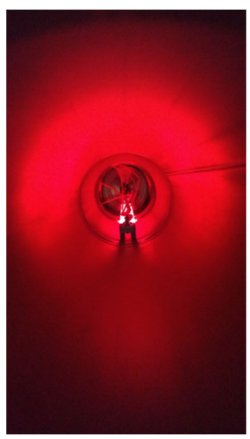

Figure 3: Pumping unit heated to 600 ºC in the middle of the cage.

At first, all gas lines were pumped by the TMP pumping station to about 10^{-3} Torr residual gas pressure. After that, the buffer chamber was filled by a gas of interest up to a pressure of about 100 Torr. The pulse duration of the electromagnetic valve controller was adjusted to drive the pressure in the main vacuum chamber up by about two orders of magnitude (typically from $2\text{-}5\cdot10^{-8}$ Torr up to $2\text{-}5\cdot10^{-6}$ Torr). In such a way, a wide enough dynamic range for measurements has been provided and the gas load on the pumps has been minimized.

The main vacuum chamber was pumped by the ZAO NEG pumping module and the TMP backed by a TMP pumping station to avoid pressure limits caused by low compression ratios of TMP for hydrogen and helium. An all-metal gate valve at the TMP input allowed to pump chamber either by TMP and ZAO NEG module when the valve was open or by only the ZAO NEG module when the valve was closed. The volume of the vacuum chamber was

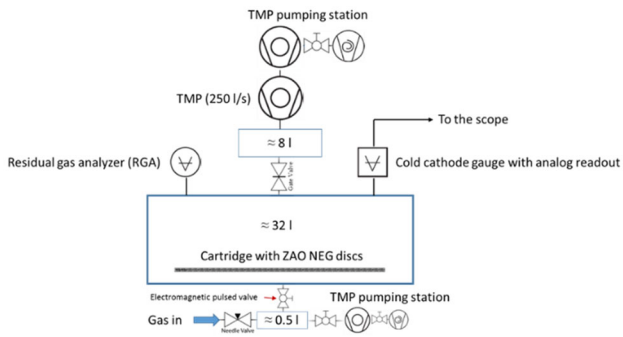

Figure 4: Schematic of experimental setup for pumping speed measurements.

equal to 40 l and 32 l respectively in these cases. An SRS RGA200 residual gas analyser and an MKS 421 cold cathode ion gauge with analog readout were attached to the vacuum chamber to record pressure time dynamics.

If some amount of gas is injected into vacuum chamber, the pressure inside the chamber will raise and then after the end of injection pulse will decrease exponentially (in molecular flow regime) according to following equation:

$$P(t) = P(t=0) \cdot e^{-\frac{S}{V} \cdot t} \quad (1)$$

where *P(t)* is pressure at the detector location (RGA or cold cathode (CC) gauge in our case) at time *t*, *t = 0* is time right after the end of the injection pulse, *S* is pumping speed at the detector location, and *V* is the volume of vacuum chamber.

Time dynamics of hydrogen pressure recorded by the RGA when the chamber was pumped by the ZAO NEG module only (TMP gate valve closed) is presented in Fig. 5 (a, b, c, d) both in linear and logarithmic scale.

ISBN: 978-3-95450-226-4 ISSN: 2222-5692 doi:10.18429/JACoW-ECRIS2020-NACB01

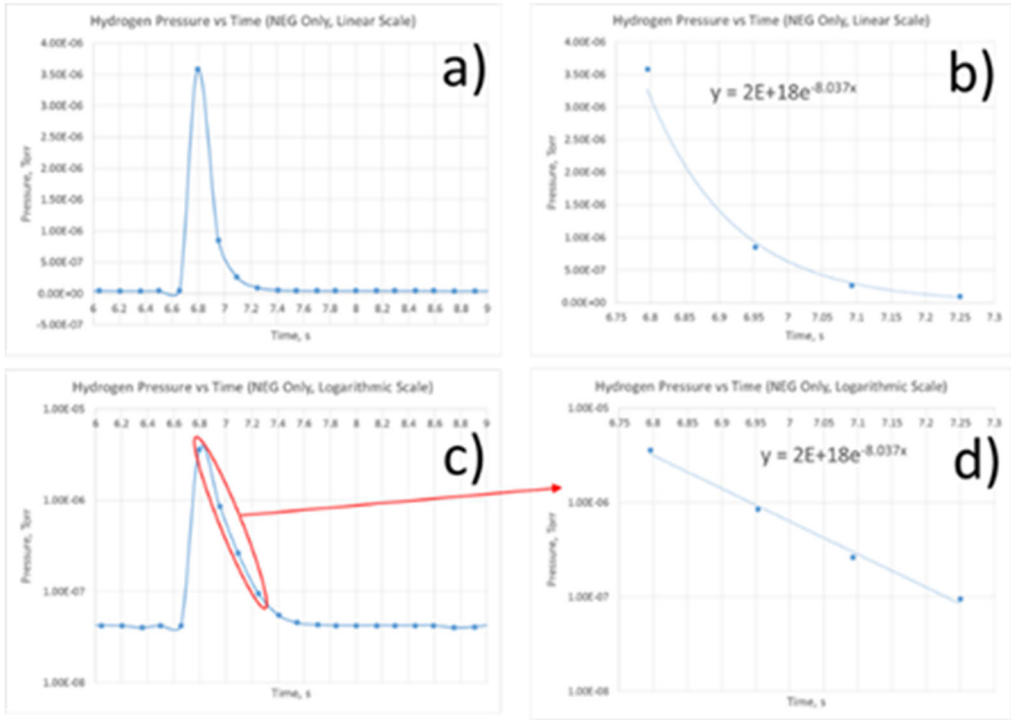

Figure 5 (a, b, c, d): Time dynamics of hydrogen pressure recorded by RGA when chamber was pumped by ZAO NEG module only (a – full pulse (linear scale), b – pressure decay part of pulse (linear scale), c - full pulse (logarithmic scale), d - pressure decay part of pulse (logarithmic scale)).

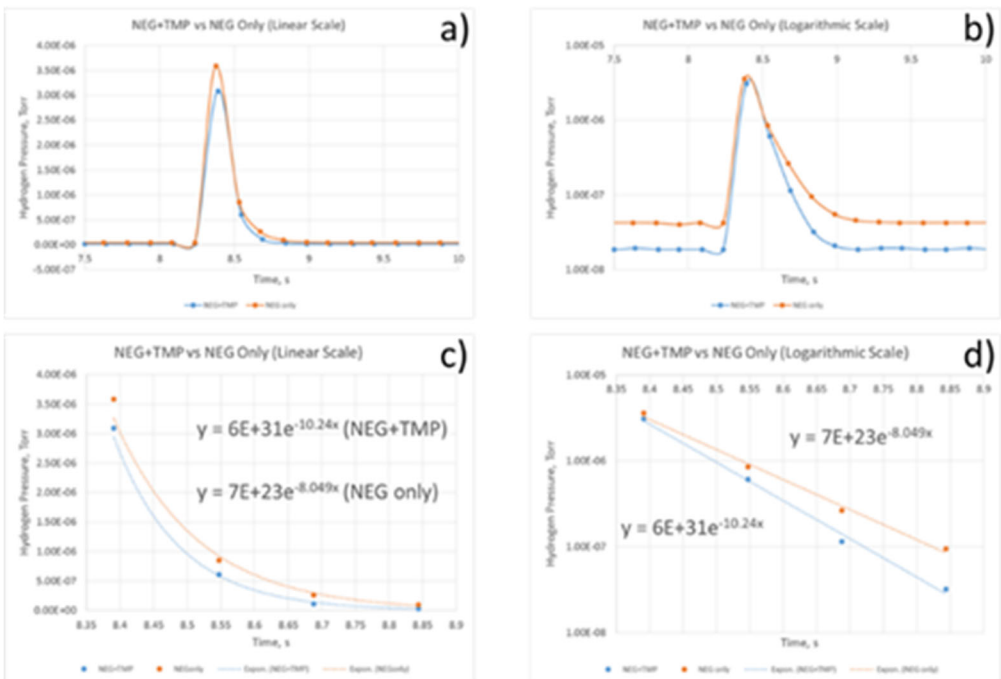

Figure 6 (a, b, c, d): Time dynamics of hydrogen pressure recorded by RGA when chamber was pumped by ZAO NEG module only (red dots and lines) and by ZAO NEG module together with TMP (blue dots and lines) (a – full pulse (linear scale), b – full pulse (logarithmic scale), c - pressure decay part of pulse (linear scale), d - pressure decay part of pulse (logarithmic scale)). Lines on lower plots are exponential fittings.

ISBN: 978-3-95450-226-4 ISSN: 2222-5692 doi:10.18429/JACoW-ECRIS2020-NACB01

RGA has been used at highest for this model recording rate (8 points/s) for all measurements described in this paper. Even in this case only 4 points were recorded for the pressure decay part of the pulse in Fig. 5 (b, d) because pressure decay time is quite short and just slightly exceeds 0.5 s. The purity of hydrogen gas injection was confirmed by recording RGA traces of atoms and molecules with other masses during injection pulse. The number of other atoms and molecules didn't exceed 1% compared to that of the injected hydrogen.

As one can see from Fig. 5, measured pressure decay is exponential with very high accuracy. The pumping speed of ZAO NEG module for hydrogen was found to be 257 l/s in this measurement since the vacuum chamber volume was equal to 32 litters. One should mention that pumping speed is measured at the RGA location and it is lower than the pumping speed inside the vacuum chamber because of limited vacuum conductance from the chamber to the RGA.

Comparison of pumping speed for hydrogen in case of pumping by both NEG module and TMP (TMP gate valve is opened) with pumping by NEG module only (TMP gate valve is closed) is illustrated in Fig. 6 (a, b, c, d).

Measured pumping speeds with hydrogen are 410 l/s for both NEG module and TMP, and 258 l/s for NEG module only. Average measured pumping speed for hydrogen is 259 l/s if chamber is pumped by NEG module only and 396 l/s if pumped by both NEG module and TMP. Statistical fluctuations of measured pumping speed are less than 6%.

Pumping speed has been measured for nitrogen as well. Average measured pumping speed for nitrogen is 87 l/s if the chamber is pumped by the NEG module only and 232 l/s if pumped by both the NEG module and TMP. Statistical fluctuations of measured pumping speed are less than 15%. The ratio of measured pumping speeds of NEG module for hydrogen (259 l/s) and nitrogen (87l/s) is in good agreement with the ratio of about factor three specified by SAES Getters.

Influence of Vacuum Conductance

The measured pumping speed for hydrogen (260 l/s) is significantly lower than pumping speed for hydrogen specified by SAES Getters (500 l/s). As was already mentioned above, pumping speed is measured at the RGA location which has limited vacuum conductance to the chamber where the NEG module is located. For this reason, pumping speed inside of the vacuum chamber can be significantly higher than measured pumping speed at a different location.

Pumping speed at the RGA location can be derived from following expression:

$$\frac{1}{S(RGA)} = \frac{1}{S(Ch)} + \frac{1}{C} \qquad (2)$$

where *S(RGA)* and *S(Ch)* are pumping speed at the RGA and at the NEG module locations, and *C* is vacuum conductance between the RGA and NEG module locations.

The RGA has been mounted on a pipe with a diameter of 31 mm and a length of 170 mm which is connected to the large vacuum chamber where the NEG module is located. Vacuum conductance of this pipe for hydrogen can be estimated to be about 374 l/s. There is always some uncertainty in the vacuum conductance value because real geometry is complex and should be somehow simplified for estimations. The dependence of the NEG module pumping speed inside the vacuum chamber on vacuum conductance between the RGA and NEG module locations is presented in Fig. 7 (using equation (2) and measured pumping speed of 259 l/s for hydrogen at the RGA location).

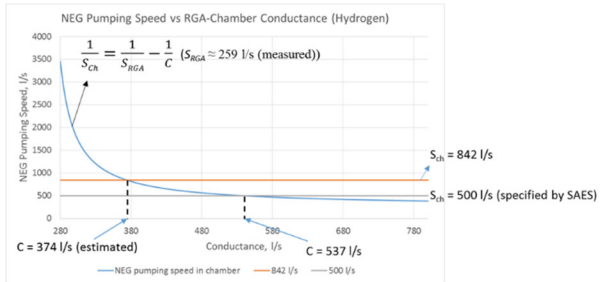

Figure 7: Dependence of NEG module pumping speed inside vacuum chamber on vacuum conductance between RGA and NEG module locations.

As one can see, any error in vacuum conductance estimation give significant uncertainty in re-calculated pumping speed. The main conclusion from this consideration is that pumping speed of the NEG module for hydrogen inside of the vacuum chamber is higher than 260 l/s and can be close to 500 l/s as specified by SAES Getters.

Can One Identify if the NEG is Saturated?

Pumping speed of NEG-based vacuum pumps can be reduced over their operation lifetime due to NEG saturation. There is always practical question exist: what is present pumping speed of NEG-based vacuum pumps after some period of operation? Pumping speed measurements using pulsed gas injection allow in situ monitoring of NEG-based pump conditions in EBIS or any other UHV device. Such an opportunity is illustrated by Fig. 8 where the pumping speed of the NEG module has been measured before and after NEG re-activation. As one can see, the degree of NEG saturation can be easily identified using this method.

Comparison of Pumping Speed Measurements by RGA and Ion Gauge

There is a significant practical interest to compare pumping speeds measured by RGA and ion gauge because RGA is not always part of UHV installation, but ion gauge is always there. MKS 421 cold cathode (CC) ion gauge with analog read-out was mounted right near RGA to cancel vacuum conductance issue and properly compare results of pumping speed measurements.

ISBN: 978-3-95450-226-4 ISSN: 2222-5692 doi:10.18429/JACoW-ECRIS2020-NACB01

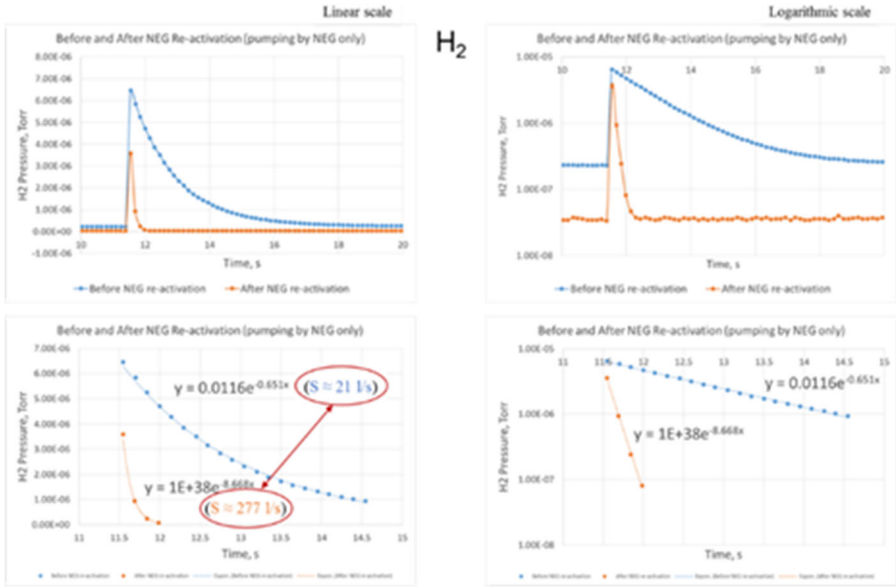

Figure 8: Pumping speed of ZAO NEG module for hydrogen before (blue dots and lines) and after (red dots and lines) re-activation.

Time dynamics of nitrogen pressure recorded by RGA and CC gauge is presented in Fig. 9 in linear and logarithmic scales. Vacuum chamber was pumped by TMP only because NEG was not activated yet.

One can see that time dynamics of pressure recorded by RGA and CC gauge are in good agreement. Some discrepancy at rising slope can be explained by limited time resolution of RGA (only 8 points per second). Comparison of pumping speed measured by RGA and CC gauge for conditions mentioned above is presented in Fig. 10. One can see that results of pumping speed measurements by RGA and CC gauge are in good agreement with each other and with specified pumping speed corrected by vacuum conductance for TMP model used. One should conclude that ion gauge can be used for pumping speed measurements although RGA would be preferable choice because it records time dynamics for gas specie of interest only thus providing more transparent results.

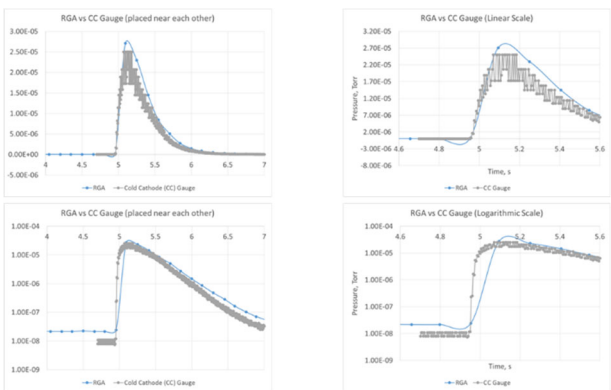

Figure 9: Time dynamics of nitrogen pressure recorded by RGA (blue dots and lines) and CC gauge (grey lines) in linear and logarithmic scales (right side plots are zoomed to show better time resolution of rising pressure slope).

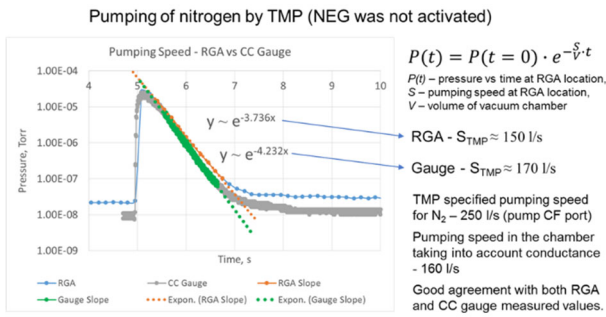

Figure 10: Pumping speed of nitrogen by TMP measured by RGA (blue dots and line, red line – approximation by exponential function) and CC gauge (grey line, green line – approximation by exponential function).

CONCLUSION

Recently introduced by SAES Getters ZAO NEG linear module is very attractive for EBIS applications due to large sorption capacity, high pumping speed and transverse compactness. It has been shown that module can be activated and regenerated by DC (or AC) current passing through the cage which contain ZAO NEG discs. We have developed in-situ method of pumping measurements using injection of limited amount of gas into vacuum chamber. Either residual gas analyzer or ion gauge can be used to record time dynamics of pressure. High pumping speed of the module for hydrogen and nitrogen has been measured. Developed method of pumping speed measurements can be used to monitor in situ NEG saturation level in EBIS or any other UHV device.

ISBN: 978-3-95450-226-4 ISSN: 2222-5692 doi:10.18429/JACoW-ECRIS2020-NACB02

STATUS OF THE HIGH-CURRENT EBIS CHARGE BREEDER FOR THE FACILITY FOR RARE ISOTOPE BEAMS*

H.J. Son†, A. C.C. Villari, A. Henriques, C. Knowles, Facility for Rare Isotope Beam (FRIB), Michigan State University (MSU), East Lansing, USA
A. Lapierre, D. Crisp, S. Nash, National Superconducting Cyclotron Laboratory (NSCL), Michigan State University (MSU), East Lansing, USA
E. N. Beebe, Brookhaven National Laboratory, Upton, USA

Abstract

The ReA post-accelerator of the National Superconducting Cyclotron Laboratory (NSCL) at Michigan State University includes an Electron-Beam Ion Trap (EBIT) operating as a charge breeder. The Facility for Rare Isotope Beams (FRIB) is being implemented. After completion, rare-isotopes beam rates are expected to exceed in some case 10^{10} particles per second (pps). The charge capacity of the ReA EBIT is insufficient to handle those rates. Therefore, parts of the TEST EBIS from the Brookhaven National Laboratory (BNL) were transferred to the NSCL to build a High-Current Electron-Beam Ion Source (HCEBIS). The HCEBIS features an electron gun that can provide a current up to 4 A for an estimated trap charge capacity of 10^{11} elementary charges. This paper presents the HCEBIS specifications, electron-beam current measurements to test its cathode, and simulation results for its implementation in the ReA post-accelerator. It also presents charge-capacity measurements conducted with the ReA EBIT that demonstrate that the HCEBIS will be able to handle beam rates of more than 10^{10} pps.

INTRODUCTION

The ReA post-accelerator [1] of the National Superconducting Cyclotron Laboratory (NSCL) at Michigan State University includes an Electron-Beam Ion Trap (EBIT) operating as a charge breeder. At the NSCL, Rare-Isotope Beams (RIB) are currently produced by fast-projectile fragmentation and fission with the Coupled-Cyclotron Facility (CCF). After production, these beams are then separated in-flight and thermalized in a helium gas cell before being transported to the ReA post-acceleration for charge breeding and then reacceleration with a linear accelerator up to several MeV/u for the nuclear physics program. The Facility for Rare Isotope Beams, FRIB, is being implemented based on a 400-kW heavy-ion linear accelerator (LINAC) [2]. After the transition from CCF-to-the FRIB LINAC, the production yield of rare isotopes will significantly increase. In some cases, rates are expected to exceed 10^{10} particles/s (pps). In addition, the user community for the Separator for Capture Reactions (SECAR) recoil separator [3] has requested stable-isotope ion beams with rates up to 10^{10} pps.

The ReA EBIT [4] has a limited charge capacity of 10^{10} elementary (1+) charges, which is insufficient to efficiently charge breed to high charge states RIB of high rates from FRIB. To increase the charge capacity of the ReA charge breeder, a new High-Current Electron-Beam Ion Source (HCEBIS) is being built. The HCEBIS uses the "backbones" of the TEST EBIS [5], which was transferred from the Brookhaven National Laboratory (BNL) in 2018. The HCEBIS can operate with an electron-beam current exceeding 4 A and has a trap length of 0.7m, allowing the device to deliver highly charged ion beams of intensities expected to be more than 10^{10} ions per second. The specifications of the HCEBIS are summarized in Table 1.

Table 1: HCEBIS Specifications

Electron-beam current	≤ 4 A
Electron-beam energy	≤ 20 keV
Magnetic field (trap center)	≤ 5 T
Electron-beam current density	≤ 200 A/cm^2
Trap length	0.7 m

The assembly of the HCEBIS has recently been completed from the electron gun to the collector, as shown in Fig. 1. The normal conducting solenoids were installed at the electron gun and the collector side. Preliminary vacuum tests for the electron gun and trap section have been completed. The control system is currently being implemented.

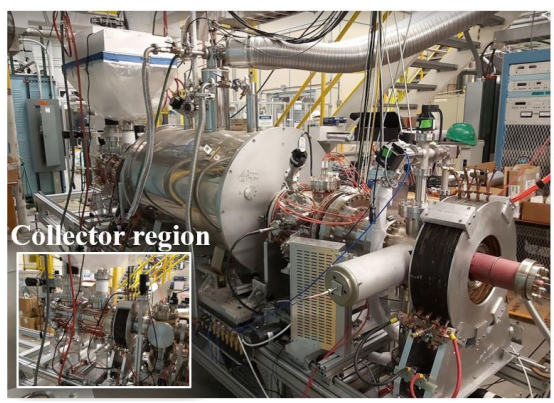

Figure 1: Assembled HCEBIS from the electron gun to the collector.

CATHODE TEST

The HCBIS will use for operation a magnetically immersed electron gun providing up to 4 A in current. The magnetic field near the cathode can suppress large radial beam oscillations, therefore the cathode is immersed in the

* Work supported by the National Science Foundation under Grant No. PHY-1565546.
†son@frib.msu.edu

ISBN: 978-3-95450-226-4 ISSN: 2222-5692 doi:10.18429/JACoW-ECRIS2020-NACB02

magnetic field of approximately 0.15 T [6]. The dispenser cathode material is made of lanthanum hexaboride (LaB6), and the cathode diameter is 9.2 mm. The LaB6 cathode currently installed was tested without magnetic fields in a test configuration.

The electron-beam is produced from the cathode by an applied high voltage onto the anode. The emitted electrons diverge due to the absence of magnetic field near the cathode. They are then accelerated and intercepted by the anode, as illustrated in Fig. 2. A pulsing circuit including a fast switch was employed to produce short electron-beam pulses of less than 10 μs to minimize the beam power on the anode and minimize the charge required to be stored in the pulsing circuit capacitors. In the turn-off period of the switch, the anode was biased to -100 V to suppress the thermal electron emission from the cathode. The pulsed emitted electron current was measured using a current transducer (Pearson, Current Monitor Model 110). Figure 2 presents the result of an electron-beam simulation in the test configuration using TRAK (see next section) and a diagram of the pulsing circuit.

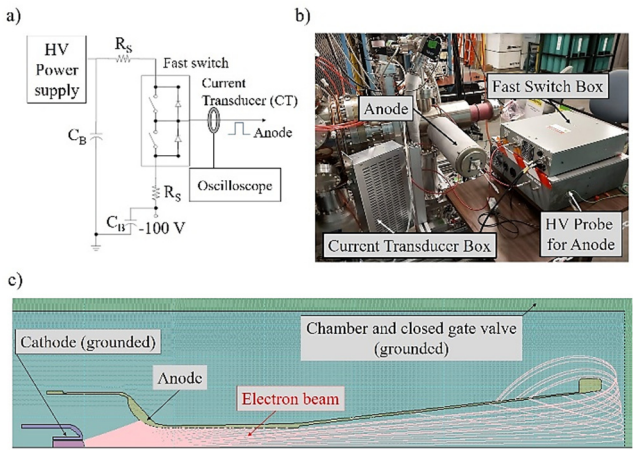

Figure 2: a) Pulsing circuit diagram, b) a photo of the experimental set-up, and c) TRAK simulation result.

Figure 3 shows the electron-beam current as function of the anode voltage with the cathode on ground potential. The anode voltage was varied from 0 V to 10 kV. With the low heater power, the emission current is limited by the temperature of the cathode surface. For higher heater power, the emitted beam current becomes only limited by the electron-beam space-charge. The I-V (current vs. voltage) curve can then be reasonably fitted with the Child-Langmuir law. The emission current is 1.12 A at the anode voltage of 10 kV with 137.4 W of heater power, corresponding to a perveance value of 1.12×10^{-6} A/V$^{3/2}$. With the heater power of 114.3 W and 137.4 W, the emission current values were the same. The emitted beam current was already limited by electron-beam space-charge with the heater power of 114.3 W. The dash line in Fig. 3 shows a simulated I-V curve having a perveance of 1.45×10^{-6} A/V$^{3/2}$. According to the perveance value measured at high heater power, the required potential difference between the cathode and the anode is 23.3 kV to obtain the electron-beam current of 4 A.

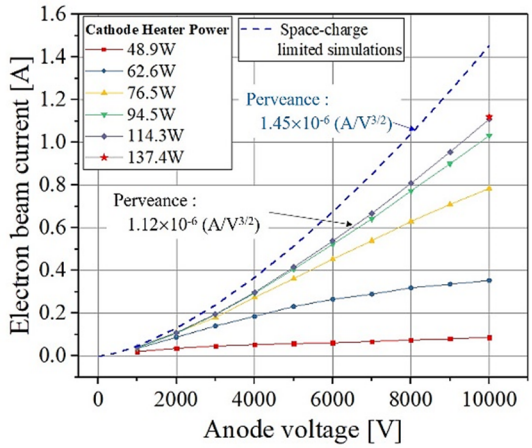

Figure 3: I-V curve of the cathode with different cathode heater powers.

HCEBIS BEAM SIMULATIONS

Beam simulations are a crucial step to verify the characteristics of the HCEBIS system to be integrated into ReA. An electron gun (e-gun) produces an electron-beam with small energy spread (quasi-mono-energetic). The electron-beam is then transported to the trap and compressed by a high magnetic field in its center. The compressed electron-beam plays two roles in the EBIS charge breeder. The electron-beam space-charge due to the compressed electron-beam, generates a strong radial potential well that traps ions radially. Trapped ions are quickly ionized to high charge states with the high current density of the electron-beam which generates a narrow charge-state distribution, increasing the breeding efficiency. Important characteristics are the electron-beam emission from the e-gun, electron-beam transport from the cathode to the collector, ion trap capacity, and current density distribution in the trap. The beam acceptance of the HCEBIS and emittance of the HCEBIS are also significant characteristics. Simulations have been conducted using Field Precision programs: ESTAT, PERMAG, and TRAK [7].

Electron-Beam Simulation

The simulation domain was two dimensional, and a single domain was used from the cathode to the collector to prevent discontinuities. All components in the simulation were assumed to be ideally axi-symmetric. Figure 4. a) shows the magnetic field and electric potential distributions in the HCEBIS along the beam axis. The cathode surface is positioned at z=0. The axial magnetic field near the cathode is approximately 0.15T and the potential difference between the cathode and the anode is near 20.6 kV. With this potential difference, the emitted beam current converged to 4 A.

The radial mesh size near the beam axis was set 10 times smaller than the outside mesh size for accurate beam trajectory calculations. The time step was set to 5×10^{-14} s. The electron-beam was transported from the cathode to the collector, as shown in Fig. 4. b). The electron-beam radius varied with the magnetic field along the beam axis and was

ISBN: 978-3-95450-226-4 ISSN: 2222-5692 doi:10.18429/JACoW-ECRIS2020-NACB02

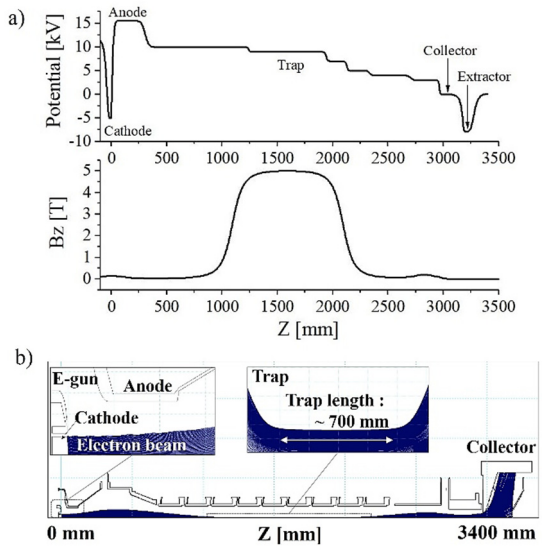

Figure 4: a) Axial magnetic field and electric potential distributions along the beam axis, and b) electron-beam trajectories from the cathode to the collector.

compressed by the magnetic field of 5T at the trap center. Figure 5 shows the radial electron-beam current density in the trap area. These current density values were averaged values of 40 axial points along the trap length. The current density is around 192 A/cm^2. The electron-beam radius according to the beam current density is estimated to be around 0.8 mm.

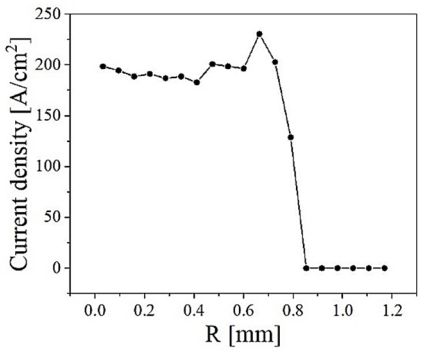

Figure 5: Electron-beam current density in the trap center (5-T magnetic field).

For an immersed electron gun of low space-charge potential, the electron-beam radius at an arbitrary z position can be expressed as [8]

$$r_z = r_{cathode}\sqrt{\frac{B_{cathode}}{B_z}} \quad (1)$$

where $r_{cathode}$ is the cathode radius, $B_{cathode}$ is the axial magnetic field at the cathode surface, and B_z is the axial magnetic field at the z position, respectively. The beam radius at the trap center can be calculated with Eq. (1) as 0.796 mm with the cathode magnetic field of 0.15T and the trap magnetic field of 5T. This value agrees well with the radius obtained from the simulations.

The theoretical charge capacity of an EBIS is given by [9]

$$C_{trap} = \frac{1.05\times10^{13}\times I_e\times L}{\sqrt{E_e}} \times f \quad (2)$$

It follows that the charge capacity of the HCEBIS is expected to be 2.4×10^{11} elementary charges, assuming a trap length (L), electron-beam current (I_e), compensation ratio (f), and electron-beam energy (E_e) of 0.7 m, 4 A, 1, and 15 keV, respectively. This capacity is sufficient to charge breed injected beam rates of 10^{10} pps of light ions. For instance, the HCEBIS could confine 3×10^{10} particles of Ne^{8+}. Even if losses are considered in the HCEBIS and during transport through the ReA LINAC, beam intensities of more than 10^{10} pps could be delivered to experimental facilities.

Beam Acceptance of the HCEBIS

The ReA EBIT in operation employs a Pierce-type gun in a magnetically semi-immersed configuration [10, 11]. The electron-beam size in the ReA EBIT trap is significantly smaller than that of a magnetically immersed electron gun. Hence, the acceptance of the ReA EBIT is smaller than the HCEBIS acceptance. ReA includes a beam cooler-buncher (BCB) [4] for pulsed injection into the ReA EBIT. Although for injected beams of low intensity the BCB beam emittance is smaller than the EBIT acceptance, its emittance is expected to significantly increase for high-intensity beams. Evaluating the acceptance of the HCEBIS is needed to understand its limits in capturing high-intensity pulsed beams from the BCB [12].

Figure 6 shows axial electric potential distributions. The dash-dot line represents the distribution without the electron-beam space-charge. When the electron-beam is on, the electron-beam space-charge changes the spatial electric potential, as shown by the solid line. This potential distribution with the electron-beam space-charge was obtained in the previous electron-beam simulation and was used for the injection simulation.

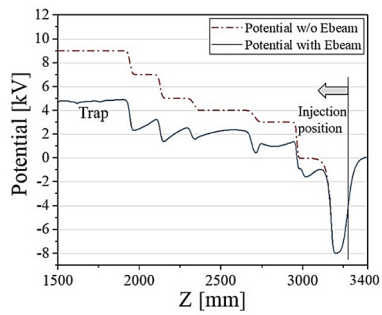

Figure 6: Axial electric potential distributions for the injection simulation with electron-beam current of 4 A and electron-beam energy of 14 keV.

A Ne^{1+} beam is injected from the injection position located at the end of the extractor shown in Fig. 6 and Fig. 7. The injected Ne^{1+} beam stops in the middle of the trap at z = 1500 mm. The initial injected ions were distributed uniformly in a x-x' phase-space rectangular that covered a 30mm×150mrad domain. The number of ions was 18272. The initial kinetic energy was set to 12 keV, and the averaged kinetic energy in the trap was around 0.9 keV. The accepted ion beam trajectory within the electron-beam in the trap is shown in Fig. 7. As shown in Fig. 8, the injected

ISBN: 978-3-95450-226-4 ISSN: 2222-5692 doi:10.18429/JACoW-ECRIS2020-NACB02

ions have a different overlap factor ($f_{overlap}$) with the electron-beam. Some ions are moving within the electron-beam over the whole trap length. In this case, the overlap factor is 1. Other ions partially overlaps with the electron-beam. Most, however, are not overlapping with the electron-beam or being accepted into the trap area (zero overlap factor).

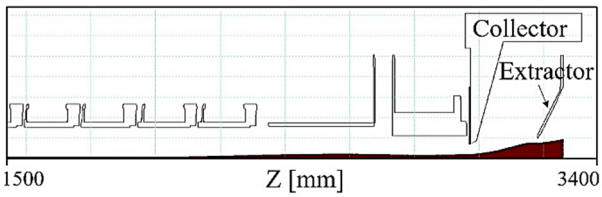

Figure 7: Injected ion beam trajectories with overlap factor of 1.

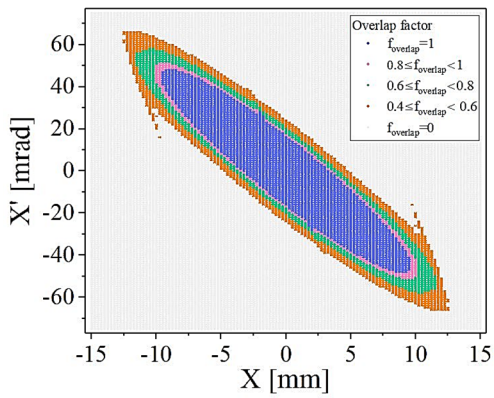

Figure 8: Acceptance ellipse with different overlap factor with the electron-beam: $f_{overlap}$=1 represents a full overlap.

The overlap factor is depended on the initial radial position and angle. All particle trajectories were tracked, and the overlap factors were obtained for each ion. The acceptance ellipse with a different overlap factor is shown in Fig. 8. The 4 times root-mean-square (4·RMS) acceptance for ions having an overlap factor 1 is 167 mm·mrad. The 4·RMS acceptance for all accepted ions having different overlapping factor is 518 mm·mrad. The 4·RMS acceptance was obtained by calculating 4·RMS emittance of the injected ions accepted with different overlap factors using the expression [13]:

$$\varepsilon_{4\cdot RMS} = 4 \cdot \sqrt{\overline{x^2} \cdot \overline{x'^2} - \overline{x \cdot x'}^2}\ mm \cdot mrad \qquad (3)$$

Wenander *et al.,* [9] obtained an analytical expression to estimate the maximum geometrical acceptance of an EBIS:

$$\alpha_{max} = x_{outmax} x'_{outmax} = \frac{r_{ebeam}}{\sqrt{2U_{ext}}} \cdot \left(Br_{ebeam}\sqrt{\frac{q}{m}} + \sqrt{\frac{qB^2 r_{ebeam}^2}{4m} + \frac{\rho_l}{2\pi\varepsilon_0}} \right) \qquad (4)$$

where r_{ebeam}, U_{ext}, q, m and ρ_l represent the electron-beam radius, ion injection potential, ion charge, ion mass and electron-beam charge per meter, respectively. The equation accounts for the electron-beam space-charge potential and was derived for ions having an overlap factor of 1 with a non-compensated electron-beam. From this equation, the HCEBIS maximum geometrical acceptance is 217 mm·mrad with the trap magnetic field at 5T and the electron-beam radius of 0.796 mm in the trap.

An acceptance comparison with the TEST EBIS is shown in Table 2 [14]. The 4·RMS acceptance of HCEBIS is larger than that of the TEST EBIS by a factor of 2 due to mainly our estimated electron-beam radius being also larger by a comparable amount (see Eq. (4)). For the maximum geometrical acceptance, the difference of the acceptance is reduced because the electron-beam space-charge potential of the TEST EBIS is deeper than that of the HCEBIS. It is complementary to the smaller electron-beam radius.

Table 2: Acceptance Comparison

	HCEBIS	TEST EBIS
Electron-beam radius	0.796 mm	0.55 mm
Electron-beam current	4 A	9 A
Ion injection potential	12 keV	22 keV
4·RMS acceptance ($f_{overlap}$=1)	167 mm·mrad	81 mm·mrad
Maximum geometrical acceptance	217 mm·mrad	165 mm·mrad

CHARGE BREEDER FOR HIGH INTENSITY BEAM

EBIT Operation for High-Intensity Ion Beams

To predict the capability of the HCEBIS, the production of high-intensity beams was tested and the electron-beam compensation ratio of the ReA EBIT was measured. When the BCB [4, 15] is operated in the pulsed mode for injection into the EBIT, the maximum beam rate capability is between 10^8–10^9 ejected ions per pulse. For the studies presented here, the BCB was operated in the continuous-injection mode to maximize the injected beam current. After optimization, a maximum Ne^{8+} beam rate after the Q/A separator of 1.748×10^{10} pps was obtained with a breeding time of 20 ms and a repetition rate of 33 Hz. The electron-beam current was set to 425 mA.

Figure 9 shows the optimized number of extracted Ne^{8+} ions as function of the number of ions ejected from the BCB. The number of extracted Ne^{8+} ions increases with the injected rate until it reaches a saturation limit. This could be explained by the electron-beam space-charge potential being largely neutralized and hence no longer efficiently confining and charge breeding injected ions.

Figure 10 shows a mass-over-charge (A/Q) scan performed during the tests. Ne^{8+} accounts for about 27 % of the total number of charge in the A/Q spectrum. Based on the achieved beam rate of 1.748×10^{10} pps in Fig. 9, the total charges of all extracted ion can be estimated as 1.569×10^{10} charges. With an electron-beam current of 425 mA, energy of 12 keV, and trap length of 0.635 m, the total charge ca-

ISBN: 978-3-95450-226-4 ISSN: 2222-5692 doi:10.18429/JACoW-ECRIS2020-NACB02

pacity of the ReA EBIT is 2.587×10^{10} charges. If we assume a 10 % loss in beam transport, the compensation ratio is estimated as approximately 69 %. This value is comparable, but more than twice higher than the compensation ratio reported by the REXEBIS group as 30 % with injected $^{40}Ar^{+}$ beam [16]. With a current of 4 A, the charge capacity of the HCEBIS is higher than that of the ReA EBIT by factor of 10. Therefore, the HCEBIS is expected to be able to charge bred and produce intense beams exceeding 10^{11} pps.

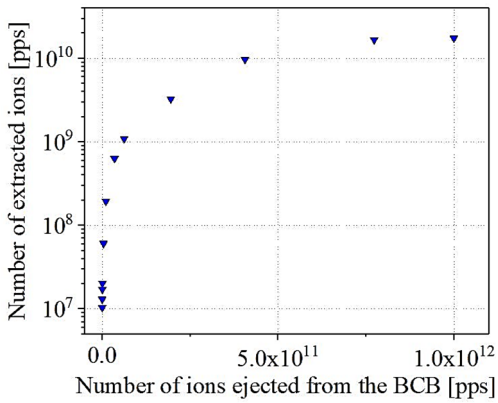

Figure 9: Ne^{8+} intensity after the Q/A separator.

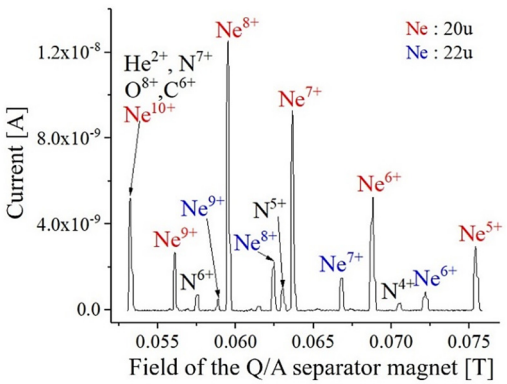

Figure 10: Mass-over-charge spectrum of highly charged ions resulting from external injection of.

CONCLUSION

A High-Current EBIS (HCEBIS) is being implemented for the ReA post-accelerator for charge breeding of intense beams. Over the last months, the cathode was tested in a test configuration up to 1.12 A. The beam acceptance and emittance were also simulated. To confirm the capability if the HCEBIS to handle high beam rates, the production of high-intensity beams of up to 10^{10} pps was studied with the ReA EBIT. Those studies confirm that the HCEBIS will be able to charge breed and produce intense beams exceeding 10^{11} pps. Firtst transport if an electron-beam through its superconducting magnet and ion extraction is expected early next year.

ACKNOWLEDGEMENTS

This material is based on work supported by the National Science Foundation under Grant No. PHY-1565546.

REFERENCES

[1] A. C. C. Villari, "Reacceleration of Rare Isotope Beams at Heavy-Ion Fragmentation Facilities," presented at EMIS-2018, Geneva, Switzerland, Sep. 2018.

[2] J. Wei, "The Facility for Rare Isotope Beams," presented at at APS April Meeting 2020, Washington D.C., MD, Apr. 2020.

[3] H. Schatz *et al.*, "SEparator for CApture Reactions (SECAR) Pre-Conceptual Design Report," FRIB, East Lansing, USA, Rep. FRIB-M41600-RP-000055-R002, Oct. 2014.

[4] A. Lapierre *et al.*, "First two operational years of the electron-beam ion trap charge breeder at the National Superconducting Cyclotron Laboratory," *Phy. Rev. Accel. Beams*, vol. 21, p. 053401, May 2018. doi.org/10.1103/PhysRevAccelBeams.21.053401

[5] E. N. Beebe *et al.*, "TEST EBIS Operation and Component Development for the RHIC EBIS," *Journal of Physics: Conference Series 2*, pp. 164–173, 2004. doi:10.1088/1742-6596/2/1/020

[6] A. Pikin, "EBIS for high intensity stable beams," *International Committee for Future Accelerators Beam Dynamics Newsletter*, no. 73, pp. 101-112, Apr. 2018.

[7] Field Precision LLC, http://www.fieldp.com

[8] F. Wenander *et al.*, "REXEBIS the Electron Beam Ion Source for the REX-ISOLDE Project Design and Simulation," CERN, Geneva, Switzerland, Rep. CERN-OPEN-2000-320, 1999.

[9] G. Zachornack *et al.*, "Electron beam ion source," *Proceedings of the CAS-CERN Accelerator School*, CERN-2013-007, pp. 165-202, Senac, Slovakia, Dec. 2013. doi:10.5170/CERN-2013-007

[10] S. Schwarz *et al.*, "A high-current electron gun for the electron beam ion trap at the National Superconducting Cyclotron Laboratory," *Rev. Sci. Instrum.*, vol. 85, p. 02B705, 2014. doi.org/10.1063/1.4827109

[11] T. M. Baumann *et al.*, "Determination of the ReA Electron Beam Ion Trap electron beam radius and current density with an X-ray pinhole camera," *Rev. Sci. Instrum.*, vol. 85, p. 073302, 2014. doi.org/10.1063/1.4885448

[12] C. Dickerson *et al.*, "Simulation and design of an electron beam ion source charge breeder for the californium rare isotope breeder upgrade," *Phy. Rev. ST Accel. Beams*, vol. 16 p. 02420, 2013. doi: 10.1103/PhysRevSTAB.16.024201

[13] R. Baartman, "Emittance Convention," TRIUMF, Vancouver, Canada, Rep. TRI-BN-15-07, June 2015.

[14] R. Kponou *et al.*, "Determining the acceptance of the Brookhaven EBIS test stand for primary ions by computer simulation," *Journal of physics: Conference Series 2*, pp. 165-172, 2014. doi.org/10.1063/1.1148714

[15] G. Bollen, "Beam Development," presented at SECAR Collaboration Meeting, MSU, East Lansing, MI, 2015.

[16] J. Pitters *et al.*, "Summary of charge breeding investigations for a future 11C treatment facility," CERN, Geneva, Switzerland, Rep. CERN-ACC-NOTE-2018-0078, Nov. 2018.

ISBN: 978-3-95450-226-4 ISSN: 2222-5692 doi:10.18429/JACoW-ECRIS2020-NACB03

DETERMINING THE FRACTION OF EXTRACTED ^{3}He IN THE $^3He^{2+}$ CHARGE STATE*

Matthew K. Gronert[1] †, Drew University , Madison, New Jersey, USA
Edward N. Beebe, Brookhaven National Laboratory, Upton, New York, USA
[1]also at Collider-Accelerator Department Brookhaven National Laboratory, Upton, New York, USA

Abstract

The parameter space of the TOF was explored using analytic methods as well as computer simulation to improve the design and functionality of a similar device that was constructed as a prototype for the Electron Beam Ion Source (EBIS) in 2019. A simulation of the beam line optics was produced in Opera-2D CAD software to show that other optical elements would not materially affect the operation of the TOF. This will allow for true measurements of the charge state ratios of helium for EBIS and extended EBIS operation in support of the Electron Ion Collider. EBIS operators will use the device to maximize the fraction of ^{3}He ions in the $^3He^{2+}$ state. Different geometries were explored as well to maximize the effectiveness of the device and to meet the performance criterion and physical constraints of the EBIS beam line.

INTRODUCTION

The Electron Beam Ion Source (EBIS) provides highly charged ions to the Relativistic Heavy Ion Collider (RHIC), and the NASA Space Radiation Laboratory (NSRL). It will also provide polarized ions for the future Electron Ion Collider (EIC). The ion with the correct charge-to-mass ratio and velocity is accelerated by the RFQ to high energy into the accelerator complex (LINAC, Booster, AGS ring, RHIC). It is therefore important for EBIS operators to be able to easily determine ion beam composition, specifically charge state ratios. Currently a magnetic, high resolution mass spectrometer is available to use. However, this takes on the order of several minutes to collect spectra, making it impractical due the many iterations it would take to properly tune the machine. An in-line time of flight spectrometer (TOF) allows for tuning on a pulse-to-pulse basis with lower resolution. The TOF consists of a Bradbury-Nielsen Gate (BNG), and a faraday cup. A BNG is a set of parallel equally spaced wires with alternating positive and negative voltages of the same magnitude. As an ion travels through the gate it is deflected and misses the faraday cup down the beam line. When the BNG wires are pulsed to 0 V the ions travel undeflected and are focused to the faraday cup [1]. The time savings allow EBIS operators to make many adjustments that would otherwise take several hours or days. A position monitor can also be affixed to the BNG about a centimeter away. It would be highly transparent so that gas injection and ion extraction can both be viewed. Last year, a BNG was tested at the Hollow Cathode Ion Source (HCIS). It was unable to deflect the entire beam. However, if one assumes homogeneity in the beam, it gave relative amounts of each ion by showing small changes on a DC background. Therefore, even a partially functioning BNG is sufficient to see desired effects. It would be beneficial to have the entire beam deflected. Simulations using Opera CAD 2D show that the entire beam can be deflected for true measurement of beam composition. These simulations further showed that other electrostatic elements in the beam line will not affect the functionality of the BNG as a chopper for TOF measurements, and established robust working conditions.

THEORETICAL REVIEW

Time of flight spectroscopy separates ions based on their charge-to-mass ratio by establishing a characteristic time to travel a specified distance. The characteristic time is given by

$$qV_0 = \frac{1}{2}mv^2 = \frac{1}{2}m\left(\frac{d}{t}\right)^2,$$

$$t = \sqrt{\frac{m}{q}}\frac{d}{\sqrt{2V_0}},$$

where V_0 is the voltage the ion of charge q and mass m is accelerated through, d is the distance traveled, and t is time. In this case, a BNG is used as a chopper to select a small sample of the beam to evaluate, so that each ion's trajectory along the specified distance starts at the same place and time. The average deflection is given by,

$$\tan\alpha = k\frac{V_p}{V_0},$$

with

$$k = \frac{\pi}{\ln\cot\frac{\pi R}{2D}},$$

where R is the radius of the wire and D is the is the distance between the centers of two adjacent wires. Here each parameter is as seen in Fig. 1.

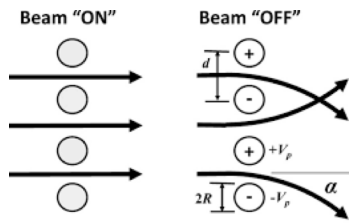

Figure 1: Schematic diagram of a Bradbury-Nielsen Gate [2].

* Work supported by Brookhaven National Laboratory and the Department of Energy
† matthewgronert@gmail.com

ISBN: 978-3-95450-226-4 ISSN: 2222-5692 doi:10.18429/JACoW-ECRIS2020-NACB03

The average particle experiences this deflection [2]. We need for $\tan\alpha > \frac{d_{\text{cup}}}{l}$ where d_{cup} is the radial distance that must be deflected over which in this case is about 20 mm, and l is the distance between the BNG and Faraday cup which is 1542 mm.

PRELIMINARY TEST

Last year, a prototype BNG was tested at the Hollow Cathode Ion Source, with gold on tungsten wire of radius 0.0254 mm, wire spacing 1 mm and V_p = 300 V. The BNG wires were at V_p and are pulsed to ground by positive and negative power supplies for 50 ns, through high pass filters (Fig. 2).

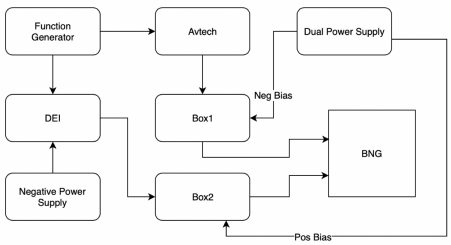

Figure 2: Box Diagram of the supporting electronics to the BNG.

Before each signal reached its set of wires, it passed through a resistor and capacitor in series to control rise times. Quadrupoles are tuned to increase beam intensity on the cup. Here a problem occurs. The rise time of the signal is not fast enough to resolve different peaks, as seen in Fig. 3. It is

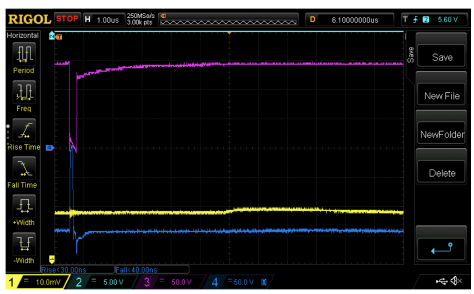

Figure 3: Voltage on the sets of BNG wires in magenta and blue, are normally held at $+V_p$ and $-V_p$, respectively, and pulsed to common during a 50ns gating pulse. The yellow trace shows the poorly resolved Faraday Cup signal, without the use of a pre-amp to drive the long signal cable capacitance.

evident that the signal increases after a few microseconds, but this does not give us any useful information about the contents of the beam. The problem is that we are terminating the scope in 1 MΩ, and therefore the RC time is large. Instead we put the Faraday Cup signal through a pre-amp, and terminate it in 50 Ω. After we add the pre-amp we get the desired spectrum, as seen in Fig. 4. We can see that the first peak is helium, then we have Nitrogen, Oxygen, and water, followed by Copper 63 and 65. These are expected

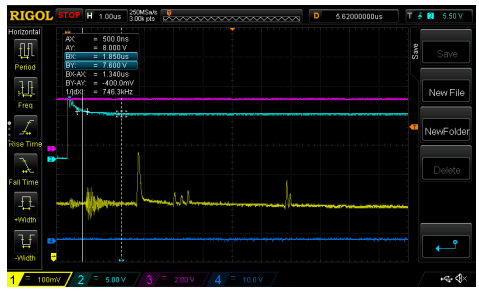

Figure 4: Time of flight data for ^{4}He, followed by C, N, O, and, ^{63}Cu and ^{65}Cu. Note that the relative abundances of ^{63}Cu and ^{65}Cu are are 69.2% and 30.8% respectively.

contaminants. We can know that the TOF is working at least partially, since the peaks have a width equal to the pulse time, and since Copper 63 and 65 appear in their relative abundances. Since, we do not deflect the entire beam this signal comes over a DC background. If we assume homogeneity in the beam, these are the proportions of the ion species.

Also, in this preliminary study, another set of parallel wires was on the same frame about 6 mm. This did not evidently alter the effects of the BNG, since this set of wires was at common, and the fields from the BNG decay to approximately 0, 1 wire spacing away from the device axially.

SIMULATION STUDIES

Opera-2D CAD was used to simulate beam optics. First, we did a study of just the BNG. Previously, we explored the ratio of R/D. It is desirable for this ratio to be such that $k > 1$. We have chosen R = 0.2 mm and D = 1 mm so that k = 1.40. The required voltage V_p is therefore 312 V. We start with V_p = 500 V.

BNG

First, we can see the BNG isopotential lines in Fig. 5.

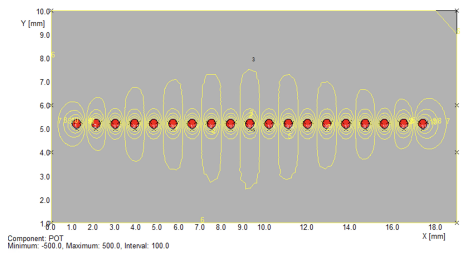

Figure 5: Isopotentials of the Bradbury-Nielsen Gate

An ion extracted at 25 kV can be sufficiently deflected by the this BNG. However, we can achieve better results by increasing V_p. We increased V_p to 850 V. It is likely that the beam will be expanding as it enters the BNG. Therefore the BNG needs to be robust in response to an expanding beam. We calculated ion trajectories entering the BNG at a variety of angles. As seen in Fig. 6, the BNG is robust to expanding beams.

ISBN: 978-3-95450-226-4 ISSN: 2222-5692 doi:10.18429/JACoW-ECRIS2020-NACB03

We can see that as long as the magnitude of the exit angle is greater than 1°, the ion is sufficiently deflected. When

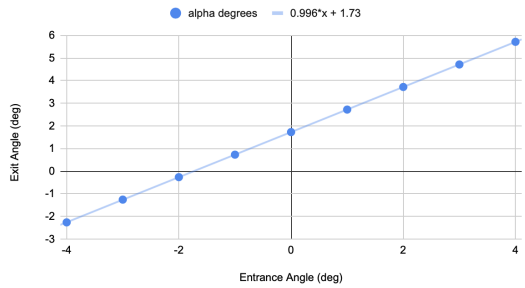

Figure 6: Exit angle vs. Entrance angle for an ion extracted at 25 kV.

modelling the BNG in opera by itself we use an X-Y symmetry so that we are viewing a cross section of the wire going into and out of the page. However, the other beam optics are cylindrically symmetric. Because the software is only 2D we must pick one symmetry system. We pick cylindrical symmetry. In this case the BNG is no longer modelled by a set of parallel wires, but by concentric circles. This does not give exactly the same deflection as the original case. However, it is nearly the same and without loss of applicability and in the interest simplicity, during the simulation, we used the cylindrically symmetric model.

Gridded Lens

The gridded lens was modeled as a transparent plane at the lens voltage with rings at common near the periphery to reduce spherical aberrations, to reflect the actual construction. We work with a gridded lens at −2 kV. A diagram of the gridded lens can be viewed in Fig. 7.

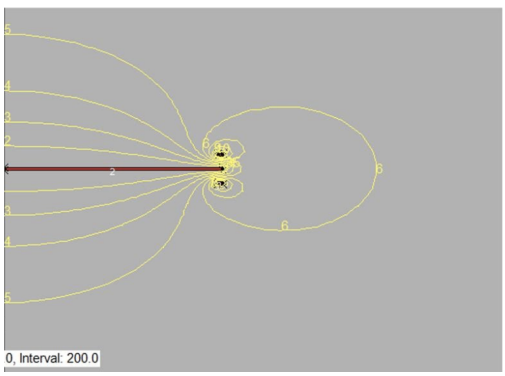

Figure 7: Iso potentials of the gridded lens gridded lens at −2 kV. Two rings on the right edge of the lens are at common to reduce spherical aberrations.

Acceleration Break

For ions to be properly accelerated by the RFQ they need to have an energy of 17 keV/nucleon. For $^{3}He^{2+}$, each ion needs to have 51 keV. Therefore it needs to drop through 25.5 kV, which can be achieved by using only internal EBIS electrodes during the extraction process. For $^{197}Au^{32+}$ each ion requires approximately 105 kV. This is achieved by biasing the entire EBIS source to HV during ion extraction, resulting in an additional voltage of approximately 80 kV across the acceleration break. A drawing of this element can be see in Fig. 8.

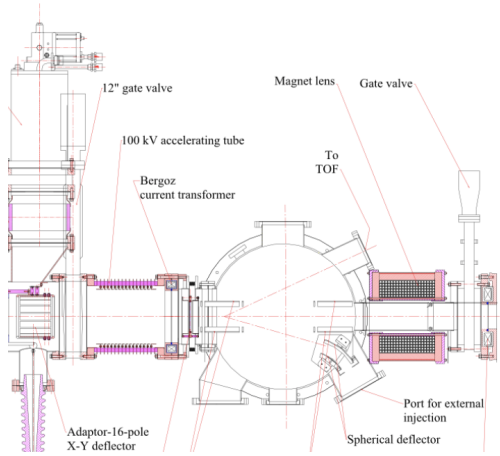

Figure 8: The 100 kV accelerating tube can be see on the left-hand side. We model the electrodes which are attached to the ceramic shown here in magenta.

If there is an 80 kV drop across the acceleration break then the total drop is divided linearly among the electrodes, with the first two electrodes being at EBIS common. Also note that if there is an 80 kV drop then the gridded lens is at −2 kV relative to this drop or at −82 kV relative to EBIS common. We only model the electrodes as thin conductors whose size and spacing are faithful to the drawing in Fig. 6.

Modelling the Entire Beam Line

Next, we calculate ion trajectories through the entire relevant beam line. Success is defined by being able to focus a beam onto the Faraday cup when the BNG is off, and preventing the beam from hitting the Faraday cup when the BNG is on. The first case we will study is the simplest, $^{3}He^{2+}$, because it does not require any voltage drop over the acceleration break. With −3.75 kV on the lens we are able to focus $^{3}He^{2+}$ to the Faraday cup when the BNG is off and deflect the beam from hitting the cup when the BNG is on, as can be seen in Figs. 9 and 10.

We have now shown that we can focus or deflect a beam of $^{3}He^{2+}$ ions as desired. Next we will show that we can do the same with $^{197}Au^{32+}$. This requires us to have an 80 kV drop across the acceleration break, so that $^{197}Au^{32+}$ will have 17 keV/nucleon entering the RFQ. In this case the gridded lens is at −2 kV relative to the acceleration break (i.e. −82 kV relative to EBIS common). Although this is not the main focus of the study, it is important that the TOF detector is functional in all modes of EBIS operation. The TOF will not be able to discriminate individual peaks for $^{197}Au^{31+}$ and $^{197}Au^{32+}$. This is because the difference in travel time is less than the time the chopper is off. However, it will be able to see the envelope of the set of Au peaks.

ISBN: 978-3-95450-226-4 ISSN: 2222-5692 doi:10.18429/JACoW-ECRIS2020-NACB03

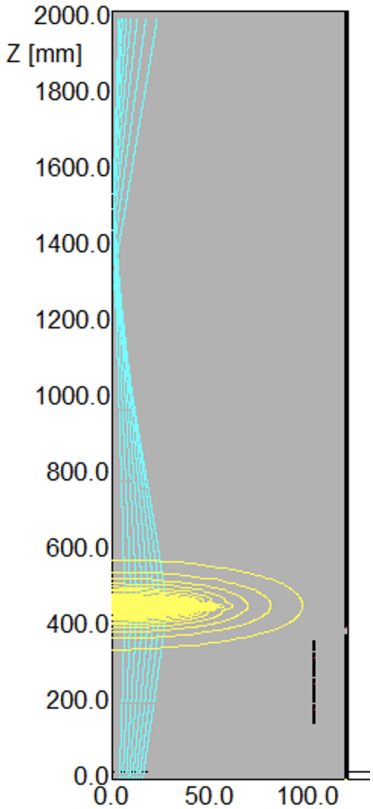

Figure 9: $^3He^{2+}$ focused to the 13 mm diameter Faraday Cup at axial position 1542 mm , with the BNG off.

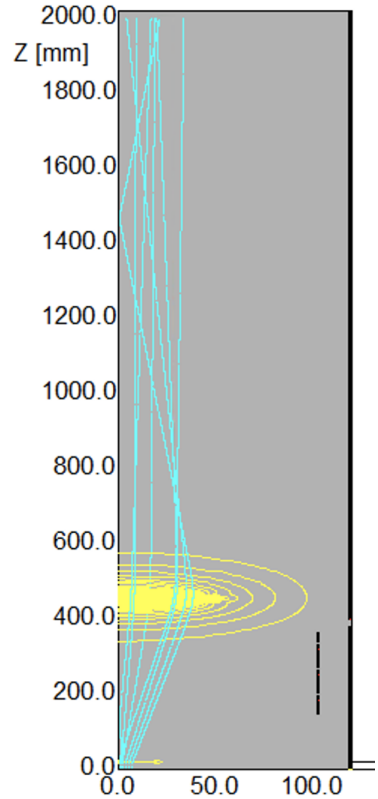

Figure 10: $^3He^{2+}$ deflected from the Faraday cup by the BNG. The ions were extracted at 25.5 kV with 0 V over the acceleration break, −3.75 kV on the gridded lens, and V_p = 850 V. The Faraday cup is located at Z = 1542 mm and has radius 6.5 mm

Simulations show that the BNG successfully deflects Au as well, with slight adjustments to the gridded lens, necessary to account for focusing due to acceleration.

Other Considerations

We intend to eventually install a harp style position/profile monitor about 1 cm axially from the BNG. Simulations have shown that it would not significantly affect the trajectories. The same considerations must be taken into account when the BNG or position monitor is inserted or removed from the beam line.

This also does not significantly affect the trajectories of the ions. The time of flight detector makes measurements use to the normal operational EBIS extraction optics except for the solenoidal lens focusing into the RFQ, which will be off during the TOF measurements.

CONCLUSION

We have now demonstrated that a Bradbury-Nielsen Gate can successfully deflect a slightly diverging beam from hitting a Faraday cup. After a suite of simulations, it is evident that the BNG can function properly with a variety of ions. We are now in the final design and construction process of the BNG for installation at the to EBIS. As previously stated, the TOF offers significant time savings to EBIS operators to see $^3He^{2+}/^3He^{1+}$ ratio for the Electron Ion Collider-and other charge state ratios for RHIC and NSRL- with only minor and easily pre-programmed changes to the EBIS operating conditions.

ACKNOWLEDGMENTS

This work was supports by Brookhaven National Laboratory and the Department of Energy Office of Science.

REFERENCES

[1] N. E. Bradbury and R. A. Nielsen, “Absolute values of the electron mobility in hydrogen”, *Phys. Rev.*, vol. 49, p. 388, 1936. doi:10.1103/PhysRev.49.388

[2] Oh Kyu Yoon, I. A. Zuleta, M. D. Robbins, G. K. Barbula, and R. N. Zare, “Simple template-based method to produce bradbury-nielsen gates”, *J. Am. Soc. Mass. Spectrom.*, vol. 18, pp. 1901–1908, 2007. doi:10.1016/j.jasms.2007.07.030

ISBN: 978-3-95450-226-4 ISSN: 2222-5692 doi:10.18429/JACoW-ECRIS2020-NACB04

ION SIMULATIONS, RECENT UPGRADES AND TESTS WITH TITAN'S COOLER PENNING TRAP

R. Silwal[1,*], S. F. Paul[1,2], B. K. Kootte[1,3], T. Joseph[1,4], R. Simpson[1,5], A. A. Kwiatkowski[1,6], G. Gwinner[3], J. Dilling[1,4], and the TITAN collaboration
[1] TRIUMF, Vancouver, BC Canada
[2] Ruprecht-Karls-Universität, Heidelberg, Germany
[3] University of Manitoba, Winnipeg, MB Canada
[4] University of British Columbia, Vancouver, BC Canada
[5] University of Waterloo, Waterloo, ON Canada
[6] University of Victoria, Victoria, BC Canada

Abstract

TRIUMF's Ion Trap for Atomic and Nuclear science (TITAN) facility has the only on-line mass measurement Penning trap (MPET) at a radioactive beam facility that uses an electron beam ion trap (EBIT) to enhance mass precision and resolution. EBITs can charge breed exotic isotopes, making them highly charged, thereby improving the precision of atomic mass measurement as the precision scales linearly with the charge state. However, ion bunches charge bred in the EBIT can have larger energy spread, which poses challenges for mass measurements. A cooler Penning trap (CPET) is currently being developed off-line at TITAN to sympathetically cool the highly charged ions (HCI) with a co-trapped electron plasma, prior to their transport to the MPET. To evaluate the integration of the CPET into the TITAN beamline and to optimize the beam transport, ion trajectory simulations were performed. Hardware upgrades motivated by these simulations and previous test measurements were applied to the off-line CPET setup. Ions and electrons were co-trapped for the first time with the CPET. Progress and challenges on the path towards HCI cooling and integration with the on-line beam facility are presented.

INTRODUCTION

Atomic mass measurements of short-lived radioactive isotopes are useful to study nuclear structure, test existing nuclear models, explore the nuclear astrophysics reaction paths, and test predictions of fundamental physics beyond the Standard model [1–4]. TRIUMF's Ion Trap for Atomic and Nuclear Science (TITAN) facility [5], is dedicated to high precision mass measurements as well as in-trap decay spectroscopy of radioactive ion beams (RIB). The TITAN system (see Fig. 1) is comprised of the following ion traps:

- A radio-frequency quadrupole (RFQ) cooler and buncher,
- A measurement Penning trap (MPET),
- An electron beam ion trap (EBIT),
- A cooler Penning trap (CPET), and
- A multiple-reflection time-of-flight mass spectrometer (MR-TOF MS)

* roshanisilwal@gmail.com

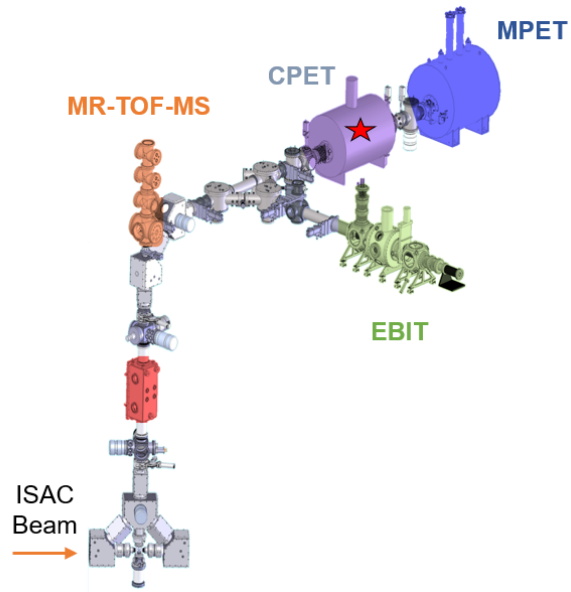

Figure 1: The TITAN beamline shown with different traps color-coded (the star indicates that the trap is not currently coupled to the radioactive beamline).

The RFQ cooler and buncher [6] receives the radioactive beam from the isotope separator and accelerator (ISAC) facility [7] at TRIUMF at a beam energy of 20 keV. It then cools the ions via collisions with He buffer gas, and bunches the beam. Downstream of the RFQ, a pulsed drift tube reduces the energy of the ion bunches to roughly 2 keV to match the acceptance of the other ion traps. The MR-TOF MS [8, 9] is used to either clean isobaric contaminants from the radioactive beam or for highly sensitive mass measurements and is advantageous for low-intensity or highly contaminated RIB species. TITAN-MPET [10] can perform extremely precise mass measurements using a time-of-flight ion-cyclotron-resonance (ToF-ICR) method [11, 12] by measuring the cyclotron frequency (ν_c) of the ion. Since $\nu_c = qB/2\pi m$, the mass values can be extracted from ν_c. For singly charged ions, the MPET has achieved ppb precision [10], which is sufficient for nuclear structure and astrophysics studies. However, in order to test fundamental symmetries, an even high precision can be required [13].

ISBN: 978-3-95450-226-4 ISSN: 2222-5692 doi:10.18429/JACoW-ECRIS2020-NACB04

The mass measurement precision in the MPET is limited by the charge state of the species (q), the number of ions observed during the measurement (N_{ions}), the RF excitation time (T_{rf}), and the magnetic field (B) as shown in Eq. (1).

$$\frac{\delta m}{m} = \frac{m}{qBT_{rf}\sqrt{N_{ions}}}. \quad (1)$$

Of these parameters, the superconducting magnet of 3.7 T is fixed, N_{ions} depends on the measurement cycle time, the RIB production rate and the contaminants, and (T_{rf}) is limited by the half-life of the exotic ions. The charge state of the species can be increased to enhance the mass precision and resolving power [14–17]. TITAN has the only on-line Penning trap at a RIB facility, coupled to the EBIT to charge breed ions in order to increase the charge state [4, 18–22]. The highly charged ions (HCI) can charge-exchange with neutral atoms in the MPET, damping and/or shifting the ToF-ICR resonances [23], hence deteriorating mass precision and resolving power. To reduce the probability of charge-exchange, TITAN-MPET is currently being upgraded to a cryogenic trap which will significantly reduce the residual gas level.

Currently, TITAN-EBIT [24, 25] can operate at 65 keV beam energy, 500 mA electron beam current, and 6 T magnetic field. The existing electron gun will be upgraded to a newly designed system that can provide up to 6 A beam current. Singly charged ions transported to the EBIT are ionized to high charge states by electron impact ionization. The electron beam is compressed to roughly 100 µm radius by the 6 T field as it passes through the trapping region that consists of several drift tubes. These HCI are axially trapped by an electric field applied across the drift tube electrodes and radially confined by the combined effects of the magnetic field and the space-charge of the electron beam. These charge-bred ions are then extracted by an extractor electrode at the collector region and transported to the MPET for mass measurements.

The transversal and longitudinal emittance of ion bunches extracted from the EBIT can exceed the acceptance of the MPET. The ~20 eV/q energy spread of the highly charged ion beam [26] extracted from the EBIT can lead to reduced injection efficiency and smeared TOF resonances. The mass precision is reduced as the ions probe a larger volume in the trap and therefore more magnetic field inhomogeneities. For maximal mass precision, it is essential to cool the HCI bunch before extraction in order to reduce its energy spread. Most of the available cooling techniques such as buffer cooling [27] and optical cooling [28] do not apply to HCIs due to the large charge exchange cross-sections and limited availability of appropriate atomic transitions for laser cooling. In an effort to cool HCIs, a practical solution based on electron cooling [29, 30] is being pursued at TITAN. HCIs are cooled by Coulomb collisions between ions and electrons that self cool in the 7 T magnetic field through emitting cyclotron radiation [31, 32].

The CPET [33] consists of 29 cylindrical trap electrodes where both ions and electrons are trapped simultaneously in nested potential wells. A schematic of the CPET is shown in Fig. 2. The gate electrodes (G1, G2) confine injected electrons which then cool into the nested positive potential well. The pulsed drift tube (DT1) is used to reduce the energy of incoming ion bunches from ~ 2 keV to a few 10 eV thus making them trappable within the CPET. After the cooling process, the energy of extracted ion bunches is elevated with another pulsed drift tube (DT2) for transport to the MPET. The off-line setup comprises an ion source to inject stable singly charged ions into the trap which will be replaced by the EBIT in the on-line system. Several efforts were made in optimizing the trap, characterizing the electron plasma, enhancing electron injection, and improving the beam diagnostics. The most important developments include the design of an off-axis electron gun for electron injection that provides an unobstructed extraction of cooled ions towards the MPET [34], and a harp detector [35] built to diagnose the electron plasma without obstructing the transport of the ions into the trap.

Previous studies with the CPET have provided insight into plasma instabilities and oscillation modes that may be enhanced by asymmetries in the system [31]. This study revealed ~minute trapping times and suggested that even longer trapping times without losing the plasma can be achieved by applying a counteracting rotating wall drive [36]. Successful electron plasma creation was demonstrated using an on-axis [34] and off-axis [37] electron gun with the first signs of self-cooling in electrons. Characterizing the ion trapping, however, posed a challenge due to high voltage sparks/discharges in the system. With many electrodes, a compact vacuum feed-through wiring section, and high voltage switching among multiple electrodes, the system is fairly complex. Motivated by a need to simplify the setup and to optimize the ion-electron dynamics, we performed ion trajectory simulations followed by a few hardware changes in the system. Here, we present the current status, recent results, and upgrades of the off-line CPET setup. We also discuss the challenges and upcoming plans for commissioning and online integration into the TITAN beamline.

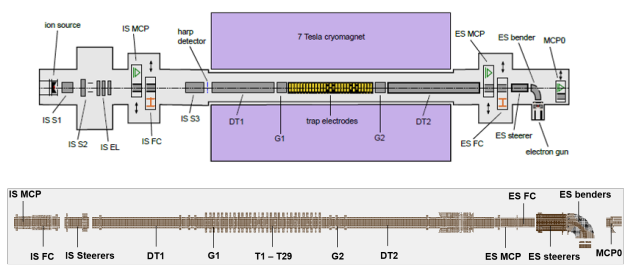

Figure 2: Schematic of the CPET [38] (top) and SIMION geometry shown without the ion source (bottom).

ION TRAJECTORY SIMULATIONS

The ion trajectory simulations were performed using the SIMION package [39], which incorporated both electric and

ISBN: 978-3-95450-226-4 ISSN: 2222-5692 doi:10.18429/JACoW-ECRIS2020-NACB04

magnetic fields to understand the beam properties during ion injection and extraction.Previously, the 29 trap electrodes were floated to 1 kV or higher during normal operation, potentially leading to HV discharges. To avoid this, we developed a new scheme with the trap near ground potential. This scheme adds a complication of having to pulse the drift tube (DT1) to inject the ions. The first goal of the simulations was to find suitable settings for ion injection with the new scheme. To do so, a simulated 2 keV ion beam, with ~20 eV energy spread was injected into the trap using the SIMION geometry. DT1 was pulsed from +1 kV to −1 kV during injection to reduce the beam energy. Strong accelerating negative voltage was required to avoid magnetic field reflection when the ion beam enters the high B regime and to maximize the beam transmission.

Upon interaction with the self-cooled electrons, the ions would cool in the 2 ion wells next to the end caps as seen in Fig. 3. The cooled ions will be extracted from one of the wells by lowering the end cap (E2). Assuming the ion bunches cool to ~ 1 eV, the second goal of the simulations was to obtain an extracted beam with small energy spread and a time focus (i.e. longitudinally compressed bunches) in the MPET (or on the off-line detector). The ions were initialized at the ion well position as a cylindrical beam of a finite length (ranging from 1 to 3 trap electrodes) and a radius of 0.5 mm. Uniform energy spread averaging to ~1 eV/q was used, assuming cold ions, and the extraction of the cooled beam was optimized accordingly. It was found that applying a voltage gradient across a few electrodes is an ideal way of extracting the ion bunch without adding additional energy spread. Extracted ion bunches were brought to a suitable transport energy of 2 keV by pulsing drift tube DT2 from −1 kV to +1 kV. The simulations showed that pulsing the DT2 bias with appropriate timing did not affect the beam energy spread.

Figure 3 shows the on-axis potential on the trap electrodes optimized for trapping ions. Proper analysis of the applied voltages was required since the trap electrodes were affected by the field penetration of the nearby gate electrodes. In order to account for this field penetration, three trap electrodes on either end of the gate electrodes were set to the same potential and used as end cap electrodes to trap the ions. Two modes of extraction, shown in Fig. 3 (bottom), produced good beam properties. The optimum condition was obtained when a linear voltage gradient along four trap electrodes was created (red). Pulsing a few electrodes to a constant negative potential (blue) also resulted in ~2 eV energy spread of the extracted ion bunch.

The third goal of the simulations was to check if the TOF signal on the off-line detector on the electron side (ES MCP0) could be used to probe changes in beam energy of cooled (1 eV/q) bunches versus uncooled (20 eV/q) bunches. An energy spread of ~1 eV and a time focus of 200 ns were achieved for the cold beam. Figure 4 shows a Gaussian fit for the energy spread of the extracted beam with and without cooling.

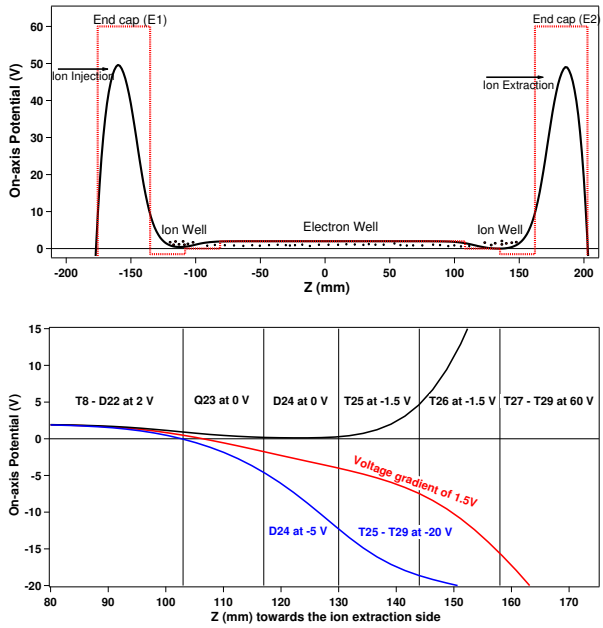

Figure 3: On-axis potential during ion trapping in black and the applied voltages in red (top) and extraction with a linear voltage gradient in red and fixed potential in blue (bottom). Note the trap center is located at z = xy; labels T, D and Q refer to the type of the trap electrode (unsegmented ring electrode, two-fold segmented dipole electrode and 4-fold segmented quadrupole electrode).

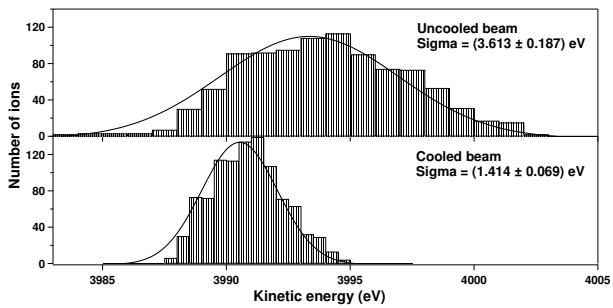

Figure 4: Energy spread of the extracted ions (here the MCP biased at −2 kV to image the beam) for cooled vs uncooled ions (from simulations). The uncooled beam has larger energy spread as expected.

The positive simulation results motivated the realization of the above operation scheme for the CPET. To this end with the goal of increased robustness against HV discharges in mind and to accommodate the simulation results, the following hardware changes were applied to the system. The three trap electrodes on either end of the gate electrodes were biased with the same voltage. The respective segments of several azimuthally split electrodes were shorted within the vacuum chamber, hence reducing the number of HV carrying cables within the magnet bore. Among them were a pair of dipoles forming a regular trap electrode and the adjacent electrodes in the two octupoles to form quadrupoles. The first quadrupole was kept at the trap center to apply the

ISBN: 978-3-95450-226-4 ISSN: 2222-5692 doi:10.18429/JACoW-ECRIS2020-NACB04

rotating wall drive to the electrons. The second quadrupole was moved to the ion extraction end, where the potential minimum of the trap occurs, with a set of dipole electrodes on either side to allow for mass selective dipole cleaning [31]. The careful arrangement of electrode wires allowed maximum spacing between HV-carrying wires. The ones requiring high voltage switching were placed closer to the outer chamber to avoid possible sparking. The ceramic tubes surrounding the copper wires and the wire lengths were changed according to the new trap configuration to avoid open wire ends. As motivated by the simulation results, a resistor chain for the creation of linear voltage gradients was built.

CHARACTERIZING THE ELECTRON AND ION TRAPPING

Electron Plasma Studies

First tests of trapping and detection of over 10^8 electrons were reported in [40], using an on-axis electron gun. Further tests with an upgraded off-axis electron gun [34] were performed to quantify electron loading and trapping. Recent tests were conducted with a typical emission current of 70 µA that resulted in a DC current of ~1 µA at the harp detector. Loading and trapping were optimized to allow maximum transmission and storage times inside the magnetic field. A scan of the number of trapped electrons at various storage times recorded by the harp detector is shown in Fig. 5, for a 3 s loading time. We achieved a storage time of over 3 minutes, much longer compared to any previous tests. The initial increase in the electron number is due to the damping of an azimuthal asymmetry related m=1 diocotron motion caused by a E × B drift [37, 40]. Early studies by Chowdhury *et al.* [37] showed that the radial displacement of the plasma column recorded on a phosphor screen (inside the magnet bore) decreased on a timescale of 2 s due to this damping. Additionally, the extraction through the diverging magnetic field lines amplifies the initial radial displacement of the plasma and can cause electrons to get lost against the electrode surfaces (of DT1) before reaching the detector.

Longer electron storage times will be necessary when the CPET is coupled with the charge bred HCI and the MPET for mass measurements. Since faster electron cooling requires a large ratio between the number of electrons and ions, and high electron density in the trap [32], the trap was re-loaded to maintain a number of 10^8 trapped electrons or higher with shorter loading times (few hundred ms) for electron related studies. As detailed in [34], we deploy a continuous electron loading mechanism first described by [41]. Electrons were successfully confined in nested potential wells of various shapes formed with the 15 central trap electrodes, thus confirming the self-cooling of electrons in the magnetic field. This was achieved using a floating 16 channel digitally controlled voltage (DAC) supply box developed using a Raspberry Pi controlled Analog Devices evaluation board.

Electron plasma is known to have plasma instabilities triggered by asymmetries in the setup such as misalignments

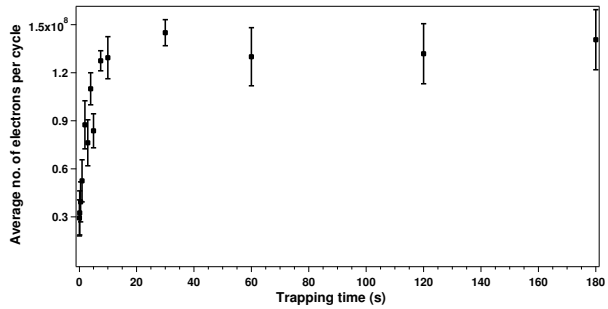

Figure 5: More than 10^8 electrons were trapped for over 3 minutes with an electron loading of 3 s.

in the magnetic and optical axes, off-axis plasma injection, residual gas in the trap, interactions with ions, and application of dipole excitations [42]. Various plasma oscillation modes (radial, azimuthal, and axial) related to the plasma rotations, instabilities, and temperatures exist [43]. The diocotron mode created by the interaction of electrons with their image charge can move the plasma away from the axis leading them to diffuse radially. A counteracting force, created by a rotating-wall drive [36, 42] is needed to ensure a centered plasma with even longer storage times. Another plasma mode in the axial direction, termed the TrivelPiece-Gould mode [43] can be used to diagnose the plasma temperature. Currently, efforts are underway to extract additional information about the electron plasma from the image currents that these plasma oscillations induce on the trap electrodes.

Ion Trapping

A Na surface ion source was used to inject ions into the trap. The ion source emitted a range of ion species that were chopped and steered by a set of electrostatic Lorentz steering elements. Ions of 2 keV energy were reduced to ~100 eV in the drift tube, before sending them to another Lorentz steerer placed inside the magnetic field. These steerers were primarily used to localize the beam in the center of the trap. The three shorted trap electrodes on either end (E1 and E2) were used to trap these ions. By lowering the E2 potential after the desired trapping time, the ions were extracted and recorded by a MCP detector at the end of the beamline. A scan of ion counts for different storage times resulted in a lifetime of nearly 3 s, as shown in Fig. 6. This is the first demonstration of successful ion trapping with the CPET.

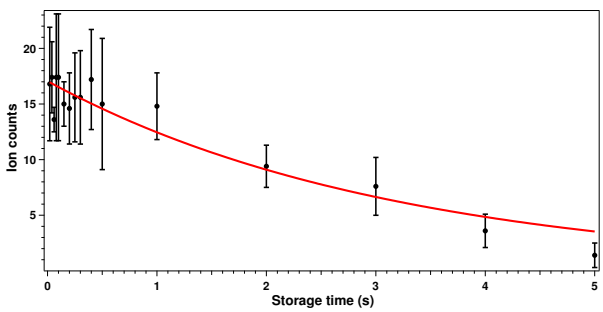

Figure 6: Ions were trapped for several seconds in the trap.

ISBN: 978-3-95450-226-4 ISSN: 2222-5692 doi:10.18429/JACoW-ECRIS2020-NACB04

Co-trapping Ions and Electrons

Once the ions and electrons were successfully trapped for reasonably long times, the next steps involved trapping both species simultaneously and evaluating the co-trapping of the two species. The electron/ion loading, trapping, and extraction operation required a robust control to execute these steps. As such, we upgraded the programmable pulse generator software that controls the TTL logic and updated the controls for the power supplies to a Labview interface. It was found that rapid switching of electrode voltages with Behlke HV switches increased the likelihood for HV discharges. Therefore, the rise and fall times of the switches were increased from <50 ns to 300 ns – 1 µs by adding appropriate resistance in series with the HV switches.

Following these improvements to the system, we performed several tests of co-trapping electrons and ions in the CPET. A schematic of the on-potential during the measurements at different CPET electrode positions is shown in Fig. 7. While we successfully detected the presence of both

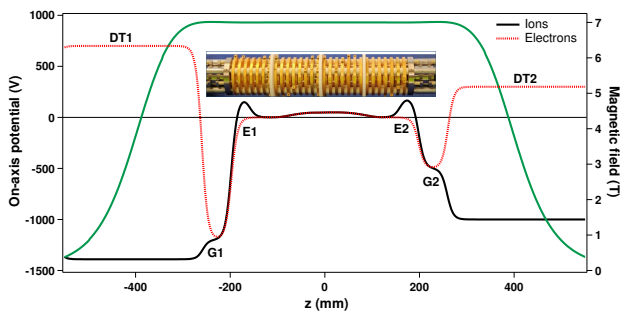

Figure 7: On-axis potentials during the measurements for ions(black solid) and electrodes (red dotted) along with the magnetic field strength (green).

trapped ions and electrons when injected simultaneously, no clear signs of ion cooling have been observed. To observe the signs of cooling, we monitored the TOF signal on the MCP, where the cooled ions are expected to have a longer ToF. We also used the DAC box to bias the trap electrode in the ion extraction end for use as an improvised retarding field analyzer to block ions with lower kinetic energy. A decrease in the energy spread of the extracted ions will provide a clear indication of cooled ions. Challenges faced during these tests include a broad energy profile of the injected ions from an ion source, multiple mass species emitted from the source, and generation of spurious ion signals in the trap when electrons are present. The latter is either caused by electron-impact ionization when electrons collide with the residual gas or is an indication of plasma-induced discharge. Unfortunately, the TOF of the spurious ion counts coincided with the injected ion counts, hence prohibiting a clear indication of cooling. Further studies by adding a Wien filter or a Bradbury-Nielsen gate [44, 45] to the system is needed to identify the masses of the observed signal. Additionally, the resistor chain will be added in the extraction electrodes to improve the beam profile of the extracted ions. A systematic study of the spatial overlap of the two species will also be conducted as the overlap is needed for maximum cooling power.

CONCLUSION AND OUTLOOK

Ion trajectory simulations and hardware modifications were performed to optimize the beam transmission and minimize high voltage discharge. Electrons and ions were trapped simultaneously with the TITAN-CPET. Systematic studies of charged particle transport and trapping were performed to optimize loading and transmission efficiency. To improve the trapping settings and gain more control when co-trapping both species, and ultimately achieve cooling of ions, several tests are ongoing and planned. These include improving the ion extraction to achieve better time focus, applying the rotating wall drive to store plasma for a longer time and improve plasma compression, diagnosing the source of spurious electron-induced ion signals, and confirming the spatial overlap of the two species. Additionally, an in-situ plasma generation scheme by applying an RF excitation to a CPET electrode is currently being tested.

ACKNOWLEDGEMENTS

We would like to thank the National Research Council of Canada (NRC) for funding. This work was partially supported by the Natural Sciences and Engineering Research Council of Canada (NSERC) and the Canada Foundation for Innovation (CFI). We thank TRIUMF's technical staff, especially M. Good, for the mechanical changes. T. Joseph and R. Simpson would like to thank TRIUMF's cooperative education program.

REFERENCES

[1] K. Blaum, "High-accuracy mass spectrometry with stored ions", *Phys. Rep.*, vol. 425, no. 1, pp. 1-78, 2006. doi:10.1016/j.physrep.2005.10.011

[2] K. Blaum, J. Dilling, and W. Nörtershäuser, "Precision atomic physics techniques for nuclear physics with radioactive beams", *Phys. Scr.*, vol. 2013, p. 014017, 2013. doi:10.1088/0031-8949/2013/T152/014017

[3] J. Dilling *et al.*, "Mass measurements on highly charged radioactive ions, a new approach to high precision with TITAN", *Int. J. Mass Spectrom.*, vol. 251, pp. 198–203, 2006. doi:10.1016/j.ijms.2006.01.044

[4] A. A. Kwiatkowski *et al.*, "Precision mass measurements at TITAN with radioactive ions", *Nucl. Instrum. Methods Phys. Res., Sect. B*, vol. 317, pp. 517–521, 2013. doi:10.1016/j.ijms.2006.01.044

[5] A. A. Kwiatkowski *et al.*, "TITAN: An ion trap facility for on-line mass measurement experiments", *Hyperfine Interact.*, vol. 225, pp. 143–155, 2014. doi:10.1007/s10751-013-0892-8

[6] T. Brunner *et al.*, "TITAN's digital RFQ ion beam cooler and buncher, operation and performance", *Nucl. Instrum. Methods Phys. Res., Sect. A*, vol. 676, pp. 32–43, 2012. doi:10.1016/j.nima.2012.02.004

ISBN: 978-3-95450-226-4 ISSN: 2222-5692 doi:10.18429/JACoW-ECRIS2020-NACB04

[7] M. Dombsky *et al.*, "Commissioning and initial operation of a radioactive beam ion source at ISAC", *Rev. Sci. Instr.*, vol. 71, p. 978, 2000. doi:10.1063/1.1150364

[8] C. Jesch *et al.*, "The MR-TOF-MS isobar separator for the TITAN facility at TRIUMF", *Hyperfine Interact.*, vol. 235, pp. 97–106, 2015. doi:10.1007/s10751-015-1184-2

[9] E. Leistenschneider *et al.*, "Dawning of the $N = 32$ Shell Closure Seen through Precision Mass Measurements of Neutron-Rich Titanium Isotopes", *Phys. Rev. Lett.*, vol. 120, p. 062503, 2018. doi:10.1103/PhysRevLett.120.062503

[10] M. Brodeur *et al.*, "New mass measurement of ^{6}Li and ppb-level systematic studies of the Penning trap mass spectrometer TITAN", *Phys. Rev. C*, vol. 80, p. 044318, 2009. doi:10.1103/PhysRevC.80.044318

[11] G. Gräff, H. Kalinowsky, and J. Traut, "A direct determination of the proton electron mass ratio", *Zeitschrift für Physik A: Atoms and Nuclei*, vol. 297, p. 35–39, 1980. doi:10.1007/BF01414243

[12] G. Bollen, R. B. Moore, G. Savard, and H. Stolzenberg, "The accuracy of heavy-ion mass measurements using time of flight-ion cyclotron resonance in a Penning trap", *J. Appl. Phys*, vol. 68, p. 4355, 1990. doi:10.1063/1.346185

[13] M. P. Reiter *et al.*, "High-precision Q_{EC}-value measurement of the superallowed β^{+} emitter ^{22}Mg and an *ab initio* evaluation of the $A = 22$ isobaric triplet", *Phys. Rev. C*, vol. 96, p. 052501(R), 2017. doi:10.1103/PhysRevC.96.052501

[14] I. Bergström, "SMILETRAP—A Penning trap facility for precision mass measurements using highly charged ions", *Nucl. Instrum. Methods Phys. Res., Sect. A*, vol. 487, pp. 618-651, 2002. doi:10.1016/S0168-9002(01)02178-7

[15] S. Sturm *et al.*, "High-precision measurement of the atomic mass of the electron", *Nature*, vol. 506, pp. 467-470, 2014. doi:10.1038/nature13026

[16] F. Heiße *et al.*, "High-Precision Measurement of the Proton's Atomic Mass", *Phys. Rev. Lett.*, vol. 119, p. 033001, 2017. doi:10.1103/PhysRevLett.119.033001

[17] J. Repp *et al.*, "PENTATRAP: a novel cryogenic multi-Penning-trap experiment for high-precision mass measurements on highly charged ions", *Appl. Phys. B*, vol. 107, pp. 983–996, 2012. doi:10.1007/s00340-011-4823-6

[18] S. Ettenauer *et al.*, "First Use of High Charge States for Mass Measurements of Short-Lived Nuclides in a Penning Trap", *Phys. Rev. Lett.*, vol. 107, p. 272501, 2011. doi:10.1103/PhysRevLett.107.272501

[19] A. T. Gallant *et al.*, "Highly charged ions in Penning traps: A new tool for resolving low-lying isomeric states", *Phys. Rev. C*, vol. 85, p. 044311, 2012. doi:10.1103/PhysRevC.85.044311

[20] D. Frekers *et al.*, "Penning-trap Q-value determination of the ^{71}Ga$(\nu, e^{-})^{71}$Ge reaction using threshold charge breeding of on-line produced isotopes", *Phys. Lett. B*, vol. 722, pp. 233-237, 2013. doi:10.1016/j.physletb.2013.04.019

[21] S. Ettenauer *et al.*, "Penning trap mass measurements utilizing highly charged ions as a path to benchmark isospin-symmetry breaking corrections in ^{74}Rb", *Phys. Rev. C*, vol. 91, p. 045504, 2015. doi:10.1103/PhysRevC.91.045504

[22] C. Babcock *et al.*, "Mass measurements of neutron-rich indium isotopes toward the $N = 82$ shell closure", *Phys. Rev. C*, vol. 97, p. 024312, 2018. doi:10.1103/PhysRevC.97.024312

[23] E. Leistenschneider, A. A. Kwiatkowski, and J. Dilling, "Vacuum requirements for Penning trap mass spectrometry with highly charged ions", *Nucl. Instrum. Methods Phys. Res., Sect. B*, vol. 463, pp. 496-498, 2020. doi:10.1016/j.nimb.2019.03.047

[24] G. Sikler *et al.*, "A high-current EBIT for charge-breeding of radionuclides for the TITAN spectrometer", *Eur. Phys. J. A - Hadrons and Nuclei*, vol. 25, p. 63, 2005. doi:10.1140/epjad/i2005-06-072-6

[25] A. Lapierre *et al.*, "The TITAN EBIT charge breeder for mass measurements on highly charged short-lived isotopes—First online operation", *Nucl. Instrum. Methods Phys. Res., Sect. A*, vol. 624, pp. 54–64, 2010. doi:10.1016/j.nima.2010.09.030

[26] Ruben Schupp, "Determination of beam properties of highly-charged ions extracted from TITAN's electron beam ion trap", M.Sc. thesis at University of Heidelberg, Germany, Winter 2016. https://titan.triumf.ca/research/publications/RubenThesis2016.pdf

[27] A. Kellerbauer *et al.*, "Buffer gas cooling of ion beams", *Nucl. Instrum. Methods Phys. Res., Sect. A*, vol. 469, pp. 276-285, 2001. doi:10.1016/S0168-9002(01)00286-8

[28] D. J. Wineland and W. M. Itano, "Laser cooling of atoms", *Phys. Rev. A*, vol. 20, p. 1521, 1979. doi:10.1103/PhysRevA.20.1521

[29] S. L. Rolston and G. Gabrielse, "Cooling antiprotons in an ion trap", *Hyperfine Interact.*, vol. 44, pp. 233–245, 1989. doi:10.1007/BF02398673

[30] J. Bernard *et al.*, "Electron and positron cooling of highly charged ions in a cooler Penning trap", *Nucl. Instrum. Methods Phys. Res., Sect. A*, vol. 532, pp. 224–228, 2004. doi:10.1016/j.nima.2004.06.049

[31] U. Chowdhury, "A Cooler Penning Trap to Cool Highly Charged Radioactive Ions and Mass Measurement of ^{24}Al", PhD thesis, University of Manitoba, 2016. https://hdl.handle.net/1993/31511

[32] Z. Ke *et al.*, "A cooler ion trap for the TITAN on-line trapping facility at TRIUMF", *Hyperfine Interact.*, vol. 173, pp. 103–111, 2006. doi:10.1007/s10751-007-9548-x

[33] V. V. Simon *et al.*, "A cooler Penning trap for the TITAN on-line trapping facility", *J. Phys.:Conf. Series*, vol. 312, p. 052024, 2011. doi:10.1088/1742-6596/312/5/052024

[34] S. F. Paul *et al.*, "Off-axis electron injection into a cooler Penning trap", *Hyperfine Interact.*, vol. 240, p. 50, 2019. doi:10.1007/s10751-019-1587-6

[35] D. Lascar *et al.*, "A novel transparent charged particle detector for the CPET upgrade at TITAN", *Nucl. Instrum. Methods Phys. Res., Sect. A*, vol. 868, pp. 133–138, 2017. doi:10.1016/j.nima.2017.07.003

[36] R. G. Greaves and C. M. Surko, "Inward Transport and Compression of a Positron Plasma by a Rotating Electric Field", *Phys. Rev. Lett.*, vol. 85, pp. 1883–1886, 2000. doi:10.1103/PhysRevLett.85.1883

ISBN: 978-3-95450-226-4 ISSN: 2222-5692 doi:10.18429/JACoW-ECRIS2020-NACB04

[37] U. Chowdhury *et al.*, "A cooler Penning trap for the TITAN mass measurement facility", *AIP Conf. Proceedings*, vol. 1640, pp. 120-123, 2015. doi:10.1063/1.4905408

[38] S. F. Paul, "Off-axis electron injection into a cooler Penning trap", Master's thesis, University of Heidelberg, 2017.

[39] D. A. Dahl, "SIMION for the personal computer in reflection", *Int. J. Mass Spectrom.*, vol. 200, pp. 3-25, 2000. doi:10.1016/S1387-3806(00)00305-5

[40] B. Kootte *et al.*, "Quantification of the Electron Plasma in TItan's Cooler Penning Trap", in *Proc. Int. Workshop on Beam Cooling and Related Topics (COOL'15)*, Newport News, VA, USA, Sep. 2015, pp. 39–42. doi:10.18429/JACoW-COOL2015-MOPF06

[41] T. Mohamed *et al.*, "Fast electron accumulation and its mechanism in a harmonic trap under ultrahigh vacuum conditions", *Phys. Plasmas*, vol. 18, p. 032507, 2011. doi:10.1063/1.3562501

[42] G. Maero *et al.*, "Stabilizing effect of a nonresonant radio frequency drive on the $m = 1$ diocotron instability", *Phys. Plasmas*, vol. 18, p. 032101, 2011. doi:10.1063/1.3558374

[43] F. Anderegg, "Waves in Non-Neutral Plasma", in *Physics with Trapped Charged Particles*, World Scientific, Singapore, 2014, pp. 173-193. doi:10.1142/9781783264063_0006

[44] N. E. Bradbury and R. A. Nielsen, "Absolute Values of the Electron Mobility in Hydrogen", *Phys. Rev.*, vol. 49, pp. 388–393, 1936. doi:10.1103/PhysRev.49.388

[45] J. R. Kimmel, F. Engelke, and R. N. Zare, "Novel method for the production of finely spaced Bradbury–Nielson gates", *Rev. Sci. Instrum.*, vol. 72, p. 4354, 2001. doi:10.1063/1.1416109

ISBN: 978-3-95450-226-4 ISSN: 2222-5692

List of Authors

Bold papercodes indicate primary authors; ~~crossed out~~ papercodes indicate 'no submission'

ISBN: 978-3-95450-226-4 ISSN: 2222-5692

ISBN: 978-3-95450-226-4 ISSN: 2222-5692

ISBN: 978-3-95450-226-4 ISSN: 2222-5692

ISBN: 978-3-95450-226-4 ISSN: 2222-5692

Institutes List

AEC
Chiba, Japan
- Hashizaki, S.
- Kondo, T.
- Ouchi, F.
- Sasano, T.
- Shiraishi, T.
- Suzuki, T.
- Takahashi, K.

ANL
Lemont, Illinois, USA
- Scott, R.H.
- Vondrasek, R.C.

Atomki
Debrecen, Hungary
- Biri, S.
- Perduk, Z.
- Rácz, R.

BNL
Upton, New York, USA
- Beebe, E.N.
- Coe, B.D.
- Gronert, M.K.
- Kondrashev, S.A.
- Ritter, J.
- Rodowicz, T.
- Schoepfer, R.
- Trabocchi, S.M.

Catania University
Catania, Italy
- Naselli, E.

CNAO Foundation
Pavia, Italy
- Maugeri, C.
- Russo, F.

CNRS LPGP Univ Paris Sud
Orsay, France
- Minea, T.

Drew University
Madison, New Jersey, USA
- Gronert, M.K.

DU
Debrecen, Hungary
- Pálinkás, J.

ESS Bilbao
Zamudio, Spain
- Miracoli, R.

FRIB
East Lansing, Michigan, USA
- Bultman, N.K.
- Henriques, A.I.
- Knowles, C.
- Lund, S.M.
- Machicoane, G.
- Morrison, P.
- O'Brien, W.R.
- Omelayenko, M.
- Rao, X.
- Ren, H.T.
- Son, H.J.
- Villari, A.C.C.

GANIL
Caen, France
- Bajeat, O.
- Barue, C.
- Damoy, S.
- Dubois, M.
- Frigot, R.
- Hormigos, S.
- Jacquot, B.
- Kamalou, O.
- Lechartier, N.
- Leduc, A.
- Lemagnen, F.
- Maunoury, L.
- Metayer, V.
- Michel, M.
- Osmond, B.

GHMFL
Grenoble, France
- Debray, F.

GSI
Darmstadt, Germany
- Hollinger, R.H.
- Lang, R.
- Mäder, J.
- Maimone, F.
- Patchakui, P.T.
- Tinschert, K.

Gunma University, Heavy-Ion Medical Research Center
Maebashi-Gunma, Japan
- Kawashima, M.

HNLPSM
Hefei, People's Republic of China
- Jiang, W.

IAP/RAS
Nizhny Novgorod, Russia
- Bokhanov, A.
- Golubev, S.
- Izotov, I.
- Kazakov, M.Yu.
- Kiseleva, E.M.
- Lapin, R.L.
- Razin, S.

ISBN: 978-3-95450-226-4 ISSN: 2222-5692

- Shaposhnikov, R.A.
- Shlepnev, S.P.
- Skalyga, V.
- Vybin, S.S.

IMP/CAS
Lanzhou, People's Republic of China
- An, J.R.
- Chang, J.J.
- Chen, Y.
- Fang, X.
- Feng, Y.C.
- Guan, M.Z.
- Guo, J.W.
- Guo, Y.H.
- Hitz, D.
- Hu, Q.
- Huang, W.
- Jia, Z.H.
- Li, J.B.
- Li, L.B.
- Li, L.X.
- Li, Y.J.
- Liu, Y.G.
- Lu, W.
- Ma, H.Y.
- Ma, J.D.
- Ma, Y.M.
- Mei, E.M.
- Ou, X.J.
- Qian, C.
- Shen, Z.
- Sun, L.T.
- Wang, H.
- Wang, X.D.
- Wu, B.M.
- Wu, Q.
- Wu, W.
- Xin, C.J.
- Yang, Y.Y.
- Yang, Y.
- Zhan, T.X.
- Zhang, J.Q.
- Zhang, W.H.
- Zhang, X.Z.
- Zhao, H.W.
- Zhao, H.
- Zheng, S.J.
- Zhu, L.

INFN-Pavia
Pavia, Italy
- Costanzo, G.

INFN/LNL
Legnaro (PD), Italy
- Galatà, A.
- Gallo, C.S.

INFN/LNS
Catania, Italy
- Calabrese, G.
- Castro, G.
- Celona, L.
- Chines, F.
- Gammino, S.
- Leonardi, O.
- Manno, G.
- Mascali, D.
- Massara, A.
- Mauro, G.S.
- Mazzaglia, M.
- Mishra, B.
- Naselli, E.
- Passarello, S.
- Pidatella, A.
- Russo, F.
- Siliato, D.
- Sorbello, G.
- Torrisi, G.

INP NNC RK
Almaty, Kazakhstan
- Abdigaliyev, M.B.
- Ivanov, I.A.
- Koloberdin, M.V.
- Kurakhmedov, A.E.
- Mustafin, D.A.
- Sambayev, Y.K.
- Zdorovets, M.V.

Institute for Plasma Research
Bhat, Gandhinagar, India
- Abhangi, M.
- Bandyopadhyay, M.
- Kumar, R.
- Vala, S.J.

JINR
Dubna, Moscow Region, Russia
- Bogomolov, S.L.
- Bondarchenko, A.E.
- Efremov, A.A.
- Kuzmenkov, K.I.
- Lebedev, N.
- Loginov, V.N.
- Mironov, V.
- Pugachev, D.K.

JYFL
Jyväskylä, Finland
- Bhaskar, B.S.
- Ikonen, A.
- Julin, J.
- Kalvas, T.
- Koivisto, H.A.
- Kosonen, S.T.
- Kronholm, R.J.
- Marttinen, M.S.P.
- Tarvainen, O.A.
- Timonen, O.P.I.
- Toivanen, V.

KBSI
Deajeon, Republic of Korea
- Kim, S.J.

ISBN: 978-3-95450-226-4 ISSN: 2222-5692

Korea Basic Science Institute
Busan, Republic of Korea
- Hong, J.G.
- Ok, J.W.
- Park, J.Y.
- Won, M.

LBNL
Berkeley, California, USA
- Benitez, J.Y.
- Covo, M.K.
- Felice, H.
- Hafalia, R.R.
- Hodgkinson, A.
- Juchno, M.
- Pan, P.
- Phair, L.
- Prestemon, S.
- Todd, D.S.
- Wang, L.
- Xie, D.Z.

LPSC
Grenoble Cedex, France
- André, T.
- Angot, J.
- Baylac, M.A.
- Bhaskar, B.S.
- Leduc, A.
- Migliore, M.
- Méndez, J.A.
- Sole, P.
- Thuillier, T.

MSU
East Lansing, Michigan, USA
- Isherwood, B.C.

NIRS
Chiba-shi, Japan
- Iwata, Y.

NSCL
East Lansing, Michigan, USA
- Crisp, D.B.
- Lapierre, A.
- Machicoane, G.
- Nash, S.

ORNL
Oak Ridge, Tennessee, USA
- Wong, C.Y.

Osaka University, Graduate School of Engineering
Osaka, Japan
- Harisaki, S.
- Kato, Y.
- Kubo, W.
- Okumura, K.
- Omori, T.
- Owada, I.
- Sato, K.
- Tsuda, K.

PKU
Beijing, People's Republic of China
- Chen, J.E.
- Cui, B.J.
- Guo, Z.Y.
- Jiang, Y.X.
- Li, K.
- Ma, T.H.
- Peng, S.X.
- Wen, J.M.
- Wu, W.B.
- Xu, Y.
- Zhang, A.L.
- Zhang, J.F.
- Zhang, T.

QST-NIRS
Chiba, Japan
- Kitagawa, A.
- Muramatsu, M.

R&K Company Limited.
Shizuoka, Japan
- Sei, M.

RIKEN Nishina Center
Wako, Japan
- Higurashi, Y.
- Kamigaito, O.
- Nagatomo, T.
- Nakagawa, T.
- Ohnishi, J.

STFC/RAL/ISIS
Chilton, Didcot, Oxon, United Kingdom
- Faircloth, D.C.
- Letchford, A.P.
- Tarvainen, O.A.

TEMF, TU Darmstadt
Darmstadt, Germany
- Andreev, A.

Texas A&M University Cyclotron Institute
College Station, Texas, USA
- Ärje, J.E.
- May, D.P.
- Roeder, B.T.
- Yennello, S.J.

Texas A&M University, Cyclotron Institute
College Station, Texas, USA
- Abegglen, F.P.
- Clark, H.L.
- Gagliardi, C.A.
- Henderson, L.E.
- Kim, G.J.
- Tabacaru, G.

Toyo University
Kawagoe-shi, Saitama, Japan
- Yoshida, Y.

ISBN: 978-3-95450-226-4 ISSN: 2222-5692

TRIUMF
Vancouver, Canada
- Adegun, J.A.
- Ames, F.
- Dilling, J.
- Kester, O.K.
- Kootte, B.A.
- Kwiatkowski, A.A.
- Paul, S.F.
- Silwal, R.

UBC & TRIUMF
Vancouver, British Columbia, Canada
- Dilling, J.

UCAS
Beijing, People's Republic of China
- Huang, W.
- Shen, Z.
- Sun, L.T.

UNIFE
Ferrara, Italy
- Gallo, C.S.

University Debrecen
Debrecen, Hungary
- Pálinkás, J.

University of Catania
Catania, Italy
- Sorbello, G.

University of Chinese Academy of Sciences
Beijing, People's Republic of China
- Qian, C.

University of Electronic Science and Technology of China
Chengdu, People's Republic of China
- Jin, X.L.
- Lei, L.

University of Manitoba
Manitoba, Canada
- Gwinner, G.
- Kootte, B.A.

USTC,SNST
Anhui, People's Republic of China
- Lu, Z.T.

UW/Physics
Waterloo, Ontario, Canada
- Simpson, R.